GENERAL ATOMIC

GA-A13950
UC-77

GAS TURBINE HTGR PROGRAM

SEMIANNUAL PROGRESS REPORT FOR THE PERIOD JANUARY 1, 1976 THROUGH JUNE 30, 1976

by
PROJECT STAFF

Prepared under
Contract E(04-3)-167
Project Agreement No. 46
for the San Francisco Operations Office
U.S. Energy Research and Development Administration

GENERAL ATOMIC PROJECT 3227 DATE PUBLISHED: JULY 30, 1976

[redacted]

ABSTRACT

This report describes the work accomplished under ERDA Contract E(04-3)-167, Project Agreement No. 46, during the period January 1, 1976, through June 30, 1976.

The ERDA program is directed to investigations supporting the tech nology for, and establishing the reference baseline design of, the helium Gas-Turbine High-Temperature Gas-Cooled Reactor (GT-HTGR). These investigations include reactor plant systems and dynamics, bottoming cycles, plant safety, primary pressure boundary, turbomachinery, helium valves and heat exchangers, fission product effects, materials, power conversion loop test alternatives, and program planning.

This report documents specific subtasks completed during the reporting period and describes the progress of ongoing work.

CONTENTS

FIGURES

TABLES

1. INTRODUCTION AND SUMMARY

This report describes the work on the Gas-Turbine High-Temperature Gas-Cooled Reactor (GT-HTGR) accomplished under ERDA Contract E(04-3)-167, Project Agreement No. 46, during the period January 1, 1976 through June 30, 1976.

The ERDA-sponsored program is directed toward investigations of reactor plant systems and dynamics, plant safety, primary pressure boundary, turbomachinery, materials, fission product effects, and the requirements for testing components of the power conversion loop. Previous work in this program is described in Refs. 1-1 through 1-4.

The Reactor Plant Technology task, described in Section 2, was significantly restructured during the reporting period in order to identify plant arrangements and parameters having improved economic performance over the reference design. This effort has included the study of N_2O_4 as a secondary-cycle working fluid in recuperated and nonrecuperated configurations. It was concluded that the efficiency was highest in the recuperated arrangement and that any improvement over the ammonia bottoming cycle was small. Furthermore, it was concluded that the high chemical activity of N_2O_4 raised enough safety and material questions that its use in the subject application had insufficient incentives relative to the technical risk.

Other studies of more economic plants have concentrated during the past six months on steady refinements to the basic design presented in Ref. 1-1. These have included reoptimizing the system parameters in a concerted manner with the primary system configuration, upscaling the plant to a 4000-MW(t) unit, adopting a twin-unit arrangement, and in the binary-cycle version utilizing a common bottoming cycle. Of particular note is the selection of a compressor pressure ratio of 2.5, a top system pressure of 7.91 MPa (1150 psi), and a turbine inlet temperature of 850°C (1562°F). The older parameters

were 2.35, 6.89 MPa (1000 psia), and 816°C (1500°F), respectively. These studies resulted in a 40% plant efficiency and a large improvement in plant economics.

Other efforts in the Reactor Plant Technology task have included improving the design definition of bottoming cycle components and the balance of plant, areas in which cost and technical uncertainties have heretofore been significant. A core physics and performance study directed at a case with a reactor outlet temperature (ROT) of 950°C (1742°F) has been initiated in order to develop an information base pertinent to long-term fuel development requirements.

Finally, under the Reactor Plant Technology task, investigations have established that sequential loop startup and shutdown are both feasible and useful and that the power required per machine is not significantly greater than the power per machine required for simultaneous loop startup. Furthermore, it was shown that the peak startup power is determined by the low-speed performance characteristics of the turbine and compressor and not by the peculiarities of reversing the flow of the down loop into the forward direction.

The Power Conversion Loop Test Alternatives task completed work to prepare test requirements for the Helium Component Test Facility (HCTF) and to review the HCTF design proposed by NASA. This task has been extended into a study to define alternative and lower-cost methods of testing critical components in the power conversion loop. These studies, reported in Section 3, describe favorably the possibilities offered by coupling a nonnuclear heat source to the demonstration plant prior to the loading of the nuclear core.

The Primary Pressure Boundary task has concentrated on developing details of the square (4 x 1000 MW(t)) and delta (3 x 1000 MW(t) turbomachinery cavity arrangements within the prestressed concrete reactor vessel (PCRV) designs. Layouts of components, tendons, and ducts have been so prepared in this work and are described in Section 4. A stress analysis of the delta

design has been completed showing the feasibility of this arrangement. Furthermore, it is believed that the PCRV arrangement will be satisfactory at the higher pressure levels now under consideration. Also described in Section 4 is the approach to thermal barrier design and alternative means of obtaining a technically satisfactory hot (turbine inlet) duct design.

Section 5 describes the Materials task, which has concentrated on screening materials for the critical components in the power conversion loop. Preliminary results have been obtained showing that carburization of Hastelloy X leads to substantial degradation in creep-rupture properties at 900°C (1652°F) in controlled impure helium compared with literature values for air. Little effect is observed at 800°C (1472°F) in impure helium. The behavior of cast turbine blade and vane materials such as IN100 presently appears to be consistent with air properties.

Section 6 describes the current effort to measure the sorption isotherm of cesium over ducting and turbine materials. Preliminary data have been obtained which lead to a different behavior with temperature from that calculated with older isotherm data for stainless steel. Explanations for this difference are offered, and studies to resolve this difference are proposed. Also given in Section 6 are a literature search and a report on the current status of decontamination with recommendations for experimentation in this important area.

A summary of the investigations of turbomachinery design performed during the past six months is presented in Section 7. This work, done by United Technologies Corporation, will be described more fully in a separate report. The major accomplishments include conceptual bearing and seal designs for the 1000-MW(t) machine and a corresponding test plan, the development of parametric information for the design alternative studies of Section 2, and a more detailed study of a machine for a 950°C turbine inlet temperature as a basis for determining a development path.

Section 8 describes the effort on helium control valves. During the reporting period, a system design description for the valves was prepared,

and a package was sent out to vendors for technical comments and a cost estimate. The requirements for these valves for plant designs having a 950°C ROT was also examined. Finally, preliminary integration arrangements of the valves in the various PCRV design alternatives were prepared.

The heat exchanger studies are reported in Section 9. The most significant factor in these studies was the identification of a practical headering arrangement which would permit a near full field of heat exchanger tubes, arranged in the form of contiguously packed hexagonal modules. This allows the heat exchangers to be made smaller for a given heat transfer. This in turn offers opportunities for reductions of cavity size and hence the PCRV, for a reduction of the pressure loss in each heat exchanger, for selection of a fewer number of tubes, or combinations of these options. These choices were exploited through an optimization study, the results of which are presented in Section 2.

Other efforts in heat exchanger technology during the reporting period included the preparation of designs for the alternate configuration study of Section 2, for both the dry-cooled single-cycle plant and the wet-cooled binary-cycle plant.

The program planning effort is described in Section 10 and has emphasized the documentation of planning through the design definition phase (now called Phase II). The effort is continuing with the objective of updating the preliminary development plan report.

The safety research studies are reported in Section 11. These studies include a description of significant risk sequences for the GT-HTGR which appear to be below the probability-consequence envelope of the Steam-Cycle (SC) HTGR. This decrease arises because of the lower probability for fluid ingress into the primary system and because the GT-HTGR requires no external pressure relief in the PCRV. Confirmation that internal pressure relief is permissible provided that all other code requirements are met has been obtained from the American Society of Mechanical Engineers (ASME) Code Committee. Other safety research efforts have been directed to preparing

safety-related design criteria and to an analysis of turbine fission product deposition and mass transfer.

A brief study of the safety of the binary-cycle plant has been performed emphasizing the consequences of ammonia leaks. The results indicate that although ammonia raises more problems than water, the problems have potential solutions. Finally, a PCRV seismic analysis has been performed which indicates no appreciable differences from the results of seismic analyses for the SC-HTGR PCRV. These new data will provide the forcing functions to determine the seismic response of critical power conversion loop components.

In summary, significant progress has been made during the reporting, period. Design improvements have been identified and are being implemented; technical and safety problems are being resolved on a steady basis.

REFERENCES

1-1. "Gas Turbine HTGR Program, Semiannual Progress Report for the Period July 1, 1975 through December 31, 1975," General Atomic Report GA-A13740, January 1976.

1-2. "Gas Turbine HTGR Program, Semiannual Progress Report for the Period January 1, 1975 through June 30, 1975," General Atomic Report GA-A13485, July 1975.

1-3. "Gas Turbine HTGR Program, Quarterly Progress Report for the Period October 1, 1974 through December 31, 1974," General Atomic Report GA-A13301, January 1975.

1-4. "Gas Turbine HTGR Power Plant Control and Safety Studies, Quarterly Progress Report for the Period July 1, 1974 through September 30, 1974," General Atomic Report GA-A13191, November 1974.

2. REACTOR PLANT TECHNOLOGY
(Task 189a, No. SU010)

2.1. INTRODUCTION

The Reactor Plant Technology task has hitherto emphasized two major subtasks:

A. Dynamics analysis, system definition, and control

B. Maintenance configuration

This emphasis has been consistent with the objectives of developing base GT-HTGR technology packages that are applicable for use in the subsequent phased development program. The development program was envisaged to comprise the following:

1. Utilize existing HTGR technology, Fort St. Vrain and the large 3000-MW(t) steam-cycle units then planned to the fullest extent possible in preparing a GT-HTGR design.

2. Test the major power conversion loop components, particularly the turbomachinery, in a fossil-fired helium component test facility (HCTF).

3. Proceed directly to a commerical-size nuclear plant utilizing the technology and components developed under Items 1 and 2.

During the latter part of CY-1975, it became necessary for General Atomic (GA) to withdraw from existing commercial orders for large SC-HGTRs. This created additional uncertainty in the timing of an aggressive initial

plant program for the GT-HTGR. It therefore is appropriate to utilize this period to reevaluate both improved plant configurations and program planning alternatives. The Reactor Plant Technology task was thus restructured in early CY-1976 with the objective of seeking alternate plant designs to define the full longer-term economic incentives in addition to improvements in initial plant design. This restructuring is described briefly below.

Under sub-task A above, the preparation of a control system report was deleted, as was the specification of the plant behavior under protective action. However, other work under this sub-task has been completed including the documentation of the plant transient computer code REALY2, the determination of the behavior of the plant during startup and shutdown, and an assessment of turbine startup power and system requirements. This work is described in Section 2.2.

A new sub-task C was initiated to look at plants having improved economics. This sub-task included the study of an N_2O_4 cycle as an alternative to the presently proposed ammonia bottoming cycle. N_2O_4 is a dissociating fluid with enhanced heat transfer properties. Since the Russians had reported very good results and potential with this fluid, a study was undertaken, the results of which are reported in Section 2.3.

Alternative system parameters, to accompany those changed plant arrangements that have evolved over the last year, have been studied and are reported in Section 2.4. The purpose was to determine a more optimal set of parameters in order to obtain plant designs giving higher economic incentives. Such studies include twin dry-cooled units of 4000-MW(t) and 3000 MW(t) unit rating with reactor outlet temperatures (ROT) of 850°C (1562°F) and also include a case with an ROT of 950°C (1742°F) at the larger unit rating. A binary-cycle plant, i.e., twin units of 4000 MW(t) operating with an ROT of 850°C (1562°F) and having a common secondary cycle, was also studied. The results are very promising.

Further plant design studies have been performed emphasizing improved economic incentives and improved design definition and detail in previously less defined areas. The design studies have encompassed components for the ammonia bottoming cycle and the balance of plant. This work is described in Section 2.5.

Another area of technical effort undertaken during the reporting period is GT-HTGR specific core design. Previously, the SC-HTGR core had been utilized. Since there was interest in achieving higher temperatures, a core design study based on prismatic fuel was initiated with the objective of achieving a 950°C (1742°F) ROT. The results of this study are described in Section 2.6.

2.2. PLANT STARTUP AND SHUTDOWN

This section describes the studies of the startup and shutdown of the gas turbines in the GT-HTGR. The objectives of this effort have been:

1. To establish an orderly shutdown of the plant under control that keeps power conversion loop (PCL) temperature transients at acceptable levels and facilitates long-term cooling of the core

2. To compare sequential and simultaneous startup of the turbines and determine system behavior under control

3. To establish startup power and other system requirements including the possible need for demonstrating sequential startup in a nonnuclear test

The work performed to attain the above objectives is described in the following four subsections.

2.2.1. Shutdown Sequence

The basis of the shutdown sequence was described in Ref. 2-1. Phase I is the decrease from full load to approximately 10% load. Phase II involves a drop of this 10% load and shutdown of two loops with controlled speed reduction of the third loop. Phase III provides prolonged aftercooling by control of the ROT, the core temperature drop (CTD), and the turbine speed (speed). The control is accomplished by adjustment of the primary bypass valve (PBV) and the attemperation valve (AV).

Several model improvements have been made since the last reporting period, primarily in low-speed compressor performance, flow reversal transition modeling, and control system operation. Phase II has been recalculated with the improved modeling, and the data are presented in Fig. 2-1. Adequate response is achieved, and although the ROT has decreased about 11°C (20°F) from the demanded value of 593°C (1100°F) for this run, it does recover during Phase III. The inflection in the speed curve, at 93 sec, of the two loops being shut down is the result of flow reversing in those loops. The speed of the two loops at the time of flow reversal is significantly lower than the previously reported data (4% versus 13% of design speed), resulting in less severe accompanying transients.

The new results for Phase III of the shutdown sequence are similar to those given in Ref. 2-1 and hence are not presented herein.

2.2.2. Simultaneous Loop Startup

Simultaneous startup proceeds with all loops being powered to achieve essentially identical speed in each loop throughout the start. Subsequently, all loops act in a similar manner, and no flow reversal or other major transients occur. The data for a full helium inventory start are shown in Figs. 2-2 and 2-3. The required motoring power (negative on the plotted data) continues to increase with shaft speed until the increase in turbine power exceeds the increase in compressor power at about 16.3 Hz (980 rpm).

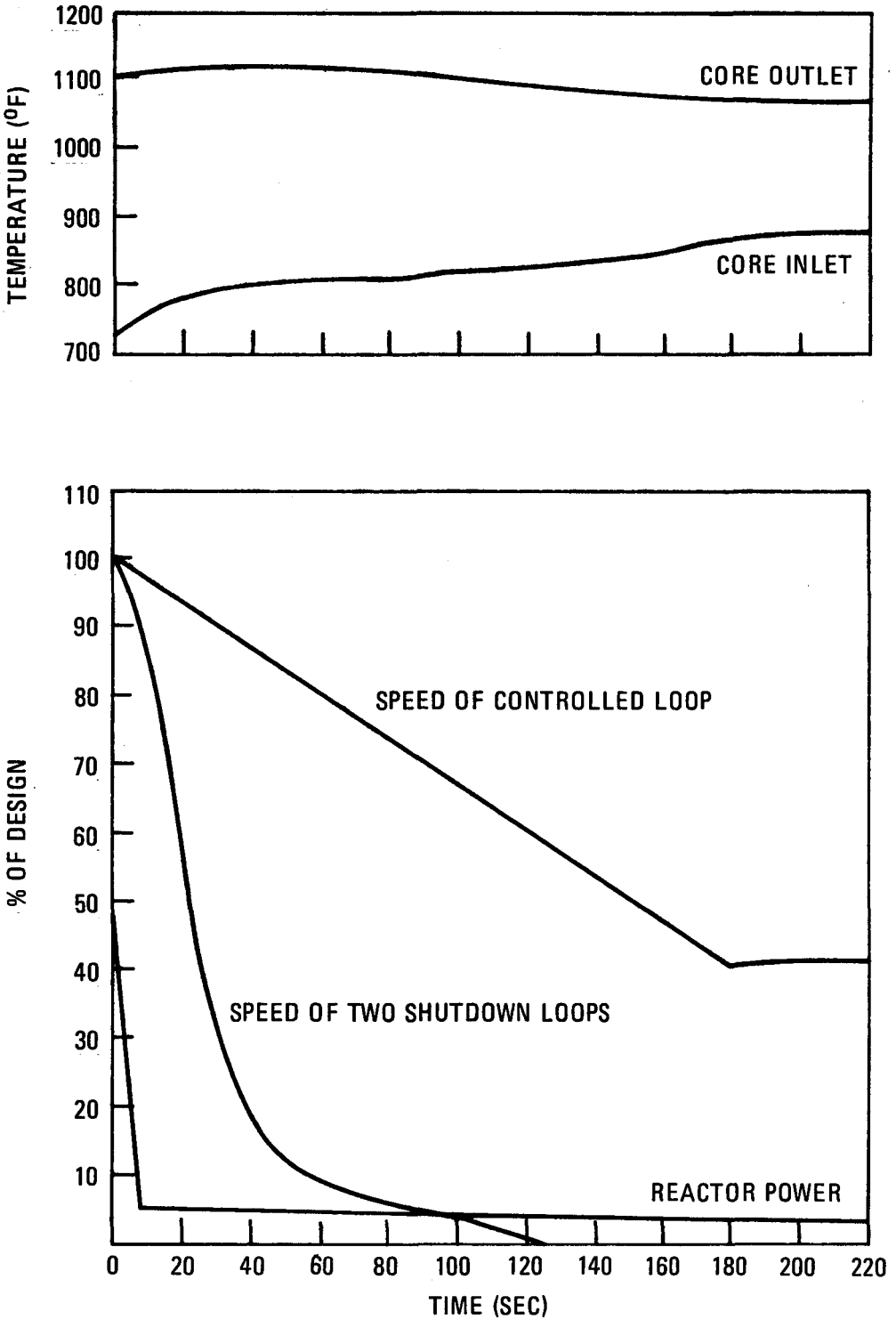

ALL MEASUREMENTS ARE IN U. S. CUSTOMARY UNITS.

GA-A13950

Fig. 2-1. Transients for Phase II of shutdown

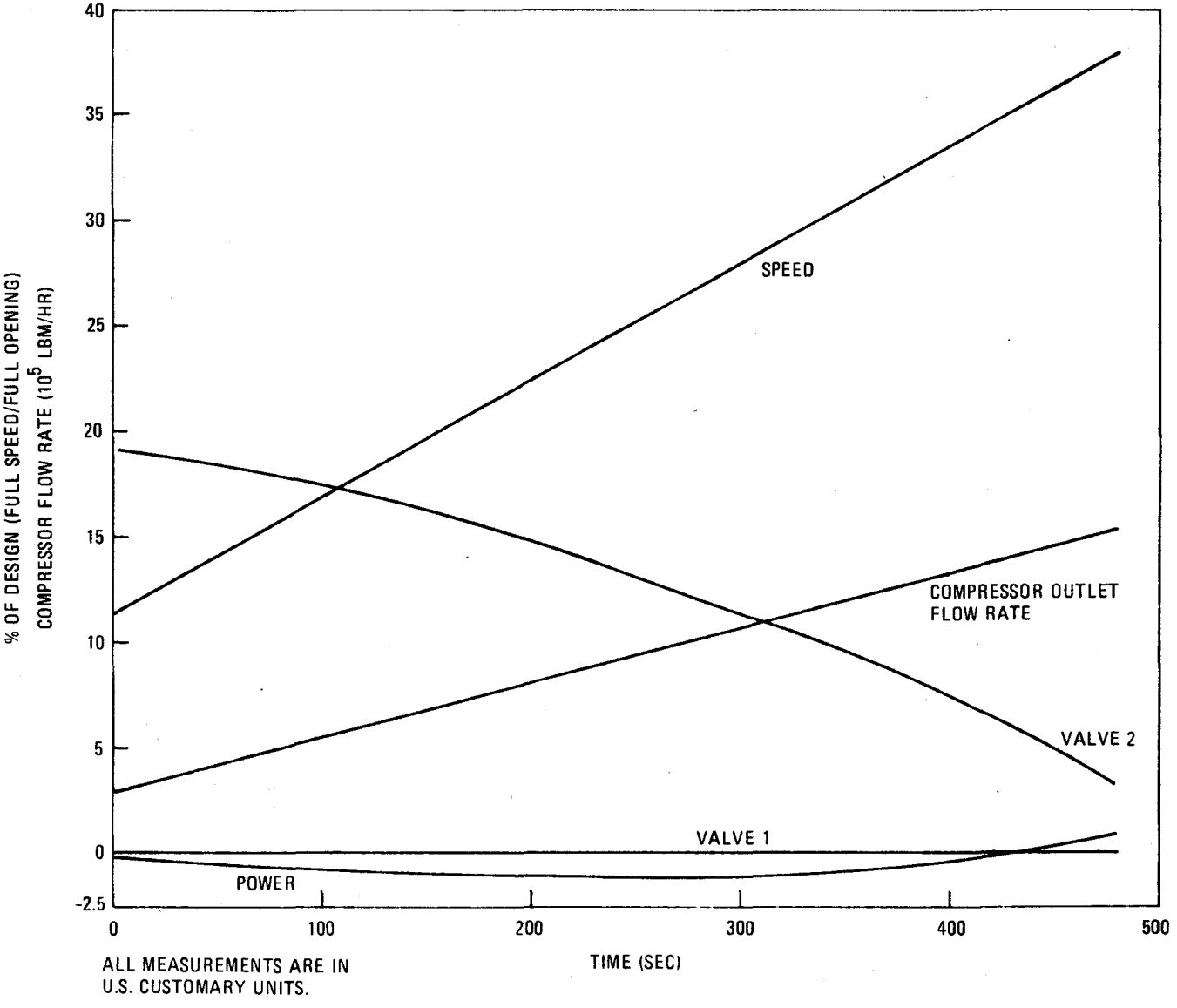

GA-A13950

Fig. 2-2. Full invenstory simultaneous startup (speed, power, flow, and valve transients)

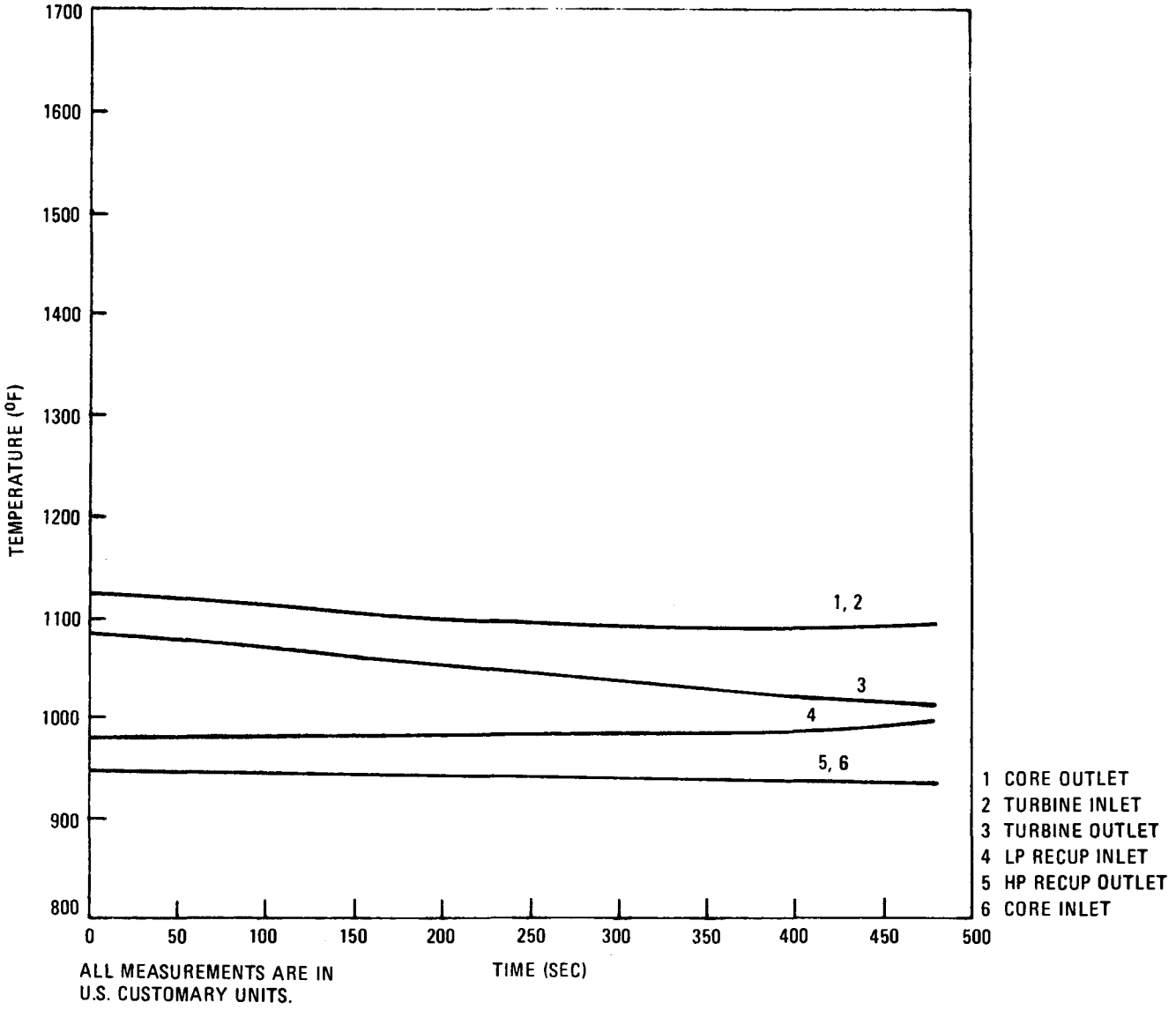

Fig. 2-3. Full inventory simultaneous startup (hot helium temperature transients)

Normally, the primary bypass valve (valve 1) would start to open shortly after this time to provide a controlled reduction in motoring power with a continued increase in speed. To illustrate the phenomenon, the run presented in Fig. 2-2 was continued with the primary bypass valve closed. As speed continued to increase, the motoring power decreased until at ≈21.3 Hz (≈1275 rpm) it crossed zero; in other words, until the turbine was supplying an acceleration power to the shaft (speed was constrained to a fixed time profile to generate the data).

Figure 2-3 presents data for helium temperatures at selected PCL locations. The data illustrate the characteristic increase in temperature drop across the turbine with increasing speed and the attendant decrease in attemperation required. The latter manifests itself in the difference between turbine outlet and low-pressure (LP) recuperator inlet temperatures, a result of the attemperation flow necessary to maintain the sum of the LP recuperator and high-pressure (HP) recuperator temperatures at a preset level. As the turbine temperature drop increases, less attemperation is required and the LP recuperator inlet and turbine outlet temperatures approach one another.

Simultaneous startup at reduced inventory provides essentially the same transient as that for full inventory. The primary difference is in the maximum motoring power that must be supplied (see Section 2.2.5 on motoring power).

2.2.3. Sequential Loop Startup

Four cases are described here for sequential startup (i.e., motoring of one loop at a time to the self-sustaining condition). Sequential start provides more options for motoring the turbines than does simultaneous start. In addition, sequential start is desirable for the restart of a down loop when the other loops are operational. The four cases discussed in the following paragraphs are exemplary of conditions covered for sequential start, considering both a refueling status startup and a re-start of a down loop.

The four cases are:

1. Start from refueling conditions; moderate ROT

2. Start of a down loop while maintaining maximum supportable electrical load (≈85% of design); ROT at design

3. Start of a down loop with electrical load dropped and operating loops reduced in speed

4. Start of a down loop with reduced inventory and ROT; electrical load at the maximum supportable by the two operating loops (≈20% of design)

Case 1. The startup of the first loop is similar to the simultaneous start sequence but with ≈10% of flow bypassed around the core through the two down loops and is therefore not described herein.

Figures 2-4 and 2-5 present the data for a startup from refueling conditions where:

1. Core outlet temperature has been raised to 593°C (1100°F)

2. One loop has already been brought to a self-sustaining speed of 24.7 Hz (1480 rpm)

3. The PCRV has been brought to full helium inventory

The flow in the second loop (the one now being started) is initially in a direction reverse to normal because of the pressure drop across the core created by the operating loop. At approximately 2.8 Hz (170 rpm), the compressor develops sufficient head to overcome the backpressure and the flow changes into the forward direction.

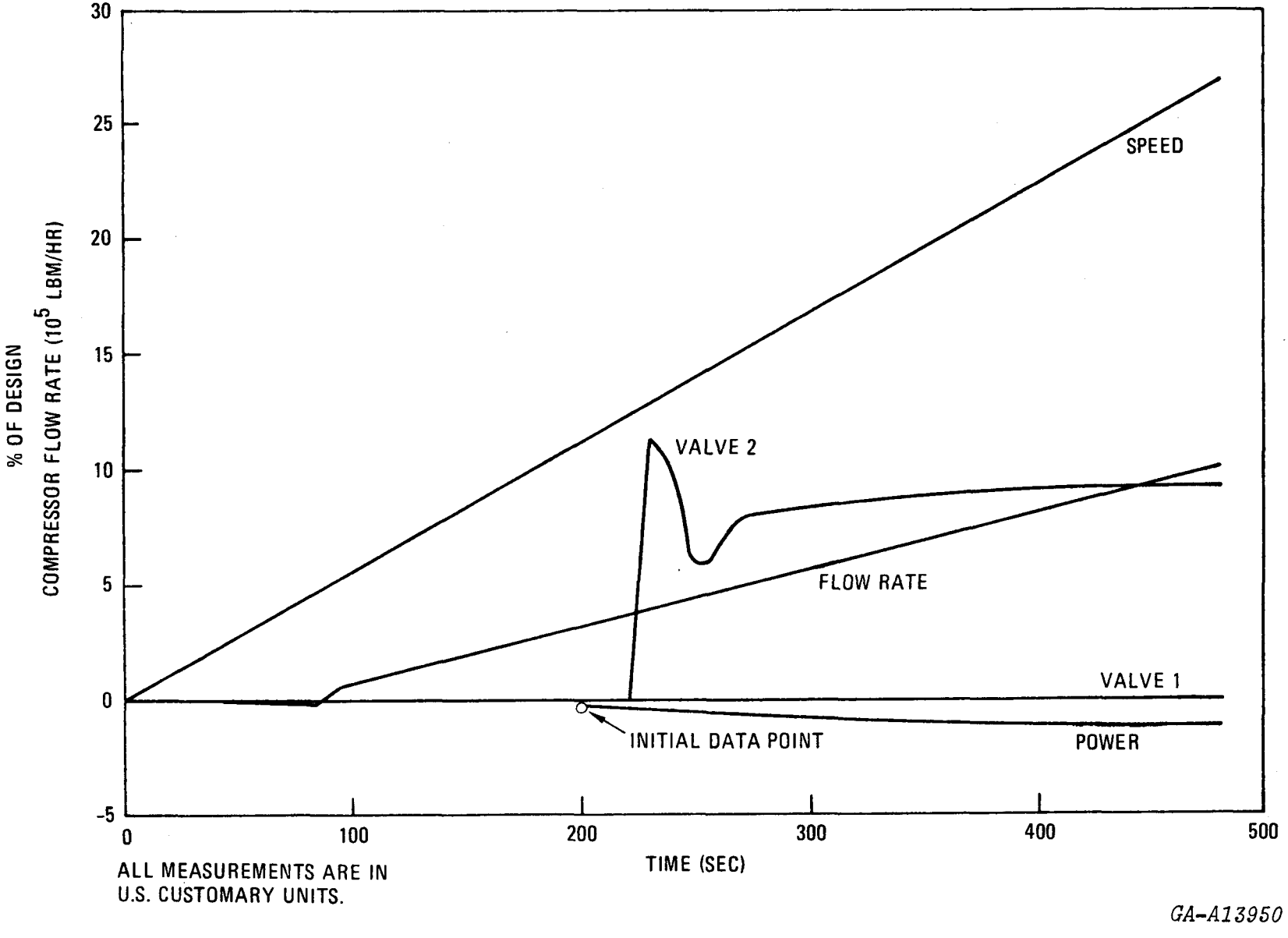

Fig. 2-4. Full inventory sequential startup of second loop (speed, power, flow, and valve transients)

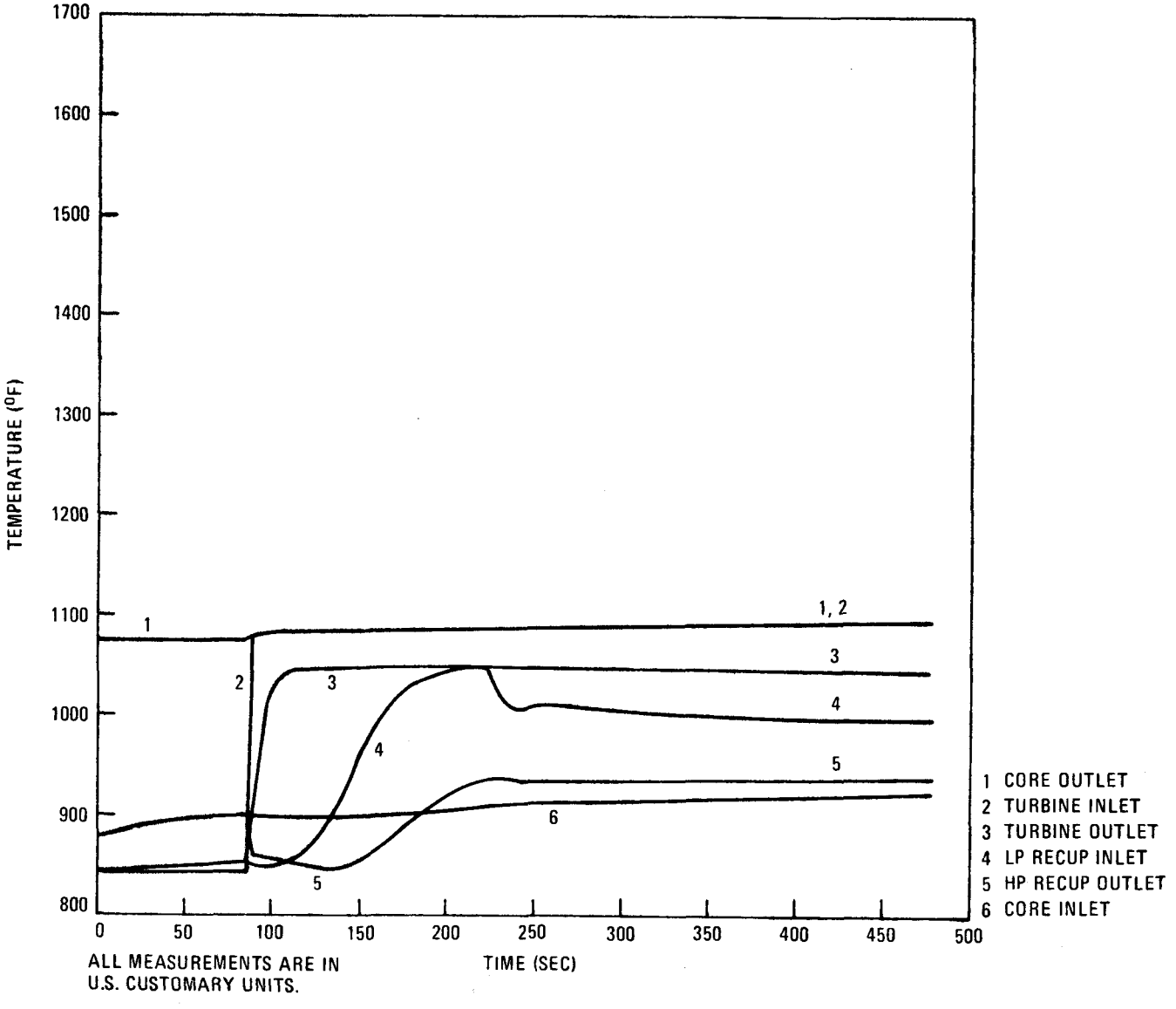

Fig. 2-5. Full inventory sequential startup of second loop (hot helium temperature transients)

Fairly significant temperature transients result in the turbine region from this flow direction change. Previously, the flow came to the turbine outlet (and through the turbine) from the recuperator. The temperature of the turbine flow was controlled by, and was somewhat lower than, the core inlet temperature. Subsequent to the flow direction change, the turbine inlet receives flow from the core outlet. This transient, which may be seen in Fig. 2-5, is being evaluated by designers to determine the acceptability of the induced thermal stresses in PCL components.

The startup of the third loop against two operating loops from the initial refueling status is essentially the same as that just described for startup of the second loop. The flow changes direction at a slightly higher speed ≈3 Hz (≈185 rpm) , and the motoring power is slightly higher (see Section 2.2.4.1).

Case 2. Consideration of the startup of a down loop leads to the logical step of simply motoring the down loop to self-sustaining, bringing it to synchronous speed, and taking up load. Figures 2-6 and 2-7 present the data for this procedure. Flow transition occurs at ≈7 Hz (≈420 rpm), and motoring power is significantly higher throughout the startup. The turbine temperature transient is much more severe (see Fig. 2-7) than it is for Case 1, and the Hp recuperator outlet temperature exceeded the 542°C (975°F) temperature currently set as a plant protection system loop shutdown trip. The reason that the trip temperature was exceeded is that the attemperation valve could not "keep up" with sufficient cooling because of the elevated turbine discharge temperature induced by this sequence. Design changes could possibly prevent exceeding the trip, and/or the trip could be raised since significant margin below damage limits exists for this peculiar short-duration transient.

Case 3. This case is intermediate to the two cases described above. Reactor outlet temperature was maintained at 816°C (1500°F), but load was dropped and speed was reduced to 40 Hz (2400 rpm). The temperature trip was still exceeded, and the turbine temperature transient was as just

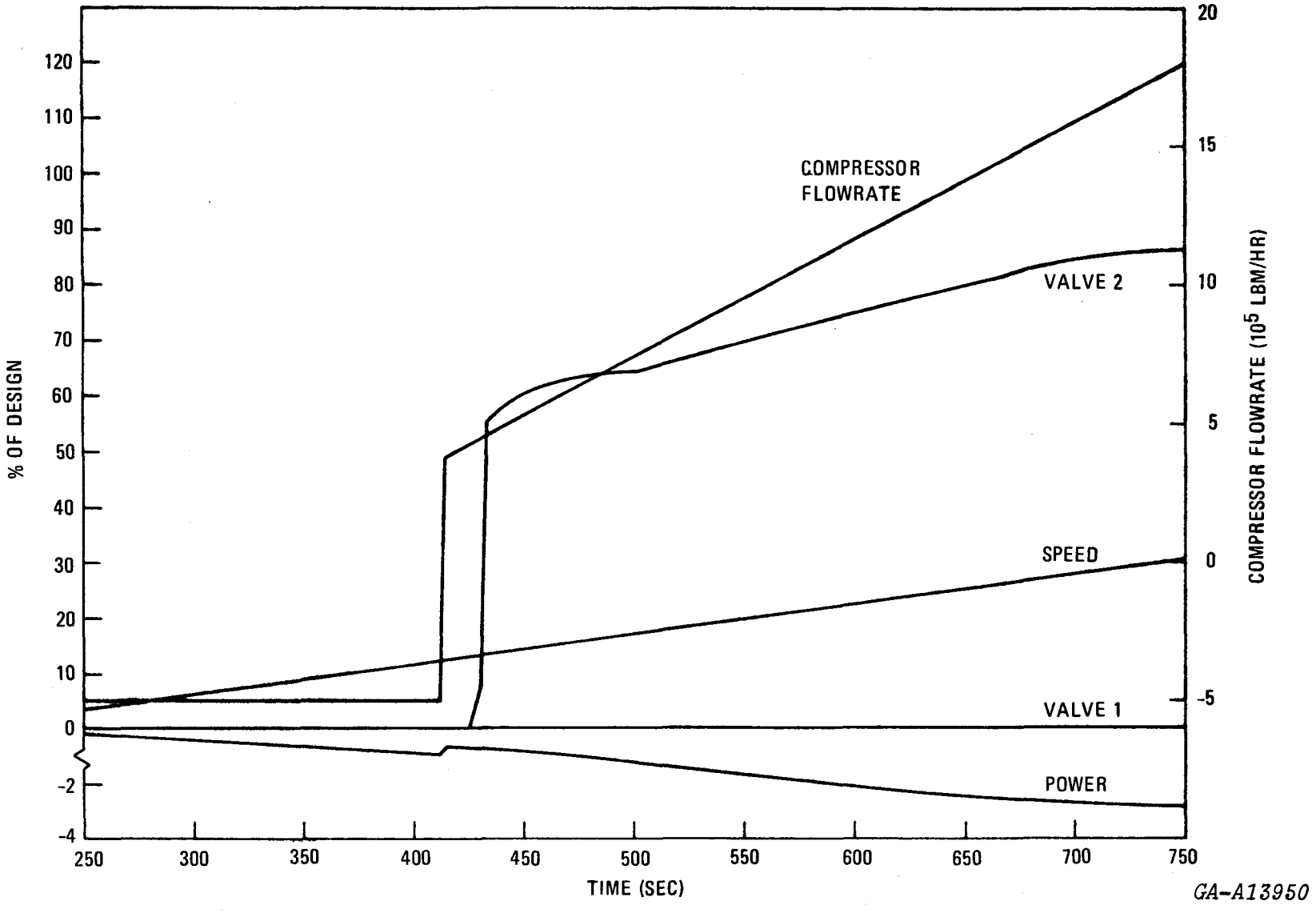

Fig. 2-6. Single-loop startup with two loops operating and loaded (speed, power, flow, and valve transients)

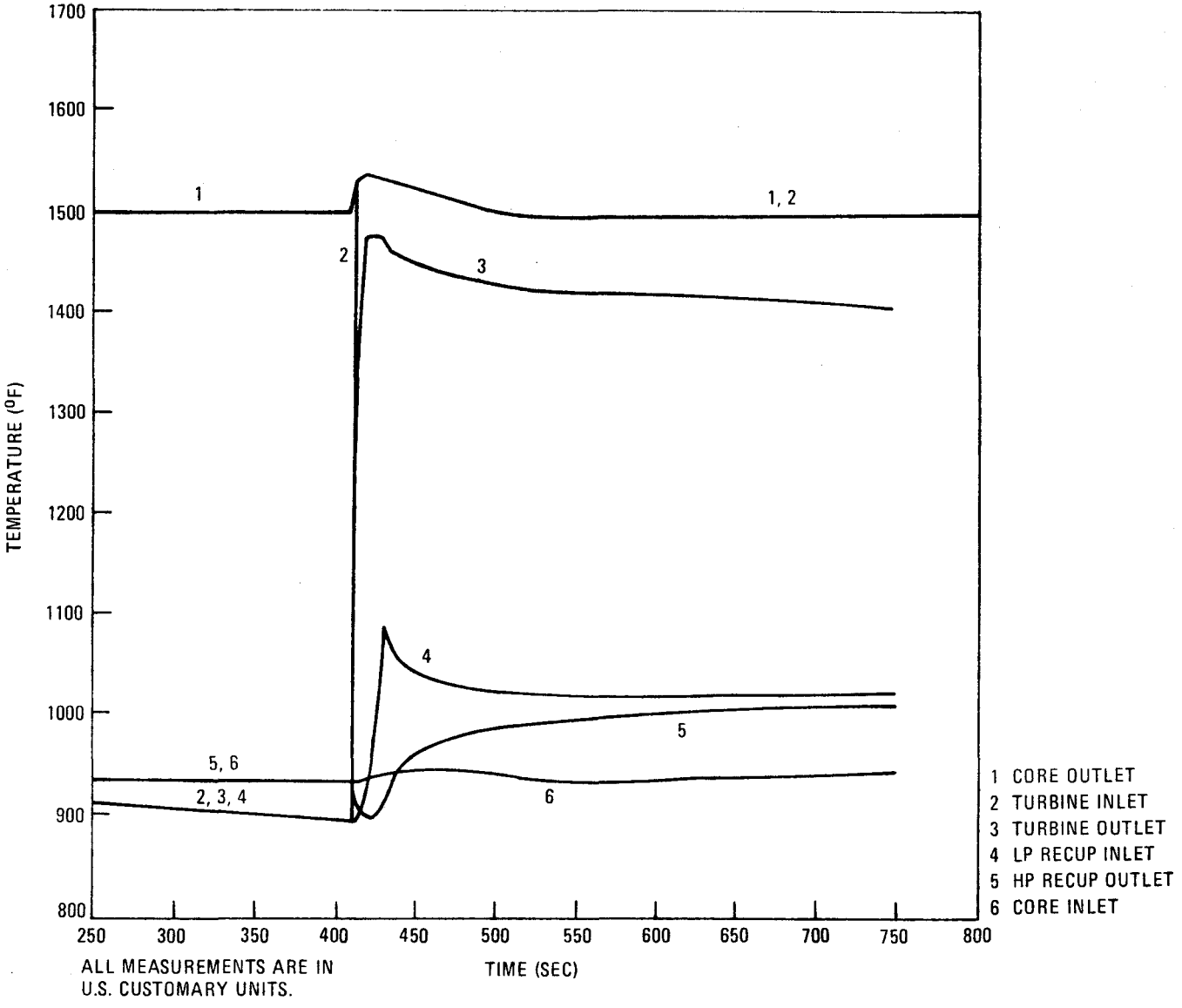

Fig. 2-7. Single-loop startup with two loops operating and loaded (hot helium temperature transients)

described, though at a lower flow (i.e., less thermal stress). Motor power was decreased (see Section 2.2.4.1) to a point nearly midway between the two previous runs.

Case 4. Reduction of inventory will reduce the motoring power requirements for the startup of one loop with the other two loops on load. However, temperatures and temperature distributions remain nearly constant with inventory change. Since the present trip levels were exceeded in the preceding runs at 816°C (1500°F) ROT, reduced inventory runs were made at reduced temperature. A run at 593°C (1100°F) and 62.5% inventory resulted in a one-third reduction in required motoring power from the corresponding full inventory condition, and the Hp recuperator outlet temperature peak was reduced to more than 14°C (25°F) below the trip value. Electrical load during the start of the down loop was approximately 20% of full load. Adequate margin remained in the attemperation control to reduce temperature further if required. Another significant difference is in the thermal transient imposed on components of the starting loop at flow reversal. The lower mass flow at reduced inventory results in a lower heat transfer to the components for a given change in the fluid temperature. This results in a lower rate of change of component temperature.

The maximum material temperature rate of change is reduced from approximately 2.8°C/sec (5°F/sec) for Case 2 to 1.7°C/sec (3°F/sec) for Case 4. Modification to the attemperation control is planned, which will reduce the temperature rate for both cases. However, the inherent reduction of thermal transients with reduced inventory will still be of significance.

2.2.4. Startup Power and Subsystem Requirements

2.2.4.1. Startup Power. In the startup runs described in Sections 2.2.2 and 2.2.3, data were generated to provide startup motoring power requirements for various conditions. Figure 2-8 presents these data for full inventory refueling condition startup at 593°C (1100°F) ROT. Negative values of power are for shaft power motoring input, whereas positive

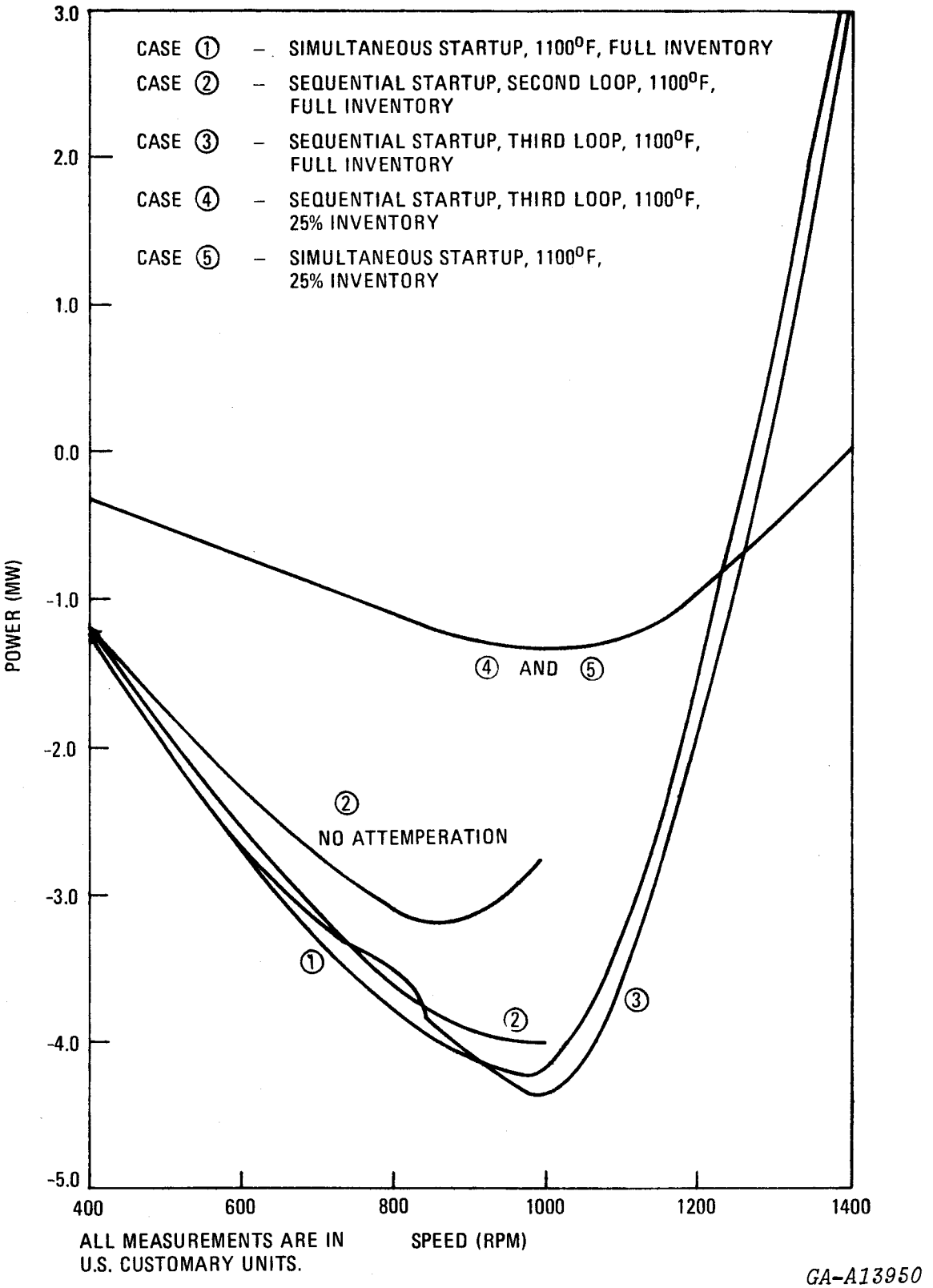

Fig. 2-8. Simultaneous and sequential plant startup power requirements

values indicate excess turbine power available for accelerating the turbomachine (i.e., at zero power, the turbine is just supplying enough power to drive the compressor). The data are for an open-loop start in that the control system would normally start opening the bypass valve after the peak motor input has been passed in order to control the decrease in motor power.

Three cases were simulated: (1) simultaneous startup of three loops from 6.7 to 23.3 Hz (400 to 1400 rpm); (2) sequential startup of the second turbomachine from 0 to 16.7 Hz (0 to 1000 rpm) with the first turbomachine running at 24.7 Hz (1480 rpm); and (3) sequential startup of the third turbomachine to 23.3 Hz (1400 rpm) with the other two turbomachines running at 24.7 Hz (1480 rpm).

The peak motor input for sequential start (Case 3) is only slightly higher than that required for simultaneous start (Case 1). Startup of the third loop in a sequential start requires the largest motoring power input because of the pressure drop of the core and the higher average pressure in the loop being started. This trend may be seen by comparing Case 2 and Case 3. The abrupt change in motor power for Case 3 between 13.3 and 14.2 Hz (800 and 850 rpm) occurred when the attemperation valve opened. In Case 2, with attemperation, the opening of the attemperation valve occurred more smoothly because of the manner in which the temperatures changed. Case 2, with and without attemperation, illustrates the additional power required when the attemperation valve is used to maintain the system temperatures.

The startups discussed above were those from essentially refueling conditions. The motoring power data for selected cases of restart of a single down loop (see Section 2.2.3) are presented in Fig. 2-9. The conditions of the cases being presented are:

Case A

1. With two loops operating at maximum load (≈85% of design) and ROT at 816°C (1500°F), bring speed of third turbomachine to 25 Hz (1500 rpm) with startup controller. Begin reactor power increase.

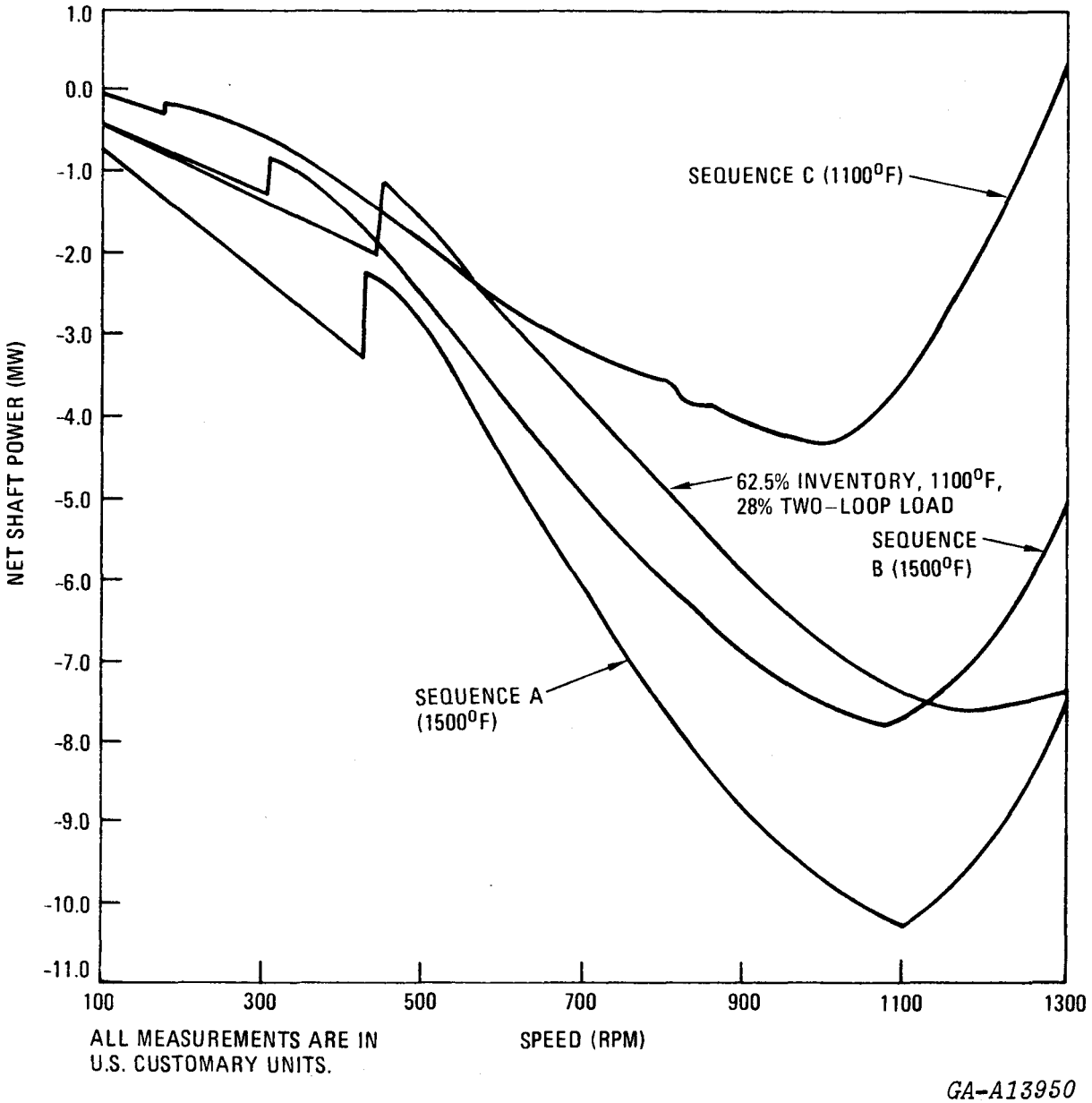

Fig. 2-9. Loop startup power requirements

2. Close bypass valves to bring machine to 60 Hz (3600 rpm).

3. Synchronize and pick up load.

Case B

1. Reduce electrical power to 10% and open load breakers. Use manual reactor outlet temperature demand to hold ROT to 816°C (1500°F).

2. Reduce speed of two turbomachines to ≈40 Hz (≈2400 rpm) with no load speed controller and simultaneously reduce reactor power.

3. Bring speed of third turbomachine to 25 Hz (1500 rpm) with startup controller and increase reactor power to maintain temperature.

4. Close bypass valves to bring these machines to 60 Hz (3600 rpm).

5. Synchronize and pick up load.

Case C

1. Simultaneously reduce electrical load to 10% and ROT to 593°C (1100°F) under automatic temperature control.

2. Open load breakers and begin reducing speed of two turbomachines to 25 Hz (1500 rpm) with no load speed controller, simultaneously reducing reactor power.

3. Same as Item 3 of Case B.

4. Same as Item 4 of Case B.

5. Same as Item 5 of Case B.

The abrupt shift in motoring power level at 3 Hz (180 rpm) for Case C, at 5 Hz (310 rpm) for Case B, and at 7 Hz (425 rpm) for Case A occurred when helium flow switched directions in the loop being started. The shaft power at the transition from reverse to forward flow was 1283 kW at 6 Hz (310 rpm) and 3309 kW at 7 Hz (420 rpm). The higher-speed operation (Case A) of the two operating loops leads to the higher speed for reversal of flow in the loop being started and a significant increase in required motor power. The shift in power level in Case C between 13 and 14 Hz (800 and 850 rpm), however, occurred because the attemperation valve opened transiently as opposed to the continuous opening, subsequent to the flow transition, in Cases A and B.

The magnitude of the motoring power for Cases A and B is dictated by three factors:

1. Higher speed of two loops results in higher pressure in the third loop, resulting in higher compressor work at a given speed.

2. Higher speed (flow) of the two loops results in larger core pressure drop for the starting loop to work against.

3. Higher temperature results in the need to open the attemperation valve, spoiling the starting loop efficiency and resulting in higher power input requirements.

The absolute magnitude of the motoring power discussed thus far (for full inventory) is subject to the uncertainties of the low-speed turbomachinery characteristics. While none of the motoring power values calculated are infeasible, the power ratio of Case A to Case C of 2.4 is indicative of the difficulty and cost associated with restart of a down loop while maintaining substantial power output from the two operating loops.

Reduced inventory results in a significant reduction in the motoring power requirements. Figure 2-8 presents a summary plot of the motoring power for two comparable reduced inventory cases.

The first reduced inventory case is a simultaneous start at 593°C (1100°F) ROT with 25% inventory. The second reduced inventory case is a sequential start of the third loop at 593°C (1100°F) ROT with 25% inventory and two loops operating at ≈24 Hz (≈1480 rpm). The motoring power requirements decrease by over a factor of 3 from those at full inventory.

A run was also made, with reduced inventory, for the start of a down loop with the two operating loops on load. This case was run at 62.5% inventory and 593°C (1100°F) ROT. The electrical load on the two operating loops was approximately 28% of their design load. The motoring power for this case is shown in Fig. 2-9. In terms of starting with two loops on load, the results may be compared with those of Case A. The reduction in ROT prevents the high reactor inlet temperature problem noted in Section 2.2.3, and the lower helium inventory reduces both the loop power at the time of flow reversal and the maximum required motoring power. As may be seen from Fig. 2-9, the motoring power at flow reversal and at the maximum point is reduced from Case A by approximately one-third, in proportion to the reduction in inventory.

2.2.4.2. Subsystem Requirements. The options for providing the necessary startup motoring power were discussed in Ref. 2-1. The three basic categories were:

1. Motor the generator with a variable frequency electrical drive.

2. Mechanically drive the turbomachine shaft.

3. Provide a means of driving the turbine with the primary fluid.

No method has yet been found to apply to option 3.

One subset of option 1 was to obtain a synchronous start or an asynchronous start from the line (i.e., constant frequency). The evaluation of these potential solutions is shown in Table 2-1.

TABLE 2-1
SUMMARY EVALUATION OF CONSTANT FREQUENCY MOTORING OPTIONS

Constant Frequency Motoring Options	Evaluation
A. Full voltage starting from main bus	The high starting torque and acceleration may cause compressor surge and/or large temperature transients. The option also precludes use of the generators fow low-speed motorized cooling.
B. Motor-generator set	Expense is similar to static frequency converter (SFC), and space, flexibility, reliability, and maintenance are considered to be worse.
C. Asynchronous start using: 1. Series choke 2. Voltage reduction 3. Starting transformer 4. Pole changing 5. Split phase starting 6. Leakage winding 7. Starting winding	All of the listed asynchronous start methods were assessed as comparable (though generally less) in cost to SFC, complex, operationally undesirable, lowerein reliability, and higher in maintenence.

The remaining options boiled down to the five schemes presented in Table 2-2. As may be observed from the table, the costs define the following choices:

1. If sequential startup is not compromised by the thermal transients discussed in Section 2.2.3, a separate static frequency converter (SFC) system should be used.

2. If simultaneous start is necessitated by thermal transients or other considerations, a motor/clutch system should be used.

2.2.5. Documentation of Transient Code

Documentation of REALY2 (Ref. 2-2) was Milestone A-1. The code will be sent to the Argonne Code Center following clearance through the California Patent Group.

The REALY2 document consists of a user's guide, an input guide, a program guide, sample REALY2 input and output, and a complete listing of the code. The document describes the version of REALY2 that was used through March of this year. Modifications to the code for the startup and shutdown studies (see Section 2.2) were tentative at that time. Thus, they were not included in the document.

TABLE 2-2
SUMMARY EVALUATION OF VARIABLE FREQUENCY MOTORING OPTIONS

Schemes	Advantages	Disadvantages	Cost Estimates
A. Static frequency changer (SFC) of core auxiliary cooling system (CACS); motorized generator; turbomachinery 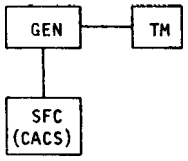 	1. Use generator as prime mover. 2. No additional length of main shaft. 3. No moving part in SFC. 4. Good reliability. 5. Take advantage of the existing SFC of CACS. 6. Speed could be easily controlled [0 to ~60 Hz (~3600 rpm)]	1. Limited power output of the existing SFC of CACS (671 kW per SFC). 2. Additional transformer and switch box are needed, since voltage requirements for CACS motor and motorized generator are different. 3. Potential licensing problem. 4. During low-speed startup, cooling efficiency in generator is low for H_2 cooling. May either be replaced by water cooling (but at increased cost of more than 10% and face possible technology development) or add an additional and separately driven gas flowing system to increase the forced cooling (but at increase in both the cost and the explosive boundary of H_2).	Per Loop / Per Plant Extra cost for motorized generator (H_2 rotor cooling) $100,000 Transformer and switch $ 20,000 Totals $120,000 $0 Total/Plant $120,000
B. SFC; motorized generator; turbomachinery 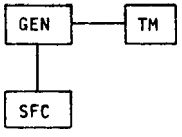 	1. SFC power output limit is open to designer. 2. No additional potential licensing problem. 3. With sequential start, only one unit (with switching) is needed for all loops. 4. Items 1, 2, 3, 4, and 6 of Scheme A.	1. Additional equipment volume. 2. Item 4 of Scheme A.	Per Loop / Per Plant Extra cost for motorized generator $100,000 Cost for SFC (two 2237-kW SFCs/plant)[a] $480,000 Total[a] $100,000 $480,000 Total/Plant $580,000 [a] Add one additional SFC as spare on line and/or for extra power output. The cost for SFC per loop would be $240,000, and the total cost per loop would be $340,000.

TABLE 2-2 (continued)

Schemes	Advantages	Disadvantages	Cost Estimates
C. Variable speed motor; clutch; generator; turbomachinery 	1. Use standard generator (less expensive than motorized generator). 2. Power output limit is open to designer. 3. Good reliability.	1. Additional length of main shaft. 2. Additional enclosure of generator coil. 3. Need one for each loop.	Per Loop / Per Plant Motor and starter (4473 kW) $300,000 Clutch $ 50,000 Extra enclosure and miscellaneous $ 50,000 Total $400,000 $0 Total/Plant $1,200,000
D. CWS pumps; hydraulic turbine; clutch; generator; turbomachinery 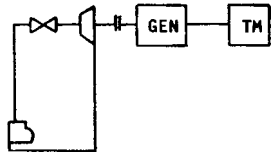	Take advantage of the existing CWS pumping facilities.	1. Startup power is limited by pumping head and capacity of CWS pumps, presently 700 kW per pump. 2. Additional length of main shaft. 3. Pumping flow stability problem in speed control. 4. Additional length of pipe routing of CWS. 5. Precooler loss of coolant during startup. 6. Need turbine for each loop. 7. Massive plumbing to each loop. 8. Limited to partial helium inventory startup.	Per Loop / Per Plant Turbine $500,000 Valves $100,000 Pipe fitting $100,000 Total $700,000 $0 Total/Plant $2,100,000
E. CWS motor; gear box; clutch; generator; switch; motorized generator; turbomachinery 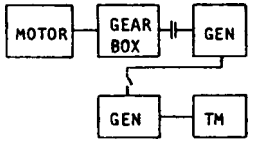	1. Take advantage of the existing CWS motor facilities. 2. No additional length of main shaft.	1. Startup power output is limited by CWS motor capacity (895 kW per motor). 2. Smooth speed control is a problem. 3. Precooler loss of coolant during startup. 4. Additional generators, transformers, and switches. 5. Additional cost for motorized generator. 6. Limited to partial helium inventory startup.	Per Loop / Per Plant Extra cost for motorized generator $100,000 Small generator (four/plant) $240,000 Transformer and switch $ 60,000 Clutch, gear box, and miscellaneous $300,000 Total $100,000 $600,000 Total/Plant $900,000

2.3. N_2O_4 COMBINED CYCLE

During this reporting period, a study of the use of nitrogen tetroxide (N_2O_4) as the working fluid in a GT-HTGR bottoming cycle was completed. The study included a survey of the literature on N_2O_4 and its use in power cycles, compilation of N_2O_4 thermodynamic and transport property data, an evaluation of several power cycle configurations, a brief assessment of the component design considerations for a typical N_2O_4 power cycle, and a brief assessment of the practical considerations involved in the use of N_2O_4 as a power cycle working fluid.

Interest in the use of N_2O_4 as a power cycle working fluid has come about primarily because of the work done in the Soviet Union over the past 15 yr. The Soviet Union is considering the use of this fluid as both a reactor coolant and a power cycle working fluid. Considerable work has been done in the USSR on the conceptual design of N_2O_4 power cycles, the development of N_2O_4 power cycle test hardware, and the determination of thermodynamic and transport properties of the fluid.

2.3.1. Thermodynamic and Transport Properties

A literature survey was performed to assess the availability of thermodynamic and transport property data. Many sources of data were found. The Soviet Union, because of its active development of N_2O_4 power cycles, had a number of books and papers on thermodynamic and transport properties. The United States also had a number of papers on properties, many of which were a result of the use of N_2O_4 as a rocket propellant. In many of the above cases, the data did not fully cover the range of interest.

A comparison of the thermodynamic data from the various sources revealed significant differences. For example, the enthalpy change for a constant pressure, temperature change varied from 40 to 58 cal/g (72 to 104 Btu/lb between the different sources of data. Both of the extremes came from Soviet Literature.

Reference 2-3 was found to contain tables of thermodynamic properties for nearly the entire range of interest. The authors of Ref. 2-3 were aware of the major Russian and American efforts to establish thermodynamic properties, and they offered reasons why their analyses were superior. The Ref. 2-3 work was carried out prior to September 1968. It is known that the Soviet Union has performed further work since that time, but this information was not available. The conditions of interest which Ref. 2-3 did not cover were pressures above 200 atm (2940 psia) and the compressed liquid region. Pressures to 300 atm (4410) were obtained by extrapolation of the Ref. 2-3 data. The compressed liquid properties were obtained by fairing existing data at supercritical temperatures with the saturated liquid properties. Transport property data were obtained from Refs. 2-3, 2-4, and 2-5.

2.3.2. Cycle Analysis

2.3.2.1. Primary Helium Cycle. The goal of the cycle analysis was to establish performance and operating conditions for a number of N_2O_4 bottoming cycles used in conjunction with a GT-HTGR. The GT-HTGR configuration which was used to evaluate the bottoming cycles was a twin 4000-MW(t), 950°C (1742°F) ROT, binary-cycle plant. The initial step in the study was to determine the performance of the primary helium cycle for a range of compressor inlet temperatures and also for a range of recuperator lengths or recuperator effectiveness. This was carried out with a modified version of the DPOINT code. The compressor pressure ratio, the compressor and turbine efficiencies, and all PCL pressure losses except those of the recuperator were held fixed. The recuperator pressure losses were varied with the recuperator length. (The effect of fixing the PCL flow resistances while allowing the pressure losses to vary was considered later in the study.)

2.3.2.2. N_2O_4 Bottoming Cycles. The N_2O_4 power cycles which were evaluated are shown in Fig. 2-10, which shows cycle diagrams along with characteristic T-s diagrams. Cycle 1 is identical to the current ammonia bottoming cycles. Cycles 2, 3, and 4 were discussed in the Russian literature. Cycles 3 and 4 are the cycles which are preferred by the Soviet Union, with Cycle 3

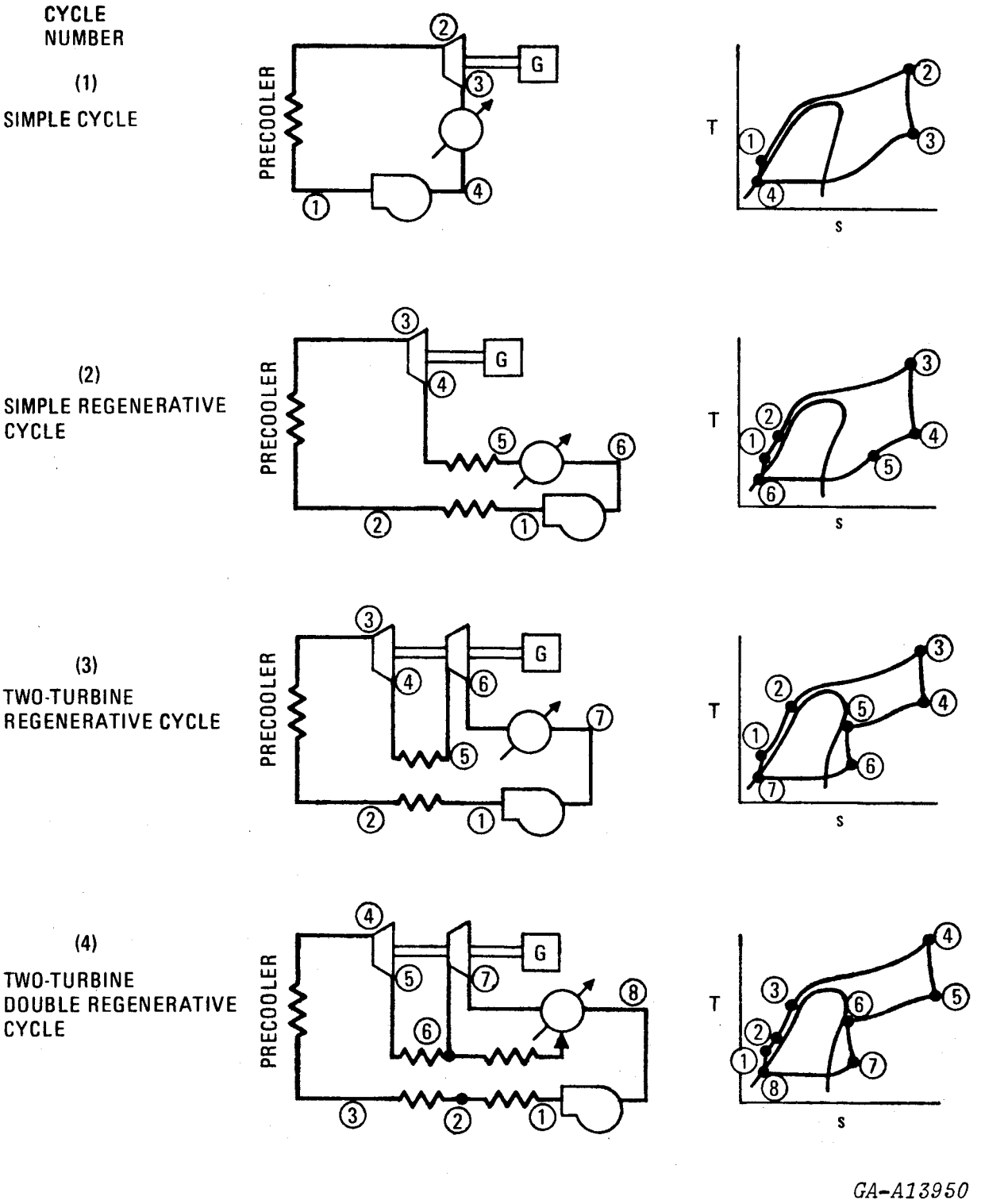

Fig. 2-10. N_2O_4 bottoming cycles

recommended for use when the N_2O_4 is heated to 450 to 500°C (840 to 1020°F) and Cycle 4 recommended when the N_2O_4 is heated to 300 to 400°C (570 to 750°F). These preferences were based on cost optimizations.

The literature contains some discussion of all-gas N_2O_4 power cycles. These cycles were not considered in this study because the literature indicated that they were lower in efficiency by approximately 8 percentage points.

The N_2O_4 cycle analysis was performed by digital computer codes written specifically for this study. These codes determined (1) the thermodynamic conditions at the inlet and outlet of all components in the N_2O_4 PCL, (2) the N_2O_4 flow rate, (3) the N_2O_4 cycle efficiency and electrical output, and (4) the overall plant efficiency and power output. A range of both primary- and secondary-cycle parameters was investigated in order to establish maximum expected efficiencies for each N_2O_4 cycle configuration.

Table 2-3 shows the cycle analysis ground rules. These were based primarily on the current ammonia binary cycle. The cycle analysis did not account for kinetic effects in the dissociation and recombination processes. Kinetic effects would reduce cycle efficiency, however, so values predicted in this study should be considered the maximum potential.

2.3.2.3. Cycle 1 - Simple Cycle. Overall plant efficiency for Cycle 1 was determined as a function of primary-cycle minimum helium temperature, primary-cycle recuperator length or effectiveness, precooler pinch point temperature difference, and maximum N_2O_4 pressure.

Figure 2-11 shows Cycle 1 performance as a function of maximum N_2O_4 pressure and minimum helium temperature. These data are for the full-length recuperator in the helium cycle (effectiveness = 0.90) and a precooler pinch point of 5.5°C (10°F). The partially dashed line for a minimum helium temperature of 60°C (140°F) is to show that, for these configurations, part of the turbine expansion is within the two-phase region. While the turbine

TABLE 2-3
N_2O_4 CYCLE ANALYSIS GROUND RULES

N_2O_4 condensation temperature	37.8°C (100°F)
N_2O_4 pump efficiency	85%
N_2O_4 turbine efficiency	90%
Secondary generator efficiency	98.8%
N_2O_4 pressure losses:	
Heater (precooler)	0.069 MPa (10 psi)
Heater inlet	0.103 MPa (15 psi)
Heater to high-pressure turbine inlet	0.552 MPa (80 psi)
Low-pressure turbine outlet to condenser	0.055 MPa (8 psi)
Condenser	0.025 MPa (3.6 psi)
Regenerative heater (if used)	0.014 MPa (2 psi) (both sides)
High-pressure turbine to low-pressure turbine ducting (if used)	0.069 MPa (10 psi)
N_2O_4 heater (precooler) pinch point Δt	5.5°C (10°F) (nominal)

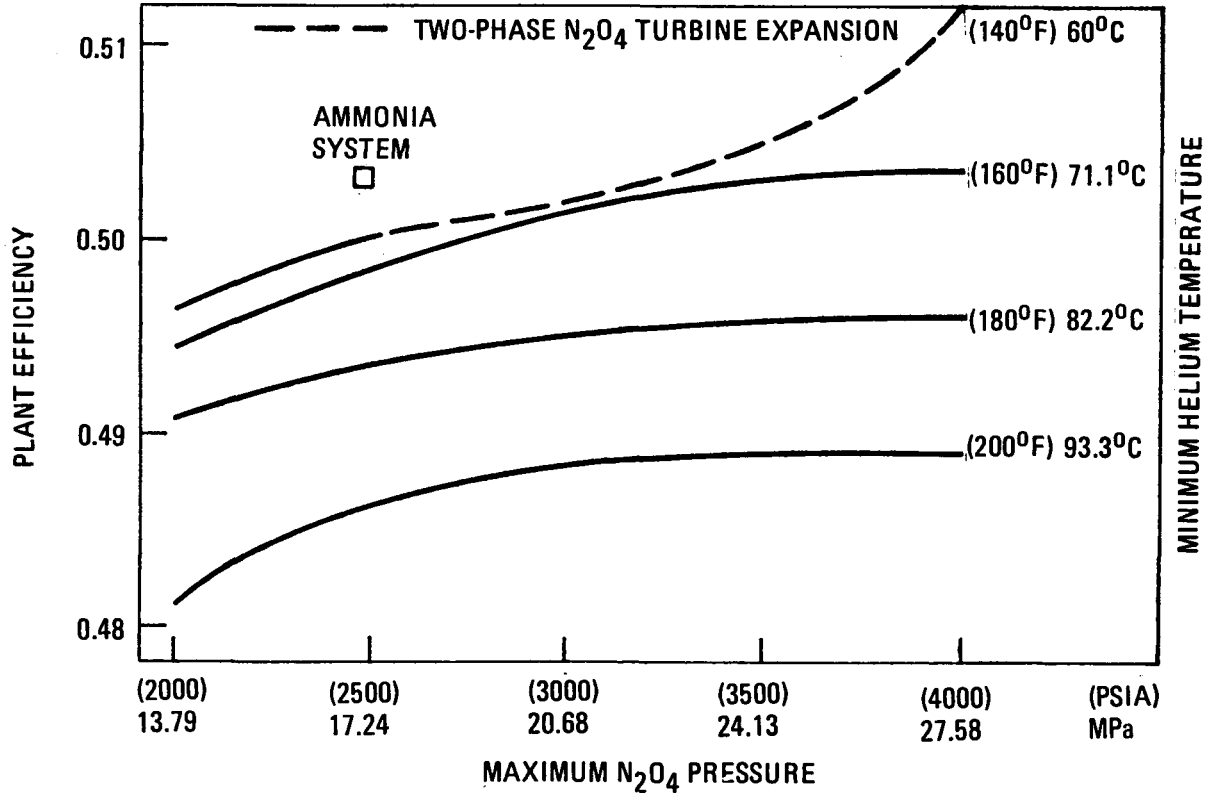

GA-A13950

Fig. 2-11. Plant performance with Cycle 1 [(full-length recuperator, precooler pinch point 5.5°C (10°F)]

discharge is in the superheat region for all cases, the shape of the N_2O_4 vapor dome is such that the turbine expansion does in some cases pass through the two-phase region. The 27.58 MPa (4000 psia) case has a turbine expansion process which passes through the critical point with resulting moisture of approximately 20%. This moisture is encountered somewhere in the middle of the turbine, and toward the exhaust it would completely revaporize. Since in the calculation procedure the turbine efficiency was not degraded when two-phase expansion occurred, the results are optimistic. Maximum N_2O_4 pressures of greater than 27.58 MPa (4000 psia) and minimum helium temperatures of less than 60°C (140°F) were not considered because they would further increase the amount of moisture encountered during the turbine expansion process.

Figure 2-11 shows that the use of an N_2O_4 bottoming cycle with the cycle 1 configuration can produce an overall plant efficiency which slightly exceeds the ammonia binary-cycle plant efficiency, but the N_2O_4 cycle must operate at considerably higher pressure and the N_2O_4 turbine expansion process must pass through a very questionable area of the two-phase region.

The effects of reducing helium cycle recuperator length (or effectiveness) and of increasing precooler pinch point temperature difference were investigated. For both, combined cycle efficiency is reduced. The point is worth emphasizing that the cycle efficiency for the nonrecuperated system is less than that with recuperation. However, the effect of pinch point is small, such that in an economic optimization the savings possible in precooler surface area might be justified. These conclusions were verified for all N_2O_4 cycles, for all minimum helium temperatures, for all maximum N_2O_4 pressures, and even in the case where helium system pressure losses were allowed to vary with helium flow rate rather than being held fixed.

2.3.2.4. Cycle 2 - Simple Regenerative Cycle. Cycle 2 differs from Cycle 1 in that it uses regenerative heating. The analysis of this cycle was somewhat more complex than the Cycle 1 analysis in that it was necessary to

consider the effects of the heat load of the regenerative heater. It was also necessary to maintain an adequate pinch point in the regenerative heater. The cycle analysis was performed in a manner similar to the Cycle 1 analysis but with the additional parameter of precooler inlet N_2O_4 temperature, which was varied so as to have an approach which was between 5.5 and 13.9°C (10 and 25°F) of the minimum helium temperature, a range sufficient to obtain maximum efficiencies.

Cycle 2 performance is shown as a function of maximum N_2O_4 pressure and minimum helium temperature in Fig. 2-12. These data are for the full-length recuperator in the helium cycle, a precooler pinch point of 5.5°C (10°F), a regenerative heater pinch point of 5.5°C (10°F) or greater, and a precooler inlet N_2O_4 approach temperature which produced the highest plant efficiency. The Cycle 2 performance was generally lower than the Cycle 1 performance. The use of regenerative heating does increase the secondary-cycle efficiency, but the higher required minimum helium temperatures reduce the primary-cycle efficiency, the combined effect being a lower overall plant efficiency. Data for minimum helium temperatures of less than 82.2°C (180°F) are not shown in Fig. 2-12 because at those conditions the maximum efficiency configuration was one in which the regenerative heater was eliminated, i.e., Cycle 1.

2.3.2.5. Cycle 3 - Two-Turbine Regenerative Cycle. Cycle 3 is still more complex in that it uses regenerative heating and two turbines. For this cycle, the pump drive turbine was assumed to be in parallel with the high-pressure power turbine. The analysis of this cycle necessitated the consideration of variations in not only the regenerative heater heat load but also the high-pressure turbine discharge pressure. The high-pressure turbine discharge pressure was varied from 1.01 to 2.53 MPa (147 to 367 psia). The upper limit of 2.53 MPa (367 psia) was sufficient to maximize efficiency, and the lower limit of 1.01 MPa (147 psia) was established because it was believed that further expansion in the high-pressure turbine would make an additional turbine uneconomic; that is, Cycle 3 would approach Cycle 2.

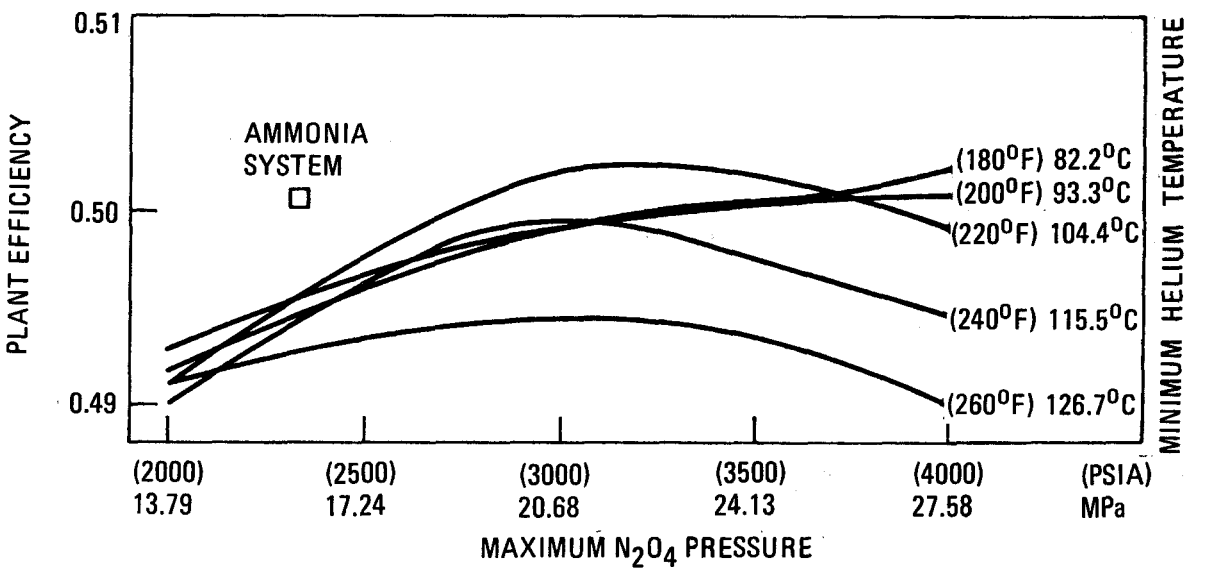

GA-A13950

Fig. 2-12. Plant performance with Cycle 2 [(full-length recuperator, precooler pinch point 5.5°C (10°F)]

Cycle 3 performance is shown as a function of maximum N_2O_4 pressure and minimum helium temperature in Fig. 2-13. These data are for the full-length recuperator in the helium cycle, a precooler pinch point of 5.5°C (10°F) and precooler inlet N_2O_4 approach temperatures and high-pressure turbine discharge pressures which produced maximum plant efficiencies. The Cycle 3 plant efficiencies were generally lower than the Cycle 2 efficiencies, the only exceptions occurring at the highest N_2O_4 pressures and the lowest minimum helium temperatures. For a minimum helium temperature of 71.1°C (160°F) and an N_2O_4 pressure above 24.13 MPa (3500 psia), the high-pressure turbine expansion process passed into and then out of the two-phase region. The maximum moisture encountered during the expansion was approximately 8%. Minimum helium temperatures of less than 71.1°C (160°F) are not shown in Fig. 2-13 because the resulting values of precooler outlet N_2O_4 temperature are so low that two-phase flow is encountered in both turbine expansion processes and in the hot side of the regenerative heater.

2.3.2.6. Cycle 4 - Two-Turbine Double Regeneration Cycle. Evaluations of Cycles 2 and 3 showed that the use of regenerative heating did not produce an increase in overall plant efficiency. This would also be the case for Cycle 4, where two regenerative heaters are used. The efficiency of Cycle 4 would, in fact, be lower than the efficiency of Cycle 3 because part of the flow which in Cycle 4 produces power in the low-pressure turbine is tapped off in Cycle 4 for use in the second regenerative heater. Since Cycle 4 is more complex and has a lower efficiency than Cycle 3, it was not evaluated in detail.

2.3.2.7. Comparison of N_2O_4 and Ammonia Cycles. Table 2-4 compares some of the significant parameters of the ammonia and N_2O_4 binary cycles. The highest N_2O_4 binary-cycle plant efficiency was produced by Cycle 1 operating with a pump discharge pressure of 27.58 MPa (4000 psia).

Table 2-4 also shows the effect on performance and operating parameters of reducing the maximum N_2O_4 pressure by 6.895 MPa (1000 psia). All cycles

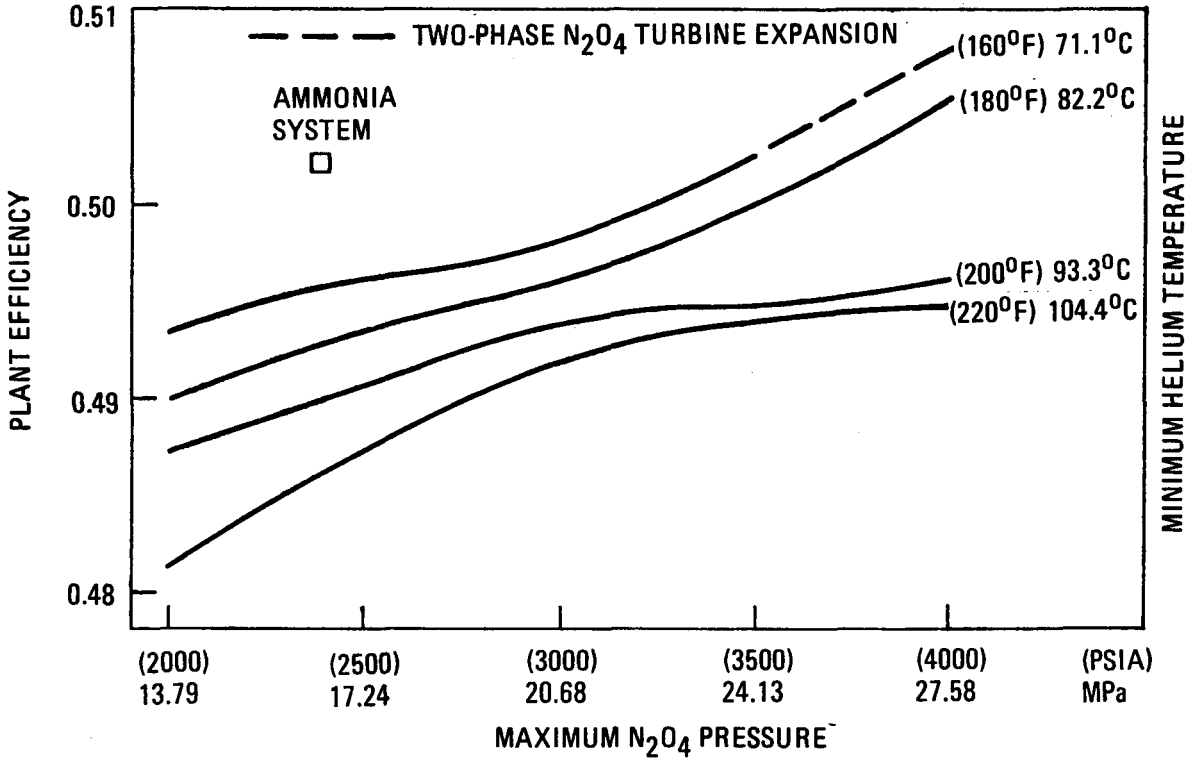

GA-A13950

Fig. 2-13. Plant performance with Cycle 3 [full-length recuperator, precooler pinch point 5.5°C (10°F)]

TABLE 2-4
CYCLE COMPARISON

Secondary Fluid	Ammonia	N_2O_4					
		Cycle 1		Cycle 2		Cycle 3	
		Case I[a]	Case II[b]	Case I[a]	Case II[b]	Case I[a]	Case II[b]
Plant efficiency, %	50.19	51.18	50.17	50.24	50.20	50.79	49.81
Helium compressor inlet temperature, °C (°F)	62.2 (144)	60 (140)	60 (140)	82.2 (180)	106.7 (220)	71.1 (160)	71.1 (160)
Primary cycle efficiency, %	38.25	38.47	38.47	35.98	33.43	37.23	37.23
Secondary Variables							
Cycle efficiency, %	20.11	21.29	19.60	22.92	25.82	22.24	20.64
Maximum pressure, MPa (psia)	16.64 (2414)	27.58 (4000)	20.68 (3000)	27.58 (4000)	20.68 (3000)	27.58 (4000)	20.68 (3000)
Maximum temperature, °C (°F)	249.2 (480.7)	207.1 (404.8)	200.5 (392.9)	256.6 (493.9)	330.8 (627.4)	219.4 (426.9)	230.7 (447.2)
Mass flow rate, kg/sec (lb/hr x 10^{-6})	2640.5 (13.02)	3534.3 (28.05)	3337.7 (26.49)	3054.2 (24.24)	2642.2 (20.97)	3507.8 (27.84)	2969.8 (23.57)
Turbine discharge volume flow rate, cm^3/sec (ft^3/hr x 10^{-6})	144.9 (18.42)	476.7 (60.60)	480.4 (61.08)	485.7 (61.75)	529.4 (67.30)	481.3 (61.19)	475.2 (60.42)
Amount of superheat to condenser, °C (°F)	0.0 (0.0)	20.2 (36.4)	26.6 (47.9)	32.4 (58.3)	45.2 (81.3)	21.5 (38.7)	36.9 (66.5)

[a] Case I: maximum system pressure = 27.58 MPa (4000 psia)

[b] Case II: maximum system pressure = 30.68 MPa (3000 psia)

lose approximately 1 percentage point in overall plant efficiency when the maximum N_2O_4 pressure is reduced from 27.58 to 20.68 MPa (4000 to 3000 psia).

Table 2-4 shows that, relative to the ammonia secondary cycle, the N_2O_4 cycles all have significantly greater mass and volumetric flow rates. The N_2O_4 cycles also have considerable superheat at the condenser inlet.

2.3.2.8. Conclusions. The following conclusions are based on the results of the cycle analysis:

1. From an efficiency standpoint, N_2O_4 is competitive with ammonia as a secondary-cycle working fluid. Overall plant efficiencies using N_2O_4 secondary cycles were essentially the same as systems using ammonia secondary cycles.

2. N_2O_4 cycles require higher operating pressures in order to attain maximum efficiency. Optimum efficiency N_2O_4 pump discharge pressures varied from 4.13 to >27.58 MPa (3500 to >4000 psia).

3. The primary-cycle compressor inlet temperatures required for maximum plant efficiency varied from 60 to 82.2°C (140 to 180°F), depending on the N_2O_4 cycle configuration.

4. The use of regenerative heating in the N_2O_4 cycle did not produce sufficient secondary-cycle performance increase to justify its use.

5. The N_2O_4 cycles had mass flow rates which were approximately twice the ammonia cycle flow rates and turbine discharge volumetric flow rates which were approximately 3.3 times the ammonia cycle values.

6. Reducing the primary-cycle recuperator effectiveness produces a reduction in primary-cycle performance and an increase in secondary-cycle performance. The net result was found to be reduced overall performance for all N_2O_4 secondary cycles considered.

Since the Russian literature emphasizes the high efficiency potential of the N_2O_4 working fluid, it was hoped that its use would produce plant efficiencies significantly greater than those of ammonia. This hope was not realized because the full potential of N_2O_4 is limited by the fact that it is being used in a bottoming cycle where the efficiencies of both primary and secondary cycles must be considered when optimizing overall plant efficiency. A good example of this is the use of regenerative heaters for which the Russian literature claims a significant increase in efficiency. The use of regenerative heaters in N_2O_4 bottoming cycles did indeed increase the secondary-cycle efficiency, but in order to attain maximum overall plant efficiency, it was necessary to increase the primary-cycle compressor inlet temperature (the N_2O_4 heater minimum hot-side temperature). This produces a reduction in primary-cycle efficiency such that the resultant overall plant efficiency is actually reduced.

2.3.3. Component Design

The design characteristics of the major components of a typical N_2O_4 bottoming cycle were evaluated. The specific system which was evaluated was for twin 4000-MW(t) GT-HTGRs with an ROT of 950°C (1742°F), a recuperator which was sized for a system which uses an ammonia bottoming cycle, a minimum helium temperature of 60°C (140°F), and an N_2O_4 bottoming cycle based on a simple cycle with no regenerative heating, i.e., Cycle 1 of Section 2.3.2.

Figure 2-14 shows a schematic of the bottoming cycle, along with typical operating conditions of the major components.

A heat transfer analysis was carried out to establish a preliminary size for the precooler. The precooler geometry was assumed to be the same as that in the ammonia binary cycle. The heat transfer correlation for the N_2O_4 (tube side) was based on experimental results for N_2O_4 heated inside smooth tubes (see Ref. 2-6). This correlation accounts for the effects of heat transfer enhancement due to diffusion through the concentration gradient

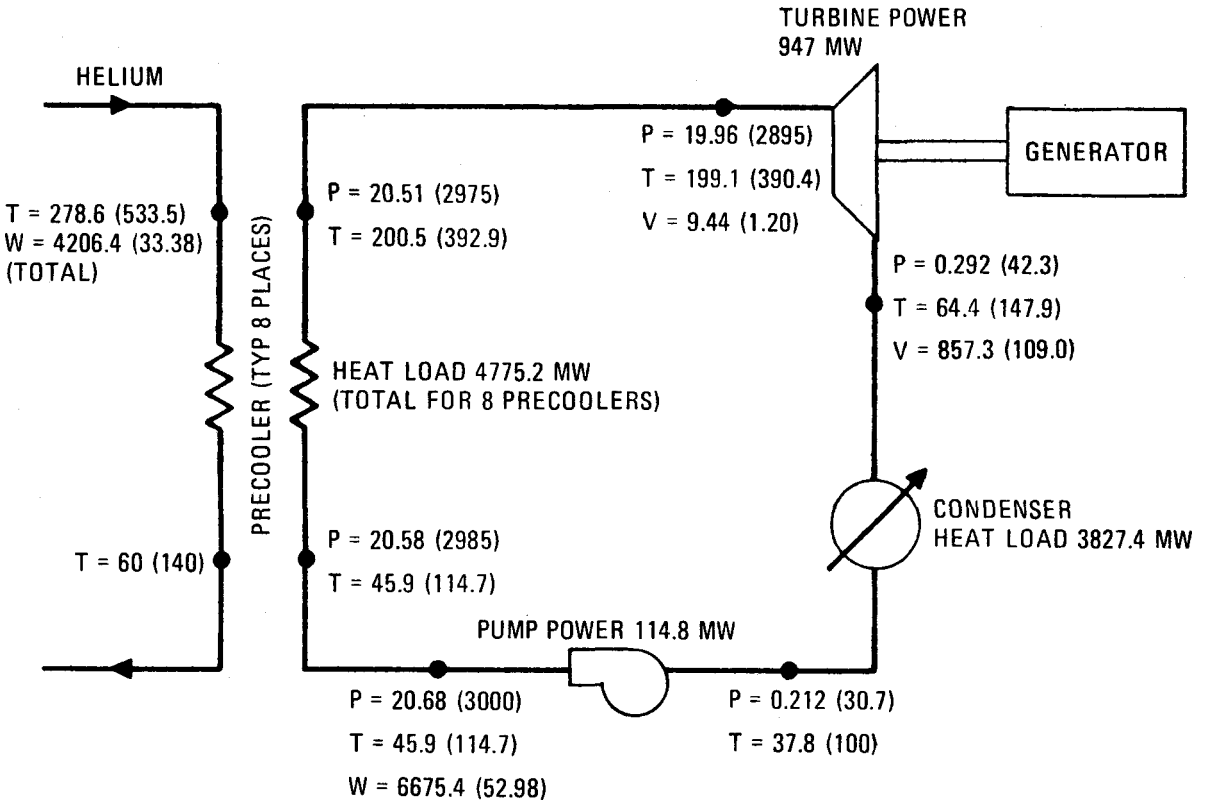

P – PRESSURE – MPa (PSIA)

T – TEMPERATURE – ^{o}C (^{o}F)

W – MASS FLOW RATE – KG/SEC (LB/HR X 10^{-6})

V – VOLUME FLOW RATE – CM^3/SEC X 10^{-6} (FT^3/HR X 10^{-6})

GA-A13950

Fig. 2-14. Typical N_2O_4 bottoming cycle operating conditions

produced by dissociation. The average overall heat transfer coefficient was 0.01899 cal/sec-cm^2-°C (140 Btu/hr-ft^2-°F). This compares with an average value for the helium/ammonia precooler of 0.02211 cal/sec-cm^2-°C (163 Btu/hr-ft^2-°F). The resulting precooler heat transfer area was 23,225.8 m^2 (250,000 ft^2) for each of eight precoolers. This compares with a helium/ammonia precooler heat transfer area of 40,700.8 m^2 (438,100 ft^2). The helium/N_2O_4 precooler was smaller because of greater temperature differences between the fluids. The overall average log mean temperature difference for the helium/N_2O_4 precooler was 32.4°C (58.3°F). This compares with a helium/ammonia precooler overall average of 15.8°C (28.4°F).

A preliminary sizing of the N_2O_4 power turbine resulted in a two-stage high-pressure turbine followed by two dual-flow turbines each with two stages. Figure 2-15 shows a diagram of this turbine configuration.

The high-pressure turbine has an inlet diameter of 0.859 m (2.82 ft) and a first-stage blade height of 4.298 cm (1.692 in.). The low-pressure turbines each have two 1.34-m (4.4-ft)-diameter outlets with a last-stage blade height of 40.1 cm (15.8 in.).

The ammonia binary-cycle turbine is a seven-stage, split-flow machine with two outlets. The N_2O_4 turbine requires more outlets because of the higher outlet volume flow rate, i.e., three times greater than that of the ammonia turbine. Fewer outlets would require an increase in outlet diameter with resulting exhaust energy and stress levels which are unacceptable. The N_2O_4 turbine requires more than one casing because for the large increase in volume flowrate, i.e., a factor of 90.8, a single-casing configuration is not feasible. The N_2O_4 turbine requires fewer stages than the ammonia turbine because the enthalpy drop across the turbine is much lower. The ammonia turbine has an enthalpy drop of 82.8 cal/g (149 Btu/lb), and the N_2O_4 turbine has an enthalpy drop of 38.0 cal/g (68.5 Btu/lb).

A preliminary design of the N_2O_4 condenser was established by a computer code which optimizes heat rejection system components. The condenser is made

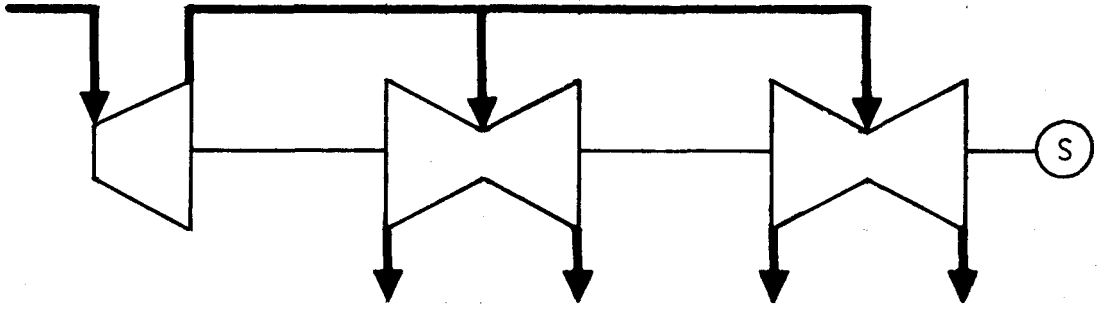

GA-A13950

Fig. 2-15. Turbine configuration

up of two U-tube, shell-and-tube-type heat exchangers with water flowing inside the tubes and N_2O_4 desuperheating and condensing in cross flow over the tube banks.

The overall dimensions of each of two condenser shells are: length = 18.9 m (62 ft), width = 10.3 m (33.8 ft), and height = 14.3 m (46.9 ft). By comparison, the ammonia condenser is made up of 24 cylindrical shells, each with a length of 12.8 m (42 ft) and a diameter of 4.57 m (15 ft). The overall heat transfer area of the N_2O_4 condensers is 277,610 m^2 (2,988,200 ft^2). The overall heat transfer area of the ammonia condensers is 224,352 m^2 (2,414,900 ft^2). The high condensation pressure of the ammonia, i.e., the design pressure of 2.07 MPa (300 psia) dictates a condenser design which has cylindrical shells. The shell diameter was dictated by shipping requirements. The N_2O_4 condenser has a design pressure of approximately 0.345 MPa (50 psia), and it was assumed that a more conventional rectangular shell configuration could be used.

Table 2-5 shows additional design data for the condensers. Each condenser has a large desuperheating section to remove the 26.6°C (47.9°F) of turbine exhaust superheat.

The vapor system for the N_2O_4 system is similar in design to the ammonia vapor system. Pipe diameters for the N_2O_4 system are smaller than those of the ammonia system because of lower volume flow rates. The turbine inlet volume flow rate for the N_2O_4 system is 9.44×10^6 cm^3/sec (1.20×10^6 ft^3/hr). This is a factor of 4.1 less than the ammonia system turbine inlet volume flow rate.

The N_2O_4 condensate system also has a lower volume flow rate than that of the ammonia condensate system. The N_2O_4 feed pump inlet volume flow rate is 4.767×10^6 cm^3/sec (0.606×10^6 ft^3/hr), which is 14% less than the ammonia feed pump inlet volume flow rate.

TABLE 2-5
N_2O_4 CONDENSER DESIGN DATA (TYPICAL FOR TWO CONDENSERS)

	Desuperheating Section	Condensing Section
Heat duty, MN	454.1	1,459.6
N_2O_4 flow rate, kg/sec (lb/hr x 10-6)	3,337.7 (26.49)	3,337.7 (26.49)
Water flow rate, kg/sec (lb/hr x 10^{-6})	7,513.4 (59.63)	24,148 (191.65)
Water inlet temperature, °C (°F)	20.3 (68.5)	20.3 (68.5)
Water temperature rise, °C (°F)	14.4 (26.0)	14.4 (26.0)
Condensate temperature, °C (°F)	—	37.8 (100.0)
Condensation pressure, MPa (psia)	—	0.212 (30.7)
LMTD, °C (°F)	24.6 (44.2)	8.3 (14.9)
Tube o.d., cm (in.)	3.175 (1.25	3.175 (1.25)
Total surface area, m^2 (ft^2)	39,186 (421,800)	99,620 (1072,200)

2.3.4. Practical Considerations

2.3.4.1. Chemical Reaction Kinetics of N_2O_4 Power Cycle. In the N_2O_4 power cycle, the following reactions take place:

$$N_2O_4 \rightleftharpoons 2NO_2 \rightleftharpoons 2NO + O_2$$

The first reaction, the dissociation of N_2O_4, is quite rapid and N_2O_4 and NO_2 are in equilibrium. The second reaction, the dissociation of NO_2, is much slower and equilibrium may not exist except at high temperatures. However, equilibrium concentrations of NO and O_2 are so small that rates of reaction for the second reaction are unimportant.

Equilibrium concentrations and rates of reaction have been calculated for the turbine inlet and outlet conditions to determine whether it is necessary to take into account nonequilibrium conditions in the power cycle. The results are shown in Table 2-6. Table 2-6 shows that the concentrations of NO and O_2 are very small in the power cycle and that, for all practical purposes, the dissociation of NO_2 to NO and O_2 can be neglected. The equilibrium gas mixtures at power cycle conditions are essentially N_2O_4 plus NO_2. The rates of reaction shown were calculated for equilibrium concentrations for the forward reaction. At equilibrium, the rates of reaction for forward and reverse reactions are equal, and there is no net change of concentration with time. The rates of reaction when compared with concentrations do give a measure of the rate at which equilibrium is approached if concentrations initially are displaced from equilibrium. For example, in the case of the outlet conditions, if the gas were all N_2O_4 (concentration = 1.039×10^{-4} mole/cm^3), 0.293×10^{-4} mole of N_2O_4 would decompose to give equilibrium concentrations of N_2O_4 and NO_2 in about 2×10^{-11} sec. Since these calculations were performed for the low-temperature part of the cycle and since the rate of reaction increases with temperature, N_2O_4 and NO_2 are always at equilibrium in the power cycle.

It is concluded that it is not necessary to take into account nonequilibrium reaction conditions in the power cycle.

TABLE 2-6
KINETIC DATA AT TURBINE INLET AND OUTLET[a]

	Turbine Inlet			Turbine Outlet		
Pressure, MPa (psia)	19.96 (2895)			0.292 (42.3)		
Temperature, °C (°F)	202 (395)			65 (148.8)		
	Equilibrium Concentration			Equilibrium Concentration		
	M %	Moles/cm^3	$dc/d\Theta$, Moles/(cm^3-sec)	M %	Moles/cm^3	$dc/d\Theta$, Moles/(cm^3-sec)
N_2O_4	19.2	0.973×10^{-3}		43.6	0.453×10^{-4}	1.68×10^{-16}[b]
NO_2	80.2	4.068×10^{-3}	2.70×10^{-5}[c]	56.4	0.586×10^{-4}	6.26×10^{-12}[c]
NO	0.4	0.021×10^{-3}		0.03	2.68×10^{-8}	
O_2	0.2	0.011×10^{-3}		0.01	1.34×10^{-8}	
Totals	100.0	5.073×10^{-3}		100.0	1.039×10^{-4}	

[a] Calculations based on ideal gas law and data for equilibrium constants and reaction rate constants given in Ref. 2-7.

[b] For reaction $N_2O_4 \rightarrow 2NO_2$

[c] For reaction $2NO_2 \rightarrow 2NO + O_2$

2.3.4.2. Impact of N_2O_4* Properties. The following properties of the working fluid in the N_2O_4 combined cycle must be considered in a plant design:

1. Toxicity
2. Reaction with moisture and organics
3. Reaction with metals (corrosion)

N_2O_4 gas is extremely toxic since it reacts with water to give nitric acid (Ref. 2-8). Animals exposed to a concentration of one part per thousand die in a few minutes. Concentrations greater than five parts per million are harmful. N_2O_4 is classed as a poisonous gas in Interstate Commerce Commission regulations and is shipped as a liquid at 0.1 MPa (14.7 psi) in high-pressure steel cylinders (Ref. 2-9).

The reaction of N_2O_4 with water produces nitric and nitrous acids which are very corrosive. Reaction with certain organics may take place to produce water and then, subsequently, the above acids (Ref. 2-8). The reaction with organics may also produce explosive products (Ref. 2-8). The only class of organics compatible with N_2O_4 are the perfluoro and fluorochloro compounds (Ref. 2-10).

The above properties of N_2O_4 have the following effects on plant design:

1. Because of the toxicity of the gas, equipment must be leak-tight (the order of "soap bubble" leak tightness), and areas housing equipment should be well-ventilated. Transfer from shipping containers to plant storage should preferably be done outdoors.

2. Equipment should be cleaned internally essentially to LOX standards to be free of moisture and organics.

*Hereinafter N_2O_4 means the equilibrium mixture of N_2O_4 and NO_2.

3. Selection of organics which can come in contact with N_2O_4 either internally or externally (such as a result of leaks) should be made with care or, where possible, avoided. For example, fluorocarbons may be best for lubricants and inorganics for insulation.

4. Equipment should be designed for vacuum as well as the working pressure. This aids in eliminating air, moisture, etc., before charging with N_2O_4 to minimize formation of nitric and nitrous acids.

The corrosion of metals by N_2O_4 is caused by either the formation of nitric and nitrous acids or the action of the oxide as an oxidizing agent. In the absence of moisture or organics no acids are formed, and this source of corrosion is eliminated. The oxide with less than 0.1% moisture is not corrosive to mild steel at ordinary temperature and pressure (Ref. 2-9). The presence of 0.3 to 10 wt % of nitric acid in the oxide (due to moisture or organics) can increase, sometimes by a factor of 10, the corrosion rate of stainless steels (Ref. 2-10). A number of metals are highly resistant to N_2O_4 because of protective oxide films formed on their surfaces (Ref. 2-10).

The Russians have studied the corrosion resistance of a large number of metals to N_2O_4 (Ref. 2-10). Most of their data are for stainless steels, which they favor for equipment in a nuclear power plant using N_2O_4 as a coolant. Such a choice was based on corrosion rates at temperatures of up to 700°C (1292°F). In the N_2O_4 combined-cycle considered here, the maximum temperature is about 200°C (392°F). In the case of stainless steels, the corrosion rates decrease with increasing temperature and increase with increasing pressure. On the basis of relatively fewer data, corrosion rates for other metals appear, in general, to vary with temperature and pressure, just the reverse. It appears that carbon steels, low-alloy steels, and stainless steels may all be satisfactory materials, at least up to 200°C (392°F) for use with N_2O_4.

It is concluded that considerations of toxicity, reaction with moisture and hydrocarbons, and reaction with metals have no insoluble impact on the design or cost of a N_2O_4 combined-cycle plant.

2.3.5. Recommendations

The studies described in this section have shown that N_2O_4 can produce overall combined-cycle efficiencies equivalent to those for the ammonia combined-cycle plant. Component sizes have been studied, and N_2O_4 has an advantage over NH_3 in the sizes of the precooler and the condenser. On the other hand, N_2O_4 is a very strong oxidizing agent, chemically very reactive, and much more toxic than ammonia. It also has more unresolved questions with respect to the choice of component materials and lubricants and the resolution of safety problems necessary to achieve licensability. For these reasons, the use of N_2O_4 as a bottoming-cycle fluid is not considered to offer enough incentives to change from the choice of ammonia and to give up the technology developed thus far.

2.4 PRIMARY AND SECONDARY SYSTEM DESIGN

2.4.1. Reference and Alternate Plant Cycle Conditions

At the beginning of CY-1976, studies were undertaken to identify and define plant configurations having improved economic incentives over the then reference design exemplified in drawing SK-169D (Fig. 5-2 of Ref. 2-1). That configuration was a 3000-MW(t), single-unit plant and was characterized by horizontal turbomachines [3 x 1000 MW(t) each] lying along radial vectors, by heat exchangers having cylindrically shaped modules, by a compressor pressure ratio of 2.35 at an ambient air temperature of 23.9°C (75°F), and by a peak system pressure of 6.89 MPa (1000 psia) and an ROT of 816°C (1500°F).

Improvements were identified in various areas including delta or square arrangement of the PCRV (see Section 4), upscaling to a 4000-MW(t) reactor size in a twin-unit plant, hexagonally packed heat exchanger modules (see Section 8), and permissible increases in top pressure, compressor pressure ratio, and ROT (see Section 7). These improvements were integrated into a new reference design and several alternate designs after suitably selecting other system parameters and component sizes to minimize the total power generating cost. The increased fuel cycle cost due to the higher price of uranium was taken into account in the selection process. Consequently, the selection has strongly emphasized high plant efficiency.

This section presents the parameters for three alternate dry-cooled (single-cycle) plants. An additional alternative design is the binary-cycle plant, which is described in Section 2.4.2.

The flow schematic and the thermodynamic cycle of the new reference dry-cooled GT-HTGR plant are illustrated in Fig. 2-16, sheet 1. The plant has a regenerative closed loop for its power conversion and an ROT of 850°C (1562°F). Sheet 2 of Fig. 2-16 lists mass flows, temperatures, and pressures of the primary helium loop and the secondary water heat rejection loop. Table 2-7 lists the performance and operating parameters of major significance. Each 4000-MW(t) power system generated 1604 MW(3) for net station efficiency of 40.1%.

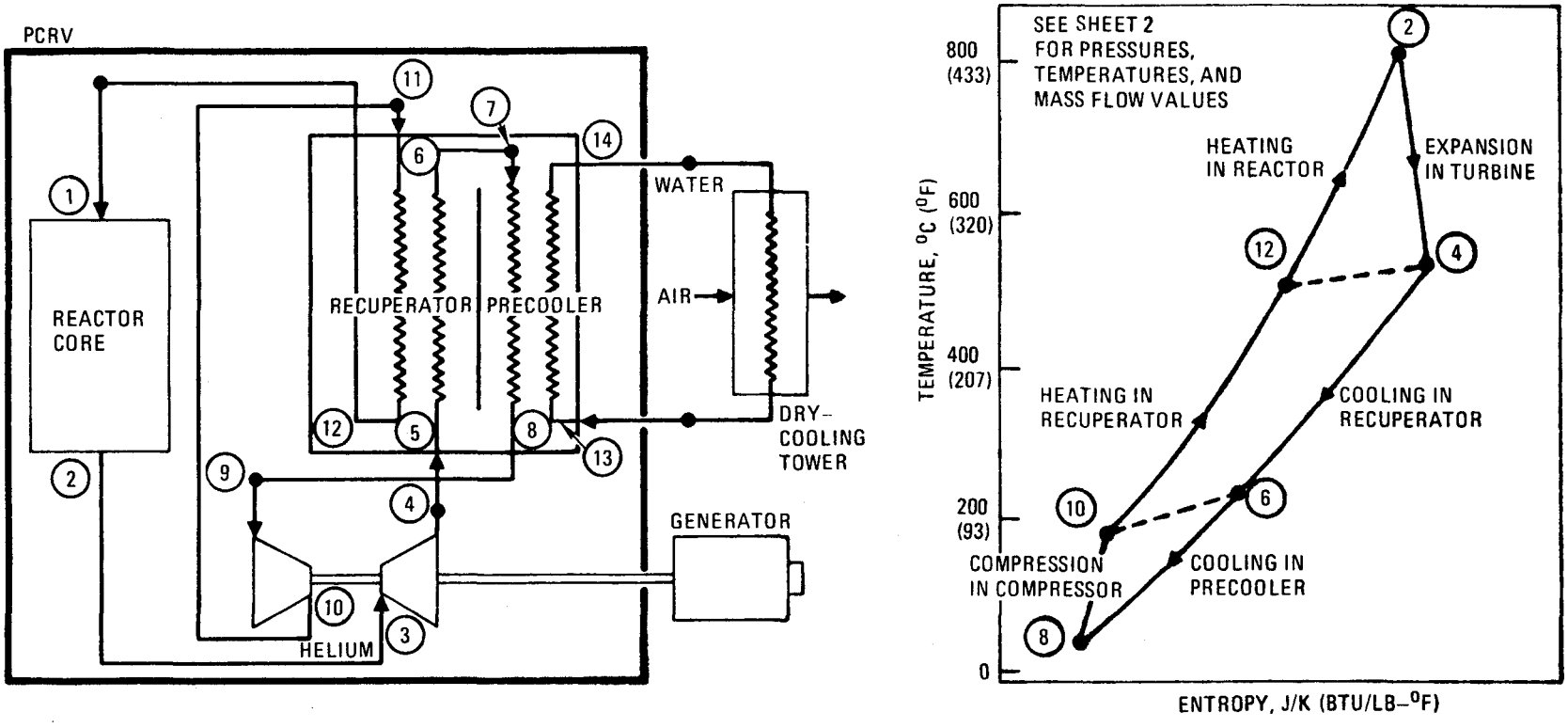

GA-A13950

Fig. 2-16. Flow schematic and heat cycle of dry-cooled GT-HTGR (sheet 1 of 2)

HELIUM LOOP PRESSURES, TEMPERATURES, AND MASS FLOWS

			PRESSURE, MPa (PSIA)	TEMPERATURE, °C (°F)	FLOW/LOOP,* KG/SEC (LB/HR)
1.	REACTOR:	INLET	7.78 (1128)	506 (943)	2,237 (17,754,000)
2.		OUTLET	7.66 (1111)	850 (1562)	2,237 (17,754,000)
3.	TURBINE:	INLET	7.62 (1105)	850 (1562)	559 (4,438,000)
4.		OUTLET	3.28 (476)	544 (1012)	573 (4,552,000)
5.	RECUPERATOR/LOW PRESSURE:				
		INLET	3.26 (473)	544 (1012)	574 (4,559,000)
6.		OUTLET	3.22 (467)	221 (430)	574 (4,559,000)
7.	PRECOOLER:	INLET	3.21 (466)	221 (430)	574 (4,559,000)
8.		OUTLET	3.19 (462)	26 (79)	574 (4,559,000)
9.	COMPRESSOR:	INLET	3.17 (460)	26 (79)	575 (4,566,000)
10.		OUTLET	7.93 (1150)	175 (347)	575 (4,566,000)
11.	RECUPERATOR/HIGH PRESSURE:				
		INLET	7.87 (1141)	175 (347)	559 (4,438,000)
12.		OUTLET	7.80 (1132)	506 (943)	559 (4,438,000)
13.	COOLING WATER:	INLET		21 (69)	932 (7,396,000)
14.		OUTLET	2.00 (290)	168 (334)	932 (7,396,000)

*4 LOOPS IN EACH REACTOR.

GA-A13950

Fig. 2-16. Flow schematic and heat cycle of dry-cooled GT-HTGR (sheet 2 of 2)

TABLE 2-7
TWIN 4000-MW(t), DRY-COOLED GT-HTGR MAJOR PERFORMANCE AND OPERATING PARAMETERS FOR 850°C (1562°F) REFERENCE CYCLE

Turbine inlet temperature	850°C (1562°F)
Compressor pressure ratio	2.50
Compressor inlet temperature	26°C (79°F)
Compressor discharge pressure	7.93 MPa (1150 psia)
System pressure loss ratio	0.0703
Recuperator effectiveness	0.898
Turbine isentropic efficiency	91.5%
Compressor isentropic efficiency	89.0%
Turbine disk cooling flow[(a)]	2.50%
Turbomachine bypass leakage[(a)]	0.3%
Recuperator plus precooler bypass leakage[(a)]	0.5%
Generator efficiency	98.8%
Primary system heat loss	2 x 17.6 Mw(t)
Station auxiliary power	2 x 14 Mw(e)
Station efficiency	40.1%
Net electrical output	2 x 1604 Mw(e)
Reactor thermal power	2 x 4000 Mw(t)
Compressor helium flow rate per loop	575 kg/sec (4,566,000 lb/hr)
Ambient temperature	15°C (59°F)

[(a)] All bypass flows based on compressor flow rate

One alternate plant has twin reactors of 3000 MW(t) each with an ROT of 850°C (1562°F). The 3000-MW(t) plant is configured with three loops using PCL components identical to those specified for the 4000-MW(t) reference plant. Thus, cycle temperatures, pressures, and helium flows per loop are the same as those shown in Fig. 2-16. Each 3000-MW(t) plant generated 1200 MW(e) for a net station efficiency of 40.0%.

Increasing the top-cycle temperature leads directly to higher power plant efficiency, by approximately 3% per 100°C (180°F). Both the reactor core and the turbomachinery are capable of achieving much higher temperatures; indeed, the HTGR core is known for its high-temperature capability. The advanced state of the art for open-cycle turbomachinery indicates that adequate research and development can extend permissible turbine inlet temperatures for the helium turbine far beyond the 850°C (1562°F) value used in this assessment. Two additional alternate designs at an ROT of 950°C (1742°F) have therefore been examined. Of primary interest is the twin 4000-MW(t) configuration. The performance of this plant is shown in Table 2-8. The remaining alternate, a twin 3000-MW(t) plant at 950°C (1742°F) ROT, is configured with three loops using PCL components identical to those of the 950°C (1742°F) ROT, twin 4000-MW(t) plant. The efficiency of this twin 3000-MW(t) plant is 42.8%.

2.4.2 Binary-Cycle Design Arrangements and Parameters

When cooling water is available, significant additional power can be produced economically from the helium-cycle waste heat. General Atomic has studied various Rankine power cycle fluids and has selected ammonia as the working fluid for this secondary power cycle. Optimization studies have shown that, to minimize the power generation cost of the binary-cycle plant, modest changes to the helium power conversion equipment are necessary. To take full advantage of the economy of scaling to higher powers, only one ammonia turbine is specified, even for twin plants.

TABLE 2-8
TWIN 4000-MW(t), DRY-COOLED GT-HTGR MAJOR PERFORMANCE AND OPERATING PARAMETERS FOR 950°C (1742°F) ALTERNATE CYCLE

Turbine inlet temperature	950°C (1742°F)
Compressor pressure ratio	2.50
Compressor inlet temperature	26°C (79°F)
Compressor discharge pressure	7.93 MPa (1150 psia)
System pressure loss ratio	0.067
Recuperator effectiveness	0.915
Turbine isentropic efficiency	91.5%
Compressor isentropic efficiency	89.0%
Turbine disk cooling flow[(a)]	4.0%
Turbomachine bypass leakage[(a)]	0.3%
Recuperator plus precooler bypass leakage[(a)]	0.5%
Generator efficiency	98.8%
Primary system heat loss	2 x 19.8 MW(t)
Station auxiliary power	2 x 14 MW(e)
Station efficiency	42.9%
Net electrical output	2 x 1716 MW(e)
Reactor thermal power	2 x 4000 MW(t)
Compressor helium flow rate per loop	531 kg/sec (4,218,000 lb/hr)
Ambient temperature	15%C (59°F)

[(a)] All bypass flows based on compressor flow rate

2.4.2.1. Performance and Cycle Parameters. The flow schematic of the 4000-MW(t), binary-cycle GT-HTGR is illustrated in Fig. 2-17, sheet 1. As shown, the ammonia power cycle takes heat from the helium-cycle at about 250°C (483°F) and produces additional electric power. Sheet 2 of Fig. 2-17 lists mass flows, temperatures, and pressures of the helium and ammonia cycles. The dry-cooled and binary-cycle plants have comparable primary system parameters, except for the helium temperatures of the binary-cycle version, which are higher in the compressor and heat exchanger sections of the loop. Each 4000-MW(t) power system generated 1923 MW(e) for a net station effi-cicney of 48.1%.

2.4.2.2. Reactor-Turbine System. Table 2-9 gives a summary for the reactor-turbine system of the 4000-MW(t) plant. The precooler and recuperator sizes change from the dry-cooled plant designs. The precooler cavity diameters and active tube lengths increase from 4.9 m (16 ft) and 12.4 M (40.2 ft) for the dry-cooled plant to 5.3 m (17.25 ft) and 15.4 m (50 ft), respectively, for the evaporatively cooled binary-cycle plant. The recuperator cavity diameter remains the same for both plant designs; however, the active tube lengths decrease from 12.9 m (41.7 ft) for the dry-cooled, single-cycle plants to 11.1 m (36.1 ft) for the binary-cycle plant designs. PCRVs for the binary-cycle plants are correspondingly shorter and larger in diameter. Outside diameters and heights, respectively, are 41.8 m (137.1 ft) by 34.0 m (111.7 ft) for the 4000-MW(t) reactor and 37.5 m (123.1 ft) by 32.2 m (105.5 ft) for the 3000-MW(t) reactor. (Note that PCRV diameters quoted above are outside the panels, whereas Table 2-9 quotes diameters inside the panels.)

2.4.2.3. Ammonia Plant. The major systems for the secondary plant are as follows:

1. Circulating water system
2. Turbine/generator system
3. Vapor system

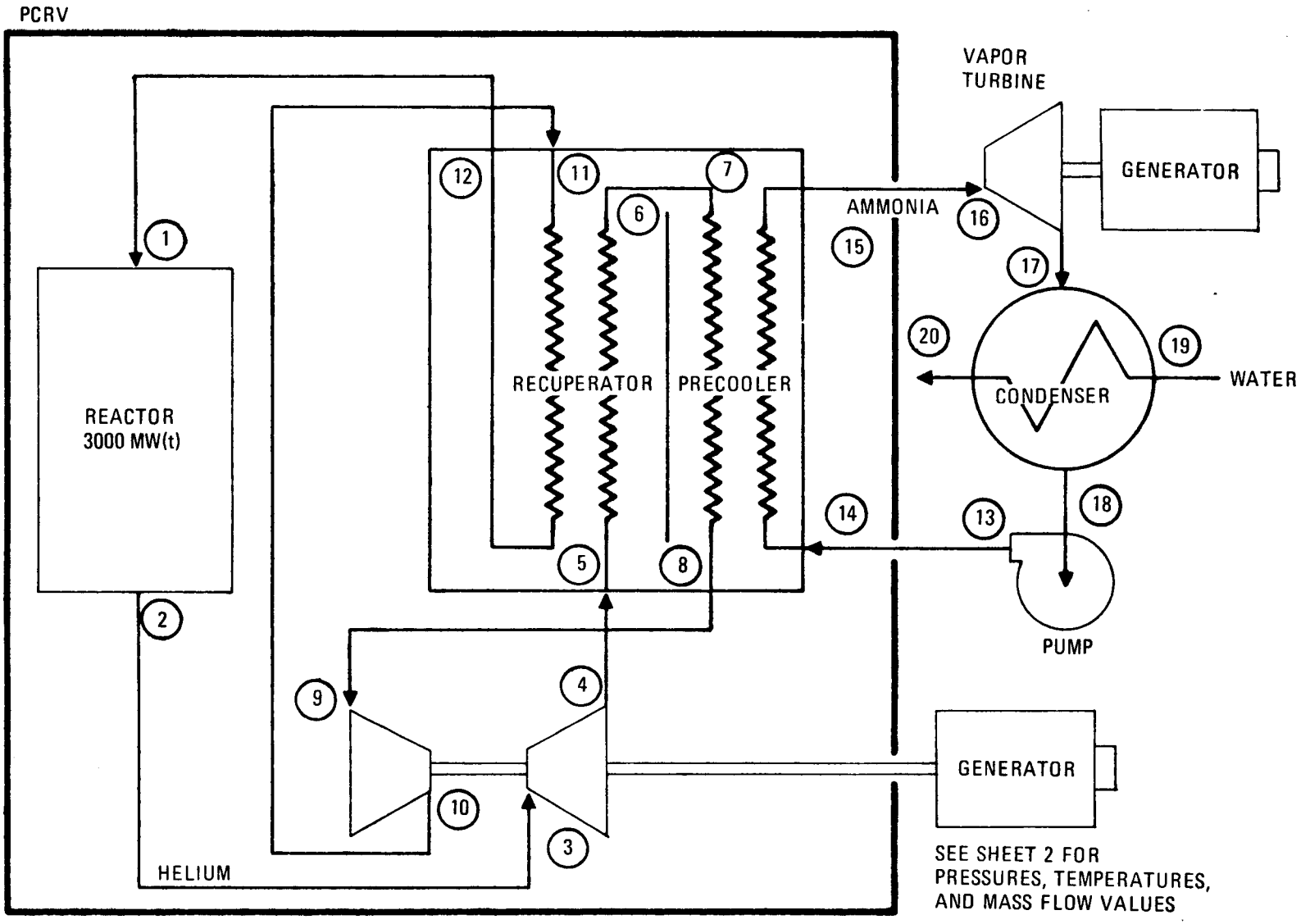

GA-A13950

Fig. 2-17. Flow schematic of binary-cycle GT-HTGR (sheet 1 of 2)

HELIUM AND AMMONIA LOOP PRESSURES, TEMPERATURES, AND MASS FLOWS

			PRESSURE MPa	PRESSURE (PSIA)	TEMPERATURE °C	TEMPERATURE (°F)	FLOW/LOOP KG/SEC	FLOW/LOOP (LB/HR)
1.	REACTOR:	INLET	7.8	(1128)	507.8	(946)	2,252	(17,837,000)
2.		OUTLET	7.7	(1111)	850.0	(1562)	2,252	(17,837,000)
3.	TURBINE:	INLET	7.6	(1105)	850.0	(1562)	563	(4,459,000)
4.		OUTLET	3.3	(476)	544.4	(1012)	577	(4,573,000)
5.	RECUPERATOR/LOW PRESSURE:							
		INLET	3.3	(473)	544.4	(1012)	578	(4,581,000)
6.		OUTLET	3.2	(467)	276.1	(529)	578	(4,581,000)
7.	PRECOOLER:	INLET	3.2	(466)	276.1	(529)	578	(4,581,000)
8.		OUTLET	3.2	(462)	64.4	(148)	578	(4,581,000)
9.	COMPRESSOR:	INLET	3.2	(460)	64.4	(148)	579	(4,587,000)
10.		OUTLET	7.9	(1150)	232.8	(451)	579	(4,587,000)
11.	RECUPERATOR/HIGH PRESSURE:							
		INLET	7.9	(1141)	232.8	(451)	563	(4,459,000)
12.		OUTLET	7.8	(1132)	507.8	(946)	563	(4,459,000)
14.	PRECOOLER:	AMMONIA INLET	16.9	(2444)	37.8	(100)	436	(3,456,000)
15.		AMMONIA OUTLET	16.8	(2434)	250.6	(483)	436	(3,456,000)
17.	CONDENSER:	AMMONIA	1.3	(188)	34.4	(94)	3,491	(27,648,000)*
19.		WATER INLET			19.4	(67)	104,293	(826,000,000)*
20.		WATER OUTLET			28.3	(83)	104,293	(826,000,000)*

*FOR TWIN 4000–MW(t) PLANT.

GA-A13950

Fig. 2-17. Flow schematic of binary-cycle GT-HTGR (sheet 2 of 2)

TABLE 2-9
REACTOR-TURBINE SYSTEM SUMMARY FOR TWIN
4000-MW(t), BINARY-CYCLE PLANT

Plant Arrangement	Reactor thermal rating, MW(t)	4000
	Number of reactors per plant	Twin arrangement
	Heat rejection	Binary-cycle plant
	Reactor outlet temperature, °C (°F)	850 (1562)
	Number of primary system loops per reactor	4
	Reactor power density, kW/liter	8.2
	Power conversion loop rating, MW(t)	1000
	Turbomachinery orientation	Horizontal
	Heat exchanger orientation	Vertical
PCRV	Arrangement (turbomachine positioning)	Square
	Diameter, m (ft) (inside panels)	40.42 (132.6)
	Height, m (ft)	34.05 (111.7)
	Hot duct replaceability	Yes
	Man access for turbomachinery bearing inspection	Yes
	Maximum system pressure, MPa (psia)	7.93 (1150)
Turbomachine	Turbomachine type	Single shaft
	Generator drive end	Compressor
	Diameter, m (ft)	3.51 (11.5)
	Length, m (ft)	11.58 (38)
	Approximate weight, kg (ton)	272,000 (300)
	Compressor pressure ratio	2.50
	Number of journal bearings	2
	Thrust bearing location	External to PCRV
Recuperator	Type (modular construction)	Tubular, axial flow
	Number per reactor	4
	Overall diameter, m (ft)	5.1 (16.75)
	Overall length, m (ft)	17.07 (56.0)
	Assembly weight, kg (ton)	353,740 (390)
	Tube material type	Ferritic 2-1/4 Cr - 1 Mo
	ASME Code class	Section VIII
Precooler	Type (modular construction)	Tubular, axial flow
	Number per reactor	4
	Coolant fluid	Ammonia (supercritical)
	Overall diameter, m (ft)	5.1 (16.75)
	Overall length, m (ft)	22.3 (73.0)
	Assembly weight, kg (ton)	689,340 (760)
	Tube material type	Medium carbon steel
	ASME Code class	Section VIII
Performance (ISO conditions)	Total plant power, MW(e)	3850
	Plant efficiency, %	48.1

4. Feed pump system
5. Condensate system

A general description of each of the above systems is given in this section.

2.4.2.4. Circulating Water System. The circulating water system provides the major means of rejecting heat, including the condensation of exhaust ammonia from the turbine/generator and feed pump turbines and heat rejected from other turbine plant equipment such as generator coolers, turbine lubricating oil cooler, exciter, etc. The circulating water system consists of the circulating water pumps, cooling tower, piping, and accessories.

The heat load imposed on the system at rated operating conditions is approximately 3873 MW(t) (13,220 BTU/hr).

The natural-draft evaporative cooling tower design parameters were selected on the basis of an optimization of the condenser/cooling tower combination. The results of this study indicate that a 10°C (18°F) approach and a 8.9°C (16°F) range based on an ISO dry bulb temperature of 15°C (59°F) [50% relative humidity and 9.7°C (49.5°F) wet bulb temperature] are near the economic optimum and are feasible from an engineering viewpoint. Because of the heat duty, two towers would be required.

The total circulating water flow is 104,290 kg/sec (826 x 10^6 lbm/hr) for the twin 4000-MW(t) binary plant.

In order to provide operating flexibility and remain within the capacity limitations of proven pump designs, the twin 4000-MW(t) plant requires 18 pumps.

The large-diameter water piping between the cooling towers and the ammonia condensers would be of concrete. The smaller ammonia piping is carbon steel or fiberglass-reinforced plastic (FRP).

2.4.2.5. Ammonia Turbine/Generator System. This sytem consits of the ammonia turbine/generator, auxiliaries, and the turbine/generator foundation. One dual-flow power turbine is utilized in the secondary plant. The power turbine output shaft work is 1113 MW for the twin 4000-MW(t) binary-cycle plant. The inlet turbine conditions are 250°C (483°F) and 16.1 MPa (2344 psia). The exit conditions are 34.4°C (94°F) and 1.3 MPa (188 psia), with a flow rate of 3232 kg/sec (25.2 x 10^6 lbm/hr). The generator efficiency was taken at 98.6%.

The turbine/generator control is a combination of turbine following and turbine bypass. Under normal operation, the turbine controls must be capable of following the precooler heat load, and, in addition, when the primary plant is tripped, the secondary plant must also drop load. Therefore, turbine bypass is utilized in this mode of control.

2.4.2.6. Secondary Vapor Systems. The secondary vapor system conveys the supercritical ammonia vapor produced in the precoolers to the secondary power turbine and feed pump turbine drives. It also includes the manifolding between the turbine exhaust and the condenser.

The vapor lines from each precooler have two precooler isolation valves, one on each side of the containment building wall. The precooler flows are then headered into a single line to the turbine. A turbine stop valve is located in the turbine inlet line to isolate the turbine during a turbine trip or a load rejection.

A vapor bypass circuit provides piping, valves, and equipment between the main vapor line and the flash tank and from the flash tank to the condenser. This bypass is utilized during startup to provide vapor for the secondary turbine. In addition, the flash tank circuit is used in a desuperheating mode when the power turbine is bypassed during a plant loss of load condition.

The feed pump turbine drives have vapor piping and valves connecting them to the main vapor line. Each branch line leading to the feed pump turbines includes a fast-acting stop valve to interrupt the vapor flow in the event of a turbine overspeed, a throttling control valve operated by the feed pump turbine speed controller, and a bypass around each feed pump turbine with a control valve to maintain automatically a constant pressure ratio across the turbine at all speeds within the normal operating range.

2.4.2.7. Condensate System. The condensate system consists of the condenser, condensate pumps, condensate storage tank, main feed pumps, booster feed pumps, piping, and valves. This system transfers the condensed ammonia from the condenser to the ammonia heater.

The condenser was sized on the basis of an optimization study of the total heat rejection system (i.e., cooling tower, circulating water pumps, and piping). The condenser is a shell-and-tube-type heat exchanger with the water flowing inside the tubes and ammonia condensing in cross flow over the tube banks. Because of the relatively high condensation pressure of ammonia, multiple shells are utilized. Each shell was constrained to a maximum diameter of 4.6 m (15 ft) and a maximum weight of 318,180 kg (350 ton), which are the limitations imposed for shop assembly and shipment. Details of the condenser design are given in Section 2.5.1.

Electric motor-driven condensate pumps are used to transfer the condensate from the hot well to the booster feed pump inlet. The booster feed pumps and main feed pumps are turbine-driven and deliver the ammonia to the precoolers at 16.8 MPa (2440 psia).

2.5. PLANT AND COMPONENTS DESIGN

2.5.1. Condenser Mechanical Design

Before proceeding with the mechanical design, a brief survey of steam condenser design and ammonia refrigeration practice was made, the results of which are summarized below.

2.5.1.1. Steam Condenser Experience. With the exception of a paper machine dump condenser, all of the steam condensers described in the references examined are structurally different from the proposed design because of the low shell-side pressure.

The above steam dump condenser is a shell-and-tube heat exchanger with a flat top bundle to provide for steam access and circular impingement baffles on top of the tubes under the inlet nozzles. There are multiple condensate drains in the bottom of the shell. While the shell side of a steam condenser is a different structural problem than the proposed ammonia unit, the tube sizes, permissible velocities, and fouling factors for plain tubes should be of the same order, and in these matters relevant industry standards were complied with.

In mechanical construction, transport, and field erection, steam condensers provide little guidance except to emphasize that once the cost penalty of multiple single shells and connecting piping is accepted, shipping and erection problems seem insignificant in contrast to those of a conventional large steam condenser which must be field assembled.

Two relevant problems discussed in the literature are water box corrosion and tube vibration, and these should be studied in any final design program.

Steam condenser practice is relevant in tube alloy selection, even though the use of ammonia rules out any copper-bearing alloys. References indicate that Type 304 stainless steel (SS) should be suitable for a cooling

tower system with adequate water chemistry control and would be recognized as such by most utility managements. Neither Type 316 SS nor titanium seem justified, and type 410 SS, while listed in the Heat Exchanger Institute Standard for Steam Surface Condensers, is not discussed in the literature on installations.

In steam condensers, pressure drop is very undesirable because it reduces turbine output and also reduces the heat transfer coefficient. The latter effect should not be important in the ammonia condenser case because, at the operating pressure of 1.24 MPa (180.6 psia) the change in density due to pressure drop is negligible.

The tube arrangement of a steam condenser has access lanes or clearances formed by leaving out tubes in the tube field. It will be seen that this feature was provided for to some extent in the ammonia condenser, and it is expected that the ultimate supplier will develop this feature further. Some of these passages in a steam condenser provide steam for deaerating and heating condensate.

Deaerating is not a problem with ammonia, but having the condensate leave at the steam condensing temperature instead of being cooled to the coolest water temperature should be as great a thermal advantage in an ammonia system as in a steam system.

2.5.1.2. Refrigeration Experience. One thing that seemed questionable was having the high-pressure ammonia on the shell side and the low-pressure water in the tubes. It is usually less expensive to have the high-pressure fluid in the tubes, but the key factor seems to be water-side fouling. Cleaning of the tube bores, at least by conventional methods, is much easier than cleaning the shell side. It is possible that a condenser could be built where the tubes would extend across an open channel containing the water. In this case cleaning would be by a water jet or brushes positioned by a moving bridge that would span the channel. Time did not permit the investigation of this alternative. In spite of the potential savings of the cost of shells, it is not clear whether there would be any net economic

gain. Small ammonia condensers with the water on the outside were common at one time, and some were mentioned where the coils were immersed in a body of water and removed periodically for cleaning.

From the published literature, the most significant large ammonia refrigeration installation was that used to cool the concrete at Boulder Dam. This installation had three shell-and-tube condensers which were four-pass units 6.2 m (20 ft) long, each having 420 25.4-mm (1-in.) tubes. The ammonia was on the shell side, and there was a cooling tower in the water circuit. It was reassuring to see that the largest ammonia system found in the literature had the same features as the system proposed here.

In discussing noncondensible gasses in ammonia systems, one reference attributes their presence to air inleakage at parts of the system that are subatmospheric and to decomposition of the refrigerant or lubrication oil at the high temperatures attained in the compressor. Consistent purging of these gasses is necessary for condenser efficiency, and that was provided for in the original study. It was evident that this is a very minor matter compared with the problem of air in a conventional condenser. The normal operating condenser pressure of 1.24 MPa (180.6 psia) and the offensive nature of leaking ammonia make air inleakage improbable once the system is in operation.

There appears to be no deaeration problem as there is with water, and the rate of decomposition was evaluated and found to present no problems.

According to another reference, extended surface tubes are becoming increasingly popular for water-cooled refrigeration condensers. The extended surface referred to as of the low fin type on the shell or refrigerant side. High water velocities are used in the tubes, and frequent tube cleaning is necessary if cooling water quality is poor.

2.5.1.3. Description of the Proposed Design. This study proposes units whose general construction follows low-pressure feedwater heater practice. The 4.57-m (15-ft) shell diameter, chosen as a shipping limit, is the same

as that of the Westinghouse PWR steam generators, and the dry weight of each of the 24 condenser units, which is about 272,000 kg (300 ton), is comparable to the 318,000 kg (350-ton) weight of the steam generators. Barge shipment is the most applicable means of transport, as it is for the PWR units.

The U-tube configuration seemed to be a more conservative way of providing for expansion between tubes and shell than a floating head or shell expansion joint.

The thick shell required for the 2.06-MPa (3000-psi) design pressure probably rules out the shell joint, and it was felt that a floating head design on so large a unit might have leakage problems. Leakage of even a small amount of ammonia into the cooling tower water would not be acceptable, and the U-tube design was therefore the logical choice. It may be of interest to note that both conventional low-pressure feed heaters and PWR steam generators are U-tube heat exchangers.

The ammonia condenser units are designed like low-pressure feedwater heaters in accordance with ASME Code, Section VIII, Division 1 and TEMA-C standards. The assumed shell material was SA-285, Grade C, and the tubesheet material was SA-201, Grade A. The tubes are Type 304 SS, 28.5 mm (1.125-in.) o.d. and 1.24-mm (0.049-in.) wall, modified to a four-flute, configuration in the heat transfer areas. The U-bend section and the tubesheet section are left plain, as are short areas 3.05 m (10 ft) apart where the tube passes through the second and fourth support plates.

The principal performance parameters are summarized in Table 2-10. The ammonia condenser unit proper is shown in Figs. 2-18 and 2-19. A possible support structure is shown in Fig. 2-20. Each condenser train consists of three units mounted one above the other as shown in Fig. 2-20. The ammonia vapor from the turbine comes in at the top of the top unit, and an equal amount is assumed to condense in each unit and be drawn off as a liquid through the four nozzles at the bottom of each shell.

Figure 2-18 shows horizontal and vertical sections and an end view of the top unit. Figure 2-19 is a cross section A-A taken through the vapor

TABLE 2-10
PRELIMINARY DESIGN DATA FOR GT-HTGR BINARY-CYCLE PLANT
CONDENSER [TWIN 4000-MW(t) REACTOR]

Plant	Reactor thermal rating, MW(t)	Twin 4000-MW(t) arrangement
	Number of condensers/plant	24
	Heat exchanger type	Tubular
	Type of construction	Shell and tube
	Flow configuration	U-tube, cross flow (shell)
	Orientation	Horizontal
Thermal Data	Heat transfer Q, MW(t)/plant	3873
	LMTD, °C (°F)	7.16 (12.9)
	Conductance UA/plant, MW/°C (Btu/hr-°F)	540.4 (1025×10^9)
	Ammonia pressure loss, kPa (psi)	8.96 (1.3)
	Water pressure loss, kPa (psi)	103.4 (15)
Surface Geometry	Number of passes	2
	Tube type	Spirally corrugated
	Tube o.d., mm (in.)	28.5 (1.125)
	Tube wall thickness, mm (in.)	1.24 (0.049)
	Number of tubes/unit	11388
	Effective tube length, m (ft)	9.3 (30)
	Surface area/plant, m^2 (ft^2)	224,358 (2.4149×10^6)
	Maximum metal temperature, °C (°F)	32.2 (90)
	Operating internal pressure differential, MPa (psi)	0.93 (135)
	Tube material type	304 SS
	ASME Code class	Section VIII
	Safety class	Nonnuclear
Overall Assembly	Shell design pressure, MPa (psig)	2.06 (300)
	Normal operating pressure, MPa (psia)	1.24 (180.6)
	Maximum vapor temperature, °C (°F)	48.9 (120)

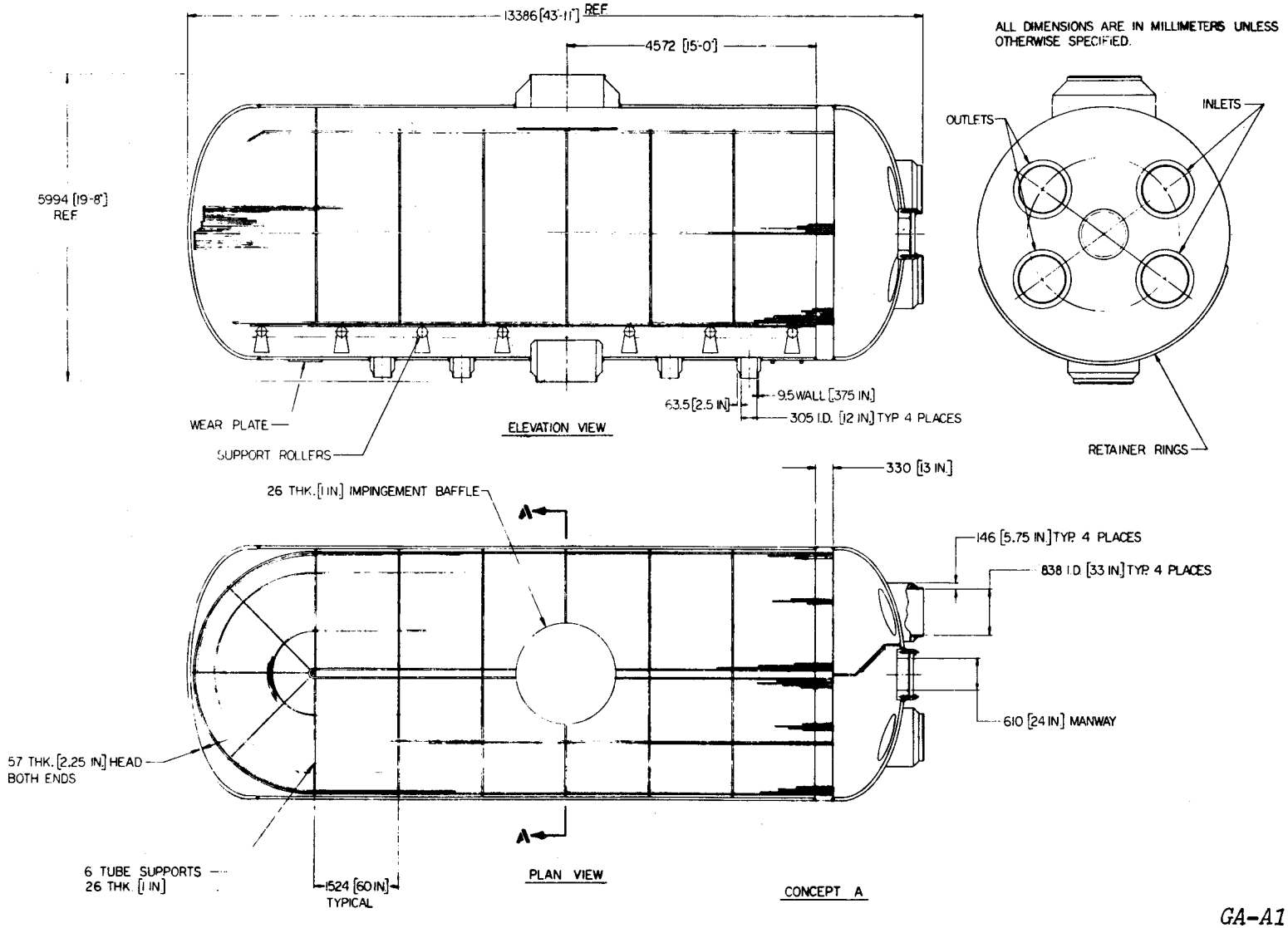

Fig. 2-18. Ammonia condenser (horizontal and vertical sections and end view of top unit)

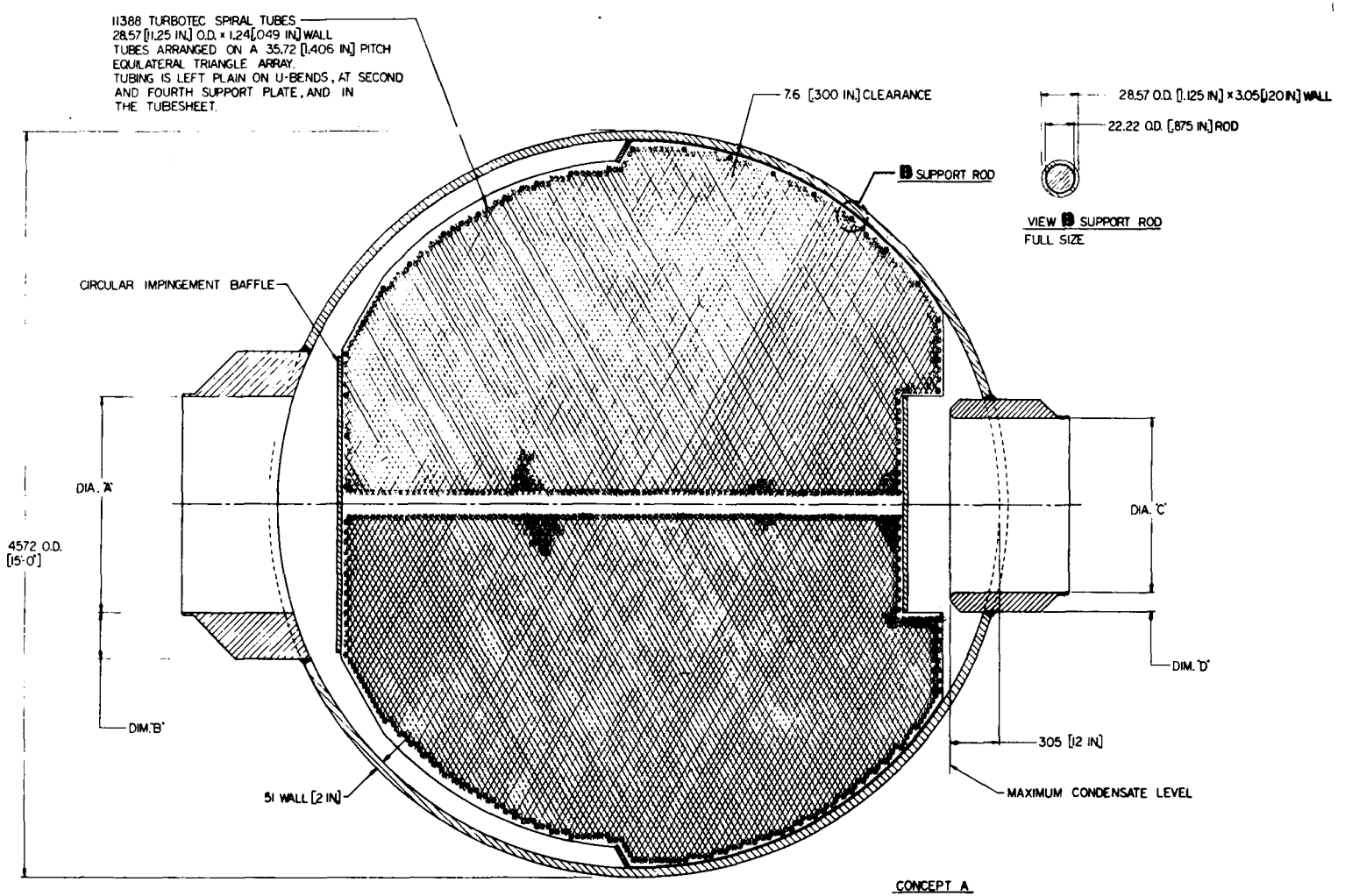

CONDENSER	DIA. A	DIM. B	DIA. C	DIM. D
UPPER (AS SHOWN)	1321 mm 52 in.	279 mm 11 in.	1067 mm 42 in.	114 mm 4.5 in.
MIDDLE	1067 mm 42 in.	229 mm 9 IN.	762 mm 30 in.	83 mm 3.25 in.
LOWER	762 mm 30 in.	165 mm 6.5 in.	—	—

NOTE

ALL DIMENSIONS ARE IN MILLIMETERS
UNLESS OTHERWISE SPECIFIED.

GA-A13950

Fig. 2-19. Ammonia condenser (section A-A)

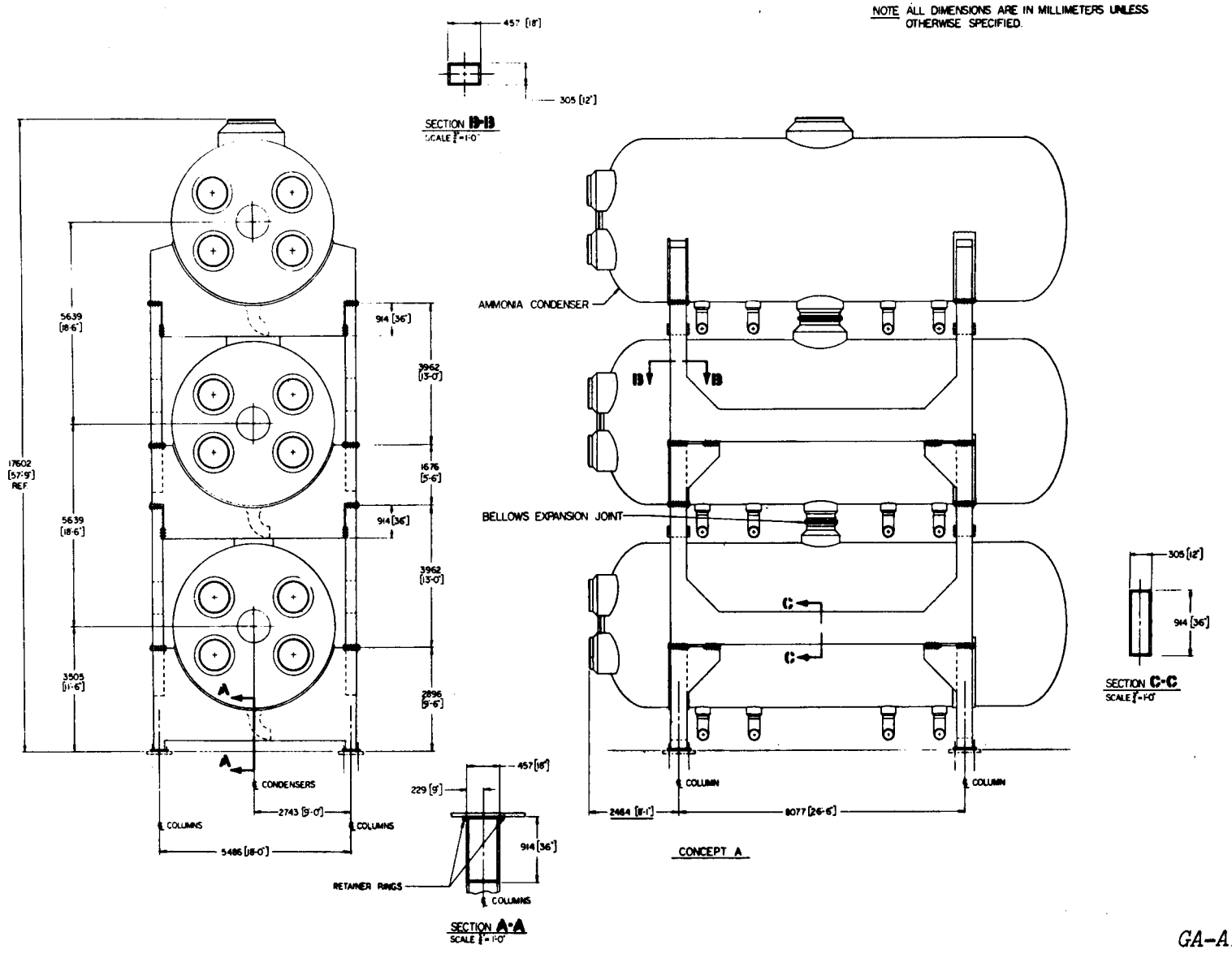

Fig. 2-20. Ammonia condenser support structure

nozzles. The U-tubes are in the horizontal plane, with the cooling water entering at one side and leaving at the other. Two inlet and two outlet pipes were provided to keep the pipe size and entry openings small, but the sizes will make it easy to provide for two half-size water circuits if they are considered desirable. On the ammonia side, the vapor enters the top nozzle and is deflected by the circular impingement plate. It then divides, some of it flowing down the sides of the bundle in the spaces shown in Fig. 2-19 and some of it entering the center part of the bundle through the void formed by the inner U-tubes. The vapor thus enters the tube field from several directions so that bypass and pressure drop are minimized. The condensate collects at the bottom of each shell below the projection of the vapor outlet nozzle shown in Fig. 2-19. The bundle is held together by tie-bolts and spacers between the support plates, which is the normal construction for a shell-and-tube heat exchanger bundle. The bundle can be removed in the same manner as in a feedwater heater bundle by cutting the inner shell-to-tubesheet weld and pulling it out on the rollers shown in Fig. 2-18. It is expected that the tube support plates at the U-bend will be a builtup construction in accordance with the manufacturer's standard design.

As shown in Fig. 2-20, each unit sits in two saddles positioned against earthquake forces by two retaining rings welded to the shell which prevent horizontal movement relative to the front saddle. At the rear saddle, the shell, which is weaker because it is not stiffened by the tubesheet, is reinforced by a wear plate. The supports and bearing plates are designed in accordance with the American Institute of Steel Construction standards.

The support design shown in Fig. 2-20 is subdivided into modular sections for ease of transport and sequential erection. The intent was that the external size of the box sections would be held constant and the plate thickness varied as the load increased from top to bottom or from one earthquake zone to another. Trial calculations indicate that plate thicknesses are satisfactory, even for pessimistic seismic assumptions.

2.5.2. Ammonia Turbine Design

2.5.2.1. Summary. This section summarizes the conceptual design study of an ammonia turbine for the advanced GT-HTGR plant with 950°C (1742°F) ROT. With heat rejection from the twin 4000-MW(t) reactors, the power recoverable from the waste heat plant (binary cycle) is on the order of 920 MW(e). The designs presented are based on a turbine inlet temperature and pressure of 250°C (481°F) and 16.1 MPa (2334 psia), respectively. The designs outlined are very conceptual in nature and were carried out to (1) check the efficiency level used in the cycle calculations, (2) develop an understanding of some of the performance and mechanical design problems, (3) solicit vendor inputs in the areas of feasibility and cost, and (4) enable the preparation of a binary-cycle plant layout to be made.

The conceptual designs have been calculated using supercritical ammonia properties from Ref. 2-11. The mechanical designs reflect modern steam turbine practice. A double-flow arrangement was chosen for the following reasons: (1) it minimizes thrust balancing requirements; (2) it results in low values of blade stresses; and (3) the double-exhaust arrangement is well-suited to the piping configuration for the multiplicity of condenser shells. The main emphasis was placed on a single turbine design of 920 MW(e), but, from the availability and practicality standpoints, two turbines may be necessary; accordingly, two 460-MW(e) units were evaluated. Compared with modern steam plants, the ammonia turbine is a compact unit and is analogous to the HP section of a modern power generating utility steam turbine.

The tentative results show that the efficiency value of 90% used in the cycle calculations should be realizable for a large ammonia turbine. For the seven-stage, double-flow design, efficiency values above 90% were predicted, but they are unrealistic and should be regarded with circumspection. The small blade heights are an inherent feature of a supercritical NH_3 turbine and are of concern because of the tip clearance effects (and general end-wall losses that adversely affect the efficiency). However, blades with a lower aspect ratio and at higher hub-tip ratios are not uncommon in steam

turbine practice. While it is not expected that the gas flow path geometries will be changed significantly with specialized vendor design attention, industry assessment of the turbine efficiency potential will be valuable.

In the mechanical design, the blading stress levels are commensurate with a machine life of 280,000 hr. Turbine layouts (see Figs. 2-21, 2-22, and 2-23) were prepared to get an appreciation for the overall size of the ammonia turbine. In this phase of the program, the mechanical design aspects of the rotor, bearings, seals, and structure were not addressed, and in these areas, inputs from a turbine company with experience in large power generating machinery are necessary.

2.5.2.2. Principal Design Parameters. The design parameters listed below have to be selected in order to define the ammonia turbine geometry and system. The nondimensional parameters such as ϕ, ψ, N_s, and D_s^*, permit one to pinpoint a high efficiency region of design alternatives. Table 2-11 gives the nondimensial turbine parameters for preliminary sizing, and Table 2-12 gives the nomenclature of terms.

The aerodynamic considerations are:

1. Height of first-stage blades
2. Distribution of work in stages
3. Flow coefficient = $\phi = Va/U$
4. Stage loading coefficient = $\psi = gJ\Delta H/U^2$
5. Specific diameter = $D_s = D\,(J\Delta H)^{1/4}/(V_s\dot{m})^{1/2}$
6. Specific speed = $N_s = N\,(V_s\dot{m})^{1/2}/(J\Delta H)^{3/4}$
7. Mach number at exit

The mechanical considerations are:

1. Height of last-stage blades
2. Type of rotor construction (drum type, welded, bolted, etc.)
3. Type of turbine casing (single or double casing, horizontal or vertical split)

*N_s and D_s are not strictly nondimensional as defined but conform to prevalent usage.

TABLE 2-11
NONDIMENSIONAL TURBINE PARAMETERS FOR PRELIMINARY SIZING

1. Flow coefficient = $\phi = \frac{Va}{U}$

2. Stage loading coefficient = $= \frac{gJ\Delta H_{st}}{U^2} = \frac{C_0^2}{2U} = \frac{g(1800)}{(\pi N_s D_s)^2}$

3. Velocity ratio = $\frac{U}{C_0} = \frac{1}{\sqrt{2\psi}} = \frac{N_s D_s \pi}{\sqrt{2g\ 60}}$

4. Volume coefficient or Gulp factor = $\frac{Q}{\omega D^3} = \frac{\pi}{2}\phi\xi$

5. Centrifugal stress coefficients (for untapered blade) = $\bar{\sigma} = \frac{\text{Blade centrifugal stress}}{\frac{\gamma\omega^2 D^2}{g}} = \frac{\xi}{2}$

6. Hub-tip ratio = $\varepsilon = \frac{\text{Hub diameter}}{\text{Tip diameter}} = \frac{1-\xi}{1+\xi}$

7. Specific speed = $N_s = \frac{N\,Q^{1/2}}{(J\Delta H)^{3/4}} = \frac{60\,g^{3/4}}{\sqrt{\pi}} \frac{(\xi\phi)^{1/2}}{\psi^{3/4}}$

8. Blade height/mean diameter = $\xi = \frac{1-\varepsilon}{1+\varepsilon}$

9. Specific diameter = $D_s = \frac{D(J\Delta H)^{1/4}}{Q^{1/2}} = \frac{1}{\sqrt{\pi}\sqrt{g}} \frac{\psi}{(\xi\phi)^{1/2}}$

10. Solidity = $\frac{\text{Blade chord}}{\text{Blade pitch}}$

11. Blade aspect ratio (AR) = $\frac{\text{Blade height}}{\text{Blade chord}}$

12. Tip clearance ratio = $\frac{\text{Tip clearance}}{\text{Blade height}}$

TABLE 2-12
NOMENCLATURE

ΔH	=	heat drop, KJ/kg (Btu/lb)
U	=	blade speed, m/sec (ft/sec)
Va	=	axial velocity, m/sec (ft/sec)
$\phi = \frac{Va}{U}$	=	flow coefficient
$\psi = \frac{gJ\Delta H_{st}}{U^2}$	=	stage loading coefficient = $\frac{\Sigma V_u}{U}$
σ_c	=	centrifugal stress in blading, MPa (psi)
R	=	degree of reaction
Q	=	turbine exhaust volume flow
D	=	mean diameter of stage
J	=	mechanical equivalent of heat, ft-lb/Btu
v_s	=	specific volume
m	=	mass
γ	=	specific weight of blade material, N/m^3 (lb/ft^3)
ω	=	rotational speed, rad/sec
C_0	=	spouting velocity, m/sec (ft/sec)
st	=	stage (subscript)
V_u	=	tangential velocity component, m/sec (ft/sec)

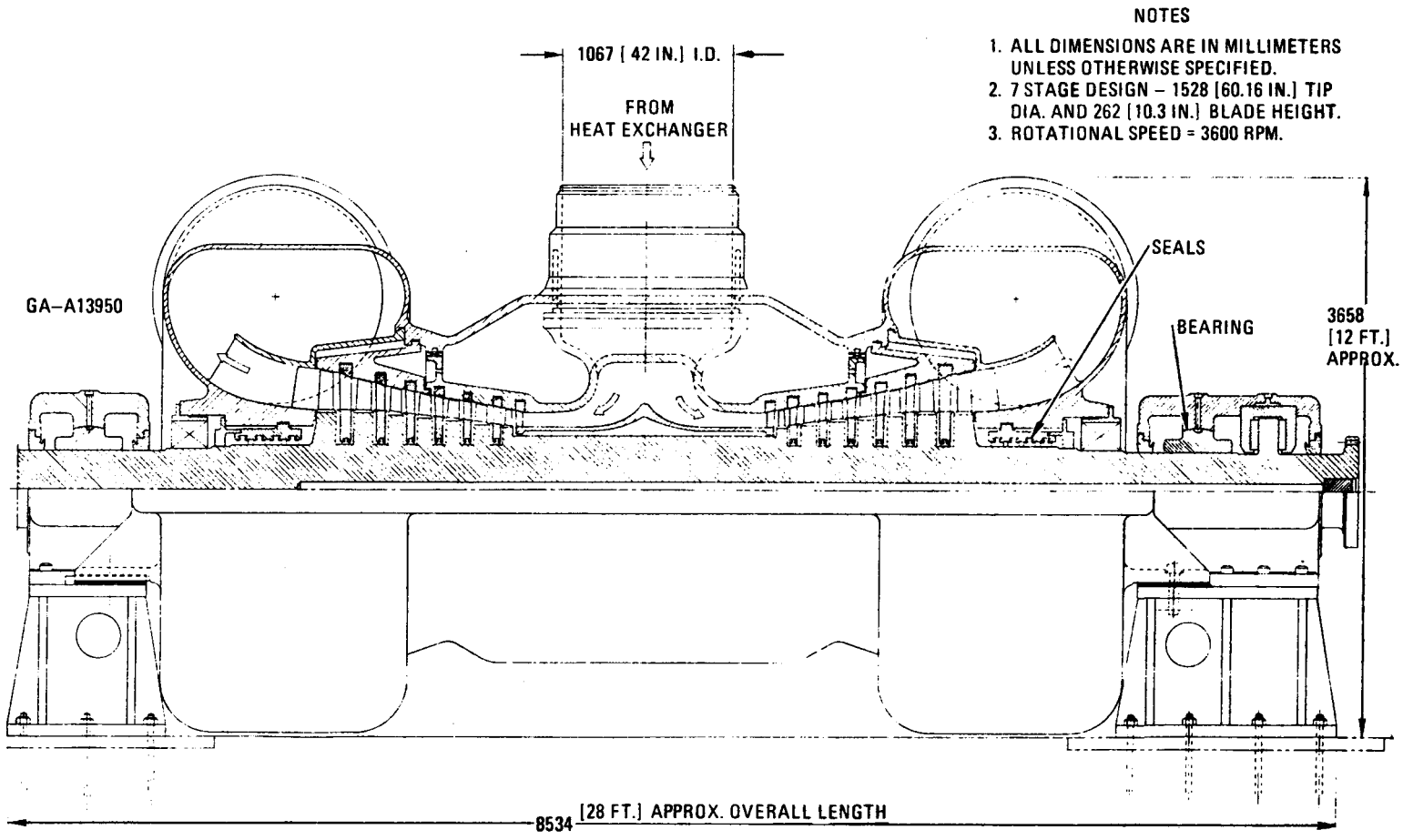

Fig. 2-21. Conceptual 920-MW(e), dual-flow NH_3 turbine design for twin 4000-MW(t), 950°C ROT GT-HTGR (elevation view)

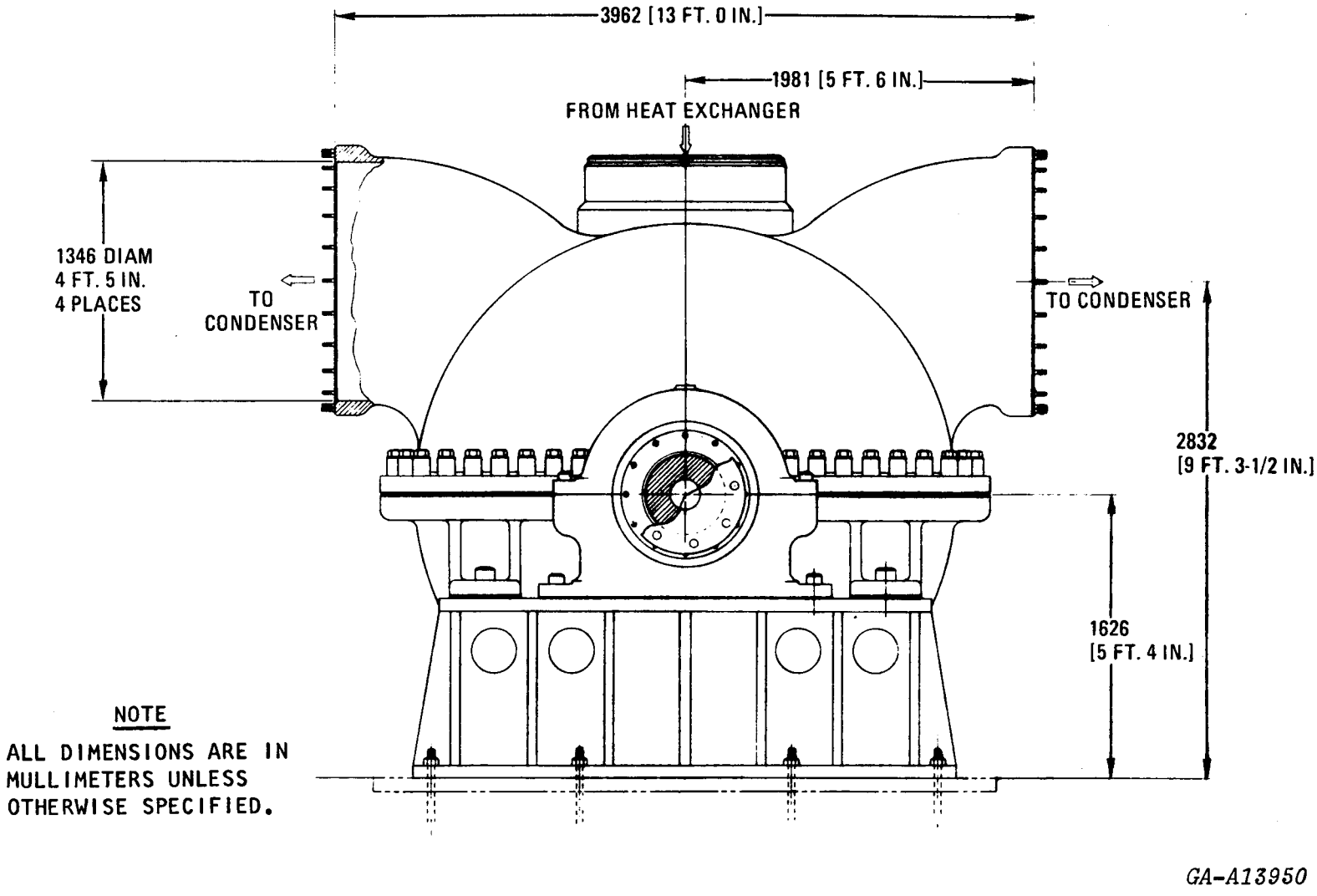

Fig. 2-22. Conceptual 920-MW(e), dual-flow NH_3 turbine design for twin 4000-MW(t), 950°C ROT GT-HTGR (end view)

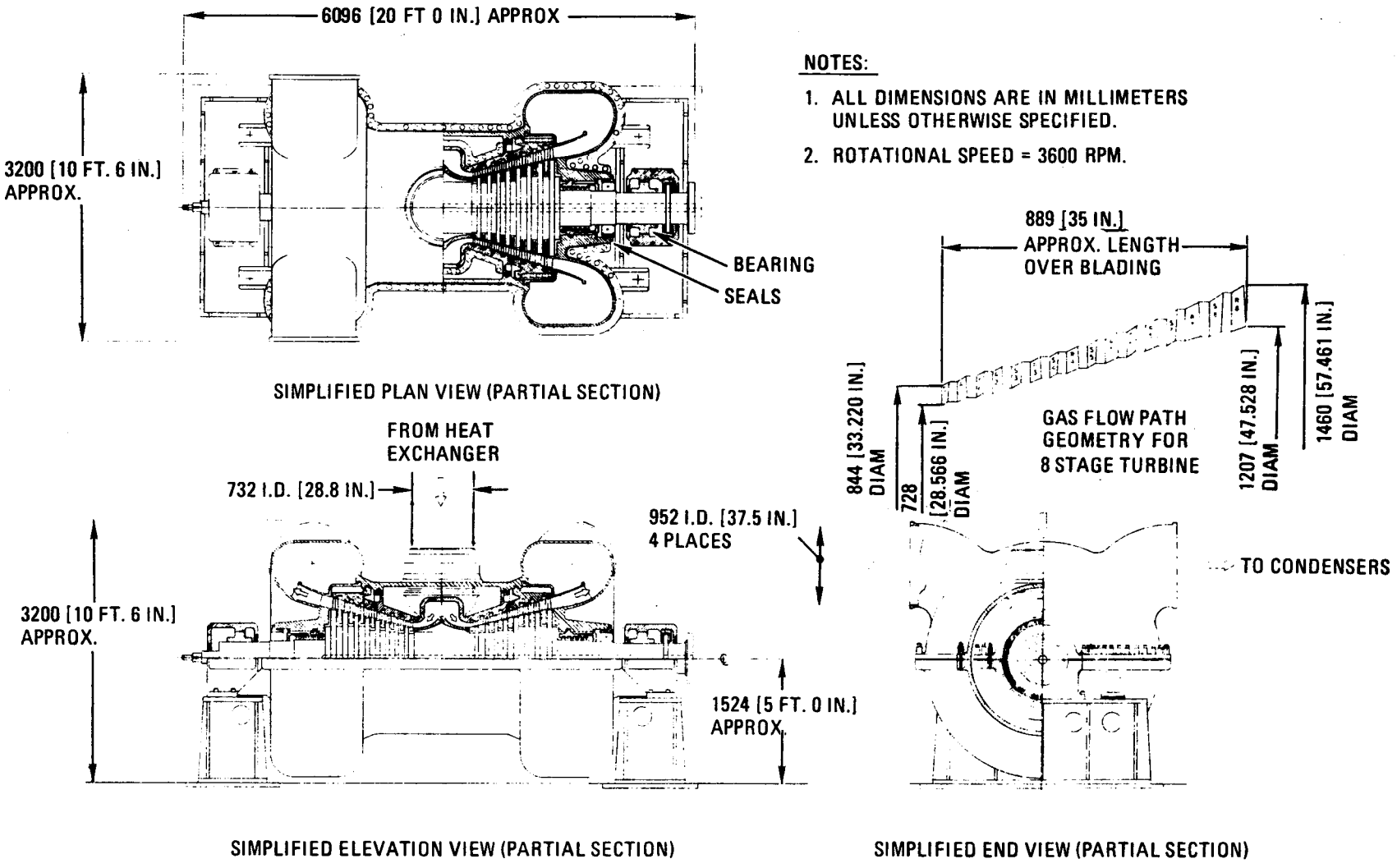

Fig. 2-23. Conceptual 460-MW(e), dual-flow NH_3 turbine design for twin 4000-MW(t), 950°C ROT GT-HTGR

4. Examination of possible rotor and blade dynamics problems
5. Bearing system definition (plain journal, tilting pad)
6. Materials and stress allowables
7. Centrifugal stress in the blade

2.5.2.3. Turbine Aerodynamic Design Considerations. Unlike the helium turbine or the air-breathing turbines, the NH_3 turbines are not limited by the stresses in the first-stage blading as a result of the low temperatures obtained at the inlet to the turbine. However, it is still necessary to have as high a blade speed as possible in order to reduce the number of stages to a minimum, which increases the stress on the last-stage blades of the turbine. There are several constraints on the design, some of which are imposed on the turbine by the cycle conditions, such as shaft speed, mass flow rate, and temperature and pressure ranges, for a certain (given) output at the turbine shaft (see Table 2-13). Other constraints are imposed on the turbine by the requirements of a good design. One such constraint is the choice of relative magnitudes of ψ (= $gJ\Delta H_{st}/U^2$), the stage loading coefficient, ϕ (= Va/U). Performance analysis of a large number of turbine rig tests produces an empirical relationship between these parameters and efficiency (Fig. 8 of Ref. 2-13) turbine stages of varying reaction and outlet swirl. The efficiencies as drawn have been corrected for zero tip leakage. Most of the measured efficiencies shown are for stages with axial entry velocity, ∿20% to ∿30% reaction, and some swirl in the exhaust. This figure shows that if high efficiency is the sole criterion, the optimum values ψ and ϕ are between 0.5 and 0.6, respectively, in order to lie in the highest efficiency region. It will be shown that in this design this is difficult to achieve without incurring the penalties of a larger number of stages. In order to increase the height of the blade, it is necessary to choose smaller rotor diameters. However, there is a constraint on the minimum value of rotor diameter that can be chosen. There are universal characteristics of each type of turbomachine which can be used to guide the conceptual design for various types of fluids and for a wide range of thermodynamic conditions. Figure 15 in Ref. 2-14 shows the efficiency as a function of specific speed and specific diameter. These are parameters which characterize the flow conditions prevalent for a large class of turbomachinery. This curve limits the least diameter permissible consistent with

TABLE 2-13
AMMONIA TURBINE DATA

Item	GT-HTGR NH_3 Turbine	De Laval Study (Ref. 2-12)
Flow, kg/sec (lbm/sec)	3071 (6764)	1840 (4044)
Inlet temperature, °C (°F)	249.5 (481)	99 (210)
Inlet Pressure, MPa (psia)	16.1 (2334)	6.09 (882)
Expansion ratio	12.1	6.0
Gross power, MW(e)	920	230
Net power, MW(e)	893	200
Primary power, MW(e)	3088	N/A
Total power, MW(e)	3981	N/A
Specific power, MW(e)/(kg/sec) [hp/(lb/sec)]	0.291 (182.347)	0.1087 (68.11)
Turbine type	Axial split flow	Axial split flow
Exhaust volume flow, m^3/sec (ft^3/sec)	299.5 (10,577.5)	127.2 (4490)
Specific power, MW(e)/(m^3/sec) [MW(e)/(ft^3/sec)]	3.07 (0.087)	1.81 (0.051)

a high efficiency design and helps to determine the appropriate number of stages. In order to lie in the high efficiency island, one must have a specific diameter greater than or equal to about 0.6.

The range of permissible rotor diameters is not very large, since a high rotor diameter implies a high Mach number for a given flow coefficient. A high Mach number introduces irreversibilities into the thermodynamic process and therefore has a deleterious effect on the efficiency. In modern steam turbine practice, supersonic velocities in the rear stages are used without undue penalties on the efficiency of the stage. It is possible to avoid these high velocities in the ammonia turbine, and it is indeed beneficial, from the point of view of acceptable blade heights and hub-tip ratios, to maintain low values of axial velocity and flow coefficient as mentioned earlier. Table 2-11 summarizes useful nondimensional parameters and their interrelationships. Their usefulness lies in the fact that the performance of a turbine can be estimated by using the results of a geometrically similar turbine with the same specific speed, specific diameter, Reynolds number, and Mach number. Table 2-14 gives a preferred range of values for some of these parameters. These are merely intended as a guide, and values outside the ranges suggested are not uncommon in modern large steam turbines ($\sim$1000-MW(e) output). For example, the exhaust area limitation is based on the assumption of a prismatic blade (with no taper of its cross-sectional area). However, by using taper ratio values characteristic of modern steam turbine practice, the exhaust annulus area can be considerably increased (for the same blade centrifugal stress). Exhaust areas of 8 to 9 m^2 (86 to 97 ft^2) are widely used in large steam turbine sets. In the ammonia turbine, centrifugal stress in the last-stage blade is not excessive, even without the use of area tapering. This is precisely the kind of insight which is immediately available upon examination of the relatively low specific speed of the last stage.

Table 2-15 indicates some more features of the preferred designs of the ammonia turbine. Indicated are two cases, one for the single split-flow turbine (see Fig. 2-21) and the other for two units each of a split-flow type (see Fig. 2-23). The high efficiency requirements predicate a

TABLE 2-14
DESIGN PARAMETER ENVELOPES

First-stage blade height = h	h > 40 mm (1.6 in.)	Tip clearance losses (secondary flows)
Hub-tip ratio = $\varepsilon = \frac{D_{hub}}{D_{tip}}$	$0.9 > \varepsilon > 0.6$	Higher limit for first-stage blades; lower limit for last-stage blades.
Stage loading coefficient = $\psi = gJ\Delta H_{st}/U^2$	<2	Should be maintained at a low value (1) for high efficiency (to avoid highly cambered blades)
Flow coefficient = $\phi = Va/U$	<0.7	Should be maintained at a low value ($\approx$0.5) in high-pressure stages for reasonable blade height and in low-pressure stages to minimize exit loss
Specific speed (fps units) = $N_s = \frac{N \times Q^{1/2}}{(J\Delta H)^{3/4}}$	$300 > N_s > 100$	Tends to low values as a consequence of favorable thermodynamic properties of NH_3 at turbine exhaust
Specific diameter (fps units) = $D_s = \frac{D\ (J\Delta H)^{1/4}}{Q^{1/2}}$	$1.5 > D_s > 0.6$	Tends to high values; same reason as above
Exhaust area = A	$<2 \cdot m^2$ ($<21 \cdot ft^2$)	Centrifugal stress limit

TABLE 2-15
DESIGN PARAMETERS FOR AMMONIA TURBINE

Item	One Turbine		Two Turbines		De Laval Turbine (Ref. 2-12)	
	First Stage	Last Stage	First Stage	Last Stage	First Stage	Last Stage
Number of stages	7		8		4	
Flow coefficient	0.5	0.5	0.45	0.45	0.2031	0.2985
Stage loading coefficient	1	1	0.9	0.9	0.62	0.76
Tip diameter, m (in.)	0.962 (37.9)	1.532 (60.3)	0.844 (33.22)	1.46 (57.5)	1.209 (47.62)	1.418 (55.84)
Hub diameter, m (in.)	0.8 (31.5)	1.008 (39.7)	0.728 (28.67)	1.207 (47.53)	0.924 (36.38)	0.867 (34.16)
Blade height, mm (in.)	82.3 (3.24)	261.6 (10.3)	61.5 (2.42)	126.1 (4.966)	142.75 (5.62)	275.3 (10.84)
Hub-tip ratio	0.829	0.659	0.863	0.844	0.764	0.6117
Hub speed, m/sec (fps)	150.63 (494.2)	190.13 (623.8)	137.3 (450.35)	227.55 (746.6)	174.2 (571.5)	163.5 (536.5)
Tip speed, m/sec (fps)	181.63 (595.9)	288.7 (947.3)	159.1 (521.8)	275.1 (902.6)	228 (748)	267.4 (877.1)
Gas axial velocity, m/sec (fps)	83.06 (272.5)	119.7 (392.7)	66.66 (218.7)	113.1 (371.1)	40.86 (134)	64.3 (211)
Rotor blade chord, mm (in.)	63.35 (2.494)	75.4 (2.968)	37.52 (1.477)	49.6 (1.954)	76.2 (3.0)	114.3 (4.5)
Rotor blade aspect ratio	1.458	3.109	1.64	2.332	1.873	2.41
Hub solidity	1.489	1.507	1.494	1.479	—	2.09
Number of rotor blades	60	146	94	100	—	50
Specific speed, N_s	100.7	160.7	91.44	114.27	108.49	150.2
Specific diameter, D_s	1.0757	0.6742	1.2481	0.9992	1.2728	0.8258
Axial thrust, MN (lb)	0.916	(205,863)	0.604	(135,802)	—	
Turbine efficiency, η_{TS}	0.9146	—	0.926		0.85	
Centrifugal stress, MPa (ksi)	49.5 (7.176)	171 (24.8)	29.23 (4.24)	88.53 (12.84)	—	57.77 (8.67)
Rotor bending stress, MPa (ksi)	137.9 (20)	137.9 (20)	137.9 (20)	137.9 (20)	—	28.8 (4.17)
Tip flare	<15 deg	—	<15 deg		—	
Degree of reaction	0.5	—	0.55		0.69	0.62
Exhaust area, m^2 (ft^2)	—	2.5 (26.935)	—	2.648 (28.503)	—	1.977 (21.28)
$\frac{\text{Power output}}{\text{Exhaust area}}$, MW/m^2 (MW/ft^2)	—	367.6 (34.156)	—	347.4 (32.277)	—	116.3 (10.81)

large number of stages (Refs 2-15 and 2-16) and stage loading coefficients on the order of 1.0. The losses in a turbine stage are proportional to the stage loading coefficients and the camber of the blade (which is itself a function of ψ/ϕ). In order to arrive at a high efficiency configuration, it is desirable therefore to reduce ψ and increase the number of stages. The most economic design can be evaluated only after detailed optimization studies involving the cost of power generation. It would appear that, faced with the certainty of increasing power generating costs, the most economic turbine is a highly efficient machine. It was therefore deemed necessary to choose a high value of R for the ammonia turbine. This can be achieved only with a larger number of stages. Furthermore, in order to ensure adequate blade height and blade aspect ratio, the axial velocity must be maintained at a low value in the high-pressure stages where the specific volume is low. The resulting low value of ϕ implies a lower stage loading coefficient for the same efficiency.

Table 2-15 also highlights the compact nature of the resulting turbine when using a dense fluid such as ammonia. The power output/exhaust area of a typical modern steam turbine is on the order of 10.0 to 30.0 MW(e)/m^2 (1.0 to ~3.0 MW(e)/ft^2), whereas for the ammonia turbine it is an order of magnitude higher. This means that for the same power output one would expect the linear dimensions of an ammonia turbine to be two to five times smaller than those of a steam turbine. The reduction in cost is therefore substantial, especially when one considers the large development costs associated with the last-stage blades of present-day steam turbines.

2.5.2.4. Performance Estimation. To evaluate accurately the stage efficiencies and overall turbine efficiency, an existing computer code for steam turbine design was used after incorporating the thermodynamic properties of ammonia. The computer code evaluates blade geometries in each stage, stage efficiencies, and overall turbine (isentropic) efficiency. Evaluation of losses in the code is based on the tests of Ainley and Mathieson (Ref. 2-17) and the modifications thereto suggested by Dunham and Came (Ref. 2-18). These tests have been well-documented in the literature, and further modifications have been suggested by various authors (Refs. 2-15, 2-16, 2-19, and 2-20). One is referred to the literature for details of the same (Ref. 2-15).

Whether these loss correlations are the most appropriate for the dense fluids which are of interest in a binary cycle is a moot point. Steam turbine practice has tended toward slightly different definitions for loss correlations; see, for instance, Kearton (Ref. 2-21) and Lee (Ref. 2-22) and also Refs. 2-23 and 2-24. From the aerothermodynamic studies, it was concluded that the minimum number of stages compatible with the high efficiency demanded was seven, with a single turbine of split-flow construction. Table 2-15 shows some of the important thermodynamic parameters of such a machine. For the seven-stage single split-flow configuration, a nominal value of 50% reaction was chosen for all of the stages (ψ = 1.0 and ϕ = 0.5). If two turbines are chosen, the mass flow through each is halved so that, in order to maintain reasonable blade heights and hub-tip ratios, it is necessary to reduce ψ (= 0.9) and ϕ (= 0.45) and to increase the number of stages to eight.

2.5.2.5. Mechanical Design Considerations. Because of the preliminary nature of the design, insufficient attention has been given to the mechanical aspects of the design. The power transmission requirements predicate a large shaft diameter. A shaft diameter in the range of 482 to 559 mm (19 to 22 in.) is used for the single split-flow design; for the two-unit split-flow design, a range of 381 to ∿444.5 mm (15 to 17.5 in.) is used. The choice of a bearing type depends on various factors including dynamic loads. Since the rotor dynamics were not evaluated at this stage of the design, a journal bearing with pressure lubricant feed has been nominally chosen. However, it must be noted that journal bearings have no resistance to an oil whip type of instability. Because of the high pressures present at the inlet of the turbine, a double casing has been employed, with intermediate pressure ammonia bled off from the fourth stage into the space between the casings. The casings are horizontally split. A thrust bearing has been provided, although the thrust has been minimized because of the opposed flow. It is necessary to provide static and dynamic seals to prevent excessive leakage of ammonia during operation and while the turbine is shutdown.

As a result of the low temperatures prevalent in the turbine, low-to-medium-alloy steels are adequate. A typical high-strength low-alloy ferritic

steel is suitable for the rotor. The relative characteristics of the three steel groups (low-to-medium-alloy, high-alloy ferrite martensite, and austenitic steels) are shown in Table 2-16. It can be seen that low-alloy steels are best suited for low-temperature use. Their resistance to corrosion is inadequate, and whether this is of significance in the relatively different environment of ammonia remains to be determined. For the blades, 12% chrome (Type 400 SS) steel is typical.

2.5.2.6. Discussion. One of the disadvantages in the use of low-pressure steam is its high specific volume. Typically, although low-pressure (LP) turbines of large turbogenerators develop only about 30% of the total power output, they represent approximately 80% of the total weight of the set. The LP turbines, in fact, cost five to six times the cost per kW of the high-pressure (HP) machines and intermediate-pressure (IP) machines. Another serious problem associated with LP steam turbines is that of blade erosion. In this conceptual design, care has been exercised to exclude moisture in the low-pressure stages of the turbine.

The use of a high-density fluid for duty at the low-temperature end of steam and gas turbines has, therefore, several technical advantages from the point of view of the turbomachinery. The main advantage is the increase in efficiency and specific power output of the basic power plant. The high density of the fluid compared with steam at LP outlet conditions gives a substantial reduction in turbine exhaust area, with an attendant decrease in centrifugal stress in the last-stage blades. Furthermore, since the hub-tip ratio is not excessively low in the last stages (>0.7), the blade root is operating at a relatively higher value of reaction (>0.15) and permits the avoidance of highly cambered blades. Since the last stages of the turbine are doing more work, a higher stage efficiency in the last stages has a beneficial influence on the overall efficiency of the turbine. Table 2-15 indicates a higher value for the efficiency of the eight-stage 460-MW(e) machine. Although the machine has smaller blades, the machine as a whole (and the first stages in particular) is very lightly loaded with a higher degree of reaction than the seven-stage machine. While the efficiency values predicted may be regarded as high, it is possible to rationalize the higher efficiency

TABLE 2-16
RELATIVE CHARACTERISTICS OF THREE STEEL GROUPS

	Group A: Low-to-Medium-Alloy Steels	Group B: High-Alloy Ferrite-Martensite Steels	Group C: Austenitic Steels
Endurance limit	Poor	Fair	Good
Cost relationship	1	3	7
Castability	Good	Satisfactory	Satisfactory
Forgability	Good	Good	Good
Weldability	Good; only in special cases with preheating and stress relieving	Only with high preheating and subsequent heat treatment	Good; stress relieving usually desirable
Susceptibility to thermal shock cracks during heat treatment or curing of heavy castings	Slight; removal of casting skin necessary in places to examine for cracks	Very susceptible; complete removable of casting skin desirable before heat treatment	Not susceptible
Adequate resistance to scaling up to about °C (°F)	560 (1040)	650 (1200)	750 (1380) and higher
Machinability	Normal	High strength at low temperatures; machining difficult	Very tough; low cutting speed with deep cut desirable
Resistance to erosion	Normal	Normal	Very susceptible
Resistance to corrosion (rust)	Bad	Good	Excellent
Sliding behavior at high temperature	Normal	Good	Tendency to seize
Relaxation behavior	Normal	Sometimes inferior to group A	Varies according to alloy and heat treatment
Coefficient of thermal expansion in $deg^{-1} \times 10^{-6}$ at 600°C (1112°F)	14.5 (normal)	12.5 (low)	18.5 (high)
Coefficient of thermal conductivity at 20°C (68°F), W/(cm-sec-°C)	3.76 (normal)	0.3 (less)	0.15 (bad)
Susceptibility to thermal stresses	Normal	More susceptible than Group A	Much more susceptible than Group A

for the turbine with the larger number of stages on physical grounds. It is in this area that vendor assessment is needed of what constitutes a realistic efficiency potential for the ammonia turbine. The chosen designs lie in the high-efficiency areas of these nondimensional plots. It may be noted that the designs embody a constant U/C_0 (blade speed/spouting velocity) for all stages in an attempt to achieve an optimal design.

The use of a high-density fluid is not free from attendant disadvantages. The high density results in higher bending stresses, and the bladings are in general more susceptible to vibration-induced failure. Furthermore, in order to achieve reasonable first-stage blade heights and hub-tip ratios, the mean diameter of the flow must be gradually increased toward the last stage so that the flow is no longer purely two-dimensional. However, the resulting flare is within established design practice.

The layout of the turbine stages with overall dimensions is shown in Figs. 2-21, 2-22, and 2-23. The bearing span of the seven-stage machine is about 6.71 m (22 ft). There are two exhaust ducts from each half of the machine leading to two horizontal headers which, in turn, pipe the ammonia into eight banks of three condensers each laid out in a vertical array. It is obvious that with the large number of condensers the two 460-MW(e) units lend themselves to a more acceptable layout. The conceptual thermodynamic and mechanical design of the ammonia condenser is described in other sections of this report (see Sections 2.4 and 2.5).

Table 2-13 gives the reference data for the designs considered, and Table 2-11 gives a summary of the salient design parameters. Also given in Table 2-11 is a summary of the conceptual ammonia turbine study conducted by the De Laval Turbine Company for the Franklin Institute Research Laboratories (Refs. 2-12 and 2-25). In summary, it may be concluded that despite the uncertainties in performance prediction the outlook for a high efficiency, low cost, ammonia turbine is very optimistic.

2.5.3. Balance-of-Plant Designs

A study has been initiated to develop preliminary building requirements and sizes and to produce conceptual plot plans for current binary-cycle and dry-cooled versions of the GT-HTGR. The purpose is to establish design criteria and layout characteristics of the GT-HTGR. Figure 2-24 shows a preliminary containment/PCRV/reactor service building elevation cross-section. Figure 2-25 is a preliminary concept of the plot arrangement for a twin 3000-MW(t) plant.

2.5.3.1. Dry-Cooled and Binary-Cycle Plant Arrangements. There are two versions of the GT-HTGR, the binary-cycle and the dry-cooled versions. Layout requirements for both are similar, except that the binary-cycle plant has a turbine building which the dry-cooled plant does not have. The study incorporates as much commonality in the layouts of both plants as possible. In fact, unless it becomes impossible or unfairly penalizes either version of the GT-HTGR, the plot plans of both versions are expected to be exactly the same except for the deletion of addition of the binary-cycle turbine building. However, the reference plant design is considered to be the dry-cooled version. Any minor differences between the binary-cycle and dry-cooled plants are being resolved to favor the dry-cooled version.

2.5.3.2. Reference and Alternate Designs. The reference plant has loops rated at 1000 MW(t) each. For 3000-MW(t) reactors, three loops are required; for 4000-MW(t) reactors, four loops are required. The data generated in this work task will be used to compare qualitatively balance-of-plant requirements and costs of twin 4000-MW(t) plants having 1000-MW(t) and possibly larger loop ratings with those of a 3000-MW(t), three-loop plant. However, the primary effort in the study is directed to the development of the arrangement for a twin 3000-MW(t) plant with three 1000-MW(t) loops per reactor.

2.5.3.3. Layout Basis. The design of the SC-HTGR is used extensively as the basis for the layout of components which are the same or similar for both plants. The PCRV arrangement and layout of other GT-HTGR specific

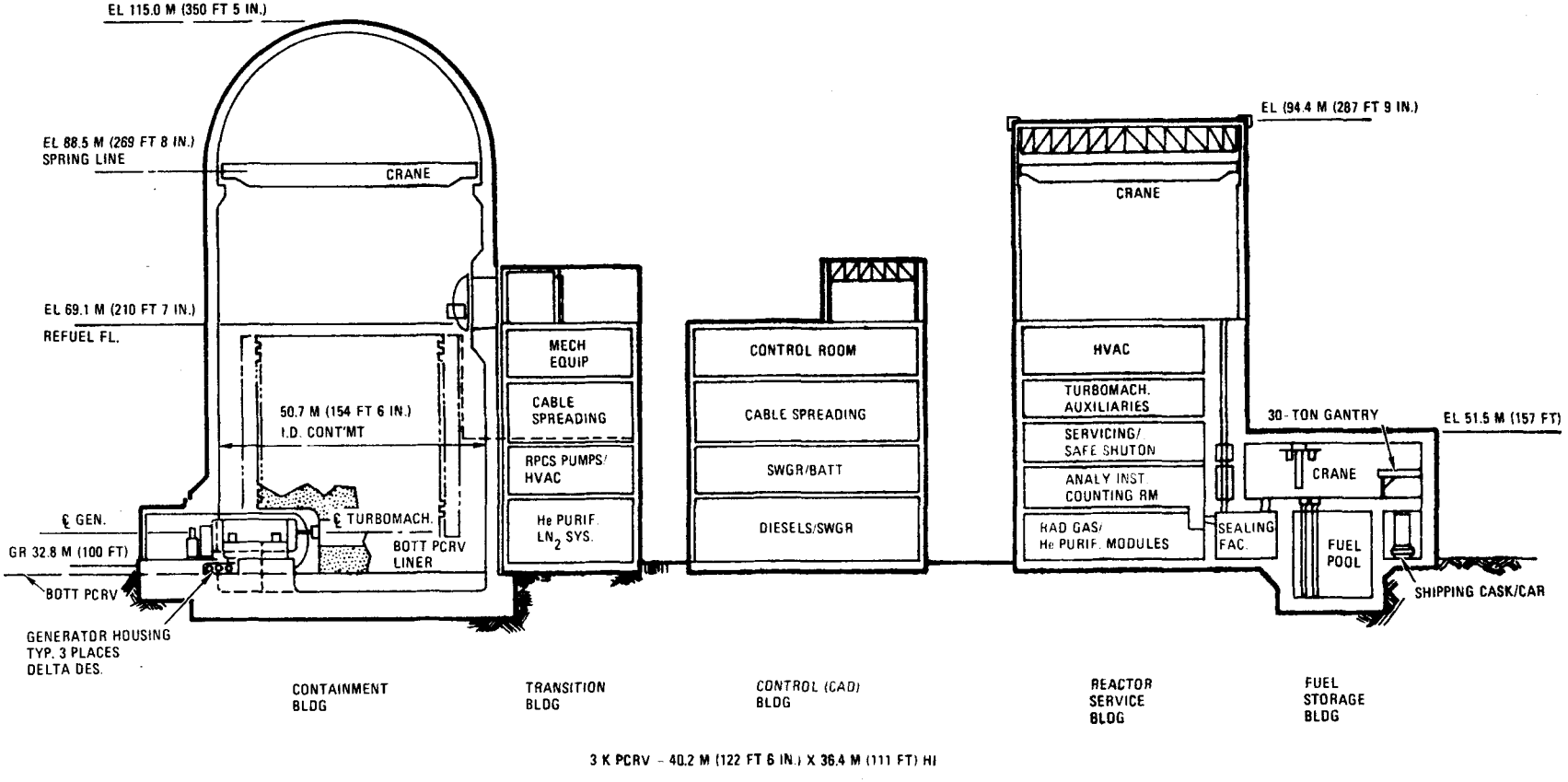

GA-A13950

Fig. 2-24. 3000-MW(t) GT-HTGR elevational relationship interface study

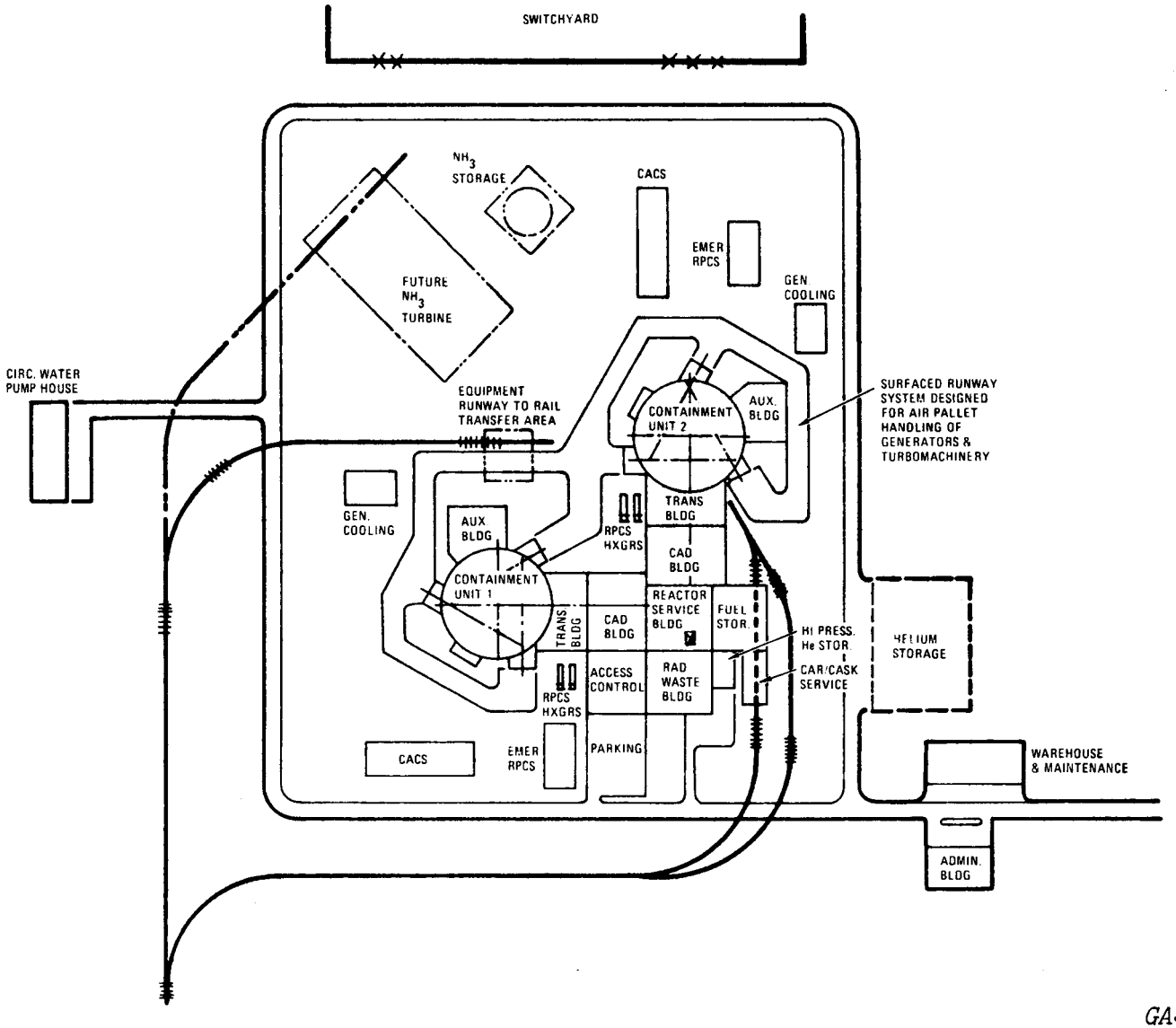

GA-A13950

Fig. 2-25. Twin 3000-MW(t) GT-HTGR showing runway system for air pallet equipment handling

components are based on the current reference GT-HTGR design concept: horizontal turbomachinery located below the reactor core cavity, with shafts oriented tangentially rather than radially with respect to the PCRV (see Section 4.2).

The following criteria are available as a natural consequence of other ongoing tasks:

1. Ammonia turbine/generator sizing and layout requirements
2. Other ammonia system equipment layout data
3. PCRV sizing
4. Containment building minimum dimensions
5. Dry-cooling tower (and wet tower for binary-cycle plant) layout data
6. Electrical system one-line diagram and load summary

Other existing criteria are being incorporated as follows:

1. Modify (or use as is) H_2 flame suppression system and generator cell
2. Modify (or use as is) existing control room layout.
3. Modify SC-HTGR helium storage building based on capacity.
4. Use SC-HTGR helium purification system.
5. Modify (or use as is) SC-HTGR service water system.
6. Modify SC-HTGR reactor plant cooling water system
7. Use SC-HTGR office and control access building(s)
8. Use SC-HTGR radiation waste system.
9. Use SC-HTGR fuel handling, fuel storage, and other containment/reactor service building features.
10. Modify SC-HTGR containment HVAC system.

The study includes the following specific tasks:

1. Compile layout criteria for significant plant components.
2. Allocate equipment to all buildings.
3. Perform general arrangement studies, including loop-size alternatives.

4. Adjust SC-HTGR control and diesel building to GT-HTGR requirements.
5. Lay out reactor service building based on SC-HTGR; budget for four plan and one elevation drawings.
6. Lay out reactor auxiliaries building (if any).
7. Lay out containment building.
8. Produce reference plot plans.
9. Compare balance-of-plant impact of 4000-MW(t) plants with loops of 1000 MW(t) and larger ratings.
10. Produce drawing(s) of turbomachine maintenance facility (conceptual space allocation only).
11. Produce layout of generator cell, including location of generator auxiliaries, bus duct routing, and provisions for generator and turbomachine handling.

2.6. INITIAL CORE DESIGN STUDIES

2.6.1. Core Design Parameter Selection

Effort to establish a new 4000-MW(t) GT-HTGR core design with an ROT of 950°C (1742°F) was initiated during this reporting period. The studies were performed at the higher of the two temperatures considered in the various design alternatives in order to provide a bound to any core difficulties and to provide a basis for fuel development requirements. Preliminary cycle analysis indicated that this new reactor would have a total coolant flow rate of 2012.4 kg/sec (15,972 x 10^6 lb/hr), an inlet pressure of 7.7938 MPa (1130.4 psia), and an inlet temperature of 568.2°C (1054.7°F).

The use of a high ROT made it necessary to incorporate several core design modifications in order to maintain satisfactory fuel temperature and fission product release. Table 2-17 shows the primary core design parameters which were selected for analysis.

In the past, 4000-MW(t) core designs at General Atomic have had a power density of 8.2 W/cm^3 and a 4-yr fuel cycle. The selection of a lower power density was made in order to reduce fission product release and also because of the fuel cycle benefits which are produced by an increased conversion ratio. The use of a 3-yr fuel cycle with one-third of the core replaced

TABLE 2-17
4000-MW(t) GT-HTGR CORE DESIGN PARAMETERS

	New GT-HTGR Design	Old GT-HTGR Design
Power density, W/cm^3	7.0	8.2
Fuel cycle, yr	3	4
Fuel block	10-row, FSV	8-row
Fuel particles	TRISO-BISO	TRISO-BISO
Number of axial fuel zones	4	4

annually was selected in order to reduce age peaking effects with resulting lower fuel temperature and lower fission product release. The use of the 10-row, Fort St. Vrain (FSV) fuel block was also selected in order to reduce fuel temperature and fission product release. The TRISO-BISO fuel particle design and the four axial fuel zone configuration are the same as current core designs for both steam plant and gas turbine applications.

In addition to the design parameters shown in Table 2-17, it was also decided that the new core design would use power rods in addition to the control rods and that the core thorium loading would be maximized. The use of power rods for reactor control has been found to be a valuable improvement for the radial control of large HTGRs and is highly beneficial in reducing fuel temperature and fission product release. The 4000-MW(t) SC-HTGR core configuration and current lead plant SC-HTGR designs also use power rods.

The use of maximum core thorium loading is desirable because the conversion ratio increases with the thorium loading.

The current effort on the new core design has been directed toward the establishment of a physics design of the core. These results provide input for thermal, stress, and fission product release analyses.

2.6.2. Core Physics Analysis

A detailed core physics design has been completed using the selected core parameters as a guideline. In addition, the power distributions, fluences, and fissions per initial metal atom (FIMA) required for fuel performance evaluation have been prepared in the appropriate format on magnetic tape. A brief description of several of the major characteristics of the design is included in the following paragraphs.

Considering the desired thermal rating [4000 MW(t)] and power density (7 W/cm^3), several possible core layouts were investigated. The round core shown in Fig. 2-26 was selected since it most closely approximated the desired parameters. The core has a power density of 7.15 W/cm^3 with three fuel segments which are well-distributed and nearly volumetrically equal. Such a layout tends to be very compatible with a power rod control system (rods grouped by age) and a standardized fuel cycle.

Several modifications of the SC-HTGR fuel cycle were made in an attempt to reduce power peaking and fuel temperature. The initial decision to use a 3-yr fuel cycle is estimated to reduce the maximum region power factor (RPF) by ∿12%. The maximization of the thorium by the appropriate choice of axial zoning and fuel dimensional parameters further reduces the RPF by ∿8%. By extending the depletion interval of the initial core from 292 equivalent full power days (EFPD) to 345 EFPD, fuel cycle costs will be reduced slightly, and the performance requirements of the third fuel segment will more closely resemble those of the equilibrium fuel segments. To reduce the number of fuel blends required and also to reduce further the maximum RFP, a single (standard) set of fuel atom densities was defined, using the GARGOYLE code (Ref. 2-26) for use in all reloads. The mass flows used for the GT-HTGR were then for an extended initial core, with a C/Th ratio of 170, having standardized reloads, with a C/Th ratio of 185.

The use of the 10-row fuel element will increase the number of fuel rods to be fabricated but will also reduce fuel temperatures by ∿111°C (∿200°F) (compared with the 8-row element). Since the 10-row element is

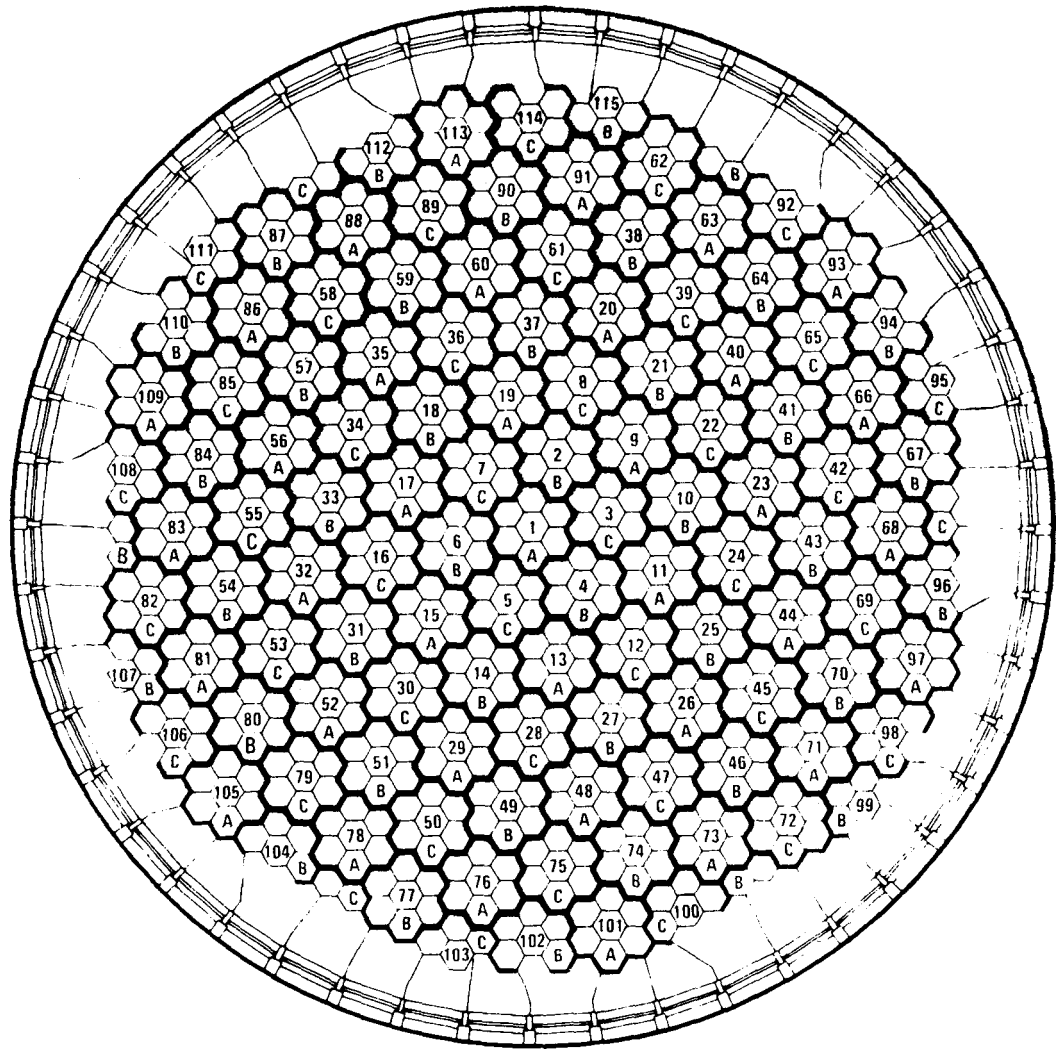

SEGMENT POSITION	7 COLUMNS	6 COLUMNS	5 COLUMNS	4 COLUMNS	2 COLUMNS	TOTAL REGIONS	TOTAL COLUMNS	VOLUME FRACTION
A	37	0	0	0	0	37	259	0.331626
B	30	3	3	3	3	42	261	0.334187
C	30	3	3	3	3	42	261	0.334187
TOTAL	97	6	6	6	6	121	781	1.000000

TOTAL CORE VOLUME = 5.591×10^8 CM^3

CORE AVERAGE POWER DENSITY = 7.15 W/CM^3

GA-A13950

Fig. 2-26. 4000-MW(t) GT-HTGR (3-yr cycle) core arrangement

the same as the FSV element, the FSV cross-section libraries, with minor modification, are suitable for the GT-HTGR core design. In summary, the GT-HTGR design calls for a 222°C (400°F) increase in gas temperatures. The proposed fuel element and fuel cycle changes can be expected to compensate for ∿167°C (∿300°F) in fuel temperatures. Reductions in local tilting are expected to achieve maximum fuel temperatures comparable with those of the steam cycle design.

A seven-year radial depletion of the proposed design has been completed with the GAUGE (Ref. 2-27) computer code. The core layout shown in Fig. 2-26 was used with the fuel segments being replaced in alphabetical order and with the mass flows previously described. Reactor control was achieved by employing power rods grouped by age. At any reload the power rods were withdrawn from the freshest fuel segment first. Typically, the core operated at full-power equilibrium with only one bank of power rods in the oldest fuel segment. The control rod pairs will be needed primarily for startup and shutdown. Preliminary shutdown margin calculations indicate that the shutdown margins will be adequate without considering the power rods.

The depletion studies indicated that the maximum RPF can be limited to less than 1.25 with four radial fuel zones requiring only 44 fuel blends over the normal 40-yr history of the plant. Available reactivity is ∿2% Δk during most of each cycle, with between 0.5% and 1.0% Δk excess available at end of cycle.

Table 2-18 presents data used in and obtained from the depletion study. When contrasted with data from previous steam cycle core designs the GT-HTGR core requires more fuel initially, but the net lifetime fissile requirements are reduced by ∿25%. The maximum region power factor is reduced by ∿25%. There also appears to have been some reduction (∿5%) in the intraregion tilting observed. By virtually every measure of technical performance, the radial characteristics of the GT-HTGR core physics design appear to be significantly improved over all previous steam cycle designs.

TABLE 2-18
INFORMATION TAKEN FROM 7-YR RADIAL DEPLETION OF
GT-HTGR CORE

Depletion Interval	Fuel Segment Charged	Mass Flows, kg				Depletion Interval Length, EFPD	Number of Unique Types	Maximum RPF	Time Averaged Maximum RPF	End of Cycle, K_{eff}
		Thorium Charged	U^{235} Charged	U^{235} Discharged	U^{235} Discharged					
Initial Core	1	25,568	1,140	649	277	345	16	1.145	1.124	1.015
	2	25,979	1,140	436	404					
	3	25,979	1,140	280	483					
Reload 1	4	23,470	1,214	310	449	270	12	1.211	1.167	1.007
Reload 2	5	23,705	1,221	291	454	275	16	1.222	1.214	1.007
Reload 3	6	23,471	1,214	304	451	330	---	1.223	1.213	1.009
Reload 4	7	23,470	1,214	---	---	285	---	1.230	1.201	1.006
Reload 5	8	23,705	1,221	---	---	296	---	1.242	1.230	1.008
Reload 6	9	23,471	1,214	---	---	300	---	1.228	1.216	1.009
Typical Reload Data From Previous SC-HTGR Design (4 yr, 8 W/cm^3, 190/210)										
Reload I	I + 4	13,324	970	106	295	292	16	1.60	1.50	1.008

On the basis of the previous steam cycle core design, the decision was made that the eight-element high core would be divided into four axial fuel zones of two layers each. Several temperature optimizations of a four-zone core were made, and it was determined that the most promising was the power split between zones which equilibrated the maximum fuel temperature in each zone for a 1.3/1.4 (RPF/local tilt) fuel channel. A study was thus made contrasting the characteristics of this shape with the shape used for the reference 3 SC-HTGR core design. As can be seen from Tables 2-19 and 2-20, the optimized shape required a much steeper power and fuel zoning profile. As a result, the maximum thorium load which could be used with the optimized shape is ∿20% less than that which can be used with the reference 3 shape. In addition, the fuel temperature decrease noted for the optimized shape is less than 28°C (50°F). On the basis of these observations, the reference 3 shape was selected as the most practical for the GT-HTGR core design.

The axial fuel zoning required to produce and maintain the desired axial shape was determined by using the GASP (Ref. 2-28) model. The axial fuel densities were employed in the BUG-RZ (Ref. 2-29) model to generate the axial power shapes as a function of power rod insertion fraction. The unrodded axial power shape for the GT-HTGR design is shown in Fig. 2-27.

In summary, a preliminary core physics design for the GT-HTGR core has been completed which is significantly better for GT-HTGR applications than any previous steam cycle core designs. RPFs are reduced by ∿25%, fast fluence is down by ∿40%, and local tilting is decreased by ∿5%. The resulting fuel temperatures are expected to be comparable with those of the steam cycle design, even though the required gas temperatures have increased by ∿222°C (∿400°F). The fission product release remains to be determined, but further improvements are possible such as power rod subgrouping and further optimization of the axial zoning/thorium loading. These may be studied if performance analysis of the proposed design should determine that lower fission product releases are necessary.

TABLE 2-19
AXIAL ZONING INFORMATION

Reference 3 Axial Shape (from SC-HTGR)				Temperature-Optimized Axial Shape (1.3/1.4 Gas Turbine Channel)			
Axial Zone	Relative Power Density	Fertile Ratio	Fissile Ratio	Axial Zone	Relative Power Density	Fertile Ratio	Fissile Ratio
1	1.22	1.22	1.40	1	1.44	1.39	1.74
2	1.16	1.07	1.07	2	1.14	1.05	0.99
3	0.94	0.91	0.81	3	0.83	0.82	0.66
4	0.69	0.80	0.72	4	0.59	0.74	0.61

TABLE 2-20
COMPARISON OF FUEL TEMPERATURES FOR
TEMPERATURE-OPTIMIZED AXIAL SHAPE AND REFERENCE 3
AXIAL SHAPE

Region Peaking Factor	Local Tilting Factor	Maximum Fuel Temperature		Temperature Advantage of Optimized Shape, °C (°F)
		Optimized Shape, °C (°F)	Reference 3 Shape, °C (°F)	
1.0	1.2	1180 (2157)	1199 (2190)	19 (33)
1.0	1.4	1296 (2365)	1318 (2405)	22 (40)
1.2	1.2	1195 (2183)	1216 (2221)	21 (38)
1.2	1.4	1313 (2396)	1337 (2439)	24 (43)
1.3	1.2	1202 (2196)	1224 (2236)	22 (40)
1.3	1.4	1321 (2410)	1347 (2457)	26 (47)

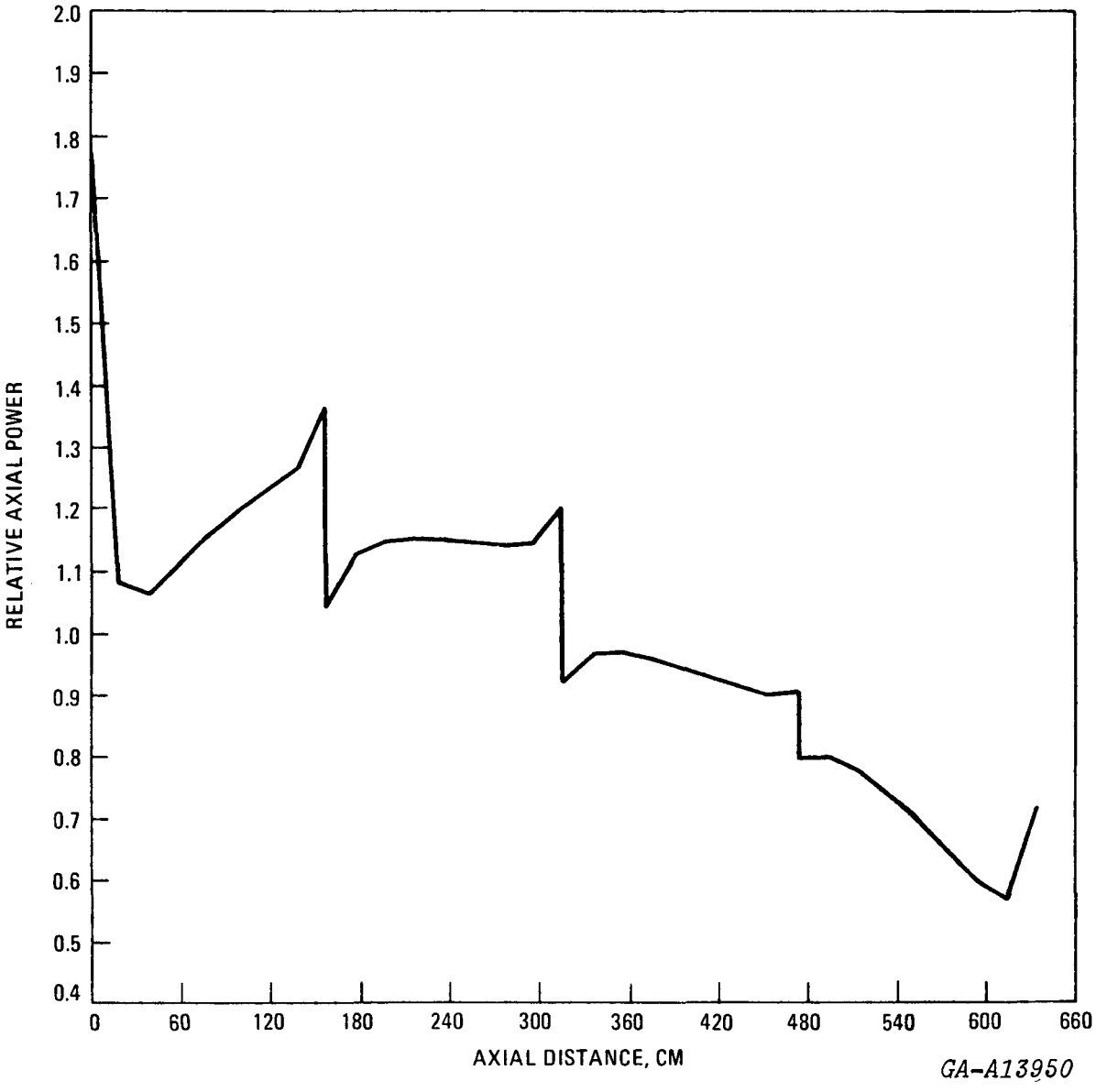

Fig. 2-27. Unrodded axial power shape for GT-HTGR core

REFERENCES

2-1. "Gas Turbine HTGR Program, Semiannual Progress Report for the Period July 1, 1975 through December 31, 1975," General Atomic Report GA-A13740, January 1976.

2-2. "REALY2: the GT-HTGR Transient Performance Analysis Program, "General Atomic Report GA-A13880, March 1976.

2-3. Seshadri, D. N., D. S. Viswanath, and N. R. Kuloor, "Thermodynamic Properties of the System $N_2O_4 = 2NO_2 = 2NO + O_2$," AIChE J. 16, 420 (1970).

2-4. Krasin, A. K., and V. B. Nesterenko, "Thermodynamic and Transfer Properties of Chemically Reacting Gas Systems," translated from Russian, UDC 621.039.534, 1971.

2-5. McCarthy, J. R., et al., "Regenerative Cooling; Characteristics of 50-50 Fuel and Nitrogen Tetroxide at Supercritical Pressures," North American Aviation, Rocketdyne Division, 1964.

2-6. Presler, A. F., "An Experimental Investigation of Heat Transfer to Turbulent Flow in Smooth Tubes for the Reacting N_2O_4-NO_2 Systems," NASA TN D-3230, 1966.

2-7. Baulch, D. L., D. D. Drysdale, and D. G. Horne, "Evaluated Kinetic Data for High Temperature Reactions," in Homogeneous Gas Phase Reactions of the H_2-N_2-O_2 System, Vol. 2, Butterworth, London, 1973, pp. 285-323.

2-8. Riebsomer, J. F., "The Reactions of Nitrogen Tetroxide with Organic Compounds," Chem. Rev. 36, 157 (1945).

2-9. Kirk, R. E., and D. F. Othmer, Enclopedia of Chemical Technology, Vol. 9, Interscience, New York, 1952, pp. 416-419.

2-10. Sukhotin, A. M., et al., "N_2O_4 Coolant Technology and Corrosion Resistance of Structural Materials," paper presented at IAEA Study Study Group Meeting on Gas-Cooled Fast Reactors, Minsk, July 24 to 28, 1972.

2-11. Canjar, L. N., and F. S. Manning, "Thermodynamic Properties of Ammonia," in Thermodynamic Properties and Reduced Correlations of Gases, Gulf Publishing Company, Houston, 1967, Chapter 14.

2-12. Troulakis, S., "Steam Ammonia Power Cycle Study," De Laval Turbine Company, September 1968.

2-13. Smith, S. F., "A Simple Correlation of Turbine Efficiency," J. Roy. Aeronaut. Soc. 69, 467 (1965).

2-14. Balje, O. E., "A Study on Design Criteria and Matching of Turbo-Machines: Part A - Similarity Relations and Design Criteria of Turbines," Trans. ASME J. Eng. Power Ser. A 84, 83 (1962).

2-15. Horlock, J. H., "Review - Losses and Efficiencies in Axial Flow Turbines," Int J. Mech. Sci. 2, 48 (1960)

2-16. Horlock, J. H., Axial Flow Turbines, Butterworth, London, 1970, Chapter 3.

2-17. Ainley, D. G., and G. C. R. Mathieson, "A Method of Performance Estimation for Axial Flow Turbines," British ARC Report R&M 2974, 1951.

2-18. Dunham, J., and P. M. Came, "Improvements to the Ainley-Mathieson Method of Turbine Performance Prediction," Trans. ASME J. Eng. Power Ser. A 92, 252 (1970).

2-19. Craig, H. R., and H. J. A. Cox, "Performance Estimation of Axial Flow Turbines," Proc. Int. Mech. Eng. London 185, 32 (1971).

2-20. Horn, G., et al., "Turbine Flow Problems of Binary Cycles Employing High Density Fluids," Proc. Int. Mech. Eng. London 185, 165 (1968).

2-21. Kearton, W. J., Steam Turbine Theroy and Practice, Pitman, London, 1958.

2-22. Lee, J. F., Theory and Design of Steam and Gas Turbines, McGraw-Hill, New York, 1954.

2-23. Lakshminarayana, B., and J. H. Horlock, "Review: Secondary Flow and Losses in Cascades and Axial Flow Turbomachinery," Int. J. Mech. Sci. 5, 287 (1963).

2-24. Spencer, R. C., K. C. Cotton, and C. N. Cannon, "A Method for Predicting the Performance of Steam Turbine Generators (16.5 MW and Larger)," ASME Paper 62-WA-209, 1962.

2-25. Slusarek, Z. M., "The Economic Feasibility of the Steam Ammonia Power Cycle," Franklin Institute Research Laboratories Report PB 184331, 1968.

2-26. Todt, F. W., "GARGOYLE-II, an Infinite Medium Fuel Cycle Analysis Code with Fuel and Poison Searches," Gulf General Atomic Report GA-9477, October 1969.

2-27. Wagner, M. R., "GAUGE, a Two-Dimensional Fuel Group Neutron Diffusion-Depletion Program for a Uniform Triangular Mesh," Gulf General Atomic Report GA-8307, March 1968.

2-28. Todt, F. W., and L. J. Todt, "GASP/M1, a One-Dimensional Program for Computing Fuel and Poison Distributions to Achieve Burnup Independent Power Distributions," Gulf General Atomic Report GA-9855, June 1970.

2-29. Dorsey, J. P., R. Froehlich, and F. W. Todt, "BUG-2/BUGTRI, Two-Dimensional Multigroup Burnup Codes for Rectangular and Hexagonal Geometry," Gulf General Atomic Report GA-8272, August 1969.

3. POWER CONVERSION LOOP TEST ALTERNATIVES (Task 189a, No. SU033)

3.1. TEST ALTERNATIVES

Three major alternatives for testing power conversion loops (PCLs) have been proposed for detail investigation. These are: (1) the Helium Component Test Facility (HCTF), which has been the basis for much of the program planning to date and which serves as a reference point for the other alternatives; (2) nonnuclear testing in the first nuclear plant in which an electric and/or fossil-fueled test of one or more PCLs is performed before the core is loaded into the PCRV; and (3) nuclear testing in the first nuclear plant, in which extended preoperational testing is followed by hot power test operations using the reactor core. For each of these alternatives, testing at reduced thermal input power can also be considered (see Section 3.3).

3.2. PRELIMINARY STUDY OF 1000-MW ELECTRIC HEATER

The following notes relate to the use of an electric heater to represent the reactor core as the energy input source for a power conversion testing loop. The case has been studied for 1000 MW with a heated gas outlet temperature of 815°C (1500°F), but the design envisages the possibility of operating at 982°C (1800°F) outlet gas temperature. The inlet conditions used were 497°C (927°F) at a pressure of 67.38 bar (977 psi) and a flow of 604 kg/sec (4.79×10^6 lb/hr). These conditions have been taken as typical.

The heater design is based on the use of carbon or graphite heating elements so that limiting material temperatures are not restrictive. Carbon elements are proposed for the heater sections because these elements can have higher electrical resistivity than graphite and so can operate at a higher

electrical voltage and a lower current, the latter having the highest impact on space and cost. In using carbon, however, the maximum temperatures within the element must not reach values which cause graphitization and hence lowering of resistivity. A temperature of 1800°C (3272°F) is regarded as safe, and little resistance change would be expected up to 2000°C (3632°F). For a 982°C (1800°F) gas outlet temperature, expected carbon temperatures are below 1650°C (3002°F).

Some trial designs have been pursued to expose the various problems and to arrive at practical solutions, and while there are a number of detail options open, there appears to be no basic problem of feasibility. Fig. 3-1a shows an outline arrangement.

3.2.1. Heater

The heater consists basically of a number of carbon elements arranged vertically with gas flowing downward over the heating surfaces. Each element is fed by one line of a three-phase power supply at its upper end where the temperature is lowest. Three elements make up a three-phase group, and their three lower ends are joined to form a neutral or star point which is at earth potential. No external connections are needed at the lower high-temperature end of these assemblies. An array of such three-phase element groups make up the complete heater.

A typical case studied uses tubular elements of 1.2 cm (0.47 in.) wall thickness with a mean tube diameter of 17 cm (6.69 in.). With a power density in the element of 140 W/cm^3, a mean heat flux of 84 W/cm^2 of surface area is produced with gas flowing on both the inside and outside faces. For 1000 MW, 61 groups of three elements (183 total) with a length of 610 cm (20 ft) are required. The power ratings chosen produce a radial temperature difference of 220°C (428°F) between the element surface and the hottest zone within the element material. This results in acceptable thermal stresses which in practice will relax somewhat with creep.

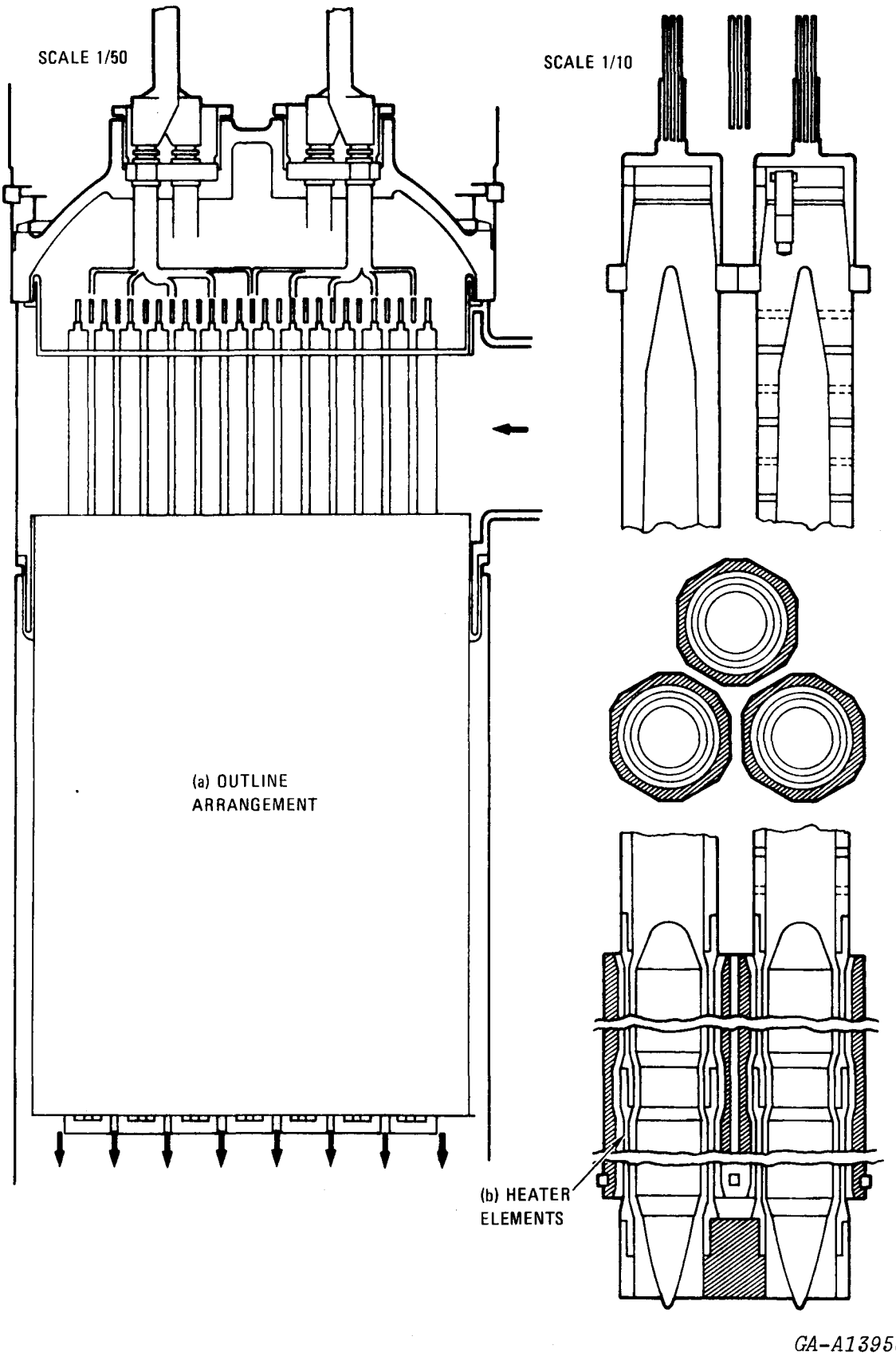

Fig. 3-1. 1000-MW electric heater unit

The first scheme placed the elements in an open array set on a 23 cm (9.1 in.) triangular pitch with gas flowing freely through the tube bores and tube interspaces. However, if an element should fracture and contact a neighbor, it could cause a very destructive short circuit. The presently favored arrangement raises the pitch to 27 cm (10.6 in.) and puts an electrically isolated shell tube around each element. This produces an annular gas path on the outside of the element tube which now requires an appropriate gas flow annulus on the inside; this is satisfied by fitting a central filler rod.

While this scheme adds complexity and involves supporting and sealing against bypass gas flows, it permits a choice of annulus size so that the gas velocity may be raised until it satisfies the required pressure drop and thereby increases the heat transfer coefficient. In the first scheme, the pressure drop through the heater was unnecessarily low. A further advantage of the shrouded element arrangement is that it allows the use of ceramic insulator pins to control the long elements against lateral movement. An element arrangement is shown in Fig. 3-1b.

3.2.2. Power Input Connections to Heater

For a power input of 1000 MW, the power input to each of 183 elements is over 5.46 MW. The EMF required for a typical carbon element 26.1 m (20 ft) long operating at the rating previously stated is about 445 V, and the current per element is about 12,290 A. The three-phase line-to-line voltage is consequently 770 V.

The total phase current is nearly 750,000 A. For convenience, entry into the pressure vessel has been split into two penetration groups, each containing the three-phase lines with each line carrying nearly 375,000 A.

While the net magnetizing ampere-turns outside a three-phase conductor group is zero, high alternating ampere-turns are applied to the material between the conductors. Hysteresis losses can be avoided by the use of

penetration plates of nonmagnetic material such as 18% nickel 13% chrome steel, but voltages will be generated and eddy-current heating will occur. The relatively high electrical resistance of the plate material will reduce the heating, but water cooling of the plates will be necessary.

The design requirements in this area have not yet been adequately evaluated, and further solutions such as the use of concentric conductors to avoid the problem have been tentatively studied and look encouraging.

Stepdown transformers are needed between the incoming supply and the heater. The heavy connections for high current on the secondary side preclude any use of circuit breaking or switching. Therefore, all circuit control must be applied to the primary side of the supply transformers.

An additional primary winding can be provided so that the locally generated power from the test loop can be fed back to the heater in parallel with the external power supply. However, the plant under test must have its generators running at synchronous speed before it can feed power back to the heater. Any degree of loading can be made by appropriate generator excitation.

The amount of heat generated in the supply bus bars to the heater is such that water cooling is required. Given this, there is every incentive to reduce the copper sections so far as possible and to design for high-current densities. Values of 1550 A/cm^2 (10,000 $A/in.^2$) can be achieved without cooling problems.

The forces between conductors are very large, but their strength is such that supporting ties at about 0.91 m (3 ft) intervals are adequate. It is desirable to mount the heater transformers as close as possible to the pressure vessel penetrations in order to minimize the self-inductance of the feeder bus bars. For a length of 6.1 m (20 ft), a power factor of about 0.95 can be achieved. The copper saving is an additional reason for keeping the lengths short.

3.2.3. Internal Bus Bars

A bus bar chamber inside the pressure vessel head is proposed that accommodates the connections between entry penetrations and the connections to the top of each heater element. Each heater element is suspended directly from a support bus bar which carries a number of elements in line. Parallel rows of support bus bars, fed in phase sequence, make up the complete array of suspended elements. The elements are rigidly mounted since the heavy conductors do not permit any connection flexibility; thus, each bottom block joining three elements makes rigid three-element assemblies. However phase loads are balanced, no significant distorting loads are envisaged, but it is recommended that initial selection for approximately matched resistances be made for each group of three. About 100°C (180°F) mean temperature difference between elements under their restrained condition is acceptable. That is a change from 0 to 200°C (0 to 360°F) over the element length.

A nominal gas barrier under the bus bar chamber is created by a non-conducting ceramic collar fitted below the connecting head of each heater element. There is no gas seal, but the barrier provides a division between the flowing gas entering the heater and the bus bar chamber above. The bus bars are cooled directly by water tubes in contact with the copper conductors, and any heat input from the gas will also be taken up by the water tubes. The effect on the copper temperature will be small because the heat transfer potential between the gas and the water will be small, since no high gas velocities can be expected in the bus bar chamber. A suitable water flow will meet the cooling load from both sources of heat.

3.2.4. Heater Elements

Each tubular heater requires fabrication from a number of sections which are of convenient size for machining and which can be joined in a manner that will carry the high current. Locally thickened sections which screw together with a jointing compound make an effectively continuous current path which bonds on heating. There are four heater sections and one entry section.

It is proposed that the upper section of each element, where gas flow enters, should be made of graphite having a much lower electrical resistance. This reduces the heating in the region above the defined heat transfer channels. Furthermore, the thickness may be increased to reduce current density and further reduce heat generated in the section.

At the top connection, the material is nearly solid. This helps to limit the local heat generated to values which help the design of the connecting heads where a tapered water-cooled cap is attached. Good contact is assured by the use of disk springs which will maintain a force on the tapered joint and keep contact resistance low. The cooled cap will remain close to the constant temperature, and any increase in contact resistance will raise the temperature of the graphite in the taper so that expansion will reestablish good contact. The contact current density in the tape connection is about 17 A/cm^2 (110 $A/in.^2$).

Gas entry into the lower of the heater tubes is through a larger number of uniformly spaced holes through the walls of each upper section. This helps to draw flow more evenly over the external surfaces, and the holes add substantially to the cooling surface. The low-resistance graphite and the lower heat rating which results give no difficult temperature problems in the upper section of the heater elements.

3.2.5. Concluding Comments

The scheme studied has not been engineered into a particular test loop design. The design has been treated as an assembly which will mount vertically into a suitable cylindrical cavity, with gas entry through one or more side ducts and with gas exit from the bottom of the cavity.

There appears to be a practical solution to each of the problems exposed; the scope of work has involved a sufficient degree of detail to establish feasibility and size on most issues and to predict that solutions are available in areas which require more work.

The work to date has been based on a single 1000-MW heater unit which has the potential for operating at higher outlet gas temperatures than those presently specified.

If the unit were required to accept power from the generator in the test loop when running at a nonsynchronous speed, then it would require another separate heater. It would not appear to be practical to put the two heaters one above the other in view of the separate electrical connections to each.

This implies two adjacent cavities, each with similar bus bar penetration heads and with the units displaced axially to suit a connecting duct between them. The second heater in series would have a much higher entry gas temperature than at present, but this could be minimized by putting the smaller heater first.

Separately loading the test loop generator at nonsynchronous speeds without recovering its power would be simpler. If this part of a testing program is not extensive, then the value of the power wasted could compare favorably with the added cost and complexity of a double heater scheme.

3.3. ALTERNATE TEST CYCLE CONDITIONS

Full power testing obviously provides the best demonstration of power conversion loop design and performance capability. However, to reduce facility cost, alternate test modes have been proposed. The alternate test modes include testing at reduced temperature, testing at reduced pressure, testing with argon instead of helium, and motoring the generator with and without external heat input. The cycle conditions for each component are shown in Tables 3-1 through 3-4. These data are to be used to judge the adequacy of less than full power testing.

TABLE 3-1
CYCLE CONDITIONS FOR HEATER

	Case 1	Case 2	Case 3	Case 4	Case 5	Case 6
	Full-Power Testing	Heating at Reduced Temperature	Heating at Reduced Pressure	Heating with Argon	Generator Motoring	Heating and Generator Motoring
Inlet temperature, °C (°F)	502 (935)	431 (808)	508 (947)	503 (938)	92 (197)	220 (427)
Inlet pressure, MPa (psia)	6.71 (973)	6.35 (921)	1.37 (199)	0.67 (97)	3.21 (466)	3.75 (544)
Inlet flow, hg/sec (10^6 lb/hr)	609 (4.83)	602 (4.78)	125 (0.99)	609 (4.83)	406 (3.22)	412 (3.27)
Outlet temperature, °C (°F)	816 (1500)	705 (1300)	816 (1500)	815 (1500)	92 (197)	303 (577)
Outlet pressure, MPa (psia)	6.61 (958)	6.25 (907)	1.34 (195)	0.66 (96)	3.16 (458)	3.70 (536)
Outlet flow, hg/sec (10^6 lb/hr)	609 (4.83)	602 (4.78)	125 (0.99)	609 (4.83)	406 (3.22)	412 (3.27)
Thermal power, MW	993	857	200	98	0	179
Net electric power, MW	356	271	71	35	150	69

TABLE 3-2
CYCLE CONDITIONS FOR TURBOMACHINERY

	Case 1 Full-Power Testing	Case 2 Heating at Reduced Temperature	Case 3 Heating at Reduced Pressure	Case 4 Heating with Argon	Case 5 Generator Motoring	Case 6 Heating and Generator Motoring
Compressor inlet temperature, °C (°F)	35 (95)	34 (93)	30 (85)	35 (95)	119 (245)	98 (207)
Compressor inlet pressure, MPa (psia)	2.94 (426)	2.83 (411)	0.59 (85)	0.30 (43)	2.33 (338)	2.28 (330)
Compressor flow, kg/sec (10^6 lb/hr)	631 (5.01)	625 (4.96)	130 (1.03)	631 (5.01)	420 (3.33)	427 (3.39)
Compressor outlet temperature, °C (°F)	177 (350)	171 (340)	172 (341)	178 (352)	199 (390)	203 (396)
Compressor outlet pressure, MPa (psia)	6.89 (1000)	6.54 (948)	1.41 (204)	0.69 (100)	3.36 (488)	3.90 (566)
Compressor outlet flow, kg/sec (10^6 lb/hr)	609 (4.83)	602 (4.78)	125 (0.99)	609 (4.83)	406 (3.22)	412 (3.27)
Turbine inlet temperature, °C (°F)	815 (1500)	705 (1300)	816 (1500)	816 (1500)	91 (195)	803 (577)
Turbine inlet pressure, MPa (psia)	6.55 (950)	6.20 (999)	1.34 (195)	0.66 (95)	3.14 (456)	3.67 (532)
Turbine inlet flow, kg/sec (10^6 lb/hr)	619 (4.91)	612 (4.86)	125 (0.99)	619 (4.91)	412 (3.27)	420 (3.33)
Turbine outlet temperature, °C (°F)	542 (1007)	463 (865)	538 (999)	542 (1007)	80 (176)	223 (432)
Turbine outlet pressure, MPa (psia)	3.08 (446)	2.97 (431)	0.62 (90)	0.31 (45)	2.39 (346)	2.34 (340)
Turbine outlet flow, kg/sec (10^6 lb/hr)	630 (5.00)	624 (4.95)	130 (1.03)	630 (5.00)	420 (3.33)	426 (3.38)
Compressor pressure ratio	2.35	2.31	2.39	2.35	1.45	1.72
Turbine pressure ratio	2.13	2.09	2.16	2.13	1.32	1.57
Shaft speed, Hz (rpm)	60 (3600)	60 (3600)	60 (3600)	19 (1140)	60 (3600)	60 (3600)

TABLE 3-3
CYCLE CONDITIONS FOR RECUPERATOR

	Case 1	Case 2	Case 3	Case 4	Case 5	Case 6
	Full-Power Testing	Heating at Reduced Temperature	Heating at Reduced Pressure	Heating with Argon	Generator Motoring	Heating and Generator Motoring
Cold inlet temperature, °C (°F)	177 (350)	171 (340)	172 (341)	178 (352)	199 (390)	203 (396)
Cold inlet pressure, MPa (psia)	6.82 (989)	6.46 (937)	1.41 (204)	0.68 (99)	3.30 (478)	3.83 (556)
Cold inlet flow, kg/sec	609 (4.83)	602 (4.78)	125 (0.99)	609 (4.83)	406 (3.22)	412 (3.27)
Cold outlet temperature, °C (°F)	502 (935)	431 (808)	509 (947)	504 (938)	91 (196)	220 (427)
Cold outlet pressure, MPa (psia)	6.74 (978)	6.38 (926)	1.38 (200)	0.68 (98)	3.22 (467)	3.76 (546)
Cold outlet flow, kg/sec (10^6 lb/hr)	609 (4.83)	602 (4.78)	125 (0.99)	609 (4.83)	406 (3.22)	412 (3.27)
Hot inlet temperature, °C (°F)	542 (1007)	463 (865)	538 (999)	542 (1007)	80 (176)	223 (432)
Hot inlet pressure, MPa (psia)	3.01 (436)	2.94 (427)	0.61 (89)	0.30 (44)	2.39 (346)	2.33 (338)
Hot inlet flow, kg/sec (10^6 lb/hr)	630 (5.00)	624 (4.95)	130 (1.03)	630 (5.00)	421 (3.34)	427 (3.39)
Hot outlet temperature, °C (°F)	228 (441)	212 (413)	212 (413)	228 (441)	183 (361)	205 (400)
Hot outlet pressure, MPa (psia)	3.01 (436)	2.90 (421)	0.60 (87)	0.30 (44)	2.37 (344)	2.32 (336)
Hot outlet flow, kg/sec (10^6 lb/hr)	630 (5.00)	624 (4.95)	130 (1.03)	630 (5.00)	421 (3.34)	427 (3.39)
Heat load, MW (10^6 Btu/hr)	1029 (3510)	815 (2780)	218 (745)	102 (348)	227 (776) [a]	37 (126)

[a] Heat flow is reversed from design condition.

TABLE 3-4
CYCLE CONDITIONS FOR PRECOOLER

	Case 1 Full-Power Testing	Case 2 Heating at Reduced Temperature	Case 3 Heating at Reduced Pressure	Case 4 Heating with Argon	Case 5 Generator Motoring	Case 6 Heating and Generator Motoring
Helium inlet temperature, °C (°F)	228 (441)	212 (413)	212 (413)	228 (441)	183 (360)	205 (400)
Helium inlet pressure, MPa (psia)	3.00 (435)	2.90 (420)	0.60 (87)	0.30 (44)	2.36 (343)	2.31 (335)
Helium inlet flow, kg/sec (10^6 lb/hr)	630 (5.00)	624 (4.95)	130 (1.03)	630 (5.00)	420 (3.33)	427 (3.39)
Helium outlet temperature, °C (°F)	35 (95)	34 (93)	30 (85)	35 (95)	119 (246)	98 (207)
Helium outlet pressure, MPa (psia)	2.95 (428)	2.85 (414)	0.59 (86)	0.30 (43)	2.34 (340)	2.28 (331)
Helium outlet flow, kg/sec (10^6 lb/hr)	630 (5.00)	624 (4.95)	130 (1.03)	630 (5.00)	420 (3.33)	427 (3.39)
Cold inlet temperature, °C (°F)	30 (85)	30 (85)	30 (85)	30 (85)	30 (85)	30 (85)
Cold inlet pressure, MPa (psia)	2.00 (290)	2.00 (290)	2.00 (290)	2.00 (290)	2.48 (360)	2.48 (360)
Cold inlet flow, kg/sec (10^6 lb/hr)	352 (2.79)	352 (2.79)	352 (2.79)	38 (0.3)	214 (1.7)	315 (2.5)
Cold outlet temperature, °C (°F)	174 (344)	159 (318)	56 (133)	174 (344)	183 (361)	203 (397)
Cold outlet pressure, MPa (psia)	2.00 (290)	2.00 (290)	2.00 (290)	2.00 (290)	2.48 (360)	2.48 (360)
Cold outlet flow, kg/sec (10^6 lb/hr)	352 (2.79)	352 (2.79)	352 (2.79)	38 (0.3)	214 (1.7)	315 (2.5)
Heat load, MW (10^6 Btu/hr)	630 (2150)	577 (1970)	123 (420)	68 (213)	138 (472)	238 (812)

3.4. PRELIMINARY EVALUATION OF TEST ALTERNATIVES

The following discussion and analysis of each alternative, although not completed in detail, generally illustrate the advantages and uncertainties expected for each approach.

3.4.1. Evaluation Criteria

The following technical and programmatic criteria are used to evaluate the alternatives:

1. Maximize the test information which can be incorporated in the design of the first nuclear plant.

2. Minimize the technical uncertainties at major decision-making points in the program.

3. Minimize capital expenditures for test facilities and test equipment.

4. Minimize total development program cost.

5. Minimize the amount of funds expended before a full-scale turbomachine is tested.

6. Minimize the time period required before large-scale commercial sales can be made.

3.4.2. Subcomponent Testing Common to All Alternatives

The objective of this task is to evaluate alternative PCL tests. However, to put the PCL testing in perspective with the whole development program, major testing of subcomponents is described in Table 3-5. The tests in Table 3-5 would be performed regardless of the PCL testing approach adopted.

TABLE 3-5
SUBCOMPONENT TESTING COMMON TO ALL ALTERNATIVES

Component	Proposed Subcomponent Tests
PCRV	Scale-model demonstration
Thermal barrier	Conductivity tests
	Depressurization tests
	Vibration tests
Materials	Screening and qualification tests
	Friction and wear tests
Turbomachinery	Scaled helium or full-size air compressor and turbine tests
	Bearing and seal rig tests
	Cooling flow bench tests
	Inlet and outlet duct air flow tests
	Blade vibration bench tests
	Disk spin tests
Heat exchangers	Module assembly vibration tests
	Module assembly air flow tests
	Module assembly air heat transfer tests
Helium control valves	Full-scale air flow tests
	Actuator qualification tests
	Assembly life tests
PCL	Preoperational systems checkout
	Low-flow generator motoring operation

In addition, a number of related programs will provide valuable operational experience relevant to PCL system design and operation. The Peach Bottom HTGR end-of-life studies will provide valuable insight into such uncertain areas as materials performance in helium and fission product plate-out characteristics. Operational surveillance of the Fort St. Vrain HTGR will provide similar valuable data. Should cooperation between the German/Swiss and U. S. gas-cooled reactor (GCR) programs be expanded, results from European facilities, such as the AVR, Oberhausen II, and the HHV gas-turbine facilities, could be factored into the design and development program.

3.4.3. Major Technical Differences between Alternatives

Significant differences between PCL test alternatives center in two areas, turbomachinery and integrated system performance aspects. Heat exchangers, valves, thermal barrier, and other components and subsystems would benefit from, but may not necessarily require, full-power integrated system testing, given the degree of testing indicated in Table 3-5.

The HCTF minimizes technical uncertainties because full-scale test results are obtained before the nuclear plant components are manufactured. Also, more PCL testing can be performed before commitment to the completion of the nuclear plant. For example, matching and optimization of turbine and compressor performances can be accomplished using the HCTF. Moreover, components might be more heavily instrumented than in a PCRV, and provision for component access and inspection can be maximized by appropriate facility design. The HCTF is defined as a single loop test. Options involving the nuclear plant can offer the possibility of a multiple loop test, depending on the selected nuclear demonstration plant rating.

The option with nonnuclear heat testing in the first nuclear plant requires that the nuclear plant design be committed and built before any full-scale PCL results are available. It is conceivable that design changes could be made following tests, but such changes would be constrained by PCRV envelopes in existence. (Alternately, oversized PCRV cavities could

be designed into the first plant for possible contingencies.) The time necessary between obtaining test results, redesigning components, remanufacturing, and reinstalling components would also be a factor weighing against desirable but nonessential design changes like turbomachinery performance optimization, because the expensive nuclear plant would be sitting idle, delaying commercial operation. These same considerations would argue for shortening the test program and reducing the amount of test results. Nevertheless, a complete demonstration test program is achievable with this approach.

The option with nuclear testing in the first nuclear plant shares the disadvantages of the nonnuclear/first nuclear plant test alternative, plus some additional uncertainties which are difficult to resolve at this time. These include estimating the operations time available before radioactivity levels will have increased to a point where maintenance and inspection are impaired, determining whether the plant will be licensed without prior full-scale component testing, and predicting the technical and programmatic implications of malfunctions in the first nuclear-powered plant.

In summary, from a purely technical and risk minimization point of view, the HCTF is preferred. Although nonnuclear heater testing at full power in the first nuclear plant makes testing and design modifications more difficult and resolves technical uncertainty later in the program, it still provides necessary full-scale testing prior to nuclear operation. Nuclear demonstration testing in the first nuclear plant would involve the greatest technical uncertainty and risk. A recommendation at this time in favor of the first full-power PCL demonstration using nuclear heat would seem to require strong programmatic advantages.

3.4.4. Major Programmatic Differences between Alternatives

The major disadvantage of the HCTF is that it requires the largest early capital expenditures for test facilities. By utilizing structures

and systems in the nuclear plant, the alternatives are superior in that testing is done with equipment some of which has subsequent commercial value. Unless the HCTF is allowed credit as a commercial electric plant or as a test facility for other test programs subsequent to gas-turbine testing, all of its cost must be charged to the development program. It is unclear whether total program cost will be larger or smaller than other alternatives. The extra costs of the alternatives due to special equipment, special plant design features, first-of-a-kind costs, interest on the first nuclear plant during testing, etc., must be addressed before this determination can be made.

Since the HCTF itself will be less expensive than the first nuclear plant, less money would have to be spent to reach the point at which full-scale turbomachinery test data were obtained.

Nonnuclear testing in the first nuclear plant could be achieved in two ways: (1) the entire plant could be constructed, with testing performed just prior to loading the reactor core; (2) a minimal amount of construction could be done, just enough to permit PCL testing, with construction to be completed after obtaining test results.

With the skeleton nuclear plant concept, test facility capital cost is reduced because some structures and systems, especially the PCRV, have subsequent commercial value. By performing testing before the full commercial plant construction is complete, less money is spent at the time when a PCL is operated at power for the first time. On the other hand, because the nuclear plant is more expensive than the HCTF, the investment when the PCL is tested is not reduced to a level comparable to the HCTF. Therefore, this alternative is intermediate with respect to this criterion.

With the fully constructed nuclear plant concept, test facility capital cost is also lower than with the HCTF. However, the funds expended by the time a PCL is tested for the first time at power is large, because the nuclear plant and the nonnuclear heater are completely constructed except for loading of the reactor core.

Nuclear testing in the first nuclear plant is concomitant with essentially no large-scale facilities or equipment for PCL testing. The funding expended to the point in time when a PCL is operated at power for the first time would be maximum, because the complete nuclear plant would be constructed. Construction and successful operation of a nuclear plant with no waiting for intermediate test results would appear to be the quickest way to verify all aspects of the concept, but this entails a greater degree of risk. However, the nuclear plant test alternative has the advantage in that a total system test of PCL and reactor is achieved. However, startup problem delays should, to some extent, be expected. Component inspection, especially if the activity levels prohibit hands-on maintenance, would be more difficult. Mechanical failures would be difficult to repair. Licensing restrictions on operation, maintenance, and inspection could be severe.

Total program cost is potentially minimized by the nuclear plant test alternative, because the prenuclear testing is minimized. However, because some startup problems must be anticipated, this potential will certainly be eroded, depending on the startup problems experienced. Also, if additional design and/or development work is undertaken to reduce the risk of initial PCL operation with a nuclear heat source, the cost of such work would add to the program cost.

4. PRIMARY PRESSURE BOUNDARY (Task 189a, No. SU037)

4.1. SUMMARY

During the reporting period, the primary pressure boundary task effort has concentrated on the development of reactor vessel layouts which would result in a lower-cost system. Several possible arrangements and numbers of loops were investigated. This investigation resulted in the selection of a new family of reactor arrangements which differ from the former arrangement in that the turbomachinery is placed normal to the PCRV radius vector rather than parallel, as previously.

The layouts of a three-loop, 3000-MW(t) and a four-loop, 4000-MW(t) reactor arrangement are presented. The advantages of the new layouts are discussed.

A preliminary finite element stress analysis of a three-loop, 3000-MW(t) delta reactor arrangement was conducted. This analysis demonstrated the feasibility of the delta arrangement.

A preliminary finite element stress analysis of the large steel closures was conducted. This analysis is used both to show the feasibility of this type of closure and to optimize the thickness of the components which make up the closure.

An investigation was made of the design of the support interface between the PCRV and the various pieces of equipment contained within the PCRV. The design of these supports is shown, along with an analysis of the loads and resulting stresses.

The results of further investigations of the design of the thermal barrier and the reactor core outlet duct are presented. A description of the various thermal barrier classes and zones is presented, along with more detailed analysis of the vented thermal barrier. Also presented are a preliminary design for the 850°C (1562°F) ROT reactor outlet duct and a discussion of alternate approaches to reactor outlet duct design for 950°C (1742°F) ROT.

4.2. PCRV DESIGN APPROACH STUDIES

A study of PCRV configurations for two-, three-, and four-loop configurations of an advanced 4000-MW(t) GT-HTGR was performed. The study included turbine inlet temperatures of 850°C (1562°F) and 950°C (1742°F). The turbomachine arrangements investigated were radial and nonradial arrangements. In the nonradial arrangement, the turbomachine cavities form a horizontal delta in case of the three-loop configuration and a square in the case of the four-loop configuration. The two-loop configurations have delta and parallel arrangements of the turbomachine cavities. This study completes Milestone B-1.

The configurations studied are given in Table 4-1.

From the results of this study, the following can be summarized:

1. None of the two-loop configurations was considered for further study for the following reasons:

    a. In the delta design, the heat exchanger diameters are too large.

    b. In the parallel design, the ducting is too problematical.

TABLE 4-1
PCRV CONFIGURATIONS STUDIED

Configuration	Arrangement	Turbine Inlet Temperature, °C (°F)	Number of Loops	Number of Recuperators per Loop	Number of Precoolers per Loop
850/2-1	Delta	850 (1562)	2	1	1
850/2-2	Parallel	850 (1562)	2	2	2
850/3-1	Radial	850 (1562)	3	1	1
850/3-2	Delta	850 (1562)	3	1	1
850/4-1	Radial	850 (1562)	4	1	1
850/4-2	Square	850 (1562)	4	1	1
950/3-1	Radial	950 (1742)	3	1	1
950/3-2	Delta	950 (1742)	3	1	1
950/4-1	Radial	950 (1742)	4	1	1
950/4-2	Square	950 (1742)	4	1	1

2. The following configurations were studied further:

   a. Delta configuration of the three-loop primary system for the following reasons:

      (1) Improved ducting

      (2) Simpler prestressing

      (3) Better access to turbomachine

      (4) PCRV diameter independent of turbomachine (turbomachine growth capability)

      (5) Minimum height of PCRV

      Uncertainty: effects of structural discontinuities in bottom part of PCRV.

   b. Square configuration of the four-loop primary system for the same reasons as in Item 2a with the exception that PCRV diameter is not independent of turbomachine (no turbomachine growth capability). Same uncertainty as in Item 2a.

A discussion of the study is given in Appendix A.

4.3. PCRV DESIGN FOR 850°C ROT

4.3.1. General

A design study of a 3000-MW(t), three-loop configuration and a 4000-MW(t), four-loop configuration of a single-cycle, dry-cooled GT-HTGR with a outlet temperature (ROT) of 850°C was performed. The purpose of this study was to confirm the data generated by the optimization code CODER for these configurations and to find out areas for improvement of this code.

In general, the study confirmed that CODER produced a viable design for these configurations. Only minor corrections due to dimensional or angular input data limitations had to be made.

Some aspects of the two configurations are discussed, and the configurations are evaluated.

4.3.2. CODER Results

For the design of the three-loop, 3000-MW(t) and the four-loop, 4000-MW(t) reactors, the data shown in Table 4-2 were given as input into the CODER program.

The results of the CODER runs are given in Table 4-3.

4.3.3. Design Description

The CODER output data were used for the designs shown in Figs. 4-1 and 4-2 for the three-loop configuration and in Figs. 4-3 and 4-4 for the four-loop configuration.

Both configurations incorporate multiple 1000-MW(t) loops consisting of a single turbomachine (TM) unit, one recuperator, and one precooler. Each recuperator and precooler of loop is connected to the TM unit by a straight vertical duct at the bottom of the cavities. The vertical compressor discharge cavity is slightly canted outward in order to reduce the bend in the recuperator-precooler connecting duct. The core inlet duct from the high-pressure side of the recuperator to the core cavity has an angle of inclination of 50 deg. This angle is larger than the 45-deg angle verified by a structural analysis and therefore represents some design uncertainty.

The PCRV diameter is determined with the code-allowable concrete stresses and limiting ligament dimensions between the cavities which are based on HTGR steam plant dimensions and on judgments from GT-HTGR PCRV stress analyses.

TABLE 4-2
CODER INPUT DATA

Item	Unit	3000-MW(t) Three-Loop Reactor	4000-MW(t) Four-Loop Reactor
Core cavity height	m (ft)	14.417 (47.3)	14.417 (47.3)
Core cavity diameter	m (ft)	11.277 (37.0)	13.564 (44.5)
Recuperator cavity diameter	m (ft)	5.258 (17.25)	5.258 (17.25)
Precooler cavity diameter	m (ft)	4.877 (16.0)	4.877 (16.0)
CACS cavity diameter	m (ft)	2.347 (7.7)	2.347 (7.7)
Turbomachine cavity diameter	m (ft)	4.225 (13.5)	4.115 (13.5)
Recuperator cavity plug thickness	m (ft)	1.829 (6.0)	1.829 (6.0)
Precooler cavity plug thickness	m (ft)	1.524 (5.0)	1.524 (5.0)
Max cavity pressure, core	MPa (psi)	7.931 (1150)	7.931 (1150)
Max cavity pressure, heat exchanger	MPa (psi)	6.269 (909)	6.269 (909)
Concrete allowable stress	MPa (psi)	15.696 (2275)	15.696 (2275)

TABLE 4-3
CODER OUTPUT DATA

Item	Unit	3000-MT(t) Three-Loop Reactor	4000-MW(t) Four-Loop Reactor
PCRV diameter (without panels)	m (ft)	35.966 (118.0)	40.173 (131.8)
PCRV height	m (ft)	33.833 (111.0) [(a)]	34.107 (111.9)
Top head thickness	m (ft)	8.230 (27.0)	9.815 (32.2)
Bottom head thickness	m (ft)	11.186 (36.7)	9.876 (32.4)
Height from bottom of turbo-machine cavity to PCRV bottom	m (ft)	3.170 (10.4)	3.170 (10.4)
Radius, PCRV center to precooler center	m (ft)	12.192 (40.0)	13.929 (45.7)
Radius, PCRV center to precooler center	m (ft)	12.192 (40.0)	13.929 (45.7)
Radius, PCRV center to recuperator center	m (ft)	12.192 (40.0)	13.929 (45.7)
Precooler center to recuperator center	m (ft)	12.409 (40.7)	12.409 (40.7)

[(a)] These dimensions could be reduced according to layout.

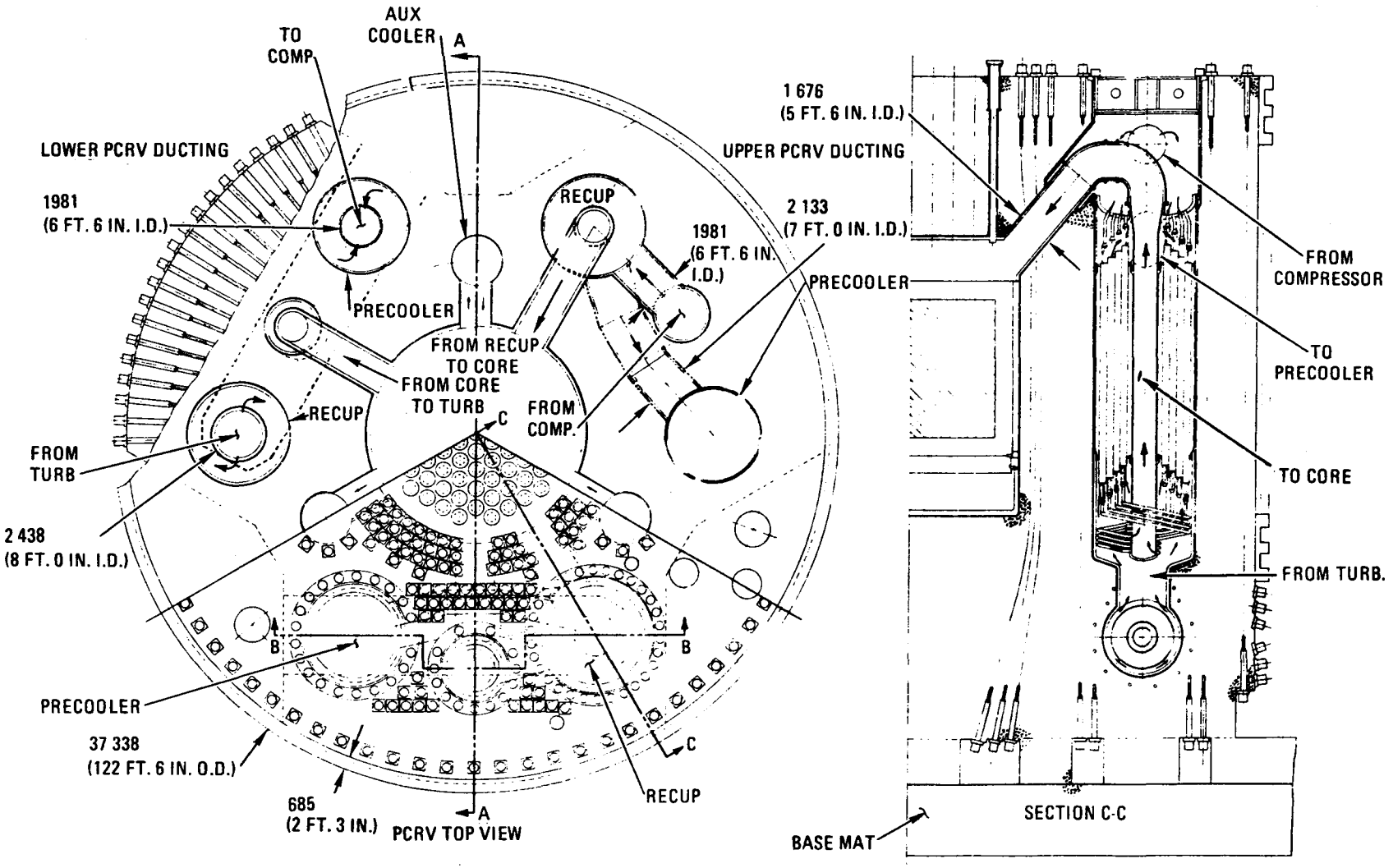

NOTE
1. ALL DIMENSIONS ARE IN MILLIMETERS UNLESS OTHERWISE SPECIFIED.

GA-A13950

Fig. 4-1. Three-loop, 3000-MW(t), 850°C ROT, single-cycle, dry-cooled GT-HTGR (drawing and section C-C)

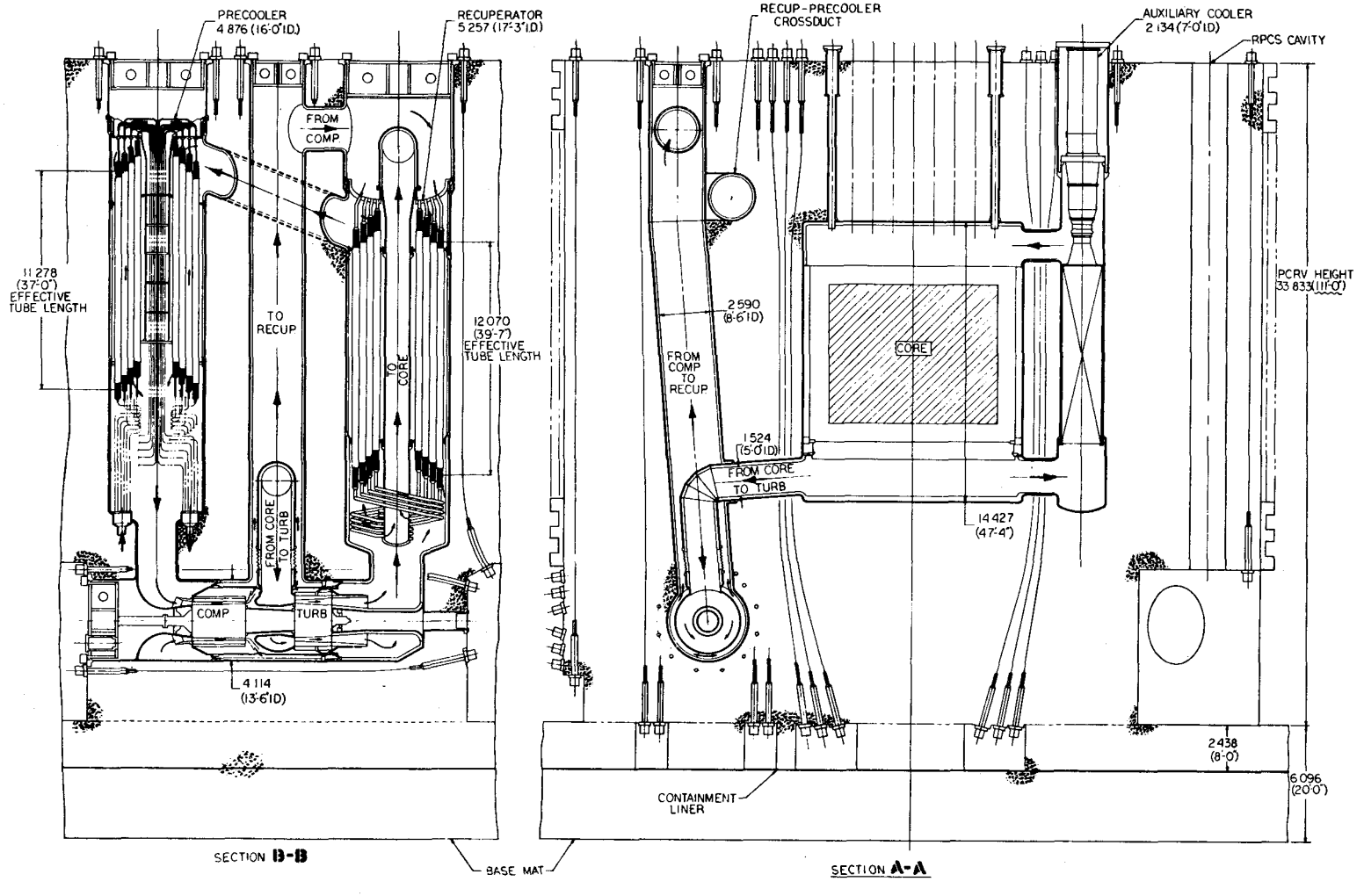

GA-A13950

Fig. 4-2. Three-loop, 3000-MW(t), 850°C ROT, single-cycle, dry-cooled GT-HTGR (sections A-A and B-B)

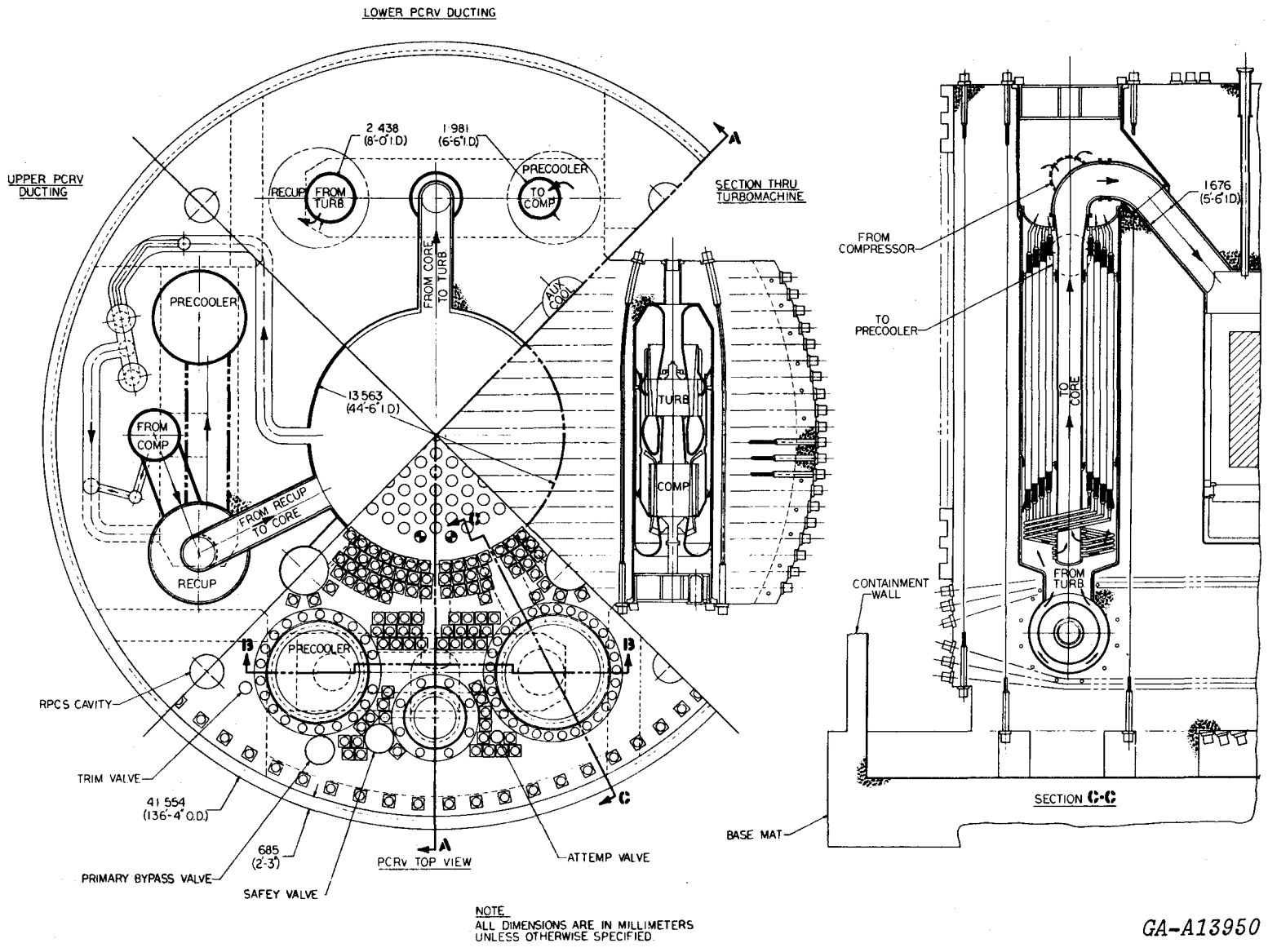

Fig. 4-3. Four-loop, 4000-MW(t), 850°C ROT, single-cycle, dry-cooled GT-HTGR (drawing and section C-C)

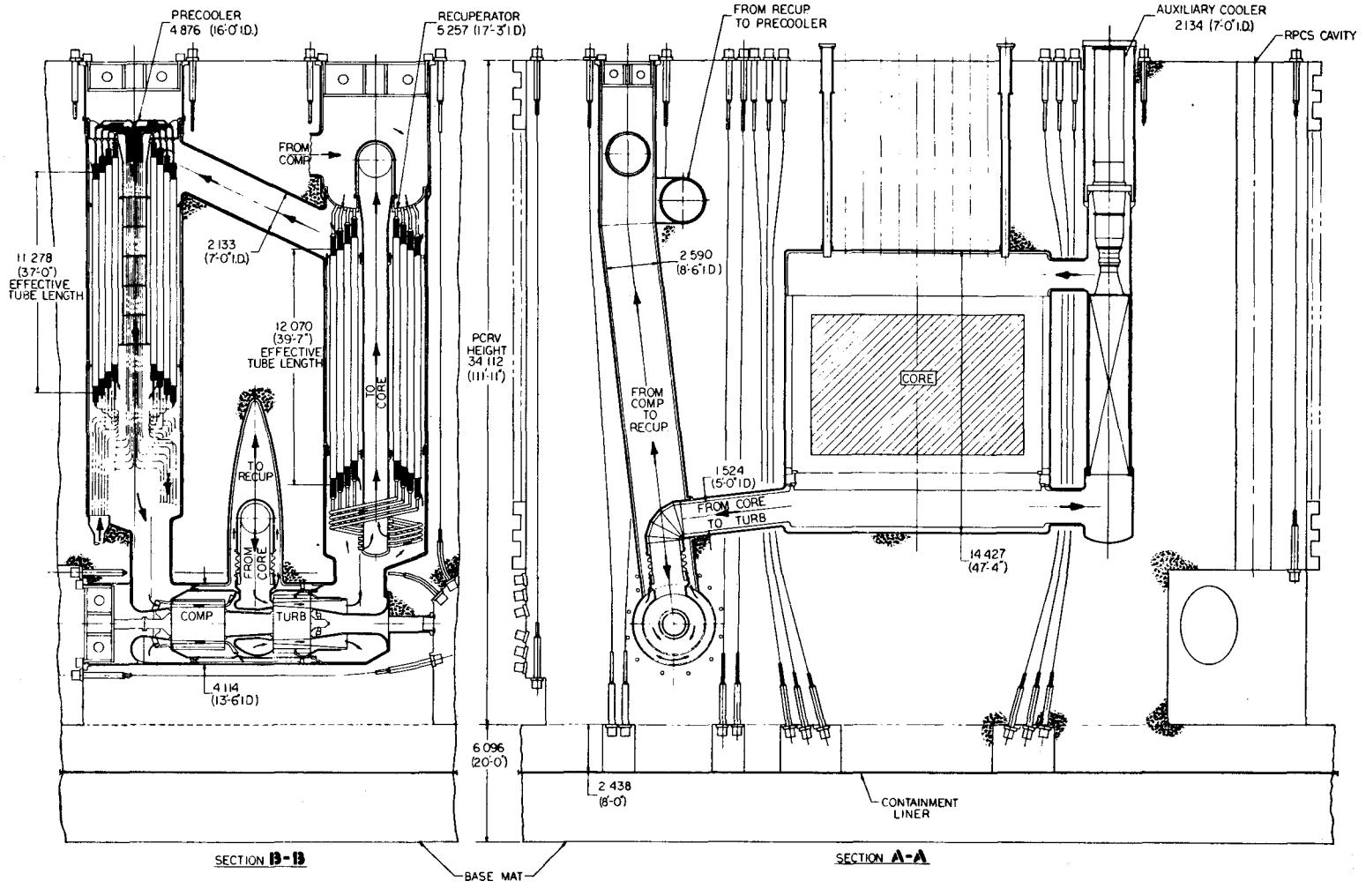

NOTE
ALL DIMENSIONS ARE IN MILLIMETERS
UNLESS OTHERWISE SPECIFIED

GA-A13950

Fig. 4-4. Four-loop, 4000-MW(t), 850°C ROT, single-cycle, dry-cooled GT-HTGR (sections A-A and B-B)

The PCRV height is established either by the total stackup required by the recuperator length and TM or by the stackup required by the PCRV head thicknesses plus the core cavity height. In the three-loop configuration, the PCRV height is determined by the former, while the latter establishes the height for the four-loop version.

For both configurations, the arrangement of the vertical tendons is difficult in the area of the compressor discharge cavity and requires more detail work in order to find an optimum arrangement. The tendon heads of the horizontal, longitudinal tendons for the TM cavity determine the design of te inner corner of the cutouts in the bottom head of the PCRV, especially at the closure end of the cavity. This is especially true for the four-loop design where the corner forms an angle of 90 deg. There is no such problem for the three-loop configuration.

The circumferential prestressing is conventional for the top part of the PCRV with wire winding in steel-lined channels of precast panels. In the bottom head section of the PCRV, the wire winding is replaced by diagonal tendons. The number of tendons is determined by the prestress required on the outer surface of the PCRV in this section. The tendons are arranged in layers, evenly separated on the circumference. The tendons lie across each other above and below the TM cavities. The pattern for the diagonal tendons is a straight-across pattern for the four-loop version, as shown in Fig. 4-5. A more complicated crossing pattern is required for the three-loop design, as shown in Fig. 4-6.

4.3.4. Comparison and Evaluation

The two configurations studied have been compared and evaluated as shown in Table 4-4. Because of the difference in power between the two configurations, most of the items in Table 4-4 can be compared on a relative basis only. In the following, the individual items in the table are discussed in more detail.

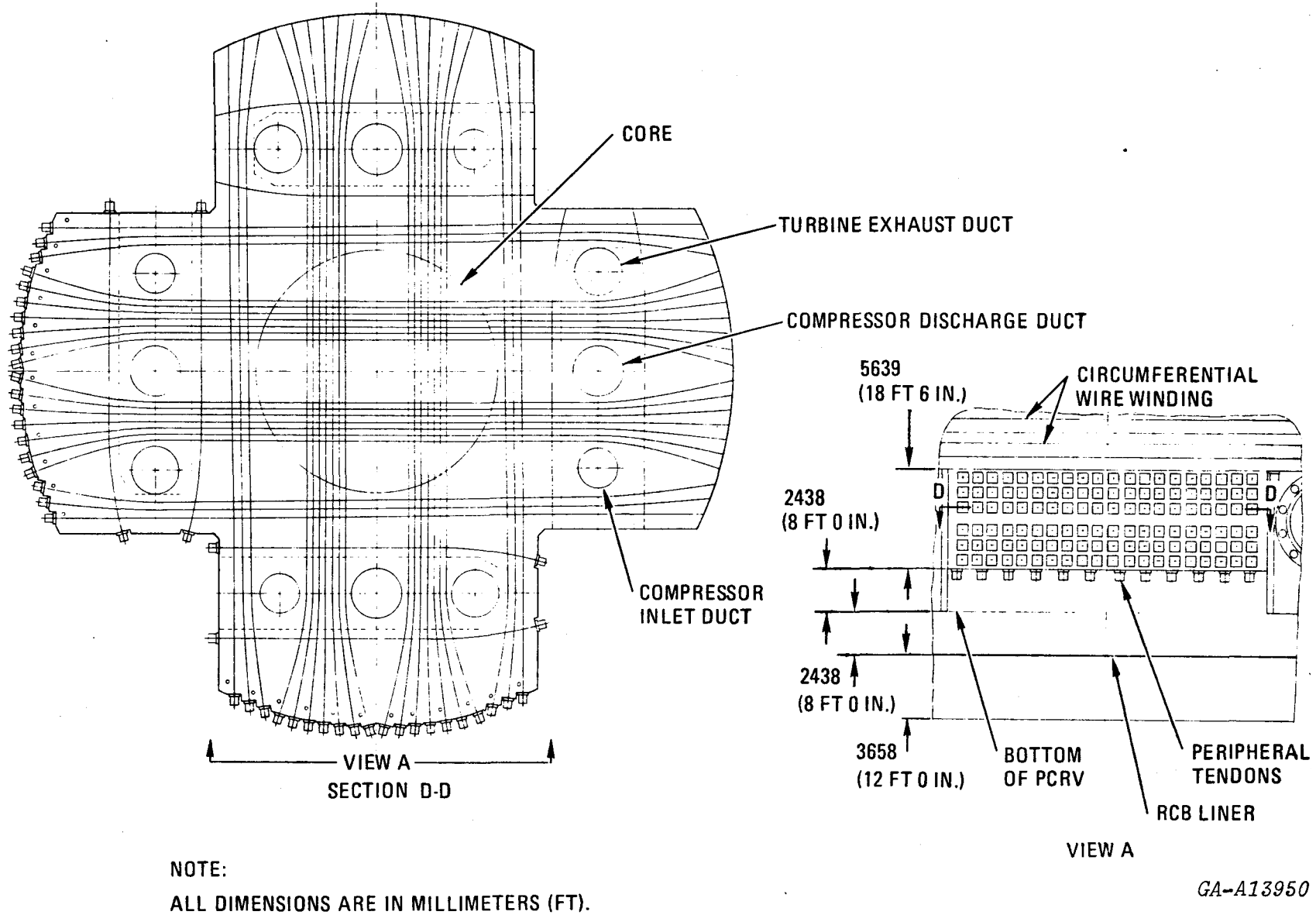

Fig. 4-5. Diagonal tendon system for four-loop GT-HTGR

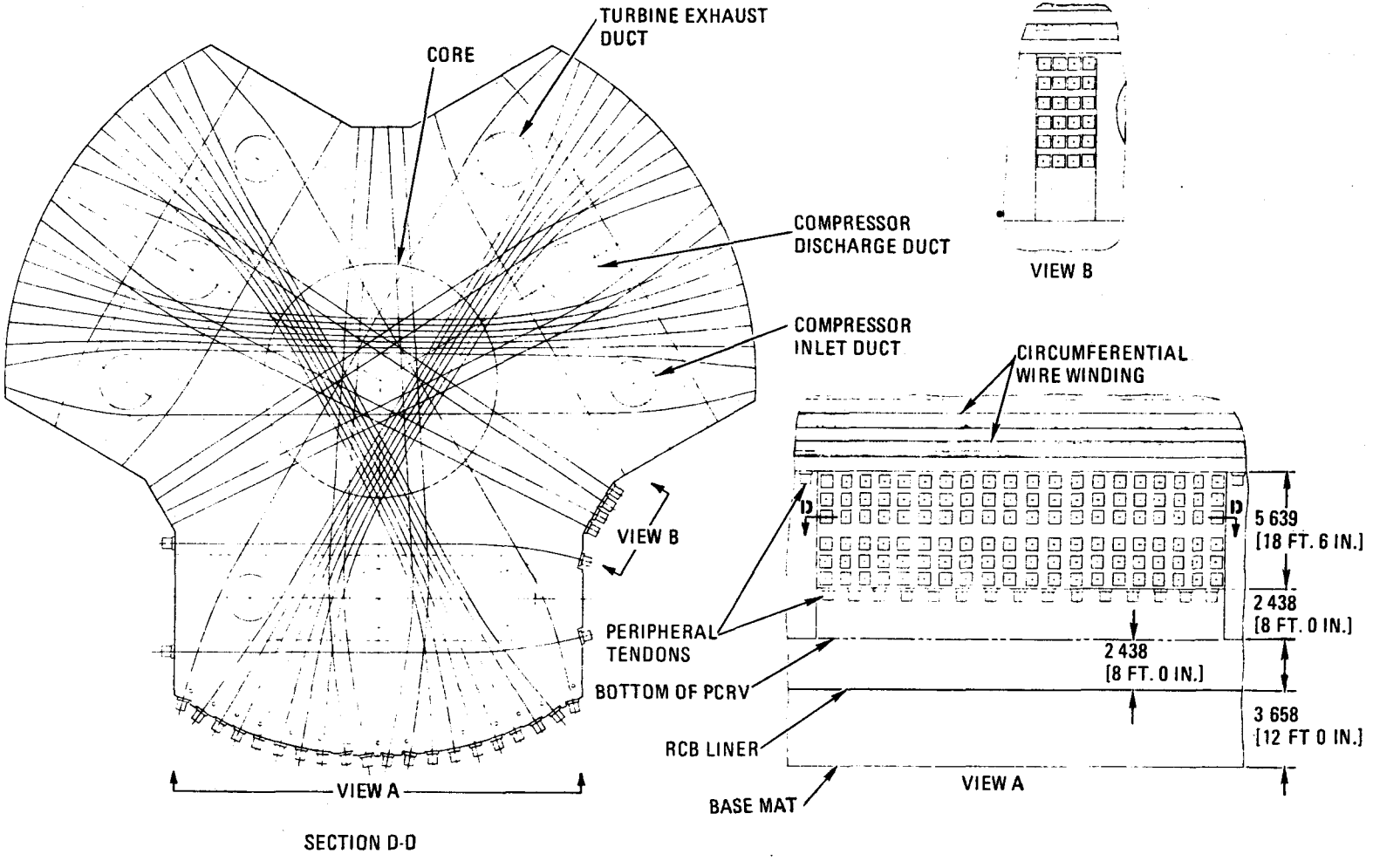

NOTE:
ALL DIMENSIONS ARE IN MILLIMETERS (FT).

GA-A13950

Fig. 4-6. Diagonal tendon system for three-loop GT-HTGR

TABLE 4-4
COMPARISON AND EVALUATION

Three-Loop Configuration:	
PCRV height determined by recuperator	Cost disadvantage
Turbomachine cavity provides growth capability for turbomachine unit	Design advantage
Complicated diagonal tendon system	Design and cost disadvantage
Adequate space for tendon heads at turbomachine cavity closure	Design advantage
Vertical ducts heat exchanger-turbomachine cavity concentric to heat exchanger cavity	Efficiency advantage
Adequate space for generator housing	Design and cost advantage
CACS cavities do not determine precooler and recuperator cavity location	Cost advantage
Four-Loop Configuration:	
PCRV height equals minimum height with present recuperator dimensions	Cost advantage
No growth capability of turbomachine unit	Design disadvantage
Simple diagonal tendon system	Design and cost advantage
Limited space for tendon heads at turbomachine cavity closure	Design disadvantage
Vertical ducts heat exchanger-turbomachine cavity eccentric to heat exchanger cavity	Efficiency disadvantage
Limited space for generator housing	Design and cost disadvantage
CACS cavities determine precooler and recuperator cavity location	Cost disadvantage

PCRV height: This is a relative evaluation. The minimum height depends on the top and bottom head thicknesses, and therefore the three-loop, 3000-KW(t) design has a relatively larger PCRV height compared with the four-loop, 4000-MW(t) design.

TM growth capability: This item can be compared directly and is fundamental for each configuration. The four-loop design provides no growth capability for the turbomachinery without influencing the PCRV size. The PCRV of this configuration is designed for a TM cavity of minimum dimensions for the compressor inlet and turbine outlet scrolls, and the cavity space available does not provide additional length for a larger TM. In the three-loop design, however, sufficient space for TM growth can be provided without influencing the PCRV diameter.

Diagonal tendons: The arrangement for the three-loop design is more complicated because each layer of tendons has six crossings in the center, while the four-loop design has only two crossings per layer (see Figs. 4-5 and Fig. 4-6).

Tendon head space: The available space for the tendon heads in the corner of the PCRV cutouts can be a major problem for the four-loop design. It will be no problem for the three-loop design.

Vertical ducts at bottom of heat exchanger cavities: The most efficient position of these ducts would be concentric to the bottom surface. Because of the required cavity arrangement in the four-loop design, these ducts had to be arranged eccentric to the heat exchanger cavities. A concentric arrangement can be provided for the three-loop configuration.

Generator housing: Adequate space for the generator housing is available for the three-loop design because the PCRV cutout forms an angle of 120 deg which provides an open space of 30 deg for the generator housing. For the four-loop design, this space will be limited because of the 90 deg corner of the cutout. An alternate solution to the four-loop generator congestion

problem would be to increase the shaft length between the TM and the generator, moving the generator away from the PCRV. This could cause critical shaft speed problems which should be investigated before taking such an approach.

Core auxiliary cooling system (CACS) cavities: Minimum ligament requirements between cavities in the PCRV determine the geometric arrangement of the precooler recuperator, CACS, and core cavity. For the four-loop design, these are all minimum ligaments, and a larger CACS cavity, if required, would result in a larger PCRV diameter. The three-loop design is not based on minimum ligament spacing of the cavities, and therefore, an increase in the CACS cavity diameter would not affect the PCRV diameter.

4.3.5. Conclusion

The result of an overall comparison of the advantages and disadvantages of the two configurations leads to the conclusion that the three-loop configuration is a more favorable design with a better growth potential.

4.4. DELTA DESIGN STRESS ANALYSIS

Elastic stress analysis of the three-loop delta design PCRV has been performed utilizing the finite element method. Two structural analysis computer codes were used in the study: i.e., MARC (Ref. 4-1) and THREED (Ref. 4-2). Both codes implement similar solution schemes, the latter being more efficient for the present analysis.

Two finite element models of the PCRV were developed for the analysis. The element used in the analyses is a 20-node isoparametric brick element with 8 corner nodes and 12 midedge nodes which provide the capability of modeling the curvature of cylindrical surfaces. The first model consists of 204 elements and 1179 nodal points, a relatively coarse mesh for the purpose of a preliminary feasibility study. The second model consists of 351 elements and 2061 nodal points. The purpose of the latter model was to verify

the results from the first model and to provide an adequate model for comprehensive design studies. The symmetric qualities of the PCRV design enable the modeling of a 60-deg sector of the PCRV from the barrel midheight to the barrel floor. The major cavities of the reactor system included in the models and the layer-by-layer finite element breakdown of the second model are shown in Fig. 4-7.

Two sets of loading conditions were applied to each model representing the two most severe combinations of PCRV loads: i.e., construction loads and end-of-life loads. Construction loading includes maximum prestressing loads without pressure loading from the reactor system. The prestress system provided for the PCRV is divided into two groups: the circumferential prestressing system (CPS) and the longitudinal prestressing system (LPS). The end-of-life loading condition consists of degraded prestress loads accompanied by maximum cavity pressure loads. Because of short-term concrete relaxation created by shrinkage and long-term creep relaxation, CPS and LPS loadings will diminish during the design life of the PCRV. On the basis of experience with the steam plant PCRV, a stress reduction of 20% is assumed for both CPS and LPS loadings at end-of-life.

Other model assumptions besides the 20% prestress degradation are as follows: The core cavity liner, the heat exchanger cavity liner, and the CPS channel stiffness are assumed to be zero; deadweight stresses are assumed to be negligible; material properties of the concrete are assumed to be isotropic and linearly elastic with a Young's modulus of 4.0×10^4 MPa (5.8×10^6 psia) and Poisson's ratio of 0.21; axial stresses created by the LPS loading are assumed to be uniform on the PCRV barrel; thermal stresses are neglected.

Preliminary stress analysis using the first model indicated that the delta layout is structurally feasible. Stress results were compared with the allowables as defined by the ASME Boiler and Pressure Vessel Code, Section III, Division 2 (Ref. 4-3) and were found to be acceptable. The coarseness of the first model resulted in questionable element geometry

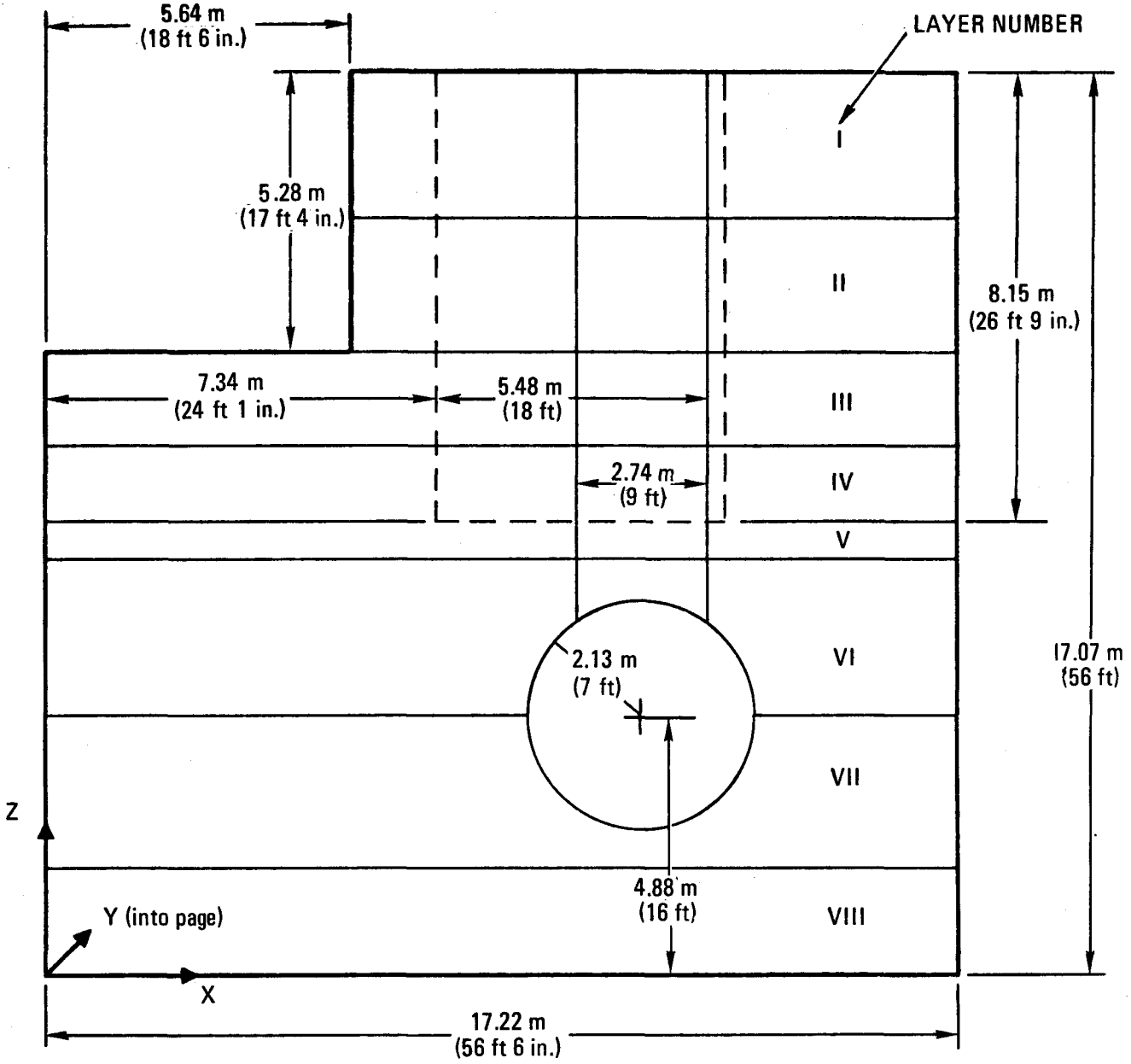

GA-A13950

Fig. 4-7. Delta layout (side view)

at some locations in the model where relatively high stresses were expected. Therefore, it was decided that a more refined model would be developed in order to verify the preliminary analysis and for use in design studies. The increased size of the second model allows accurate modeling of all important PCRV features, in particular, the critical intersections of vertical cavities with the horizontal TM cavity.

The first recommendation of the preliminary analysis has been verified using the refined model. Because the two models differ in number of elements, stresses cannot be compared on a one-to-one basis. Instead, an average principal stress along a peripheral line common to both models is compared, as shown in Table 4-5. This comparison illustrates a high degree of repeatability in the stress results. Such repeatability from two radically different models tends to verify the accuracy of the results. Furthermore, it has become apparent that accurate preliminary analysis can be performed with a relatively coarse mesh. On the other hand, because of questionable element geometry in the first model, a substantial amount of data was excluded from the results. Subsequently, a good deal of engineering judgment and interpretation was necessary in order to arrive at those results. The results from the finer mesh require far less interpretation and indicate significant trends in a much more continuous and realistic fashion.

During construction, the PCRV is subjected to maximum prestress loading without any internal pressure loading from the reactor system. The prestressing must be substantial enough to prevent tensile stresses from occurring at any time during the design life. At the same time, the prestressing cannot result in unacceptable compressive stresses.

Subjected to the loading conditions mentioned previously, the model meets the ASME Code (Ref. 4-3) requirements in all cases. A PCRV location of particular concern from conception of the delta layout is the section change (generator cutout) 7.92 m (26 ft) above the PCRV floor. The analyses indicate that compressive stresses of about 13.8 MPa (2000 psi) exist near the discontinuity; these stresses are clearly acceptable. For end-of-life loading, Fig. 4-8 illustrates the trend of local peak tensile stresses along

TABLE 4-5
COMPARISON OF STRESSES BETWEEN FIRST MODEL AND SECOND MODEL

Loading Conditions	Average Principal Stress, MPa (psi) (Max or Min)		Location
	First Model	Second Model	
Construction	-8.72 (-1264) (min)	-8.58 (-1244) (min)	Along X axis near barrel midheight
Construction	-7.94 (-1151) (min) -3.98 (-577) (max)	-8.51 (-1234) (min) -4.33 (-628) (max)	At 60 deg to X axis same height
Construction	-13.51 (-1960) (min)	-13.03 (-1890) (min)	Near cutout
Construction	-26.34 (-3820) (min)	-26.06 (-3780) (min)	Between vertical ducts
End of life	-5.83 (-846) (min) -2.34 (-340) (max)	-5.98 (-868) (min) -2.12 (-307) (max)	Along X axis barrel midheight

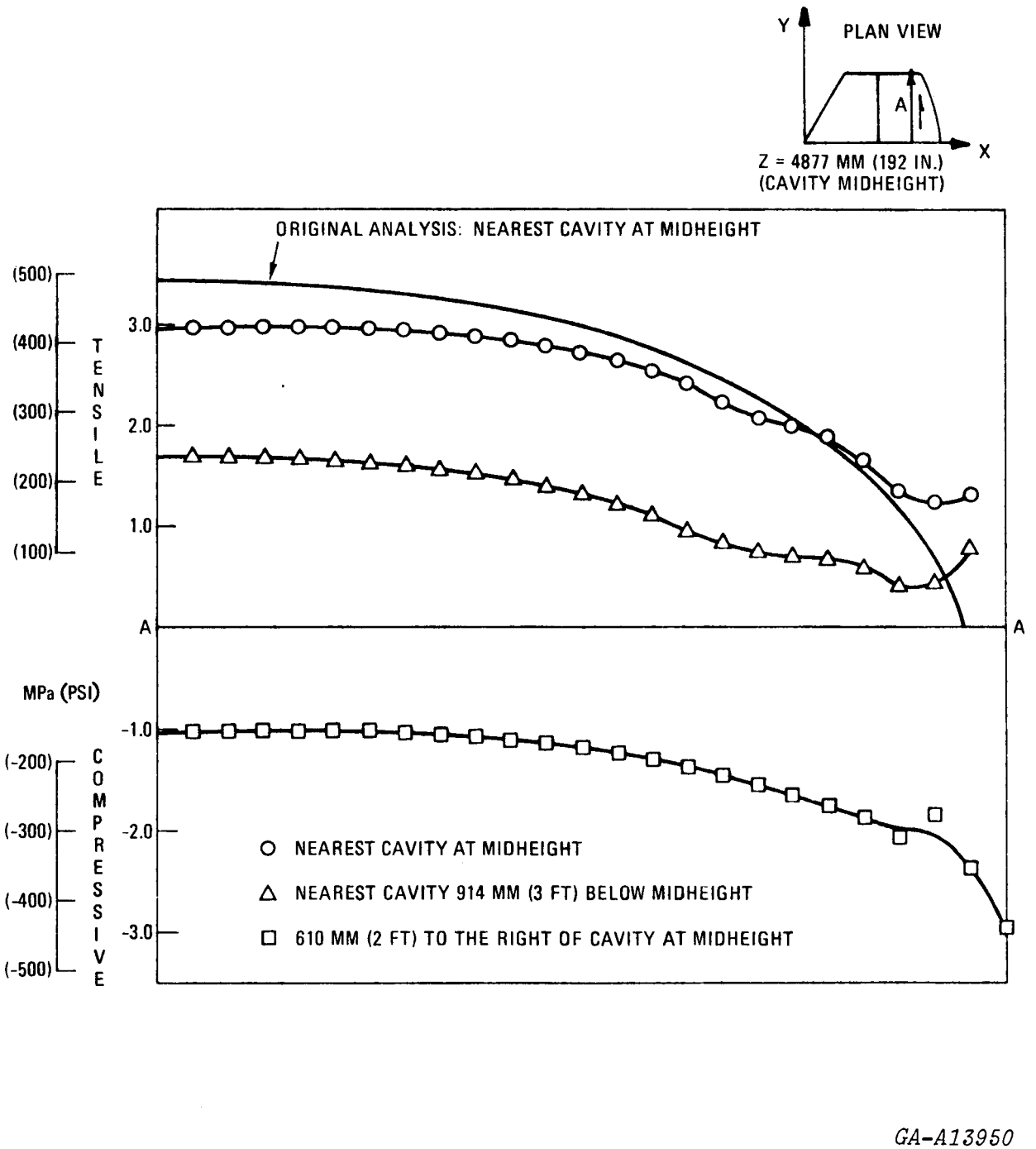

GA-A13950

Fig. 4-8. Turbomachine cavity stresses, maximum principal stress vs cavity length (end-of-life loading)

the length of the TM cavity near the cavity midheight. The upper two curves again indicate the close comparison of results from the two different models. The graph also illustrates the stress gradient near the discontinuity, emphasizing the local nature of these tensile stresses.

The conclusions which can be reached from this study are as follows:

1. The new finite element model of the PCRV provides results which require much less interpretation than the previous model.

2. The results of the new model and the previous model are comparable.

3. The delta arrangement of the PCRV is feasible because it does not introduce any stress concentrations which are unacceptable.

Recommendations of these analyses are as follows for design studies using the refined model:

1. The loading conditions should be modified to examine the model's sensitivity to variations in prestressing loads.

2. A thermal stress analysis should be performed.

3. A parametric study should be made in order to optimize the relative cavity locations in the PCRV.

A parametric study is currently under way in order to satisfy the first recommendation.

4.5. STEEL CLOSURE

4.5.1. Introduction

A preliminary stress analysis of a GT-HTGR closure was performed to demonstrate the feasibility of the steel closure design. This analysis was carried out using the SAP IV program (Ref. 4-4). This program is a finite element program which is capable of performing static as well as dynamic analyses of linear systems.

For this analysis, two different pressure laodings were considered: P = 7.03 MPa (1020 psig) and 5.55 MPa (805 psig), corresponding to the maximum pressures for the recuperator and the precooler cavities, respectively. To assess the effects of different geometrical parameters (including plate thickness, number of radial gussets, and plug height) on closure stress and deflection, a number of parametric runs were made on the precooler cavity closure. The PCRV steel closure stresses which were calculated were compared with the allowable stress limits of the ASME Boiler and Pressure Vessel Code, Section III, Division I (Ref. 4-5). On the basis of these analyses, the steel closure design for the various GT-HTGR cavities is feasible.

4.5.2. Method of Analysis

The steel closure model which was analyzed is shown in Fig. 4-9. The closure model is simulated by 228 nodal points and 188 shell elements (element No. 6 in Ref. 4-4). At each nodal point, six degrees of freedom are considered: namely, three displacements and three rotations. The stresses at the centroid of each element are calculated by determining three inplane loads (two normal loads and one shear load) as well as three bending loads. Even though this program is capable of performing analyses on structures with anisotropic material behavior, only isotropic material properties were considered in this analysis.

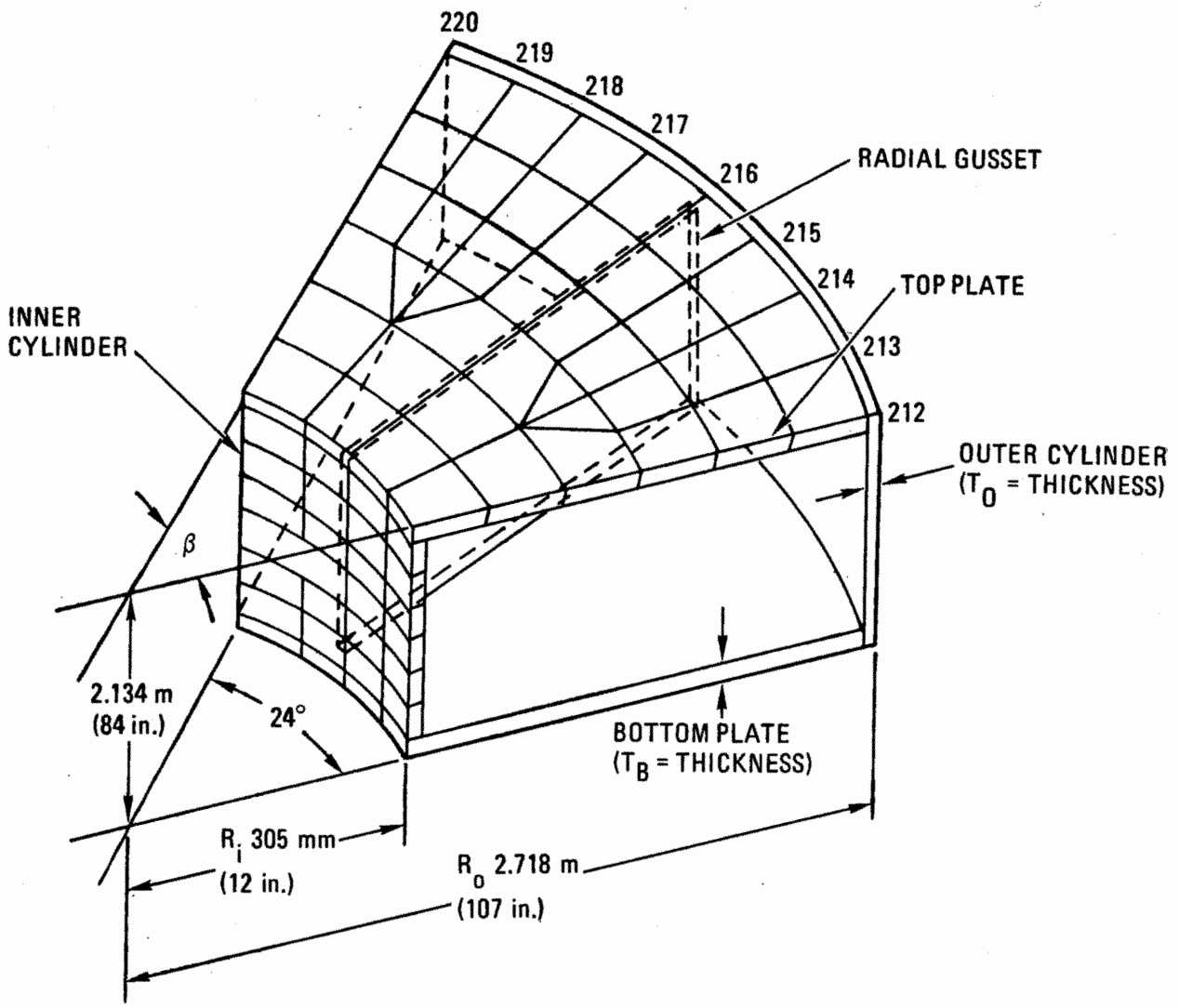

Fig. 4-9. PCRV closure plug model

GA-A13950

Various geometrical parameters such as plate thickness, number of radial gussets, and change in plug height were considered in order to assess the effect of these variables on closure stress and deflection. The change in plate thickness for a highly stressed bottom plate and the outer cylinder and the change in number of gussets (N = 12, 15, and 18) were found to have profound effects on the closure stress and the deflection. On the other hand, the stress was found to be less sensitive to variations in the closure height. This analysis is expected to provide the design guidelines for the PCRV steel closure and to be an aid in achieving the most economical closure design.

To minimize model preparation time and computer cost, a pie-shaped closure plug model with a variable circumferential angle β (β = 360/number of gussets) was prepared (see Fig. 4-9), taking advantage of the closure structural symmetry. The closure was also restrained in the axial direction by a simulated retaining ring to transmit the closure pressure loads to the PCRV.

4.5.3. Results

Various computer runs were made on the PCRV steel closures to calculate the stresses and deflections of the different recuperator and precooler cavity closure configurations. However, this report highlights only the precooler cavity closure runs.

A base case closure model was prepared for the preoooler cavity with 12 radial gussets and with bottom plate and outer cylinder thicknesses of 7.62 mm (3 in.). These parameters were determined during the preliminary design studies.

For this analysis, a pressure loading of 5.55 MPa (805 psig) was applied on the pressure boundaries. The stresses at the most critical locations, namely, bottom plate and outer cylinder, were found to exceed the allowable stress limits of Ref. 4-5. Consequently, two additional runs were made with thicker plate for the bottom plate and for the outer cylinder. The calculated stresses are given in Table 4-6.

TABLE 4-6
PRECOOLER CAVITY CLOSURE STRESS ANALYSIS

	Plate Thickness		
	T_O = 76.2 mm (3 in.) T_B = 76.2 mm (3 in.)	T_O = 101.6 mm (4 in.) T_B = 101.6 mm (4 in.)	T_O = 101.6 mm (4 in.) T_B = 114.3 mm (4 in.)
Stress Location	Stress in MPa (psi)	Stress in MPa (psi)	Stress in MPa (psi)
Bottom plate	308.0 (44,680)	180.0 (26,080)	179.2 (25,990)
Outer cylinder	333.5 (48,370)	223.6 (32,430)	186.8 (27,090)

N = 12, $T_{gussett} = T_{inner}$ = 50.8 mm (2 in.), T_{top} = 76.2 mm (3 in.), H = 2.134 m (84 in.)

Deflection plots for these runs are shown in Figs. 4-10 and 4-11. Figure 4-10 is a plot of vertical deflections in the bottom plate versus radial location. As expected, the closure vertical deflection is reduced with increased bottom plate and outer cylinder wall thicknesses.

Deflection behavior of the outer cylinder is found to be significantly different from that which was initially calculated in the preliminary design studies. It was found that the deflection of the outer cylinder is similar to that expected in a simply supported plate subjected to lateral pressure loading. Consequently, the radial deflection at the midheight (H/2) is significantly greater than the end deflection, as shown in Fig. 4-11. For the outer cylinder, two simple supports are believed to be provided by the top and bottom plates, and the remaining two supports are provided by the two radial gussets. Because of this behavior, the calculated stresses were found to be significantly higher than those calculated during the preliminary design studies.

In order to determine the effect of the number of radial gussets on the closure stress, two runs were made: one with 15 radial gussets and the other with 18. A plot of radial deflection versus axial location for the outer cylinder is shown in Fig. 4-12. This graph indicates that the closure becomes more rigid with an increase in the number of radial gussets. Consequently, both the closure deflection and the stress are significantly reduced.

As the number of radial gussets increases, the welding costs are also expected to increase. The increase in the welding costs will be partially offset by a decrease in the required plate thickness for the bottom plate and the outer cylinder. Nevertheless, on the basis of this preliminary cost analysis, the total closure cost is found to increase with an increase in the number of radial gussets.

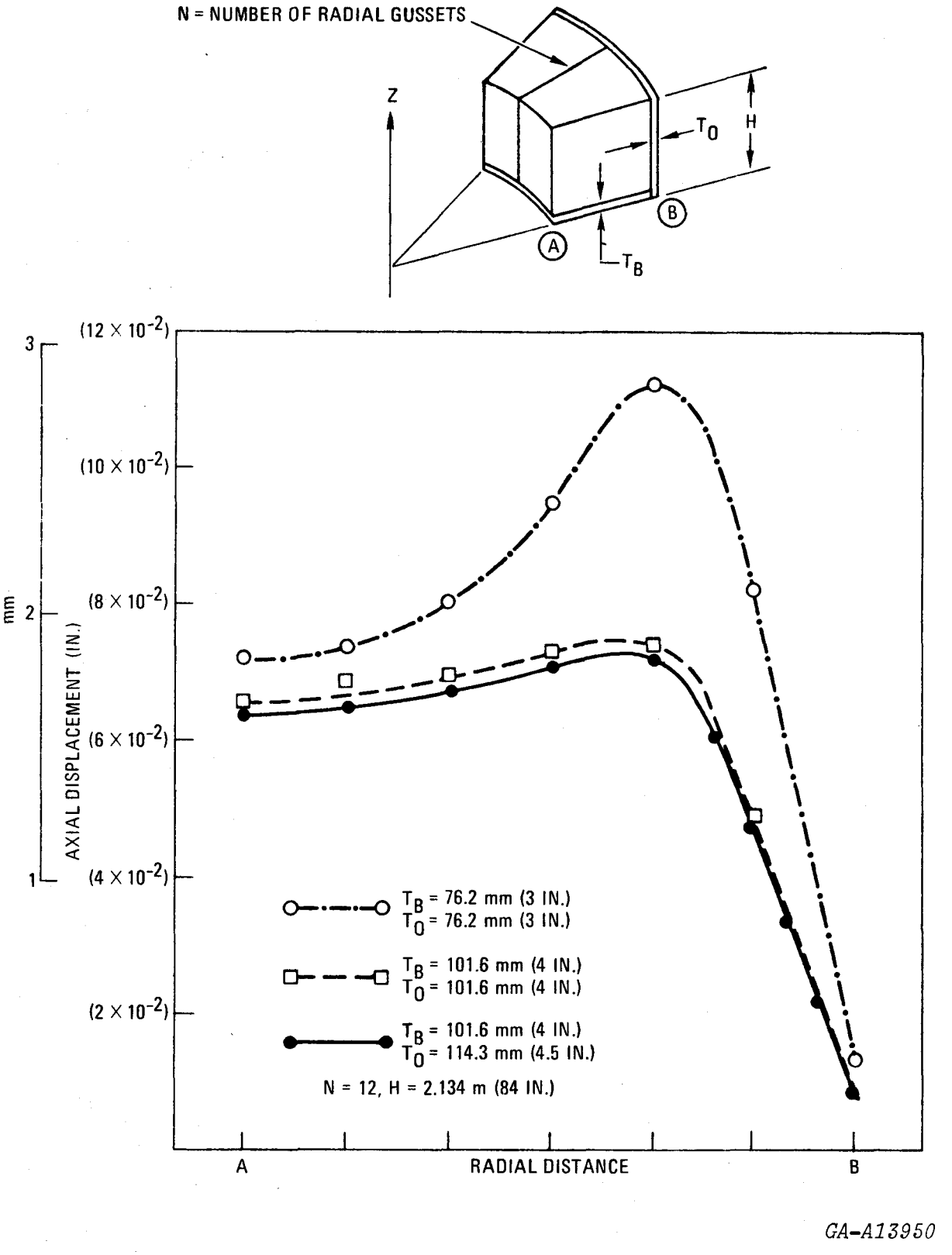

Fig. 4-10. Vertical deflection vs radial location for bottom plate

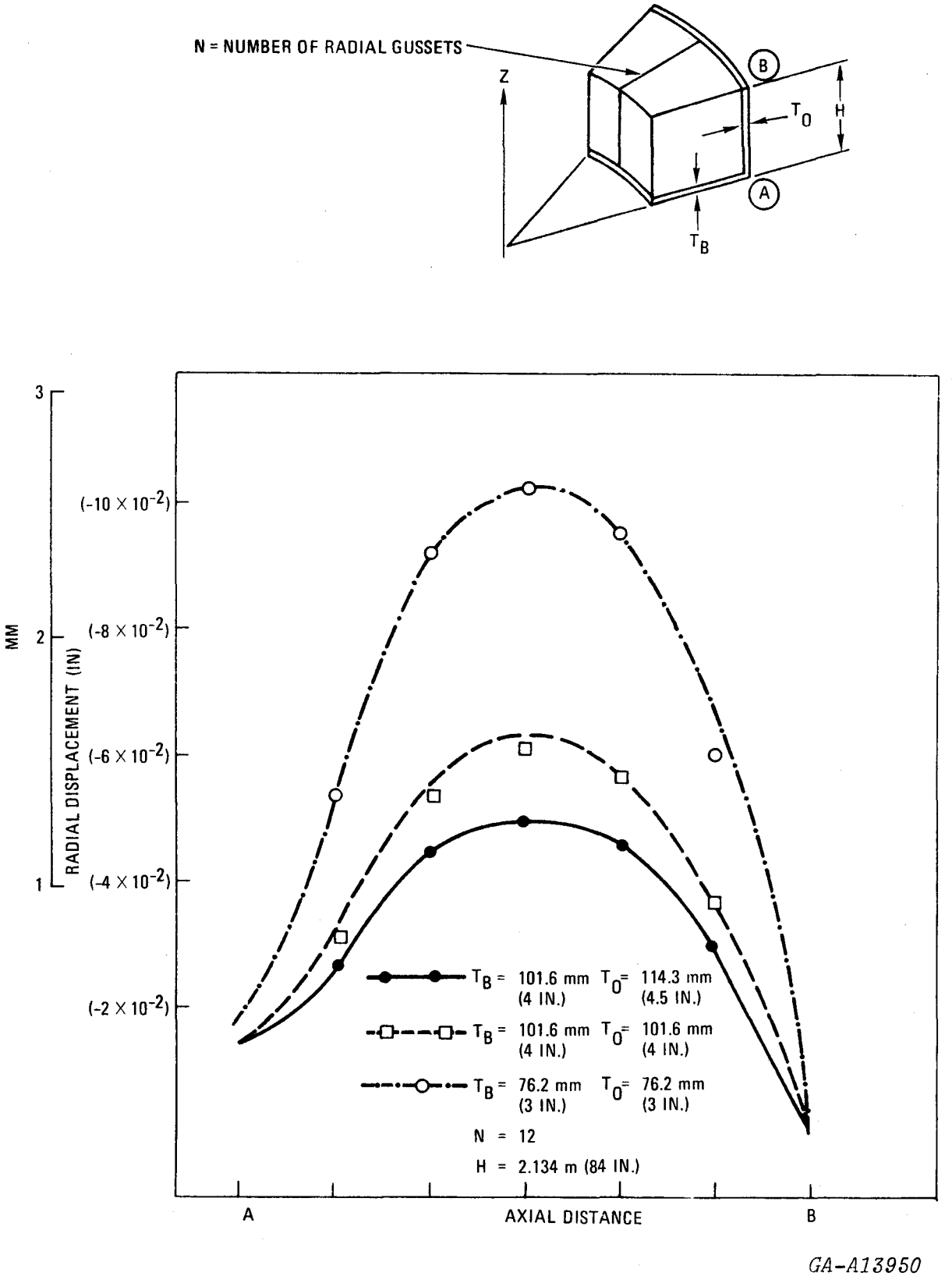

Fig. 4-11. Radial deflection vs axial location for outer cylinder (for varied plate thicknesses)

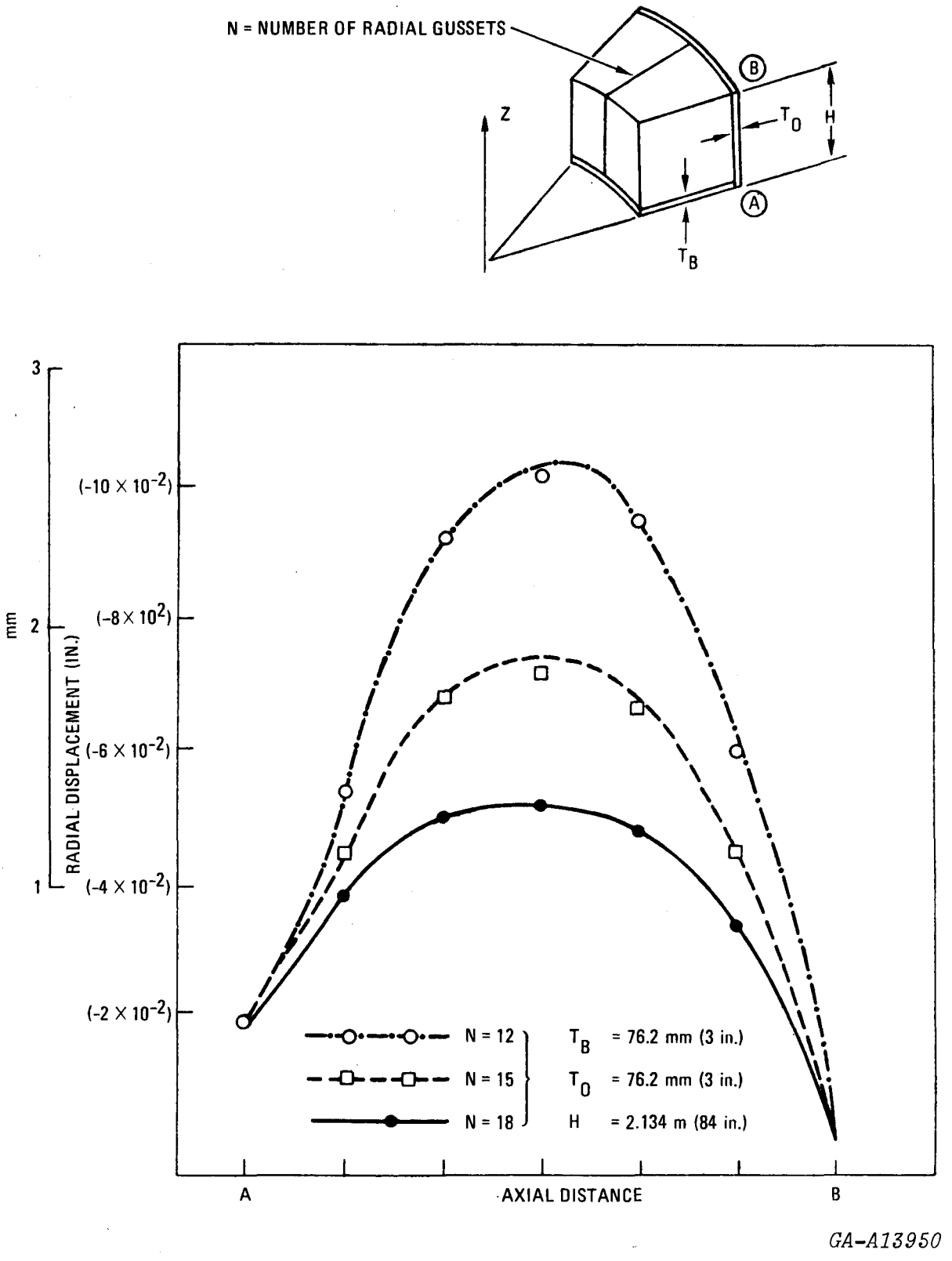

Fig. 4-12. Radial deflection vs axial location for outer cylinder (for different number of gussets)

4.6. EQUIPMENT SUPPORT INTERFACES

Equipment supports have at least three major functions: structural, thermal, and mechanical. Each support must connect the equipment to its PCRV cavity liner structurally, withstanding all anticipated loads; it must provide sufficient thermal resistance to avoid causing local liner hot spots; and the support must be accessible or otherwise designed to facilitate equipment removal and replacement. Allowance must be made in equipment support design for PCRV concrete movement caused by long-term creep of the prestressed material. Section 4.6.1 discusses this phenomenon, specifically examining the horizontal turbomachine cavity. Section 4.6.2 follows with the turbomachine mount design study results, while Section 4.6.3 treats heat exchanger support design.

4.6.1. Turbomachinery Support Displacement Analysis

4.6.1.1. Introduction. A preliminary stress analysis was performed on the turbomachinery cavity liner to determine elastic as well as inelastic displacements created by the PCRV prestressing, pressure, and thermal loads. These displacements must be determined in order to design various components, namely, compressor end flange support, turbine end support, and turbomachinery cavity closure. The total PCRV liner displacements during plant operation were calculated based on the methods outlined for the SC-HTGR PCRV. Total turbomachinery liner displacements, which include elastic as well as creep deformations, were calculated by appropriately combining the various elastic displacements as calculated in Section 4.4.

4.6.1.2. Method of Analysis. The total displacements, which include elastic as well as creep deformations, at the various turbomachinery liner locations were calculated on the basis of methods used for the SC-HTGR and the elastic displacements as determined in Section 4.4. It is well-known that if a concrete bar is subjected to an uniaxial loading either at room temperature or at elevated temperature, the bar is expected to deform continuously because of the time-dependent creep strain. The rate of creep strain will

depend on various factors such as aggregate properties, cement paste properties, concrete moisture content, time from casting, steady-state temperature, etc. Using the concrete creep data given in Ref. 4-6 and the subsequent concrete creep testing program at UC Berkeley, the SC-HTGR PCRV design group developed design methods which predict the approximate total (maximum) liner displacements (elastic as well as creep) based on PCRV elastic displacements.

4.6.1.3. Total Concrete Displacement. It was observed in the GT-HTGR PCRV stress analysis reported in Section 4.4 that the liner displacements during construction are nearly out of phase with the pressure displacements. In order to perform conservative displacement analysis, it was assumed that the PCRV is subjected to a combination of prestressing and thermal loadings without PCRV internal pressurization for the entire PCRV life of 40 yr. In that case, the maximum radial displacements (elastic plus creep) in the turbomachinery cavity at the end of the PCRV life are calculated by

$$U/r = \varepsilon_s + (1 - \delta + \Phi)\ \varepsilon_i + \varepsilon_t \qquad (4\text{-}1)$$

where U = radial displacement m/m (in./in.) (with respect to turbomachinery axis)

r = radius of turbomachinery cavity = 2.134 m (84 in.)

ε_s^* = 400 μ at the end of PCRV life

δ^* = 0.18 stress reduction factor

Φ^* = creep coefficient = 3

ε_i = circumferential strain during construction

ε_t = circumferential thermal strain $\simeq$ 275 μ

Thus, the maximum expected radial displacement can be calculated as

$$U = 400 \times 10^{-6} \times 2.134 + (1 - 0.18 + 3) \times 0.00376$$

$$+ 275 \times 10^{-6} \times 2.134 \text{ m } (400 \times 10^{-6} \times 84 + (1 - 0.18 + 3)$$

$$\times 0.148 + 275 \times 10^{-6} \times 84 \text{ in.}) = 15.8 \text{ mm } (0.622 \text{ in.})$$

*Based on SC-HTGR results

The required radial displacements in the bolted joint, namely, turbomachinery plug, compressor and flange, and turbine end support will be approximately 15.8 mm (0.622 in.). These requirements are considered to be excessive and may create problems in the bolted joint design. If this is the case, radial clearance requirements can be reduced by drilling bolt holes in the penetration liner, the compressor end flange, the turbine end support, and the turbomachinery plug after the PCRV has been prestressed, thus creating minimum mismatch between these components at the beginning of the PCRV life. Similarly, the PCRV displacements at the turbine end support and at the turbomachinery shaft bearing were also calculated. The calculated displacements are summarized in Table 4-7.

If it is found that these requirements unduly penalize the component design, the following alternatives are suggested:

1. Perform a detailed time-dependent PCRV analysis. This is expected to reduce the magnitude of these conservative displacements significantly.

2. Provide additional cooling in the vicinity of the PCRV bottom head. This will reduce the bulk temperature of the bottom head concrete and, consequently, reduce the time-dependent concrete creep displacements.

4.6.2. Turbomachine Mount Design

4.6.2.1. Summary. As part of the current major equipment interface design study, the inboard and outboard turbomachine case mount designs identified in Ref. 4-7 were examined, as well as candidate interfacing cavity liner and concrete anchor designs. Mount loads and load paths were identified, and a criterion was established by the ACD staff that disallows mount failure in order to insure turbomachine cavity seal integrity. The resulting designs for the inboard mount system (mount No. 1, turbine end) and the outboard mount system (mount No. 2, compressor end) are shown in Fig. 4-13.

TABLE 4-7
TURBOMACHINERY SUPPORT DISPLACEMENT

Location	Required Radial or Vertical Clearance	Remarks
Bolt for turbomachinery plug	15.875 mm (0.625 in.) in radial direction	Bolt holes were assumed to be drilled before the PCRV construction.
Compressor end flange and turbine end support	6.35 mm (0.25 in.) in radial direction	Bolt holes were assumed to be drilled at the beginning of the PCRV life.
Turbine end support (uplift)	6.35 mm (0.25 in.) in vertical direction	
Turbomachinery shaft	4.76 mm (0.1875 in.) in radial direction	Turbomachinery shaft was assumed to be aligned at the beginning of the PCRV life.

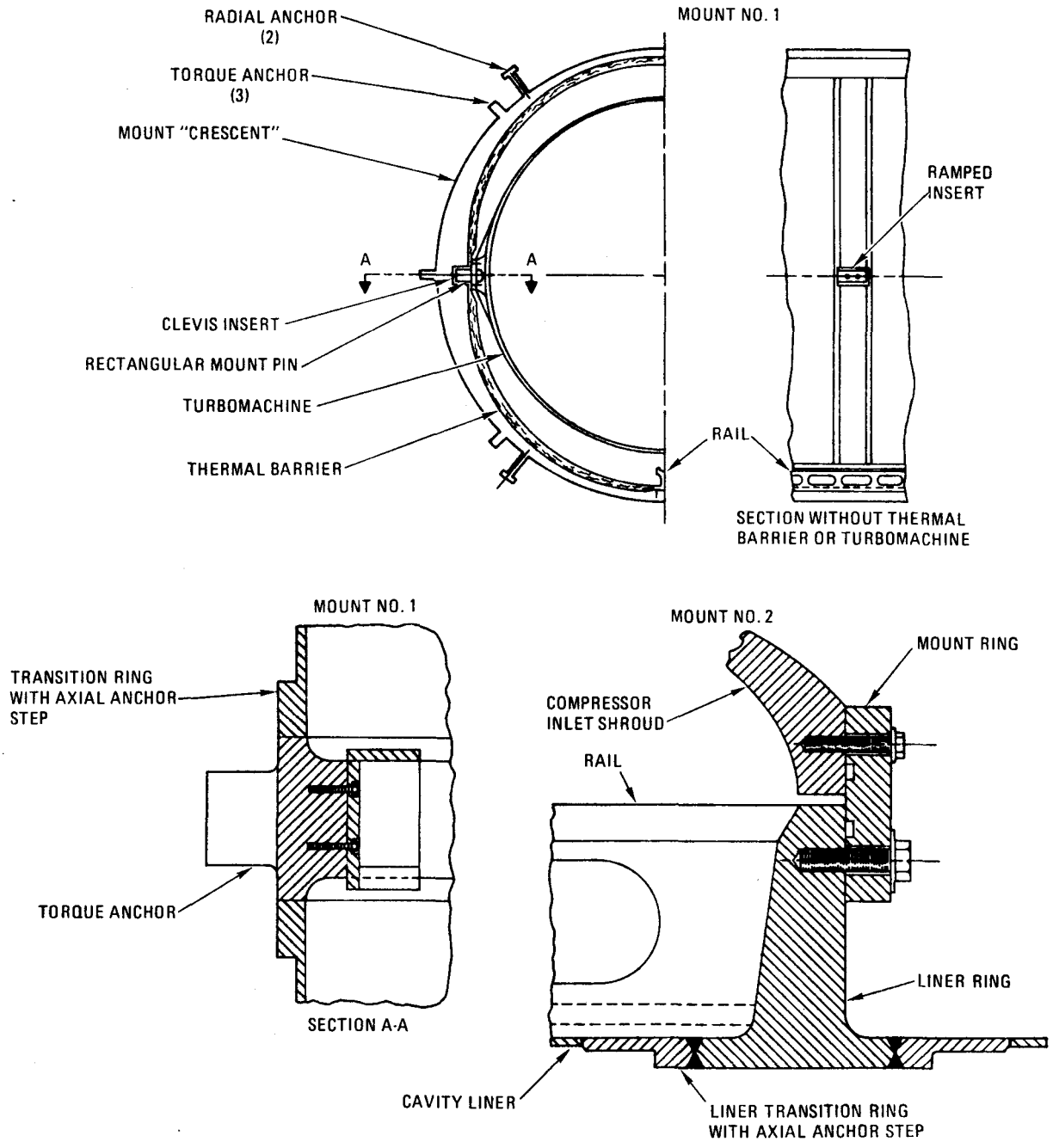

Fig. 4-13. Turbomachine mounts

Significant changes were made to the referenced mount No. 1 design to improve the load path geometry, while only minor alternations were made to the referenced mount No. 2 design.

It will be necessary to provide for pressure balancing of the maintenance spaces at each end of the turbomachine at all times, including control valve transient events, because shroud loads would otherwise become very large, approaching 45 MN (10^7 lbf).

4.6.2.2. Description. Figure 4-14 is a sketch which depicts the turbomachine in its cavity. It identifies the inboard mount as a pair of horizontal pins and the outboard mount as a bolt circle near the periphery of the compressor inlet shroud. The outboard mount acts as the axial case anchor and supports outboard radial as well as axial loads. The inboard mount pins slide in slotted clevises and support inboard case radial and all torque loads.

4.6.2.3. Loads. Turbomachine case loads, as currently known, are summarized by load type in Table 4-8, where data references are given. Table 4-9 groups the load data by events. Much data in the tables are self-explanatory; however, the following comments are relevant where assumptions were made during the subject study.

Horizontal installation loads were identified as the axial force required to move the inboard end of the turbomachine up the clevis ramps. A 15-deg ramp angle and a friction coefficient of 0.15 were assumed.

A rotor disk failure impact load of 4.45 MN (10^6 lbf) was estimated by assuming that one-third of the disk impacts the disk catcher before the other fragments do and that the catcher deforms 127 mm (5 in.) radially in arresting the missile. Knowing the mass and kinetic energy of the missile (1/3 disk at 452 rad/sec) and assuming that the missile deceleration rate would be constant (consistent with catcher plastic deformation), it was possible to estimate the force and duration (7.5 msec) of the impact load

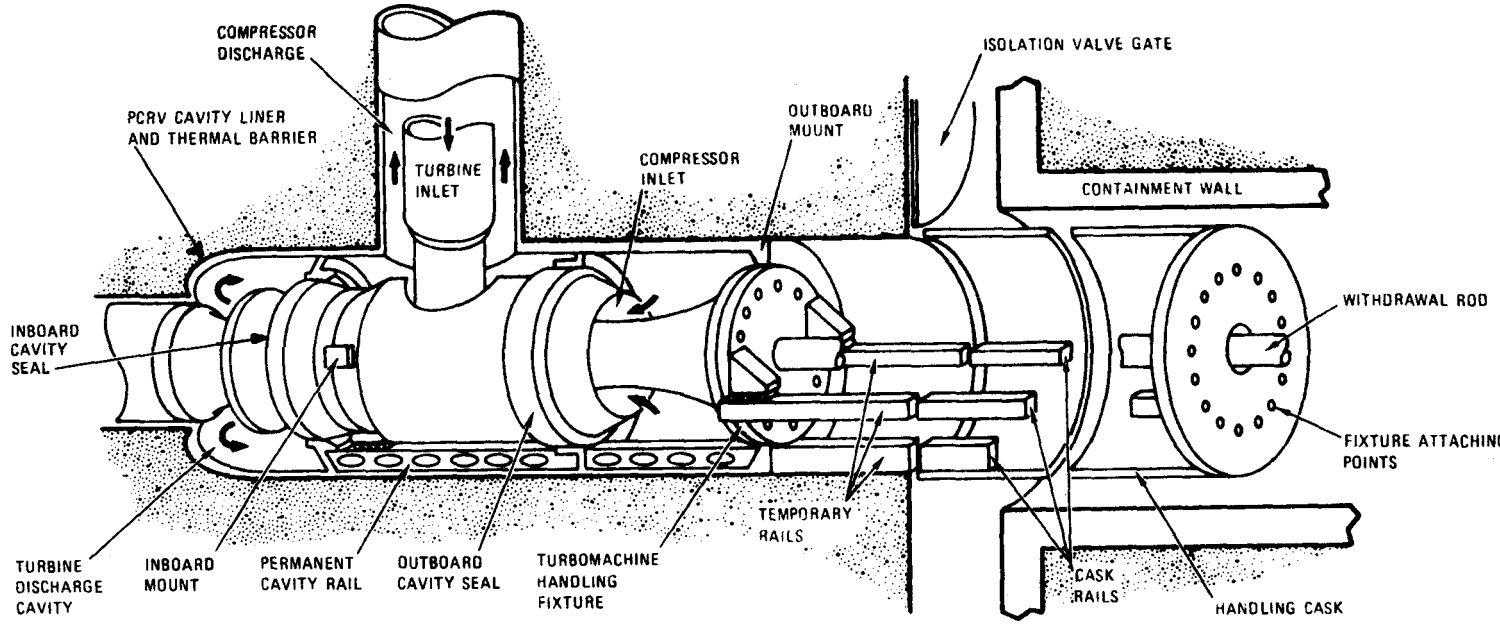

Fig. 4-14. Turbomachine removal system

TABLE 4-8
TURBOMACHINE CASE MOUNT LOAD SUMMARY

	Total	Mount No. 1 (Turbine End)	Mount No. 2 (Compressor End)	Reference
Dead weight, MN (klbf), vertically downward	244 (547)	(144) 324	(100) 223	Ref. 4-1, pp. 12 and 19, and Ref. 4-8, p. 65
Live weights				
Turbine inlet case pressure load, MN (klbf), vertically upward	0.65 (145)	0.45 (100)	0.20 (45)	Ref. 4-7, p. 11
Installation loads				
Vertically downward, MN (klbf)		1.44 (324)	1.00 (223)	Ref. 4-7, pp. 12 and 19, and Ref. 4-8, p. 65
Horizontally (TM C_L), MN (klbf)		0.63 (141)	0.63 (141)	Estimated (see text)
Max at 66.5 deg from horizontal	1.57 (354)			
Seismic loads (add to other loads, e.g., dead weight and axial), MN (klbf)				
OBE (Horizontal)		0.97 (219)	0.67 (151	Ref. 4-7, p. 67 and Ref. 4-8, p. 65
(Vertical)		1.60 (360)	1.10 (248)	
(Axial)		0.15 (34)(max)	1.65 (370)(max)	
SSE (Horizontal)		1.58 (355)	1.09 (245)	
(Vertical)		1.42 (319)	9.79 (220)	
(Axial)		0.15 (34)(max)	2.67 (600)(max)	

TABLE 4-8 (continued)

	Total	Mount No. 1 (Turbine End)	Mount No. 2 (Compressor End)	Reference
Rotor vibration loads, MN (klbf)				
Normal		Small		
Disk failure (impact)	∿4.45 (∿1000)	∿4.45 (∿1000)	4.45 (∿1000)	
Axial thrust loads, MN (klbf)				
Normal	7.56 (1700)	0.15 (34)(max)	7.56 (1700(max)	Estimated and Ref. 4-7, p. 19
Generator short	7.56 (1700)	0.20 (45)(max)	7.56 (1700)(max)	Estimated and Ref. 4-7, p. 19
Torque loads				
Normal max, MN (kftlbf)	3.27 (735)	3.27 (735)	∿0.004 (∿1)	Calculated
Generator short, MN (kftlbf)	4.36 (980)	4.36 (980)	∿0.004 (∿1)	Estimated (see text)
TM bearing sudden seisure	(a)	(a)	(a)	
Deblading, MN (kftlbf)	∿35.6 (∿8000)	∿35.6 (∿8000)	Small[(b)]	Estimated (see text)
Total vertical force, normal, MN (klbf)		±0.31 (±70)	0	Calculated
Total vertical force, generator short, MN (klbf)		±0.42 (±94)	0	Estimated (see text)
Deblading, MN (klbf)	3.38 (760)	±3.38 (±760)	Small	Estimated (see text)

[(a)] Depends on bearing housing bolt shear requirements = small.

[(b)] Compressor inlet support vanes cannot support large torque applications. Turbomachine rotor deceleration to rest in 37.5 revolutions assumed, with generator shaft coupling sheared.

TABLE 4-8 (continued)

	Total	Mount No. 1 (Turbine End)	Mount No. 2 (Compressor End)	Reference
Thermal stresses (M = 0.15 at Mount No. 1)				
Axial case expansion, MN (klbf)	0.28 (64)	0.28 (64)	0.28 (64)(max)	Estimated (see text)
Radial case expansion, MN (klbf)			(c)	
Mount ΔT	Small[d]	Small	Small	See text

(c) Force accepted by mount rig and does not require load takeout into concrete.

(d) Mount No. 1 exists in compressor discharge atmosphere and is cooled by reactor plant cooling water system. Max ΔT ∿120°C (250°F). Mount No. 1 is not externally restrained. Mount No. 2 exists in compressor inlet atmosphere and has little ΔT.

TABLE 4-9
TURBOMACHINE CASE MOUNT LOADS BY EVENT

Event/Category	Load Components		Loads	
	Mount No. 1	Mount No. 2	Mount No. 1, MN (klbf)	Mount No. 2, MN (klbf)
1. Installation			Vert 0.72 (162) Axial 0.31 (70) Comb 0.79 (177)	1.00 (223) 0.63 (141) 1.17 (264)
2. Normal max operation	Dead weight Turbine inlet pressure Axial thrust[a] Torque	Dead weight Turbine inlet pressure Axial thrust[a]	Vert 0.81 (182) Axial 0.12 (27) Comb 0.82 (185)	0.79 (178) 7.56 (1700) 7.61 (1710)
3. Generator short emergency	Normal max operation except for higher torque loads		Vert 0.92 (206) Axial 0.13 (30) Comb 0.93 (208)	0.79 (178) 7.56 (1700) 7.61 (1710)
4. OBE upset	Normal max operation + vert + horiz + axial		Vert 1.61 (362) Horiz 0.97 (219) Axial 0.22 (∿50) Comb 1.90 (426)	1.90 (426) 0.67 (151) 9.21 (2070) 9.43 (2120)
5. SSE faulted	Normal max operation + vert + horiz + axial		Vert 1.52 (342) Horiz 1.58 (355) Axial 0.22 (∿50) Comb 2.20 (495)	1.77 (398) 1.09 (245) 10.25 (2300) 10.45 (2350)
6a. Disk failure emergency	Normal max operation + fragment impact[b] (without deblading)		Vert 3.03 (682) Horiz 4.45 (1000) Axial (small) Max Comb 4.47 (1005)	5.24 (1178) 7.56 (1700) 9.21 (2070)
b. Disk failure emergency	Normal max operation + deblading torque[c] (without impact)		Vert 4.05 (∿910) (+ imbalance loads) Horiz 0.60 (135) Comb 4.09 (920)	Normal

[a] Includes axial expansion loads.

[b] Duration of impact force <10 msec and fragments hit sequentially.

[c] Assumes rotor decelerates in 37.5 revolutions (duration = 0.625 sec).

applied to the turbomachine case and mounts. The catcher deflection was estimated by assuming a 10% material strain plus deformation out of round. Finally, a downward force vector was identified as the most adverse direction, since it adds directly to the highest normal mount loads.

It was assumed that the rotor is of bolted design and that the tie bolts would loosen and/or fail following the loss of a disk, so that a deblading event would follow. The torque transmitted to the turbomachine outer case (by the inner case) was calculated by assuming that the rotor deceleration rate would be constant, that the rotor would stop in 37.5 revolutions, and that the generator rotor would decouple from the turbomachine by proper action of a shaft shear coupling. The number 37.5 revolutions was estimated by referring to an informal estimate that a generator rotor would decelerate to rest in about 0.75 revolution if a rotor segment engaged the case and by estimating that the blading failure resistance would be 10% of a generator rotor segment and that 20% of the rotor length would suffer engagement at any single instant. The rotor would, then, come in rest in 0.625 sec. It is likely that the inboard shaft bearing would become ineffective during the accident, while the outboard one (nearest the cavity plug) would not. The inboard bearing is supported by the turbine inner case, which could be destroyed by the accident, whereas the outboard bearing is supported directly by the outboard mount (compressor inlet shroud). In the event of a generator short, the shaft torque will be very large and likely variable. In addition, the turbomachine may overspeed because of a loss of real load. However, except for small bearing forces, torque can be transferred to the casing only by the gas dynamic coupling provided by the rotor blading. Since the turbomachine overspeed will be limited to about 20%, it seems unlikely that a large increase in fluid power or blading torque can occur. A 20% increase in normal casing torque was assumed for this study.

Thermal stresses on the turbomachine case mounts will be small because of the mounting scheme. Axial loads will be limited by the sliding force which can be sustained by the inboard clevises. These loads were estimated as 15% of the normal mount force, on the basis of a 0.15 coefficient of friction at the pin/clevis interfaces.

Table 4-9 lists the loads given in Table 4-8 by event. Vertical, axial, and combined loads are listed, as well as horizontal (radial) loads where applicable. Loads are listed in their maximum combination, and the data given for the mount No. 1 (inboard) are for the more heavily loaded of the two mount pins.

For the inboard mount pin, the highest vertical load of over 4 MN (900 klbf) is applied by the deblading accident, and the accuracy of this value is questionable. The maximum radial (horizontal) load could be an approximate 4.45-MN (1000-klbf) impact during a rotor burst, or a sustained but cyclical 1.56-MN (350-klbf) load during an SSE.

The outboard mount axial load would reach a maximum value of about 10.25 MN (2300 klbf) during operation just prior to shutdown caused by an SSE. The normal axial load of 7.56 MN (1700 klbf) is the major contributor and is a steady load caused by cavity segment pressure and area differences. It should be noted that these values assume that the maintenance spaces at each end of the turbomachine shrouds are pressure-balanced with the low PCL gas pressures at the machine ends, probably by use of small shroud vent holes, which would be useful for in-situ inspection. During rapid PCL pressure transients caused by abrupt control valve action, axial loads as large as 22.25 to 26.7 MN (5000 to 6000 klbf) could be exerted on the compressor inlet shroud, in combination with large radial loads, unless means are provided to balance the pressure rapidly across the shroud. A control valve bleed line to the spaces is a possibility which could provide the necessary balance function while limiting the buildup of plateout contamination in the maintenance access spaces.

4.6.2.4. Mount Design. Inboard and outboard turbomachinery mounts share several design considerations. First, neither must fail during service, lest the turbomachine cavity seals fail and cause extremely rapid loop pressure transients. Secondly, loads must be transmitted through the relatively thin cavity steel liner of 14 mm (0.5625 in.) thick to the PCRV concrete so that neither the liner nor the concrete are damaged. Concentrated loads at mount

points must, therefore, be spread to an acceptable compressive stress value of less than 28 MPa (4000 psi) at the concrete interface. The liner must also be anchored to the PCRV so that the liner cannot be pulled from the concrete locally. Liner/PCRV separating forces can arise by PCRV creep or by application of turbomachine mount loads. Design decisions which meet these criteria include the use of concrete anchors in the liner design and a mount geometry which limits the development of large bending moments so that the PCRV/liner interface "sees" little tension. Finally, the mount geometry must feature sufficient material to react shear and compressive stresses developed by the turbomachine mount loads without interfering with turbomachine installation, or being overly complex and expensive.

The inboard mount design (see Fig. 4-13) utilizes locally thickened cavity walls which are slotted to accept the turbomachine clevis pins. An insert is shown bolted to each liner slot so that post creep liner dimensions can be made to fit the insert without altering the dimension of the hardened pin. Also, the liner can be low-alloy ferritic steel, while the insert inner face can be hardened to accept high local compressive stresses.

Radial forces (horizontal) are transmitted through the shoulder around the pin to the insert vertical face and through the heavy-walled liner "crescent" to the concrete. Vertical forces are accepted from the horizontal (rectangular) pin face by the adjacent insert face and vertically through the "crescent," distributing the force radially over about 120 deg of the liner circumference to the concrete. Torque imposed on the liner in this manner is reacted by the concrete through three shear lugs cast integrally with the "crescent." The small axial forces transmitted through the clevis by friction to the liner are reacted by the concrete at the steps in adjacent liner material whose thickness changes abruptly. This design requires only welds of equal gage material during liner fabrication. Large-diameter headed studs located near the ends of the "crescent" prevent separation of the steel and the concrete at those points. The continuous internal geometry of the cavity liner permits application of the thermal barrier directly over the entire surface, except at the clevis pin insert location.

The outboard mount consists merely of a heavy section of ring integrated into the cool outboard end of the cavity liner. With the aid of a segmented

attachment ring, the compressor inlet shroud (and outboard bearing carrier) bolts to the cavity liner. An annular gap is maintained between the shroud periphery and the liner ring inside diameter, and oversized bolt holes are to be used in the mount ring so that thermal expansion and cavity creep induced radial movements can occur without rupturing the shroud. Vertical forces are transmitted directly to the concrete by the stiff ring, while the large axial loads are transmitted by a step in the cavity liner outside diameter located at the support ring.

A permanent rail is located at the bottom of the cavity to permit translation of the machine, the inboard end of the machine being supported by the rail and by a linear bearing assembly. The length of the bearing assembly and the width at the fail flange of the liner attachment will provide sufficient bearing area to avoid overloading the PCRV concrete locally as the machine is rolled in or out of the cavity.

4.6.3. Heat Exchanger Support Design

A thermal sleeve support concept has evolved for the large, vertically oriented GT-HTGR heat exchangers. Such full cavity diameter supports are shown in Figs. 4-15 and 4-16 for the recuperator and the precooler, respectively. The purpose of the current study has been to evaluate the adequacy of this concept. The study scope has not included liner support design, since the HTGR shear anchor approach appears to be well-founded.

It is recommended that the thermal sleeve support concept be pursued in detail for use with the recuperator and the precooler in GT-HTGR designs. All loads appear to be acceptable by a reasonably straightforward design. The large thermal L/d inherent in the concept mitigates conduction heat transfer from the equipment to the liner through the support itself. Location of the support near the top of the cavity allows physical access to seal rings and fastener rings.

4.6.3.1. Seismic Loads. Seismic loads are listed in Table 4-10 for for high seismic option requirements listed in Ref. 4-9. Expected loads (per Ref. 4-10) are much lower than peak loads. The lower values were used

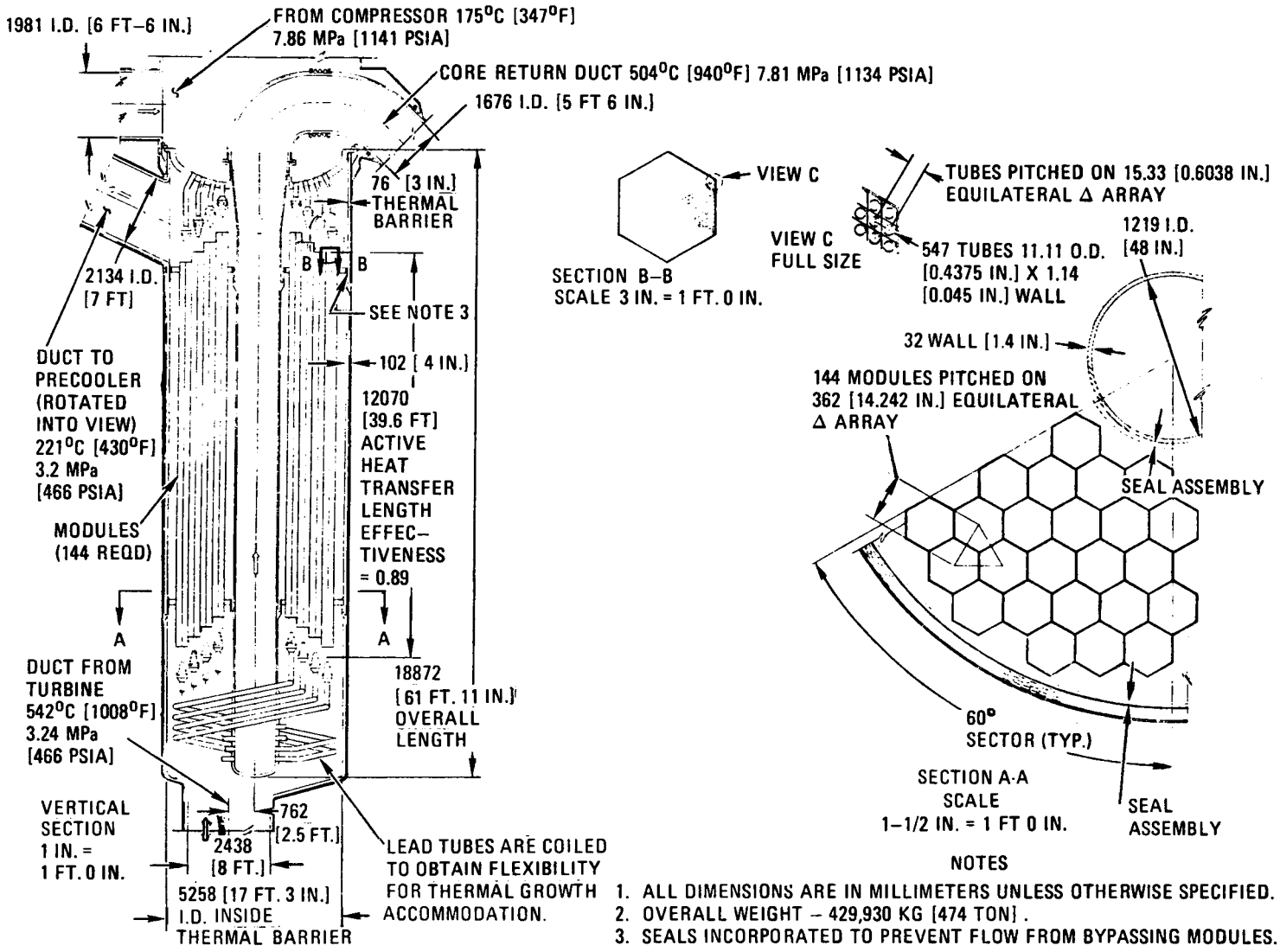

Fig. 4-15. Recuperator for twin 4000-MW(t), 850°C ROT, four-loop, dry-cooled GT-HTGR

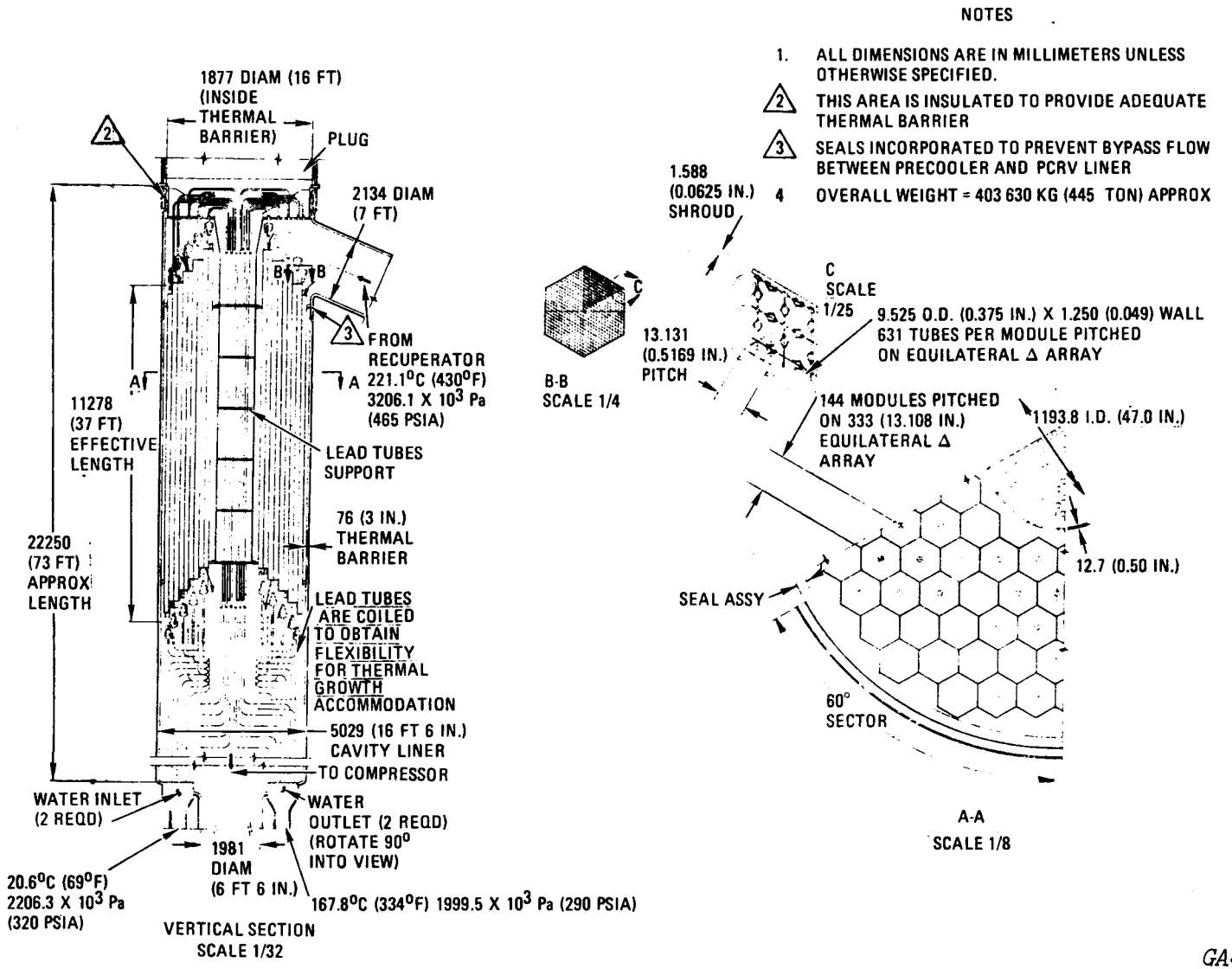

Fig. 4-16. Precooler for twin 4000-MW(t), 850°C ROT, four-loop, dry-cooled GT-HTGR

TABLE 4-10
RECUPERATOR AND PRECOOLER SEISMIC AND HANDLING LOADS[a]

	OBE	SSE
Maximum high seismic option ground excitation, g		
± Horizontal	0.25	0.50
± Vertical	0.25	0.40
Damping factors for heat exchanger equipment	2%	3%
Seismic response (at PCRV top head), g		
± Horizontal (Maximum)	48 x 0.25 = 12	25 x 0.5 = 12.5
(Expected)	3.5 x 0.25 = .87	3.5 x 0.5 = 1.75
± Vertical (Maximum)	20 x 0.25 = 5	15 x 0.4 = 6
(Expected)	2.4 x 0.25 = 0.6	2.4 x 0.4 = 0.96
Vertical seismic loads, MN (lbf x 10^{-6})		
Precooler (see Fig. 4-16)		
Upward (Maximum)	15.83 (3.56)	19.79 (4.45)
(Expected)	1.58 (0.356)	0.16 (0.035)
Downward (Maximum)	23.75 (5.34)	27.71 (6.23)
(Expected)	6.32 (1.42)	7.74 (1.74)
Recuperator (see Fig. 4-15)		
Upward (Maximum)	16.86 (3.79)	21.08 (4.74)
(Expected)	1.69 (0.379)	0.17 (0.038)
Downward (Maximum)	25.31 (5.69)	29.53 (6.64)
(Expected)	6.76 (1.52)	8.27 (1.86)
Horizontal seismic loads, MN (lbf x 10^{-6})		
Precooler (Maximum)	47.50 (10.68)	49.51 (11.13)
(Expected)	3.42 (0.77)	6.94 (1.56)
Recuperator (Maximum)	50.62 (11.38)	49.51 (11.13)
(Expected)	3.69 (0.83)	7.38 (1.66)
Vertical handling loads (assume 2 g downward), MN (lbf x 10^{-6})		
Precooler: 7.92 (1.78		
Recuperator: 8.45 (1.90)		

[a]Maximum loads are based on high seismic criteria of DC-4-4; expected loads are based on Ref. 4-9 criteria.

in this study because it is felt that the heat exchanger natural frequencies will not correspond to those of the PCRV top head. This assumption must be verified in the near future. In the current study, it is assumed that the forces act at the heat exchanger center of mass, which was found to be about 8.5 m (28 ft) below the attachment plane for the recuperator.

All quantitative study results are listed in Table 4-11. Seismic stresses were calculated at the horizontal thermal sleeve/liner interface plane by combining the horizontal seismic shear load and the vertical loads caused by vertical acceleration and horizontal acceleration induced bending. It was assumed that the support sleeve (see Fig. 4-17) is 610 mm (24 in.) tall, 17.5 mm (0.69 in.) thick, and 5335 mm (210 in.) in diameter.

A seismic restraint ring (segmented) is used to key the heat exchanger sheet to the thermal sleeve, accurately locating the heat exchanger and preventing vertical movement during an earthquake. When the ring is removed, the heat exchanger may be lifted from the cavity.

4.6.3.2. Thermal Stresses. At steady operating conditions, where $T_1 > T_0$ (see Fig. 4-17), the thermal sleeve will tend to form a conic frustum, with $D_1 > D_0$. The heat exchanger sheet will grow thermally at the same rate as the thermal sleeve, since: (1) the material of construction is the same (sheet and sleeve), (2) the sleeve is insulated against other heat input/loss, and (3) there is good thermal contact at the sheet/sleeve interface. No stresses in the sleeve will be generated by this thermal expansion process. However, there will be bending stresses at the knuckle because of the angular sleeve movement and the restraint of the shear anchor-supported liner on the knuckle. A long sleeve with a given radial expansion at its upper end will transmit a small angular motion and develop low bending stresses at the knuckle.

At steady operating conditions, a radial thermal gradient will exist through the sleeve; use of insulation will reduce its magnitude and the local heat load to the liner cooling system. If the sleeve is relatively

TABLE 4-11
PRECOOLER AND RECUPERATOR/LINER SUPPORT PRELIMINARY STUDY RESULTS

	Recuperator	Precooler
1. Dead weight, kg (lb)	431,000 (948,000) (see Fig. 4-15)	404,500 (890,000) (see Fig. 4-16)
2. Steady sleeve thermal stress, MPa (psi)	∿1.05 (∿150)	<0.7 (<100)
3. Transient sleeve thermal stress	Low	Low
4. SSE/seismic and handling knuckle shear stress, MPa (psi)	∿210 (∿30,000)	<210 (<30,000)
5. Steady thermal knuckle shear stress, MPa (psi)	∿196 (∿28,000)	<196 (<28,000)
6. OBE combined seismic and thermal knuckle shear stress, MPa (psi)	∿308 (∿44,000)	<308 (<44,000)
7. Heat loss/loop, MW(t)	∿0.05	∿0.03

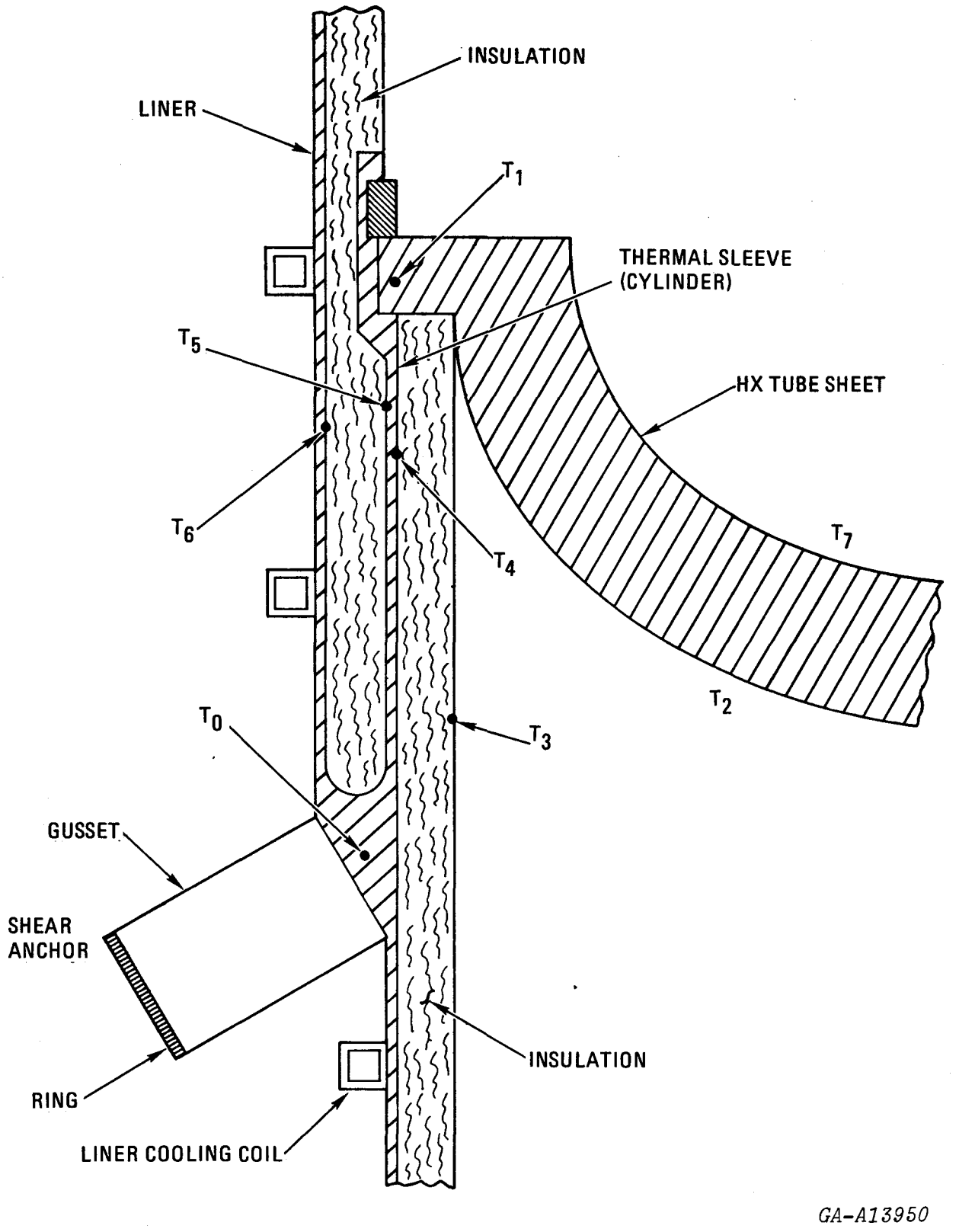

Fig. 4-17. Recuperator support

thin and long, the circumferential and longitudinal stresses developed by a linear radial thermal gradient of $(T_5 - T_4)$ are equal and are

$$S = \frac{\alpha E\ (T_5 - T_4)}{2\ (1 - \nu)}$$

where α = coefficient of thermal expansion
E = elastic modulus
ν = Poisson's ratio

with compressive stresses on the inner surface and tension on the outer surface.

The sleeve lower end should not have an abrupt change in section at the knuckle, lest large shear stresses develop at the interface caused by non-linear radial thermal gradients.

In order to evaluate steady thermal stress magnitudes, it was necessary to estimate the thermal profile in the structure. A brief heat transfer study was made with the aid of Fig. 4-17 for the 950°C ROT cycle conditions. Gas temperatures on either side of the recuperator sheet are 280°C (537°F) and 230°F (445°F) (T_2 and T_7), respectively. With 25.4 mm (1 in.) of insulation on both sides of the thermal sleeve, the radial temperature drop to a 650°C (150°F) liner through the sleeve $(T_4 - T_5)$ is about 0.5°C (1°F). The corresponding thermal stress of less than 1.05 MPa (150 psi) is listed in Table 4-11. The heat load through the sleeve itself to the liner knuckle is only about 0.035 MW(t) for a 610-mm (2-ft)-long sleeve. The radial heat load to the liner through the sleeve is about one-third of that along the sleeve, or about 0.012 MW(t). Tangential transient thermal stresses would be limited to 140 MPa (20,000 psi) for brief periods if the sleeve were uninsulated, assuming the 1.67°C/sec (3°F/sec) gas temperature transient given in Ref. 4-11 for rapid loop shutdown. Maximum thermal stresses in an insulated sleeve will be well below 140 MPa (20,000 psi) and should be entirely acceptable even during an earthquake.

Combined seismic and thermal knuckle stresses listed in Table 4-11 are within ASME Code allowable limits for Class I components when a material such as SA-537 (carbon steel) is used, which has an allowable shear stress intensity value greater than 140 MPa (20,000 psi).

4.7. THERMAL BARRIER AND CORE OUTLET DUCT DESIGN

4.7.1. Introduction

The design of the thermal barrier for the GT-HTGR can be separated into two basic categories. The first category constitutes the design of the thermal barrier for the cavity liners and the majority of the coolant ducts. The second category is the core outlet duct, whose design presents an additional set of unique problems.

Section 4.7.2 describes the overall thermal barrier system and provides a thermal barrier classification for each reactor zone and its associated area. Section 4.7.3 discusses the thermal design of the vented thermal barrier. These two sections together complete Milestone B-2.

Sections 4.7.4 and 4.7.5 treat the respective design approaches for the core outlet duct for the reference 850°C ROT case and for the advanced 950°C ROT case and completes Milestone B-3.

4.7.2. Thermal Barrier Description

The thermal barrier within the GT-HTGR reactor is divided into four major classes. The classes selected are related to the temperature capabilities of the materials of construction used in the various configurations. Table 4-12 presents the four classes of thermal barrier and lists the temperature capability of each for various reactor operation conditions.

The construction of classes A, A/B, and B is basically identical. The differences are associated with the materials of construction used for the various components.

TABLE 4-12
THERMAL BARRIER HOT-FACE TEMPERATURE LIMITS

Class	Normal and Upset Conditions: Full-Power Hot Average Surface Temperature Not Exceeding, °C (°F)	Normal and Upset Conditions: Maximum Local Continuous Hot Surface Temperature, °C (°F)	Emergency Conditions: Maximum Operational Transient Hot Surface Temperature (10-hr Transient), °C (°F)	Faulted Conditions: Critical Safety Limit, °C (°F)
A	427 (800)	427 (800)	593 (1100)	704 (1300)
A/B	593 (1100)	621 (1150)	760 (1400)	815 (1500)
B	899 (1650)	954 (1750)	1038 (1900)	1149 (2100)
C	899 (1650)	1204 (2200)	1371 (2500)	1649 (3000)

The construction of classes A, A/B, and B is of the following general type:

1. Several layers of fibrous insulation placed adjacent to the cavity or duct liner

2. A 7.5-mm (0.3-in.)-thick layer fabricated of several layers of metallic screen material

3. A 0.79-mm (0.031-in.)-thick metallic seal sheet

4. A 6.35-mm (0.25-in.)-thick metallic cover plate

The difference between the various classes is the types of fiber and metallic alloys used.

The metallic cover plate is held in place by one central fastener and eight edge fasteners which span the expansion gap between adjacent cover plates. Each of the central and edge fasteners is attached to the carbon steel cavity liner by four Nelson studs.

As a result of the cost optimization study reported in Ref. 4-12, the nominal size of a typical cavity cover plate will be 119 cm^2 (18.4 $in.^2$). The actual size will vary somewhat from location to location. A section of the thermal barrier, taken through a typical edge fastener location, is shown in Fig. 4-18.

The seal sheets used in the GT-HTGR will not cover as much as those used in the SC-HTGR. The major functions of the seal sheets in the GT-HTGR is to span the thermal expansion gap between cover plates to maintain the fibrous insulation and vent cavity material in position. A typical cover plate will contain a number of small vent holes with an aggregate area on the order of 5 cm^2 (0.78 $in.^2$) to allow the thermal barrier to vent during a rapid depressurization.

The materials used for each of the major components which make up the Class A, A/B, and B thermal barriers are given in Table 4-13. It should be

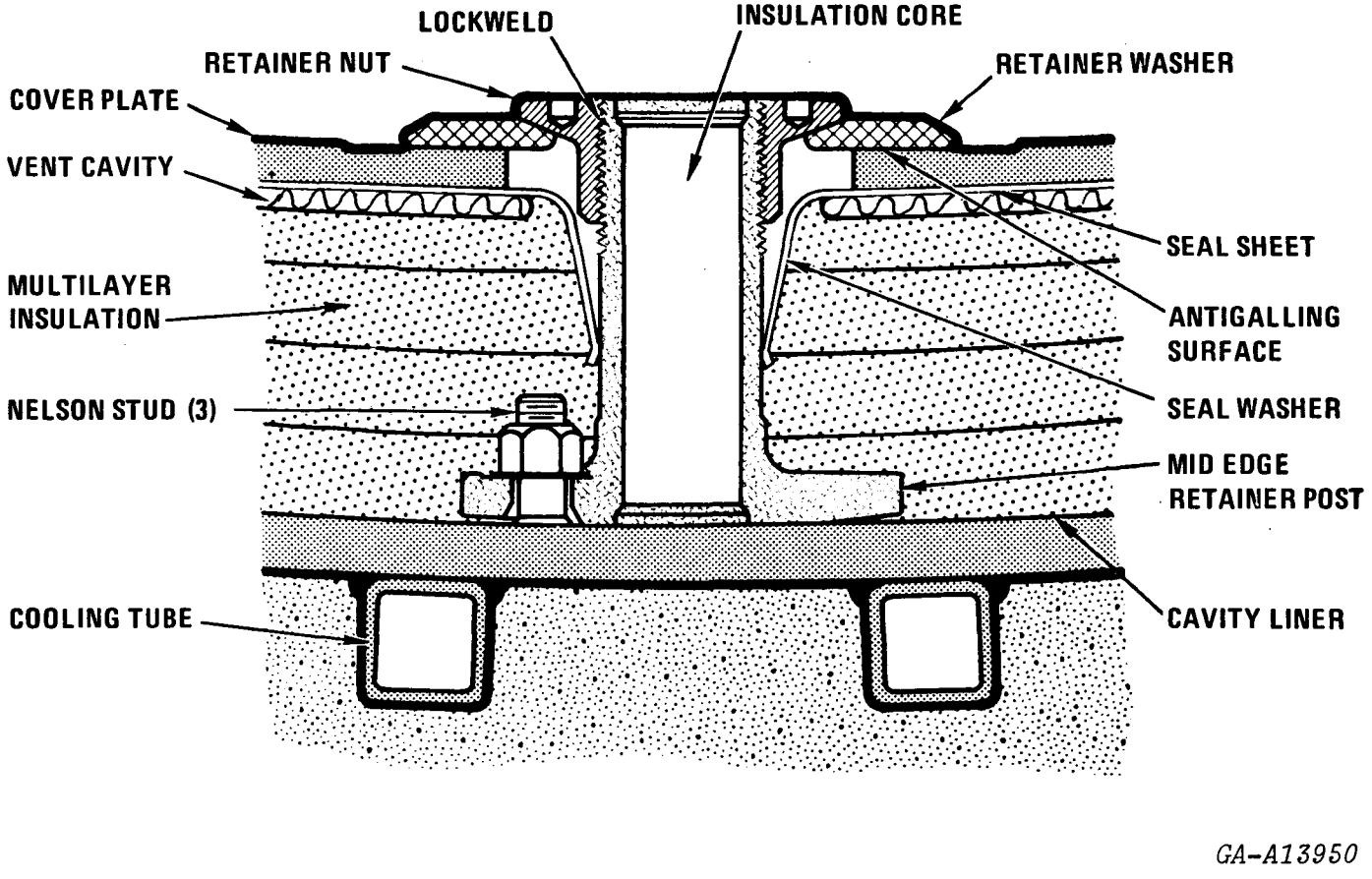

Fig. 4-18. Typical edge fastener

TABLE 4-13
THERMAL BARRIER MATERIALS FOR 850°C ROT (BY CLASS)

Components	Class		
	A	A/B	B
Fibrous insulation	Kaowool	Kaowool + Kaowool XS	Kaowool + Safel alumina
Vent cavity (wire mesh)	304 SS	316 SS	Inconel 617
Seal sheet	Carbon steel	2-1/4 Cr - 1 Mo or 304 SS	Inconel 617
Cover plate	Carbon steel	2-1/4 Cr - 1 Mo or 304 SS	Inconel 617
Fasteners	Carbon steel	2-1/4 Cr - 1 Mo or 304 SS	Inconel 617 and carbon steel
Antigalling coating	$Cr_{23}C_6$ plasma	$Cr_{23}C_6$ plasma	$Cr_{23}C_6$ plasma

noted that in the case of Class A/B, both 2-1/4 Cr-1 Mo and type 304 stainless steel are used for the metallic components. The change to stainless steel is required only in the area of the lower core cavity side wall (Zone 6).

The Class C thermal barrier is used only in the floor of the reactor core cavity. This class of insulation is constructed of Class A insulation overlaid by an additional 19 cm (7.48 in.) of silica brick (Masroc) and fibrous insulation. The locations of the various thermal barrier zones are shown in Figs. 4-19 and 4-20, along with the class designations. Zone numbering has followed SC-HTGR practice as nearly as practical.

Table 4-14 provides the listing of the thermal barrier classes and areas by zone for both the three-loop and four-loop, 850°C ROT reactor configurations.

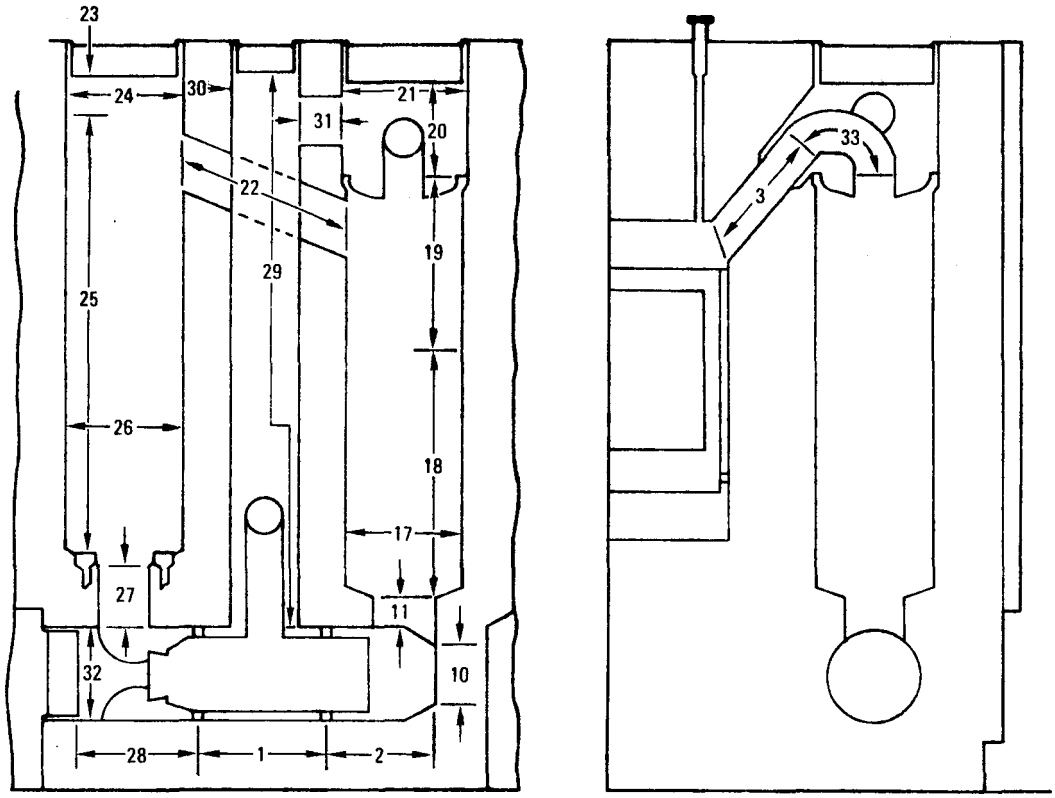

ZONE NO.	CLASS	NAME	ZONE NO.	CLASS	NAME
1	A	TURBOMACHINE CAVITY (CENTER)	23	A	PRECOOLER CAVITY UPPER SIDE WALL
2	A/B	TURBOMACHINE CAVITY (TURBINE END)	24	A	PRECOOLER CAVITY CLOSURE
3	A/B	UPPER MAIN CROSS DUCT	25	A	PRECOOLER CAVITY LOWER SIDE WALL
10	A/B	TURBOMACHINE CAVITY END WALL	26	A	PRECOOLER CAVITY LOWER HEAD
11	A/B	TURBINE TO RECUP-ERATOR DUCT	27	A	PRECOOLER TO COMPRESSOR DUCT
17	A/B	RECUPERATOR CAVITY LOWER HEAD	28	A	TURBOMACHINE CAVITY (COMPRESSOR END)
18	A/B	RECUPERATOR CAVITY LOWER SIDE WALL	29	A	COMPRESSOR TO RECUPERATOR DUCT (VERT)
19	A	RECUPERATOR CAVITY CENTER SIDE WALL	30	A	COMPRESSOR DUCT CLOSURE
20	A	RECUPERATOR CAVITY UPPER SIDE WALL	31	A	COMPRESSOR TO RECUPERATOR DUCT (HORIZ)
21	A	RECUPERATOR CAVITY CLOSURE	32	A	TURBOMACHINE CAVITY CLOSURE
22	A	RECUPERATOR TO PRE-COOLER CROSS DUCT	33	A/B	UPPER MAIN CROSS DUCT ELBOW

GA-A13950

Fig. 4-19. Thermal barrier zone description for turbomachinery and heat exchangers

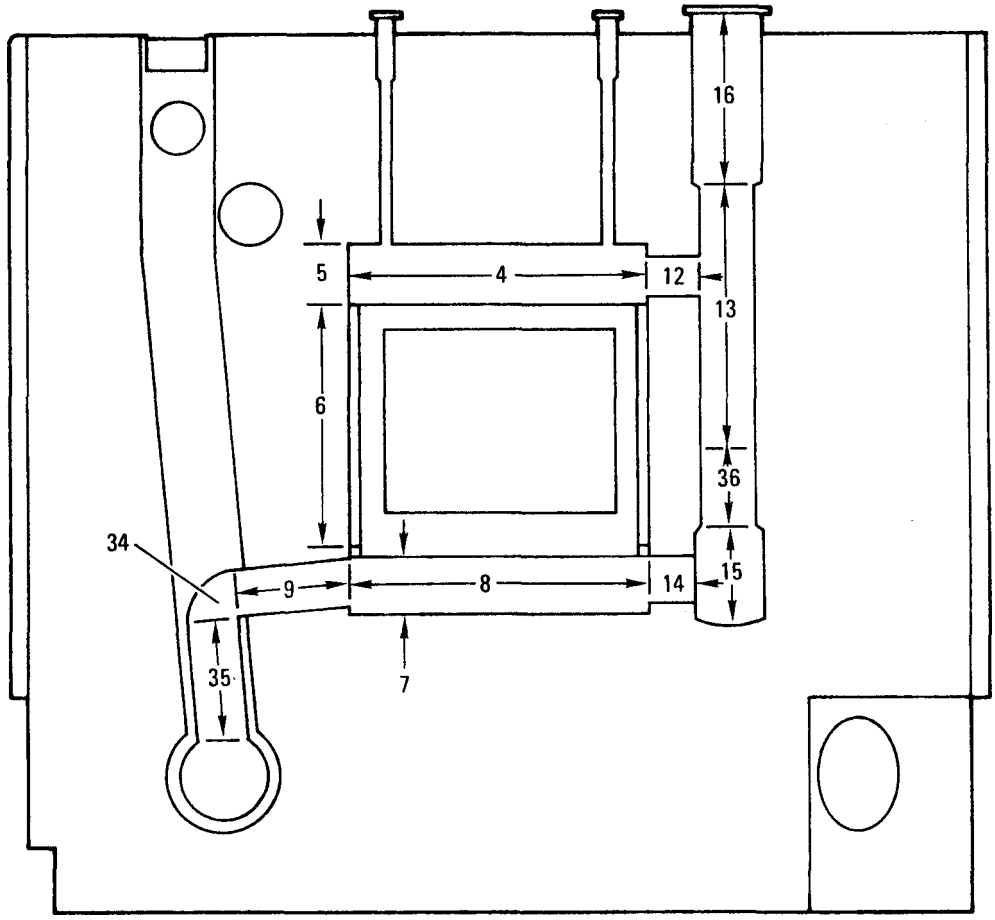

ZONE NO.	CLASS	NAME	ZONE NO.	CLASS	NAME
4	A/B	TOP HEAD	13	A/B	UPPER AUX HEAT EXCHANGER CAVITY
5	A/B	UPPER SIDE WALL	14	B	LOWER AUX CROSS DUCT (HORIZ)
6	A/B	CENTER SIDE WALL	15	B	LOWER AUX CROSS DUCT (VERT)
7	B	LOWER SIDE WALL	16	A	AUX CIRCULATOR PENETRATION
8	C	BOTTOM HEAD	34	B	LOWER MAIN CROSS DUCT (ELBOW)
9	B	LOWER MAIN CROSS DUCT (HORIZ)	35	B	LOWER MAIN CROSS DUCT (VERT)
12	A/B	UPPER AUX CROSS DUCT	36	B	LOWER AUX HEAT EXCHANGER CAVITY

GA-A13950

Fig. 4-20. Thermal barrier zone description for cross ducts and auxiliary equipment

TABLE 4-14
THERMAL BARRIER CLASS AND AREA BY ZONE FOR THREE-LOOP, 3000-MW(t) AND FOUR-LOOP, 4000-MW(t), 850°C ROT, GT/HTGR REACTORS

Zone	Class	Three-Loop Area		Four-Loop Area	
		m^2	ft^2	m^2	ft^2
1	A	294.4	2,799.0	392.6	3,732.0
2	A/B	253.2	2,406.9	337.6	3,209.2
3	A/B	149.9	1,425.5	199.9	1,900.7
4	A/B	133.1	1,075.2	159.9	1,520.5
5	A/B	78.6	747.4	93.5	888.5
6	A/B	379.0	3,603.4	450.7	4,285.1
7	B	78.0	741.6	93.3	886.9
8	C	113.1	1,075.2	159.9	1,520.5
9	B	95.4	907.1	127.2	1,209.5
10	A/B	20.1	190.8	26.8	254.4
11	A/B	39.7	377.1	52.9	502.7
12	A/B	29.0	275.1	29.0	275.7
13	A/B	187.4	1,781.3	187.4	1,781.3
14	B	38.2	362.9	38.2	362.9
15	B	111.0	1,055.7	111.0	1,055.7
16	B	186.4	1,771.9	185.4	1,771.9
17	A/B	55.8	530.1	74.4	706.9
18	A/B	480.3	4,566.3	640.4	6,088.4
19	A	595.1	5,657.2	793.4	7,542.9
20	A	196.3	1,866.1	261.7	2,488.1
21	A	80.3	763.4	107.1	1,017.9
22	A	180.4	1,715.4	240.6	2,287.1
23	A	130.9	1,244.0	174.5	1,658.8
24	A	67.5	641.5	90.0	855.3
25	A	1,015.2	9,651.0	1,353.5	12,868.0
26	A	53.8	511.1	71.7	681.5
27	A	68.2	648.0	90.9	864.0
28	A	174.0	1,654.2	232.0	2,205.6
29	A	678.1	6,446.5	90.4	8,595.4
30	A	15.9	150.8	21.2	201.1
31	A	67.7	643.2	90.2	857.7
32	A	45.2	429.4	60.2	572.6
33	A/B	37.0	352.0	49.4	469.3
34	B	28.5	271.4	38.1	361.9
35	B	44.6	424.1	59.5	565.5
36	B	118.0	1,121.6	118.0	1,121.6
Additional Insulation Not Listed by Zone					
Valve cavities	A/B	50.0	477.0	69.7	663.0
	A	5.0	48.0	6.7	64.0
Valve ducts	A/B	268.9	2,556.0	358.5	3,408.0
	A	5.9	56.0	7.9	75.2

4.7.3. Effects of Helium Permeation Flow on Vented Thermal Barriers

4.7.3.1. System Considerations. The current GT-HTGR reference thermal barrier system for 850°C ROT is based on the HTGR design with the addition of vent holes and a vent cavity between the cover plate seal sheets and the fibrous insulation (see Fig. 4-21). While the extra venting capability of the GT-HTGR thermal barrier system enables the system to accommodate a higher rate of pressure change, the thermal insulating ability may be decreased because of the increased permeation helium flow inside the system during the normal operation. A discussion of the variation in permeation flow within the insulating material as a function of various flow parameters was given in Ref. 4-12. The model used for this previous study was a simplified one-dimensional electric analogy. Subsequently, a quantitative study was conducted to identify the convective effect of the permeation flow on the characteristics of thermal insulation of the vented GT-HTGR thermal barrier system. To accomplish this, a parametric study of the several governing parameters was made.

4.7.3.2. Simulation Model and Scope of Study. A two-dimensional steady-state model was developed to study the effect of permeation flow on the thermal insulation of the thermal barrier system. The computation was made by taking advantage of the existing code POROUS (Ref. 4-13), which was appropriately modified to the GT-HTGR case. The analytical model is presented in Fig. 4-22 and is briefly described as follows:

1. The fiber insulation layer is simulated by a permeable medium with permeability K and porosity, ϕ.

2. The effects of the cover plate, seal sheet, and vent cavity are lumped together and are represented by an equivalent permeability K_c. This K_c serves as a coefficient to correlate the pressure gradient and its corresponding infiltrated helium flow across the whole layer of the cover plate system. Its value will be experimentally determined later.

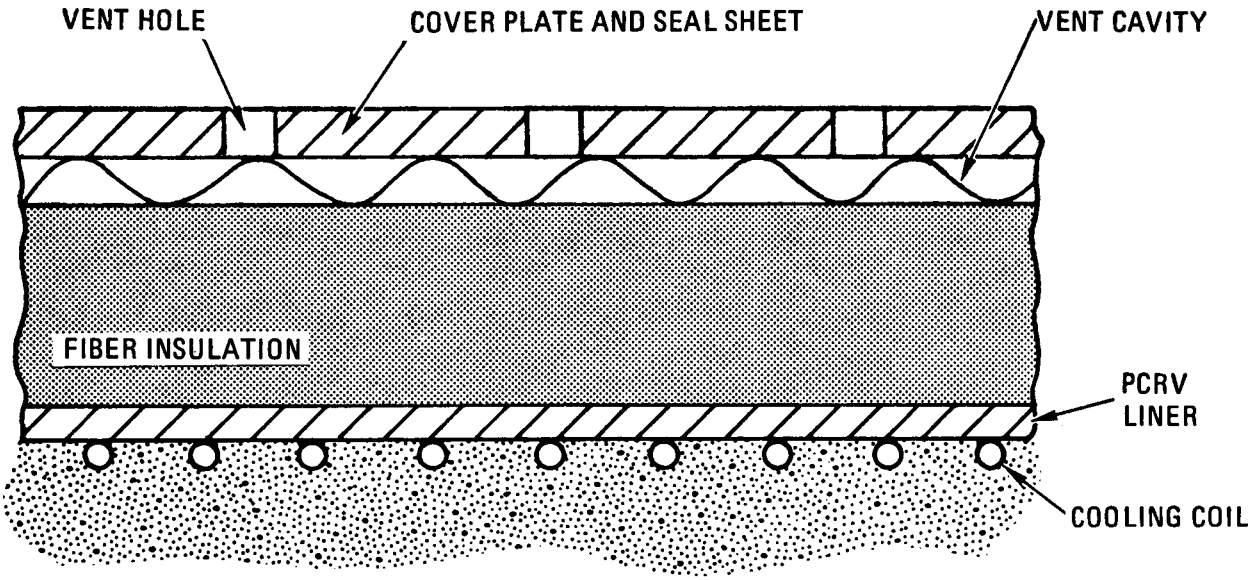

Fig. 4-21. Conceptual design of a vented thermal barrier

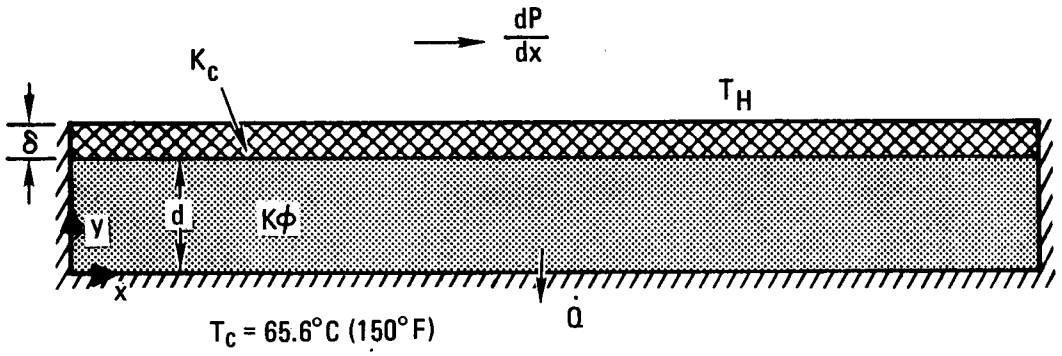

GA-A13950

Fig. 4-22. Analytical model of system of concern

3. The governing equations for this system are stated as follows:

a. Continuity equation

$$\frac{\partial(\rho u)}{\partial x} + \frac{\partial(\rho v)}{\partial y} = 0$$

b. Momentum equation

$$u = \frac{K}{\mu\phi}\left(-\frac{\partial P}{\partial x} + F_x\right)$$

$$v = \frac{K}{\mu\phi}\left(-\frac{\partial P}{\partial y} + F_y\right)$$

c. Energy equation

$$u\phi\,\frac{\partial}{\partial x}(\rho C_p T) + v\phi\,\frac{\partial}{\partial y}(\rho C_p T) =$$

$$\frac{\partial}{\partial x}\left(\lambda\,\frac{\partial T}{\partial x}\right) + \frac{\partial}{\partial y}\left(\lambda\,\frac{\partial T}{\partial y}\right)$$

where x and y are independent spatial variables, u and v are velocity components corresponding to the directions X and Y, ρ is helium density, P is pressure, μ is helium viscosity, and F_x and F_y are components of helium body force (e.g., gravitational force), T is temperature, and λ is the effective thermal conductivity [$\lambda = \lambda_{He}\phi + \lambda_{fiber}(1 - \phi)$].

A parametric study was conducted to evaluate the effects of the governing parameters on the characteristics of thermal insulation of the system of concern. The parameters are: (1) the pressure drop along the duct, dP/dx; (2) the thickness of the fiber insulation, d; (3) the temperature of the hot helium stream, T_H; and (4) the ventibility of the cover plate system, K_c/δ. The performance of thermal insulation of the thermal barrier system is characterized by the local heat flux through the thermal barrier system to the steel liner.

Several sets of results for the effects of different parameters on the local and average heat flux from fiber insulation to the steel liner have been computed and are presented in Figs. 4-23 through 4-30. These results reveal the following:

1. A high local heat flux occurs at the entrance region of the thermal barrier and decreases to a minimum near the exit region. While the local heat flux in the middle region is only slightly affected by pressure drop, the local heat flux in the end regions are both greatly influenced by pressure drop.

2. The average heat flux along the duct increases with increasing pressure drop. However, the effect is not significant.

3. As expected, the local heat flux decreases with increasing thermal barrier thickness. The zone of rapidly changing heat flux near the ends of the duct broadens with increasing thickness.

4. Not only does the local heat flux change with increasing hot gas temperature, but also the rate of change in heat flux also increases.

5. The effect of the cover plate ventibility parameter, β, defined as $1/K_c/\delta$, on the local and average heat flux is shown in Figs. 4-29 and 4-30, respectively. The nondimensional parameter has been chosen so that the larger the parameter β, the tighter or less ventible is the thermal barrier. The case of $\beta = 0$ represents a situation where the cover plate is wholly permeable, i.e., no cover plate. It can be seen that the heat flux decreases with increasing β. This is a result of a decrease of helium permeation flow within the fibrous insulation, which results in a decrease in heat flux.

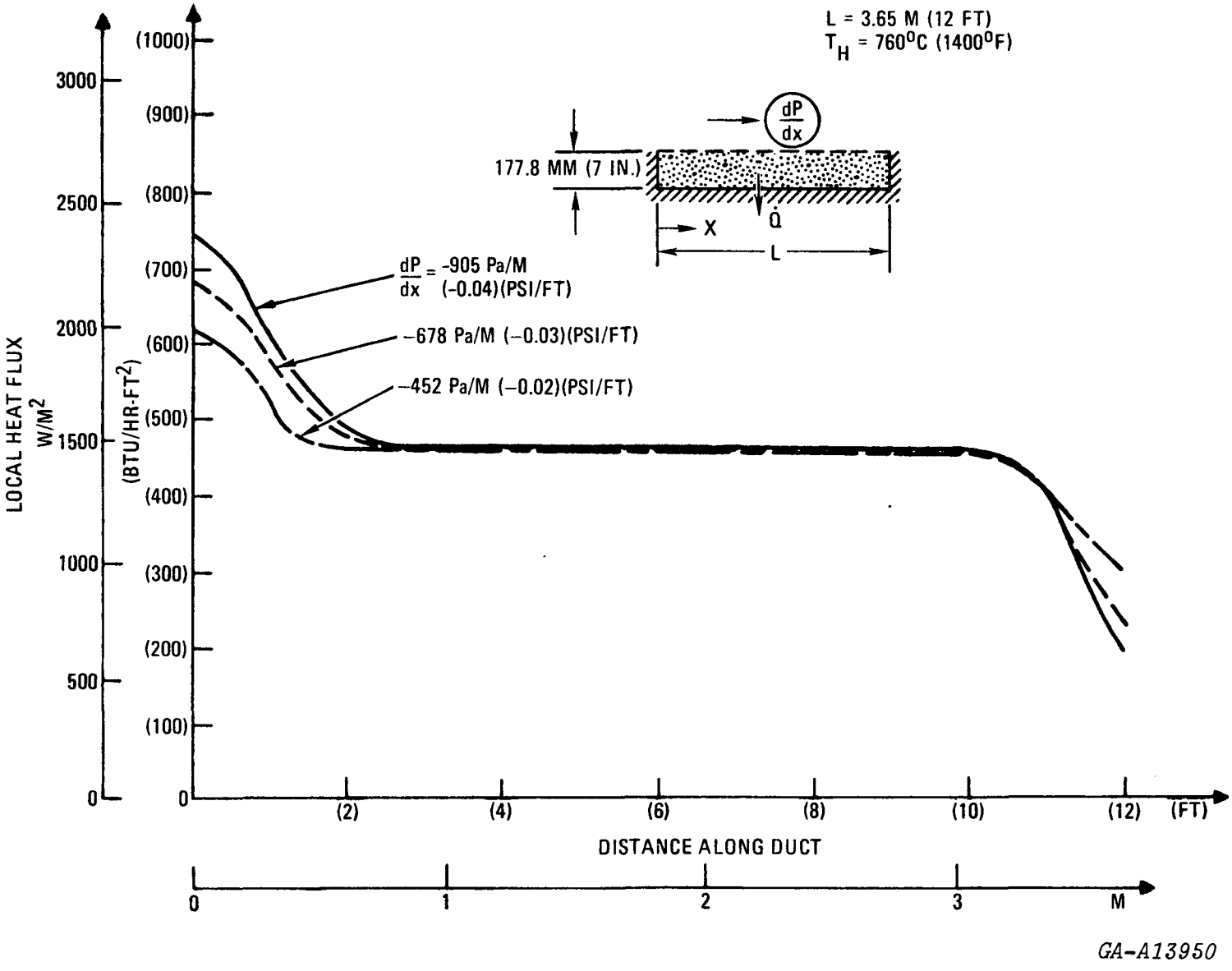

Fig. 4-23. Local heat flux as a function of distance along duct and duct pressure drop

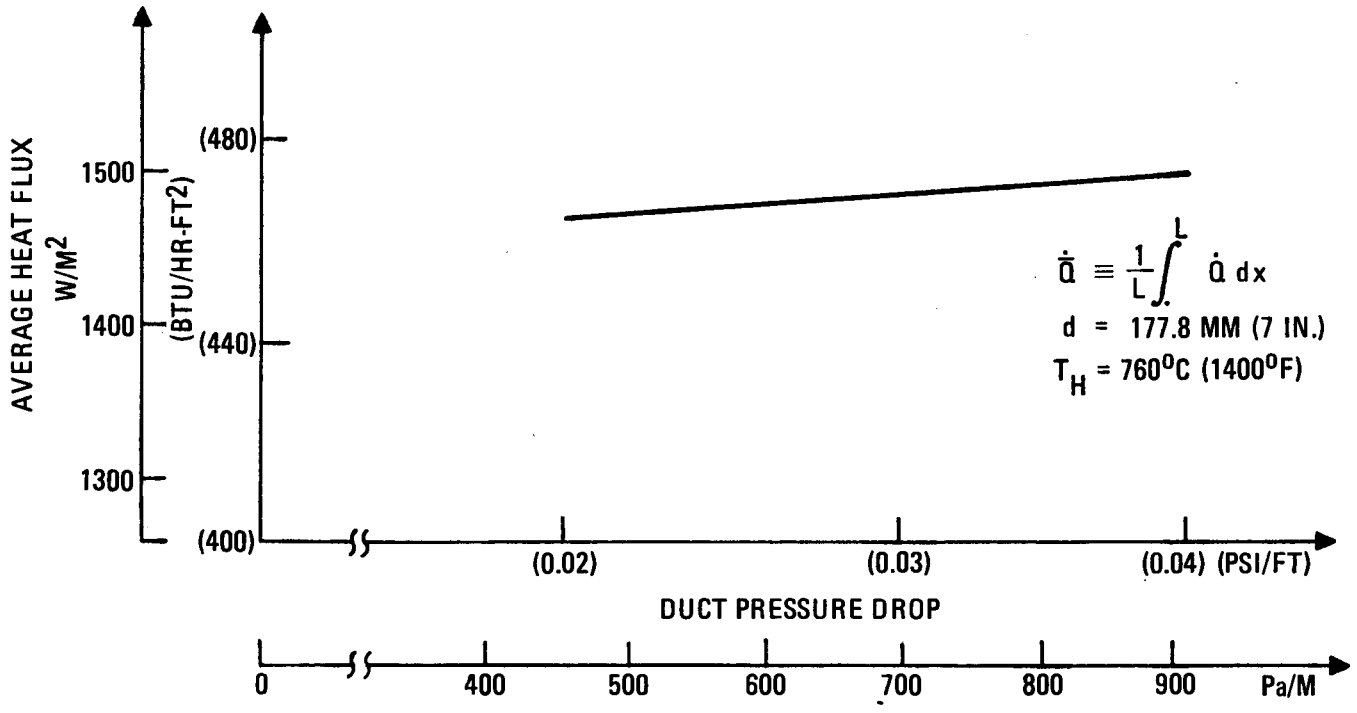

GA-A13950

Fig. 4-24. Effect of pressure drop on average heat flux

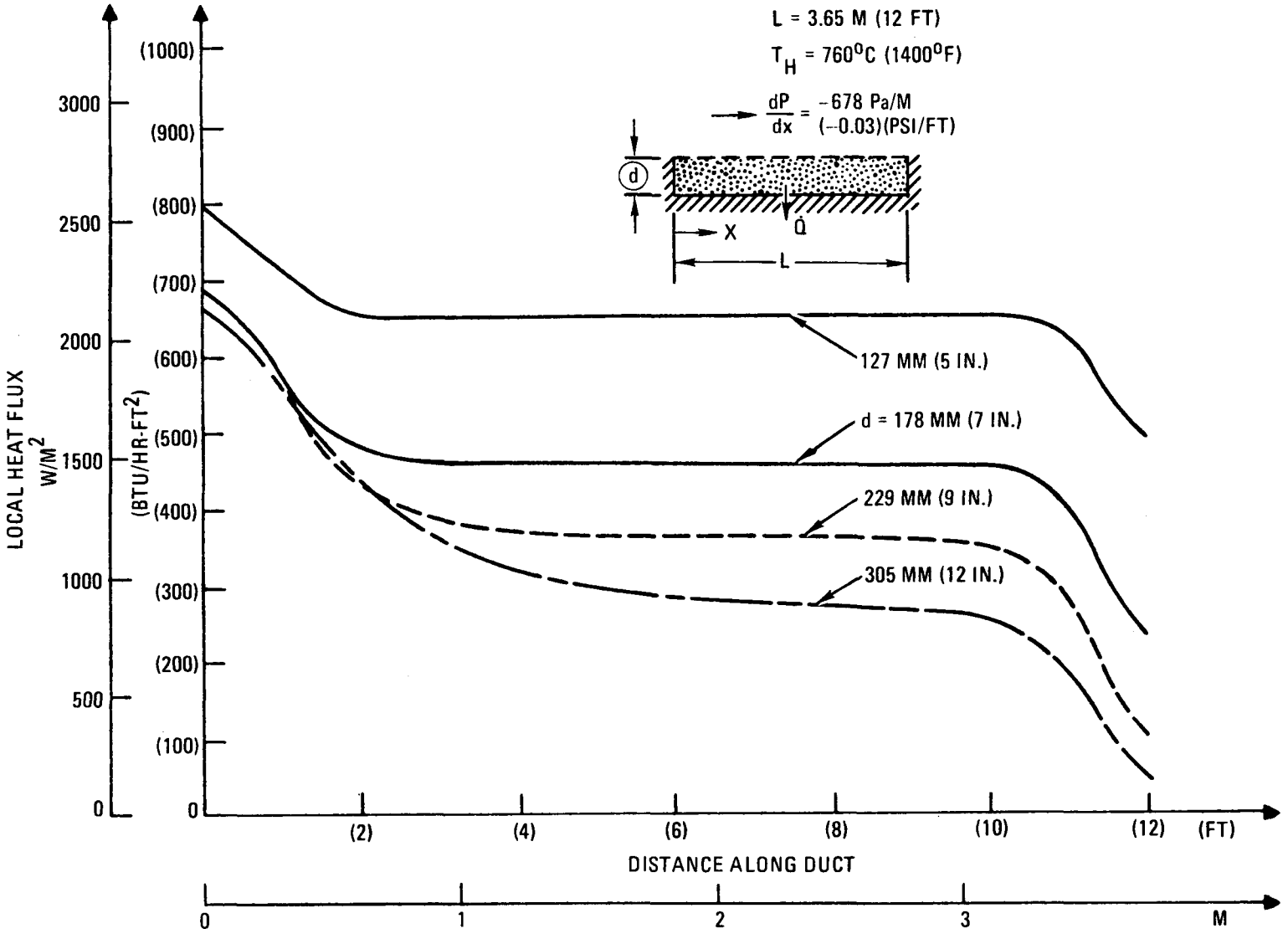

GA-A13950

Fig. 4-25. Effect of insulation thickness on local heat flux

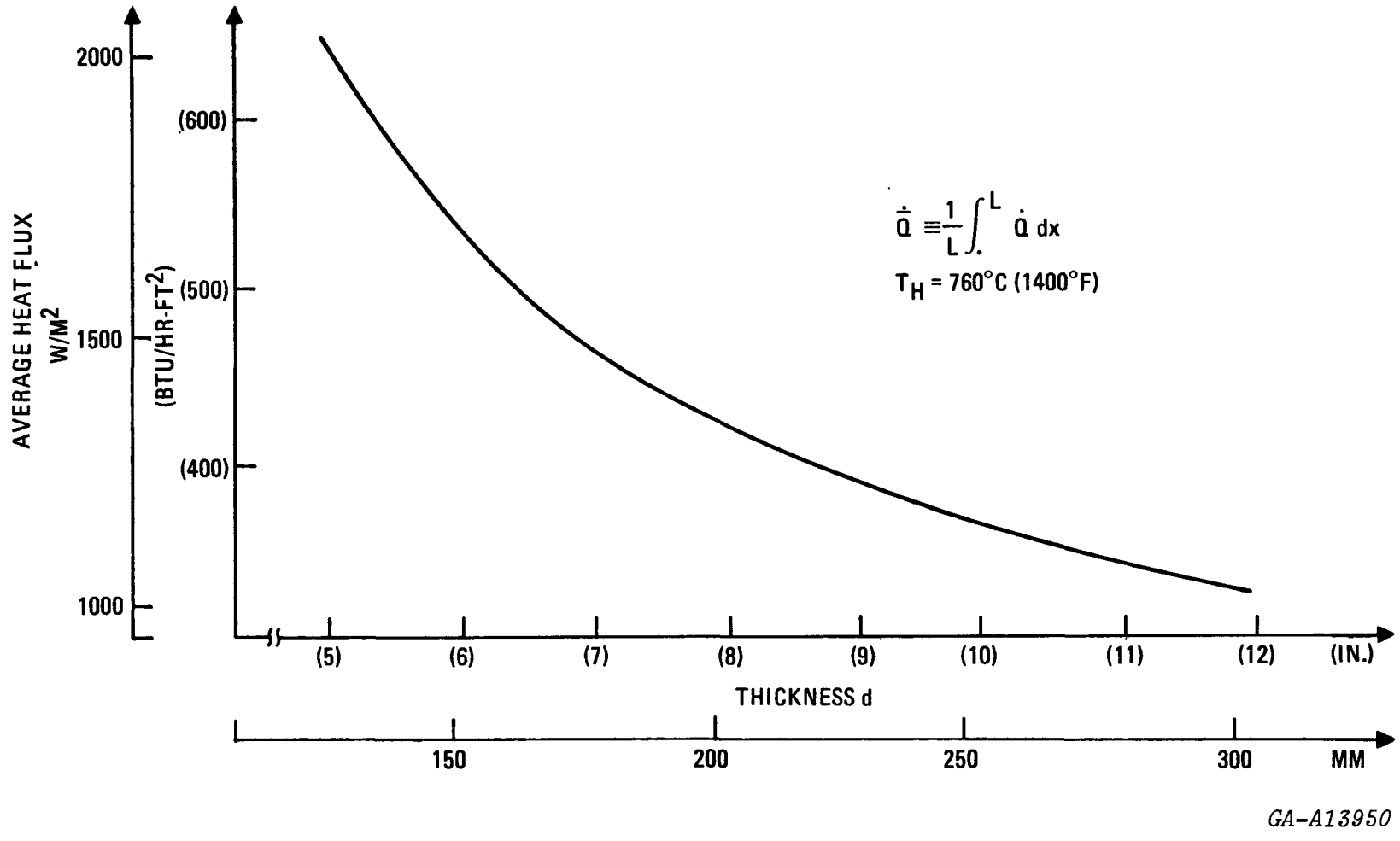

Fig. 4-26. Effect of insulation thickness on average heat flux

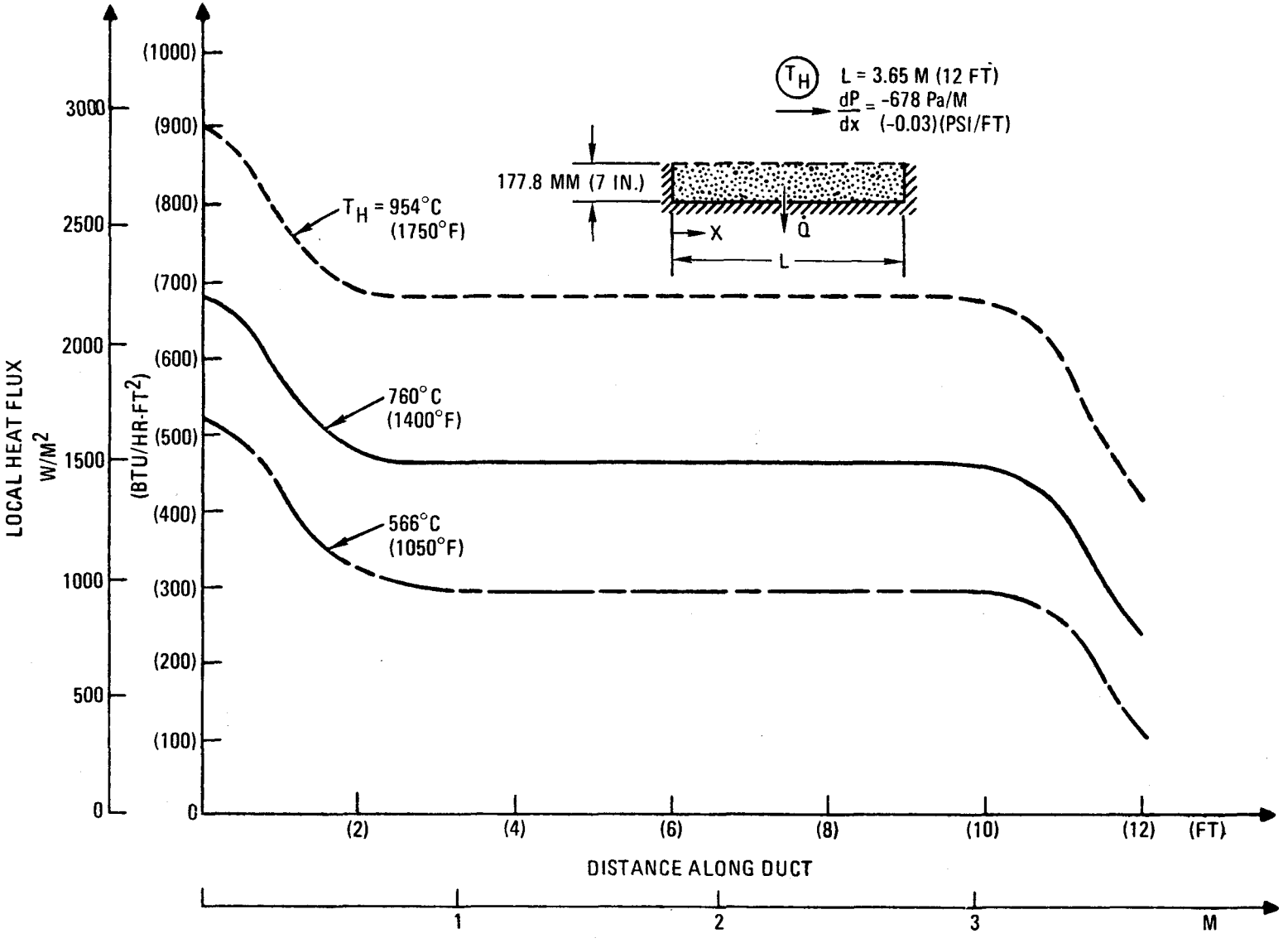

GA-A13950

Fig. 4-27. Effect of stream temperature on local heat flux

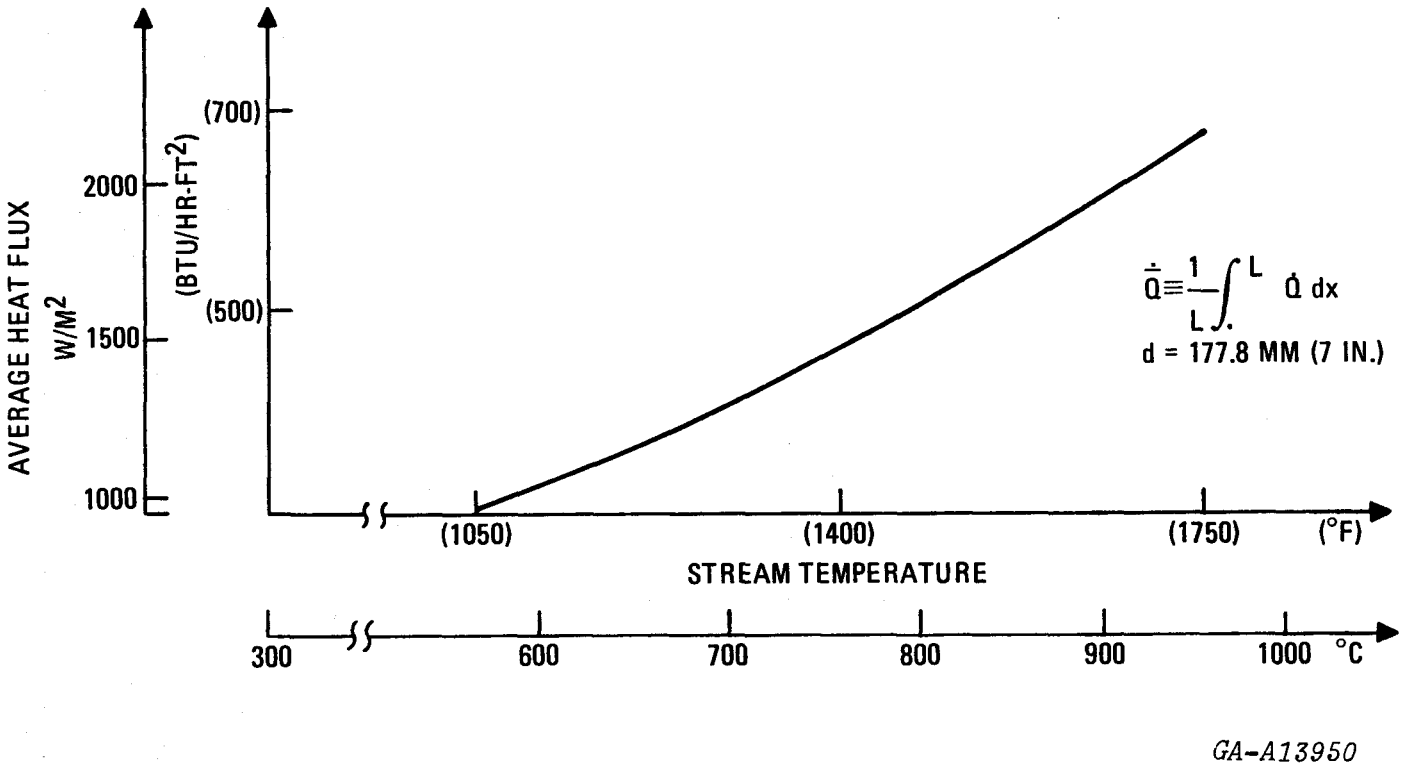

Fig. 4-28. Effect of stream temperature on average heat flux

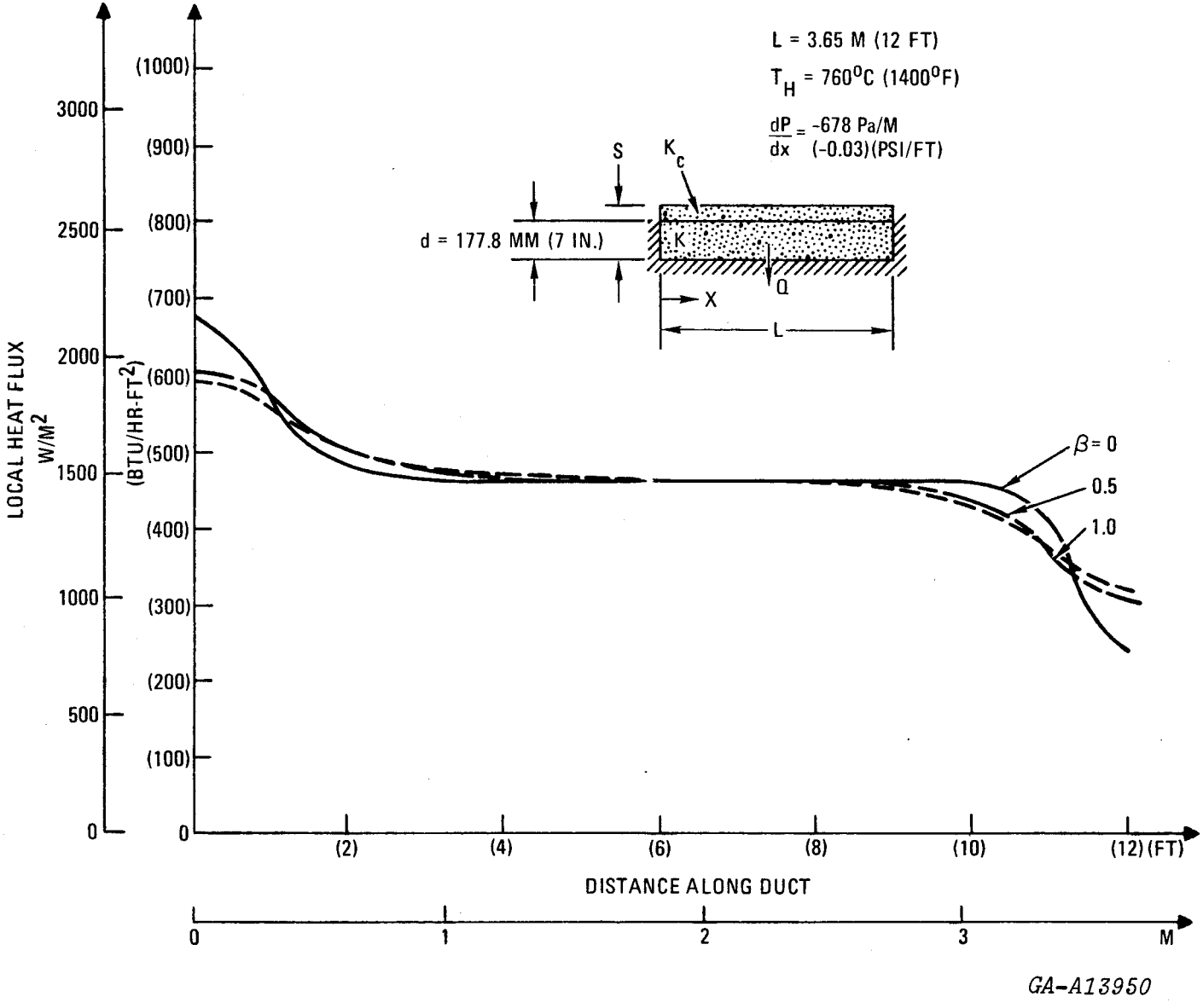

Fig. 4-29. Effect of ventability on local heat flux

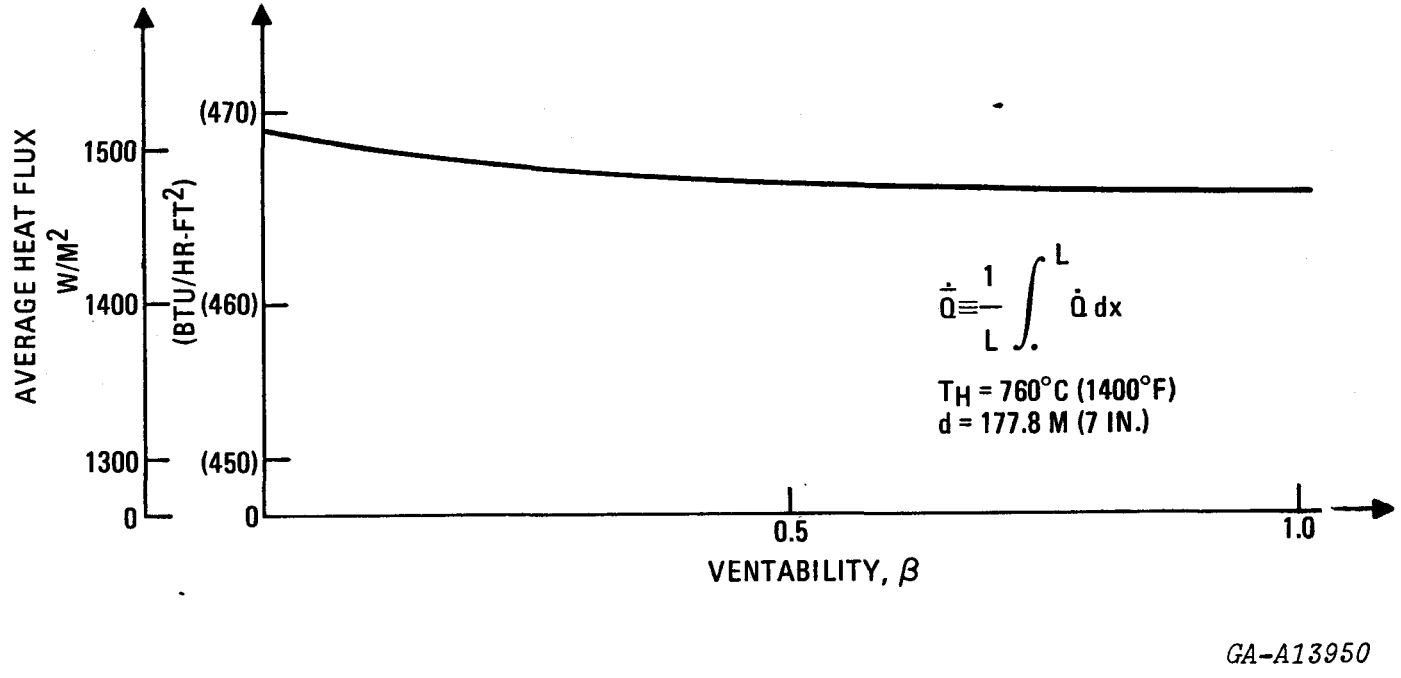

Fig. 4-30. Effect of ventability on average heat flux

The physical range of numbers assigned to the various parameters are all within the range of interest of the GT-HTGR thermal barrier design. The results presented in Figs. 4-23 and 4-24 indicate that a vented cover plate system will not cause an excessive increase in heat flux due to increased permeation flow, even at the high flux inlet end.

4.7.4. Core Outlet Duct Design for 850°C ROT

Several possible 850°C ROT core outlet duct configurations were studied. These configurations included both cooled and uncooled ducts and a variety of insulation materials. Most of the designs considered for the 850°C ROT case were also studied for the 950°C ROT case and are reported in Section 4.7.5.

The core outlet duct is considered in two sections: (1) the vertical section, which is srrounded by the relatively cool compressor effluent, and (2) the horizontal section, which is buried within the PCRV and is surrounded with water cooling channels. In all cases, several common ground rules were used as a design basis. These were:

1.	Hot helium temperature	850°C (1562°F)
2.	Hot helium pressure	7.69 MPa (1115 psi)
3.	Loop flow rate (reactor discharge considered equal to compressor discharge for this study)	567 kg/sec (4.5×10^6 lb/hr
4.	Maximum heat flux to PCRV liner	3.15 kW/m^2 (1000 Btu/hr-ft^2)
5.	Maximum liner temperature	82°C (180°F)
6.	Turbine inlet duct flow diameter (vertical and horizontal)	1.52 m (60 in.)

The vertical or free-standing duct carries helium at 850°C (1562°F) to the turbine and is surrounded by compressor discharge helium at 174°C (346°F). On entering the duct from the core discharge plenum, the helium transmits heat to the duct walls by forced convection. The film coefficient throughout this duct remains fairly high [on the order of 3.41 kW/m^2 (600 $Btu/hr-ft^2$)] because of the fairly low L/d of the duct. Coping with this heat in the vertical section is fairly straightforward, since there is an abundance of cooler compressor discharge gas available to remove it. The heat flux through the duct walls cannot be left unrestructed, however, because of the otherwise excessive thermal stresses which would be generated in the duct wall. The heat flux must therefore be limited to 142 to 170 kW/m^2 (25,000 to 30,000 $Btu/hr-ft^2$), corresponding to a ΔT across the wall of about 50 °C, (90°F) depending on the temperature of the duct wall and the material used.

Insulating the inside of the vertical duct (see Fig. 4-31) will effectively reduce both the heat flux through the duct and the temperature of the duct wall. It is possible to use a Class B type of thermal barrier using Safil alumina and Kaowool for hot core outlet duct and cooler compressor duct sections, respectively. Cover plates should be Inconel 617 for the hot core outlet duct but can be carbon steel for the cooler compressor duct liner thermal barrier. Table 4-15 indicates that if this type of thermal barrier is used, a minimum of 12.7 mm (0.5 in.) is required under a vented carbon steel cover plate to limit the heat flux to the liner to 3.15 kW/m^2 (1000 $Btu/hr-ft^2$). The principal heat source for the compressor duct liner will be convection from the compressor discharge gas at 174°C (346°F). Radiation from the core outlet duct accounts for only about 9% of the heat load in this case. The core outlet duct will require about 19.1 mm (0.75 in.) of Safil alumina (see Table 4-15) between the duct and an Inconel 617 cover plate. This reduces the heat flux to about 31.55 kW/m^2 (10,000 $Btu/hr-ft^2$) through the core outlet duct wall and its temperature to about 221°C (430°F). The minimum required insulation thickness may be increased in this section if required to decrease the overall heat loss to the PCRV cooling system.

The horizontal section, which is not concentric with the compressor discharge duct, presents somewhat more difficult heat control problems.

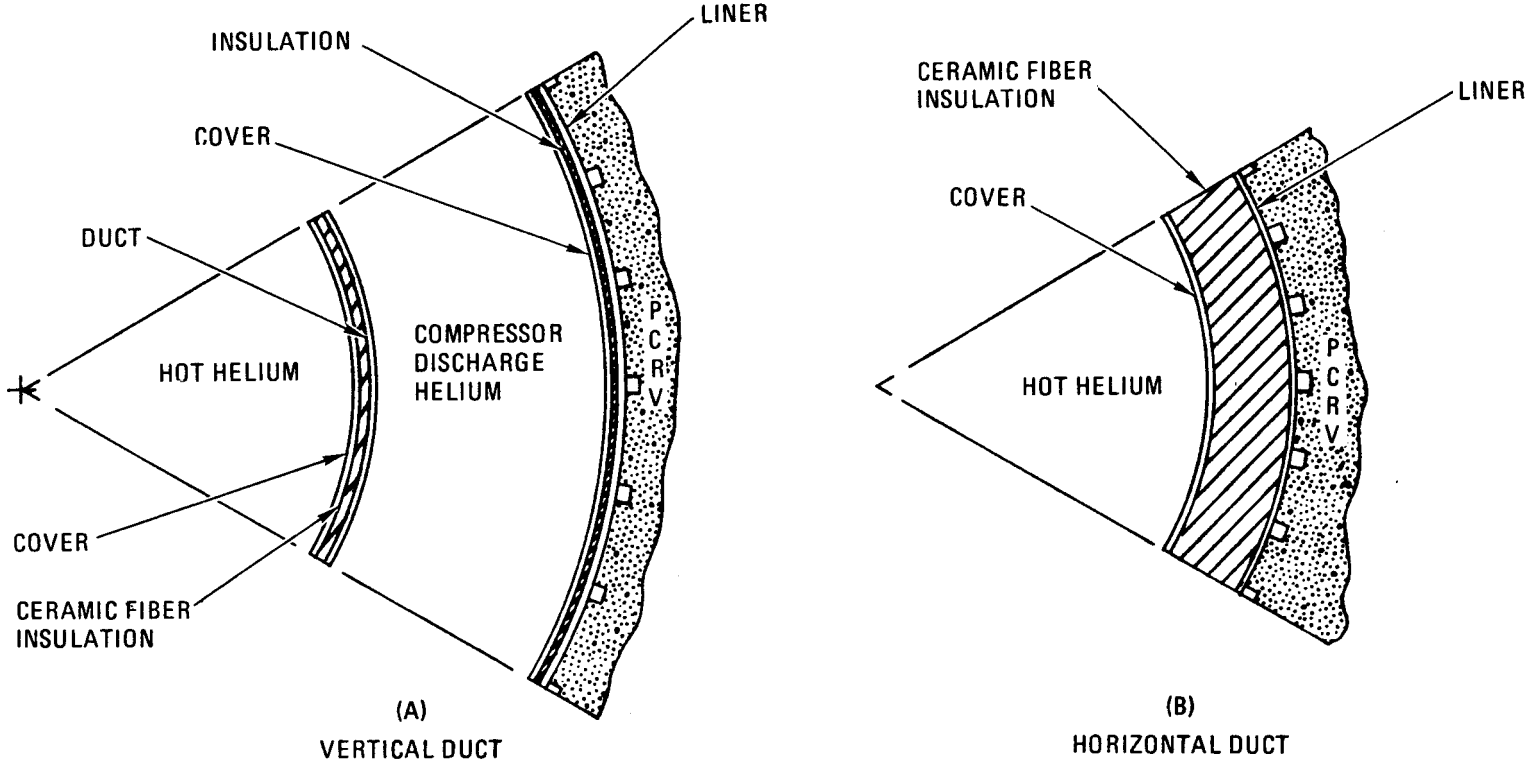

GA-A13950

Fig. 4-31. Core discharge/turbine inlet duct thermal barrier

TABLE 4-15
CORE OUTLET DUCT THERMAL BARRIER

	Vertical Section	Horizontal Section
Liner insulation material	Kaowool	Kaowool + Safil alumina
Thickness, mm (in.)	12.7 (0.5)	171.5 (6.75)
Cover plate material	Carbon steel	Carbon steel
Thickness, mm (in.)	6.35 (0.25)	6.35 (0.25)
Hot duct insulation material	Safil alumina	--
Thickness, mm (in.)	19.05 (0.75)	--
Cover plate material	Inconel 617	--
Thickness, mm (in.)	6.35 (0.25)	--
Hot duct heat flux, kW/m^2 ($Btu/hr\text{-}ft^2$)	31.55 (10,000)	3.15 (1,000)
PCRV liner i.d., m (in.)	2.7 (106.5)	1.89 (74.5)

The heat flux through the walls of this section must be limited to about 3.15 kW/m^2 (1000 $Btu/hr\text{-}ft^2$) to maintain acceptable concrete temperatures between line cooling coils. This can be done by either providing sufficient thermal resistance between the hot gas and the PCRV liner or, in addition, providing a cooling stream to carry off heat from the hot duct.

The former option is accomplished by providing a 171.5 mm (6.75 in.) composite layer of Safil alumina and Kaowool beneath an Inconel 617 cover plate (see Fig. 4-31). This, of course, provides a relatively large fiber-filled volume which must be vented sufficiently to avoid overpressuring the cover plates during rapid system pressure changes. Venting is accomplished by a vent cavity between the cover plate and the fibrous material which is constructed of layers of porous screen material.

The second option, which requires cooling flow from the compressor discharge, does not appear to be cost effective for the 850°C ROT case since it greatly complicates the construction of the thermal barrier. A more complicated construction of this type may, however, be justified for other reasons, such as additional core cavity side-wall cooling or higher core outlet temperatures, as will be discussed in Section 4.7.5.

4.7.5. Core Outlet Duct Design for 950°C ROT

When higher core outlet temperatures are to be considered [up to 135°C (242°F) increase from the former reference of 815°C (1500°F)], the limits of current HTGR thermal barrier technology would be exceeded. It appears that new cover plate materials which have improved long-term creep strengths will be required. Also, available ceramic fibrous insulation materials themselves have very marginal resiliance at 950°C (1742°F). While current technology may be retained with 850°C (1562°F) ROT systems, it is recommended that nonmetallic cover plate concepts be strongly considered for higher-temperature duty. This study evaluates a graphite composite thermal barrier based system at 950°C (1742°F).

4.7.5.1. Insulation Problem. The subject duct requires internal insulation. Without such a thermal barrier and with 950°C (1742°F) ROT, the free-standing duct mean wall temperature will exceed 650°C (1200°F) at steady conditions, and this is well into the creep range. Steady-state duct wall thermal stresses [caused by more than 110°C (200°F) temperature drop through the wall] would exceed 560 MPa (80,000 psi), which when combined with primary pressure and thermal expansion stresses could approach 630 MPa (90,000 psi) total stress. This level is far in excess of that allowed by Section III ASME Code Case 1592 (high-temperature Class I nuclear components). This is felt to be significant, because although the subject duct is classified as a non-nuclear component and could be designed to Section VIII of the ASME Code, Section VIII design rules fail to consider all failure modes; the alternate, Section III ASME Code Case 1592 does consider all failure modes. Another factor in favor of insulating the subject duct is that a forced convective heat shunt from turbine inlet gas to compressor discharge gas would otherwise occur at a rate of about 20 MW(t) and would reduce the turbine inlet temperature by about 8°C (14°F). The cold-end recuperator temperature would increase by a similar amount. While the performance losses inherent in this heat shunt rate have not been calculated, it is evident that they would be substantial and are undesirable.

4.7.5.2. Cooling Problem. A large portion of the subject duct is cooled by compressor discharge flow, it being concentric with the vertical compressor outlet duct. When the subject duct is internally insulated, it attains a low metallic duct wall temperature, very near that of the cooling flow. The resulting situation is advantageous to the entire system, because:

1. Subject duct wall properties are good (at low temperature).

2. Thermal stresses are low in the duct (because of low thermal expansion loads and low thermal gradients).

3. Heat shunt induced system performance losses are low.

4. Concentric embedded duct temperatures are not affected by (radiant) heat transfer from the subject duct.

A cooling scheme has not been identified for the horizontal section of the subject duct. Without such, Items 1 and 4 could not be realized, even if insulation were used, and Item 2 would be only partially satisfied with insulation. It is therefore important to identify candidate cooling schemes for this portion of the duct and eventually to select one for the plant design which is mechanically reasonable and satisfies the above conditions.

4.7.5.3. Duct Cooling Methods. Figure 4-32 illustrates the approximate geometry of the reactor cavity outlet duct; region II is to be cooled. It is apparent that since regions I and III are cooled with the compressor discharge flow, region II could make use of the same coolant. Less apparent, however, are the choice of the coolant flow sink and what the coolant flow rate should be. Reference to Fig. 4-33, a GT-HTGR PCL flow schematic, provides a clearer view of the flow sink choices, which are discussed below.

1. Bleed a small portion of the compressor discharge flow from region III through the annulus around the core, and dump the coolant into the core inlet plenum. Ideally, the coolant gas flow would be such that its outlet conditions are similar to the high-pressure recuperator outlet gases. The coolant would be heated by a portion of core reject heat otherwise transferred to its cylindrical cavity liner as well as by the subject duct. The need for normal core bypass flow to cool the core cavity annulus would therefore be eliminated or reduced.

2. Bleed all of the compressor discharge gas through the region II annulus, upward around the core (capturing a greater portion of the core reject heat than with scheme 1), concentrically around the core inlet duct (cooling this hot duct as well), and dumping the gas into the high-pressure recuperator inlet cavity above the recuperator main tubesheet. This scheme does not require the current reference design vertical compressor discharge duct nor the connecting cross duct to the recuperator inlet cavity, and it cools the core seismic restraints without bypassing core coolant through the core cavity annulus.

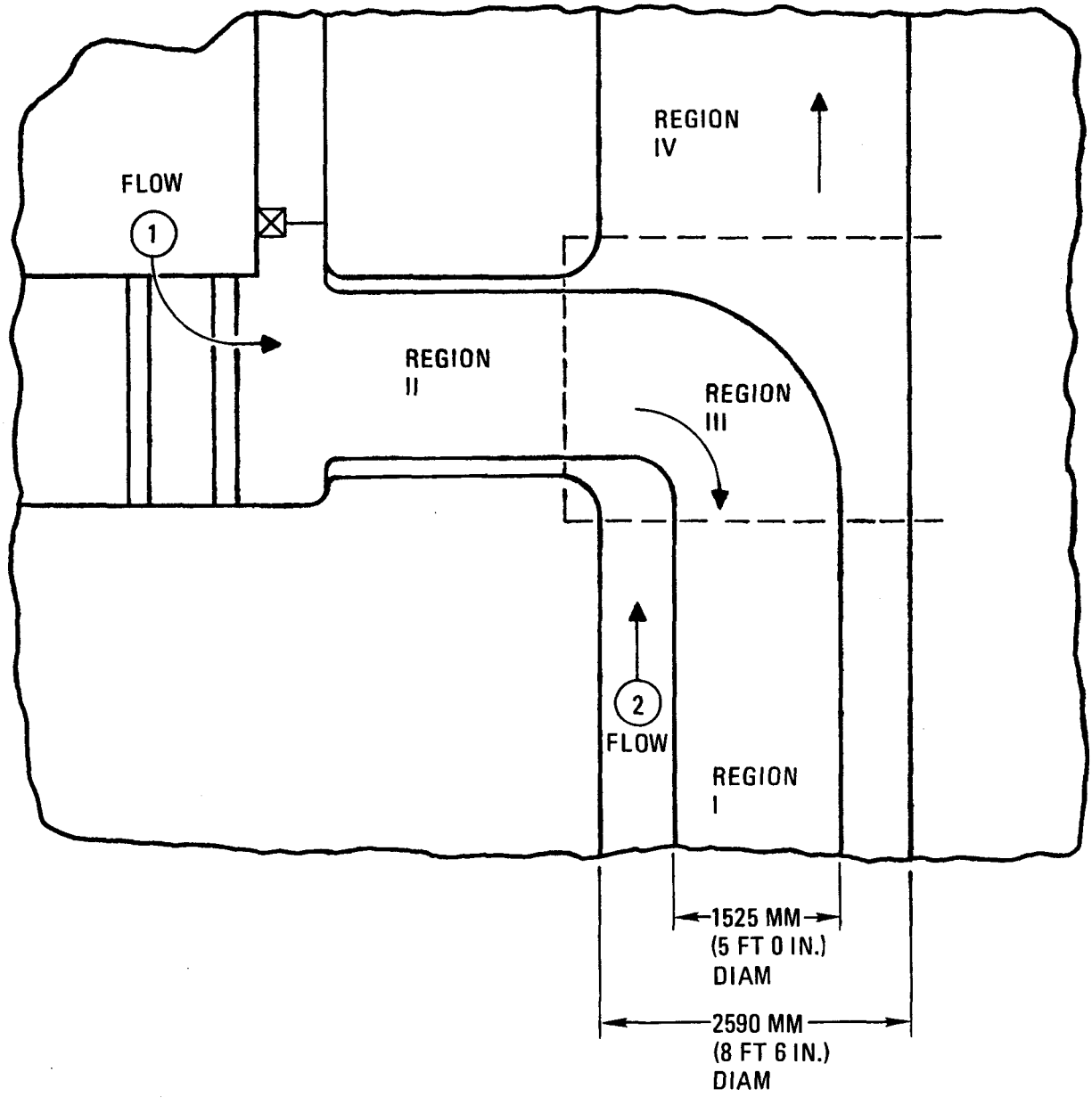

GA-A13950

Fig. 4-32. Reactor cavity outlet duct geometry

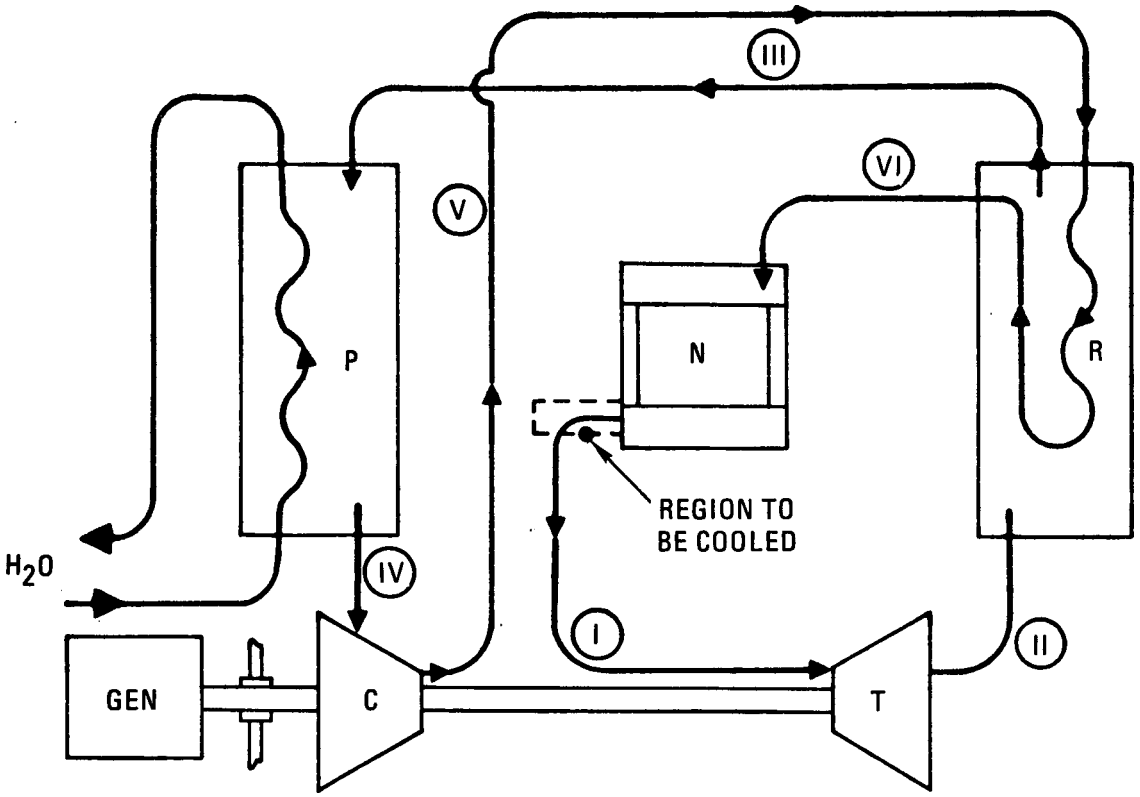

COOLING METHOD NO.	CD BLEED SINK	REMARKS
1	NI	PF
2	HP RI	FF (AROUND CORE)
3	NO	PF
4A	V	PF (ASPIRATION)
4B	V	PF (INDUCTION)
4C	V	PF (ASP. & IND.)
5	–	NF (RADIATION SHIELD)

I – INLET
O – OUTLET
PF – PARTIAL FLOW
NF – NO FLOW
FF – FULL FLOW
HP – HIGH PRESSURE
LP – LOW PRESSURE
R – RECUPERATOR
P – PRECOOLER
N – CORE
CD – COMPRESSOR DISCHARGE

GA-A13950

Fig. 4-33. GT-HTGR PCL flow schematic

3. Bleed a small portion of the compressor discharge gas from region III, through the region II annulus, and dump the flow into the nearby reactor core cavity outlet plenum. This method could be mechanically simple.

4. Bleed a small portion of the compressor discharge gas from region I or IV, through region II, back through region II, and discharge into region III. This method minimizes the impact on the system but requires some baffling in the annulus. There appear to be at least three ways to provide the flow potential required to force cooling gas circulation through the annulus. All rely upon the existence of a velocity head in the vertical compressor discharge duct. The three ways are:

   a. The minimum vertical duct flow area occurs near the center line of the horizontal hot duct (region III), where the highest gas velocity and the lowest static pressure exist. Cooling gas bled into the horizontal annulus (from region IV where the static pressure is highest) will have a potential to flow through the annulus to the low-pressure outlet region. (This is the aspiration method.)

   b. Cooling gas which is collected parallel to the vertical compressor duct flow stream lines (region I) will have a pressure nearly equal to the total pressure of the gas in the duct-free stream. If the gas is bled back and forth through the horizontal annulus and is returned to the vertical duct at right angles to the flow stream lines, the gas velocity head will provide the driving potential for cooling flow. (This is the induction method.)

c. If insufficient potential can be developed with either of the two above schemes, then they could be combined, which will increase the coolant flow potential as shown in Fig. 4-34. In any case, it would be desirable to attach a diffusion cone to the top of the hot duct elbow to reduce the pressure loss in the vertical compressor discharge duct. Otherwise, the coolant would flow around the elbow and undergo a subsequent rapid expansion.

5. If the major duct cooling considerations were to prevent horizontal duct embedded liner overheating and to reduce system performance losses, concentric radiation shields could be positioned in the horizontal annulus. The duct wall would run very hot and promote thermal expansion induced bending loads to the vertical duct. A large thermal gradient would exist at the elbow, which could greatly increase the stresses at that location. No forced convective cooling would be used.

4.7.5.4. Nonmetallic Thermal Barrier. The free-standing duct internal insulation system assumed for this study is composed of a 76-mm (3-in.)-thick graphite composite inner sleeve, surrounded by a 13 mm (0.5-in.)-thick cushion of fibrous insulation, which is encircled by the 13 mm (0.5-in.)-thick duct wall. Tentative material selections are Pyrocarb 400, Kaowool, and ferritic steel, or rough equivalents. With this thermal barrier system, the approximate heat transfer in region I would be reduced from about 20 MW(t) (uninsulated) to 0.5 MW(t). The duct outer wall would run below 190°C (375°F) with a thermal stress of about 7.7 MPa (1100 psi) caused by a radial temperature difference of less than 55°C (10°F). The major temperature drop of 555°C (1000°F) would occur through the fibrous insulation, which can develop little mechanical stress; its maximum internal temperature would be limited to 760°C (1400°F). The remaining 195°C (350°F) ΔT exists through the graphite composite cover. Although relatively thick, the graphite's low modulus limits the steady thermal stress through the wall to less than

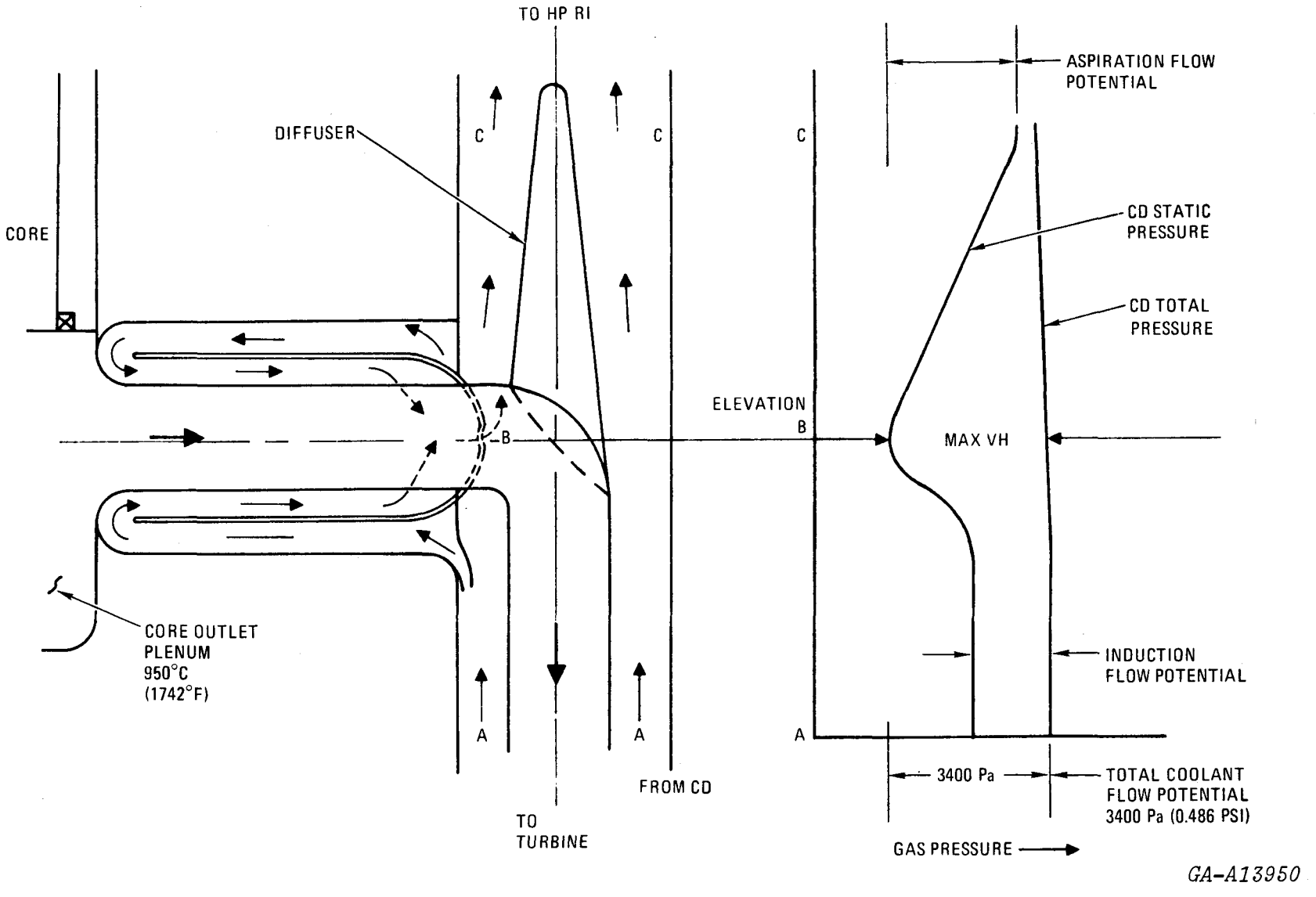

Fig. 4-34. Cooling method No. 4C

7 MPa (1000 psi), or to about 10% of its strength. It is likely that a fibrous insulation with higher temperature capabilities than Kaowool would be selected for a long-life design. An attractive candidate is Safil, an alumina fiber product.

During heatup from room to operating temperatures, the graphite and metallic wall expansions are well-matched, being nearly equal. As a result, only a small (acceptable) amount of fibrous insulation precompression will be required to assure liner support at all times.

4.7.5.5. Cooling Methods Evaluation. The various cooling methods are evaluated below.

1. The first hot duct cooling method is somewhat difficult to evaluate mathematically because it is a function of the unknown coolant bleed flow rate. However, it is interesting to compare point design results with the current core cavity annular bleed system used to cool the seismic spring packs in the 3000-MW(t) HTGR liner. The HTGR bleeds 1.5% of the core inlet plenum flow downward around the outer reflector blocks. The cooling gas enters the 102-mm (4-in.)-wide annulus at about 338°C (640°F), driven by the 70 kPa (10 psi) core pressure drop. Of the total flow, 1% exits the annulus into the bottom core plenum via an intentionally leaky log seal at about 440°C (825°F), while the remaining 0.5% flow leaks into the core between the various side reflector blocks. Nearly 10 MW(t) of otherwise lost core heat is recovered by the bypass coolant (more than 0.3% of core heat), and the reflector block outer surface temperature is reduced, thereby somewhat limiting the radiant heat transfer to surrounding liner and spring packs.

   On the basis of the 3000-MW(t) HTGR data, a 1% coolant flow was assumed to be bled from the compressor discharge duct, through the region II annulus and upward through the 4000-MW(t)

core cavity annulus to the inlet plenum. In this case, about 20 MW(t) of reject core heat (or 0.5% of core heat) is gathered by the coolant from all four loops. The coolant gas temperature gains 222°C (400°F) and enters the inlet plenum at about 400°C (750°F), which is 149°C (300°F) below the bulk gas temperature in the inlet plenum. If the reflector block inleakage were greater than assumed or if the lower log seal leakage were significant, the gas temperature entering the inlet plenum would be greater. Otherwise, it would be necessary to reduce the coolant flow below 1% to match the 565°C (1050°F) inlet plenum gas temperature. The reflector block outer surfaces are cooled to about the same temperature as the HTGR blocks without bypassing core coolant through the core annulus.

Orificing of some type would be required to limit coolant bleed flows to the 1% range. With a 12.7-mm (0.5-in.)-wide annular flow space around the subject duct, the coolant velocity would be about 9.15 m/sec (30 ft/sec). Adequate duct cooling would result, however, because the heat transfer coefficient and coolant gas temperatures approximate those outside the vertical section of the subject duct.

During CACS operation with all loops down, the core bypass flow would reverse and join the reversed loop flows at the compressor discharge duct. Core annulus flow with one loop down and three loops operating would be complex; probably, reduced coolant flow to the inlet plenum and around the core would result, with a portion of the coolant leaking into the down loop at the subject cross duct. Reduced core cavity annulus cooling could result.

2. The second hot duct cooling method looks attractive if core cooling related safety issues can be satisfied. With 100% of the compressor discharge flow directed around the subject

duct, upward through the core cavity annulus, and annularly around the core inlet ducts to the recuperator high-pressure inlet, a total of nearly 150 MW(t) or more than 3.5% of core power is recuperated from the core outer periphery. This raises the high-pressure recuperator inlet temperature by about 4.5°C (8°F) to about 180°C (355°F). The core reflector block outer temperature is reduced to about 205°C (400°F) so that total heat transfer to the liner and plant cooling system is greatly reduced. The reflector blocks operate with a high radial temperature difference of over 1110°C (2000°F), but since they are stacked and are relatively unrestrained, the thermally induced loads should be small.

A fortunate result of the analysis is that the normal core annulus width of 102 mm (4 in.) is sufficient to allow passage of all compressor discharge gas without affecting the system pressure loss. The annular gas velocity will be about 61 m/sec (200 ft/sec).

In addition to the core annulus seal normally required, it is apparent that either an upper seal or an outer core shroud would be required in conjunction with an upper manifold to duct the gas to the core inlet duct annuli. Simultaneous failures of upper and lower flow resistors could possibly lead to CACS ineffectiveness. This cooling method could increase plant costs slightly.

3. A very small bleed flow (of less than 0.1%) would be required to cool the subject duct itself, from the standpoint of the thermal capacity of the coolant, because the duct wall area is small. This factor makes the third coolant scheme attractive, because system performance losses would tend to be small, on the order of 0.1%. Low gas velocities, if used, would limit the coolant-side heat transfer coefficient so that metal duct temperatures would remain high. Simple

flow orificing with discharge into a large coolant annulus does not look feasible.

A major design factor will involve duct wall fabrication. It is apparent that the duct wall itself should contain small-diameter coolant flow passages so that low-flow-rate, high-velocity coolant can pass from the compressor discharge duct to the core outlet plenum or the subject duct inlet plane. If the duct wall were fabricated, for example, as a shell of parallel tubing, the requisite tube i.d. would be about 5 to 6 mm (0.1875 to 0.25 in.). A spiral wrap of tubing would allow larger sizes to be used, on the order of 25.4 mm (1 in.) diameter. It would be convenient to dump the coolant, heated to about 260° to 315°C (500° to 600°F), into the fibrous insulation located between the cover plate and the duct wa-l at the core outlet plenum end of the duct. The gas could, then, seep along the insulation and into the main coolant stream through the cover plates, providing a measure of transpiration cooling. As the duct wall temperature could run as warm as about 315°C (600°F), a layer of low-temperature insulation material should be used between the duct wall and the embedded water-cooled liner.

4. Thermal/hydraulic estimates of scheme 4c have been made, wherein cooling flow is induced from the main compressor discharge stream via a diffusing pitot and flows annularly back and forth over the duct length to aspirating outlets at the maximum velocity section of duct region III. Results are favorable and show that when 12.7-mm (0.5-in.)-wide flow annuli are used outside the subject duct, 1% of the compressor discharge gas can be caused to flow around the duct at 9.15 m/sec (30 ft/sec). This will cause a gas temperature rise of only about 5.5° to 8.5°C (10° to 15°F) and will provide cooling nearly equal to that of the vertical section of the duct (in the compressor discharge duct).

While schemes 4a and 4b may provide less potential for cooling flow, it is evident that either could adequately cool the subject duct. The mechanical complexity of cooling method 4 may be greater than covering method 3, but its performance and safety impacts will be negligible. As with the other cooling methods presented, a layer of thermal insulation will be required around the cooled assembly to limit local concrete temperatures.

5. Mechanical assembly of a series of concentric radiation shields would be as complex as other schemes, and the fact that no coolant flow may be required is not seen as a significant advantage. Because the duct wall will run hot, the concept does not appear to be attractive.

4.7.5.6. Conclusions. System performance estimates are to be made for cooling methods 1 through 4, including heat transfer and pressure changes. Safety studies are to be made on cooling methods 1 and 2 to determine whether these are viable candidate methods. With these studies and the information presented herein, it should be possible to select a preferred subject duct cooling method.

Conclusions that are apparent at this time include the following:

1. The subject duct should be internally (and externally) insulated, as recommended above.

2. Cooling methods 1 through 4 appear to have the capability to cool the subject duct satisfactorily and appear to be mechanically feasible.

3. The carbon composite/fibrous internal thermal barrier scheme presented for the subject duct appears to meet all current thermal and mechanical requirements for use with 950°C (1742°F) ROT systems.

REFERENCES

4-1. "MARC-CDC Nonliner Finite Element Analysis Program," Marc Analysis Corporation, Providence, Rhode Island.

4-2. Young, R., General Atomic, "THREED - Three-Dimensional Finite Element Analysis Program," unpublished data, 1975.

4-3. ASME Boiler and Pressure Vessel Code, Section III, Division 2, 1975.

4-4. Bathe, K., el al. "SAP IV, a Structural Analysis Program for Static and Dynamic Response of Linear Systems," University of California, Berkeley Report EERC 73-11, June 1973.

4-5. ASME Boiler and Pressure Vessel Code, Section III, Division 1, 1974.

4-6. Browne, R. D., and R. Blundell, "The Behaviour of Concrete in Prestressed Concrete Pressure Vessels," Nucl. Eng. Des. 20, 459 (1972).

4-7. "HTGR Direct Cycle Turbomachinery Technology Final Report," UTCR-0080, June 1975.

4-8. "HTGR Direct Cycle Turbomachinery Technology Mid-Program Progress Report," PSD-R-101, UTCR-0082, January 1976.

4-9. "Seismic; Nuclear Steam System," General Atomic Design Criteria DC-4-4, January 1975.

4-10. Vepa, K., General Atomic, "Nodal Analysis of Horizontal Seismic Motion in the Recuperator," unpublished data, April 1975.

4-11. Williams, K., General Atomic "GA-HRB Bypass Valve System Comparison," unpublished data, September 1975.

4-12. "Gas Turbine HTGR Program, Semiannual Progress Report for the Period July 1, 1975 through December 31, 1975," General Atomic Report GA-A13740, January 1976.

4-13. Baxi, C. B., General Atomic, "POROUS, a General Purpose Code to Calculate the Steady State Velocity and Temperature Distributions in a Porous Medium," unpublished data, February 1974.

5. DIRECT-CYCLE GAS-TURBINE MATERIALS (Task 189a, No. SU034)

5.1. INTRODUCTION

The purpose of the GT-HTGR Materials Screening Test Program is to identify and evaluate structural alloys for application in PCL components. The general approach is to establish the applicability of candidate materials by determining possible environmental effects on pertinent structural properties through screening tests, diagnostic metallurigcal evaluations, and analyses. The results of this program will provide the foundation for additional work that will be required to select and qualify materials for each component of the GT-HTGR.

The experimental program includes parallel screening tests at the Central Institute for Industrial Research (CIIR) in Oslo, Norway, and at the GA Advanced Materials Laboratory. The first effort represents a collaboration between GA and the European High-Temperature Materials Program (formerly a part of the OECD High-Temperature Reactor Dragon Project) and includes creep-corrosion environmental screening tests on candidate alloys supplied by GA. In the investigations at GA, possible environmentally induced evaporation, corrosion, and aging effects on the strength, deformation, and fracture characteristics of the candidate alloys are being studied by means of a series of screening tests.

Significant scheduled milestones achieved during the reporting period include:

1. Completion of a report documenting the interim results of controlled impurity helium tests and the results of 3000-hr specimen destructive testing and metallurgical diagnostic evaluation.

2. Initiation of the 900°C (1652°F) controlled impurity helium aging tests at GA

5.2. TEST PROGRAM STATUS

5.2.1. Collaborative Tests

There were significant developments during the reporting period in the collaborative creep-corrosion screening test program being conducted at CIIR. Due to the termination of the OECD Dragon Project on March 31, 1976, the testing at CIIR has been reorganized and is being continued under the combined funding of ERDA, KFA (Julich, West Germany), and EEC, (Petten, Holland). The former Dragon Metals Program staff, now stationed at Wimborne, United Kingdom, is continuing to coordinate the program.

The test matrix for the collaborative program, including alloys, temperatures, stresses, times, and helium environment, was discussed in Ref. 5-1. Briefly, uninstrumented creep and corrosion control tests are being conducted on candidate alloys at 650°C (1202°F), 800°C (1472°F), and 900°C (1652°F) in controlled impurity helium and in air at design stress levels for times up to 10,000 hr.

The status of the GT-HTGR creep-corrosion screening tests at CIIR is summarized in Table 5-1. As of June 1, 1976, the tests on the cast turbine alloys, IN100, Rene 100, IN713, M21, and IN738, on the cast ducting alloy IN519, and on the wrought ducting alloy Inconel 617 in helium at 800°C (1472°F) and 900°C (1652°F) had progressed to 8000 hr. The wrought alloy Hastelloy X specimens had ruptured in 2760 and 3300 hr, respectively. The 650°C (1202°F) helium tests on the above alloys had reached durations of 6000 hr. Helium testing on other alloys such as molybdenum TZM, MA753, and MA754 had progressed to various times from 1000 to 6000 hr. Air tests on most alloys had reached at least 3000-hr durations.

Several additional candidate ducting alloys were sent to CIIR for creep-corrosion testing at 800°C (1472°F), 900°C (1652°F), and 1000°C (1832°F) in

TABLE 5-1
STATUS OF GT-HTGR CREEP-CORROSION SCREENING TEST PROGRAM AT CIIR AS OF JUNE 1976

Alloy	Type	Accumulative Hrs at Specified Temperature							
		650°C (1202°F)		800°C (1472°F)		900°C (1652°F)		1000°C (1832°F)	
		He	Air	He	Air	He	Air	He	Air
IN100*	Vacuum	6000	3000	8000	3000	8000	4000	--	--
Rene 100*	Shell cast	3000	3000	8000	3000	8000	4000	--	--
IN713*		6000	3000	8000	3000	8000	4000	--	--
MM004*		3000	3000	8000	3000	5000	4000	--	--
M21*		6000	3000	8000	3000	8000	4000	--	--
IN738*		3000	3000	8000	3000	8000	4000	--	--
Hastelloy X (HT.081)*	Wrought	6000	3000	8000	3000	3000(a)	4000	--	--
Hastelloy X (HT.086)	Solid solution	--	--	IP.(0)	IP.(0)	IP.(0)	IP.(0)	IP.(0)	PL.
Inconel 617*	Strengthened	6000	3000	8000	3000	8000	4000	--	--
Hastelloy S		--	--	IP.(0)	IP.(0)	IP.(0)	IP.(0)	IP.(0)	PL.
RA333		--	--	IP.(0)	IP.(0)	IP.(0)	IP.(0)	IP.(0)	PL.
HD556		--	--	IP.(0)	IP.(0)	IP.(0)	IP.(0)	IP.(0)	PL.
MA753+	Mechanically alloyed	6000	PL.	3000	3000	4000	1000	--	--
MA754+	Dispension strengthened	3000	PL.	3000	3000	4000	1000	PL.	PL.
Mo TZM+	Wrought	3000	--	3000	--	1000	--	PL.	--
IN519+	Centrifugally cast	6000	3000	8000	3000	8000	4000	PL.	PL.
HK40		--	--	IP.(0)	IP.(0)	IP.(0)	IP.(0)	IP.(0)	PL.
Supertherm		--	--	IP.(0)	IP.(0)	IP.(0)	IP.(0)	IP.(0)	PL.
Manaurite 36X		--	--	IP.(0)	IP.(0)	IP.(0)	IP.(0)	IP.(0)	PL.
Manaurite 36XS		--	--	IP.(0)	IP.(0)	IP.(0)	IP.(0)	IP.(0)	PL.
Manaurite 900		--	--	IP.(0)	IP.(0)	IP.(0)	IP.(0)	IP.(0)	PL.
Inconel 718+	Wrought	6000	3000	--	--	--	--	--	--
Inconel 706+	Precipitation strengthened	6000	3000	--	--	--	--	--	--
A286+		6000	3000	--	--	--	--	--	--
316+	Austenitic	3000	PL.	3000	PL.	--	--	--	--
Incoloy 800+	Stainless steel	3000	PL.	3000	PL.	--	--	--	--

KEY: IP.(0) - Test in progress (initiated June 1976). Accumulated time ~0 to 100 hr.

PL. - Test planned. Specimens at CIIR awaiting installation in RIG.

* - Detailed metallurgical analysis on 3000-hr specimens completed and reported in Ref. 5-2.

\+ - Detailed metallurgical analysis on 3000-hr specimens in progress.

(a) - Replacement specimen (original two specimens failed at ~3000 hr).

NOTE: Total number of specimens currently in test ~ 268.

controlled impurity helium and in air. These alloys included a new heat of Hastelloy X in addition to the wrought alloys RA333, HD556, and Hastelloy S. Centrifugally cast alloys HK40, Supertherm, Manaurite 36X, Manaurite 36SX, and Manaurite 900 will also be evaluated as possible ducting alloys with potentially increased carburization resistance. The test stresses will be 30.3 MPa (4.4 ksi) at 800°C (1472°F), 13.1 MPa (1.9 ksi) at 900°C (1652°F), and 4.8 MPa (0.7 ksi) at 1000°C (1832°F). It is hoped that times in excess of 3000 hr will be achieved on the new specimens before the end of September 1976.

A report documenting the creep, weight change, tensile, and impact test data as well as the detailed metallurgical specimen analyses of two wrought alloys and six cast alloys has been issued (Ref. 5-2). Some pertinent results and conclusions are summarized in Section 5.3.

5.2.2. Screening Tests at GA

The screening test program being conducted at the GA Advanced Materials Laboratory complements the parallel creep-corrosion screening tests being conducted at CIIR. The GA tests (described in detail in Refs. 5-3 and 5-4) are being conducted as part of an investigation of the effects of simulated GT-HTGR environmental exposure on the strength, deformation, and fracture behavior of candidate materials. Results from these tests supplement the CIIR creep data. These tests include environmental aging in vacuum (to simulate the evaporative behavior of materials in high-velocity helium), in controlled impurity helium, and in air.

During the reporting period, the 800°C (1472°F) unstressed aging tests in controlled impurity helium and in air reached over 6000-hr duration. The 900°C (1652°F) controlled impurity helium unstressed aging tests were initiated. Tensile and instrumented impact testing on the 3000-hr 800°C (1472°F) specimens were completed, along with detailed metallurgical evaluation.

Unstressed vacuum aging tests at 800°C (1472°F) and 900°C (1652°F) have progressed to over 8000 and 7000 hr, respectively, Tensile tests on 3000-hr specimens have been completed, and detailed metallurigcal evaluation of specimens is in progress.

5.3. PERTINENT RESULTS

5.3.1. Controlled Impurity Helium Tests

The results of the controlled impurity creep and unstressed aging tests at 650°C (1202°F), 800°C (1472°F), and 900°C (1652°F), subsequent room temperature tensile and impact tests, and detailed diagnostic metallurgical specimen evaluation on eight key GT-HTGR candidate alloys have been documented in Ref. 5-2. The alloys include the vacuum cast candidate turbine blade and vane alloys IN100, Rene 100, IN713, MM004, M21, and IN738 and the wrought candidate ducting alloys Hastelloy X and Inconel 617. The most significant results are summarized in Table 5-2, which includes mean reaction depths for oxidation and carburization, weight change results, changes in tensile and impact properties, and estimated creep rates compared with literature air data (Refs. 5-5, 5-6, and 5-7).

The controlled impurity helium creep curves obtained to date are shown in Figs. 5-1, 5-2, and 5-3, respectively, for 650°C (1202°F), 800°C (1472°F), and 900°C (1652°F). The percentages of change in room temperature tensile yield strength and ultimate strength and plastic strain to failure for specimens exposed to 3000 hr in controlled impurity helium are plotted as a function of temperature in Figs. 5-4 and 5-5, respectively. An example of the diagnostic metallurgical analyses performed to determine the extent and mode of helium impurity/metal interactions is shown in Fig. 5-6 for cast alloy IN100 aged for 3000 hr at 900°C (1652°F).

The following tentative conclusions pertinent to the potential applicability of the cast alloys IN100, Rene 100, IN713, MM004, M21, and IN738 and

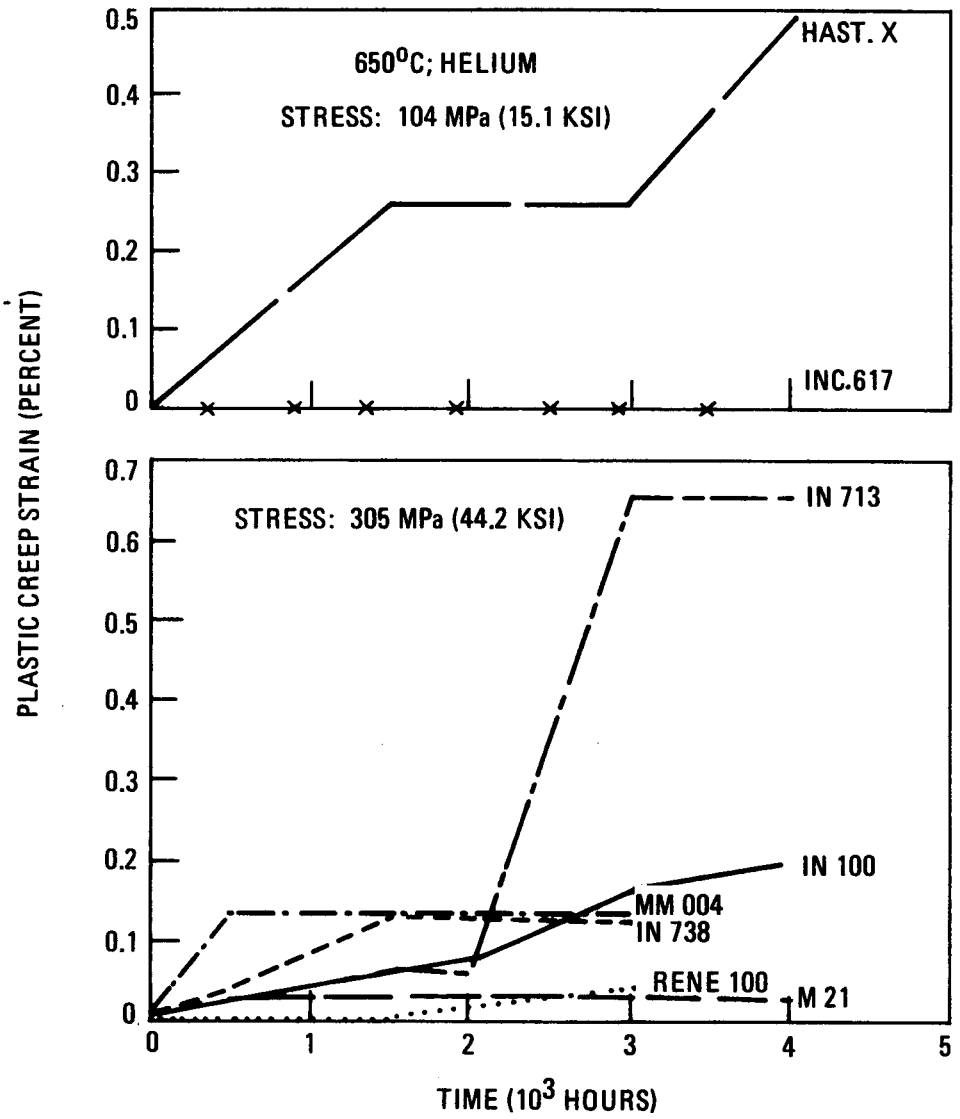

GA-A13950

Fig. 5-1. Creep curves for uninstrumented tests in 650°C (1202°F) controlled impurity helium at CIIR

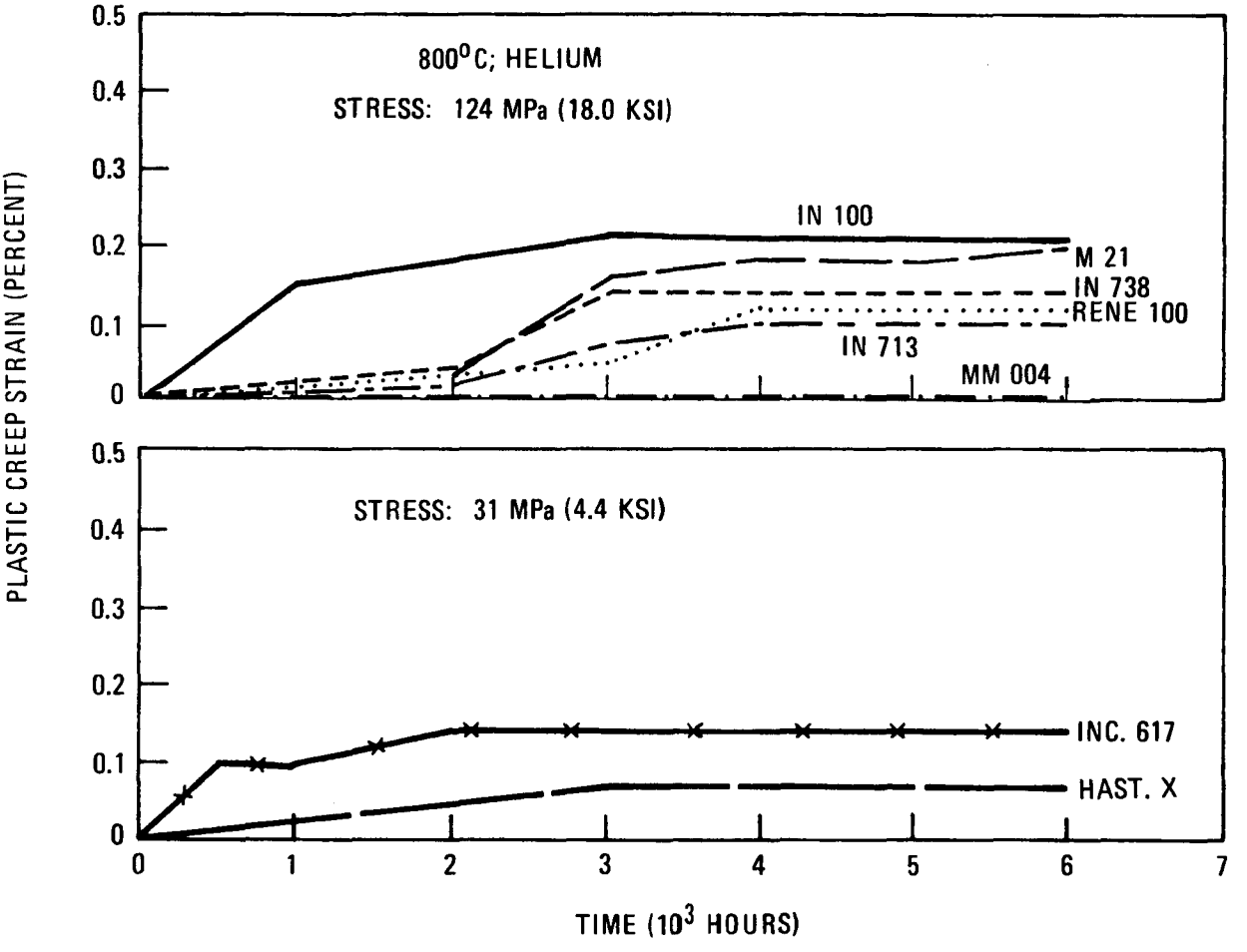

GA-A13950

Fig. 5-2. Creep curves for uninstrumented tests in 800°C (1472°F) controlled impurity helium at CIIR

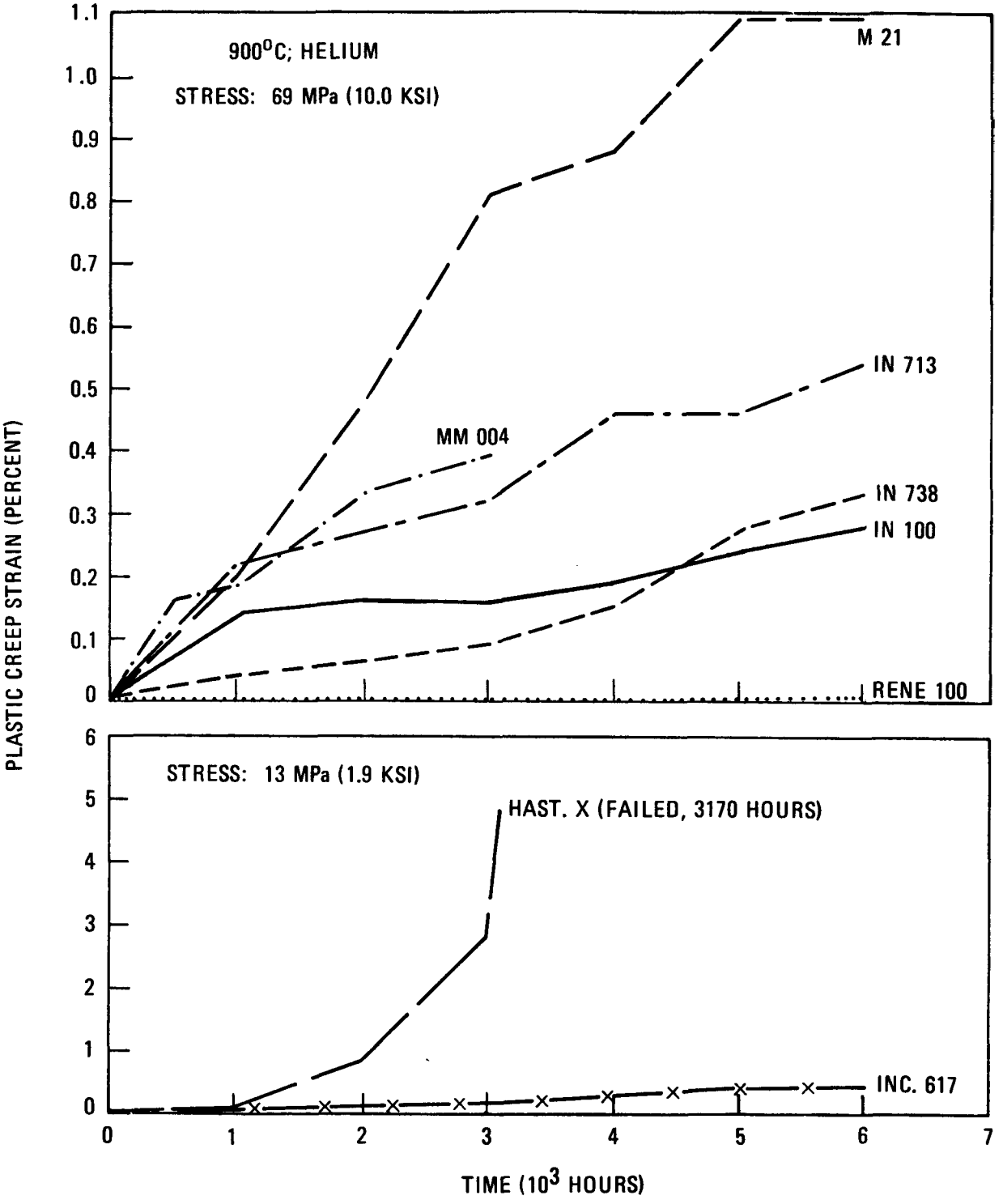

GA-A13950

Fig. 5-3. Creep curves for uninstrumented tests in 900°C (1652°F) controlled impurity helium at CIIR

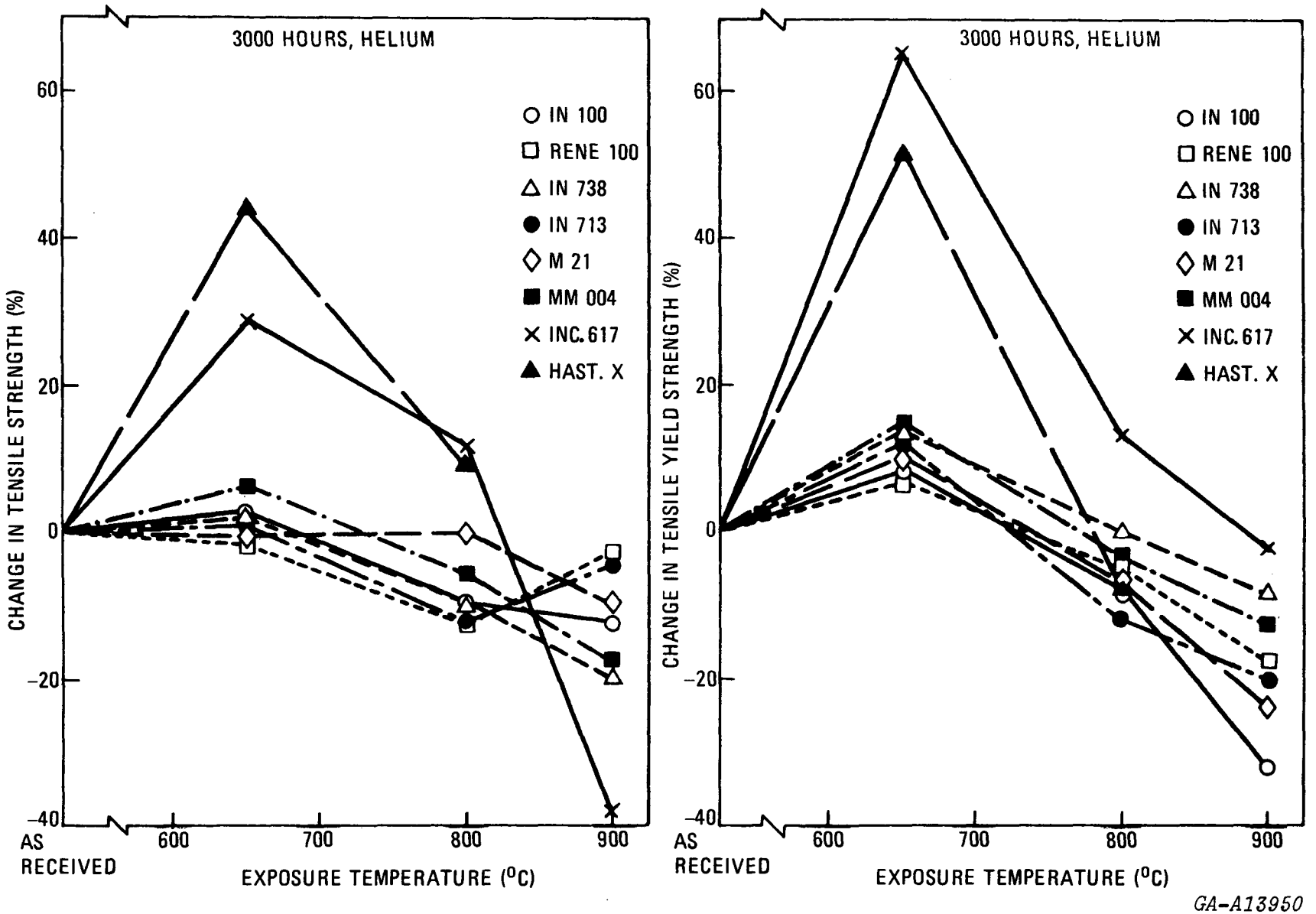

Fig. 5-4. Change in tensile strength and 0.2% tensile yield strength as a function of exposure temperature for specimens

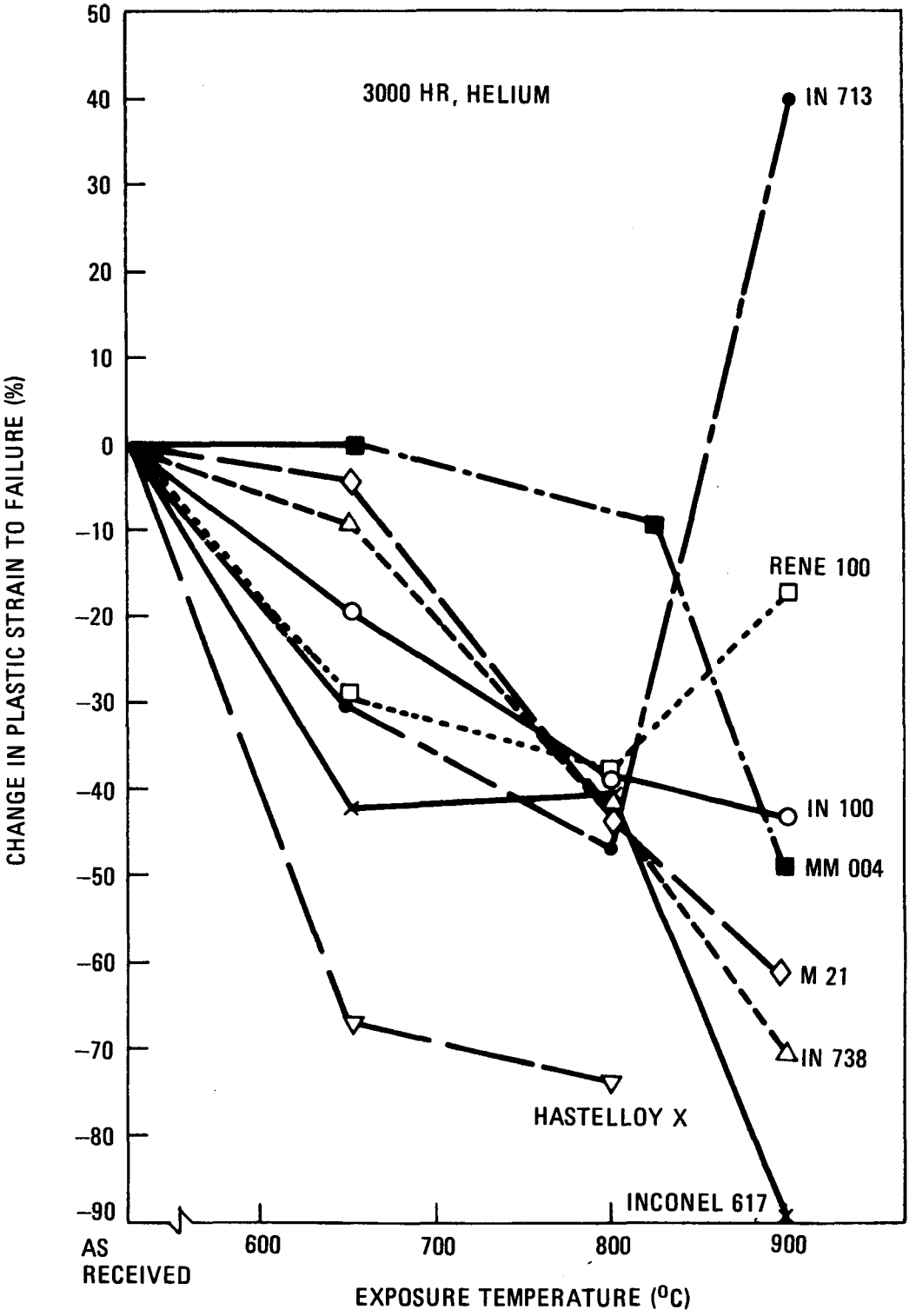

Fig. 5-5. Change in plastic strain to failure as a function of exposure temperature for specimens aged 3000 hr in controlled impurity helium

IN100 (01144) Marble's Etch 250X

(a) Microstructure shows general extent of surface corrosion and alloy depletion.

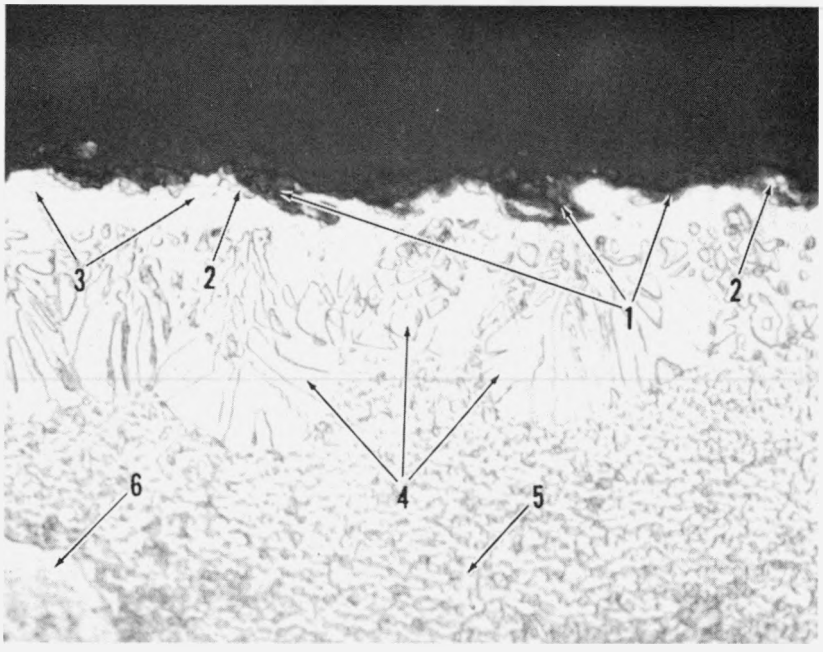

IN100 (01144) Marble's Etch 1000X

(b) Microstructure shows surface corrosion products and subsurface microstructural constituents tentatively identified by SEM microprobe analysis: 1) Al-rich oxide (contains some Ti, Cr, and C), 2) carbides, 3) Ni-rich γ-matrix (alloy-depleted region), 4) agglomerated γ' (within alloy-depleted region), 5) precipitated γ' in γ-matrix, and 6) primary γ' or γ'-engloved carbide.

GA-A13950

Fig. 5-6. Optical photomicrographs showing surface condition and etched subsurface microstructure of alloy IN100 after 3000-hr exposure in controlled impurity helium environment at 900°C (1652°F)

TABLE 5-2
SUMMARY OF CONTROLLED IMPURITY HELIUM SCREENING TEST RESULTS[a]

Alloy	Temp, °C	Mean Reaction Depth,[b] μm			Carbon Wt Change, %	Total Wt Change, mg/cm²	Carbon Wt Change, % of Total Wt Change	Room Temperature Property Change Relative to As-Received Material, %				Estimated Minimum Creep Rate,[c] (%/hr) x 10⁵	
		Oxidation	Denuded Zone	Carburization				Tensile Strength	Yield Strength	Elongation	Impact Strength	Controlled Impurity Helium, 3000 to 6000 hr	Air (Literature)[d]
IN100	650	—	—	—	—	+0.05	—	+2.8	+8.5	-19.2	—	—	—
	800[b]	2	13	50	0	+0.32	0.5	-8.7	-6.4	-38.5	-47.5	—	—
	800	2	13	50	0	+0.32	0.5	-9.8	-8.4	-38.5	—	0.0	0.1
	900	5	24	80	29	+0.43	90.7	-12.1	-32.0	-42.3	—	4.0	0.7
Rene 100	650	—	—	—	0	+0.11*	0.0	-1.4	+6.9	-29.2	—	—	—
	800	1	8	50	-6	+0.23	0.4	-12.4	-4.5	-37.5	—	2.3	0.1
	900	3	22	95	29	+0.52	82.2	-2.4	-17.4	-16.7	—	0.0	0.7
IN738	650	2	10	—	0	+0.21	0.0	+2.7	+14.0	-0.1	—	—	—
	800	6	12	45	0	+0.32	0.0	-9.3	+0.4	-41.8	—	0.0	00
	900	3	18	70	9	+0.66	14.5	-19.7	-8.0	-69.7	—	8.0	—
M21	650	—	—	—	18	+0.16	—	-0.2	+10.1	-4.1	—	—	—
	800[b]	17	23	175	36	+2.77	15.6	+4.5	-6.8	-30.1	-3.6	—	—
	800	17	23	175	36	+2.77	15.6	-4.1	-7.3	-56.2	—	1.7	—
	900	23	46	400	55	+2.92	20.5	-9.8	-23.8	-61.6	—	9.3	—
IN713	650	—	—	—	0	+0.10	—	+1.8	+12.2	-29.6	—	—	—
	800[b]	15	19	125	31	+1.14	32.6	-10.9	-12.2	-29.6	-42.0	—	—
	800	15	19	125	31	+1.14	32.6	-13.7	-10.8	-63.0	—	1.0	1.0
	900	24	31	225	39	+1.78	26.2	-4.2	-20.0	+40.7	—	7.3	2.0
MM004	650	—	—	—	0	+0.04*	0.0	+6.6	+14.2	0.0	—	—	—
	800	16	23	125	79	+1.38*	30.5	-5.2	-2.9	-8.3	—	—	—
	900	31	44	350	150	+2.81	29.0	-17.2	-12.1	-48.3	—	—	—
Inconel 617	650	0.5	9	35	18	+0.13	—	+28.9	+65.0	-42.1	—	—	—
	800[b]	10	19	110	25	+0.33	50.3	+12.0	+12.8	-40.7	>46.0	—	—
	800	10	19	110	25	+0.33	50.3	+11.5	+14.0	-40.3	—	0.0	0.03
	900	20	40	700	110	+2.14	31.3	-38.0	-2.0	-88.6	—	7.7	0.3
Hastelloy X	650	1	8	100	9	+0.04	—	+44.4	+51.8	-66.9	—	—	—
	800[b]	5	16	135	30	+0.96	29.4	+13.8	-4.1	-69.1	-91.3	—	—
	800	5	16	135	30	+0.96	29.4	+4.7	-10.1	-78.6	—	0.0	5.0
	900	6	38	3170 (to center)	63	+1.75	33.3	—	—	—	—	Failed (~3000 hr)	8.0

[a] All results are for 3000 hr exposures unless otherwise indicated. Weight change, reaction depth, and carbon determinations were made on unstressed specimens. Weight change represents average for two specimens unless marked with * (one specimen).

[b] All reaction depths were measured from outer surface. Carburization depth represents region of heavy carbide precipitation.

[c] Creep stresses are given in Figs. 5-2 and 5-3.

[d] Air values for IN100, Rene 100, and IN713 from Ref. 5-1; for Inconel 617 from Ref. 5-2; for Hastelloy X from Ref. 5-3.

the wrought alloys Hastelloy X and Inconel 617 in GT-HTGR components were made on the basis of the analyses of the interim test results of up to 6000 hr duration.

1. Interactions with impurities in the helium occur to varying degrees in all of the cast and wrought alloys during exposure at 650°C (1202°F) to 900°C (1652°F). Oxidation and carburization are both active mechanisms, with the extent of both increasing with increasing temperature. In all cases, carburization occurs to a significantly greater depth than oxidation, and the former is potentially more harmful to structural integrity.

2. The rates of oxidation/carburization in the cast alloys decrease significantly with time at all temperatures with the exception of those for M21 and MM004. The alloys IN100, Rene 100, and IN738 have the best carburization resistance in controlled impurity helium of the eight alloys analyzed and gain significant carbon only at 900°C (1652°F). These alloys also have excellent oxidation resistance in controlled impurity helium at 650°C (1202°F) to 900°C (1652°F). The resistance of IN100, Rene 100, and IN738 to helium impurity effects is apparently due to the combination of relatively high initial carbon content and to the protective nature of their titanium and chromium containing aluminum-rich oxide surface scale. The presence of titanium in the scale appears to be particularly effective in preventing carburization.

3. The estimated minimum creep rates of IN100, Rene 100, and IN713 in controlled impurity helium at 800°C (1472°F) and 900°C (1652°F) are not significantly different from air creep rates calculated from available data in the literature. (No pertinent air creep rate data were located for the cast alloys IN738, M21, and MM004).

4. The wrought alloys Hastelloy X and Inconel 617 carburize significantly at 800°C (1472°F) and to a greater degree at 900°C (1652°F) during exposure in controlled impurity helium. The rates of oxidation/carburization (i.e., weight gain) at 900°C (1652°F)

remain high and nearly constant after 6000 hr of aging. However, the oxidation depths of the wrought alloys after 3000 hr in controlled impurity helium are within the range observed for the six cast alloys. Both wrought alloys form carbide outer surface scales over apparently nonprotective chromium-rich oxide inner scales after aging at 800°C (1472°F) and 900°C (1652°F) in controlled impurity helium.

5. The creep-rupture properties of Hastelloy X in controlled impurity helium at 900°C (1652°F) are significantly degraded by in-depth carburization. The rupture life at 900°C (1652°F) is more than an order of magnitude less than the predicted life in 900°C (1652°F) air. The estimated creep rate of Inconel 617 at 900°C (1652°F) in controlled impurity helium is an order of magnitude greater than the creep rate of the same heat in 900°C (1652°F) air. The 800°C (1472°F) creep rates of Hastelloy X and Inconel 617 in controlled impurity helium are at least as low as corresponding 800°C (1472°F) creep rates in air.

6. Changes in room temperature tensile properties of the cast alloys after aging or creep testing for 3000 hr in controlled impurity helium at 650°C (1202°F) to 900°C (1652°F) can be attributed to microstructural changes caused by well-known thermal aging effects, including coarsening of precipitation hardening intermetallic compound phases (γ') and/or carbide precipitation. The changes in room temperature tensile properties of the wrought alloys after 3000-hr 650°C (1202°F) and 800°C (1472°F) aging or creep testing in controlled impurity helium agree with available air thermal aging data. However, the room temperature tensile properties of Inconel 617 after creep testing at 900°C (1652°F) for 3000 hr in controlled impurity helium are apparently reduced by in-depth carburization and the formation of semicontinuous grain boundary carbides.

7. The limited impact properties of specimens aged at 800°C (1472°F) for 3000 hr in controlled impurity helium generally agree with air thermal aging data in the literature.

The substantiation of these tentative conclusions awaits the completion of the 10,000-hr duration air and controlled impurity helium creep and unstressed aging tests, the availability of parallel air data, and the detailed metallurgical analyses of the test specimens.

5.3.2. Vacuum Aging Tests

Weight change as a function of time after aging in vacuum at 800°C (1472°F) and 900°C (1652°F) is plotted for several alloys in Fig. 5-7. The weight losses in the cast and wrought alloys after 6000 hr at 800°C (1472°F) were quite small, and the weight loss rates in M21, IN100, and Inconel 617 were approaching zero after this time period. Hastelloy X and IN519 were losing weight at a low but nearly linear rate at 800°C (1472°F) and at 900°C (1652°F). All alloys lost significant weight after 6000 hr, but the weight change rates of the lower chromium cast alloys M21 and IN100 decreased to zero after 6000 hr. The wrought alloy Hastelloy X and the centrifugally cast alloy IN519 were still losing weight at rates of 5.6×10^{-4} and 7.0×10^{-4} mg/cm^2/hr, respectively, after 6000 hr. Metallurgical analyses of 3000-hr specimens are in progress, and it appears that most of the weight loss is due to vaporization of chromium from the alloy.

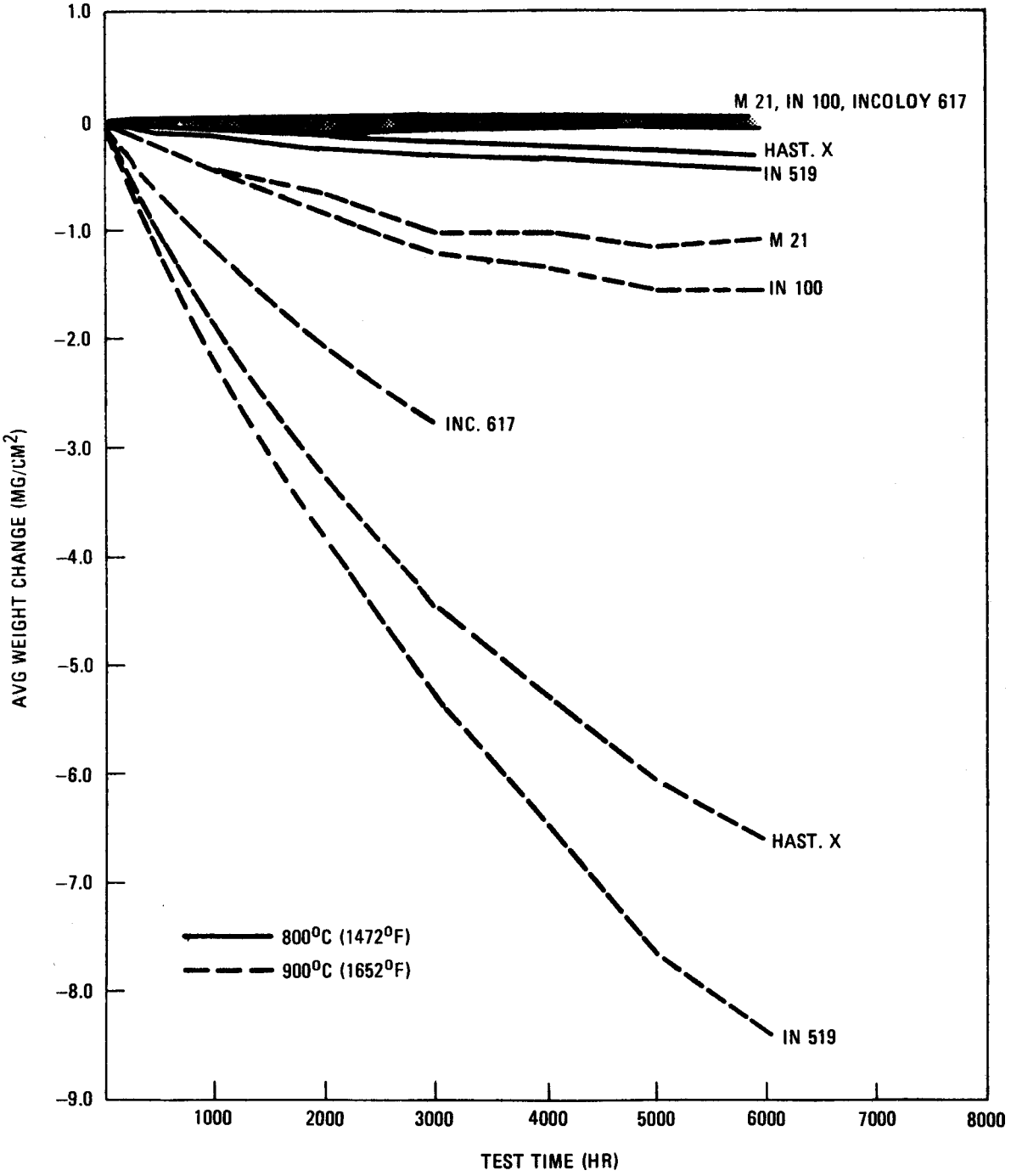

Fig. 5-7. Weight change of several alloys as a function of time after aging in 10^{-8} torr vacuum at 800°C (1472°F) and 900°C (1652°F)

REFERENCES

5-1. "Gas Turbine HTGR Program, Quarterly Progress Report for the Period October 1, 1974 through December 31, 1974," General Atomic Report GA-A13301, January 1975.

5-2. Rosenwasser, S. N., and W. R. Johnson, "Gas Turbine HTGR Materials Screening Test Program Interim Results," General Atomic Report GA-A13931, June 1976.

5-3. "Gas Turbine HTGR Power Plant Control and Safety Studies, Quarterly Progress Report for the Period July 1, 1974 through September 30, 1974," General Atomic Report GA-A13191, November 1974.

5-4. "Gas Turbine HTGR Program, Semiannual Progress Report for the Period January 1, 1975 through June 30, 1975," General Atomic Report GA-A13485, July 1975.

5-5. Aerospace Structural Metals Handbook, Vol. 4, Department of Defense Materials Information Center, Mechanical Properties Data Center, Belfour Stulen, Inc., Traverse City, Michigan, December 1974 (Rev.).

5-6. Tillack, D. J., Huntington Alloys, Inc., Huntington, West Virginia, personal communication, July 1975.

5-7. Tackett, J. N., "The Creep Rupture Properties of Hastelloy X Sheet," Technical Report 8745, Stellite Division, Cabot Corporation, Kokomo, Indiana, January 1975.

6. FISSION PRODUCT EFFECTS STUDIES (Task 189a, No. SU035)

6.1. FISSION PRODUCT SORPTION MEASUREMENTS

6.1.1. Introduction

Calculational methods used for predicting fission product plateout distribution in the primary circuit of a GT-HTGR require as input the adsorption characteristics of the condensible fission products on the alloy components. The actual distribution of plateout activity is quite complex and involves circuit geometry, prevailing fluid dynamics, physical and chemical properties of the fission products, and temperature, surface chemistry, and physical nature of the alloy substrates. The dynamics of plateout depends on whether contact with the surfaces leads to reversible or irreversible deposition. The fission product sorption studies are aimed at providing the necessary experimental input data on the dynamics of fission product deposition in terms of equilibrium adsorption isotherms.

The adsorption studies to date have been focused on the behavior of cesium isotopes, the most important condensible fission product, on the various candidate alloys for the GT-HTGR (Ref. 6-1). The alloys tested include Hastelloy-X, IN100, and M21LC, in the form of as-received (implying degreased and cleaned) 0.05-mm (0.002-in.)-thick foil shape (when available) and cast rods. Two experiments on Hastelloy-X, one pretreated with once-through flowing helium containing expected reactor coolant impurities and the other air-oxidized, were also completed. The adsorption data obtained over a range of expected service temperatures are presented.

During the adsorption experiments, qualitative indications were observed on the diffusion of cesium into the bulk of the alloy material.

This behavior was seen consistently at high-temperature [approximately 800°C (1472°F)] exposures of the specimen to cesium vapor. The bulk diffusion, however, does not appear to contribute additional cesium plate-out on the alloy substrate surface. These results are also discussed.

6.1.2. Experimental

The adsorption isotherms were measured by the pseudoisopiestic method discussed earlier (Ref. 6-1). However, a number of design improvements have been made. The new design incorporates several adsorption furnaces mounted on a rack and a single traveling detector on rails. The detector has a 19 (0.75 in.) x 19 mm (0.75 in.) slit and can be positioned under the specimen at each adsorption furnace at any desired time for the measurement of in-situ cesium (tagged with Cs-137) loadings. A view of the new equipment is shown in Fig. 6-1. The advantage of the movable detector system is that it allows easy calibration checks and avoids overheating of the detector crystal due to extended exposure to furnace heat. It has also increased GA's experimental capability for simultaneous experiments by at least fourfold. This is significant realizing that one adsorption experiment on the average takes from three to five months to complete. Additional details of the equipment design and operation and the specimen degreasing and cleaning procedure for representative surface preparation are given in Ref. 6-2.

The specimens of Hastelloy-X were in the form of a 0.05-mm (0.002-in.)-thick foil to provide large surface area per specimen. This also enabled GA to determine complete adsorption isotherms in one experiment. The alloys IN100 and M21LC were available only as cast rods and were therefore used as such for only single-point determinations. Single-point measurements were also done on Hastelloy-X foil specimens to correlate the data. The sources and nominal compositions of the various alloys were given in the materials program section of Ref. 6-1.

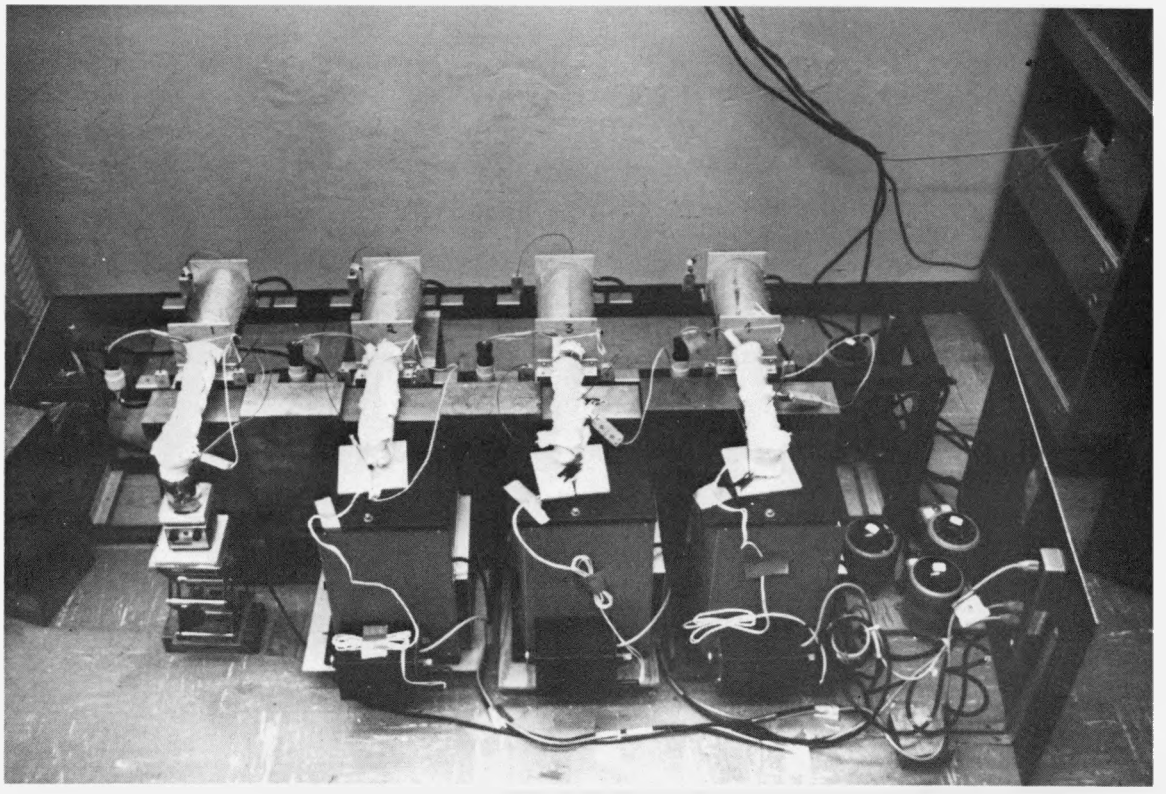

GA-A13950

Fig. 6-1. New design of pseudoisopiestic cesium adsorption assembly

The cesium adsorption data are reported for three different specimen surface conditions: namely, as received, air-oxidized, and gas-turbine helium-pretreated. The helium pretreatment was done at near atmospheric pressure and at 800°C (1472°F) for 750 hr using a gas flow rate of 100 cm^3/min (6.10 $in.^3$/min), once through only. The impurity content of helium was that expected in a GT-HTGR primary circuit, i.e., CO (50 ppm), CH_4 (50 ppm), H_2 (500 ppm), O_2 ($\leq$1 ppm) at 0.1 MPa (1 atm.).

The relative roughness factors, i.e., the ratio of the true surface area to the geometric surface area, for the specimens were measured by a stylus technique (Ref. 6-3) using Surf-analyzer equipment with a fine-point diamond stylus. Scans at various surface locations were averaged to give a representative surface roughness factor. The maximum sensitivity of the NBS-calibrated surface analyzer stylus is 25 nm (1 μin.) of surface deformation. The BET method for determining the roughness factors was found to be inadequate for these specimens because of the inherently small measurable surface area per unit weight.

At the end of an experiment, quantitative determination of in-situ cesium loadings on the specimen were made by twice leaching the adsorbed cesium with hot 50% hydrochloric acid and measuring the Cs-137 activity of the solution using a well counter. Subsequently, the specimen was also counted to determine the cesium activity not removed by the hot acid treatment. The correlation of the activity remaining on the sample after the hot acid treatment and the activity leached was subsequently used for qualitative judgment on the possible bulk diffusion of cesium into the specimen.

6.1.3. Results and Discussion

The cesium adsorption data on as-received Hastelloy-X obtained from various experiments are summarized in Tables 6-1 through 6-4. The cesium loadings are given in terms of both geometric area as well as true area.

TABLE 6-1
CESIUM ADSORPTION ON AS-RECEIVED HASTELLOY-X FOIL MATERIAL OF GEOMETRIC AREA OF 554.84 CM^2 AND ROUGHNESS FACTOR OF 5.4. RESULTS FROM EXPERIMENT NO. 3 AND PRESENTED IN THE ORDER IN WHICH THEY WERE TAKEN. SPECIMEN OUTGASSED AT 500°C (932°F) FOR 5 HR.

Specimen Temperature °C (°F)	Cesium Vapor Pressure		Cesium Loading[a]	
	Pascal	Atm	Geometric Area $\mu g/cm^2$	True Area $\mu g/cm^2$
500 (932)	1.5×10^{-1}	1.5×10^{-6}	1.2300	0.2280
612 (1134)	1.5×10^{-1}	1.5×10^{-6}	1.0900	0.2020
400 (752)	4.8×10^{-4}	4.8×10^{-9}	0.8970	0.1660
515 (959)	4.8×10^{-4}	4.8×10^{-9}	0.8700	0.1610
618 (1144)	4.5×10^{-4}	4.5×10^{-9}	0.8250	0.1530
725 (1337)	4.6×10^{-4}	4.6×10^{-9}	0.3500	0.0650
825 (1517)	6.1×10^{-4}	6.1×10^{-9}	0.1100	0.0204

[a] Corrected data from Ref. 6-4. See text for details.

TABLE 6-2
CESIUM ADSORPTION ON AS-RECEIVED HASTELLOY-X FOIL MATERIAL OF GEOMETRIC AREA OF 277.42 CM^2 AND ROUGHNESS FACTOR OF 5.4. SPECIMEN OUTGASSED AT 725°C (1337°F) FOR 7 HR. RESULTS FROM EXPERIMENT NO. 6.

Specimen Temperature °C (°F)	Cesium Vapor Pressure		Cesium Loading[a]	
	Pascal	Atm	Geometric Area $\mu g/cm^2$	True Area $\mu g/cm^2$
400 (752)	4.0×10^{-4}	4.0×10^{-9}	0.1610	0.0298
500 (932)	2.0×10^{-1}	2.0×10^{-6}	0.5240	0.0970
500 (932)	1.5×10^{-2}	1.5×10^{-7}	0.2157	0.0399
500 (932)	7.8×10^{-4}	7.8×10^{-9}	0.1950	0.0361
500 (932)	4.8×10^{-4}	4.8×10^{-9}	0.1428	0.0264
500 (932)	2.0×10^{-5}	2.0×10^{-10}	0.1800	0.0333
600 (1112)	4.1×10^{-4}	4.1×10^{-9}	0.1256	0.0233
700 (1292)	2.2×10^{-1}	2.2×10^{-6}	0.4535	0.0840
700 (1292)	2.3×10^{-2}	2.3×10^{-7}	0.1333	0.0247
700 (1292)	5.4×10^{-4}	5.4×10^{-9}	0.1106	0.0205
825 (1517)	2.4×10^{-1}	2.4×10^{-6}	0.1970	0.0365
825 (1517)	2.5×10^{-2}	2.5×10^{-7}	0.1127	0.0209
825 (1517)	3.5×10^{-3}	3.5×10^{-8}	0.0994	0.0184
825 (1517)	8.3×10^{-4}	8.3×10^{-9}	0.0922	0.0171
825 (1517)	5.7×10^{-4}	5.7×10^{-9}	0.0951	0.0176
825 (1517)	2.4×10^{-5}	2.4×10^{-10}	0.0758	0.0140

[a] Corrected data from Ref. 6-4. See text for details.

TABLE 6-3
CESIUM ADSORPTION ON AS-RECEIVED HASTELLOY-X FOIL MATERIAL OF GEOMETRIC AREA OF 129.03 CM^2 AND ROUGHNESS FACTOR OF 5.4. SPECIMEN OUTGASSED AT 325°C (617°F) FOR 24 HR. RESULTS FROM EXPERIMENT NO. 12.

Specimen Temperature °C (°F)	Cesium Vapor Pressure		Cesium Loading[a]	
	Pascal	Atm	Geometric Area $\mu g/cm^2$	True Area $\mu g/cm^2$
600 (1112)	3.3×10^{-3}	3.3×10^{-8}	0.1910	0.0354
600 (1112)	2.0×10^{-5}	2.0×10^{-10}	0.1190	0.0220
600 (1112)	1.7×10^{-6}	1.7×10^{-11}	0.0996	0.0184
600 (1112)	3.4×10^{-7}	3.4×10^{-12}	0.0970	0.0180
700 (1292)	3.0×10^{-7}	3.0×10^{-12}	0.0455	0.0084
300 (572)	1.4×10^{-6}	1.4×10^{-11}	0.1760	0.0326
400 (752)	1.5×10^{-6}	1.5×10^{-11}	0.1510	0.0280
500 (932)	1.6×10^{-6}	1.6×10^{-11}	0.1250	0.0231
600 (1112)	1.7×10^{-6}	1.7×10^{-11}	0.0997	0.0185
700 (1292)	1.8×10^{-6}	1.8×10^{-11}	0.0627	0.0116
800 (1472)	1.9×10^{-6}	1.9×10^{-11}	0.0165	0.0031

[a] Corrected data from Ref. 6-4. See text for details.

TABLE 6-4
CESIUM ADSORPTION DATA FOR AS-RECEIVED IN100 AND M21LC ALLOYS (CAST RODS) AND HASTELLOY-X (FOIL) SPECIMENS FROM VARIOUS SINGLE-POINT EXPERIMENTS. SPECIMENS OUTGASSED AT 325°C (617°F).

Experiment No.	Alloy	Roughness Factors	Specimen Temperature, °C (°F)	Cesium Vapor Pressure		Cesium Loading	
				Pascal	Atm	Geometric Area, $\mu g/cm^2$	True Area, $\mu g/cm^2$
17	IN100	52.8	800 (1472)	3.4×10^{-4}	3.4×10^{-9}	0.703	0.0133
	M21LC	52.8	800 (1472)	3.4×10^{-4}	3.4×10^{-9}	0.563	0.0107
20	IN100	52.8	800 (1472)	3.4×10^{-4}	3.4×10^{-9}	0.514	0.0097
	M21LC	52.8	800 (1472)	3.4×10^{-4}	3.4×10^{-9}	0.598	0.0113
22	Hastelloy-X	5.4	800 (1472)	1.6×10^{-3}	1.6×10^{-8}	0.075	0.0136

The results in general indicate that cesium adsorption on Hastelloy-X involves the Freundlich mechanism. This is evidenced by the adsorption isotherms plotted in Fig. 6-2 in terms of a linear relationship between log C (cesium loading) and log P (cesium vapor pressure). Data from several experimental samples are used in the development of the isotherms, and possible sample-to-sample variations have not been fully quantified. The isotherm at 825°C (1517°F) also includes two data points at 800°C (1472°F). Similarly, the isotherms at 500°C (932°F), 600°C (1112°F), and 700°C (1292°F) include the data at neighboring temperatures from Table 6-1.

As is evidenced in Fig. 6-2, the cesium adsorption data show some degree of nonreproducibility from different experiments. The adsorption isotherms derived are, therefore, preliminary and subject to improvement when more data become available. The current spread in the data could be a result of nonreproducibility of a clean specimen surface, even though precautions were taken to adhere to a standard degreasing and cleaning procedure. Some hysteresis effects due to vacuum baking at high temperature during an adsorption run were also evidenced; i.e., the specimen after being exposed to high temperatures [$\geq$800°C ($\geq$1472°F)] showed relatively lesser cesium loadings. This effect was found to be more pronounced during cesium adsorption on Incoloy 800 and on empty Inconel 625 adsorption tube in parallel studies (Ref. 6-2).

Another reason for the scatter in the data could be associated with the method used for estimating in-situ activity due to cesium adsorbed on the specimen relative to that on the specimen tube. The small tube portion that contains the specimen could provide significant surface area for cesium adsorption if the surface roughness factor were to be large. The roughness factor of the tube material has not been measured, but on the basis of experience it is estimated to be approximately 40 and would thus provide comparable true area. In the earlier work, therefore, a number of simultaneous empty tube experiments were conducted so that the tube contribution could be directly subtracted from the tube plus specimen data. This approach was used in reporting the data from experiments No. 3 and No. 7 in Ref. 6-4.

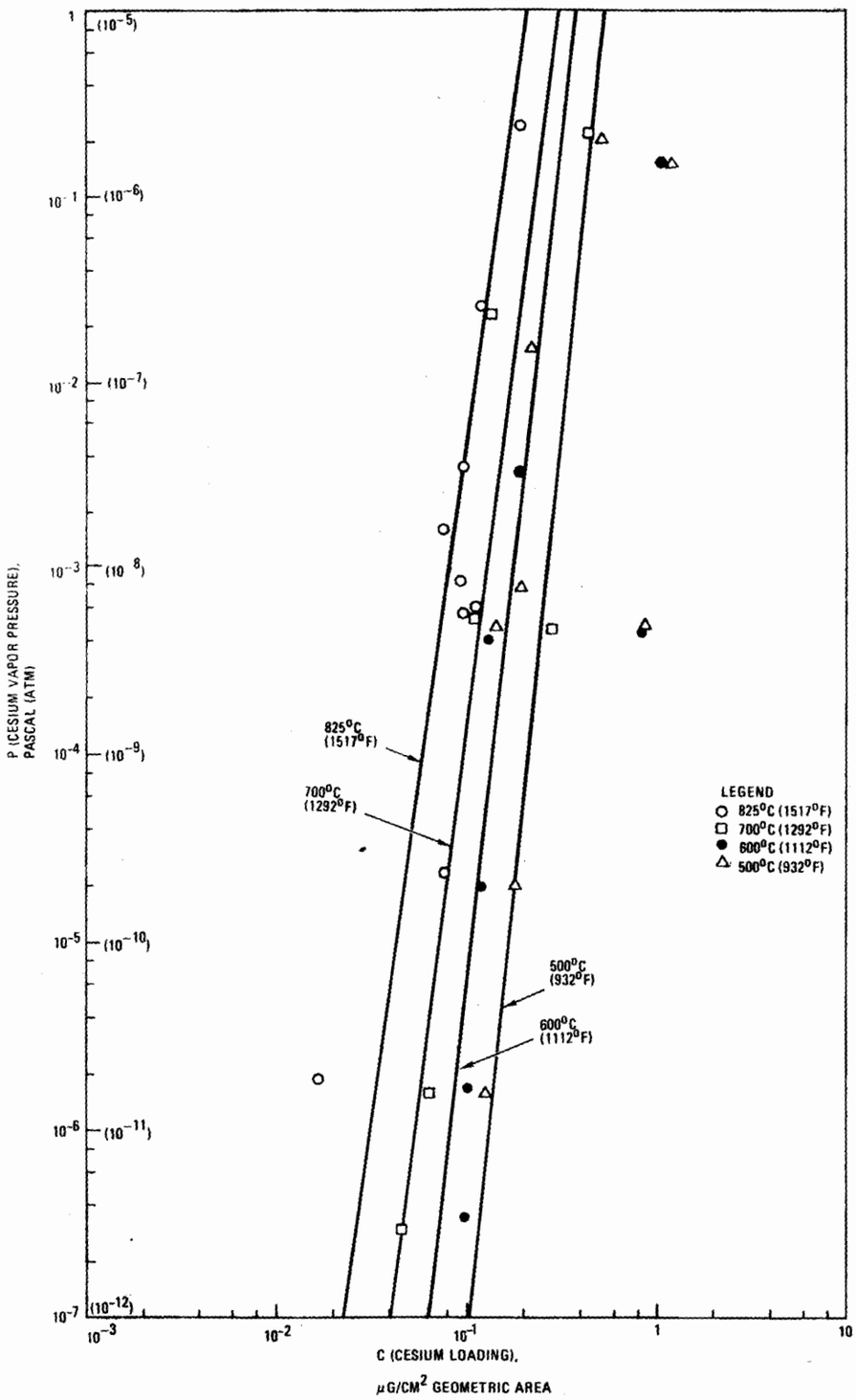

GA-A13950

Fig. 6-2. Cesium adsorption isotherms for as-received Hastelloy-X foil with roughness factor of 5.4

However, this approach proved to be very cumbersome and inaccurate, the major reasons being the irreproducibility of important parameters such as the detection geometry (and hence in-situ counting efficiency), the cesium metal specific activity, and the tube surface conditions due to welding effects at the capped end. Subsequently, the method for calculating in-situ specimen loading was changed to the one used in this report. In the present method, the natural background count rate is subtracted first from all equilibrium count rates to obtain tube and specimen contribution. At the end of the experiment, the in-situ count rate is measured both with and without the specimen in the tube. From the end-of-experiment data after subtracting laboratory background, a fraction indicating the ratio between the count rate due to the specimen and the count rate due to the specimen plus tube is calculated. This fraction is then used for estimating the in-situ specimen count rate from the specimen-plus-tube data. This method, though more appropriate, is also inadequate. It inherently assumes that the specimen and the tube material have the same adsorption characteristics under all conditions of the experiment. To make the tube effect less significant would require unusually large surface area specimens. In the present series of experiments, tube contributions of from 15% to 40% of the total in-situ activity were observed depending on the specimen size.

The wide spread in the cesium adsorption data indicates the difficulty of typical adsorption experiments. The reproducibility can perhaps be improved by conducting single-point tests instead of a full adsorption isotherm. However, this requires several independent experiments to develop an isotherm. A few single-point experiments were also attempted, and the data are reported in Table 6-4. The single-point test for Hastelloy-X at 800°C (1472°F) shows relatively lesser cesium loading than that at 825°C (1417°F) observed under similar conditions in earlier experiments. Because of the lack of more single-point tests, the 800°C (1472°F) data points were conservatively included in the development of an adsorption isotherm at 825°C (1517°F) in Fig. 6-2. On the basis of these isotherms, the isosteric Clausius-Clapeyron heat of adsorption at a cesium loading of 0.15 $\mu g/cm^2$ geometric area on as-received Hastelloy-X is observed to be 52 kcal/mole. It should be noted that this is not the true heat of adsorption.

Single-point cesium adsorption data were also obtained for cast rod materials of IN100 and M21LC, the candidate alloys for the turbine (see Table 6-4). The data at 800°C (1472°F) and 3.4×10^{-4} P (3.4×10^{-9} atm) cesium vapor pressure suggest no significant differences in the adsorption characteristics of these alloys and Hastelloy X foil when cesium loadings per unit true surface area are compared (see Table 6-4). However, it should be noted that because of the higher roughness factor of cast specimens, higher cesium loadings were observed per unit geometric area of the specimen. More experiments are needed to confirm this effect and the similarity of the three alloys.

The results of cesium adsorption on air-oxidized and GT-HTGR helium-pretreated Hastelloy-X are presented in Table 6-5. Both pretreated specimens show definite evidence of higher cesium loadings. The increase, however, amounts to only about a factor of 5 over the as-received samples. The surface analysis of the simultaneously pretreated coupons is not yet available.

The ease of cesium removal from various specimens at the end of each experiment for quantitative analysis could be used as qualitative evidence for cesium migration into the bulk of the specimen alloys. It was consistently observed that the longer the time a specimen was exposed to cesium vapor at temperatures $\geq$800°C ($\geq$1472°F), the larger was the cesium fraction that could not be easily leached with hot 50% hydrochloric acid. Typical examples are given in Table 6-6. The specimen exposed at lower than 800°C (1472°F) or for shorter durations at 800°C (1472°F) showed lesser evidence of strongly adherent adsorbed cesium. However, it should be noted that the bulk diffusion phenomena in these experiments did not create additional surface for further cesium adsorption. This conclusion is based on the relative adsorptions observed.

In summary, the results from the present series of cesium adsorption experiments reveal that more work is needed to fully characterize the adsorption phenomenon. It is perhaps significant that the behavior of

TABLE 6-5
CESIUM ADSORPTION ON PRETREATED HASTELLOY-X FOIL MATERIAL
WITH SURFACE ROUGHNESS OF 5.4 PRIOR TO PRETREATMENT

Experiment No.	Pretreatment	Specimen Temperature, °C (°F)	Cesium Vapor Pressure		Cesium Loading	
			Pascal	Atm	Geometric Area, $\mu g/cm^2$	True Area, $\mu g/cm^2$
13	Air-oxidized at 825°C (1517°F) for 20 hr	300 (572)	1.7×10^{-5}	1.7×10^{-10}	0.232	0.0430
		400 (752)	1.9×10^{-5}	1.9×10^{-10}	0.219	0.0406
		500 (932)	2.0×10^{-5}	2.0×10^{-10}	0.211	0.0391
		700 (1292)	2.3×10^{-5}	2.3×10^{-10}	0.177	0.0328
		800 (1472)	2.4×10^{-5}	2.4×10^{-10}	0.124	0.0230
		800 (1472)	4.2×10^{-8}	4.2×10^{-8}	0.266	0.0493
21	GT-HTGR helium-pretreated at 800°C (1472°F) for 750 hr	800 (1472)	4.9×10^{-4}	4.9×10^{-9}	0.416	0.0770

TABLE 6-6
EFFECT OF SPECIMEN EXPOSURE TO CESIUM VAPOR AT 800°C (1472°F) ON EASE OF CESIUM REMOVAL BY TWO HALF-HOUR LEACHING OPERATIONS WITH 50% HOT (NEAR BOILING) HYDROCHLORIC ACID

Experiment No.	Alloy Specimen	Length of Exposure, hr	% of Total Activity Not Removed
20	As-received IN100 and M21LC	312	∿23.4
17	As-received IN100 and M21LC	388	27 to 33
22	As-received Hastelloy X	677	22.4
21	Helium pretreated Hastelloy X	936	38.7

pretreated specimens (especially with simulated reactor coolant environment) should be studied in greater detail because of their direct applicability to the GT-HTGR primary system. The adsorption also shows evidence of strong dependence on available true surface area. More importantly, the isotherms show only a modest pressure dependence over a large range of cesium vapor pressure [10^{-7} to 10^{-1} P (10^{-12} to 10^{-6} atm)], while the maximum variation in cesium loadings between 500°C (932°F) and 825°C (1517°F) at any vapor pressure appears to be within an order of magnitude. Regarding the bulk diffusion of cesium into the metal, the evidence is only preliminary, and much more work would be required to confirm this phenomenon. The details of the bulk diffusion of cesium at high service temperatures [>800°C (>1472°F)] need to be investigated by combination of ion sputtering methods with chemical analysis techniques such as ESCA and Auger spectroscopy.

6.2. DECONTAMINATION STUDIES FOR GT-HTGR COMPONENTS

6.2.1. Summary

Most of the components in a GT-HTGR facility, i.e. those made of conventional metals (mild steel or austenitic stainless steels) and those which have been exposed to only moderate temperatures [≥400°C (≥752°F)], should present no great problems for decontamination, since conventional approaches should be suitable. The greatest challenge will arise from the turbomachinery, where sophisticated metal alloys may be required and fission product plateout will occur at high temperatures [>800°C (>1472°F)] at large helium flows. Decontamination is expected to be required because of the potentially large radioactivity levels and the probable requirement for contact rather than remote maintenance approaches.

Decontamination studies will initially need to be exploratory in nature because of the lack of prior experience, since materials of construction are not yet selected and since plateout deposits have not been fully characterized. Of great significance is whether or not extensive diffusion of the fission products will occur into the base metals; normal decontamination approaches are not expected to remove such activity unless the material is etched off. Another difficulty facing the experimental decontamination studies is obtaining representative samples which are prototypical of the equipment (problems) which would be encountered in actual reactor operation.

On the basis of literature findings, two recommendations are offered relative to further activities in this area: (1) concentrate on developing the Turco Products 4501 (three-step) process for applicability to GT-HTGR requirements, taking advantage of the vendor's expertise and (2) cooperate with the HHT program, which currently includes decontamination studies.

6.2.2. General Criteria

Many power conversion loop components which need to be repaired will be too valuable for mere discard and replacement, especially the turbomachinery. There will be an urgency for rapid turnaround of the damaged equipment, and the disposal of large items (including decontamination, packaging, transportation, and burial) will be costly. Prior studies indicated that $15 of equipment could be decontaminated for $1 spent on recovery (Ref. 6-5) and that major pieces of chemical processing equipment could be decontaminated and repaired (Ref. 6-6) (including the cost of storage of waste liquids) for 60% of the 1974 replacement cost.

Sophisticated equipment in the GT-HTGR will demand highly reliable decontamination approaches. The treatments must be strong enough to remove radiactive deposits to permit the required maintenance, but gentle enough to prevent damage to the base metal.

6.2.3. Background Experience Related to LWR and HTGR Equipment

Early in the development of power reactors, it was recognized that radioactive contamination would tend to build up on the surfaces of components within the primary coolant circuit (Ref. 6-7). The AEC sponsored decontamination studies by several organizations including Turco Products. This research resulted in technology which permitted the development of reagents which were effective in removing PWR contamination films without danger of corrosion damage to the system. The early literature is dominated with these efforts, including several excellent surveys (Refs. 6-8 through 6-11).

The AEC provided significant impetus to decontamination technology with the formation of the Reactor Decontamination Information Exchange Group. Formed in June 1960, it initially consisted of representatives from the AEC and four government laboratories. These meetings, held about once or twice a year, continued until about 1967. The group was expanded at its third meeting to include representatives from five additional

organizations, including GA. The efforts reported at these meetings were published in the form of minutes, e.g., Refs. 6-12 through 6-14. Results of these meetings subsequently culminated in the preparation of a book (Ref. 6-15) commissioned by the AEC which is an all-inclusive guide and history of the technology of decontamination.

The AEC-commissioned book (Ref. 6-15) has sections devoted to PWR (mostly), BWR, and HTGR decontamination experience. Several LWR decontamination processes are described, most of them being two-step procedures involving an alkaline permanganate treatment to oxidize and loosen the scale for subsequent action by an inhibited acid. Because of differences in the nature of the contamination films (i.e., "crud" scales formed from water systems at relatively low temperatures on probably different base metals, with much of the activity being activation products), it is felt that this experience will probably not be too applicable to GT-HTGR requirements.

In early studies directed at HTGR component decontamination, GA's general approach has been the use of representative samples to test commercial reagents, using established procedures or variants of such procedures rather than the formulation of new reagents. Several GA documents (Refs. 6-16 through 6-20) describe such efforts. Various metal parts or coupons were contaminated either in GAIL (General Atomic In-Pile Loop) at GETR or in a GA-constructed laboratory apparatus (with tagged isotopes) and decontaminated in a special laboratory loop installed at GA. Mild steel, austenitic and ferritic stainless steels, copper, and Cr/Mo alloys were contaminated with various radioactive or tagged isotopes (i.e., Cs-134, Cs-137, Ta-182, I-131, Ba-133, and Ba-140) by particulates, vapor deposition, etc., at temperatures of up to $\sim$1050°C ($\sim$1922°F). Different decontamination agents were evaluated in various screening tests. On the whole, the best results were usually obtained with one of the Turco Products two-step procedures, though the same two-step process was not consistently

superior and often variations in the subsequent decontamination were evident because of differences in the exposure conditions or metal surfaces. The following general conclusions were indicated in these studies:

1. Carbon-steel HTGR components can be decontaminated satisfactorily and to higher DFs than similarly treated stainless steels.

2. There is usually an inverse relationship of attainable decontamination with contamination temperature.

3. Heavier deposits are usually easier to remove than light deposits.

4. Particulate matter activities are more easily removed than those deposited from the vapor phase.

5. Contamination is more easily removed when deposited on clean, smooth surfaces.

6. Activities, e.g., cesium, which have reacted with and diffused into the oxide film present on stainless steels can be removed effectively only if the surface oxides are removed.

7. Ultrasonic decontamination techniques offer no advantage, considering the additional costs involved.

Encouraging decontamination results were obtained from a single-step, descaling reagent, RD-16, a neutral proprietary solution recommended by the Electric Boat Division of General Dynamics Corporation (Ref. 6-19).

After considerable experimental work at ORNL, oxaplate-peroxide solutions were developed (Refs. 6-21 and 6-22) and recommended as UO_2 solvents and general decontaminants for mild steel and aluminum surfaces. The most effective mixture was an aqueous solution of 0.4 mole oxalic acid, 0.16 mole ammonium citrate, and 0.34 mole H_2O_2, adjusted to pH 4.00 with NH_4OH

and used at 85°C (185°F). The solution was developed primarily to prepare equipment, e.g., the fuel handling machine for direct maintenance operations. No suitable noncorrosive method could be found for the decontamination of laboratory-contaminated stainless steel coupons baked at >500°C (>932°F), in helium.

In a Harwell symposium, Turco Products described (Ref. 6-23) its procedures in developing and testing new radioactive decontamination processes. It was stressed that the metal coupons used must be exposed to the anticipated environment for extended periods of time. Experience has shown that though film thicknesses in PWR systems reach an equilibrium value in about three weeks, the tenacity of the film to the substrate increases with time, and decontamination becomes most difficult after about two year's exposure.

6.2.4. Aircraft Nuclear Propulsion Program Decontamination Experience

Highly applicable experience related to GT-HTGR components is not available, since equipment materials and expected plateout levels have not yet been determined. However, preliminary conservative estimates have been made at GA (Ref. 6-24); this report also included approximate temperatures and pressure which would exist at various portions of the primary circuit.

The only direct decontamination information on turbomachinery which could be found was that related to GE's ANP program. In one document (Ref. 6-25), components of GE's turbomachinery were classified into a group of materials which included the 300 Series stainless steels, heat-treatable stainless steels, and many high-content chromium, nickel, and cobalt base steels. It was stated that this group of materials had been effectively decontaminated at the Idaho Test Station by use of the Turco 4501 Process.

A second, similar document (Ref. 6-26) describes the nature of the contamination including the formation of tenacious surface scales due to the temperatures encountered, diffusion of the plateout into the surface scale, and partial migration into the base metals. Removal of the contaminants is

guaranteed only by removal of the scale. The effectiveness of the Turco 4501A Decontamination Process was verified by the complete decontamination of three complete X-39 jet engines, which were returned to operation. No damage to the base metals or materials such as excessive corrosion, intergranular attack, pitting, or loss of tolerances was encountered in the process. A list of steps was outlined for decontamination the turbine assembly and a lesser number of steps for the compressor. The list of steps for the turbine assembly included degrease, alkaline clean, Turco 4501A (alkaline chelating agents for conditioning), Turco 4502 (alkaline permanganate oxide bath), Turco 4518 (inhibited oxalic acid bath), Versene and possibly vapor blast, with a rinse after each step. Each procedure is described, and the number of steps depends on the complexity of the part, the obduracy of the contamination, the skill of the operator, etc.

6.2.5. HHT Reactor Experience

Several Swiss groups have been working on decontamination approaches for components for an HHT (helium-cooled, high-temperature) reactor with gas turbine, and they have already obtained some promising results (Ref. 6-27). Six fission products (Cs-134, Cs-137, Ag-110m, I-131, Sr-89, and Sr-90) and five activation products (Cr-51, Mn-54, Co-60, Zn-65, and Ta-182) are deened to be significant from a contamination standpoint.

To date, many hundreds of samples have been prepared, including 12 material types (stainless steels, molybdenum alloys, and nickel alloys). These have been fabricated into 13 shapes for various tests, contaminated differently in a reactor or out-of-pile, decontaminated, and examined for mechanical changes, corrosion effects, etc. Chemical effects caused by contaminants (e.g., H_2O, CO_2, H_2, CO, CH_4, and N_2) in the helium are even factored into the studies. The Swiss groups have demonstrated that sample contamination (at least for cesium) by different treatments is comparable, whether carried out in-pile (Dragon or AVR) or out-of-pile, with respect to the tenacity of the nuclide and its ease of decontamination.

Just as contamination occurs in the corrosion scale of water-cooled reactor equipment and requires removal of the oxide layers to effect satisfactory decontamination, similar contamination can occur in gas-cooled reactors due to impurities in the helium, and effective decontamination demands removal of these layers (oxides, carbides, etc.).

Other significant preliminary conclusions include:

1. Oxide layers of several microns have been found on stainless steel specimens after 1000-hr exposure to contaminated helium, but molybdenum alloys (TZM) were practically unchanged. The oxide layers contain mostly chromium and titanium; therefore, a suitable solution is required to dissolve the chromium oxide to effect good decontamination.

2. The extent of contamination for five nuclides varied considerably on reactor exposed samples, depending on the material composition and its preliminary surface treatment.

3. When stainless steel specimens were used, ∿90% of the cesium is removed by water washing if they have not been oxidized, compared with only 15% to 35% removal if the samples were oxidized before the cesium contamination.

4. Molybdenum alloys are susceptible to corrosion, but stainless steels and nickel alloys provide good resistance. Also, by obtaining stress/strain diagrams of notched (stressed) samples while they are immersed in the decontamination solution, one can determine whether the materials are subject to stress corrosion cracking.

5. To evaluate diffusion effects, iron, nickel, and molybdenum alloys were treated with cesium and contaminated helium; at 900°C (1652°F), cesium containing oxygen made the iron samples brittle, but they remained ductile if the cesium contained no oxygen.

6. The use of cobalt alloys in the gas turbine or hot duct materials is strongly disfavored. Such alloys could become so highly activated as to prevent direct accessibility, even with decontamination. The Swiss groups specify a maximum cobalt content of 200 ppm in their test specimens and 500 ppm and 2000 ppm maximum for Ta and H_f, respectively.

The following were considered to be pertinent from other data from the HHT reactor program (Ref. 6-28):

1. The highest radiation field is expected on the surface of the rotor from a turbomachine removed from the circuit. It is believed that a DF of 10^3 will be required for Cs-134 and Cs-137 to avoid exceeding the maximum allowable does of 3 rem/person over a three-month period.

2. Brown Boveri suggests a maximum metal loss of 5 μm (0.0002 in.) per decontamination operation. Thsi was inferred to be a nominal specification relative to turbine blade tolerances.

3. Decontamination tests were carried out on stainless steel samples (Type 4541) exposed to helium flow for 37 days in the AVR-VAMPYR reactor at surface temperatures of up to 500°C (932°F). Very high DFs of $>10^3$ were obtained by an unspecified process, with negligible loss of base metal. It was concluded that diffusion into the base metal would not be a problem for these reactor conditions. However, additional plateout tests will have to be carried out for longer time periods at higher temperatures to evaluate this problem.

6.3. UPDATED PLATEOUT DISTRIBUTION

The updated fission product plateout distribution neither confirms nor refutes the results of the previous study (Ref. 6-24). It does indicate the present incomplete understanding of the physical phenomena which

control the sorption process as well as the need for additional data. The effect of surface conditions is a possible area where further investigation could prove fruitful. The present uncertainty is evidenced by a five-order-of-magnitude variation in surface activities, depending on the data used.

The plateout distribution of Cs-137 and Cs-134 can have a significant impact on the maintenance approach taken for the GT-HTGR components. If it can be adequately demonstrated that the amount of plateout on the turbomachines is small, then contact maintenance could be considered reasonable. On the other hand, if the amount of plateout is large, then the problems of remote handling must be appropriately considered early in the plant design.

In Ref. 6-24, the PAD (Plateout and Distribution) code was used to obtain a preliminary assessment of the plateout distribution in the GT-HTGR system. Because sorption isotherms for the high-temperature alloys in the GT-HTGR were not available, the existing sorption isotherm for oxidized Type 304 stainless steel was used to predict the plateout distribution on the turbine inlet duct and turbine. The validity of using this isotherm was questionable. Therefore, studies were initiated to determine the sorption isotherms for several of the GT-HTGR candidate alloys. The results of these studies are presented in Section 6.1 and were incorporated into the PAD code to reanalyze the cesium plateout distribution.

The amount of plateout on the turbine inlet duct and turbine is a small fraction of the total plateout in the system. Consequently, changing the turbine inlet duct and turbine sorption isotherms does not significantly alter the plateout distribution in the rest of the system. The results of both the updated and the Ref. 6-24 cesium plateout distribution calculations for the turbine inlet duct and turbine are shown in Fig. 6-3.

Reference 6-24 calculations, as stated earlier, were based on oxidized Type 304 stainless steel. These results are shown in Fig. 6-3 as curve A. To show the effect of reduced surfaces on the distribution, the surface activity in Ref. 6-24 was reduced by an assumed factor of 100. This reduced

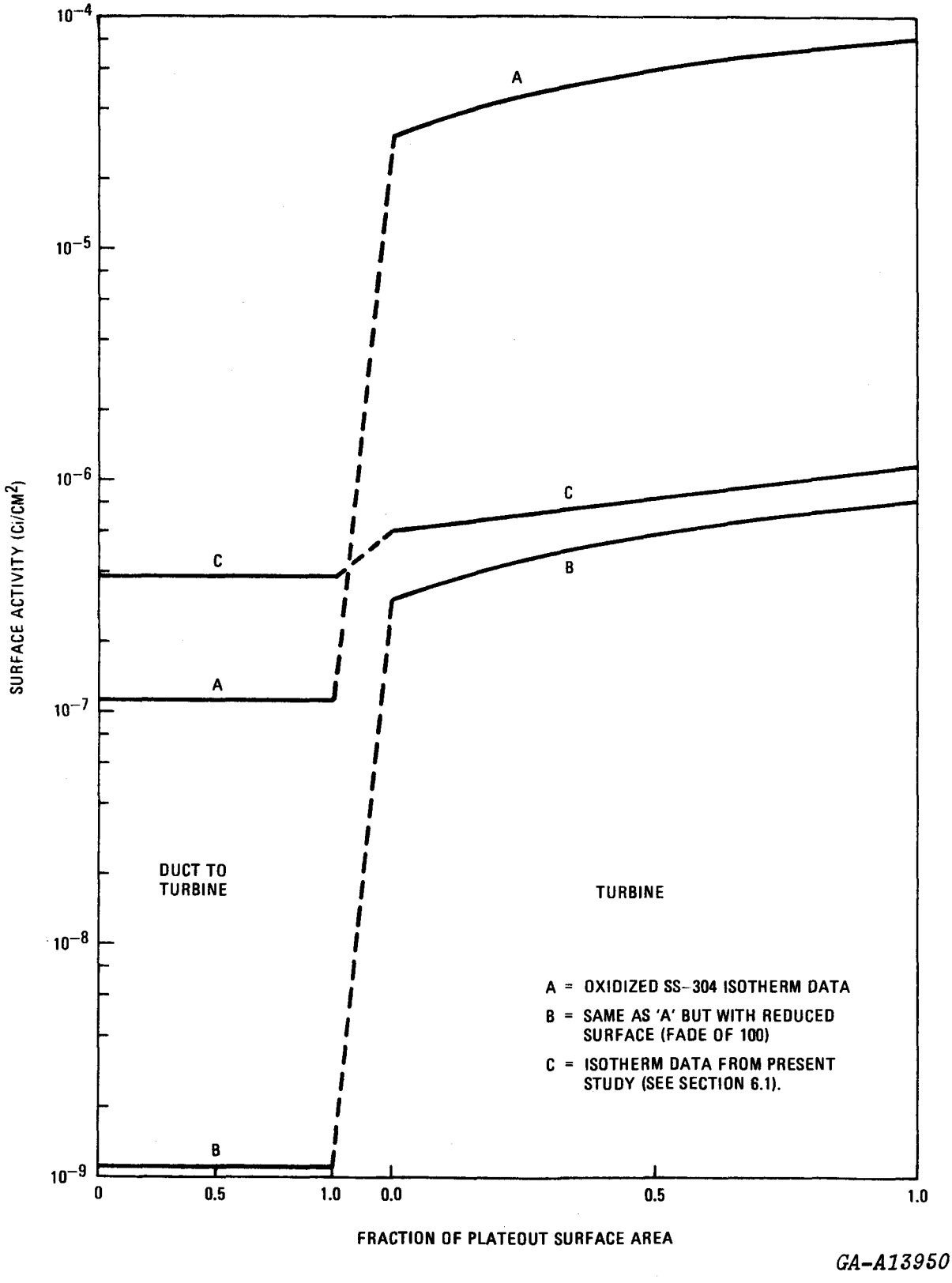

Fig. 6-3. Updated duct-to-turbine/turbine plateout distribution

distribution is shown in Fig. 6-3 as curve B. The isotherm used for the present updated calculation given as curve C was based on investigations of nearly reduced surfaces. Therefore, it is not necessarily inconsistent to find the updated calculation for the turbine plateout levels falling between the previously generated oxidized and reduced calculations. However, for the turbine inlet duct there is clearly a large difference in the plateout predicted by the two sets of isotherm data. This difference could be the result of one or more of the observations discussed below.

The sorption isotherms used in Ref. 6-24 were based on data generated below 732°C (1350°F) which are sensitive to small temperature changes at the temperatures used in this study. The new data were generated at temperatures more representative of the temperatures experienced in the GT-HTGR and show a much reduced sensitivity to temperature changes. It can be postulated that it is not valid to extrapolate the sorption isotherm used in Ref. 6-24 to the temperatures required for this study.

Another facet of the sorption isotherm data is the surface roughness. The surface roughness may cause the actual surface area of a sample to be many times larger than the geometric surface area. For the updated calculation, data from plateout on foils were used. These foils had 5.4 times more effective surface area than geometric surface area. The sorption isotherm used in Ref. 6-24 was also based on foil data. However, the surface roughness of these foils was not measured. The amount of plateout is proportional to this effective surface area rather than to the geometric surface area. On an actual cast turbine blade. this effective surface area could be more than 50 times larger than the geometric surface area. This effect is also shown in Fig. 6-3. Consequently, surface roughness is a factor that can significantly alter the interpretation of plateout experiments.

The effect of surface oxidation must also be considered. Reference 6-24 noted an early work which observed drastic changes in the amount of plateout due to surface oxidation. These changes were not investigated

to the extent that they could be fully understood. Nonetheless, it was noted that hundredfold changes in sorptivity could be observed. Reference 6-24 assumed a constant factor of 100 for the reduction in sorptivity when going from an oxidized surface to a reduced surface. In the early works, it appears that the temperature dependence of the isotherm is changing as well as its absolute value. Furthermore, the change in temperature dependence appears to be moving in a direction of less sensitivity to temperature changes as the surface becomes more reduced. It can also be speculated that as the surface becomes oxidized the sorption becomes a function of the changing activation energy of the oxidized surface.

Another point is the difference in the materials used for generating the new sorption data compared with the Type 304 stainless steel used in Ref. 6-24. The present data were developed from Hastelloy-X, Incoloy 800, IN100, and M21LC samples. Although these samples all exhibited similar sorptivity, the sorptivity of Type 304 stainless steel may be significantly different. Directly comparable tests are being made using Type 304 stainless steel as a check.

Finally, the new data shows some qualitative evidence of diffusion of cesium into the base metal at 800°C (1472°F) and not at 600°C (1112°F). This diffusion may allow more cesium to plateout on the surface of the 800°C (1472°F) sample than would be expected from extrapolating 600°C (1112°F). Therefore, a sorption isotherm model using the 800°C (1472°F) data may not adequately represent the overall phenomenon.

From the above discussion, it becomes evident that a large investment in experimental work will be needed before accurate plateout distributions can be determined. The present uncertainty in results is large and effects the viewpoint as to whether the plateout/maintenance problem is insignificant or major. The above observations and differences should therefore be verified by additional work.

REFERENCES

6-1. "Gas Turbine HTGR Program, Quarterly Progress Report for the Period October 1, 1974 through December 31, 1974," General Atomic Report GA-A13301, January 1975.

6-2. "HTGR Fuels and Core Development Program, Quarterly Progress Report for the Period Ending June 30, 1976," General Atomic Report GA-A13941, June 1976.

6-3. Kane, P. F., and G. B. Larrabee, Characterization of Solid Surfaces, Plenum Press, New York, 1974, Chapter 3.

6-4. "Gas Turbine HTGR Program, Semiannual Progress Report for the Period July 1, 1975 through December 31, 1975," General Atomic Report GA-A13740, January 1976.

6-5. White, J. M., "Decontamination Principles and Techniques," Atomic Energy of Canada Limited Report AECL-1427, August 1961.

6-6. Hershey, J. H., "Separations Canyon Decontamination Facilities," in Proceedings of the First Conference on Decontamination and Decommissioning (D&D) of ERDA Facilities, Idaho Falls, Idaho, August 19 to 21, 1975, CONF-750827, p. 207.

6-7. Watkins, R. M., "Recent Trends in the Development of Nuclear Reactor Decontamination Procedures," General Dynamics, General Atomic Division Report GA-3457, September 1962.

6-8. Meservey, A. B., "Procedures and Practices for the Decontamination of Plant and Equipment," Oak Ridge National Laboratory Report ORNL-CF-60-12-71, January 1961.

6-9. Davis, F. W., "Reactor Decontamination: a Literature Review with Recommendations for Decontamination of the N. S. Savannah Reactor," BAW-1217, December 1960.

6-10. Bost, W. E., "Radioactive Decontamination, a Literature Search," TID-3535, September 1959.

6-11. Raleigh, H. D., "Radioactive Decontamination, a Literature Search," TID-3535, Supplement 1, April 1965.

6-12. Meservey, A. B., "Minutes of the Third Meeting of the Reactor Decontamination Information Exchange Group at ORNL, June 1 to 2, 1961," Oak Ridge National Laboratory Report ORNL-CF-61-7812, July 1961.

6-13. Carlson, A. B., "Minutes of the Fourth Meeting of the Reactor Decontamination Information Meeting Exchange Group, November 30 to December 1, 1961," Savannah River Report DPST62-162, February 1962.

6-14. Sammarone, D. G., "Minutes of the Seventh Meeting of the Reactor Decontamination Information Exchange Group at WAPD, February 26 to 28, 1964," Westinghouse Report WCAP-2673, September 1964.

6-15. Decontamination of Nuclear Reactors and Equipment, J. A. Ayres (ed.), Ronald Press, New York, 1970.

6-16. Busch, D. D., and R. M. Watkins, General Dynamics, General Atomic Division, "Decontamination Studies at General Atomic," unpublished data, December 1961.

6-17. Watkins, R. M., and D. D. Busch, "Decontamination of High-Temperature Gas-Cooled Reactor Components," General Dynamics, General Atomic Division Report GA-2912, February 1962.

6-18. Busch, D. D., et al., "Decontamination Studies at General Atomic, April to August, 1962," General Dynamics, General Atomic Division Report GA-3433, August 1962.

6-19. Busch, D. D., "Decontamination Studies at General Atomic, April 1963 to February 1964," General Dynamics, General Atomic Division Report GA-5740, February 1964.

6-20. Busch, D. D., "Decontamination Studies at General Atomic, January 1965 to August 1965," General Dynamics, General Atomic Division Report GA-6700, April 1966.

6-21. Meservey, A. B., "Peroxide-Inhibited Decontamination Solutions for Carbon Steel and Other Metals in the Gas-Cooled Reactor Program: Progress Report, November 1959 to July 1962," Oak Ridge National Laboratory Report ORNL-3308, January 1963.

6-22. Meservey, A. B., "Corrosion Inhibition by Hydrogen Peroxide in Decontamination Solutions," Oak Ridge National Laboratory Report ORNL-TM-120, January 1962.

6-23. Newman, K. P., "Development and Testing Techniques for Radioactive Decontamination Compounds," in Proceedings of the First International Symposium on the Decontamination of Nuclear Installations, H. J. Blythe (ed.), Cambridge University Press, London, 1967, p. 25.

6-24. Chmielewski, R. D., and C. G. Hoot, "Fission Product Plateout Calculations for a Gas Turbine HTGR," General Atomic Report GA-A13213, Nobember 1974.

6-25. Plastino, G. G., "Equipment, Material, and Facilities Requirement for Decontamination of D141A-1 Power Plant," DC59-12-734, December 1959.

6-26. Plastino, G. G., "Procedure, Material, Equipment, and Facilities Requirement for Decontamination of D140E-1 Power Plant," DC60-10-726, October 1960.

6-27. Schenker, E., et al., "Development of a Method for Decontaminating the Primary Circuit of a Helium-Cooled, High-Temperature Reactor," in French, in Proceedings of a Symposium on Gas-Cooled Reactors with Emphasis on Advanced Systems, Vol. I, International Atomic Energy Agency, Vienna, 1976, p. 221.

6-28. Krase, J. M., General Atomic, "HHT Project Paper on Fission Product Release, Plateout, Decontamination," unpublished data, July 1975.

7. TURBOMACHINERY TECHNOLOGY (Task 189a, No. SU036)

7.1. INTRODUCTION AND SUMMARY

As in the last reporting period, most of the design studies on the turbomachinery were carried out during the present reporting period by the Power Systems Division and the Pratt and Whitney Aircraft Division (P&WA) of United Technologies Corporation (UTC). The preliminary design of bearings and seals, the planning of bearing and seal tests, and the preliminary design of bearing and seal test rigs were continued from the previous reporting period into the first two months of the present reporting period. In March 1976, in response to a need to investigate direct-cycle HTGR power plants with higher performance incentives, the subcontract effort was redirected to provide an analysis of design approaches for helium turbines having inlet gas temperatures in the 900°C (1652°F) to 1000°C (1832°F) range and a parametric study of compressor and turbine designs appropriate to this range of temperatures and to compressor pressure ratios between 2.3 and 2.9.

The bearing and seal preliminary design tasks were virtually complete at the time of redirection of the program, as was the preliminary design of the journal bearing and seal test rigs. The bearing and seal test plan was completed, but the design of the thrust bearing test rig was carried through only to the conceptual level.

Supporting turbomachine design arrangement studies were continued, culminating in the conceptual layout for a high-temperature version of the turbomachine.

The principal results of these studies carried out by the subcontractor are summarized in this section of this report. A more detailed description

of the work will be given in a report to be prepared by the subcontractor in September 1976. As required in the overall statement of work for the Turbomachinery Technology, short-range turbomachinery R&D tasks are also identified in this section.

Supporting tasks carried out at General Atomic under funding from the Turbomachinery Technology task were:

1. Review of main shaft and shutdown seal designs
2. Turbomachinery support structure studies

These tasks are reported in other sections of this report.

7.2. BEARING AND SEAL PRELIMINARY DESIGNS

7.2.1. Journal Bearing Preliminary Design

Additional detail was developed for the 508 mm (20 in.) five-pad preliminary design turbomachine main bearings. Using input data from the bearing support design work, it was found that a slight change in the bearing pivot design was required to increase overall bearing stiffness and satisfy rotor critical speed criteria. Bearing damping response to subsynchronous excitation was estimated for use in the rotor stability analysis. Bearing off-design performance has been predicted, and considerable additional mechanical detail has been added to the bearing layout. Foolproofing provisions, removable oil supply nozzles, and sideplate and seal details have been added. All service connections have been defined. Some additional detail has also been developed on an alternate four-pad design because this design, while less conservative, does offer lower bearing power losses.

7.2.2. Thrust Bearing Preliminary Design

The preliminary design of the thrust bearing was completed. The thrust bearing configuration as illustrated in Ref. 7-1 is actually a pair of identical thrust bearings separated by a journal bearing. The integral journal

bearing serves to support the shaft and position it relative to the thrust bearing pads. The dual thrust bearings are required to handle the change of load direction which occurs during seismic events.

Performance of the bearing has been described with two lubrication systems: (1) flooded lubrication and (2) jet lubrication. Flooded lubrication is more widely used but requires very high oil flows and has almost twice the power loss of a jet lubrication system. Oil film thickness, power consumption, bearing spring rate, and damping coefficient have been defined over a range of loads and speeds including 20% overspeed. The jet lubrication system has been selected as the preferred system, and a full-size mechanical layout has been prepared showing all major elements of the design. Figure 7-1 shows a reduced-size version of this layout. The bearing is 762 mm (30 in.) in outside diameter, and the collars and support have been designed to provide adequate strength for seismic survival. Maximum runner misalignment has been estimated and is within the alignment capability of the pads. The jet spray system has been patterned, but additional work will be required during development to minimize oil flow and assure acceptable pad temperatures.

Thrust collar stress concentrations and deflections were analyzed using a finite element technique and were found to be within acceptable limits.

7.2.3. Preliminary Design of Bearing Seals and Buffer System

The preliminary design of the Ljungstrom-type labyrinth seals for the turbomachinery journal bearing compartments has been completed. Knife-edge seal clearances have been estimated considering shaft movement within the bearing, elastic deflections of the bearing supports, shaft unbalance, seal deflections, and assembly tolerances. The results of this study are shown in Figs. 7-2 and 7-3 for the worst case, which is the maximum overspeed of 4320 rpm. Figure 7-2 shows the scheme of dynamic deflections of the seal elements and various methods of compensating for the deflections. Figure 7-3 shows numerical values of the deflections at various points on the seal

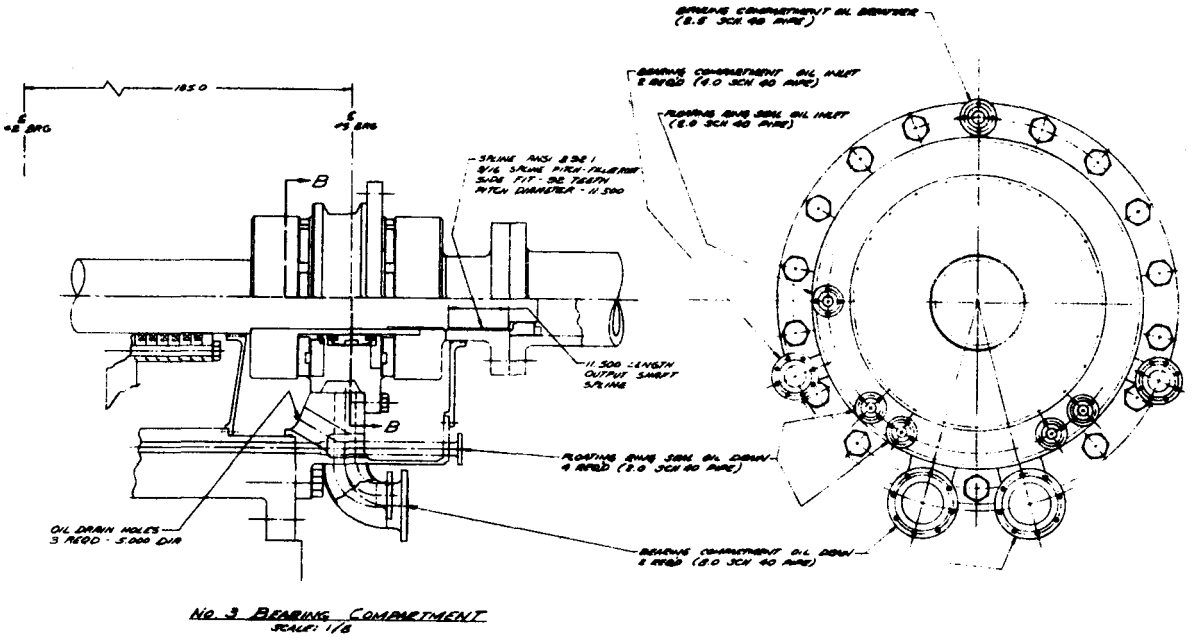

ALL MEASUREMENTS ARE IN U. S. CUSTOMARY UNITS.

GA-A13950

Fig. 7-1. Preliminary design layout of thrust bearing (sheet 1 of 4)

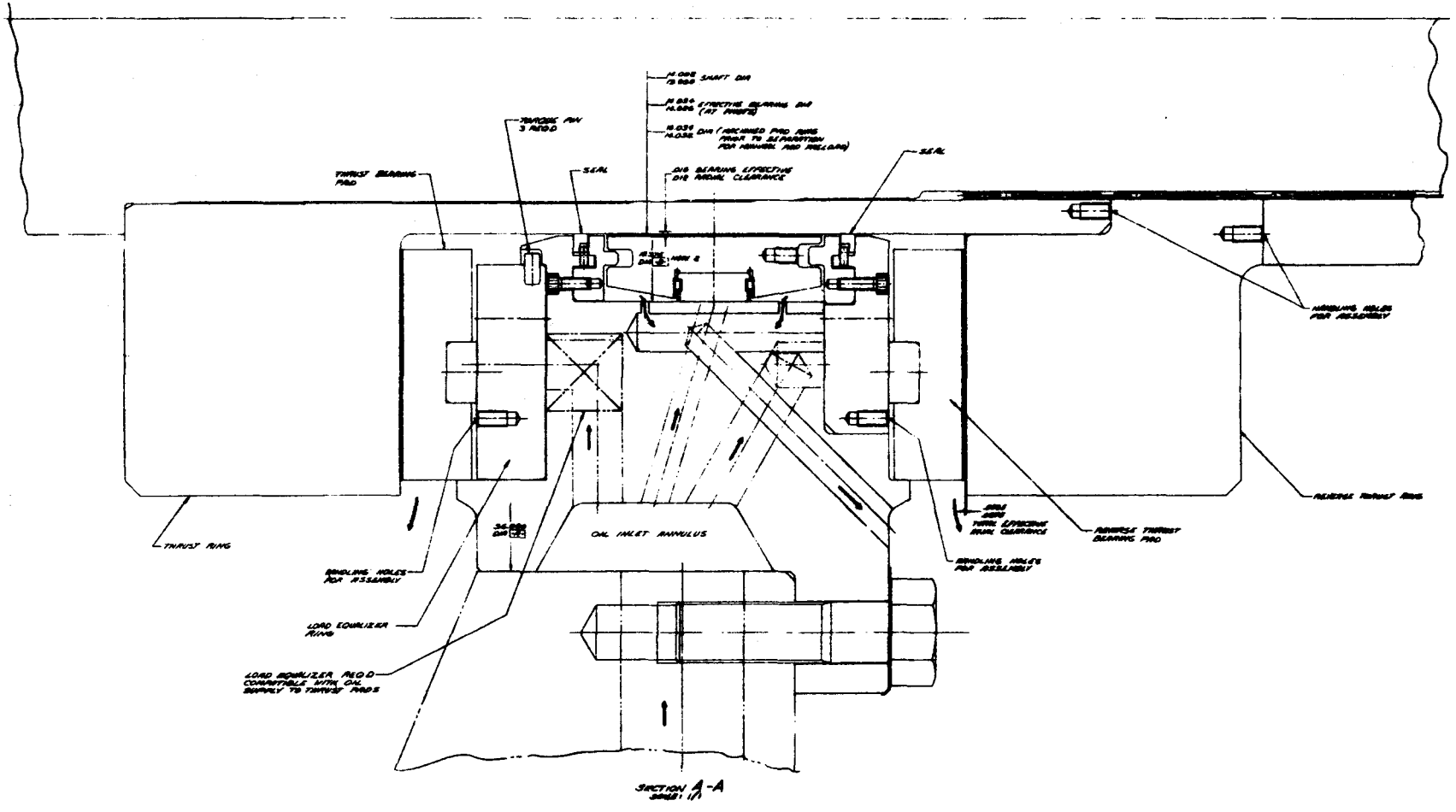

GA-A13950

Fig. 7-1. Preliminary design layout of thrust bearing (sheet 2 of 4)

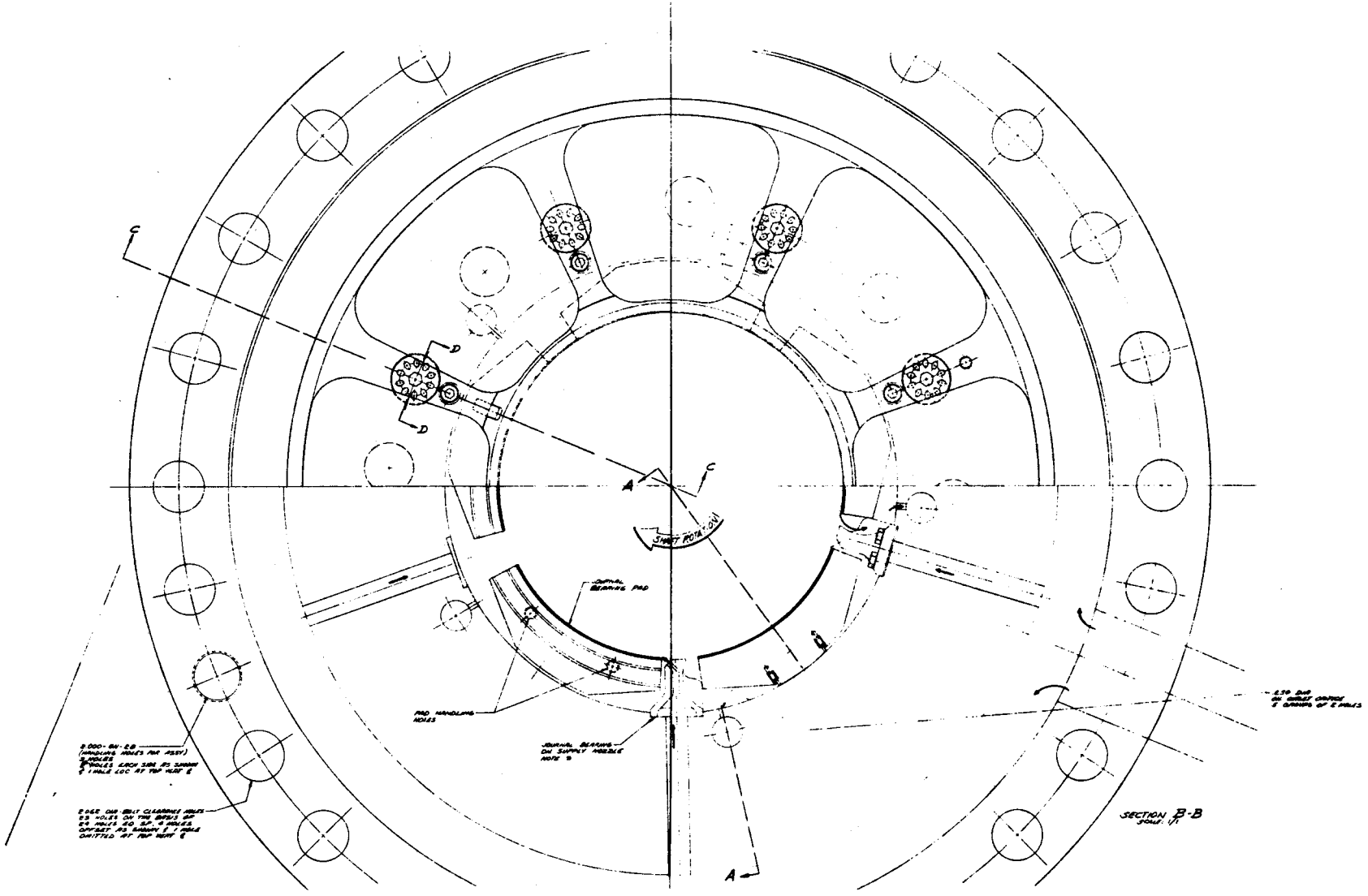

Fig. 7-1. Preliminary design layout of thrust bearing (sheet 3 of 4)

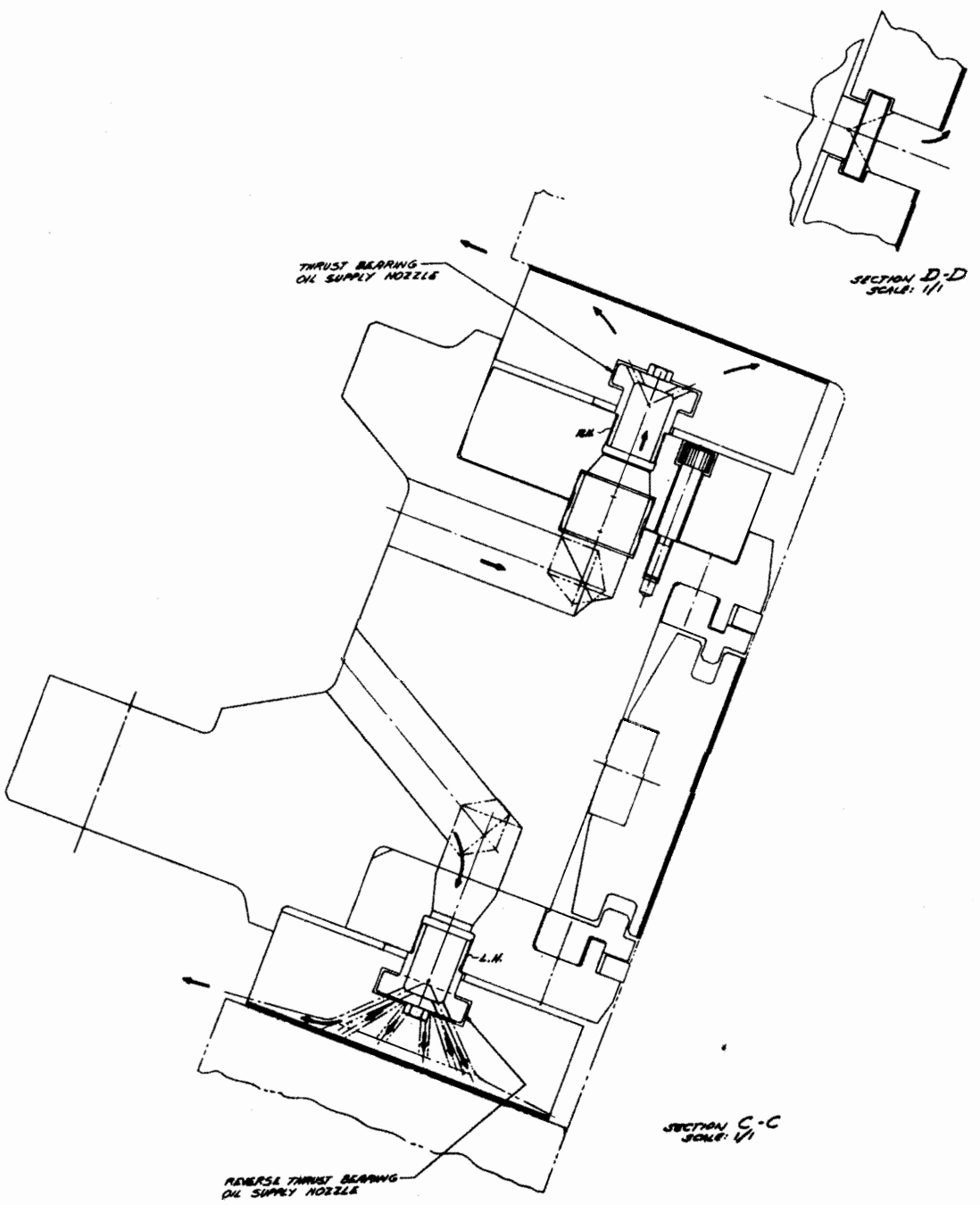

GA-A13950

Fig. 7-1. Preliminary design layout of thrust bearing (sheet 4 of 4)

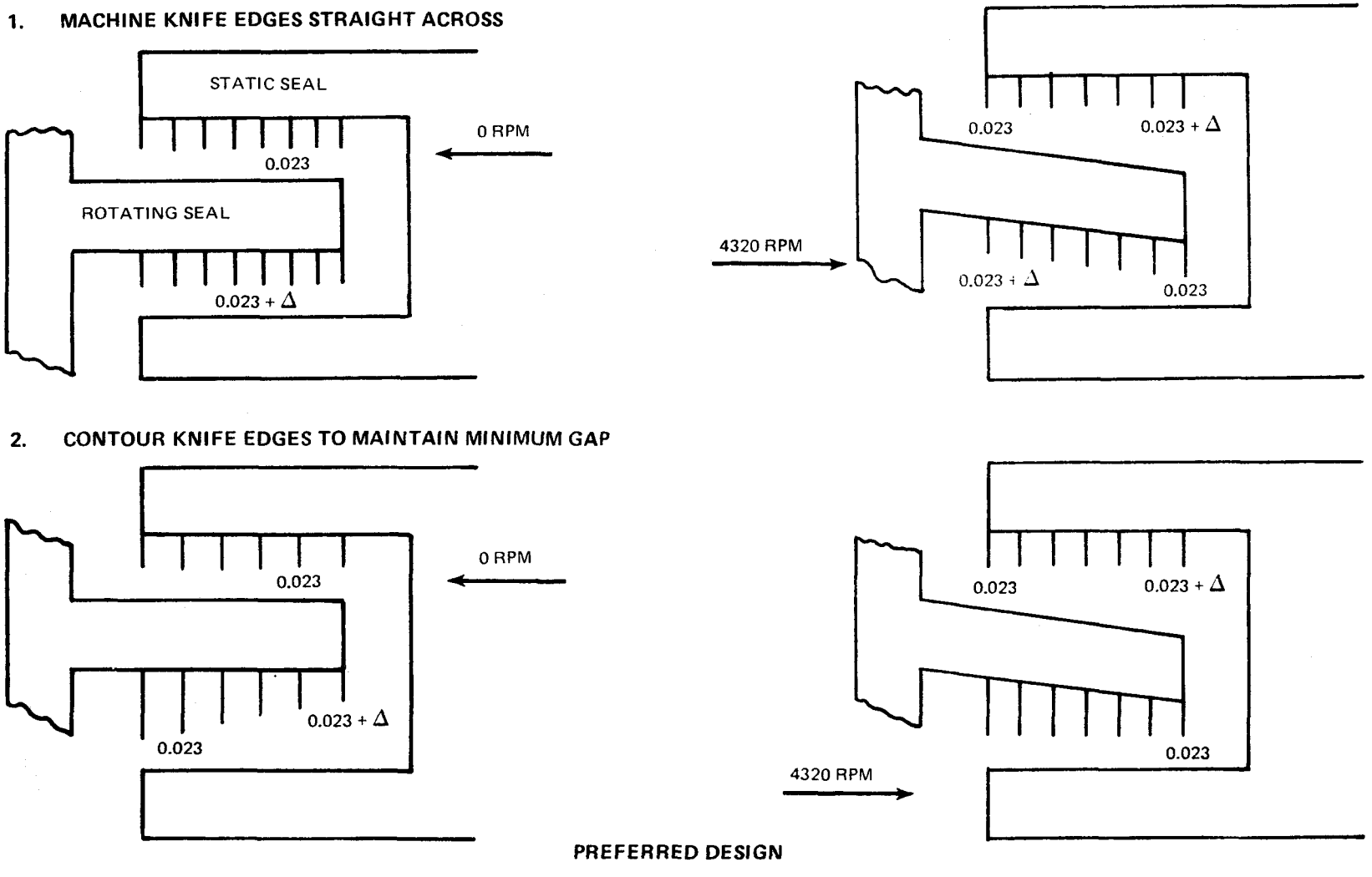

ALL MEASUREMENTS ARE IN U. S. CUSTOMARY UNITS.

GA-A13950

Fig. 7-2. Labyrinth seal dynamic growth

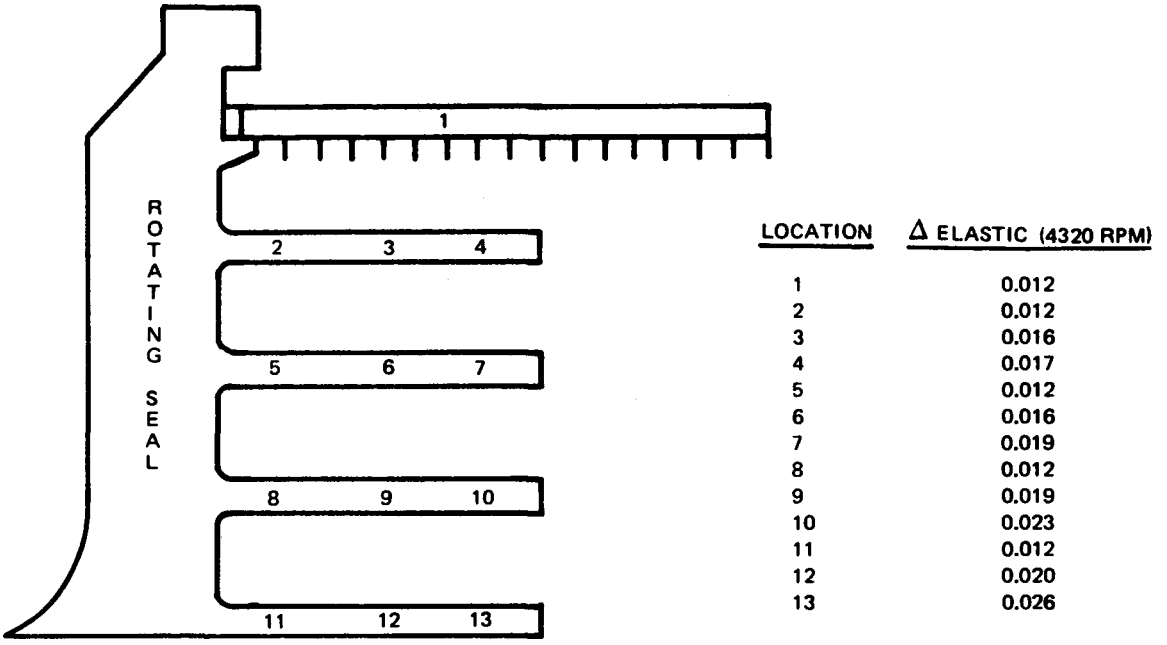

LOCATION	Δ ELASTIC (4320 RPM)
1	0.012
2	0.012
3	0.016
4	0.017
5	0.012
6	0.016
7	0.019
8	0.012
9	0.019
10	0.023
11	0.012
12	0.020
13	0.026

GA-A13950

Fig. 7-3. Labyrinth seal elastic deflections

rotating members. Buffer flow requirements using a statistical approach to seal clearances are now estimated to be less than 1814 kg/hr (4000 lb/hr) for a three-loop power plant under the worst condition of operation (i.e., two turbomachines at full power, one turbomachine shut down). A preliminary structural analysis showed seal hoop stresses within acceptable limits. Alternate seal designs were studied to determine if further reductions in buffer flow were possible. When axial space for alternate configurations is held constant, as it must be for critical speed reasons, no improvement in seal buffer flow can be shown.

7.2.4. Preliminary Design of Drive Shaft Seals

The preliminary design of the floating ring dynamic seal was completed. The seal is an assembly of six individual carbon rings in steel carriers. The seal can provide an absolute barrier to helium leakage around the shaft at speeds from 0 to 4320 rpm with very modest buffer oil flows. Furthermore, the seal can still contain a full 6.2 MPa (900 psi) pressure drop with only four of the six individual elements intact with a 30% increase in buffer oil flow. The seal mechanical layout was completed, and all pertinent dimensions and clearances were defined. Sufficient seal mobility has been provided to permit the seal to survive a seismic event.

The seal support system was refined, and some simplification was effected by permitting the atmospheric end of the seal to terminate in a wet sump. Solubility data for the oil showed that the amount of air absorbed at 0.1 MPa (14.7 psi) would be less than 1 kg/hr (2 lb/hr). Since this is the lowest pressure in the system, the air would be unlikely to outgas into the helium in the PCRV.

The preliminary design of the static stutdown shaft seal was completed. The seal radius has been defined for a reasonable pressure balance when the seal is seated, and the secondary sealing surfaces have been defined in greater detail to assure minimal leakage around the seal carrier. The mechanical layout of the seal was completed showing all of the essential elements of the seal, the seal actuators, and actuator synchronizer system.

The seal has been designed to permit limited axial motion without loss of engagement. Axial motion is likely to occur only when the thrust bearing is removed for service or inspection.

Both the static and dynamic seals can be assembled with the shaft and thrust bearing in a single module and inserted as a unit at the power plant site.

7.2.5. Secondary Containment Shaft Penetration Seal Analysis

Two seal designs were considered for the power output shaft penetration through the secondary containment boundary. The first is a static seal which is engaged by a pyrotechnic squib. This system is inactive until a depressurization occurs, at which time actuation would be initiated by a signal from the plant protection system or by the plant operator. This signal would cause an explosive charge to cut the shaft between the generator and the turbomachine and then drive a permanent seal into the gap between the shaft and the secondary containment. The seal is a one-time device and would have to be replaced before operation could resume.

The second seal design is similar to the floating ring shaft seal located in the PCRV plug just inboard of the thrust bearing. As shown in Fig. 7-4, this is a full-duty three-element seal which operates at all times and requires a supporting oil buffer system of tanks, pumps, and valves. It has the advantage of providing a seal even during normal operation and does not have to be activated when a plant upset occurs. The design is also compatible with rapid return to normal operation following plant upset. Its major disadvantage is that it requires a protected power supply for operation when the power plant is shut down.

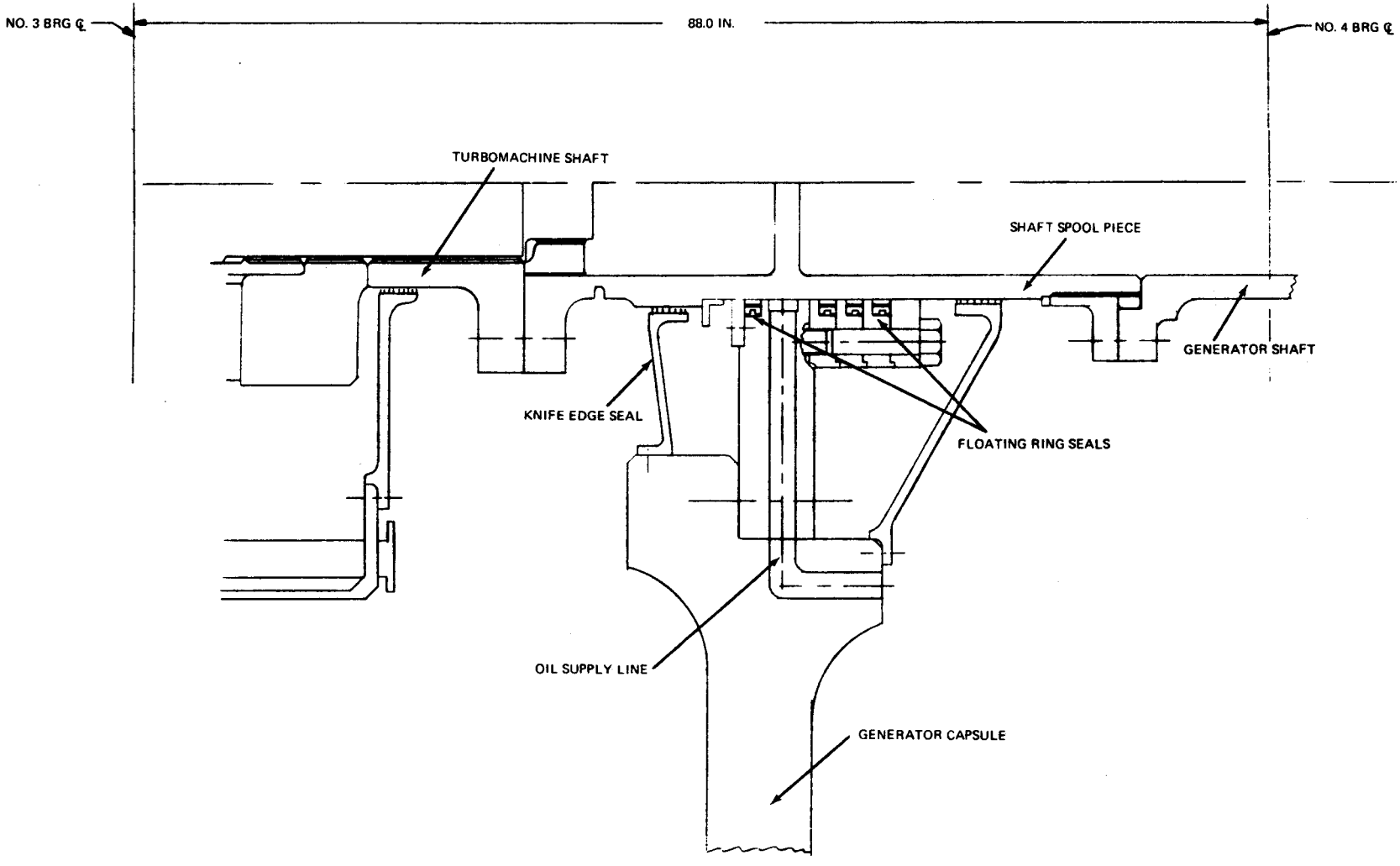

ALL MEASUREMENTS ARE IN U. S. CUSTOMARY UNITS.

GA-A13950

Fig. 7-4. Layout of floating ring shaft seal for secondary containment

7.3. SUPPORTING MACHINE DESIGN

7.3.1. Rotor Stiffness Review

The rotor stiffness review was completed. The initial work on this task defined the effect of coupling stiffness on rotor critical speed. The effect was found to be small. This study led, however, into an evaluation of the size and number of rotor tiebolts required to carry the worst combination of rotor pressure loads, seismic bending loads, torque loads, and thermal gradient effects. The result was an increase in tiebolt requirements from 16 bolts 63.5 mm (2.5-in.) in diameter to 24 bolts 76.2 mm (3-in.) in diameter. This required a substantial change in disk thickness and weight. A change in turbine disk and tiebolt material to a higher strength ferritic alloy solved the problem and resulted in a final requirement for 16 tiebolts at 76.2 mm (3 in.) o.d., and disk sizes returned to more reasonable dimensions.

A companion study of a welded, rather than a bolted, design yielded very promising results. Disk sizes were reduced further, and the ferritic material (Ladish D6AC) had better weldability than the previously proposed Tinidur. As a result of this comparison study and the advantages of balance, stiffness, weight, wear, and cost enjoyed by the welded design, this approach has been selected as the primary design for all future turbomachine analyses.

7.3.2. Shaft Design Review

The power output shaft was analyzed for potential reduction in diameter on the basis of the short-circuit torque analysis reported previously. The results of this review are that no size reduction is possible. Although the torsional stress in the shaft is relatively low, there are rather high contact stresses in the spline outboard of the No. 3 journal bearing which require the full shaft diameter. The shaft diameter, therefore, has not been reduced.

The desirability of soft-mounting the No. 3 journal bearing was also studied to determine what benefits such a design would have in avoiding bearing damage resulting from a hydrogen explosion in the electric generator capsule. A bearing damper system was examined for possible application. The original design was felt to be unacceptable, but a modified version was devised that would provide mobility when required but still maintain adequate stiffness when critical speeds were traversed. The idea was not incorporated in the reference design because it has the disadvantages of requiring separation of the thrust bearing and the No. 3 journal bearing, which are now integrated in a single bearing compartment, and it represents a design approach with significantly lower background experience than the hard-mount system.

7.3.3. Turbine Disk Design Review

The turbine disk design review has been completed for the first-, seventh-, and eight-stage disks of the 816°C (1500°F) turbine temperature design. Layouts of the disks have been prepared but are for the bolted design approach taken in the early portion of this contract.

7.3.4. Bearing and Seal Support Definition

The bearing and seal support definition was completed. During this reporting period, the No. 1 bearing support received the greatest attention because the exhaust gas from the turbine must pass over the struts that connect the inner bearing support ring to the outer cool case and turbomachine mount. Thermal gradients have been estimated for the inner ring, hot strut, and outer ring during drop load and have been found to be beyond the limits for the materials employed. Nickel allows would have adequate strength for this application, but cost and part size are such that this material change is considered to be impractical. The common industrial approach of putting a nonstructural shield around the hot strut and passing spent outer case cooling through the region between the shield and the strut was investigated as an alternative. This system was found to be feasible and has been adopted for the reference design.

7.3.5. Support Design Update

The reference 816°C (1500°F) design layout has been updated as inputs have been received from the bearing, shaft, and support design studies. The last changes to be incorporated as this work was concluded were the shielded exhaust strut design and some modifications required in the turbine exhaust case to resolve a local thermal stress problem.

7.3.6. Failure Mode and Effects Analysis

The failure mode and effects analysis (FMEA) was concluded during this reporting period with an FMEA of the main shaft static and dynamic seals. The principal failure effect which the analysis sought to detect was the escape of buffer helium outside the PCRV.

For the dynamic seal, it was found that a failure in the open position of float valve and level indicator in the high-pressure oil sump could result in blowdown of the No. 2 bearing compartment and escape of buffer helium. Redundant valves and pressure switches can be used to control or eliminate this fault.

For the static shutdown seal, it was found that a failure of the hydraulic motor that positions the seal against the shaft collar would permit helium to escape. Seal cocking during positioning could also produce a helium leak. Redundant hydraulic motors and synchronized operating rods provide solutions for these faults, along with proper pressure balancing to fully seat a partially seated seal.

7.3.7. Review of Turbine-End Mount Design

The design of the turbine-end mount system was reviewed to determine if some alternate system could be found that could distribute the loads over a larger area of the PCRV liner. The current design uses two mount points at 90 deg and 270 deg on the PCRV turbomachinery cavity liner to carry the

turbine-end loads to ground. The alternate design carries the same two point loads into an annular conical support which would be permanently attached to the PCRV liner. The ring serves to distribute the load before it is actually picked up by the PCRV liner. This design is highly conceptual, and substantial structural and heat transfer work remains to be done to verify its acceptability.

7.4. BEARING AND SEAL TEST PLANS

7.4.1. Journal Bearing Test Plan

The journal bearing test plan was defined for the reference design configuration. The plan calls for development tests of the basic five-pad 508-mm (20-in.)-diameter design with testing of a four-pad 457-mm (18-in.)-diameter design recommended as a backup offering lower losses. The possibility of adapting the jet lube supply planned for the thrust bearing will be evaluated in an attempt to minimize oil flow and power losses of the journal bearings. Rig drive requirements have been reviewed, and UTC facility capabilities have been reviewed and found to be adequate for conducting the tests.

Test load range, speeds, and misalignment were defined. Instrumentation location and variety were identified consistent with the degree of design available.

7.4.2. Thrust Bearing Test Plan

The thrust bearing test plan was defined for the double-acting thrust bearing described in Section 7.2. The plan calls for development and demonstration testing of the 762-mm (30-in.) o.d. eight-pad design and includes steady and transient loading, misalignment, and jet nozzle pattern optimization. All testing is to be full-scale, and the drive system for the journal bearing rig or a similar unit can be used to drive the thrust bearing rig. The rig size is such that with relatively minor modifications UTC facilities should be adequate to conduct the tests. Less detail exists for the thrust

bearing tests than for the journal bearing tests because of the later timing of this work and the contract effort redirection that occurred in March 1976. The general instrumentation requirements, thermocouple pressure transducer, and proximity pickup location and number have been defined.

7.4.3. Drive Shaft Seal Test Plans

The test plan for the floating ring seal has been defined and depends on two seal rigs which have a high degree of commonality. A seal element rig will be used to test single seal elements for performance and durability, while a multi-element rig will be used to verify the total seal performance, refine clearances, and assure seal survivability during maximum shaft excursions. The oil buffer supply system that provides the high-pressure oil on which the seals float will be tested, along with the seal rings and valve and float settings verified prior to full engine testing. Pressure, flow rate, temperature, and misalignment ranges were identified for the single-element and multi-element seal rigs. Instrumentation requirements were described in general terms, and an endurance test period for seal material evaluation has been selected.

A relatively simple test plan for the static seal has been defined. Items of greatest interest are leakage past the primary seal and secondary seals and behavior of the actuation mechanism. Testing will be at the full pressure of 6.89 MPa (1000 psi) on a full-scale seal, and variables such as primary seal material dimensions and finishes will be evaluated. The seal will be cycled open and closed under a range of pressures and temperatures consistent with the plug cavity operating conditions. The size of the rig is such that suitable UTC facilities should be available for conducting the test. Test instrumentation is required to measure pressure temperature, actuation time, and travel.

7.4.4. Buffer System Test Plan

The buffer seal test plan was defined to provide a comprehensive description of the tests and test conditions required to simulate the operating

environment of the buffer seals. The tests will use full-scale hardware and involve a rig which has a rotating shaft and seal dimensionally accurate in all seal clearances. Five areas of investigation are incorporated in the plan: (1) buffer seal flow calibration, (2) tank and valve calibration, (3) contaminated helium back-diffusion evaluation, (4) bearing oil loss to engine evaluation, and (5) buffer seal flow with increased clearances. The order of these tests, the number of runs required, and the operating conditions have been specified. UTC facilities appear to be adequate to conduct these tests, and the general instrumentation requirements have been defined. Special techniques will be required to measure contaminated helium backflow and oil leakage, and the specifics of this equipment have not yet been defined.

7.5. TEST RIG DESIGNS

7.5.1. Journal Bearing Test Rig Design

The preliminary design of the journal bearing test rig was completed. An illustration of the design appears in Fig. 7-5. In this reporting period, the loading frame which loads the shaft against the test bearing pads was defined in greater detail, the oil distribution system was added, and the rig cabinet was defined. The rig is capable of imposing a steady vertical load of 0.445 MN (100,000 lb) and an impulsive load of up to 1.334 MN (300,000 lb). Speeds from 0 to 4320 rpm can be set, and shaft misalignments of 0.0005 unit per unit of bearing length can be introduced.

7.5.2. Main Shaft Ring Seal Test Rig Designs

The preliminary designs of single-element and multi-element floating ring seal test rigs were completed during this reporting period. As shown in Fig. 7-6, the single-element and multi-element rigs retain about 80% parts commonality and can use the same general support system tanks and lines and the same drive system. Both rigs can be operated from 0 to 4320 rpm with misalignments of 0.001 unit per unit of seal length. Pressure and oil flow requirements for the single-element rig are lower than those for

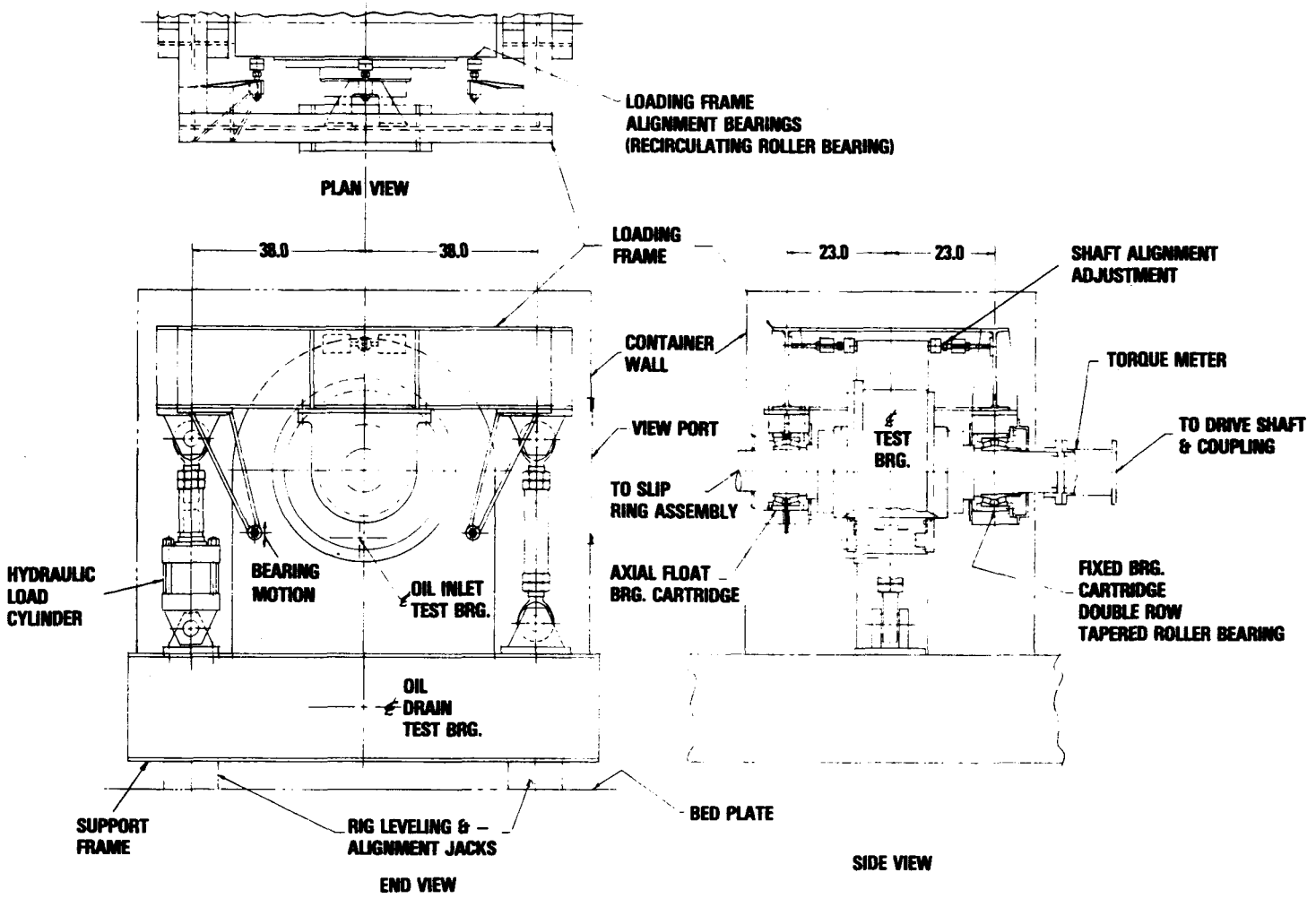

ALL MEASUREMENTS ARE IN U. S. CUSTOMARY UNITS.

GA-A13950

Fig. 7-5. Journal bearing test rig

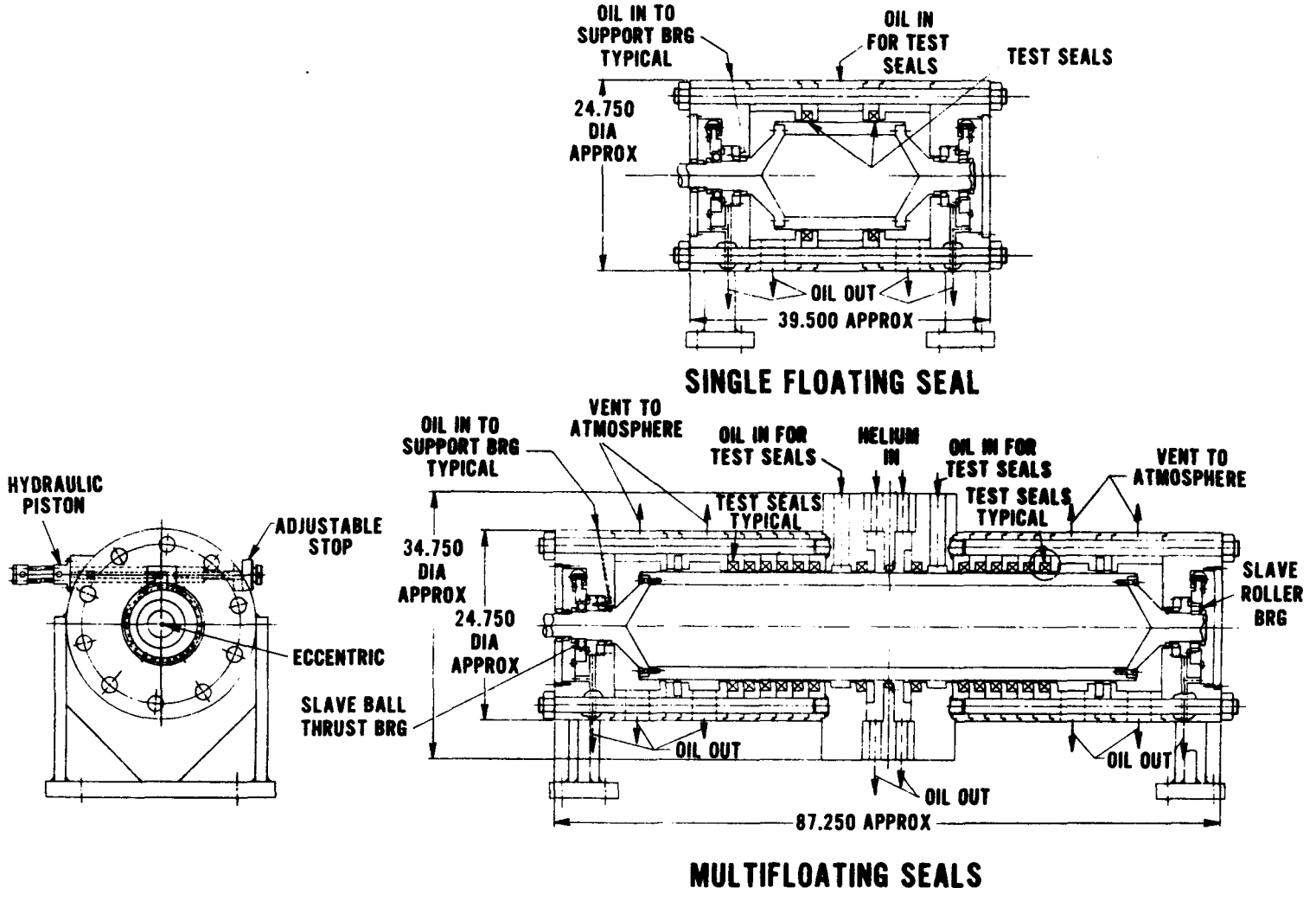

ALL MEASUREMENTS ARE IN U. S. CUSTOMARY UNITS

GA-A13950

Fig. 7-6. Main shaft ring seal test rigs

the multi-element rig and the rig itself is somewhat shorter in length. The drive motor requirements are up to 37.3 kW (50 hp) for the single-element rig and 186.4 kW (250 hp) for the multi-element rig.

As described in Section 7.4.3, the single-element rig is primarily for evaluation of oil flows, clearances, materials, and seal durability. The multi-element rig is primarily for demonstration of full pressure integrity, misalignment capability, and final trimming runs on clearance and oil flow.

The preliminary design of the static shutdown seal rig was completed. This rig, shown in Fig. 7-7, is designed to operate at pressures of up to 6.89 MPa (1000 psi) to simulate full internal PCRV pressure and to demonstrate the reliable functioning of the seal under these conditions. During the testing, the leak rates will be identified at the primary seal and secondary seals. The hydraulic motor action will be tested, and single motor failures can be simulated to verify the adequacy of the redundant motor operation. The rig itself is essentially a pressure vessel with an interior configuration similar to the power output shaft and static seal in the turbomachine. The vessel is sealed at both ends, and the simulated shaft does not rotate. Its operation is identical to that of the actual turbomachine; i.e., the vessel is charged to 6.2 to 6.9 MPa (900 to 1000 psi), and the hydraulic motors are actuated to allow the seal to move into contact with the seal collar. The downstream cavity is then depressurized and the leakage measured.

7.5.3. Thrust Bearing Test Rig Design

A conceptual design was completed for the thrust bearing test rig. The concept, shown in Fig. 7-8, was chosen from five proposed designs as most successful in meeting two primary rig design criteria: (1) to simulate the actual operating conditions in service and (2) to minimize rig drive and horsepower requirements. The rig uses a load cell composed of the shaft end and a nine-element floating ring seal identical in size and design to the six-element seal actually used in the turbomachine design. This load cell is pressurized to 10.3 MPa (1500 psi) by a high-pressure oil pump. The load

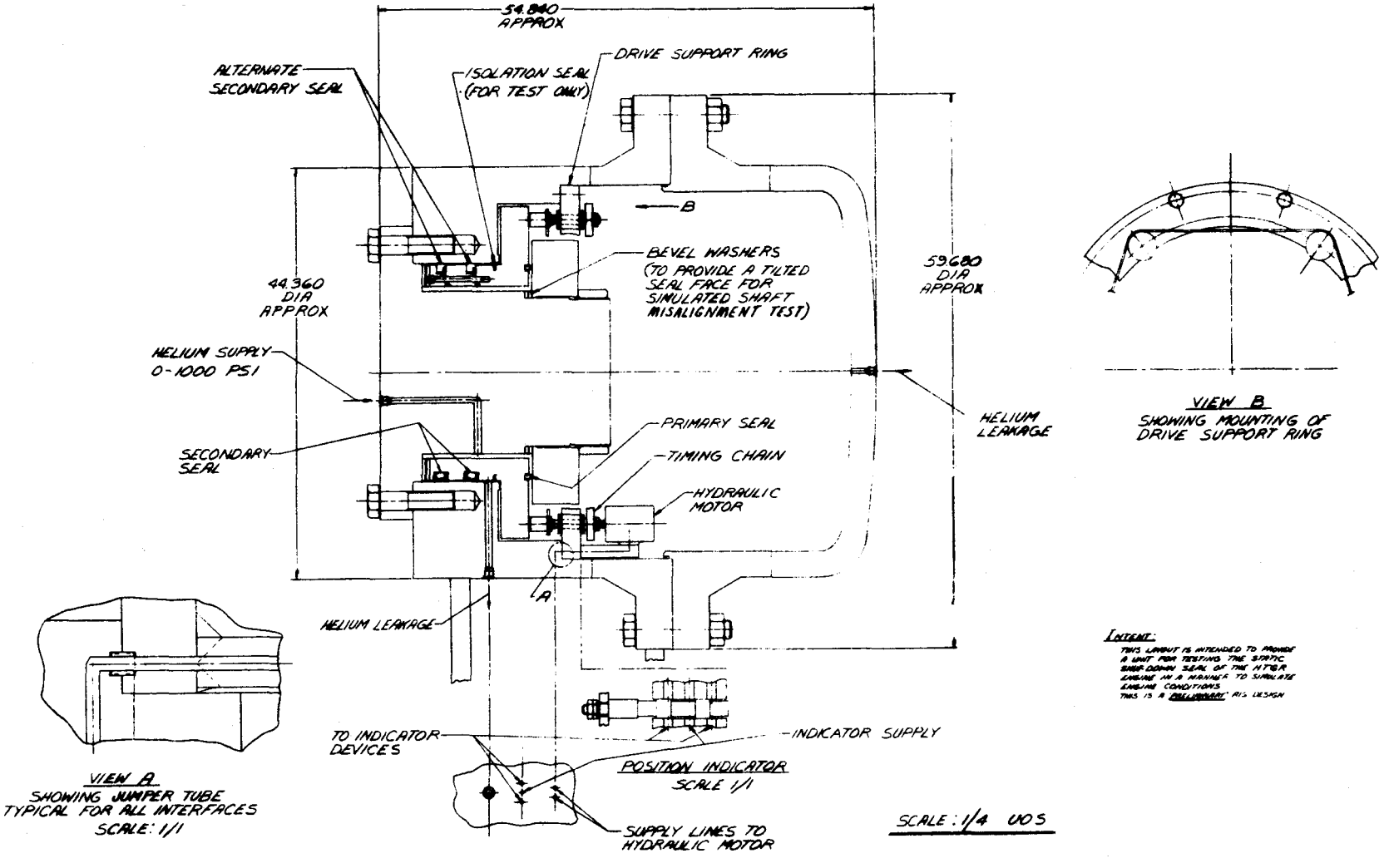

ALL MEASUREMENTS ARE IN U. S. CUSTOMARY UNITS.

GA-A13950

Fig. 7-7. Preliminary design layout of test rig for main shaft shutdown seal (sheet 1 of 2)

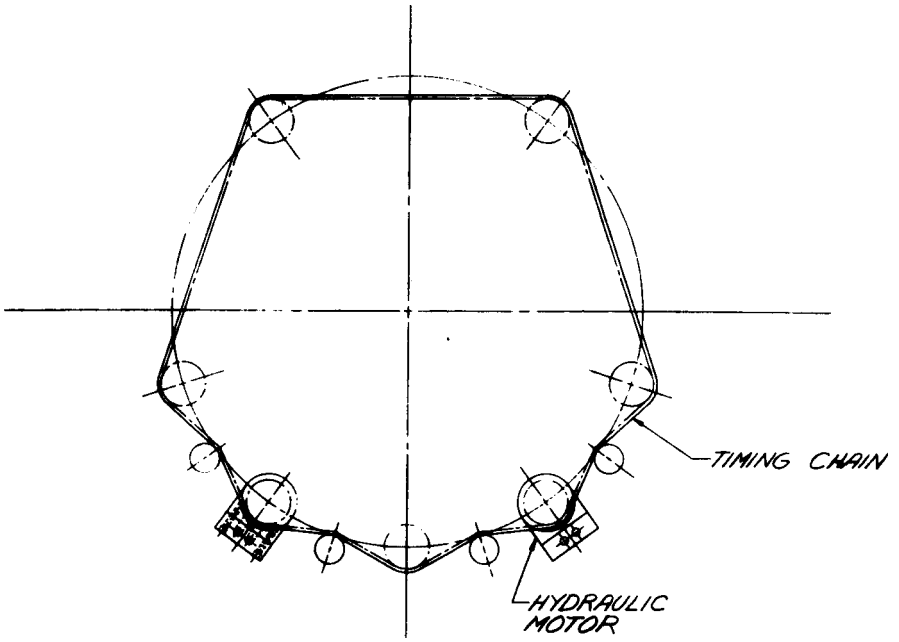

SECT THRU TIMING CHAIN

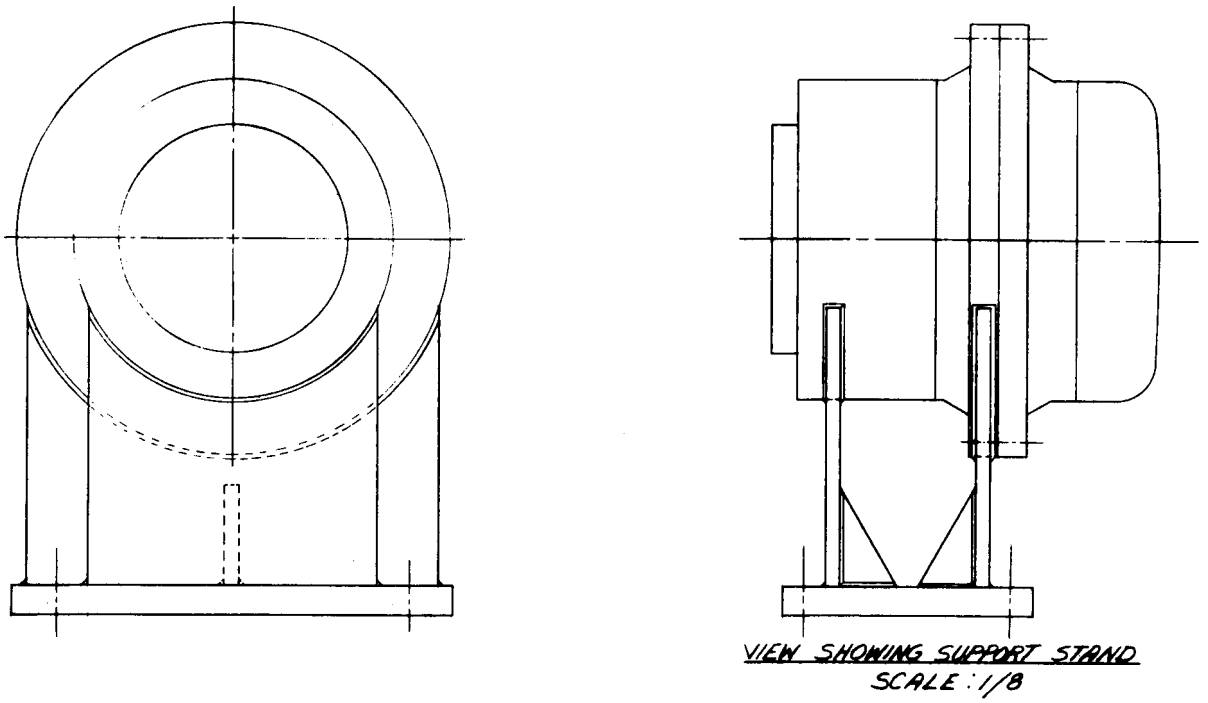

VIEW SHOWING SUPPORT STAND
SCALE: 1/8

GA-A13950

Fig. 7-7. Preliminary design layout of test rig for main shaft shutdown seal (sheet 2 of 2)

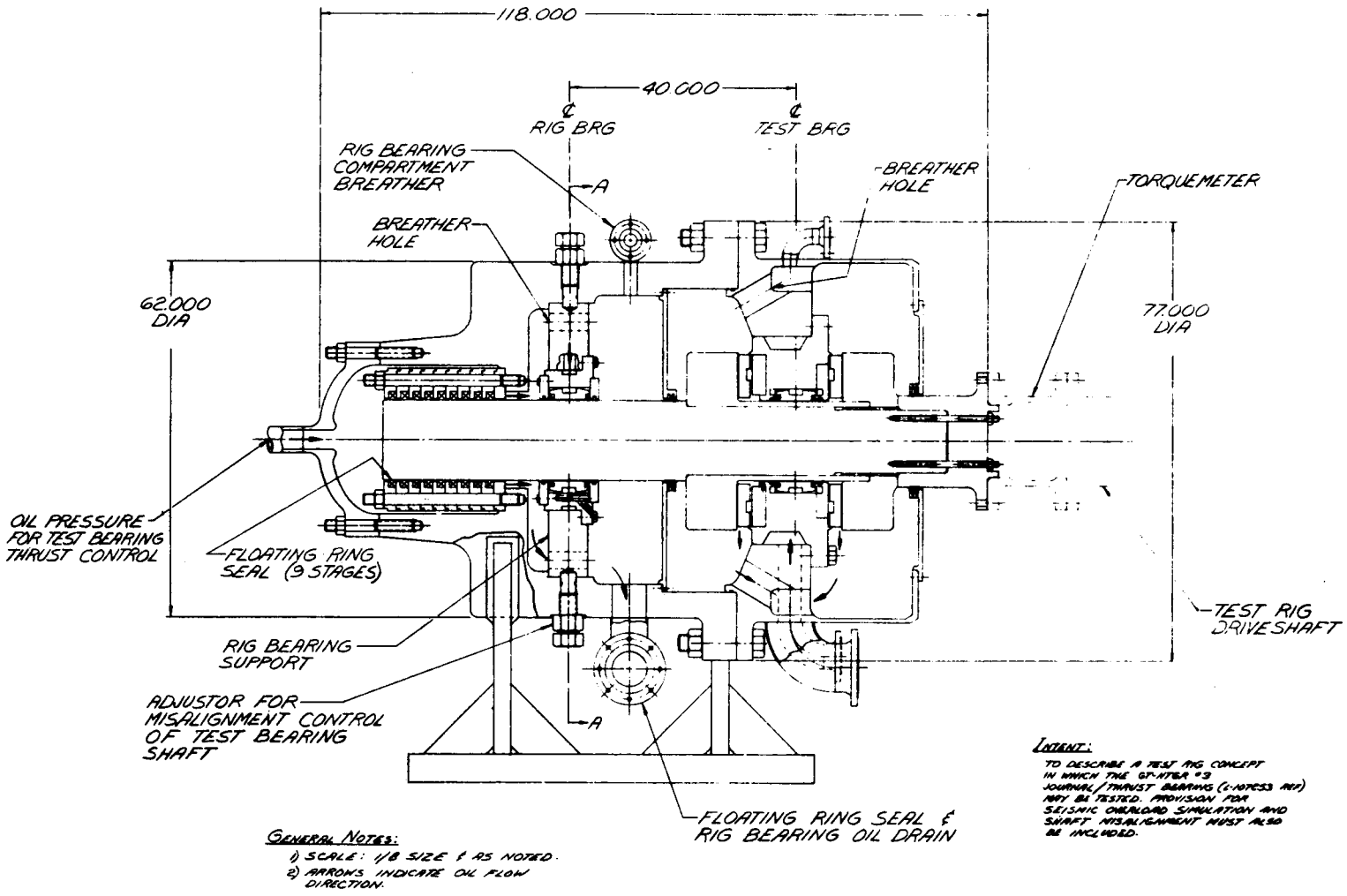

ALL MEASUREMENTS ARE IN U. S. CUSTOMARY UNITS.

GA-A13950

Fig. 7-8. Conceptual layout of thrust bearing test rig (sheet 1 of 3)

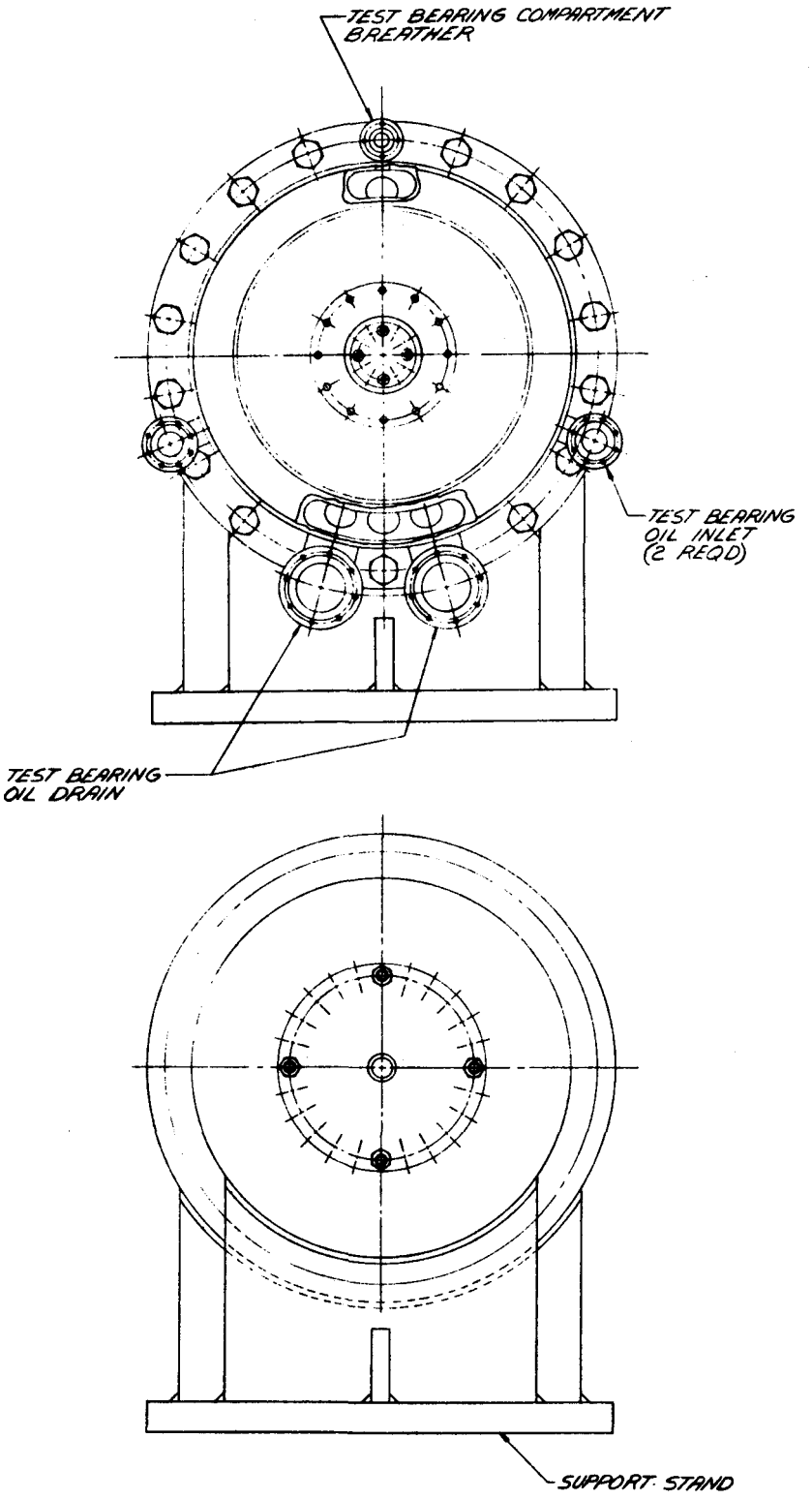

Fig. 7-8. Conceptual layout of thrust bearing test rig (sheet 2 of 3)

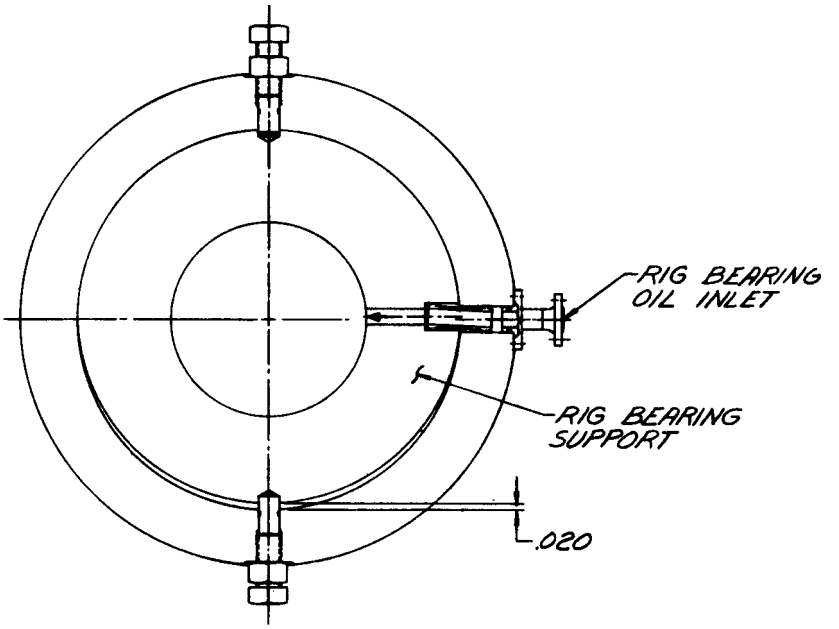

SCHEMATIC SECT. A-A
SHOWING RIG BEARING SUPPORT IN MAX MISALIGNED POSITION FOR TEST BEARING MISALIGNMENT TEST

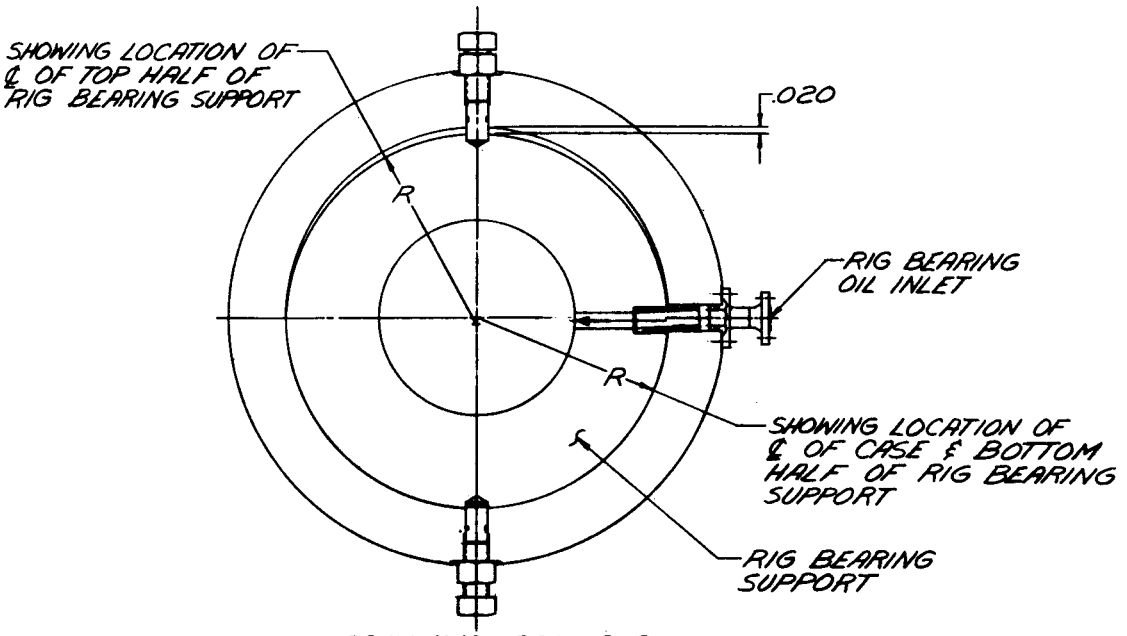

SCHEMATIC SECT A-A
SHOWING RIG BEARING SUPPORT IN NORMAL TEST POSITION

GA-A13950

Fig. 7-8. Conceptual layout of thrust bearing test rig (sheet 3 of 3)

can be varied from 0 to 0.667 MN (0 to 150,000 lb) at any rpm from 0 to 4320. This permits simulation of the startup and shutdown events, as well as steady-state operation, drop load, and to a limited degree, seismic overload. The vertical support for the shaft is provided by the integral No. 3 journal bearing in the thrust bearing assembly and by another No. 3 journal bearing located near the floating ring seal. The second journal bearing can be adjusted up or down to produce any degree of shaft misalignment desired for the thrust bearing test.

7.6. ANALYSIS OF HIGH-TEMPERATURE DESIGNS

7.6.1. Preparation of Design Tables

As a basis for an orderly design analysis of the matrix of high turbine inlet temperature closed cycles resulting in the parametric studies described below, it was necessary to define the state points around the power conversion loop and to iterate with the compressor and turbine design groups as the initial input assumptions were refined. In the course of this study, 16 compressor and turbine combinations covering turbine temperatures from 816 to 1000°C (1500 to 1832°F) and pressures ratios from 2.3 to 2.9 were investigated. Several sets of design tables were prepared for each of the cycles as the component efficiencies, turbine cooling estimates, and duct pressure losses were refined in the overall power conversion loop simulation.

7.6.2. Preparation of Off-Design Data

Off-design data were generated for four cycles selected from 16-cycle matrix. Two cycles did not require airfoil cooling. These were for designs having compressor pressure ratios of 2.35 and 2.5 at a turbine inlet temperature of 850°C (1562°F). The other two cycles were at 2.5 pressure ratio and 950°C (1742°F) turbine inlet temperature with and without a bottoming cycle for waste heat recovery. Part-load steady-state performance has been generated at four points from 0 to 100% power output. These data are useful only for general information about temperature and pressure around the

power conversion loop because the actual off-design compressor and turbine characteristics have not yet been defined. The data discussed here were generated using normalized off-design characteristics taken from the reference design, which has a pressure ratio of 2.35 and a turbine inlet temperature of 816°C (1500°F).

7.6.3. Review of Duct and Scroll Pressure Losses

The efficiency of the power conversion loop and the size of the turbomachine components are dependent on the pressure losses in the PCRV and in the turbomachine ducts and scrolls. Since the envelope of the turbomachine is limited by shipping considerations, the pressure losses were estimated assuming no change in ducting or scroll size. An approach which varied the duct and scroll sizes from cycle to cycle would have required a continuing mechanical review to ensure that shipping limits were not exceeded. Pressure losses were lowest for the high turbine temperature, high compressor pressure ratio designs, and highest for the low turbine temperature, low pressure ratio designs. In all, 16 cycles were evaluated, including 14 higher temperature cycles, the reference design 816°C (1500°F) cycle, and a high-temperature cycle with a bottoming ammonia cycle. The initial estimates of PCRV pressure losses were based on the reference 950°C (1742°F) cycle and were held constant for all turbomachine cycles. Later work was based on fixed PCRV duct sizes, and pressure loss was then found to vary with cycle temperature and pressure ratio, as shown in Fig. 7-9. All duct and scroll loss estimates must be treated as preliminary at this time, because they depend heavily on the physical size and shape of the ducts and because mechanical studies of the rotor dynamics and static structure, along with aerodynamic optimization of the compressor and turbine, will certainly produce changes in the ducts relative to the assumed configurations.

7.6.4. Analysis of Secondary Cooling Requirements

Turbomachine secondary cooling is defined as any cooling requirement except direct turbine blade and vane cooling. The elements requiring secondary cooling in the high turbine temperature cycles are the turbine inlet

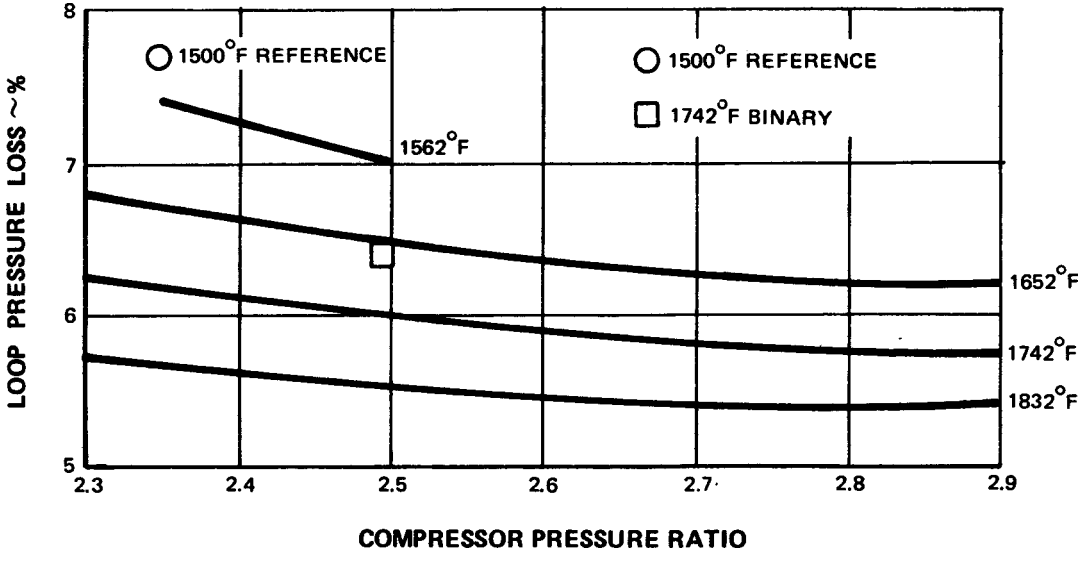

ALL MEASUREMENTS ARE IN U. S. CUSTOMARY UNITS.

GA-A13950

Fig. 7-9. Loop pressure loss variation

scroll, turbine disks, blade and vane attachments, turbine case, and turbine exhaust strut (bearing support).

The turbine cooling requirements, excluding blade and vane gas path region cooling, varied from about 9% of compressor flow at the highest turbine inlet temperature cycle to about 5% for the lowest turbine temperature cycle. The physical model for the cooling analysis was a welded rotor turbine with conventional fir tree attachments. The cooling flow requirements are not optimized, and potential exists for some reduction in these requirements. The data are based on actual experience with air-breathing open cycle designs and show the trend of cooling required as temperature increases, as well as absolute cooling levels. The data include real-engine cooling leakages which occur in areas such as the vane i.d. diaphram and o.d. attachments.

The cooling flows shown in this study for a turbine inlet temperature of 816°C (1500°F) are higher than those quoted in the study of the reference design at this temperature because of the change in disk material from A286 to Ladish D6A. The latter material has a higher ultimate tensile strength at room temperature than that of A286 and has several other advantages for this application, but it requires a slightly lower running temperature and hence a higher cooling flow. All cooling flows are based on design point (base load) pressures and temperatures. The cooling flows at part load were not examined in detail, but a brief analysis showed operation at reduced power using bypass control rather than reactor core temperature reduction would increase the cooling requirements.

The inlet scroll and turbine exhaust strut designs are discussed in Section 7.6.6, but the point to be reiterated here is that their designs are such that no additional cooling flow needs to be bled from the compressor to maintain satisfactory temperature gradients and absolute temperatures in these parts.

7.6.5. Review of Thrust Balance Loads

The analytical determination of the thrust loads created by differing pressures on the individual turbomachinery components is summed up to define the net thrust load to be carried by the thrust bearing. This work is now in progress on the four turbomachinery cycles selected for further study. The thrust load studies in the past have shown that opposing forces in the turbomachine are on the order of thousands of meganewtons (millions of pounds), and the net force which has been around 0.667 MN (150,000 lb) can vary considerably when component sizes are changed. This is not a cause for concern, however, since many techniques are available to bring these forces down to manageable levels.

7.6.6. Cooled Turbine, Case, and Strut Design Approach

The range of temperatures encountered in the high turbine temperature study is such that the approach to cooling the turbine, turbine case, turbine inlet scroll, and turbine support struts varies only in degree from one turbine inlet temperature to the next. Therefore, the following descriptions of these components generally apply to all temperatures studied.

1. Turbine cooling. In the stages where gas temperature exceeds 816°C (1500°F), a simple convective cooling scheme using radial cooling passages has been applied to the blades and vanes. The flow is taken from the compressor high-pressure discharge.

2. Turbine case. Cooling for the turbine case and cooled vanes is taken from the turbomachine cavity (center section) where compressor discharge flow is collected prior to being ducted to the recuperator. The case is convectively cooled, and some flow is bled off at the vane attachments to convectively cool the outer gas seal which is just outboard of the turbine blade tips.

3. Turbine inlet scroll. As described in Section 7.6.5, a double-wall design with insulation between the walls is proposed to keep the temperature gradient across the scroll outer wall low enough to prevent excessive thermal stresses. The outer wall carries the compressor discharge to turbine inlet pressure difference, while the inner wall runs hot and protects the insulation from the viscous forces produced by the gas flow.

4. Turbine support struts. The shielded strut design developed for the 816°C (1500°F) configuration is also required for these higher temperature designs. In all cases, it appears that spent turbine case cooling gas is sufficiently cool and available in sufficient quantities to maintain the inner structural member below 538°C (1000°F).

Preliminary structural analyses of all of the above components were conducted using the 950°C (1742°F) design as a model. Blade stress and temperature have been estimated; case temperatures have been estimated; inlet scroll vibration, buckling, and overall stresses have been analyzed; and turbine support strut temperature, stress, and spring rate have been examined. All results indicate that the design is basically feasible.

7.7. PARAMETRIC STUDY OF HIGH-TEMPERATURE DESIGNS

7.7.1. Compressor Designs

A total of 14 compressor configurations have been defined using the compressor mean line analysis program. This program provides both a mechanical configuration of the compressor and an efficiency prediction. The mechanical configuration includes definition of the flow path (i.e., o.d., number of stages, and axial length) and the required number of airfoils. The efficiency prediction is based on empirical correlations from a large data base of axial flow compressor experience and includes the effects of loading, gap/chord, aspect ratio, tip clearance, Reynolds number, and boundary layer growth.

The 14 compressor configurations defined represent compressors providing pressure ratios of 2.4, 2.5, 2.7, and 2.9 at each of the three turbine inlet temperatures of 900°C, 950°C, and 1000°C (1652°F, 1742°F, and 1832°F) plus a reference-cycle compressor at 2.35 pressure ratio and 816°C pressure ratio and 950°C (1742°F) turbine inlet temperature. The required flow at each condition was determined from a performance analysis of the HTGR cycle.

In this parametric study, several compressor design variables were fixed to complete the study within the required time and budget constraints. The variables which were fixed for all configurations are:

1. Flow path shape (constant i.d.)
2. Axial velocity distribution
3. Tip clearance = 1.6 mm (0.635 in.)
4. Axial gapping = 19 mm (0.75 in.)
5. Aspect ratio = 1.6
6. Surge margin = 11%
7. Reacticn = 0.75

In addition, constraints were placed on the design variables of gap/chord ratio and exit hubtip ratio in order to define a compressor for each point in the compressor matrix. Gap/chord ratio was constrained to be between 0.85 and 0.93, while exit hub/tip ratio was constrained to be less than 0.91. These represent design experience and are consistent with the P&WA industrial compressor design.

The results of the analysis, presented in Figs. 7-10 and 7-11, show that the diameter and the efficiency of the compressors decrease as turbine inlet temperature and compressor pressure ratio are increased. The diameter reduction is due to the reduced gas flow required as turbine temperature is increased and is the fixed upper limit on exit hub/tip ratio. The variation of efficiency with pressure ratio represents the change in adiabatic efficiency at a constant polytropic efficiency as a function of pressure ratio. The variation of efficiency at a constant pressure ratio represents the effect of tip clearance as the diameter of the machine varies as a

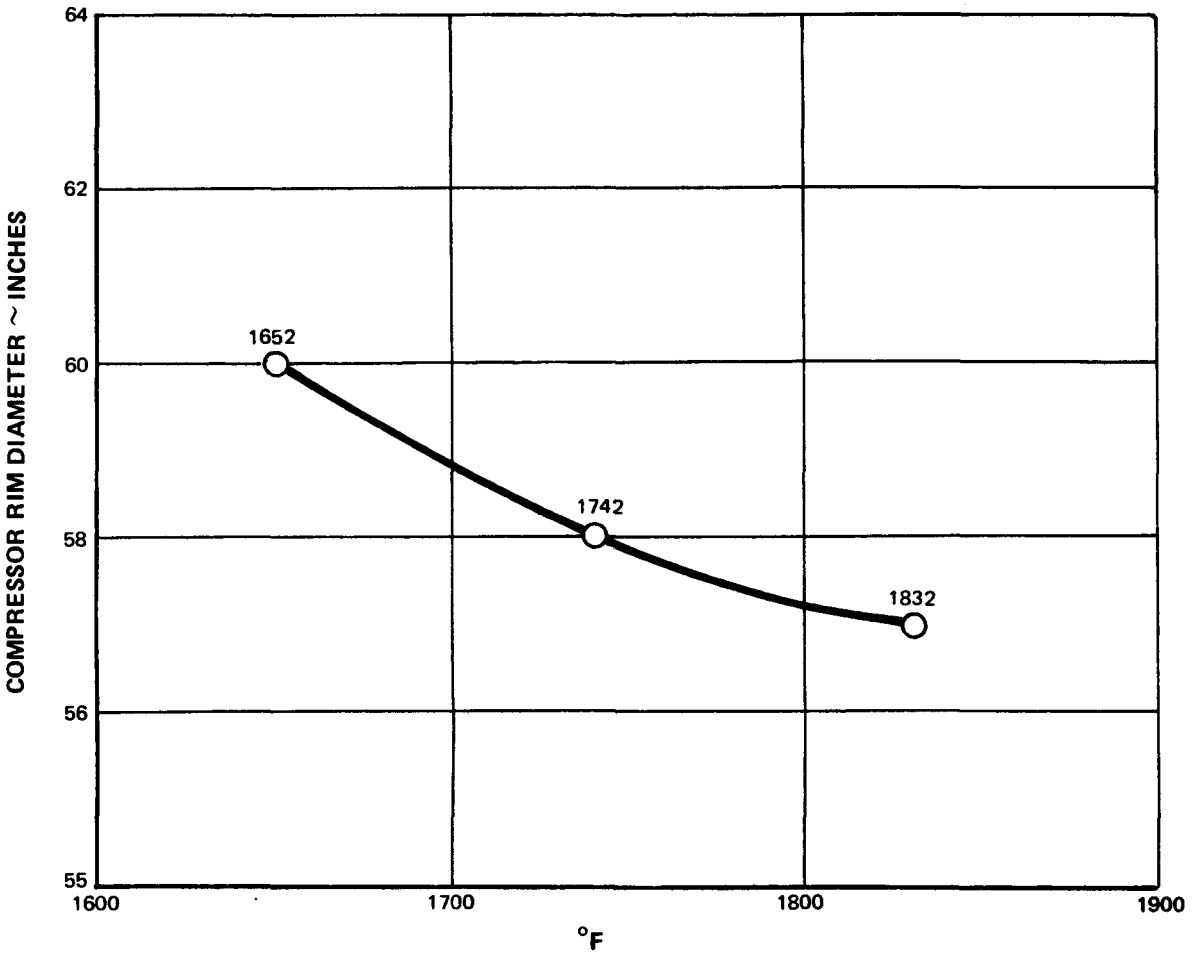

ALL MEASUREMENTS ARE IN U. S. CUSTOMARY UNITS.

GA-A13950

Fig. 7-10. Variation of compressor disk size with turbine inlet temperature

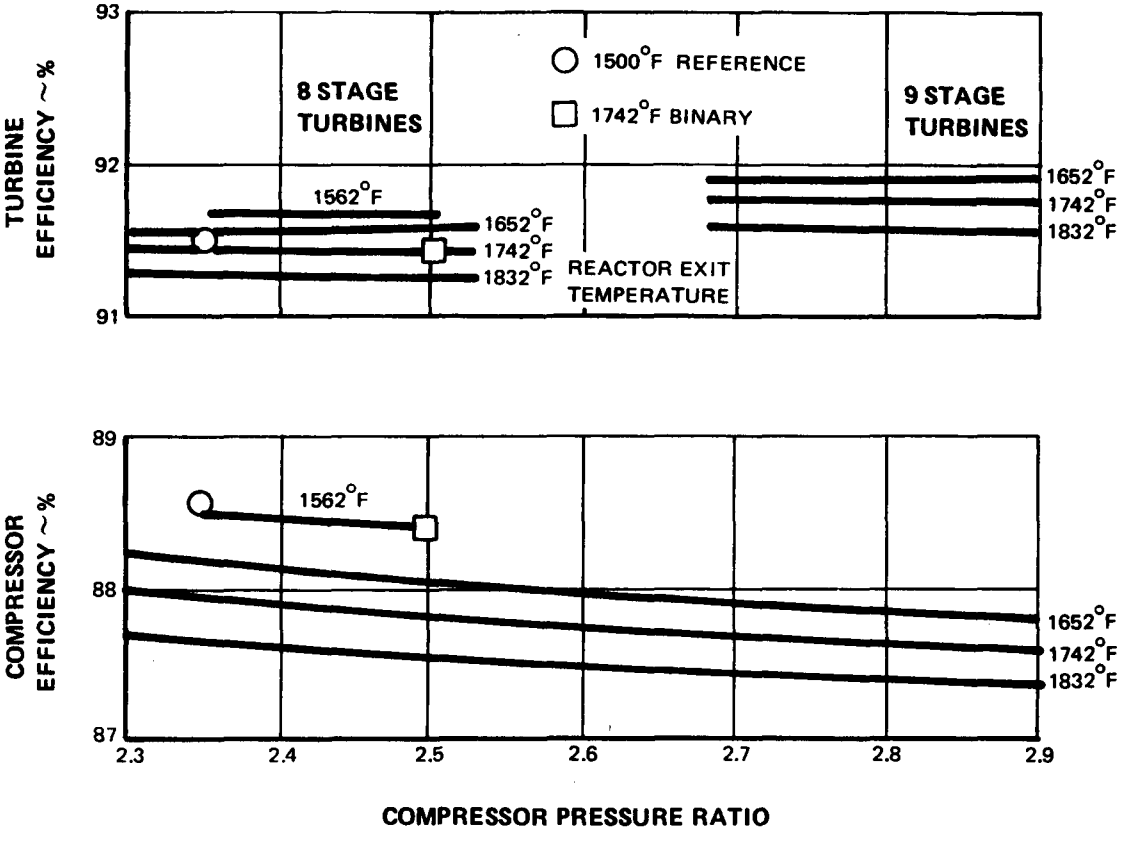

ALL MEASUREMENTS ARE IN U. S. CUSTOMARY UNITS.

GA-A13950

Fig. 7-11. Variation of efficiency for turbines and compressors (unoptimized designs)

function of turbine temperature. It should be noted that the total variation of the efficiency for the parametric study cases is only 0.9 point.

The number of compressor stages increased as turbine temperature and pressure ratio were increased. The dependence of number of stages on turbine inlet temperature is a result of the diameter being a function of turbine inlet temperature. At the higher turbine temperatures, the allowable diameter is reduced. This lower diameter coupled with a fixed mechanical speed results in less available wheel speed and consequently more stages for a given pressure ratio.

The dependence of number of stages on pressure ratio is due to the fixed-stage loading and increased work required.

7.7.2. Turbine Designs

A matrix of turbines has been designed using the turbine mean line analysis program to match each of the compressors described above. Loading factors, reaction, spacing, and tip clearance have been held constant at the levels used in the turbine design review of the 816°C (1500°F) reference design. Both eight-stage and nine-stage turbines were analyzed for the lower pressure ratio cycles. No attempt to optimize the flow path was made. The flow path elevation was held constant, since the range of helium flows was essentially identical with previous work. The only flow path change made was to add a stage when the Mach numbers and gas turnings exceeded the range of current design experience.

A nine-stage turbine was found to give better turbine efficiency at the low pressure ratios than an eight-stage design, but, when the additional cooling required for the extra stage was considered, the net cycle efficiency was unchanged.

A brief study was also conducted to determine the effects of removing a stage from the basic eight-stage turbine of the 2.5 pressure ratio cycle

at 950°C (1742°F). The first stage was redesigned to absorb the extra work, and the loading of the remaining stages was unchanged. The resulting overall efficiency loss was 1.2%. The increased work resulted in a higher temperature drop for the first stage, which would allow a reduction in airfoil cooling flows in subsequent stages. The reaction level was varied in an effort to improve stage and overall efficiency. As reaction levels were lowered to 30%, the overall efficiency did not improve, while the stage efficiency continued to fall off. The reduced cooling required could not offset the 1.2% loss in turbine efficiency.

In general, the results presented in Fig. 7-11, show that increasing turbine temperature tends to lower turbine efficiency slightly and that increasing turbine expansion ratio (to match increasing compressor pressure ratio) had no significant effect. The effects of blade tip clearance on turbine performance were also examined. At the current tip clearance of 2.5 mm (0.100 in.) the efficiency has been debited by 2.6% relative to zero tip clearance. A clearance reduction of 1.3 mm (0.050 in.) would increase turbine efficiency by 1.3%. Any actual reduction would have to be determined in a detailed turbine design study.

7.7.3. Turbine Cooling Requirements

Turbine aerodynamic and cooling characteristics were estimated with several iterations to tune performance levels with cooling and secondary system parameters. For the most part, the analyses were conducted using the latest mean line tools with helium real gas properties. For the 950°C (1742°F) turbine inlet temperature and 2.5 overall pressure ratio cycle, a stream line analysis was conducted, and selected airfoil cross sections were designed in order to incorporate the proposed cooling schemes. In addition, some preliminary heat transfer and stress analysis was done to verify structural integrity of the cooled airfoils.

Relatively simple radial flow cooling schemes were selected to minimize resulting airfoil cost increases. Cooling flows were sized to meet life

goals of 1% local creep in 280,000 hr. Airfoil skin temperature maximums were allowed to exceed the 816°C (1500°F) limit established in earlier work, since the average cross-sectional temperature is the governing factor in creep life. PWA 658 (IN100) remains the airfoil material because of its excellent creep strength. Furthermore, mechanical coupling of the vanes is recommended. Vane coupling is a simple means of reducing the effective tip bending stress and thus also reducing axial and tangential vane deflections. Lower effective bending stresses increase airfoil creep life for a given metal temperature with a minimal increase in manufacturing cost.

Three typical airfoils (first vane, first blade, and third vane) were analyzed to verify that simple convective cooling configurations are applicable in a high-temperature helium environment and to provide a base for estimating all of the stage cooling requirements. In all cases, the required metal temperature reduction was achieved with 0.15% of compressor discharge flow per row. However, for cooled vanes other than the first stage, the actual flows will be higher, since the vanes are used as cooling transfer paths for the secondary cooling system.

The heat transfer parameters were found to differ from air-cooled applications in two important respects: (1) low coolant supply temperature and (2) convective heat transfer coefficients that are approximately five times that of air. The low coolant temperature, combined with high hot gas to coolant gradients, provides significant metal cooling with a minimum of flow. In all cases, the turbine life goal was exceeded with 0.15% coolant flow per row; however, further reductions in flow level are impracticable. Total airfoil cooling required for the turbine was found to vary from zero at 816°C (1500°F) to 1.2% of compressor flow at 1000°C (1832°F) turbine inlet temperature. The increased level of film coefficient causes temperature gradients in excess of air-cooled experience. A stress analysis was performed to assess the temperature gradient effect on airfoil life. This analysis has shown that these gradients cause high initial thermal stresses which are rapidly reduced as a result of creep relaxation and which are not expected to limit airfoil lives.

7.7.4. Definition of Optimum Cycles

After the compressor and turbine characteristics had been defined and the turbine primary and secondary cooling had been evaluated, the overall performance of the various cycles was compared to determine which cycles offered the greatest thermodynamic improvements. At each turbine temperature, the optimum compressor pressure ratio was defined. The results presented in Fig. 7-12, showed that turbine inlet temperature had a much stronger influence on cycle efficiency than compressor pressure ratio. The results also showed that increasing turbine inlet temperature beyond 950°C (1742°F) yielded very small improvement in cycle efficiency. This result was due partly to reduced compressor and turbine efficiencies but more especially to increased gas bleed from the compressor discharge for turbine blade cooling, to interstage seal dilution flow, and to associated leakages. Gas for cooling the actual turbine airfoils was a smaller proportion of this flow. The larger portion was used to control ingestion of hot main stream gas into the spaces around the interstage seals, and other considerable portion was taken up in gas leaking between blade roots and other openings in the cooling gas flow path. This high bleed flow would probably be reduced considerably in a program of development leading to machines employing turbine inlet temperatures at this and higher levels.

After these results were reviewed, three cycles were selected for further analysis. Two cycles were for machines with a turbine inlet temperature of 850°C (1562°F) and compressor pressure ratios of 2.5 and 2.35 respectively. The third cycle is for a machine with a turbine inlet temperature of 950°C (1742°F) and a pressure ratio of 2.5. A limited mechanical study is being performed on these cycles to determine if critical speed or thrust balance problems exist.

7.7.5. Definition of Critical Speeds

The work completed in this task consisted of generating critical speeds and mode shapes for each of the candidate configurations at 850°C (1562°F) and 950°C (1742°F). The baseline rotor frame description included welded rotor construction in both the compressor and the turbine. The effects of both weight and stiffness changes for this type of rotor were estimated and

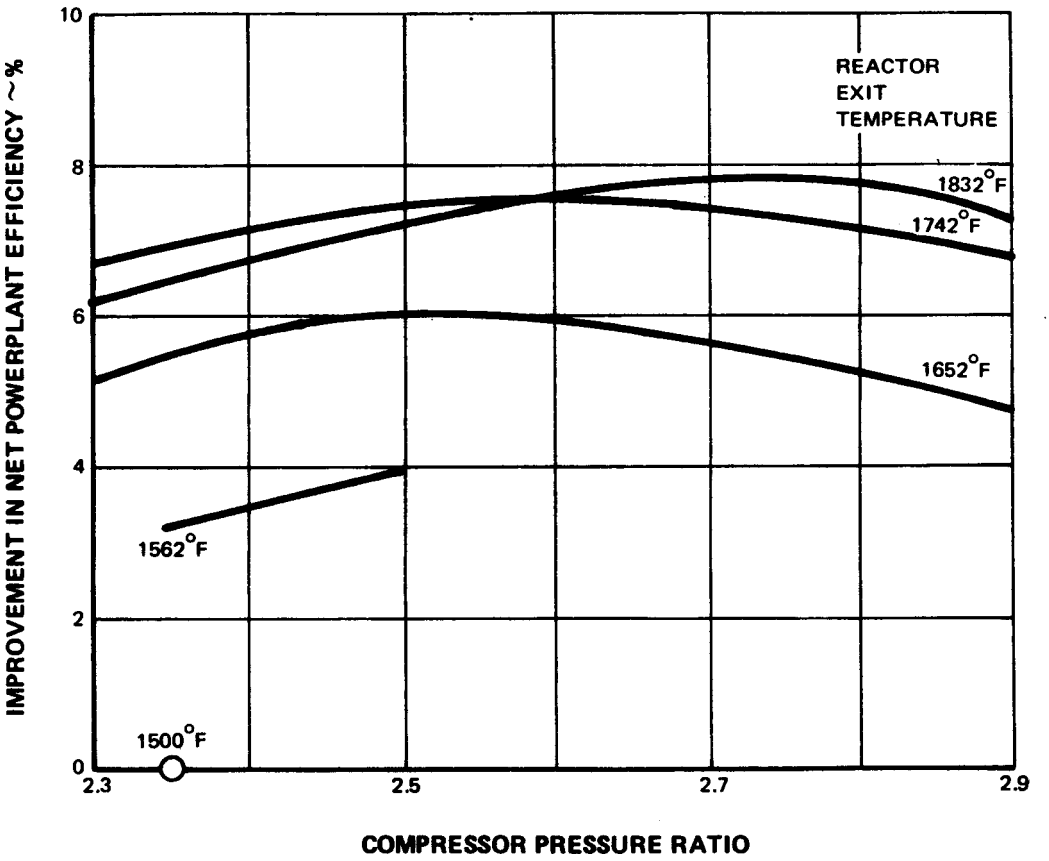

ALL MEASUREMENTS ARE IN U. S. CUSTOMARY UNITS.

GA-A13950

Fig. 7-12. Variation of improvement in power plant efficiency

included in the analyses. Some initial stiffness changes in the compressor-to-turbine shaft and the No. 3 journal bearing were made in an attempt to improve optimization of the baseline before the parametric studies were started. This was done in anticipation that some of the higher-temperature machines would have less desirable mechanical characteristics, that is, longer rotors with possibly smaller diameters. The resulting margin on a 20% overspeed for the free-free rotor bending mode was 19.5% versus an allowable 15%.

The optimized baseline design was altered for the analysis of the selected machines resulting from the cycle comparison described in Section 7.7.4. The alterations included changes in rotor length, diameter, and weight. A preliminary review of the rotor frame results shows that the 850°C (1562°F) machines at 2.35 and 2.5 pressure ratios have adequate critical speed margins (>15%) relative to the rotor bending mode. The machines at 950°C (1742°F) all appear to have less than acceptable margins. The lower modes of vibration have not been significantly affected by any changes made to date. Analyses are incomplete, and work is continuing.

7.7.6. Review of Bearing Requirements

A review of the journal bearing requirements was conducted for the cycles selected as described in Section 7.7.4. Since rotor speed is fixed, the items of major concern were bearing load and stiffness. Only limited weight data were available, and these indicated that the bearing sizes defined for the 816°C (1500°F) reference design would be adequate for the higher-temperature designs. Preliminary results from the critical speed analysis of the rotors for the higher-temperature designs indicated the need for increased stiffness in the No. 3 journal bearing. The No. 3 journal bearing stiffness was therefore increased substantially to meet this requirement.

7.7.7. Bearing and Shaft Review

The impact of the high turbine temperature cycles on shaft and bearing design was reviewed to identify any serious problems arising from the higher torques resulting from increased cycle efficiency or from anticipated weight changes. Shaft torques were found to be about 10% higher than that of the 816°C (1500°F) design, and although some splines on the output shaft are stressed higher than desired, no real problems are expected. No weight estimates have been completed, but on the basis of the welded rotor design and material changes in the turbine, it is felt that no increase in bearing size will be required and that the current bearing definition will be adequate or may even be conservative.

7.7.8. High-Temperature Study Conceptual Drawings

The design for a turbine inlet temperature of 950°C (1742°F) and a compressor pressure ratio of 2.5 has been selected from the matrix of higher turbine inlet temperature turbomachinery cycles for description by conceptual drawing. A cross-sectional view of this cycle is being prepared. The design differs from the 816°C (1500°F) reference design in several major areas. The compressor is longer because 24 stages are required at a 2.5 pressure ratio and smaller in diameter because the mass flow required to absorb 1000 MW(t) is lower. The turbine inlet duct is an insulated double-wall structure, and the rotor construction is a welded rather than a bolted design. The turbine itself is a cooled disk, blade, and vane design, and additional cooling is supplied to the disk rims and blade outer gas seals. The cross-sectional layout of this configuration will be shown in the more detailed report to be prepared for General Atomic by the subcontractor.

7.8. SHORT-RANGE R&D ITEMS

Certain items of turbomachinery technology required early in the preliminary design phase of the program have been designated as short-range R&D items. These items, for which an early test program is feasible, are:

1. Development of turbomachinery inlet and exit duct configurations giving minimum pressure losses consistent with space limitations

2. Determination of fretting and wear properties of various metal pair combinations in the high-temperature helium environment

A detailed description of these R&D items follows.

7.8.1. Turbomachinery Volute and Plenum Chamber Development

Two series of model tests are planned to assess the flow characteristics of the turbomachine inlet and exit ducts of the GT-HTGR. These tests will be done in the range of 0.1 to 0.2 scale, using air as the working fluid and an existing low-pressure compressor as the means of circulating air through the model ducts. For the first test series, the model duct will contain large segments of Plexiglas, and the emphasis will be on flow visualization to determine if there are any basic flow problems. Full-scale Mach numbers will be duplicated, but the work will be done at substantially atmospheric pressure. Smoke, tufts, and conventional pressure rakes will be used to assess the character of the flow at various points in the test loop.

For the second test series, the Plexiglas duct sections will be replaced with metal sections, the test loop will be operated in a high-pressure environment, and the emphasis will be on characterizing the flow at higher Reynolds numbers. Test data will consist principally of multiple static and total pressure measurements at selected stations in the duct so that the losses associated with inlets, discharge scrolls, and elbows can be evaluated. It is expected that a limited number of dynamic pressure measurements will

be made to assess any tendency of the duct to rumble or produce disturbances at discrete frequencies. This work is separate and distinct from the acoustic monitoring which will be done in subsequent component and prototype testing.

It is expected that any serious flow problems which are observed in the first series will lead to duct modifications which in turn will be evaluated and incorporated in the second test series. Likewise, duct elements will be further modified, as deemed necessary, in the second test series to achieve acceptable losses and flow characteristics and to define elbow, inlet, and discharge configurations which are satisfactory for use in the full-scale turbomachinery installation.

7.8.2. Materials Fretting and Wear Investigation

An essential need exists to assess material wear characteristics in helium in order to ensure that highly loaded joints such as blade/disk attachments do not deteriorate and fail prematurely due to such phenomena as spontaneous welding induced by the helium.

As a first step, the available literature pertaining to the effects of helium on candidate materials will be reviewed and potential problem areas identified. In parallel with this review, it is planned to design three test rigs for evaluating wear in a helium environment. The three rigs will be conceptually similar, each having a base with six simulated blade/disk attachment points and six dummy blades. All rigs will have provisions for loading the blades in tension, vibrating them transversely and heating them to representative temperatures in a helium atmosphere. One rig will simulate the first turbine stage, one will simulate the last turbine stage, and one will represent a typical compressor stage.

The base material in each rig will be the same as the disk which it is intended to represent. Present plans are that three of the dummy blades in each rig will be of one material and will experience three different load

levels. One other dummy blade will be of an alternate material and will experience the intermediate (nominal) load. Two additional dummy blades will be used to test a candidate coating on each of the two blade materials, at the nominal load level. It is expected that the rigs can be set up to operate unattended for extended periods of time and that each of the simulated blade/disk attachments will experience on the order of 10^8 vibratory cycles per day. The simulated blade/disk attachments will be examined periodically for evidence of wear or other form of deterioration.

This R&D item will be separate from and in addition to the ongoing longer-range investigation into the effects of the helium atmosphere on material properties.

7.8.3. Schedule of Short-Range R&D Items

A schedule for the performance of the short-range R&D items is given in Table 7-1.

7.9. CONCLUSIONS

The continued studies on turbomachinery technology show that the design of the GT-HTGR turbomachinery for the plant with 816°C (1500°F) RDT is conservative and almost completely within the current state-of-the-art. The only exception to this assessment is the thrust bearing, which can be developed through a routine test program representing a minor advance in thrust runner rim speed. The remaining bearings are within present design and manufacturing capabilities. Rigs for the testing of the bearings and seals are shown to be within the capabilities of the subcontractor's test facilities.

The studies of designs for higher turbine inlet temperatures have demonstrated that advances in plant cycle efficiency can be made by raising turbine inlet temperature and using present-day cooling and construction methods. Further studies are required to investigate the full potential of turbines with increased inlet temperature using more highly developed methods of cooling gas supply and flow control.

TABLE 7-1
MAJOR MILESTONES FOR SHORT-RANGE R&D ITEMS

Task and Milestone	Time to Milestone (months from start of development program)
1. Turbomachinery duct and volute tests	
Rig design	3
Rig and model fabrication	5
Start test	5
Complete analysis and model rework	9
Complete all tests and analysis	12
2. Materials fretting and wear properties	
Start rig design	3
Complete rig design	7
Complete rig fabrication	9
Complete testing and analysis	21

REFERENCES

7-1. "Gas Turbine HTGR Program, Semiannual Progress Report for the Period July 1, 1975 through December 31, 1975," General Atomic Report GA-A13740, January 1976.

8. CONTROL VALVE TECHNOLOGY (Task 189a, No. SU042)

8.1. INTRODUCTION

Milestone B-2 in the control valve technology studies during the past six months involved the selection of integrated valve concepts for alternative plant arrangements. The plant arrangements being evaluated are three- and four-loop variants with reactor outlet temperatures of 850°C (1562°F) and 950°C (1742°F), respectively. Detailed control studies leading to identification of valve flow areas were not carried out in this phase of the program. For valve conceptual design purposes, the previously established valve areas were retained (Ref. 8-1). The main thrust of the valve design effort was to establish a viable concept that was adaptable to three- or four-loop plant configurations and that would operate in a high-temperature helium environment. Milestone B-2 was completed with the selection of a valve concept in which the four main control valves are integrated in the PCRV structure. Each of the valves is installed in a separate cavity in the PCRV top head, and aspects of the integration such as valve location and interpipe routing were resolved for both delta (three-loop) and square (four-loop) plant arrangement.

Section 8.2 presents the control valve scheme for the GT-HTGR power plant, with the cycle conditions corresponding to the 950°C (1742°F) reactor outlet temperature case. The functions of the four valves are briefly outlined.

Sections 8.3 and 8.4 present the design conditions and requirements for the four valves. As mentioned above, the valve flow areas and opening times were assumed to be those established from previous control studies. This assumption was considered to be valid, since the valve studies were directed toward selection of a concept rather than detailed design. Minor changes to

the control requirements due to changes in the cycle conditions would not influence the selection of valve concept (i.e., linearly actuated, integrated in PCRV, etc.).

Section 8.5 presents the valve conceptual designs. Since the design of the valves is an evolutionary process, alternate approaches are discussed and the rationale for selection of the proposed concept is outlined.

Section 8.6 describes the integration of the valves in the PCRV. Since integration of the valves in cavities in the vessel is an inherent part of the basic valve design, attention here is essentially addressed to location of the valves in the PCRV. This was done in conjunction with the primary system design, since the valves and interconnecting pipes must be located such that they have a minimum impact on the PCRV design (i.e., tendon location, accessibility, etc.).

Section 8.7 presents the selected valve concepts and briefly discusses their adaptability to the alternate plant configurations.

8.2. CONTROL VALVE SCHEME

The GT-HTGR control valve scheme for the various dry-cooled and binary plant variants remains essentially the same as that established for the initial valve design study (Ref. 8-1). The main requirements of the valves in the plant control and protection system are to limit turbine overspeed and to minimize transient temperature excursions to the major components during the control mode.

As shown in the simplified control valve diagram in Fig. 8-1, the valves essentially connect the high-pressure and low-pressure parts of the primary system. With the exception of the attemperation valve, the other three valves are positioned in a medium-temperature part of the loop, and this has a significant effect on the design of the valves. The temperature shown in Fig. 8-1 are for the 950°C (1742°F) reactor outlet temperature case, since

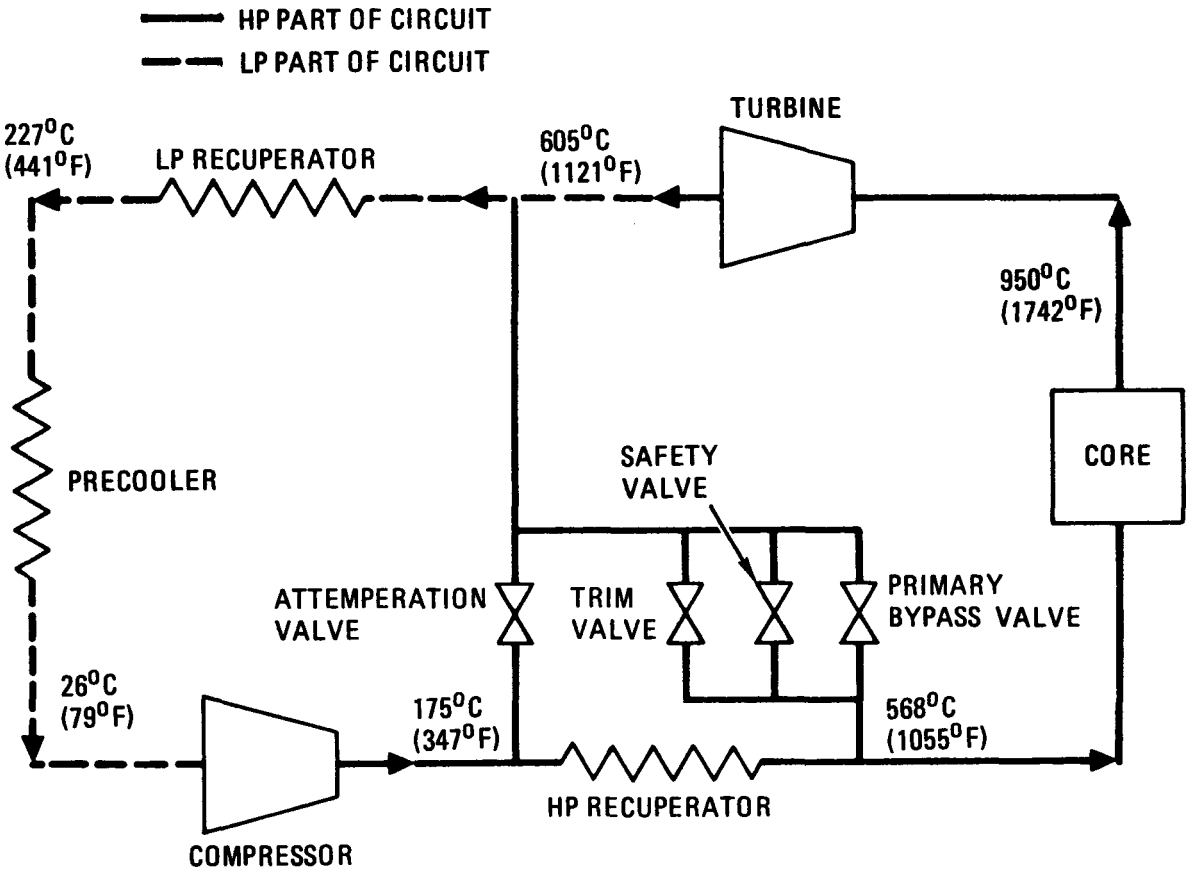

Fig. 8-1. Simplified control valve diagram (single-cycle plant)

these are considered to be the most severe steady-state operating conditions from the standpoint of valve design.

As shown in Fig. 8-1, the trim, safety, and primary bypass valves are in the medium-temperature region and connect the core inlet to the turbine exit. The attemperation valve connects the cool compressor exit to the low-pressure recuperator inlet. The primary bypass valve can be used in two modes: (1) it can be modulated by the control system for plant load control; or (2) it can be operated in a binary (open/shut) mode, if the safety valve fails to open, by a separate actuator as part of the plant protection system. The safety valve (nonmodulated) is actuated by the plant protection system and is a binary (open/shut) valve used primarily for turbine overspeed/overpressure protection. This valve cannot be used for load control purposes. The small trim valve makes fine adjustments of turbine speed and load and is of particular use when synchronizing with the electric power network. The attemperation valve is used to mix gases (compressor discharge and core inlet), thereby minimizing thermal shock to the heat exchangers and core internals.

8.3. BYPASS VALVE DESIGN CONDITIONS

The control valves are integrated in the PCRV and must operate in a dry helium environment, with a high degree of reliability for the full life of the plant. Operation at elevated temperature is considered to be the most severe of the design considerations from the standpoint of valve design. Cooling of critical parts of the valves to prevent galling, together with identification of symmetrical geometries to prevent thermal distortion, is strongly influenced by the valve operating temperature. All of the conclusions reached here for the 950°C (1742°F) reactor outlet temperature case are equally applicable to the slightly less severe design conditions associated with the 850°C (1562°F) reactor outlet temperature case. The design requirements for the four valves are briefly discussed in the following section.

8.4. BYPASS VALVE DESIGN REQUIREMENTS

The functional requirements for all four valves are listed in Table 8-1. The main effort of the last six months has been directed to identifying valve design concepts suitable for the plant with higher reactor outlet temperatures. Therefore, performances and environmental requirements have not been determined, but a good approximation of these requirements can be made from Section 9.3 of Ref. 8-1.

8.4.1. Safety Valve Design Requirements

The two functions of the safety valve are turbine overspeed protection and PCRV pressure relief. To reduce the turbine speed, the safety valve quickly opens, venting high-pressure helium to the turbine exhaust and thus rapidly reducing the turbine's expansion ratio and therefore its speed. To reduce the maximum PCRV pressure should it tend to rise above the prescribed safe limit, the safety valve opens to bypass gas from the high-pressure core inlet region to the low-pressure turbine outlet region.

The safety valve also must fail open when a high pressure differential ($\Delta P > 20$ psi) ($\Delta P > 13{,}800$ Pa) exists across the valve and must automatically fail closed or be powered closed when a low valve pressure differential exists ($\Delta P < 20$ psi) so as to prevent interference with CACS operation.

8.4.2. Primary Bypass Valve Design Requirements

The primary bypass valve, operated by a dual-mode actuation system, serves as an independent backup safety valve (see Section 8.4.1) and as a coarse control valve. In the safety mode, the safety actuator for this valve must be capable of overriding the control actuator at all times and under any conditions.

When operated by the control actuator, the primary bypass valve provides normal load and speed control for the turbine and fast-acting turbine speed control following a loss of electrical load. The valve must open

TABLE 8-1
FUNCTIONAL REQUIREMENTS FOR INDIVIDUAL BYPASS VALVE SYSTEM VALVES

All Bypass Valve System Valves	
Limiting of maximum bypass valve system flow to 120% of maximum flow through safety valve	
Control Mode	**Safety Mode**
1. Primary Bypass Valve - Control Actuator a. Normal load and speed control b. Fast-acting control of turbine speed following loss of electrical load c. Failed closed 2. Trim Valve a. Fine adjustment for normal load and speed control b. Failed closed 3. Attemperation Valve a. Minimize thermal transients b. Surge margin control c. Fail closed when $\Delta P < 20$ psi; fail open when $\Delta P > 20$ psi	1. Safety Valve a. Turbine overspeed protection b. Overpressure protection c. Fail closed when $\Delta P < 20$ psi; fail open when $\Delta P > 20$ psi 2. Primary Bypass Valve - Safety Actuator a. Backup to safety valve b. Failed closed when $\Delta P < 20$ psi; fail open when $\Delta P > 20$ psi

quickly to prevent the turbine speed from reaching the safety valve trip level and must partially reclose to return the turbine to a hot standby condition.

The valve is positioned for coarse control in order to regulate turbine power throughout the normal load range. Only 40% of the maximum flow area is utilized for normal load and speed control.

In the control mode, it is desirable, but not critical, to have the primary bypass valve fail closed to minimize the effects of valve failure on the remainder of the plant components and on CACS operation.

8.4.3. Trim Valve Design Requirements

The trim valve operates in conjunction with the primary bypass valve and provides a fine control adjustment for turbine load and speed about the operating point established by the primary bypass valve. This fine adjustment also enables the turbine to maintain synchronization with the electric power network. Because the valve operates in conjunction with the primary bypass valve, some operations will require slow, accurate positioning of the trim valve, while some will require fast, full-stroke, reversible movement.

The trim valve is designed for the same failure mode and design conditions as the primary bypass valve in the control mode.

8.4.4. Attemperation Valve Design Requirements

The main purpose of the attemperation valve is to minimize the thermal transients experienced by the remainder of the plant components. When turbine inlet temperature is increasing, the valve is opened to allow cool compressor exit gas to mix with turbine exhaust gas. A second purpose of this valve is to provide surge margin control. Opening the valve increases the compressor surge margin by reducing the compressor pressure ratio.

Another functional requirement is to limit the maximum flow through the bypass valve system from any and all combinations of open valves so as to prevent excessive pressure transients.

It is desirable, though not critical, that the attemperation valve fail open under a high pressure differential ($\Delta P > 20$ psi) to assure that transients cannot thermally shock the plant components. It is also desirable that the valve fail closed when $\Delta P < 20$ psi to minimize the possibility of degrading CACS effectiveness.

8.5. VALVE CONCEPTUAL DESIGNS

The selection of valve conceptual designs was derived largely from previously reported studies (Ref. 8-1). The main design activities were directed toward (1) operation at higher temperatures than reported previously, (2) simpler valve mechanical arrangement, (3) reduced size, and (4) adaptability to the alternate plant concepts currently being evaluated. The four valves are integrated into the PCRV. The PCRV is the primary system pressure boundary, with the pressure load being transmitted to the concrete, and serves as the valve body. The elimination of conventional valve bodies simplifies the design of the valves, reduces their weight, and substantially reduces concern about the use of hot valves. The thermal expansion problems of the valves are alleviated, and shock effects during transient operation are minimized. The integrated approach also allows the valves to be installed in separated, smaller cavities in the top head, with minimum effect on the PCRV.

In the previously established valve conceptual designs (Ref. 8-1), cool purified helium was introduced into the valve stem and ejected in the vicinity of the seat. The purpose of this small purge flow was to allow the use of a standard seating arrangement and standard materials, to reduce heat transferred to the actuator assembly, to aid in cooling the valve bonnet, and to minimize the effect of thermal gradients. Establishing a cooling scheme to satisfy all modes of operation and ensuring that thermal stresses are acceptable in the structure, valve stems, guide, and critical valve seat

area require very detailed transient thermal analyses. Such an analysis was beyond the scope of this phase of the program, which consists of the selection of a conceptual design. While recognizing the merit of transporting helium down the center of the valve stem and allowing direct impingement in the vicinity of the seat, this approach was not pursued for the conceptual design. At a later stage, when the valve geometries have been well-defined and all of the transient modes of operation are analyzed, stem and seat cooling of this type will be investigated in detail.

The valve arrangement shown in Fig. 8-2 is representative of the design approach for the four valves identified in this phase of the program. The valve is linearly actuated and embodies insulation features that will allow the assembly to reach a uniform temperature in the hot helium environment. Cool purge helium is introduced through the bonnet to minimize leakage of primary coolant along the stem and ease the upper sealing requirements. Incorporation of a self-alignment feature in the valve seats will assure more accurate seating and will minimize leakage. A simple ball joint has been incorporated into the valve stem assembly to give the valve plug rotational freedom relative to the valve stem. To ensure compatibility between the bearing surfaces and to avoid galling, etc., the materials and/or coatings must be well-matched. To eliminate the need for a separate stem guide, six small guide ribs are incorporated in the cage structure to facilitate alignment through the full stroke of the valve. In an effort to reduce the valve assembly diameter, an insulation scheme was adopted to eliminate a previously established bolted flange arrangement. This was achieved by bolting the valve cage to the thermal sleeve and welding the actuator cage to the bonnet. The pressure load on the bonnet is also eased by the reduction of the valve assembly diameter.

8.5.1. Alternative Design Concepts

The merits of the integrated valve concept having previously been established, there are several approaches to the mechanical design of the linearly actuated plug type of valve which are strongly influenced by the operating conditions. For the different plant arrangements under evaluation,

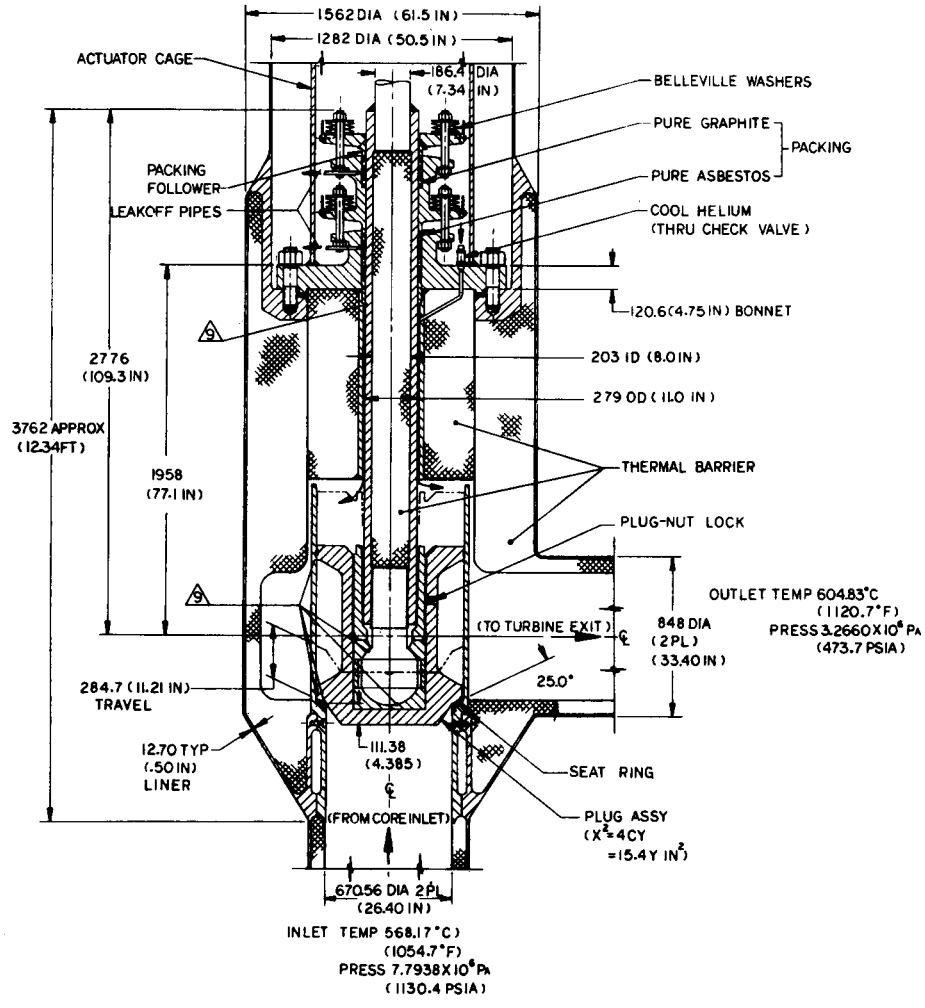

NOTES:

1. THIS VALVE PROVIDES:
   A) NORMAL LOAD AND SPEED CONTOL FOR THE TURBINE
   B) BACKUP OVERSPEED PROTECTION FOR THE TURBINE
2. VALVE FAILS OPEN UNDER HIGH PRESSURE AND FAILS CLOSED UNDER LOW PRESSURE FOR BOTH CONTROL AND SAFETY MODES
3. MINIMUM FLOW AREA = 353155 mm² (547.4 SQ IN) WHEN VALVE IS FULLY OPEN
4. DESIGN ACCORDING TO ASME CODE 1481 FOR CLASS 2 COMPONENTS
5. ACTUATION TIME 1.0 SEC FOR SAFETY MODE
6. SEAT REMOVABLE WITH CAGE
7. CAGE GUIDED AND SELF ALIGNING PLUG ASSY
8. ALL DIMENSIONS ARE IN MILLIMETERS UNLESS OTHERWISE SPECIFIED

9 HARD-SURFACED WITH NON-GALLING MATERIAL

GA-A13950

Fig. 8-2. Primary bypass valve, safety and control, integrated configuration

the most significant parameters that affect the valve design are operating temperature and pressure. Higher values of both, compared with the data used in the previous valve design (Ref. 8-1), are now being considered. Alternate mechanical arrangements were investigated in an effort to select a viable design approach for the most severe of the advanced gas turbine operating conditions. The primary bypass valve (safety and control) was selected as the base case for alternative design approaches. It was felt that the findings from this study would be generally applicable to the other three valves, since the valves essentially all embody similar overall features.

Alternative A is shown in Fig. 8-3 and embodies many of the features discussed in Section 8.5. In an effort to obtain a uniform temperature throughout the valve assembly, the bonnet was moved closer to the valve seat. This was made possible by the elimination of the stem guide and return springs (the actuator will return the plug to its seat). The thermal barrier, necessary to minimize heat conduction to the upper seals, is supported on the bonnet and retained by the actuator support. This requires an additional structural member to support the stem packing. The cage structure is essentially a rigid member. Downward axial thermal growth is accommodated by a sliding ring seal at the bottom of the valve assembly.

Alternative B in Fig. 8-3 has the bonnet located in the cool region, which eliminates the additional support structure necessary in Alternative A. The thermal barrier is located between the plug and the bonnet and is retained in position by the valve cage. Alternative B also has a sliding ring seal arrangement at the bottom of the assembly.

Because of the complexity of low-leakage ring seals capable of operating with a high pressure differential and at elevated temperature, Alternative C shown in Fig. 8-4 embodies a different approach for accommodation of thermal expansion. In this variant, the valve cage assembly is a separate structure which is bolted in position prior to installation of the valve plug body. The cage has a close tolerance fit into the thermal sleeve at the bottom of the valve cavity. The valve cage is not constrained in the vertical direction and is thus free to expand upward to accommodate thermal growth. This

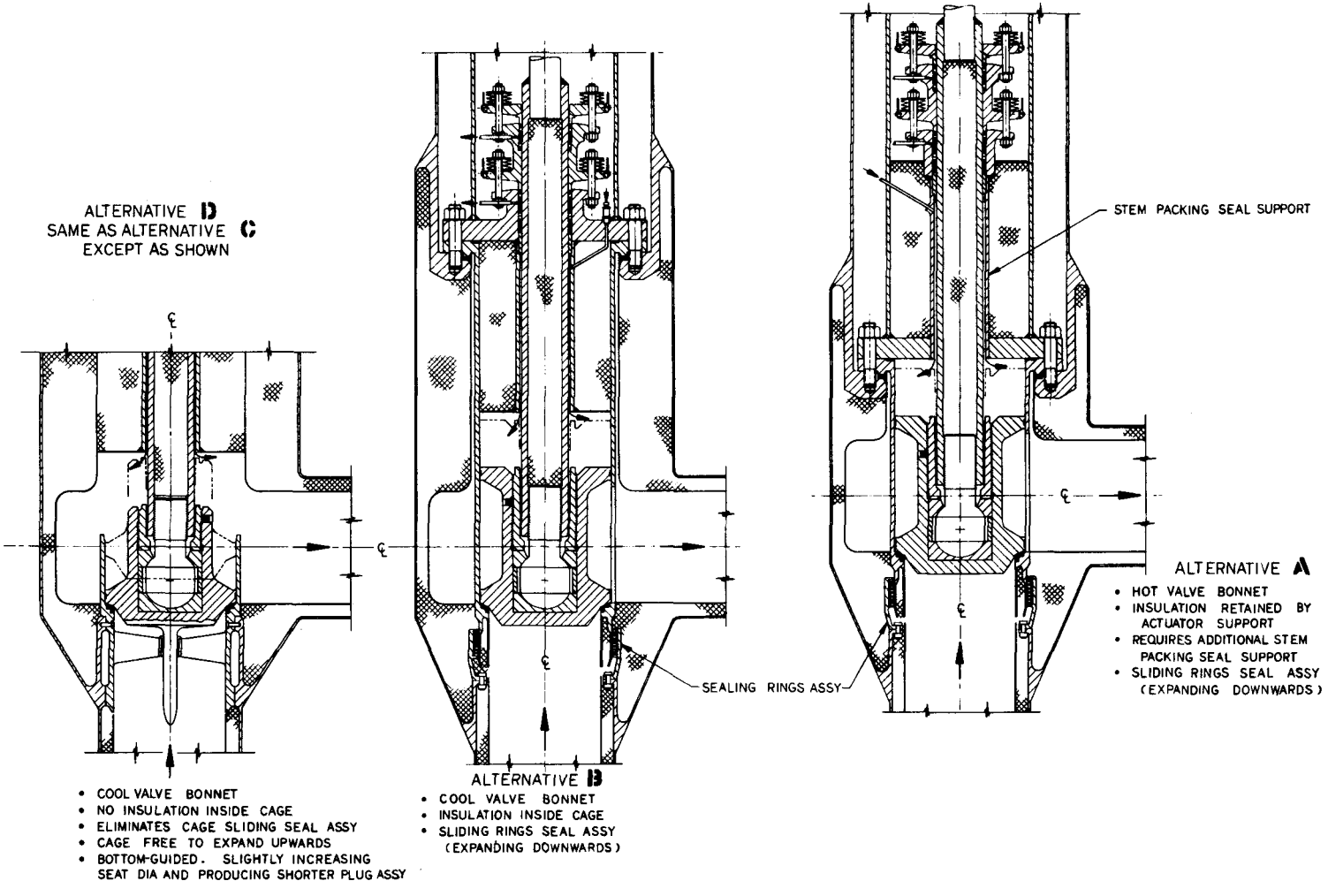

Fig. 8-3. Primary bypass valve, safety and control, design alternatives A, B, and C

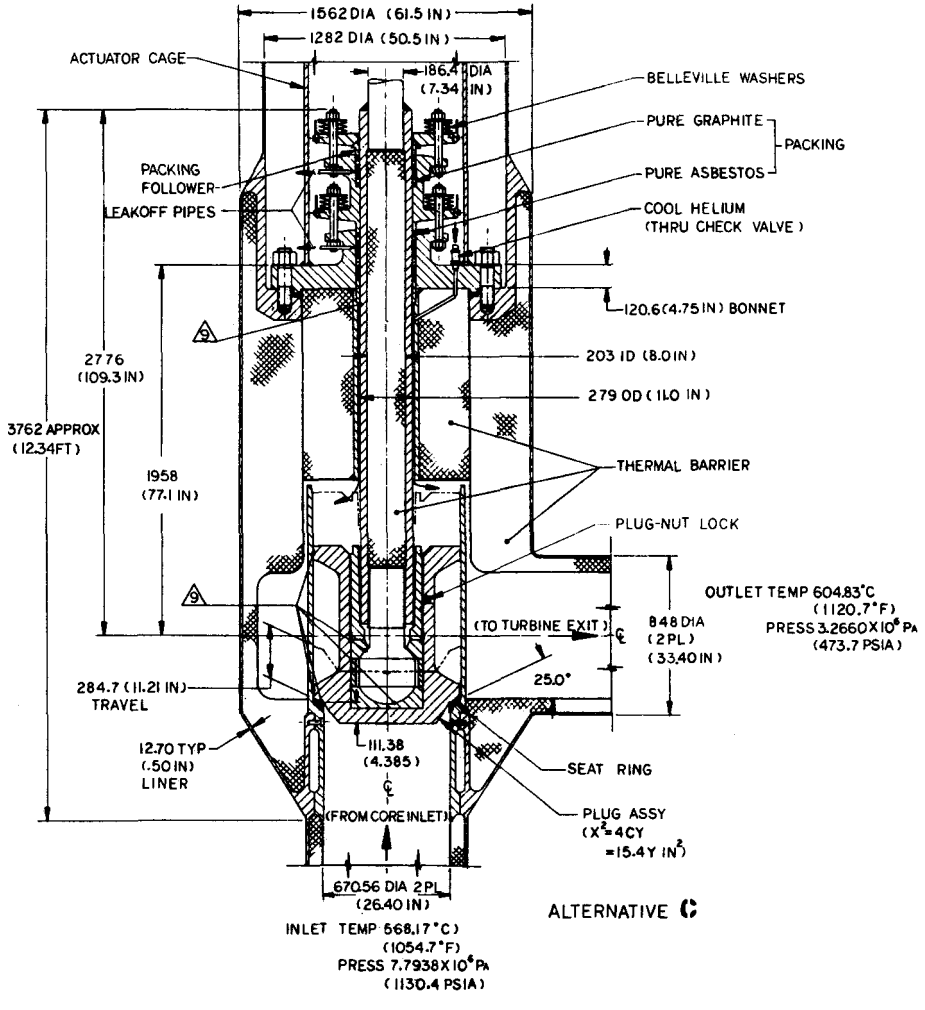

NOTES:

1. THIS VALVE PROVIDES:
   A) NORMAL LOAD AND SPEED CONTOL FOR THE TURBINE
   B) BACKUP OVERSPEED PROTECTION FOR THE TURBINE
2. VALVE FAILS OPEN UNDER HIGH PRESSURE AND FAILS CLOSED UNDER LOW PRESSURE FOR BOTH CONTROL AND SAFETY MOLES
3. MINIMUM FLOW AREA = 353155 mm² (547.4 SQ IN) WHEN VALVE IS FULLY OPEN
4. DESIGN ACCORDING TO ASME CODE 1481 FOR CLASS 2 COMPONENTS
5. ACTUATION TIME 1.0 SEC FOR SAFETY MODE
6. SEAT REMOVABLE WITH CAGE
7. CAGE GUIDED AND SELF ALIGNING PLUG ASSY
8. ALL DIMENSIONS ARE IN MILLIMETERS UNLESS OTHERWISE SPECIFIED

△9 HARD-SURFACED WITH NON-GALLING MATERIAL

GA-A13950

Fig. 8-4. Primary bypass valve, safety and control, design alternative C

arrangement obviates the need for multiple sliding ring seals. Alignment of the valve seat and stem becomes necessary because these components are in separate subassemblies, but it is felt that this can be achieved with close tolerance control on the relatively simple and symmetrical machined assemblies.

Alternative D in Fig. 8-3 is a variant of Alternative C that utilizes top and bottom guides for more positive centering of the plug and seat. The bottom guide support ribs would be aerodynamically designed to minimize pressure loss. The cage is shorter and stronger but more complex than that of Alternative C.

The conceptual design studies led to the conclusion that Alternatives B and C were viable solutions that satisfied both the control and safety and the integration criteria. The decision as to which variant should be selected and applied to the other three valves was centered around the method for accommodating thermal expansion. From the standpoint of a unitized valve assembly with the seat and valve plug being integrated in the same structure, the sliding ring seal concept (Alternative B) has merit. Because this multiple piston ring seal assembly must take the full system pressure differential and must have very low leakage for the full life of the plant, a considerable design effort is needed to identify its geometry and main features. The bolted-in-place cage concept (Alternative C) eliminates the seal leakage problem but, in turn, requires an additional subassembly that must be installed in the vessel cavity and also requires close tolerance for alignment. Because of the uncertainty of the multiple sliding ring seal arrangement, Alternative C was selected in this phase of the program. This does not exclude Alternative B from further contention; indeed, when the cycle conditions and plant configuration have been selected and more detailed valve design efforts are initiated, in-depth studies of thermal growth accommodation will be carried out.

8.5.2. Safety Valve Design

The safety valve shown in Fig. 8-5 is designed to meet the requirements of Section 8.4.1. The valve plug is shaped to give a quick opening characteristic. The normally closed valve actuator is assisted in opening by the

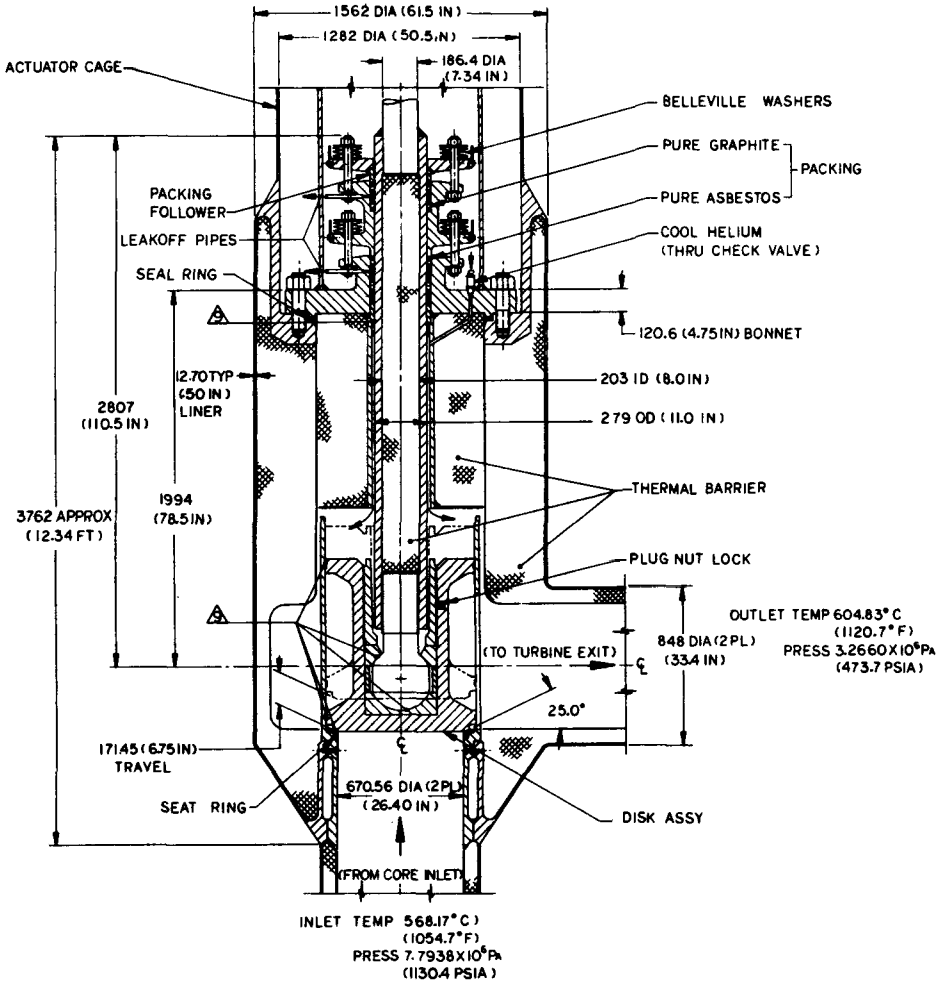

NOTICE:

1. THIS VALVE PROVIDES TURBINE OVERSPEED AND PCRV OVERPRESSURE PROTECTION
2. VALVE FAILS OPEN UNDER HIGH PRESSURE AND FAILS CLOSED UNDER LOW PRESSURE
3. MINIMUM FLOW AREA = 353155 mm^2 (547.4 SQ IN) WHEN VALVE IS FULLY OPEN
4. DESIGN ACCORDING TO ASME CODE CASE 1481 FOR CLASS 2 COMPONENTS
5. ACTUATION TIME 1.0 SEC
6. SEAT REMOVABLE WITH CAGE
7. CAGE GUIDED AND SELF ALIGNING DISK ASSY
8. ALL DIMENSIONS ARE IN MILLIMETERS UNLESS OTHERWISE SPECIFIED

A HARD-SURFACED WITH NON-GALLING MATERIAL

GA-A13950

Fig. 8-5. Safety valve, binary, integrated configuration, bypass valve system

the high-pressure helium below the seat. The actuator recloses the valve on command. The safety valve is designed, in general, as a Class 2 component in accordance with the ASME Boiler and Pressure Vessel Code, Code Case 1481, for elevated-temperature service of Class 2 and 3 components.

8.5.3. Primary Bypass Valve Design

The primary bypass valve shown in Fig. 8-2 is designed to meet the requirements of Section 8.4.2. When the plant is operating at design conditions, the valve is closed with high-pressure helium below the seat and low-pressure helium above the seat. When off-design plant performance is encountered, the valve is opened upward to provide adjustment of bypass flow for turbine control.

In the safety mode, the valve is controlled by a separate overriding actuator. The primary bypass valve must open fully from any position quickly. The pressure differential across the valve will open the valve in case of actuator failure. The valve must also return to the control position quickly. The plug is shaped to give approximately an equal percentage flow characteristic for the first 40% of the stroke in order to satisfy the normal load and speed control requirements. The remainder of the plug is truncated to give the maximum flow area with minimum additional stroke.

The primary bypass valve is designed, in general, as a Class 2 component in accordance with the ASME Boiler and Pressure Vessel Code, Code Case 1481.

8.5.4. Trim Valve Design

The trim valve used for fine control adjustments is shown in Fig. 8-6. It is designed to meet the requirements of Section 8.4.3. This valve opens upward, with high-pressure helium below the seat and lower-pressure helium above the seat. In the event of actuator failure, the valve will open, assisted by this pressure differential. The plug is contoured to give approximately an equal percentage flow characteristics. It has a flow area

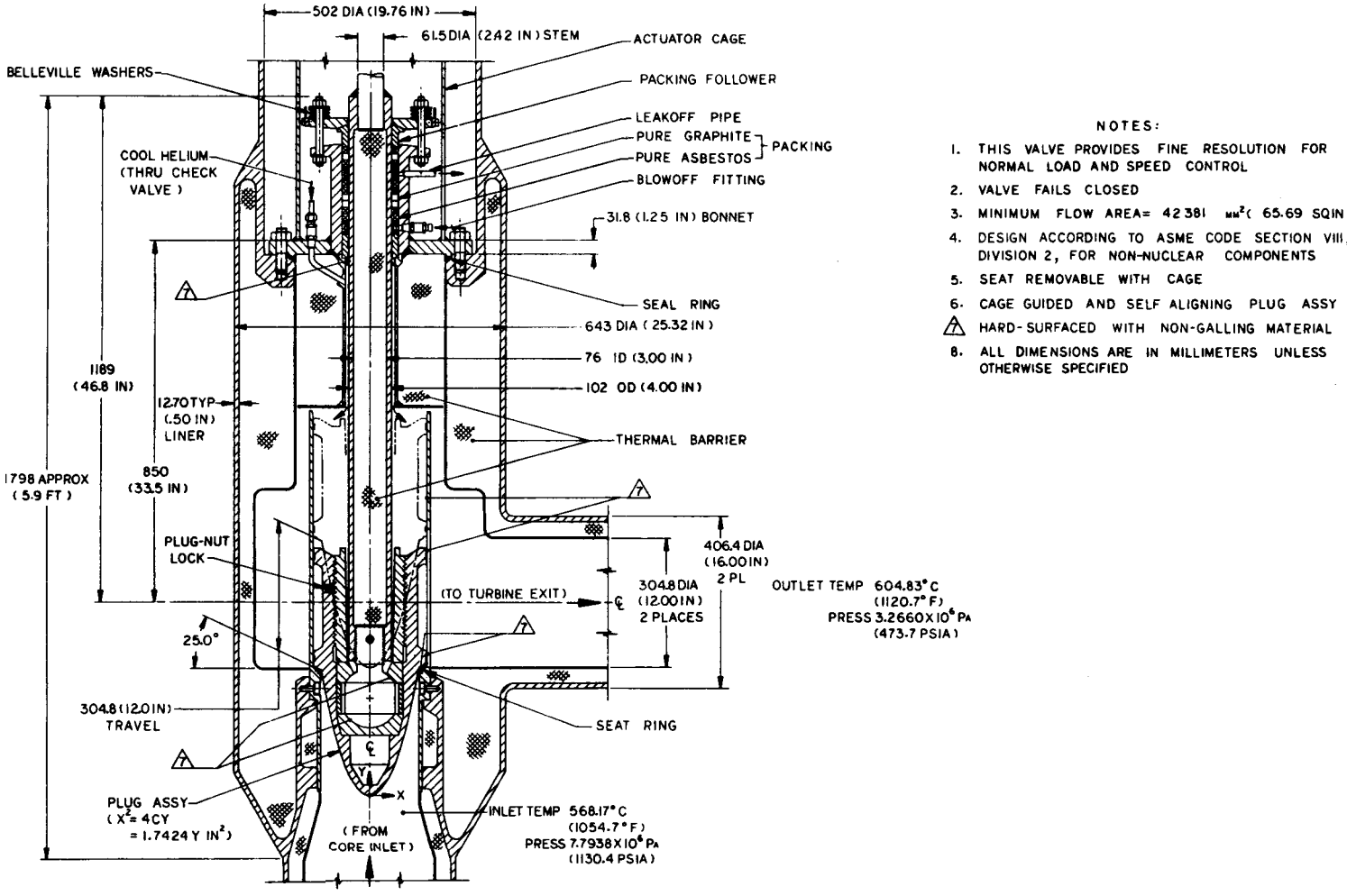

NOTES:

1. THIS VALVE PROVIDES FINE RESOLUTION FOR NORMAL LOAD AND SPEED CONTROL
2. VALVE FAILS CLOSED
3. MINIMUM FLOW AREA= 42381 MM² (65.69 SQIN)
4. DESIGN ACCORDING TO ASME CODE SECTION VIII, DIVISION 2, FOR NON-NUCLEAR COMPONENTS
5. SEAT REMOVABLE WITH CAGE
6. CAGE GUIDED AND SELF ALIGNING PLUG ASSY
7. HARD-SURFACED WITH NON-GALLING MATERIAL
8. ALL DIMENSIONS ARE IN MILLIMETERS UNLESS OTHERWISE SPECIFIED

GA-A13950

Fig. 8-6. Trim valve, integrated configuration, bypass valve system

resolution of ±0.04% of the maximum primary bypass valve flow area, with a position accuracy of ±1.02 mm (±0.04 in.).

8.5.5. Attemperation Valve Design

Shown in Fig. 8-7 is the attemperation valve. It is designed to meet the requirements of Section 8.4.4. The attemperation valve is larger than the trim valve but identical in physical design. The seat and plug diameters give the required flow areas. The plug is shaped to give approximately an equal percentage flow characteristic. A flow area resolution of ±0.02% of the maximum flow area is obtained with a position accuracy of ±0.76 mm (±0.03 in.). Even though the attemperation valve's physical design is identifal with that of the trim valve, its material requirements are quite different because of the lower temperature environment. The attemperation valve is designed, in general, in accordance with the ASME Boiler and Pressure Vessel Code, Section VIII, Division 2, for nonnuclear components.

8.5.6. Valve Assembly Details

During the conceptual design stage, one of the ground rules observed was to maintain simplicity of valve design consistent with satisfying all of the control and safety requirements. While it is obviously premature at this stage to initiate detailed design work on the control valves, fabrication and assembly considerations must be included in the conceptual phase to ensure that the selected approach is viable. For a representative control valve assembly (of the type selected and described in previous sections), a layout of the various subassemblies was prepared as shown in Fig. 8-8. This figure shows the simplicity of the integrated valve concept. The various subassemblies can be readily machined and fabricated using standard industry procedures. The structure is generally symmetrical, and large changes in section have been avoided to ensure thermal inertia compatibility and thus give uniform heating and avoid thermal stresses. The valve can be quickly assembled and economically tested prior to installation in the PCRV. If necessary, minor changes in the valve geometry can be provided to satisfy slight changes in the control mode that might show up during development testing.

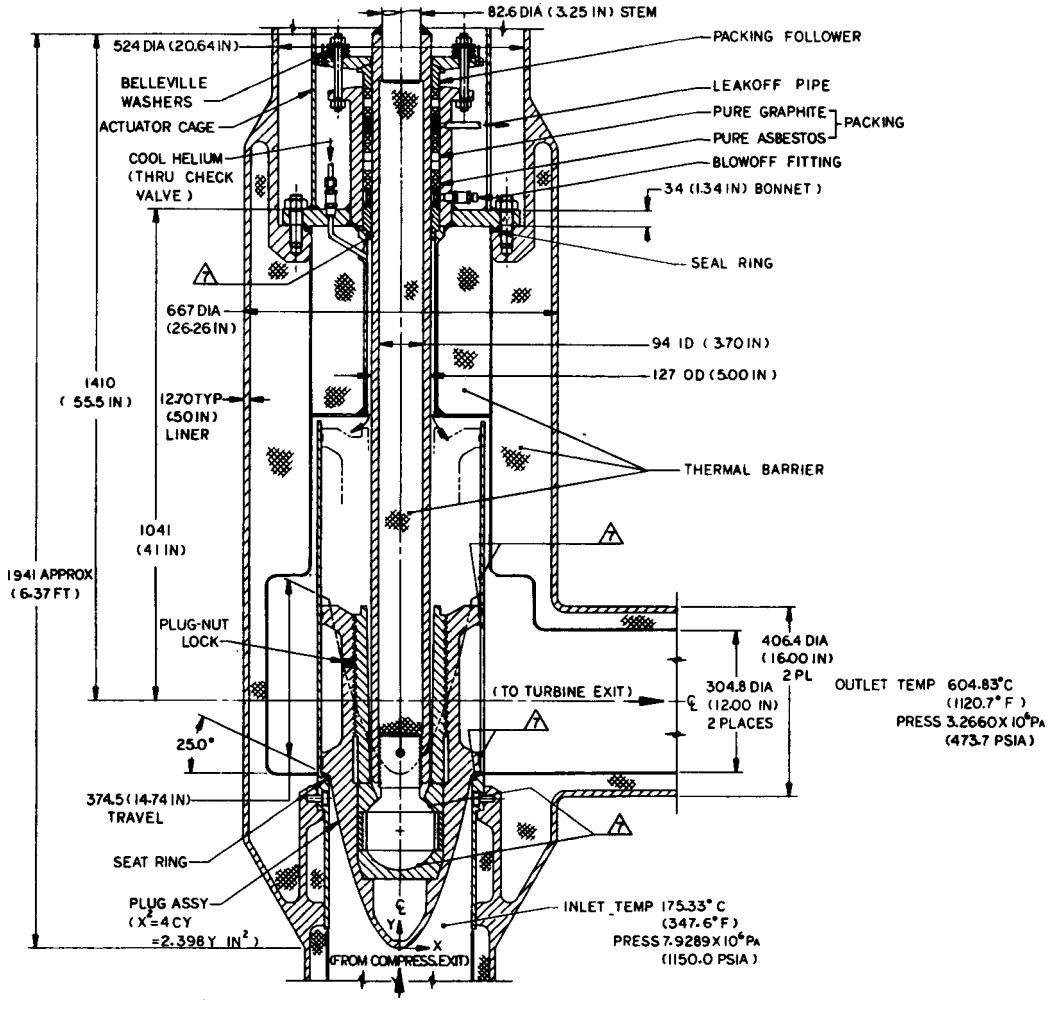

NOTES:

1. THIS VALVE: A) MINIMIZES THERMAL TRANSIENTS SEEN BY PLANT COMPONENTS
   B) PROVIDES COMPRESSOR SURGE MARGIN PROTECTION
2. VALVE FAILS OPEN UNDER HIGH PRESSURE AND FAILS CLOSED UNDER LOW PRESSURE
3. MINIMUM FLOW AREA = 72 966 mm^2 (113.1 SQ IN) WHEN VALVE IS FULLY OPEN
4. DESIGN ACCORDING TO ASME CODE SECTION VIII, DIVISION 2, FOR NON NUCLEAR COMPONENTS
5. SEAT REMOVABLE WITH CAGE
6. CAGE GUIDED AND SELF ALIGNING PLUG ASSY
7. HARD-SURFACED WITH NON-GALLING MATERIAL
8. ALL DIMENSIONS ARE IN MILLIMETERS UNLESS OTHERWISE SPECIFIED

GA-A13950

Fig. 8-7. Attemperation valve, integrated configuration, bypass valve system

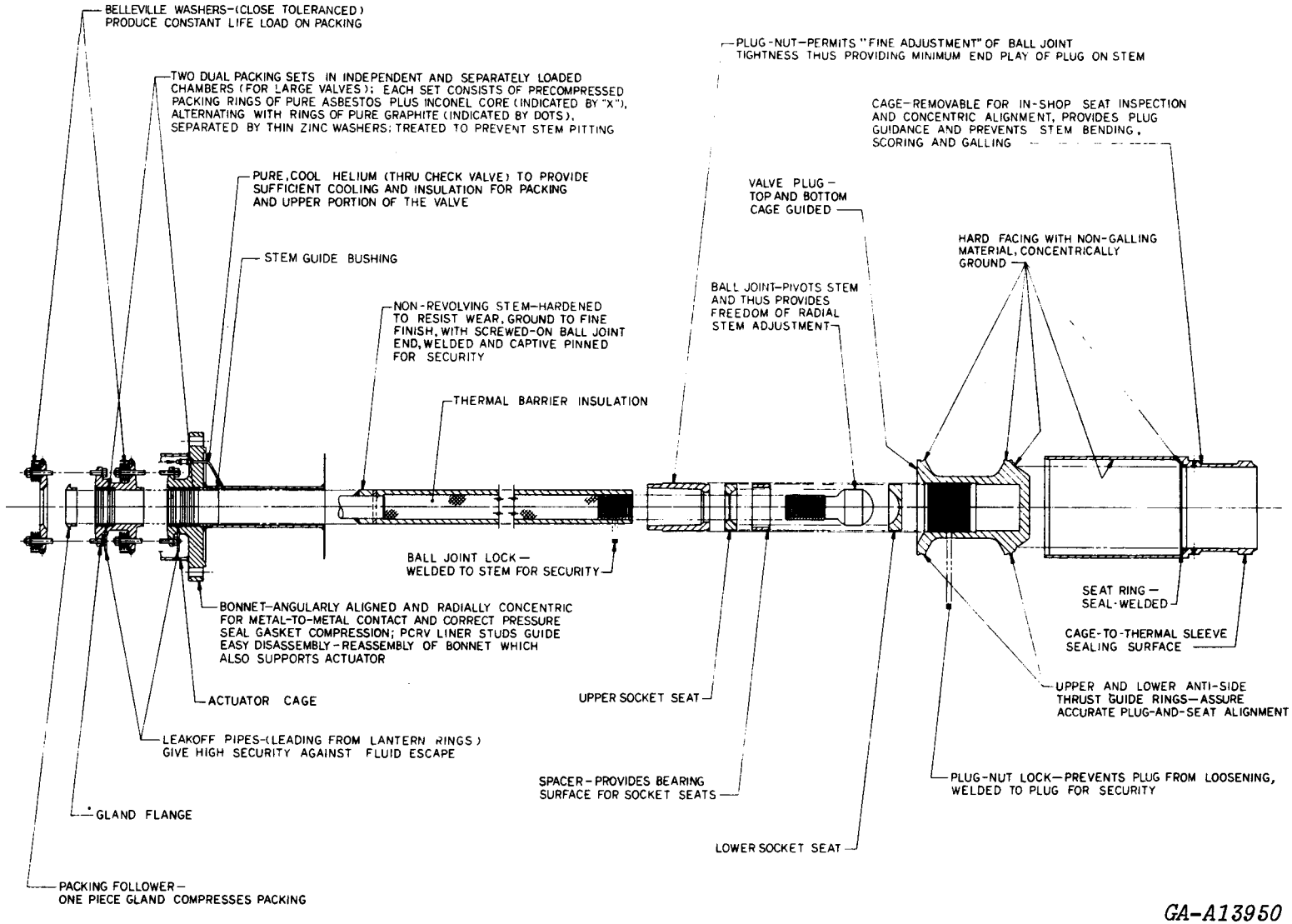

Fig. 8-8. Exploded view of typical integrated valve concept for GT-HTGR

The exploded subassembly layout was useful in (1) establishing an assembly sequence, (2) identifying areas where close tolerance control is necessary (3) identifying material interfaces (where coatings may be required to prevent galling), and (4) ensuring that fabrication and maching were feasible, a point often overlooked in the conceptual design stage. It is concluded that the selected conceptual design approaches for the four valves are feasible, satisfy the control and safety requirements, and are basically simple. The basic simplicity of the approaches is important from the standpoint of reliability and availability. With further analysis and design, the view shown in Fig. 8-8 will clearly reflect more design definition, but, at this stage, the concept is considered to be basically simple from the fabrication, assembly, testing, and installation standpoints.

8.6. INTEGRATION OF VALVES IN PCRV

Since the selected valve approach embodies an integrated concept in which the PCRV itself acts as the pressure boundary for the valve assemblies, the integration of the valves in the PCRV essentially consisted of an installation study. The design criteria for installation of the four valves in the PCRV top head were as follows:

1. Installation within defined PCRV dimensions

2. Valve accessibility for inspection and maintenance

3. Simple internal duct routing for minimum pressure loss and gas mixing, as appropriate

4. Minimum impact on tendon layout

5. Installation concept applicable to alternate plant variants currently being studied

As outlined below, the valve conceptual designs were fully integrated for both four-loop and three-loop PCRV arrangements.

8.6.1. Valve Integration in Four-Loop (Square) PCRV

As shown in the plan view of the four-loop PCRV, the four valves are installed in separate cavities, their positions being defined in Fig. 8-9. In the elevation view (Fig. 8-10), the valves are located in the top head of the vessel for ease of access for inspection and repair. The routing of the valve interconnecting ducts is in accordance with the control valve scheme in Fig. 8-1. The main task of the installation study was to determine the internal gas flow paths to avoid interference with the previously determined tendon layout. As shown in Figs. 8-9 and 8-10, the high-pressure core inlet gas is routed through the primary bypass valve, the safety valve, and the trim valve to a vertical duct that transports the bypass helium into the turbomachine cavity in the vicinity of the turbine exit. High-pressure, cooler helium from the compressor discharge is routed via the attemperation valve into the same vertical duct. The length of this vertical duct is such that good mixing of the two gas streams should take place before the bypass dump into the turbine discharge, thus minimizing recuperator thermal stresses during the control mode.

The positioning of the valves and the bypass flow ducts in the four-loop PCRV necessitated strong interaction with the PCRV layout studies. Valve installation locations were established to avoid intersection with the critically located vertical tendons directly adjacent to the cavities. While an obvious goal in the layout studies was to minimize the length of the interconnecting valve gas flow paths, the actual geometry of the initial ducts was essentially dictated by the complex tendon pattern. In the initial installation layout shown in Fig. 8-9, the four valves (per loop) were integrated in the PCRV without interference to the major components and the vessel internal structural elements. Continuing installation layout studies are planned to identify the optimum valve locations and bypass flow ducting geometries.

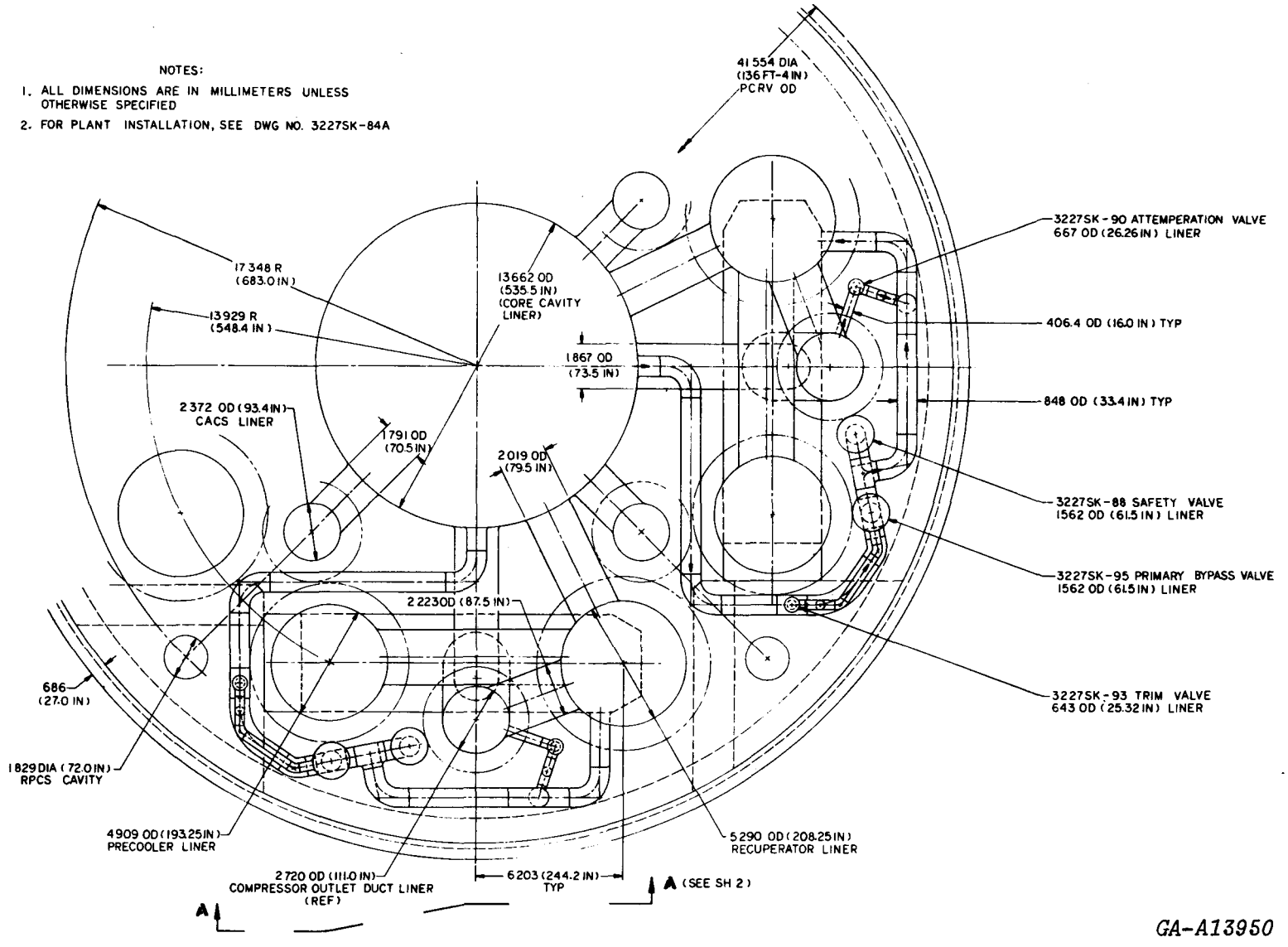

Fig. 8-9. Installation of bypass valve system valves in square PCRV (four-loop, 4000-MW, dry-cooled)

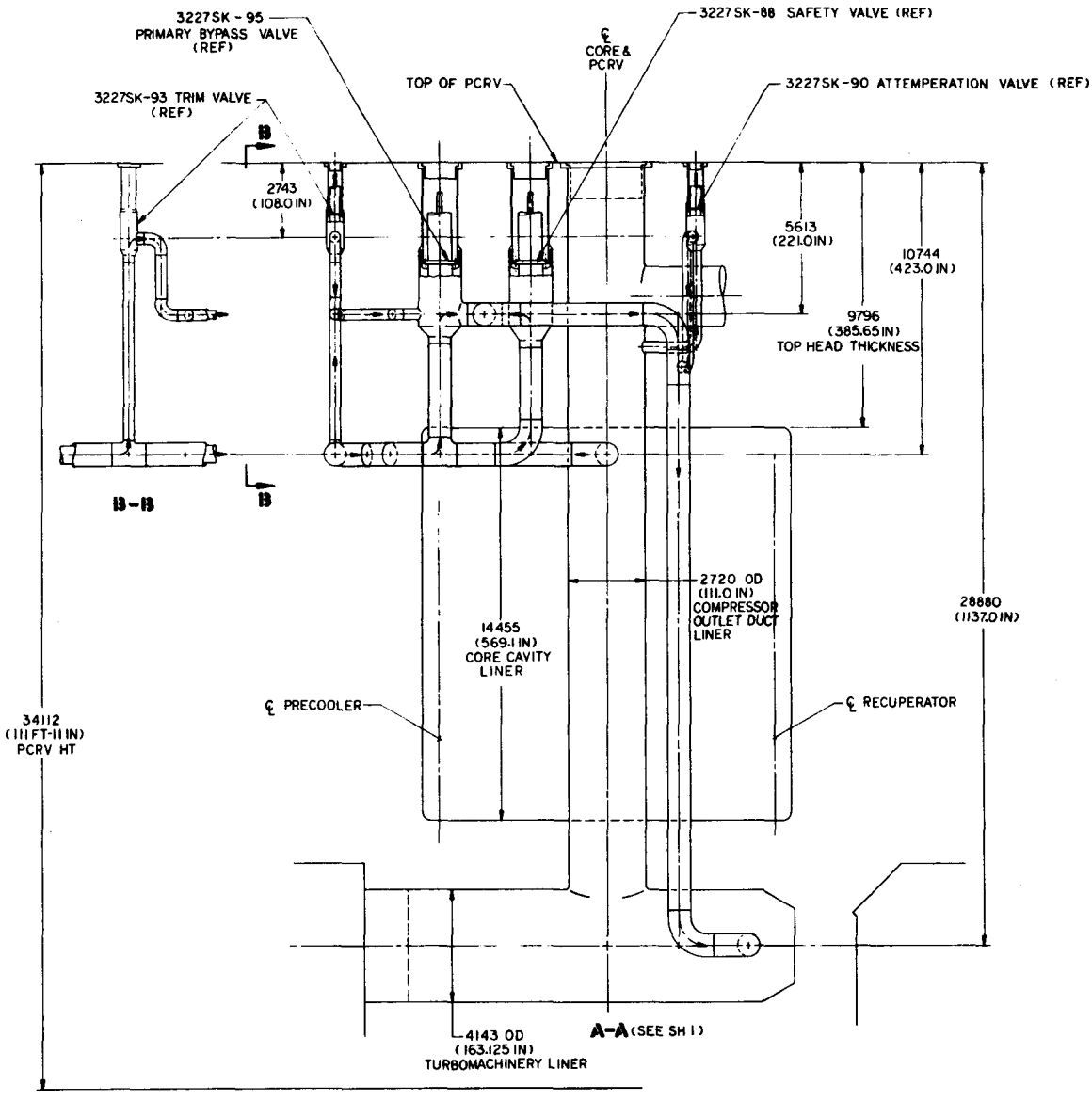

GA-A13950

Fig. 8-10. Installation of bypass valve system valves in square PCRV (four-loop, 4000-MW, dry-cooled)

8.6.2. Valve Integration in Three-Loop (Delta) PCRV

A similar valve installation study was completed for a representative three-loop primary system. The positioning of the valves for the delta PCRV is shown in Figs. 8-11 and 8-12. The layout studies followed those outlined above for the four-loop variant in that the internal bypass gas flow paths were routed within the vessel to satisfy control requirements and to have a minimum impact on structural aspects of the vessel. While the physical locations of the gas takeoff points are slightly different from those of the four-loop variant, all of the installation and integration criteria were met. The positioning of the valves in the three-loop PCRV was achieved without interference to the major component cavities and tendon layout.

8.7. INTEGRATED VALVE CONCEPTUAL DESIGN

Following the decision to adopt a fully integrated control valve configuration for the GT-HTGR (Ref. 8-1), this six-month phase of the program led to the selection of a valve concept which (1) would operate in a high-temperature helium environment, (2) had simpler mechanical features than previously identified, (3) had reduced size, and (4) was readily capable of integration in four-loop and three-loop primary systems.

The selected valve concept is applicable to the various plant configurations currently being studied (i.e., dry-cooled and binary plant, etc.). The 950°C (1742°F) reactor outlet temperature case was selected because it represented the most severe condition from the standpoint of the control valves. At 850°C (1562°F) the same valve configuration would be recommended, the lower temperature easing some of the thermal problems. When a plant configuration has been selected and the operating conditions better defined, more detailed design work on the control valves, of the type described in this report, will be carried out.

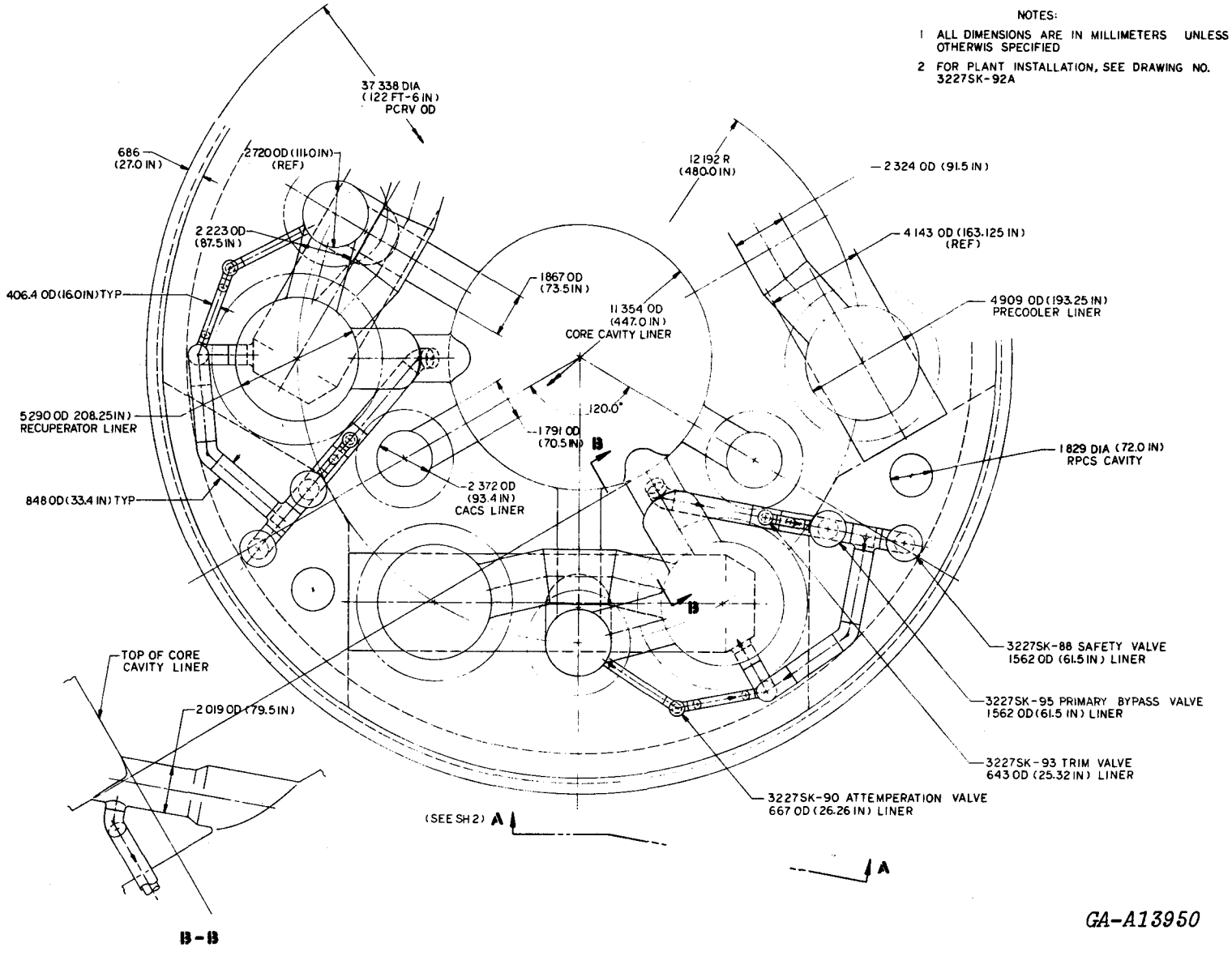

Fig. 8-11. Installation of bypass valve system valves in delta PCRV (three-loop, 3000-MW, dry-cooled)

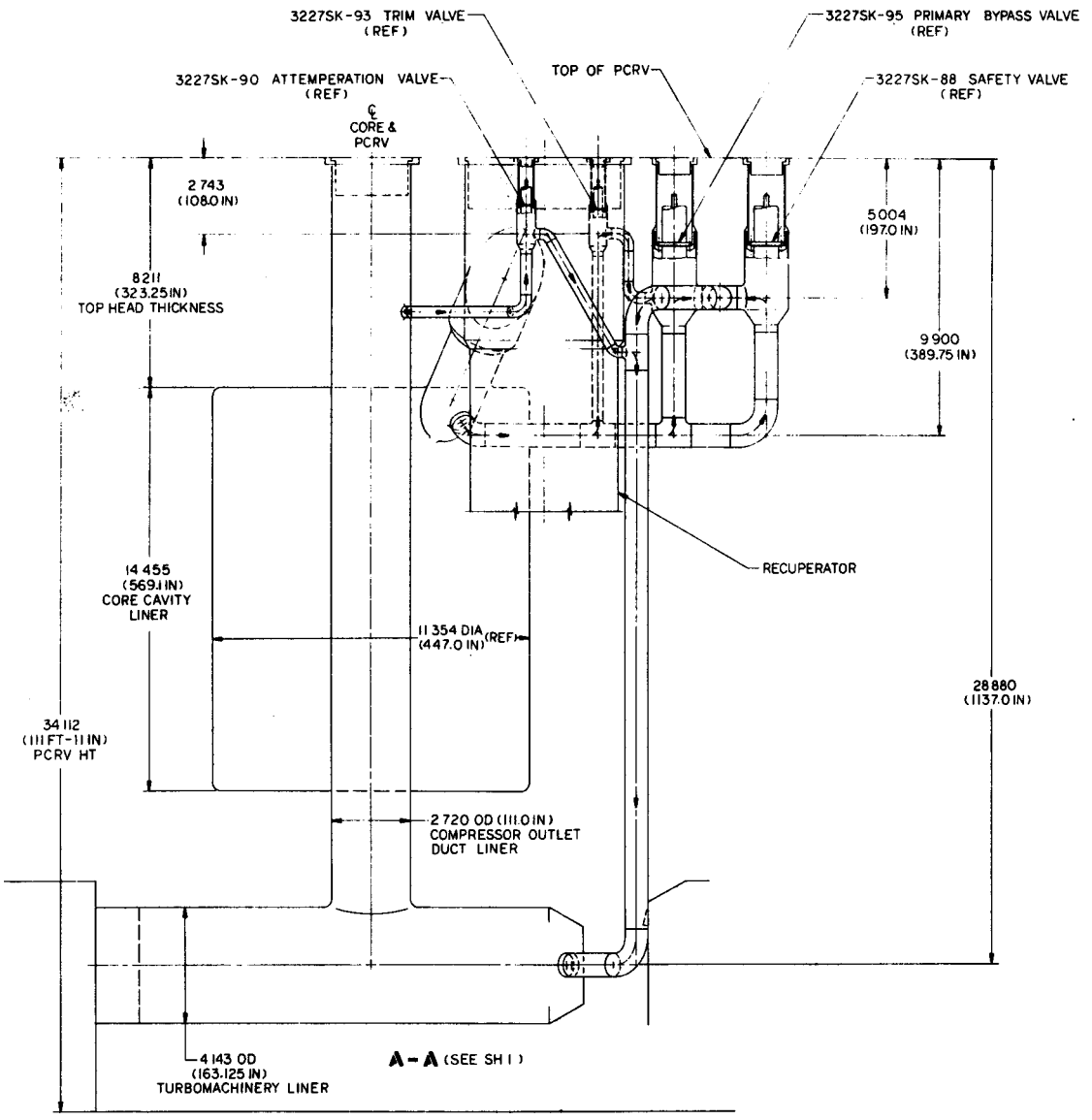

GA-A13950

Fig. 8-12. Installation of bypass valve system valves in delta PCRV (three-loop, 3000-MW, dry-cooled)

REFERENCES

8-1. "Gas Turbine HTGR Program, Semiannual Progress Report for the Period July 1, 1975 through December 31, 1975, General Atomic Report GA-A13740, January 1976.

9. HEAT EXCHANGER TECHNOLOGY (Task 189a, No. SU043)

9.1. INTRODUCTION

Milestone A was met with a document giving details of the heat exchanger base case designs for the referencee plant with a reactor outlet temperature of 816°C (1500°F). Milestone B-1 in the heat exchanger technology studies during the past six months involved the selection of integrated heat exchanger design concepts for alternative plant arrangements. The plant arrangements being evaluated are three- and four-loop variants (both dry-cooled and binary-cycle plant) with reactor outlet temperatures of 850°C (1562°F) and 950°C (1742°F). While a primary system loop rating of 1000 MW(t) was considered for the bulk of the heat exchanger design effort, the influence of varying loop size is briefly discussed. Milestone B-1 was satisfied with the selection of a heat exchanger concept with much improved packing efficiency. Retaining still the tubular, straight-tube counterflow configuration, a contiguous hexagonal array of modules was established which permitted a significant reduction in overall heat exchanger diameter to be realized without penalizing the performance. The selected design approaches for the recuperator and the precooler are adaptable to both dry-cooled and binary-cycle plant variants and have been integrated in the delta (three-loop and square (four-loop) plant configurations.

Section 9.2 presents the heat exchanger designs for the dry-cooled plant. Included in this section are the heat exchanger operating parameters and thermal requirements established from the plant optimization studies.

Section 9.3 presents the heat exchanger designs for the binary-cycle plant. The recuperator bears a close similarity to that for the dry-cooled single-cycle plant; but, for the precooler, the different thermodynamic and

heat transport properties of ammonia had an influence on the surface area requirements and the heat exchanger size.

Section 9.4 presents mechanical design aspects of the selected heat exchanger concept. Included are the much improved headering approach and module packing optimization which facilitated the reduction in heat exchanger diameter mentioned above.

Section 9.5 presents the recuperator and precooler conceptual designs selected for the advanced GT-HTGR plant. Alternate configurations considered during this phase of the program are also briefly discussed.

Section 9.6 presents the integration of the heat exchangers in the PCRV, and details are given for both the delta (three-loop) and square (four-loop) primary system layouts.

Section 9.7 presents the selected heat exchanger concepts and briefly discusses their adaptability to the alternate plant concepts.

9.2. HEAT EXCHANGER STUDIES FOR 4000-MW(t) DRY-COOLED PLANT

During this reporting period, parametric thermal size studies on the recuperator and the precooler were completed for the 950°C ROT, 4000-MW(t), dry-cooled, GT-HTGR plant. In addition, nonoptimized recuperator and precooler thermal designs were developed in support of configuration studies carried out on the 850°C ROT variant of the dry-cooled plant. The design considerations influencing this effort are discussed in the following sections.

9.2.1. Recuperator Design Considerations

The purpose of the recuperator is to reduce the reactor thermal input by recovering waste heat from the turbine exhaust helium and transferring it back into the compressor discharge helium prior to its entry into the

core. Although the recuperator is characterized by its large surface area requirement, it does not form a boundary between dissimilar fluids or between separable coolant fluid loops; thus, the consequences of small internal leaks within the recuperator can be tolerated. The overall arrangement of the recuperator assumed for these studies is based on the approaches developed and confirmed by previous studies, vis., vertically oriented, top-supported modular assembly based on a plain tubular surface geometry and configured to provide counterflow heat transfer between the high-pressure helium flowing inside the tubes and the low-pressure helium flowing outside the tubes. In addition, the designs discussed below are based on stress levels as specified in Section VIII of the ASME Code commensurate with the 280,000-hr service life associated with plant operation for 40 yr at 80% availability.

9.2.1.1. Influence of Operating Conditions. The recuperator sizing for both the 950°C ROT and the 850°C ROT cases was based on operating conditions developed from the system optimization studies discussed in Section 2.4. When compared on an equivalent loop rating basis [1000 MW(t) per loop], it is seen that the recuperator surface requirements for the current cases are comparable with those of the previous reference design, because the higher effectivenesses required in the new operating conditions tend to offset the lower mass flows. While the combinations of high effectiveness and low pressure loss create surface area requirements for the recuperator designs that are far in excess of those of steam generators for contemporary nuclear power plants, the pressure and temperature levels in the recuperator are relatively modest by comparison and offer more design latitude for utilizing less expensive alloys in thinner gages. In the 850°C ROT case, the maximum metal temperature in the heat transfer matrix is on the order of 520°F (968°F), and it is possible to utilize ferritic 2-1/4 Cr - 1 Mo alloy for all parts except for the hot end of the unit, where the subheadering lead tubes and central return duct assembly designs call for an austenitic Type 316 stainless steel alloy. In the 950°C ROT case, the maximum metal temperature of approximately 582°C (1080°F), in conjunction with the higher working pressures, necessitates the use of austenitic stainless steel for the tubular subcomponent, the domed support plate being a ferritic forging.

9.2.1.2. Thermal Requirements. Recuperator thermal design data for the four-loop case of the 950°C ROT and 850°C ROT Plant variants are presented in Figs. 9-1 and 9-2, respectively. In both cases, it can be seen that the required heat transfer rates are very large, such that the magnitude of the internal energy transfer within the cycle for the four recuperators is on the same order as the reactor thermal input. An excess surface area allowance of 10% also was adopted in the thermal size studies as a contingency to cover analytical uncertainties.

9.2.1.3. Effect of Loop Rating. The loop thermal rating selection has a direct influence on the size of the recuperator. In previous design studies based on a 3000-MW(t) reactor, it would found that the size of the recuperator that was needed to meet the performance requirements of a 1000-MW(t) loop rating was close to transportation limits. Thus, for the current studies, it was postulated that loop ratings in excess of 1000 MW(t) per loop would entail special recuperator design considerations for physical size limitations. Since there are considerable uncertainties and little published data about practical upper limits on the diameter, length, and weight of factory-assembled heat exchangers, it was necessary to assume arbitrary constraints during these studies on the basis of the best information available at the time.

From the standpoint of state-of-the-art transportation of large heat exchangers, upper limits of 5.49 m (18 ft), 22.9 m (75 ft), and 544,000 kg (600 ton) (consistent with current Schnabel railcar payload statistics) on recuperator diameter, length, and weight, respectively, were established as being consistent with current large steam generator shipping endeavors. Design solutions in excess of these values were considered to require site assembly with its attendant cost penalties.

From the standpoint of fabrication, the recuperator diameter also can be governed by the size of the top torispherical support plate forging. An upper limit of 6.1 m (20 ft) was considered to be the maximum forging capability of U. S. manufacturers for this type of forging shape and weight.

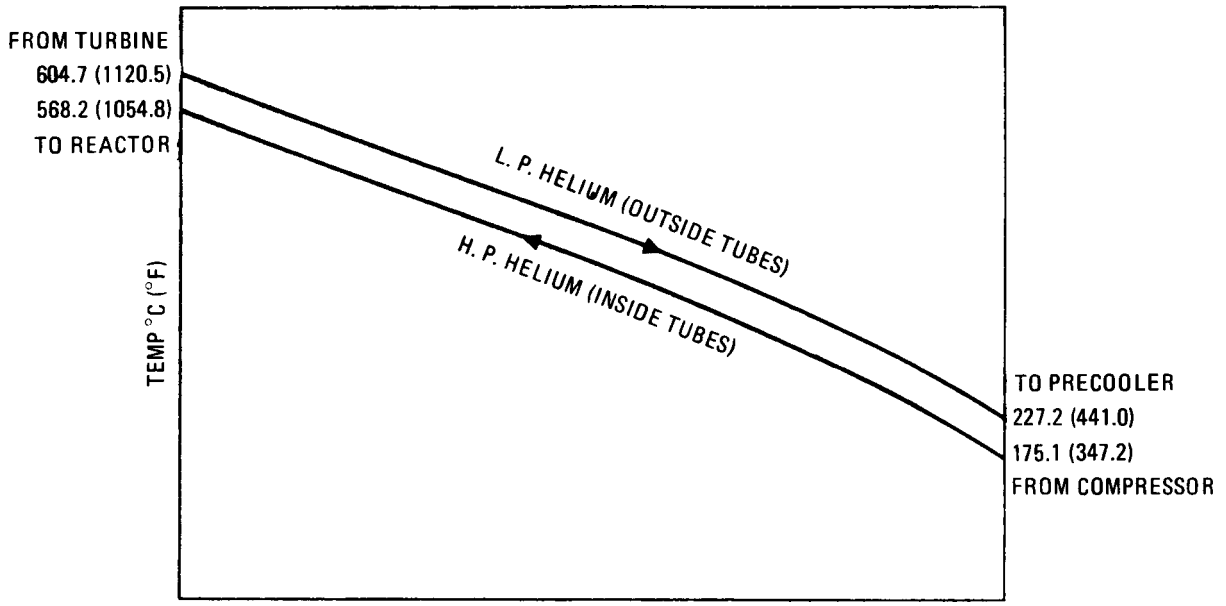

FLUID STREAM (HELIUM)	HIGH PRESSURE	LOW PRESSURE
FLOW, $\frac{KG}{HR}$ $\left(\frac{LB}{HR}\right)$ PER UNIT	1,811,225 (3,993,000)	1,880,217 (4,155,500)
T_{IN}, °C (°F)	175.1 (347.2)	604.7 (1120.5)
T_{OUT} °C (°F)	568.2 (1054.8)	227.2 (441.0)
P_{IN}, MPa (PSIA)	7.880 (1142.9)	3.248 (471.1)
LMTD, °C (°F)	43.84 (78.92)	
UA, $\frac{MW}{°C}$ $\left(\frac{BTU}{HR-{}^{o}F}\right)$ PER REACTOR	93.84 (1.7786×10^{8})	
Q, $\frac{MW}{REACTOR}$ $\left(\frac{BTU}{HR\ REACTOR}\right)$	4114.0 (1.4037×10^{10})	

GA-A13950

Fig. 9-1. GT-HTGR recuperator thermal design data for 950°C ROT, 4000-MW(t), four-loop, dry-cooled plant

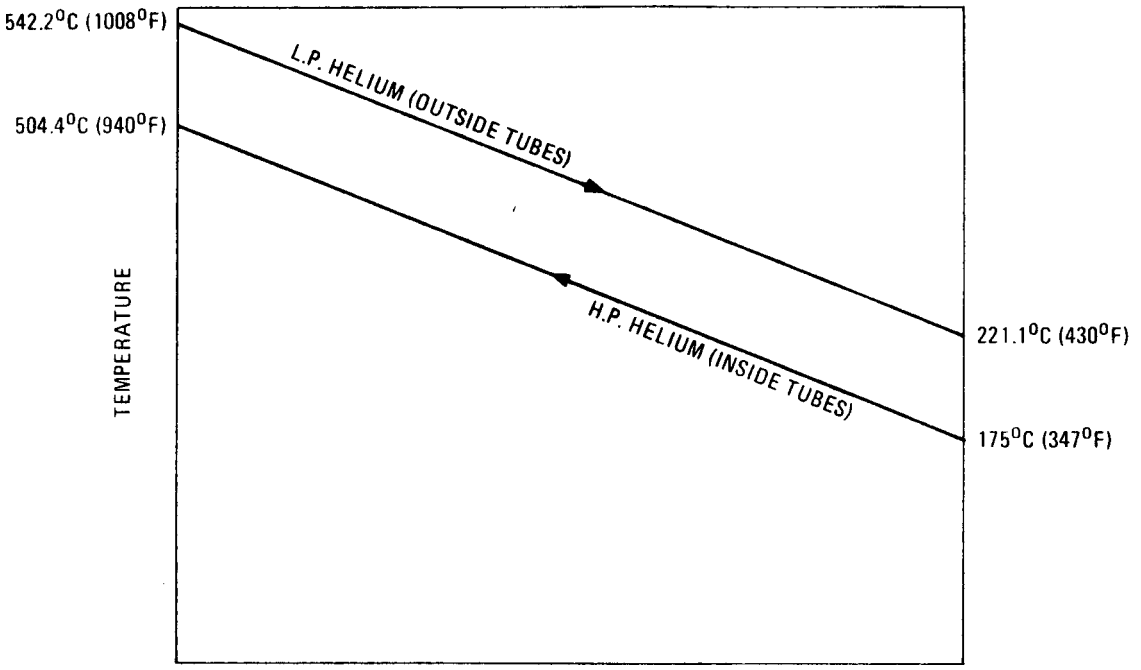

FLUID STREAM	HELIUM (HP)	HELIUM (LP)
FLOW RATE/UNIT, KG/SEC (LB/HR)	556.3 (4.414 x 10^6)	571.5 (4.53 x 10^6)
INLET TEMP, °C (°F)	175.0 (347)	542.2 (1008)
OUTLET TEMP, °C (°F)	504.4 (940)	221.1 (430)
INLET PRESSURE, MPa (psia)	7.866 (1141)	3.240 (470)
OUTLET PRESSURE, MPa (psia)	7.818 (1134)	3.212 (466)
EFFECTIVENESS	0.8975	—
HEAT TRANSFER RATE, MW(t)/REACTOR	3815	
COUNTERFLOW LMTD, °C (°F)	19.56 (35.2)	
THERMAL CONDUCTANCE, BTU/HR–°F/REACTOR	173 x 10^6	

GA-A13950

Fig. 9-2. GT-HTGR recuperator thermal design data for 850°C ROT, 4000-MW(t), four-loop, dry-cooled plant

Additional limits also must be considered for site handling and installation, and these depend largely on the approaches taken. For those studies, the limitations of 6.7 m (22 ft), 27.4 m (90 ft), and 726,000 kg (800 ton) assumed, respectively, on heat exchanger diameter, length, and weight were considered to be somewhat conservative for the handling and installation options available.

As a result of these adopted limits, it was possible to eliminate the 2000-MW(t) loop rating options from both the 950°C ROT and the 850°C ROT, 4000-MW(t) plant cases because of the impractically large heat exchanger sizes that result. The issue of whether a 1333-MW(t) loop rating is practical from the heat exchanger standpoint requires detailed study, but initial indications based on simple scaling suggest that some site fabrication would be required for these designs. The recuperators for the next available loop rating, 1000 MW(t) per loop, were analyzed in detail, and the results are discussed in the following section.

9.2.1.4. Details of Four-Loop Design. Recuperator thermal sizing based on a loop rating of 1000 MW(t) was carried out for both the 950°C ROT and the 850°C ROT, dry-cooled plant options, using the thermal design data presented in Section 9.2.1.2. While the effort for the 850°C ROT case was relatively simple, entailing the analysis and sizing of a particular recuperator configuration to support plant layout studies, the recuperator thermal design selection for the more structurally severe 950°C ROT case was made on the basis of comprehensive parametric surveys aimed at identifying the design with the minimum combination of PCRV cavity size and pressure loss consistent with the plant optimization studies discussed in Section 2.4. Significant details of both designs are summarized in Table 9-1. Both designs take advantage of the optimal qualities of hexagonal module shapes for efficient packaging of the tubular heat transfer matrix within the cavity. The virtues of hexagonal modules are discussed further in Section 9.4.3.

The parametric studies for the 950°C ROT plant case first involved surveys using the computer code PACKEM (discussed in Section 9.4.4) to identify the module sizes to give the best geometric packaging within a given PCRV cavity diameter. The best cases from this survey were then

TABLE 9-1
GT-HTGR RECUPERATOR DESIGN DATA FOR 4000-MW(t),
FOUR-LOOP, DRY-COOLED PLANT

ROT Case	950°C	850°C
Modules/heat exchanger	168	144
Hexagonal module A/F, mm (in.)	289 (11.4)	361 (14.2)
Tubes/module	328	547
Tube o.d. x wall, mm (in.)	11.1 (0.4375) x 1.14 (0.045)	11.1 (0.4375 x 1.14 (0.045)
Tube material	Austenitic Type 316 stainless steel	Ferritic 2 1/4 Cr - 1 Mo
Tube p/d	1.407	1.374
Active tube length, m (ft^2)	118,296 (1.273×10^6)	1333,438 (1.436×10^6)
Overall helium pressure loss ($\Sigma \frac{\Delta P}{P_1}$)	0.0279	0.0184
Overall heat exchanger length, m (ft)	22.3 (73.3)	18.9 (62)
Heat exchanger diameter, m (ft)	4.65 (15.25)	5.10 (16.75)
Overall dry weight, kg (ton)	404,487 (446)	429,930 (474)

analyzed individually to determine the recuperator length, overall relative pressure loss, and surface area requirement obtainable with a tube of 11.1 mm (0.4375 in.) and an idealized p/d (1.40), which has been shown previously to be near the optimum. From this group of solutions, plotted in Fig. 9-3, the case yielding the smallest heat exchanger diameter and a combination of minimum pressure loss and length was selected for a final parametric survey to determine the optimum tube diameter and pitching within the selected module geometry. This study is shown in Fig. 9-4, which indicates that the selection of 11.1-mm (0.4375-in.) o.d. tubes on a 1.407 triangular p/d (both of which are close to minimum practical fabrication limits) will have a pressure loss near the minimum. It should be noted that only the discrete solutions corresponding to prime hexagonal numbers of tubes indicated by the guarded points in Fig. 9-4 represent valid solutions and that the approach of packaging contiguous hexagonal modules removes the design alternative of treating p/d as an independent variable. Further aspects of this packaging approach are discussed in Section 9.4, which also presents the recuperator mechanical design based on the results of this study.

9.2.2. Precooler Design Considerations

The role of the precooler in the 4000-MW(t), dry-cooled plant is to cool the primary cycle helium prior to compression, while transferring this reject heat from the primary cycle to a closed cooling water loop which ultimately disposes of the heat via dry-cooling towers. In addition to ensuring total segregation of the helium and water circuits, the precooler design must provide for isolation capability and drainability of faulted water passages. The thermal size studies discussed below are based on the same overall precooler arrangement as used in previous studies, viz., vertical orientation, top support, modular assembly, counterflow tubular configuration with the water inside the tubes, and water inlet and outlet penetrations routed through the bottom head of the PCRV. The material thicknesses selected provide stress levels consistent with the requirements of Section VIII of the ASME Code for a service life of 280,000 hr.

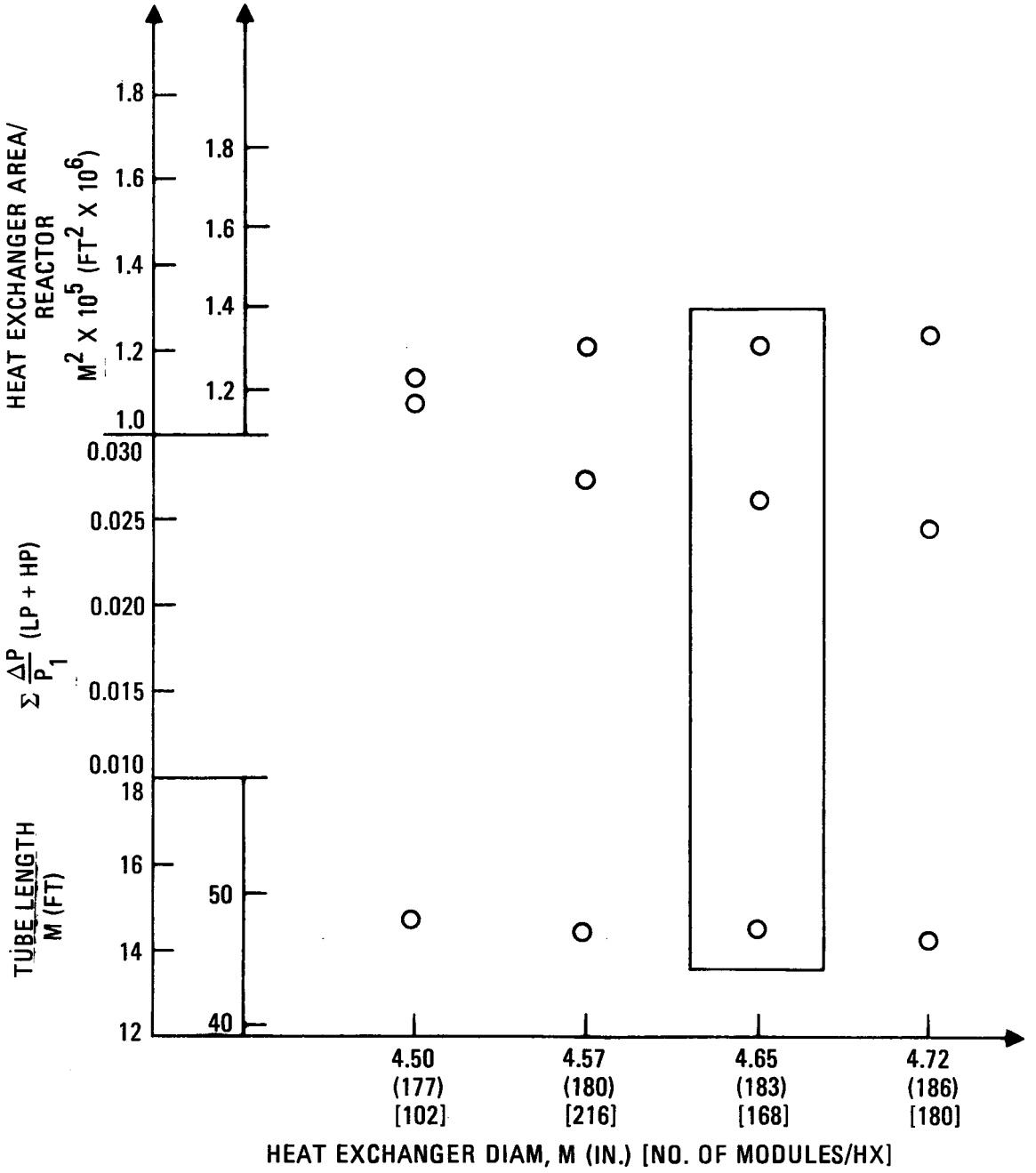

NOTES

ALL CASES HAVE A TUBE PITCH (p/d) OF 1.4.

ALL CASES HAVE TUBE O.D. (d) OF 11.1 MM (7/16 IN.)

O – GENSIZ RESULTS

GA-A13950

Fig. 9-3. GT-HTGR recuperator cavity study for 950°C ROT, 4 x 4000-MW(t), dry-cooled plant

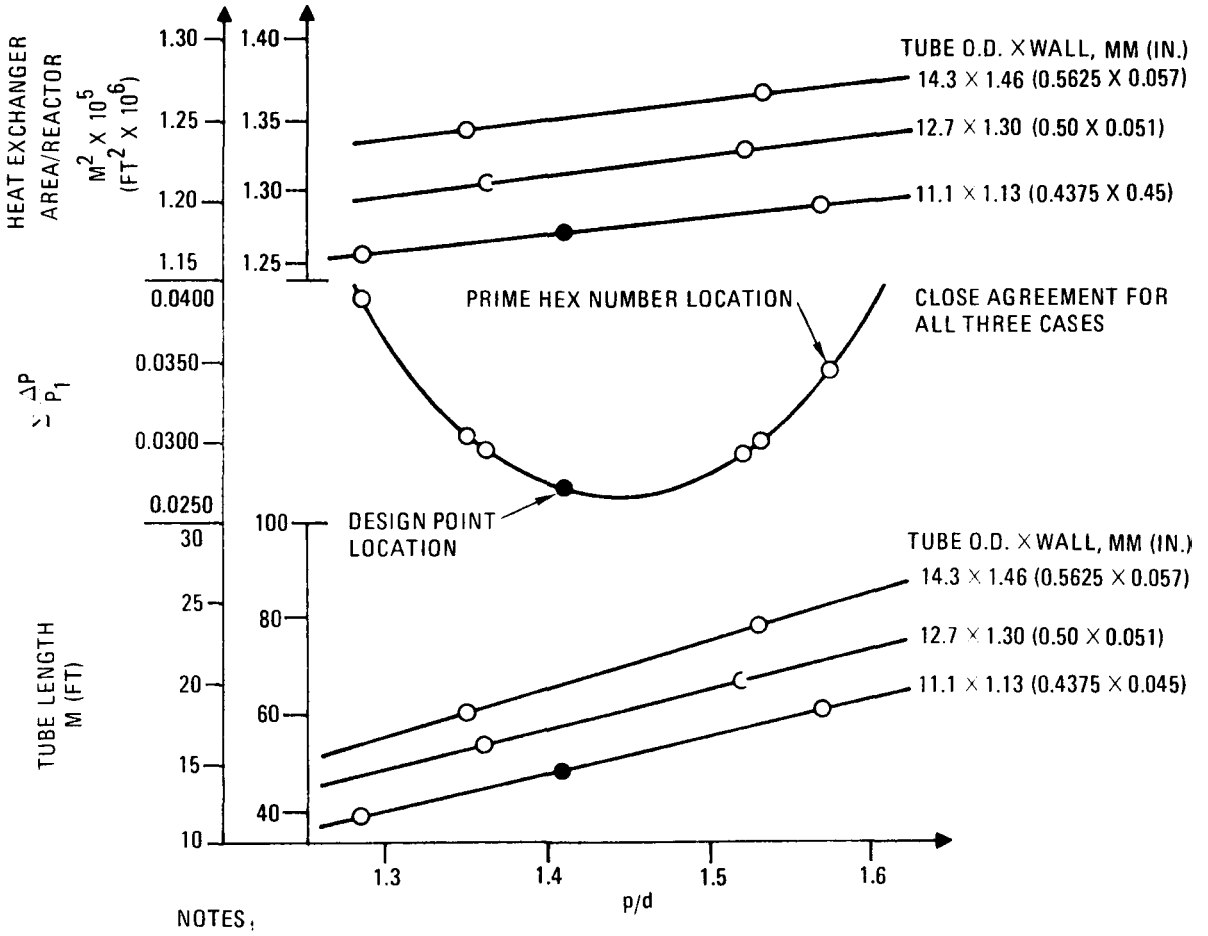

NOTES:

1. EQUILATERAL △ PITCHING.
2. AXIAL COUNTERFLOW MODULAR DESIGN.
   - 168 HEXAGON MODULES
   - MODULE PITCH = 289.1 MM (11.38 IN.)
   - 3.175 MM (1/8 IN.) THICK SHROUD SEPARATING MODULES
   - 331 TUBES PER MODULE
   - DESIGN POINT AT p/d = 1.4072
3. 10% UA MARGIN.
4. HEAT EXCHANGER CAVITY DIAM (INSIDE THERMAL BARRIER) = 4.65 M (15.25 FT)
5. FOUR LOOPS PER REACTOR, ONE RECUPERATOR PER LOOP.

GA-A13950

Fig. 9-4. GT-HTGR recuperator parametric study for 950°C ROT, 4 x 4000-MW(t), dry-cooled plant (ε = 0.90)

9.2.2.1. Influence of Operating Conditions. For both the 950°C ROT and the 850°C ROT Plant option cases, the operating temperatures and pressures in the precooler are low enough to permit the use of medium carbon steel throughout the assembly.

Previous studies have shown that the primary approach of using a straight-tube, pure counterflow configuration for the precooler design produces the most favorable combination of simplicity, conventionality, and overall geometric characteristics for an integrated PCRV installation while satisfying the requirements for minimum helium (shell-side) pressure loss. However, this approach also leads to characteristically low water velocities inside the tubes, and the low inside thermal conductances that result for plain tube surface geometries penalize the overall precooler length substantially, even though the helium side is still controlling (i.e., $hA_{He} < hA_{w}$). Thus, to generate precooler designs that do not govern the PCRV height, heat transfer augmentation is considered to be necessary, and cycle efficiency considerations make it more convenient to accommodate heat transfer enhancement pumping penalties on the water side. As a result, previous precooler reference designs have assumed water-side conductances (hA) of twice those obtainable with plain-tube turbulent flow correlations. While several enhancement methods to achieve this performance were identified (e.g., internal blockage, fins, turbulence promoters, etc.), the selection of the actual method to be used in the precooler was left for further studies. Investigations carried out during the previous reporting period toward this goal identified several promising longitudinally finned tube candidates, some of which are currently being investigated for economic and manufacturing feasibility. Meanwhile, detailed nodal analyses performed on preliminary thermal designs indicate that the axial variation of local water-side Reynolds numbers can span the turbulent-to-laminar flow transistion range, giving rise to uncertainty in the value of the heat transfer coefficients for smooth tubular surfaces. Where experimental data for the specific heat exchanger arrangement are available, heat exchangers may be designed for operation in the transition region. The mechanical and geometric constraints imposed on the precooler make transition Reynolds numbers virtually unavoidable, particularly for precoolers

sized in accordance with the thermal requirements presented in Section 9.2.2.2, which call for colder water inlet temperatures. The poorer heat transfer characteristics of transition or laminar flow occurring at the cold end of the precooler, where the minimum temperature difference (pinch point) between the helium and the water occurs, aggravates the surface area requirements, as shown graphically in Fig. 9-5. Thus, while the thermal size studies discussed in Section 9.2.2.4 are still based on inside conductances, additional checks were made to ensure that this degree of performance enhancement was still achievable at low Reynolds numbers. Data from several investigators indicate that swirl flow promoters (e.g., twisted tapes or spirally finned or fluted tubes) can produce the desired performance.

9.2.2.2. Thermal Requirements. The precooler thermal design data for both the 950°C ROT and the 850°C ROT plant cases are presented in Figs. 9-6 and 9-7, respectively. When compared with the corresponding precooler requirements for the previous three-loop, 3000-MW(t), 815°C ROT plant reference design, it is seen that the thermal duty and overall size requirements are about the same. To ensure rated performance at these conditions, an allowance of 10% excess surface area above the theoretical requirement was included in the precooler thermal size studies to cover analytical uncertainties.

9.2.2.3. Effect of Loop Rating. The loop thermal rating influences the precooler design in a manner similar to that discussed for the recuperator in Section 9.2.1.3, and the size and weight constraints adopted for the recuperator, exclusive of the forging diameter limitation, are therefore assumed to be equally applicable. This also resulted in the elimination of the 2000-MW(t) loop rating options for both the 950°C ROT and the 850°C ROT, 4000-MW(t) plant cases on the basis of impractically large precooler sizes. Because a 1333-MW(t) loop rating probably entails precooler site fabrication considerations, thermal size tradeoff studies were pursued in detail only for the 1000-MW(t) loop rating. The results are discussed in the following section.

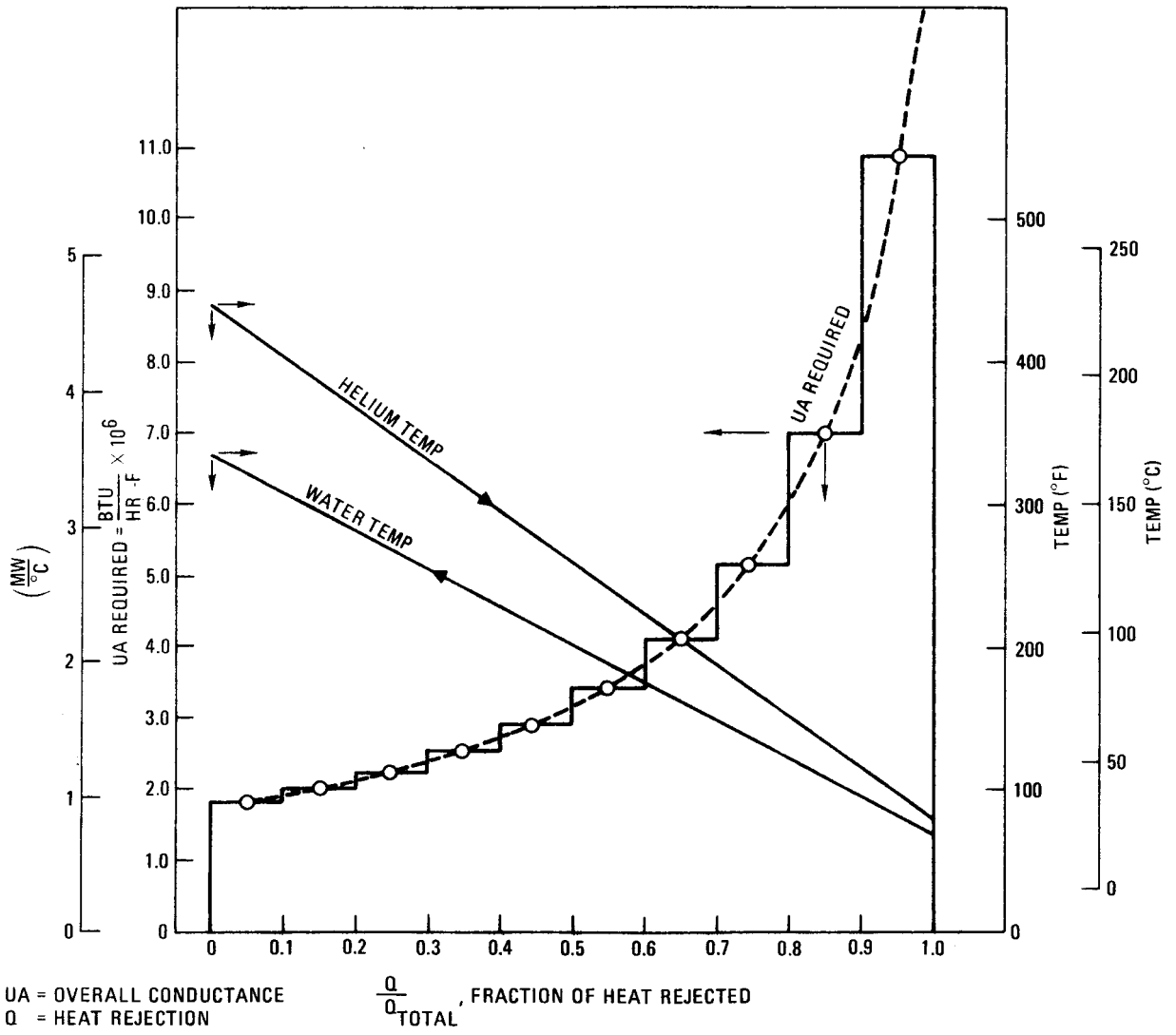

GA-A13950

Fig. 9-5. GT-HTGR precooler heat transfer requirements for 950°C ROT, 4 x 4000-MW(t), dry-cooled plant

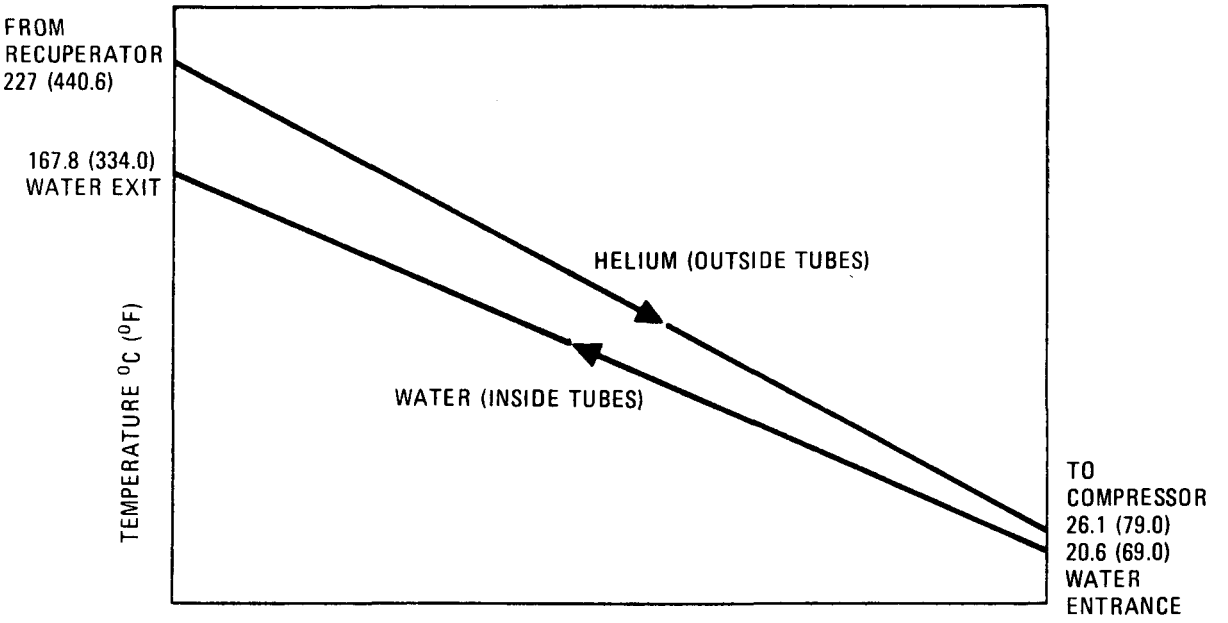

FLUID STREAM	HELIUM	WATER
FLOW, $\frac{KG}{HR}$ $\left(\frac{LB}{HR}\right)$ PER UNIT	1,339,900 (4,155,500)	3,160,600 (6,967,800)
T_{IN}, °C (°F)	227.0 (440.6)	20.6 (69.0)
T_{OUT}, °C (°F)	26.1 (79.0)	167.8 (334.0)
P_{IN}, MPa (PSIA)	3.2068 (465.1)	1.9995 (290.0)
LMTD, °C (°F)	44.16 (79.49)	
UA, $\frac{MW}{°C}$ $\left(\frac{BTU}{HR-°F}\right)$ PER REACTOR	49.54 (9.3911×10^7)	
Q, $\frac{MW}{REACTOR}$ $\left(\frac{BTU}{HR\ REACTOR}\right)$	2187.8 (7.4650×10^9)	

GA-A13950

Fig. 9-6. GT-HTGR precooler thermal design data for 950°C ROT, 4000-MW(t), four-loop, dry-cooled plant

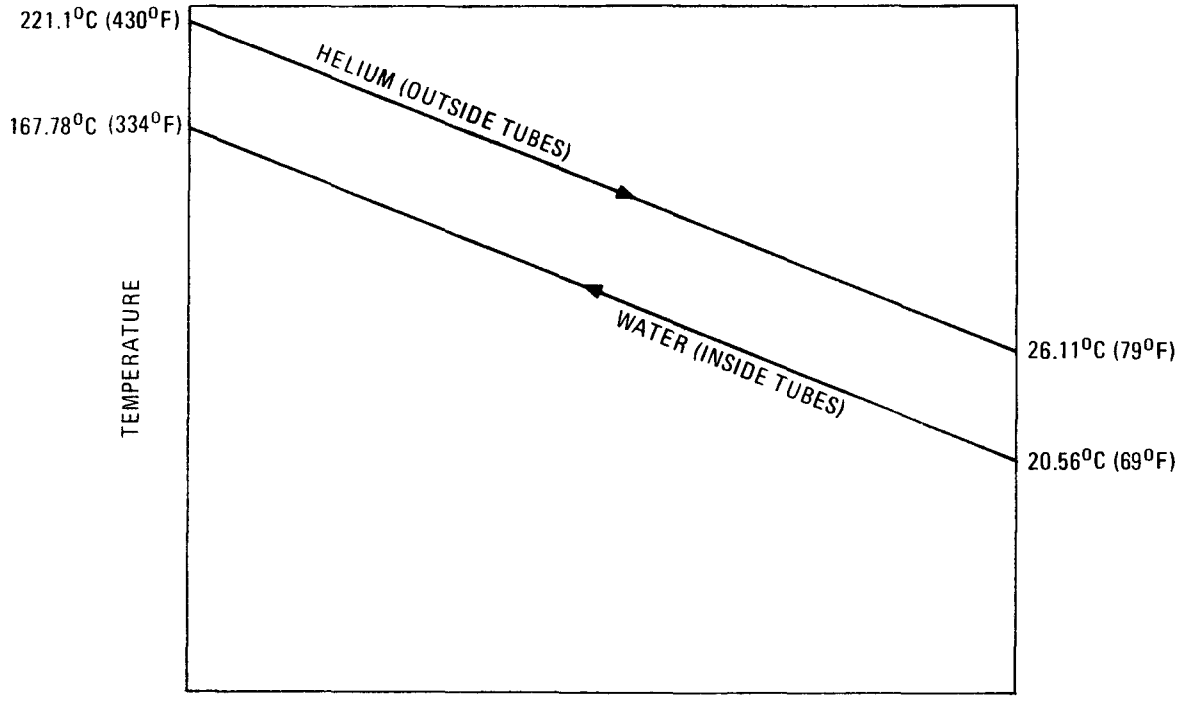

FLUID STREAM	HELIUM	WATER
FLOW RATE/UNIT, KG/SEC (LB/HR)	571.5 (4.534 x 10^6)	925.9 (7.344 x 10^6)
INLET TEMP, °C (°F)	221.1 (430)	20.56 (69)
OUTLET TEMP, °C (°F)	26.11 (79)	167.78 (334)
INLET PRESSURE, MPa (psia)	3.206 (465)	2.206 (320)
OUTLET PRESSURE, MPa (psia)	3.185 (462)	2.00 (≅290)
EFFECTIVENESS	0.972	–
HEAT TRANSFER RATE, MW(t)/REACTOR	2317	
COUNTERFLOW LMTD, °C (°F)	21.11 (38)	
THERMAL CONDUCTANCE, BTU/HR–°F/REACTOR	208 x 10^6	

GA-A13950

Fig. 9-7. GT-HTGR precooler thermal design data for 850°C ROT, 4000-MW(t), four-loop, dry-cooled plant

9.2.2.4. Details of Four-Loop Design. The information presented in this section is similar in format to the recuperator results discussed in Section 9.2.1.4 in that, while detailed studies were made only for the more severe 950°C ROT plant case, a nonoptimized 850°C ROT plant precooler design was analyzed to support plant layout studies. The 950°C ROT plant studies followed the same optimization approach described for the recuperator, using the computer code PACKEM to establish the module geometries. Inside heat transfer augmentation as discussed in Section 9.2.2.1 was taken into account in all of the thermal analyses.

The parametric results for the PCRV cavity diameter selection and the thermal size tradeoffs for the 950°C ROT plant case are shown graphically in Figs. 9-8 and 9-9, respectively, which indicate that the design selection has the minimum combination of PCRV cavity diameter, effective length, and helium-side pressure loss consistent with the adopted minimum fabrication limits of 9.5 mm (0.375 in.) and 1.40 on tube o.d. and p/d, respectively.

Details of both the 950°C ROT and the 850°C ROT precooler designs are summarized in Table 9-2.

9.3. HEAT EXCHANGER STUDIES FOR 4000-MW(t) BINARY-CYCLE PLANT

The heat exchanger studies completed during this reporting period also included preliminary parametric studies of the recuperator and the precooler for a 950°C ROT, four-loop, 4000-MW(t) GT-HTGR plant with a supercritical NH_3 Rankine bottoming cycle. In the following sections, the heat exchanger design considerations peculiar to this binary-cycle GT-HTGR plant variant are discussed, and preliminary thermal designs for the recuperator and the precooler are presented.

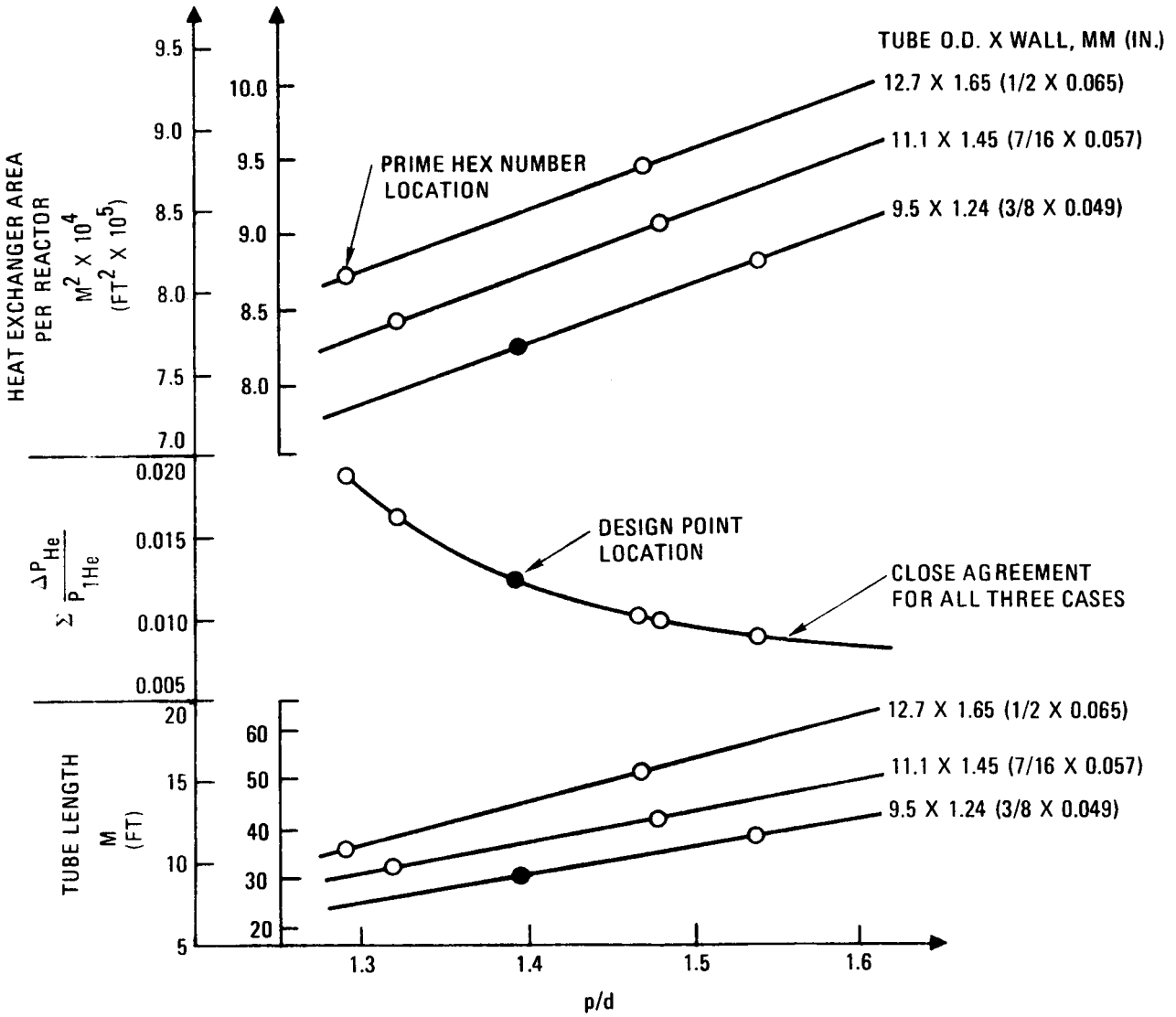

NOTES

1. EQUILATERAL Δ PITCHING.
2. AXIAL COUNTERFLOW MODULAR DESIGN.
   - 210 HEXAGON MODULES
   - MODULE PITCH = 246 MM (9.7 IN.)
   - 3.175 MM (1/8 IN.) THICK SHROUD SEPARATING MODULES
   - 331 TUBES PER MODULES
   - DESIGN POINT AT p/d = 1.3966
3. 10% UA MARGIN
4. HEAT-EXCHANGER DIAM = 4.19 (13.75 FT)
5. FOUR LOOPS PER REACTOR, ONE PRECOOLER PER LOOP

GA-A13950

Fig. 9-8. GT-HTGR precooler parametric study for 950°C ROT, 4 x 4000-MW(t), dry-cooled plant

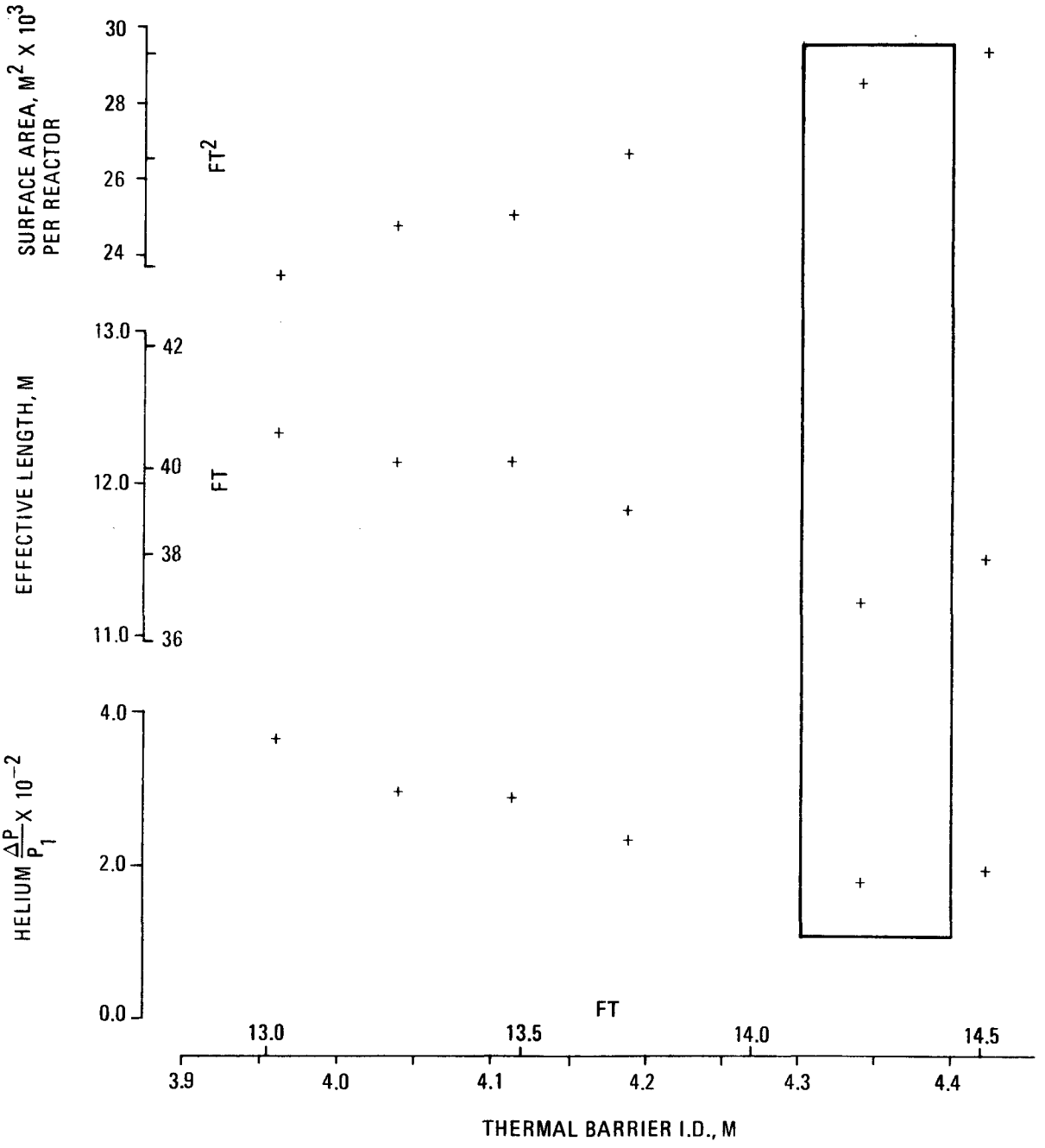

NOTES:

1. AXIAL COUNTERFLOW MODULAR DESIGN
2. UA MARGIN = 10%
3. ALL CASES HAVE PRIME NUMBER TUBES (p/d ~1.4)
4. ALL CASES HAVE TUBE O.D. OF 9.5 MM (3/8 IN.)

GA-A13950

Fig. 9-9. GT-HTGR precooler cavity sizing for 950°C ROT, 4 x 4000-MW(t), dry-cooled plant

TABLE 9-2
GT-HTGR PRECOOLER DESIGN DATA FOR 4000-MW(t),
FOUR-LOOP, DRY-COOLED PLANT

ROT Case	950°C	850°C
Modules/heat exchanger	210	144
Hexagonal module A/F, mm (in.)	246 (9.7)	335 (13.2)
Tubes/module	328	631
Tube o.d. x wall thickness, mm (in.)	9.5 (0.375) x 1.24 (0.049)	9.5 (0.375) x 1.24 (0.049)
Tube material	Medium carbon steel	Medium carbon steel
Tube p/d	1.397	1.38
Active tube length, m (ft)	9.24 (30.2)	11.28 (37.0)
Surface area/reactor, m^2 (ft^2)	77,217 (831,188)	122,514 (1.31×10^6)
Overall helium pressure loss $(\Sigma \frac{\Delta P}{P_1})$	0.0124	0.0099
Overall heat exchanger length, m (ft)	22.3 (73.0)	22.3 (73.0)
Heat exchanger diameter, m (ft)	4.19 (13.75)	4.72 (15.5)
Overall dry weight, kg (ton)	373,696 (412)	403,630 (445)

9.3.1. Recuperator Design Considerations

For the optimized GT-HTGR binary-cycle plant case under consideration, the role of the recuperator and its design requirements are very similar to those of the dry-cooled plant case discussed in Section 9.2.1. Therefore, the binary-cycle plant recuperator designs have been based on the same criteria for module packaging (contiguous hexagons), material (austenitic Type 316 stainless steel), loop rating [1000 MW(t)], and general arrangement. The thermal design data for the binary-cycle plant recuperator are presented in Fig. 9-10.

9.3.2. Precooler Design Considerations

While the precooler design for the binary-cycle plant also follows the criteria developed for the dry-cooled plant case with regard to packaging, loop rating, material, and general arrangement, its function as a heat source heat exchanger in the supercritical NH_3 bottoming cycle entails additional design considerations. Although supercritical NH_3 is a good heat transport fluid, its thermal properties are inferior to those of water, and the associated size penalty must be taken into account if the precooler is not to govern the PCRV height. This is a problem that was not encountered in the dry-cooled plant precooler designs. Because of the large variation of the specific heat (Cp) that results when the NH_3 is heated above its critical temperature, the pinch point (i.e., minimum temperature differential between the helium and the NH_3) occurs in the middle of the precooler instead of at the cold end, as is the case for helium-to-water precooler designs. The precooler end-point operating temperatures must therefore be selected with considerable care. This effect is shown graphically in Fig. 9-11, which reveals that the precooler for the 950°C ROT, binary-cycle plant has an internal pinch of 5.55°C (10°F). Other thermal design data for this precooler are tabulated in the same figure.

The binary-cycle plant precooler design is impacted further by the high working pressures on the NH_3 side which necessitate substantial

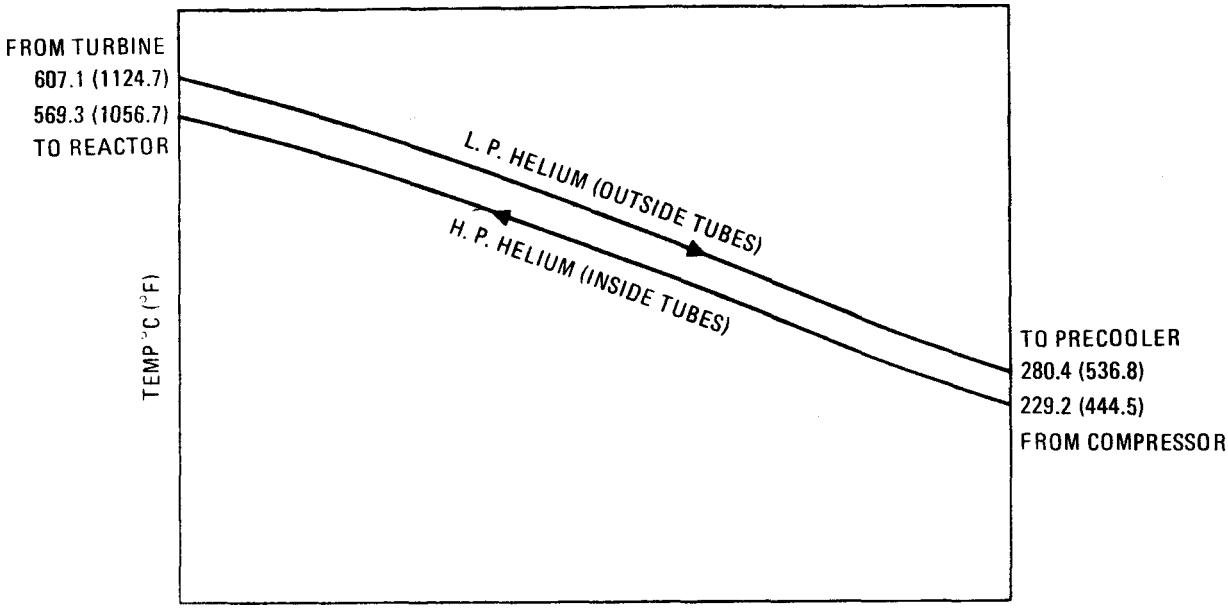

FLUID STREAM (HELIUM)	HIGH PRESSURE	LOW PRESSURE
FLOW, $\frac{Kg}{HR}$ $\left(\frac{LB}{HR}\right)$ PER UNIT	1,816,174 (4,004,000)	1,885,347 (4,166,900)
T_{IN}, °C (°F)	229.2 (444.5)	607.1 (1124.7)
T_{OUT}, °C (°F)	569.3 (1056.7)	280.4 (536.8)
P_{IN}, MPa (PSIA)	7.8738 (1142.0)	3.2543 (472.0)
LMTD, °C (°F)	44.2 (79.5)	
UA, $\frac{MW}{°C}$ $\left(\frac{BTU}{HR-°F}\right)$ PER REACTOR	80.7 (1.5318×10^8)	
Q, $\frac{MW}{REACTOR}$ $\left(\frac{BTU}{HR\ REACTOR}\right)$	3569.0 (1.2178×10^{10})	

GA-A13950

Fig. 9-10. GT-HTGR recuperator thermal design data for 950°C ROT, 4000-MW(t), four-loop, binary-cycle plant

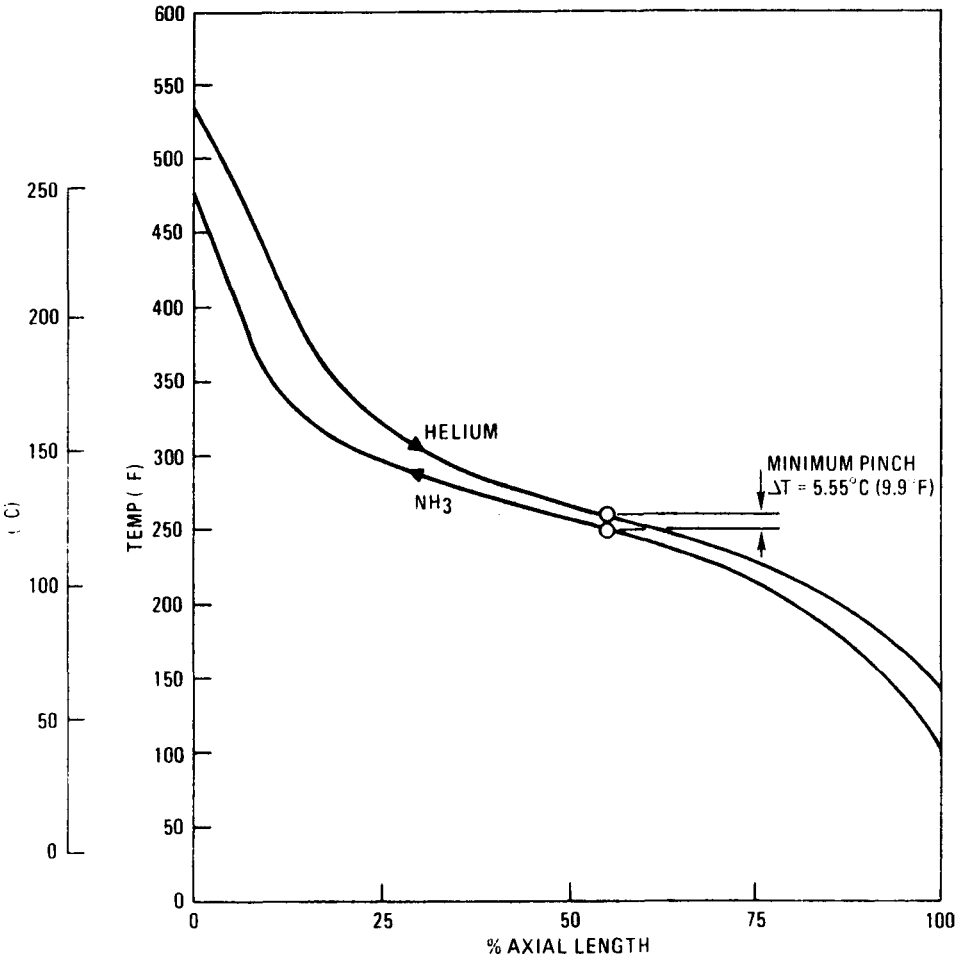

FLUID STREAM	HELIUM	NH_3
FLOW, $\frac{KG}{HR}\left(\frac{LB}{HR}\right)$ PER UNIT	1,890,100(4,166,900)	1,475,600(3,253,200)
T_{IN}, °C (°F)	280.2 (536.3)	37.9 (100.3)
T_{OUT}, °C (°F)	62.2 (144.0)	250.0 (482.0)
P_{IN}, MPa (PSIA)	3.218 (466.7)	16.7 (2424.0)
LMTD, °C (°F)	27.12 (48.81)	
UA, $\frac{MW}{°C}\left(\frac{BTU}{HR-°F}\right)$ PER REACTOR	87.76 (1.6638 X 10^8)	
Q, $\frac{MW}{REACTOR}\left(\frac{BTU}{HR\ REACTOR}\right)$	2380.0 (8.1211 X 10^9)	

GA-A13950

Fig. 9-11. GT-HTGR precooler thermal design data for 950°C ROT, 4000-MW(t), four-loop, binary-cycle plant

material thickness increases in the NH_3 pressure parts (e.g., module subheaders, tubesheets, tubes, and subheadering lead tubes), producing a significant weight increase over dry-cooled plant precooler designs. The low-alloy steel (medium carbon steel, SA-178, Grade C) utilized in the precooler for the dry-cooled GT-HTGR plant also is suitable for NH_3 heater service from both a materials compatibility and an operating temperature point of view.

Studies have shown that gravity dumping of the heat exchanger inventory is no longer a requirement, since the ammonia is in the vapor phase and the NH_3 pressure alone will empty the fluid into the dump tank. The implication of this is that the precooler could be supported from the top of the PCRV, with the ammonia inlet and outlet pipes penetrating the top closure plug. This would simplify and ease the precooler design problems and save the cost of the penetrations in the lower head of the PCRV. Tube plugging and general maintenance would be eased with this arrangement. The safety implications (and piping layout complexity) of having large-diameter ammonia pipes penetrating the top of the PCRV need to be studied before heat exchanger design work for this approach is pursued.

The NH_3 precooler also is characterized by low velocities inside the tubes, such that the considerations discussed in Section 9.2.2.1 also apply here. Heat transfer augmentation on the NH_3 side was therefore assumed in the thermal analyses, with the degree of thermal improvement being on the same order as that assumed in the dry-cooled plant precooler studies.

9.3.3. Details of Four-Loop Design

The thermal size optimization studies for the binary-cycle plant heat exchangers followed the same general approach used to establish the thermal designs for the recuperator and the precooler in the 950°C ROT, dry-cooled plant discussed in Section 9.2. First, tradeoffs were conducted using the design program GENSIZ and the optimization program CODER to identify the combination of PCRV diameter and hexagonal module size which packaged the heat transfer matric within the available envelope most efficiently without compromising performance. Contiguous packaging of the

modules was assumed for all cases, and the results are shown graphically for the recuperator and the precooler in Figs. 9-12 and 9-13, respectively. Using these results, parametric studies to determine the influence of tube diameter and pitching were then performed to provide a basis for the design selections shown in Figs. 9-14 and 9-15. In both cases, it can be seen that the design selection was governed primarily by the minimum limits on tube diameter and pitching assumed for the recuperator and the precooler. Significant features of the two selected designs are summarized in Table 9-3.

9.4. HEAT EXCHANGER MECHANICAL DESIGN

Heat exchanger mechanical design studies undertaken during this reporting period in support of the analytical effort were aimed primarily at establishing design improvements that reduce heat exchanger cross-sectional size without compromising performance. Significant progress toward this goal has been achieved through the development of a new design approach to module subheadering, which permits the reduction of PCRV diameter through more efficient module packaging. Compared with designs based on the previous approach of using conventional subheaders with flat tubesheets, the new concept, when employed in conjunction with hexagonal modules, has resulted in an overall reduction in PCRV diameter on the order of 0.3 to 0.6 m (1 to 2 ft).

With the desired design goal of packaging hexagonal modules tangent, or contiguous, to one another thus attained, follow-on mechanical design studies identified a module shrouding concept that considerably simplifies the assembly of the heat exchanger modular arrays while providing the advantages of mutually shared intermodule partitions.

Additional mechanical design studies have led to a mechanical design concept for the seals necessary to preclude gas bypass in the annular regions between the heat exchangers and their cavities.

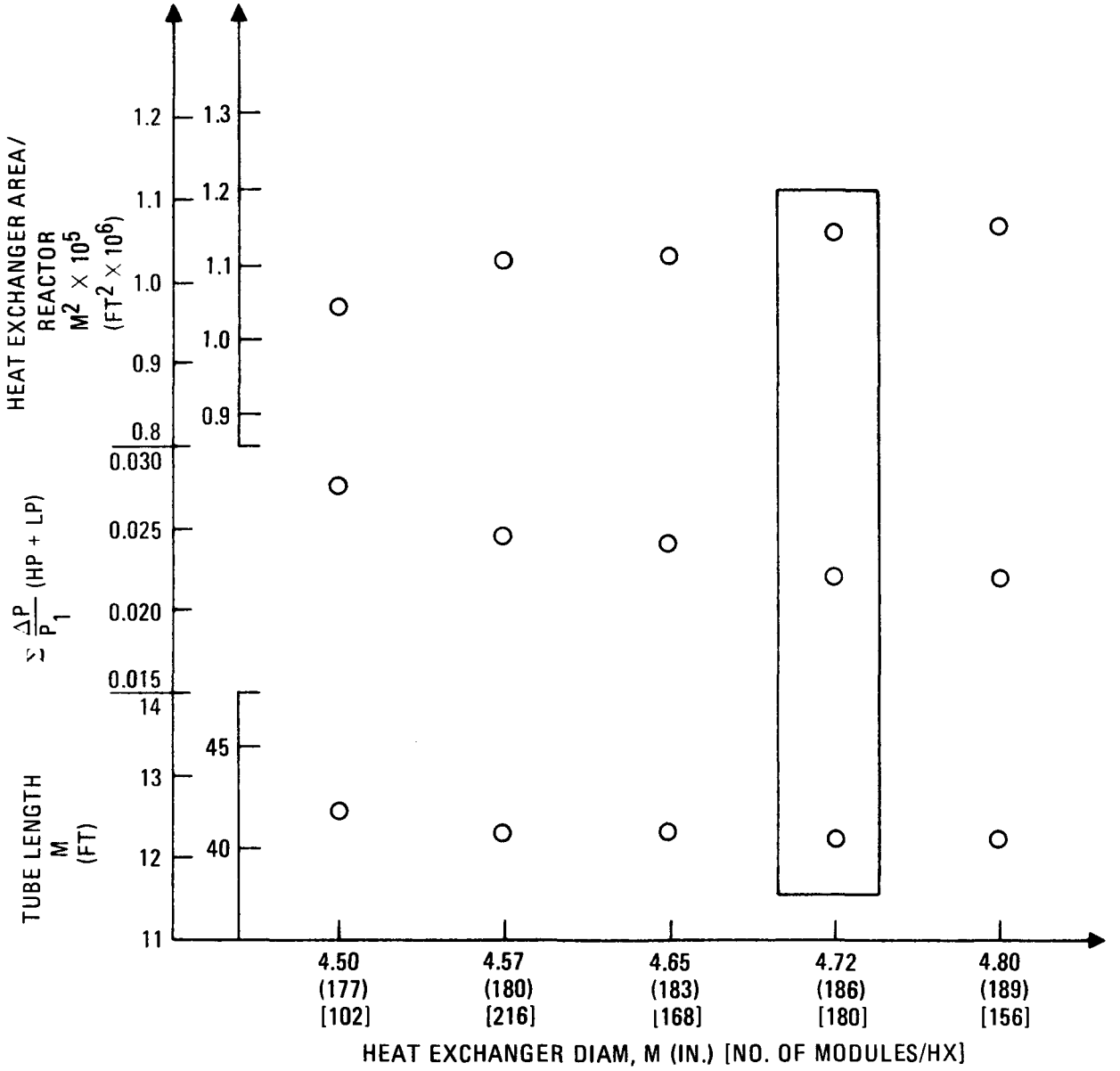

NOTES:

ALL CASES HAVE A TUBE PITCH (p/d) OF 1.4.

ALL CASES HAVE TUBE O.D. (d) OF 11.1 MM (7/16 IN.)

O – GENSIZ RESULTS

GA-A13950

Fig. 9-12. GT-HTGR recuperator cavity study for 950°C ROT, 4 x 4000-MW(t), binary-cycle plant

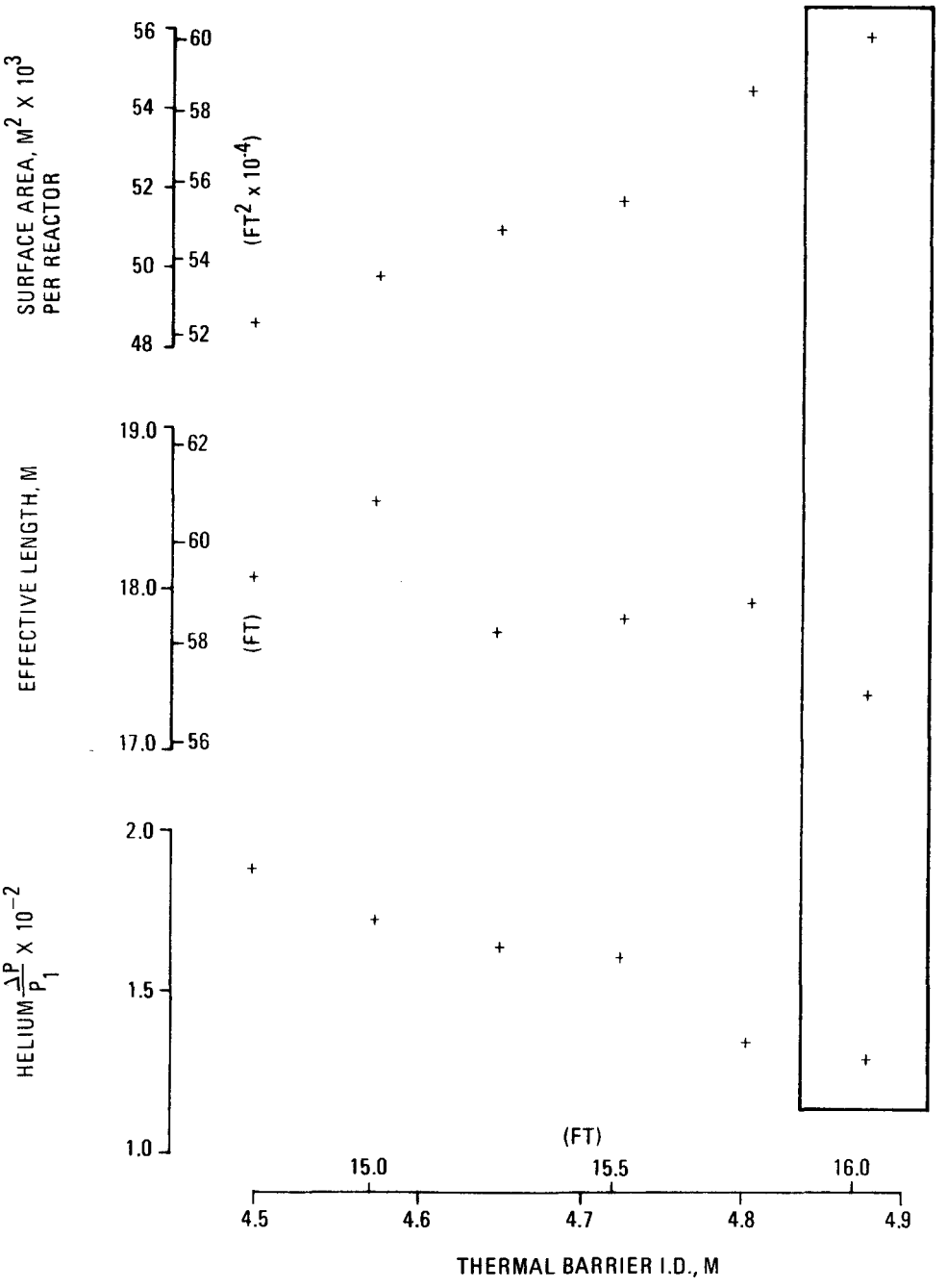

NOTES:

1. ALL CASES HAVE PRIME NUMBER TUBES (p/d ~1.4)
2. ALL CASES HAVE TUBE O.D. OF 9.5 MM (3/8 IN.)
3. AXIAL COUNTERFLOW MODULAR DESIGN
4. UA MARGIN = 10%

GA-A13950

Fig. 9-13. GT-HTGR precooler cavity sizing for 950°C ROT, 4 x 4000-MW(t), binary-cycle plant

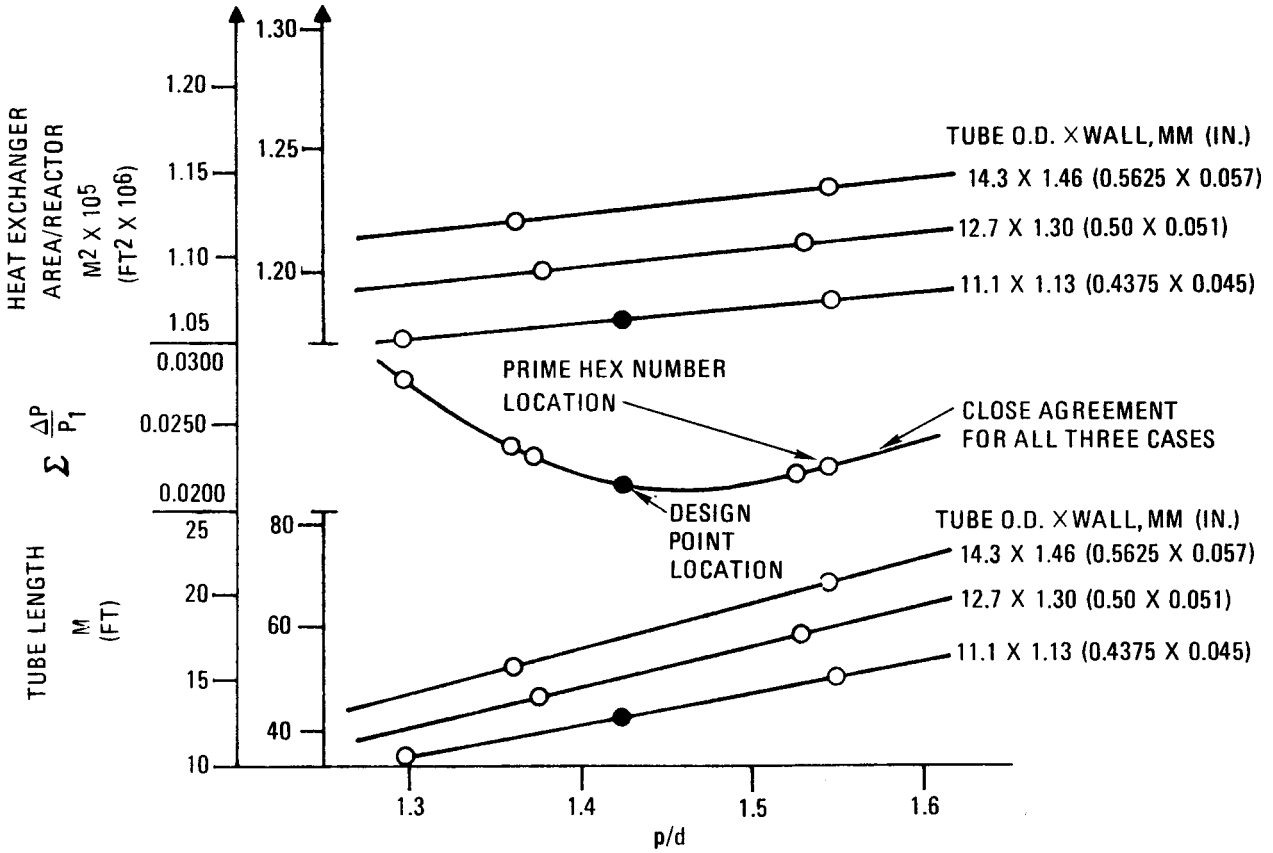

NOTES

1. EQUILATERAL △PITCHING.
2. AXIAL COUNTERFLOW MODULAR DESIGN.
   - 180 HEXAGON MODULES
   - MODULE PITCH = 292.1 MM (11.5 IN.)
   - 3.175 MM (1/8 IN.) THICK SHROUD SEPARATING MODULES
   - 331 TUBES PER MODULE
   - DESIGN POINT AT p/d = 1.4223
3. 10 % UA MARGIN.
4. HEAT EXCHANGER CAVITY DIAM (INSIDE THERMAL BARRIER) = 5.03 M (16.5 FT)
5. FOUR LOOPS PER REACTOR, ONE RECUPERATOR PER LOOP.

GA-A13950

Fig. 9-14. GT-HTGR recuperator parametric study for 950°C ROT, 4 x 4000-MW(t), binary-cycle plant (ε = 0.90)

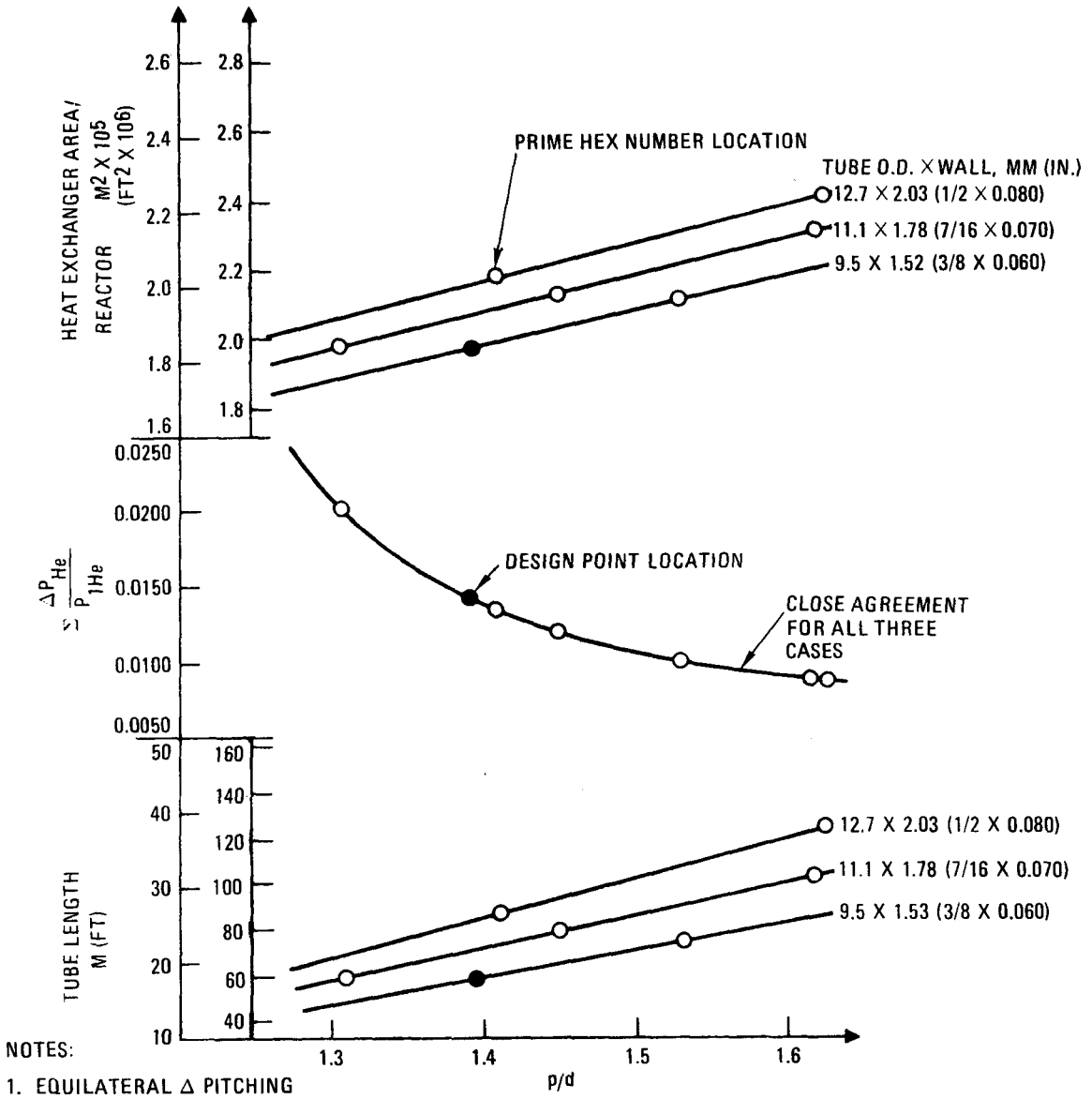

NOTES:

1. EQUILATERAL Δ PITCHING
2. AXIAL COUNTERFLOW MODULAR DESIGN
   - 222 HEXAGON MODULES
   - MODULE PITCH = 269 MM (10.6 IN.)
   - 3.175 MM (1/3 IN.) THICK SHROUD SEPARATING MODULES
   - 397 TUBES PER MODULE
   - DESIGN POINT AT p/d = 1.3956
3. 10% UA MARGIN
4. HEAT EXCHANGER DIAM = 4.72 M (15.5 FT)
5. FOUR LOOPS PER REACTOR, ONE PRE-COOLER PER LOOP
6. 0.51 MM (0.02 IN.) THICK TWISTED TAPE RUNS ALONG I.D. OF TUBES

GA-A13950

Fig. 9-15. GT-HTGR precooler parametric study for 950°C ROT, 4 x 4000-MW(t), binary-cycle plant

TABLE 9-3
GT-HTGR HEAT EXCHANGER DESIGN DATA FOR 950°C ROT,
4000-MW(t), FOUR-LOOP, BINARY-CYCLE PLANT

	Recuperator	Precooler
Modules/heat exchanger	180	222
Hexagonal module A/F, mm (in.)	292.1 (11.5)	296 (10.6)
Tubes/module	331	397
Tube o.d. x wall, mm (in.)	11.1 (0.4375) x 1.13 (0.045)	9.53 (0.375) x 3.05 (0.120)
Tube material	Austenitic Type 316 stainless steel	Medium carbon steel
Tube p/d	1.42	1.396
Active tube length, m (ft)	12.77 (41.9)	17.5 (57.8)
Surface area/reactor, m^2 (ft^2)	160,225 (1.143×10^6)	184,000 (1.989×10^6)
Overall helium pressure loss ($\Sigma \frac{\Delta P}{P_1}$)	0.0215	0.0139
Overall heat exchanger length, m (ft)	19.8 (64.9)	22.3 (73)
Heat exchanger diameter, m (ft)	4.9 (16.0)	4.72 (15.5)
Overall dry weight, kg (ton)	458,050 (505)	725,600 (800)

The design considerations involved in these studies and how their results influence the heat exchanger assemblies are discussed in the following sections.

9.4.1. Datum Case for Layout Studies

The layout work performed in support of the mechanical design studies was based primarily on the recuperator for the 950°C ROT, 4000-MW(t), dry-cooled plant, although cursory layouts of module patterns were also made in conjunction with the packaging studies discussed in Sections 9.4.3 and 9.4.4. The results of this work were applied to the heat exchanger conceptual designs reported in Section 9.5.

9.4.2. Module Packing Considerations

In an integrated plant, the heat exchangers exert a direct influence on the overall size of the PCRV, thus creating a strong incentive for surface compactness not generally imposed on ordinary industrial heat exchangers. While the counterflow tubular configuration approach used in the design of the recuperator and the precooler yields dimensions particularly suited for PCRV cavity installations, the actual packaging of the heat transfer matrix to minimize heat exchanger frontal area requirements (thus minimizing PCRV cavity diameter requirements) is of vital importance. With the possibility of packaging both heat exchangers as full, homogeneous tube arrays within their respective cavities ruled out by practical considerations, the approach taken toward modularization of the heat transfer matrix must be selected carefully. Since homogeneous tube arrays produce the minimum possible PCRV cavity diameters, the module shape and size for a given heat exchanger design should be the combination which most nearly produces the ideality of a homogeneous tube field while satisfying the mechanical design requirements for handling and thermal growth flexibility.

9.4.3. Influence of Module Shape

For the recuperator and precooler applications, there are four basic criteria that affect the selection of the shape of the modules:

1. Elimination of inactive frontal area inherent in the module shape itself

2. Minimization of inactive frontal area caused by edge effects created when the modules are packaged within the annular heat exchanger envelopes

3. Minimization of inactive frontal area produced by incompatibilities between the tubular matrix and its modular boundry

4. Maximum heat transfer matrix compactness per unit frontal area

In the initial heat exchanger studies, circular modules were chosen in order to simplify the subheader structure, recognizing that circular modules, per se, did not necessarily produce optimal packaging. The resulting modest (on the order of 60%) packing efficiencies* reflected the inefficiencies of the circular module shape attributable to tricusp area losses and to combined internal and external edge effects.

Recent innovations in module subheadering and shrouding techniques which now permit contiguous packaging of the modules have made it possible to consider more attractive alternatives, leading to the hexagonal modular arrays evolved for the conceptual designs presented in Section 9.5. The packing efficiencies for the recuperator and the precooler have been improved to 77% and 87%, respectively, the improvements being almost completely exploited to reduce the heat exchanger cavity diameters. Fig. 9-16 shows schematically how this was accomplished.

*Defined as the ratio of actual deployment of heat transfer surface within a given frontal area to the maximum theoretically possible within the same area.

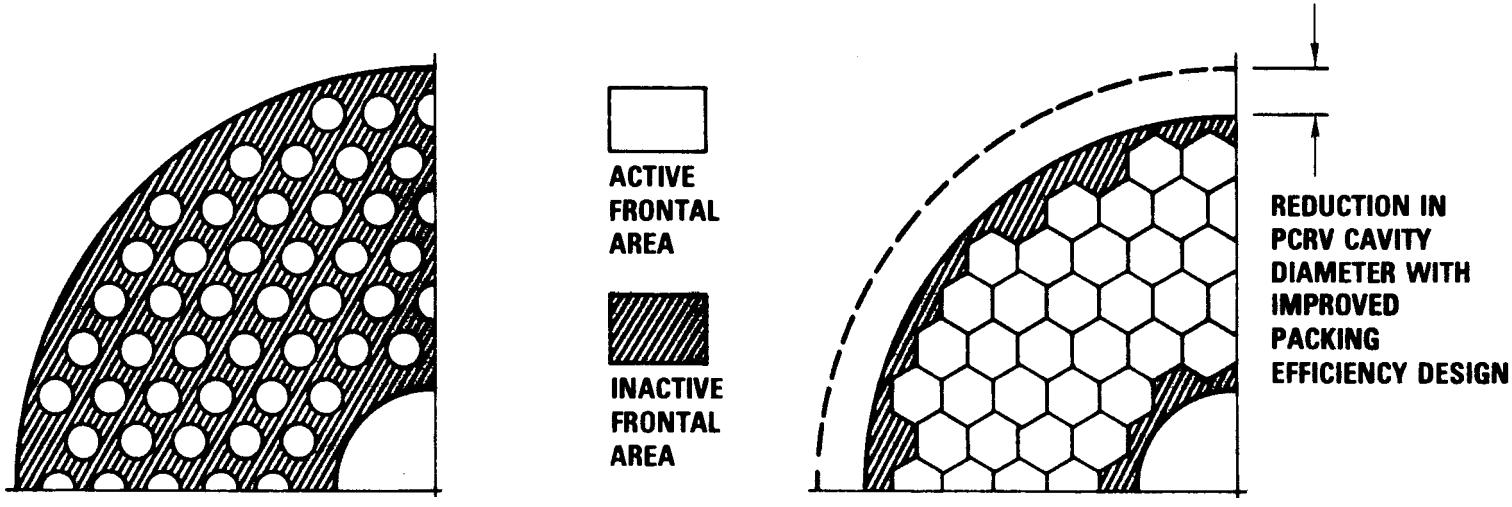

Fig. 9-16. GT-HTGR heat exchanger design improvements

From the standpoint of the criteria set for the above, the hexagonal module shape offers the following advantages:

1. No frontal area blockages attributed to the shape itself

2. Inherent compatibility with triangularly pitched tube arrays, thus minimizing frontal area losses due to internal edge effects while ensuring matrix compactness

The influence of the hexagonal shape on the frontal area blockage at the inner and outer peripheries of the modular array is controlled to a large extent by the module size, which is discussed further in the following section.

9.4.4. Influence of Module Number

The number of modules that can be packaged within a given envelope is a function of the module cross-sectional size as well as its shape, and for a given tube diameter and p/d, it is obvious that reducing the module size increases the quantity of modules possible within the envelope. However, the overall packing efficiency, which does not necessarily increase with reductions in module size, and mechanical design considerations for headering and thermal growth flexibility in the subheadering lead tubes also have to be taken into account. If the tubes within the bundle are closely pitched, as is the case in both the recuperator and the precooler designs, the incorporation of mutually shared shell-side flow guides (shrouds) between the modular tube bundles introduces frontal area blockage that has an increasingly detrimental effect on the packing efficiency as the module size is reduced (see Fig. 9-17). On the other hand, increases in module size introduce more inactive frontal area because of external edge effects and also increase the diameter and wall thickness of the lead tubes correspondingly to the point where additional PCRV cavity height may be required to achieve the coiled lead tube flexibility needed for accommodating differential thermal growth. In addition, the specification of hexagonal modules of a given size for a particular heat

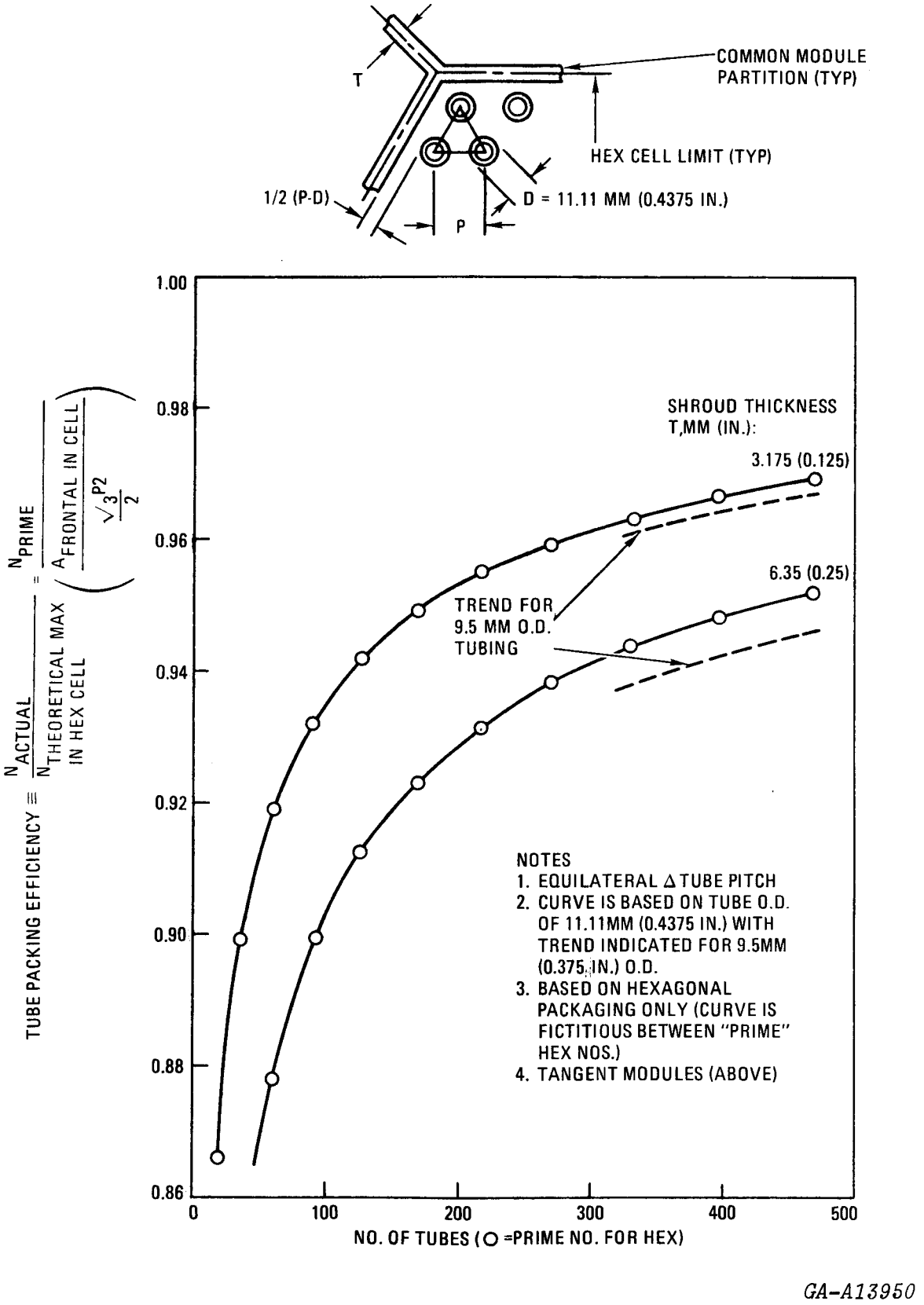

Fig. 9-17. Influence of tube count and shroud thickness on tube packing efficiency within hexagonal modules

exchanger envelope and tube diameter removes the opportunity for treating the tube p/d as an independent variable, thus imposing an additional constraint on the thermal sizing of the unit. The optimal module count for a given heat exchanger design, therefore, entails several factors which have to be examined in considerable detail.

Toward this end, the computer code PACKEM was developed to expedite hand-generated layout studies aimed at identifying heat exchanger module arrangements with high packing efficiencies. Given a circular of annular envelope, PACKEM surveys a specified range of hexagonal across-the-flats dimensions by packaging the hexagons within the envelope, after which it then packages tubes of a given diameter within the hexagons to arrive at tube pattern p/d values corresponding to prime hexagonal numbers. Cases with optimal packaging are identified with pseudopacking efficiency computations based on the ratio of the hexagonal frontal area summation to gross frontal area, together with the actual tube count per heat exchanger. After optimal packaging combinations are established by PACKEM, layout studies are performed to confirm visually that the computer results have not overlooked significant improvements available through finer survey increments. The final results are used as the basis for PCRV cavity tradeoffs similar to those discussed in Section 9.2.

Although the techniques are considerably less refined for selecting optimal module quantities from the subheadering lead tube standpoint, considerations for handling, lead tube plugging, and general complexity have historically kept the quantity of modules per heat exchanger in the range of 96 to 222. The imposition of this range, in conjunction with the PACKEM studies and the thermal size tradeoffs, generally reduce the field of acceptable module sizes to a small number, thus greatly simplifying the selection process.

9.4.5. Module Subheader Details

The ability to exploit the advantages of contiguously packaged hexagonal modules in the gas turbine heat exchanger designs to effect PCRV cavity diameter reductions has long been a desirable design feature. Early designs were not able to capitalize on this approach because they employed

relatively conventional module subheaders with flat tubesheets. Regardless of the module shape chosen, it was discovered that the subheader tubesheet edge distance mandated by structural considerations resulted in the extension of the subheader beyond the boundaries of the module proper, thus infringing on the space requirements of adjacent modules. Although this problem was relieved to some extent by staggering the modules axially and tucking the overhanging portions of their subheaders underneath one another, it was still necessary to maintain gaps between the modules to avoid mechanical interference. This not only penalized the designs substantially from a frontal area standpoint but also introduced mechanical complexity by creating a need for individual shrouds on the modules with interstitial seals between them to prevent shell-side bypass.

In the present designs, these problems have been circumvented through a subheadering innovation, details of which will be presented in a later report.

The rewards accompanying this solution to the module subheadering problem are considerable:

1. As discussed previously, significant PCRV diameter savings (on the order of 0.3 to 0.6 m (1 to 2 ft) have been realized through the ability to package hexagonal modules contiguously.

2. Mutually shared partitions between modules, rather than individual cans or shrouds, are possible, thus eliminating the need for intermodule bypass seals, increasing the structural rigidity of the modular array, and facilitating provision for shell-side gas mixing (via perforated or discontinuous partitions).

9.4.6. Seal Arrangement

A necessary feature of the heat exchanger design is a seal between the hot inlet gas and the cool outlet gas. This seal is not a static seal but must provide for the movements due to temperature changes in the connections to the support flange where a true static seal is possible.

The concept chosen is based on the design of the core top seal of the Peach Bottom HTGR, which was tested first at GA and then in the field and which performed satisfactorily for the life of the plant. It will be seen from the location of the seal in Fig. 9-18 that the high-pressure hot gas is in the bottom and that the cool low-pressure gas is on the top. The seal is made up of graphite segments, as shown in Fig. 9-19, which are confined in a carefully machined annulus. The segments seal on their upper and outer surfaces and are held against the mating metallic parts by the differential helium pressure. The springs keep the blocks correctly positioned when there is no pressure differential.

During installation it is anticipated that it will be desirable to hold the seal segments in the collapsed position until the seal gets within a few inches of the seat. The lowering of the heat exchanger unit will be stopped when it is 457 mm (18 in.) above the installed position and the segment restraint is removed as shown in the upper position of Fig. 9-19. The segment restraint may be a circular steel ring supported on cords from the top flange. If continuous, it can be cut in segments for removal. An alternative restraint would be an endless nylon rope about 25.4 mm (1 in.) in diameter that would roll off the segments as they entered the taper. It would be lifted out, cut in two, and removed. The seal segments slide on the smooth sealing surface as the heat exchanger is lowered the last 457 mm (18 in.) to its final position.

The seal concept described above applies to both the recuperator and the precooler, since each of these heat exchangers embodies a multiplicity

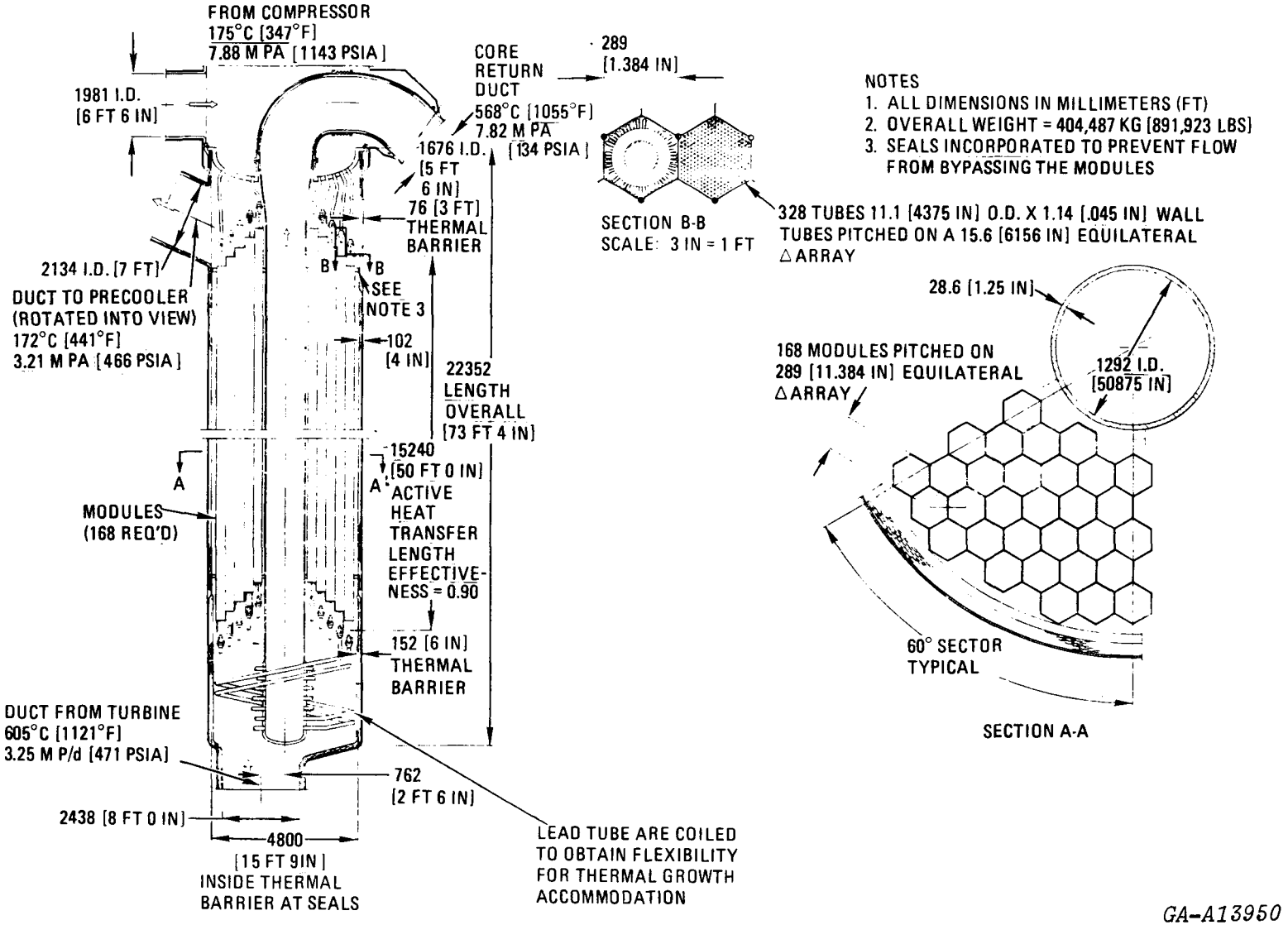

Fig. 9-18. GT-HTGR recuperator for twin 4000-MW(t), 950°C ROT, four-loop, dry-cooled plant

NOTE: ALL DIMENSIONS IN MILLIMETERS (FT)

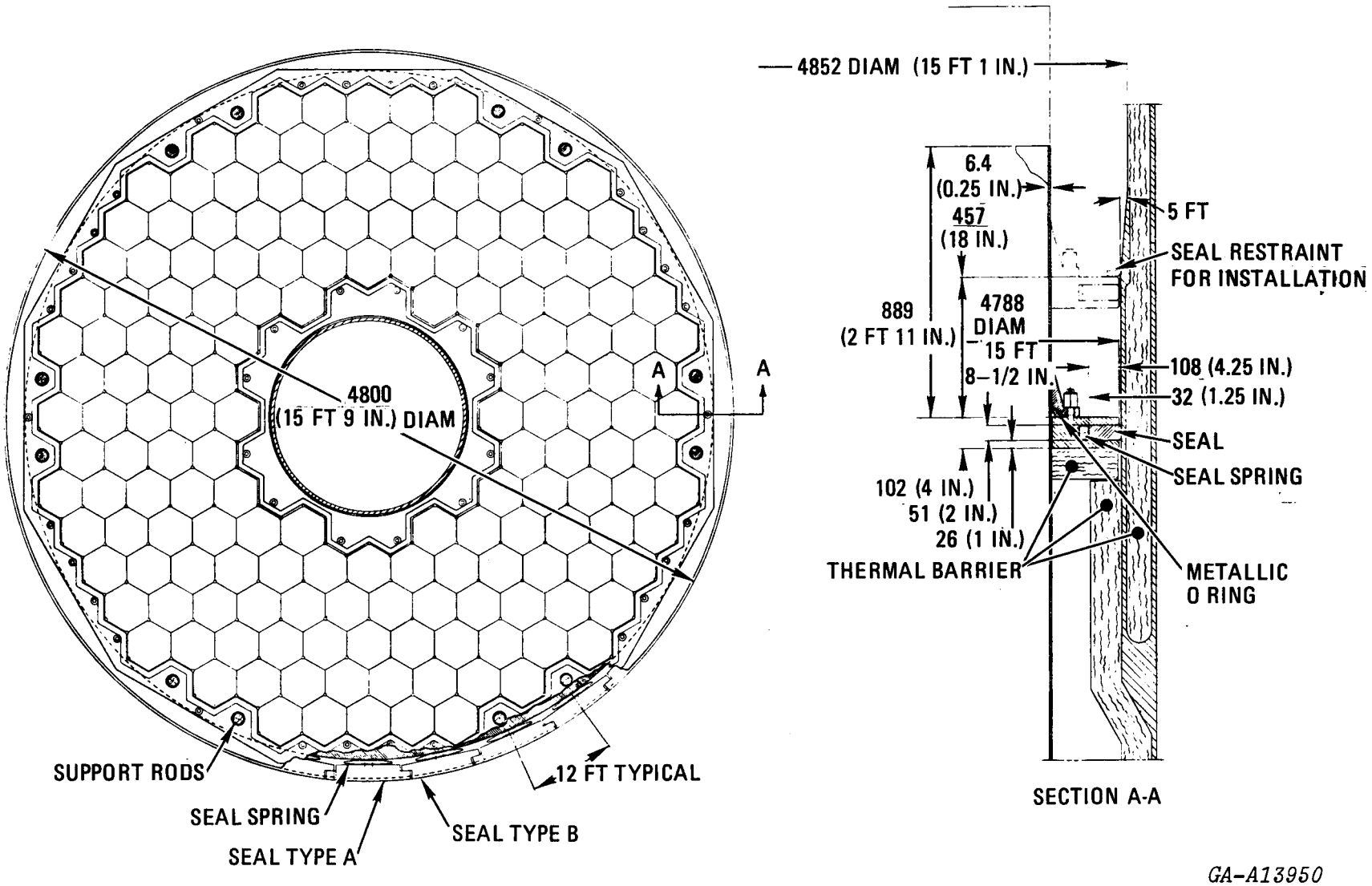

Fig. 9-19. Seal arrangement

of hexagonal modules that are installed in a cylindrical cavity, it being necessary to minimize secondary leakage to avoid performance degradation. Neither of the heat exchangers requires a seal to take the full system pressure differential.

9.5. HEAT EXCHANGER CONCEPTUAL DESIGN

Conceptual designs of the recuperator and the precooler for the 950°C ROT, four-loop, 4000-MW(t), dry-cooled plant are presented in the following sections. Both designs embody the improved tube packing efficiency approach described in Section 9.4 and reflect the thermal size optimization information reported in Section 9.2. The mechanical designs shown call for top-supported modular assemblies with thermal growth flexibility provisions located at the bottom. These general features are applicable to all of the heat exchanger designs, regardless of the plant configuration or loop rating. In addition to the selected recuperator and precooler designs presented below, alternate approaches which might offer substantial improvements are briefly discussed.

9.5.1. Recuperator Configuration

The recuperator design presented in Fig. 9-18 calls for a contiguous array of 168 hexagonal modules to be supported from a torispherical tubesheet which rests on a support ledge provided in the PCRV cavity liner. Each module contains 328 11.1-mm (0.4375-in.) o.d. x 1.14-mm (0.045-in.) wall tubes closely pitched on a 1.407 p/d triangular pattern and supported at 0.6-m (2-ft) axial intervals by cellular spacer grids along their 15.2-m (50-ft) effective lengths. The configuration provides for pure counterflow heat transfer between the high-pressure helium from the compressor flowing downward inside the tubes and the low-pressure helium flowing upward on the shell side. To facilitate shell-side entry and exit flow the modules are arranged in axially stepped hexagonal layers to reduce the flow resistance created by the modular tube bundles. Differential thermal growth is accommodated by the flexibility of the lower subheadering

lead tubes which connect the high-pressure discharge sides of the modules to the center return duct assembly. Because the modules share common partitions, sealing to preclude flow bypass around the recuperator is required only in the peripheral regions of the heat exchanger. Except for the torispherical tubesheet, upper lead tubes, and nonstructural members, which are designed on the basis of using a ferritic (2-1/4 Cr - 1 Mo) alloy, the recuperator is a stainless steel assembly. Salient details of the recuperator design are given in Table 9-1.

9.5.2. Precooler Configuration

The heat transfer matrix for the precooler design presented in Fig. 9-20 is a contiguous array of 210 hexagonal modules which are supported from a top support plate and ring assembly suspended from a ledge provided in the PCRV cavity liner. Each module contains 331 9.5-mm (0.375-in.) o.d. x 1.24-mm (0.049-in.) wall tubes with an effective heat transfer length of 9.24 m (30.2 ft) closely pitched on a 1.397 p/d triangular pattern and supported at 0.6-m (2-ft) axial intervals by cellular spacer grids. Helium from the recuperator enters the precooler cavity via a side-wall opening near the top and flows downward into the shell side of the modules where it is cooled to the compressor inlet temperature by water from the CWS flowing upward inside the tubes. The module water circuits are connected to their inlet and outlet waterbox interfaces by means of subheadering lead tubes which are coiled to achieve the necessary thermal growth flexibility. To provide drainability and rapid dump capability, the two sets of inlet and outlet waterboxes are located at the bottom of the precooler cavity where they are connected to plumbing penetrations extending through the PCRV bottom head. The location of both water inlet and the water outlet plumbing interfaces at the same end of the precooler made it necessary to transfer the water discharging from the individual modules at their top ends to the outlet waterboxes by gathering the upper lead tubes and routing them down through space provided in the center of the modular array. The modules are mitered to facilitate shell-side flow entry and exit in the same manner as that of

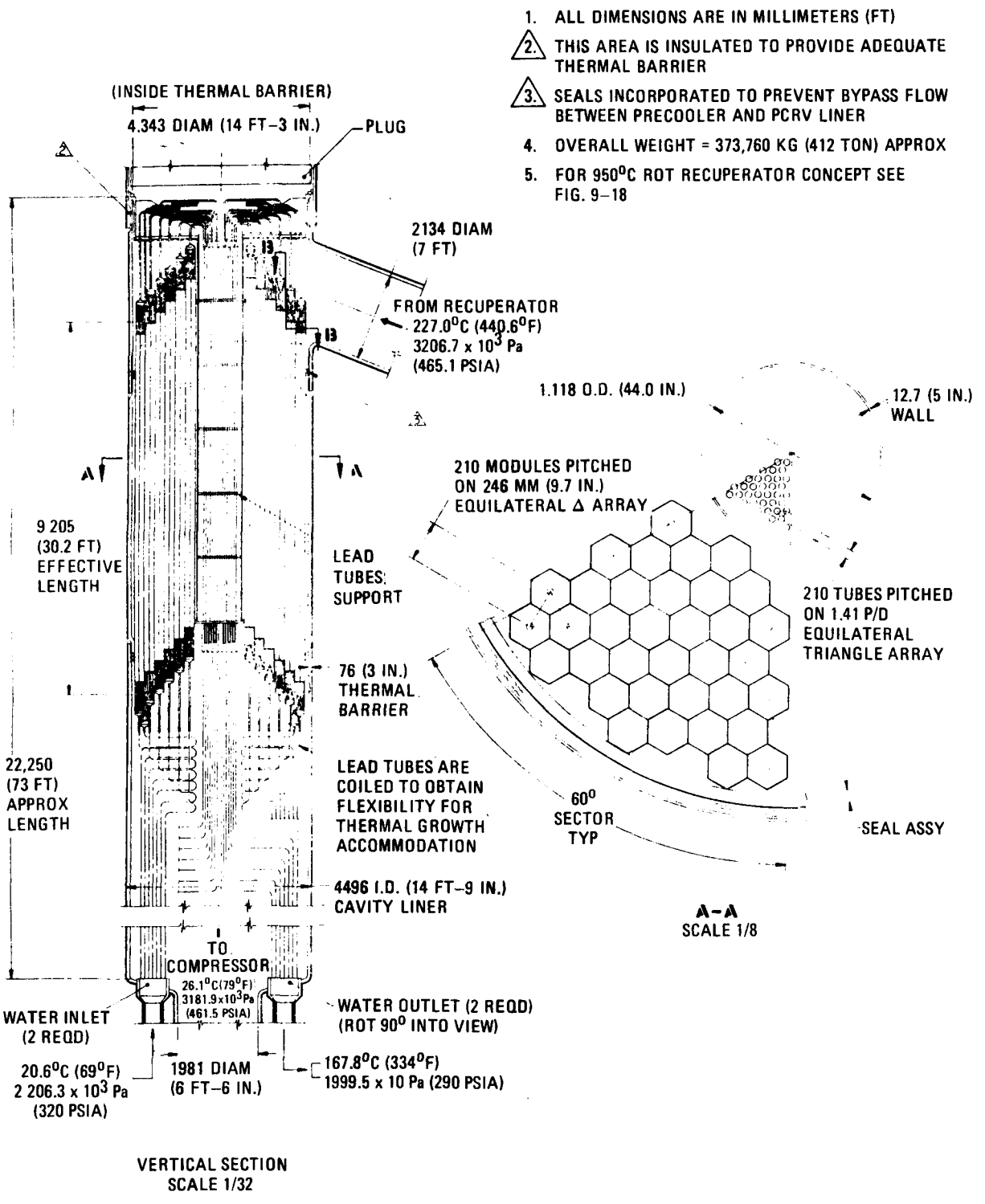

Fig. 9-20. GT-HTGR precooler for twin 4000-MW(t), 950°C ROT, four-loop, dry-cooled plant

the recuperator; the simplification of the bypass sealing afforded by the contiguous hexagonal module packing arrangement is also the same. A summary of the important precooler design features is provided in Table 9-2.

9.5.3. Alternate Configuration Concepts

In the course of the design studies carried out during this reporting period, conceptual approaches that appear to have potential for improving the recuperator and precooler subheadering lead tube arrangements were identified and documented for future reference as alternate concepts requiring further study.

9.5.3.1. Alternate Recuperator Configuration. From a structural standpoint, the main feature of the recuperator is the support of the assembly from the top, with sufficient flexibility in the coiled lower lead tubes to accommodate differential thermal expansion, as shown in the conceptual design of Fig. 9-18. With the modules fabricated from a ferritic material (2-1/4 Cr - 1 Mo), stress analyses in support of the recuperator design have shown the need for austenitic material (Type 316 stainless steel) for the lower-end lead tubes, where the metal temperature is high.

Although in-depth fluid dynamic and flow distribution analyses have not been performed for the shell-side gas flow, the blockage and complexity of the bottom-end lead tube geometries are of concern. The approach shown conceptually in Fig. 9-21 attempts to deal with this problem by transferring the lead tube flexibility to the cold (upper) end of the recuperator. The unit is still supported from the top-domed tube plate, but now the center duct becomes a load-carrying member. At the bottom of the assembly a grid support structure is attached to the center duct, and the weight of the modules is taken in this plane. With the modules essentially propped up from the bottom, they are free to grow (thermally) upward, and the thermal expansion capability is provided at the top end. The lower maximum metal temperatures at this end permit the flexible top-end lead tubes to be made from a lower-cost ferritic material.

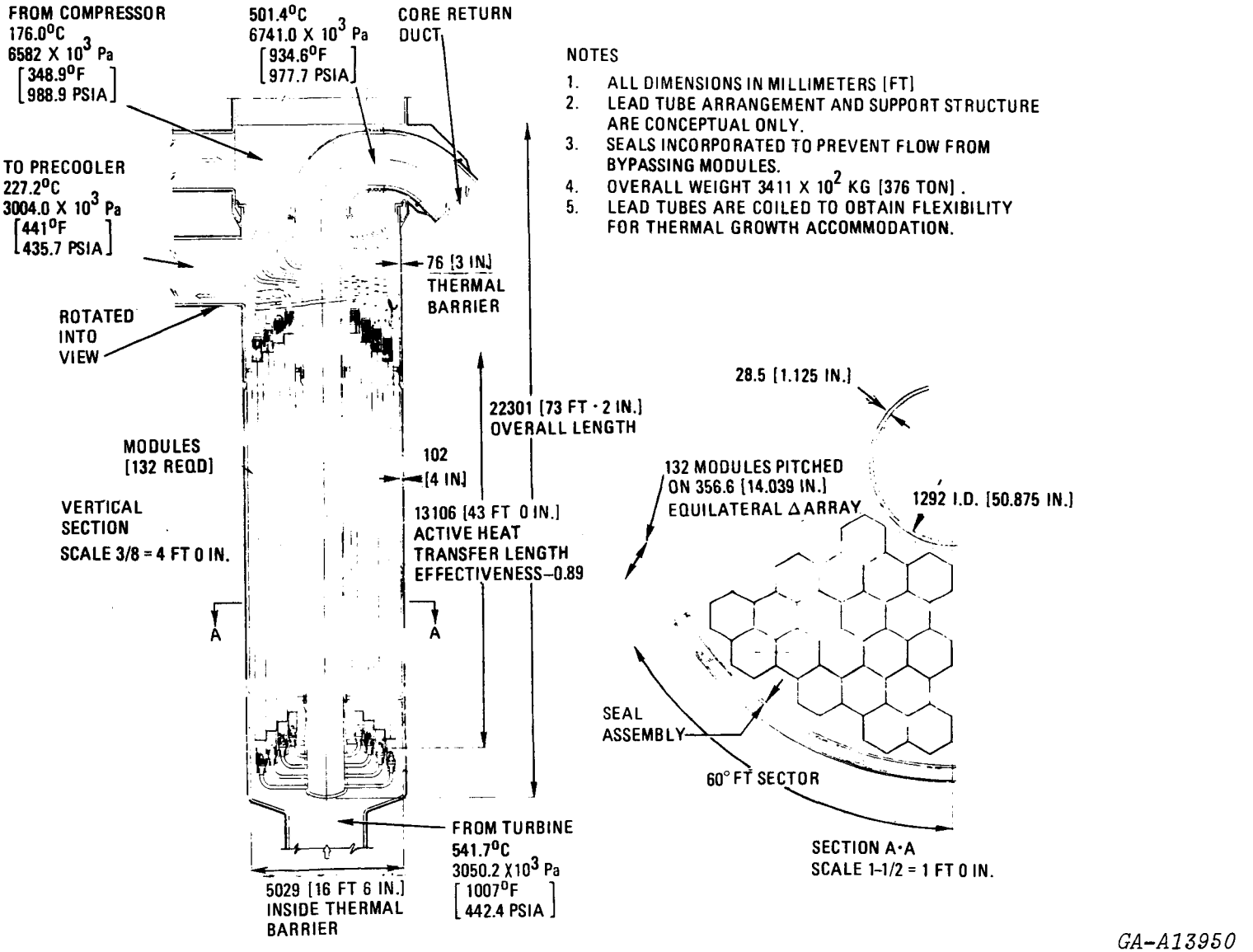

GA-A13950

Fig. 9-21. Upper lead tube flexibility concept for GT-HTGR recuperator

The merits of this variant are tentatively identified as: (1) reduced lead tube blockage and congestion at low-pressure gas inlet and (2) somewhat eased flexibility requirements because of cold-end location. There are some serious unknowns which imply that substantial design work is necessary before this approach can be considered viable. The main areas of concern are: (1) added structural loading of the pressurized central return duct, (2) geometry of bottom support grid (for low-pressure loss), (3) ability of hexagonally headered modules to be compressively loaded as columns, (4) low-pressure exit gas pressure loss flowing transversely over the coiled lead tubes, and (5) response during seismic events.

9.5.3.2. Alternate Precooler Configuration. Considerations for rapid dumping capability and gravity-motivated drainability of the water passages have essentially dictated the present precooler design approach calling for an "inverted U" arrangement, with the water inlet and outlet pipes penetrating the bottom head of the PCRV as shown in Fig. 9-22. While the precooler is a low-temperature heat exchanger [i.e., metal temperature less than 200°C (392°F)] with a rigid top support and fixed tube plates at the bottom, provision must be made for thermal expansion. This is done by incorporating flexibility in the 41.4-mm (1.63-in.)-diameter lead tubes as shown simply in Fig. 9-22. Routing the multiplicity of lead tubes to two water inlet and outlet tube plates with thermal expansion capability results in a complex headering array that requires considerable parasitic cavity height.

An alternate concept that appears to reduce the amount of thermal expansion that must be provided in the design is shown in Fig. 9-22. With support at the bottom and no mechanical constraint (except seismic stops) at the top, the precooler is free to grow upward during its rise from ambient to operating temperature. Minimum flexibility in the lead tubes is required to accommodate differential thermal expansion and to provide for growth over the small length between the support plane and the bottom tube plates. With this simplified lead tube geometry, extra height is available in the precooler cavity. Recent studies based on the

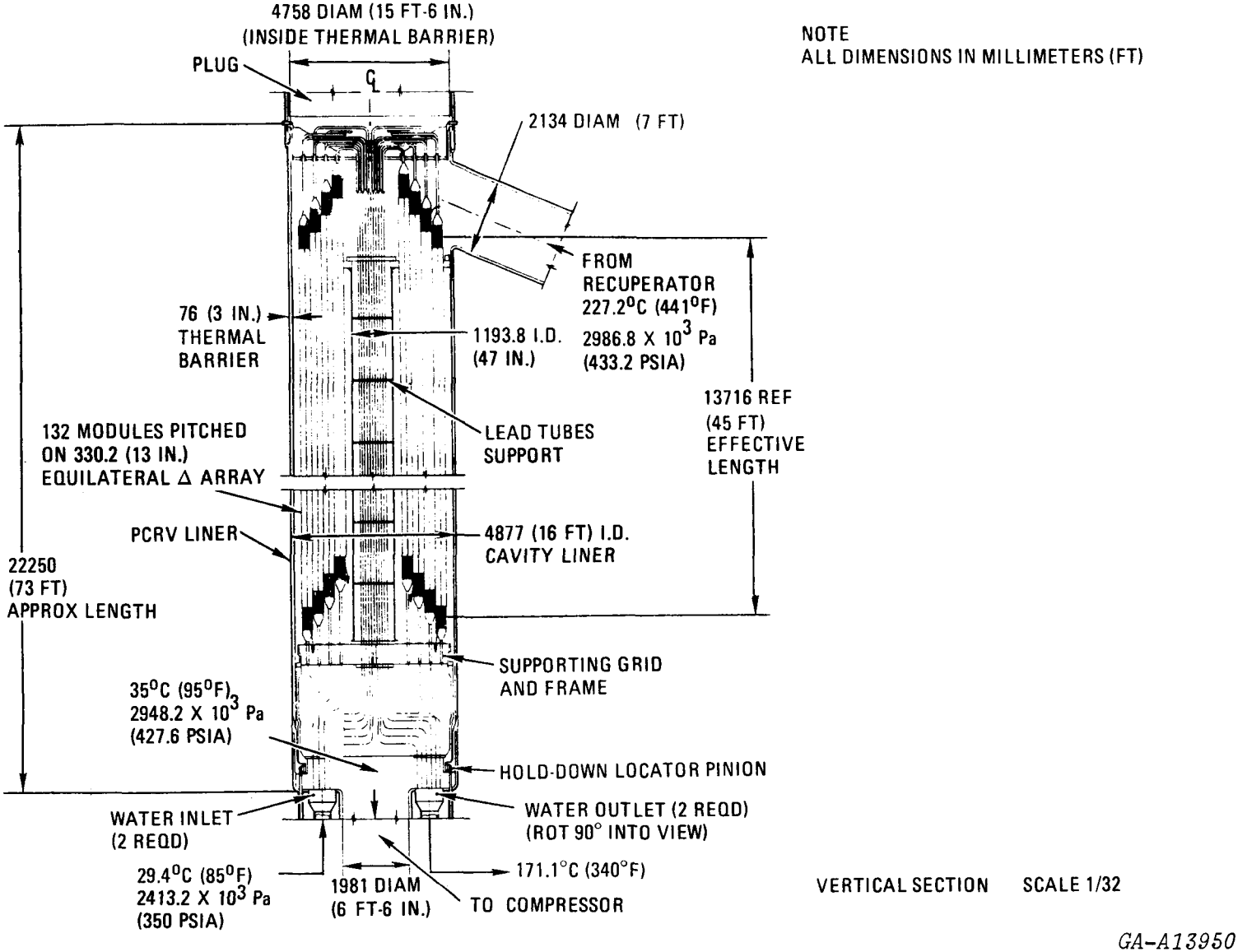

Fig. 9-22. Precooler-hexagonal module, bottom-supported

reference precooler design discussed in the previous report indicate that a potential precooler height savings on the order of 3.35 m (11 ft) for that design may be available with this approach. This savings can be exploited in several ways: e.g., (1) increased effective tube length for improved thermal performance (not recommended) or utilization of larger tube diameters to reduce the number of tube ends or (2) duct simplification obtainable through lowering the precooler assembly below its present station in the PCRV cavity.

The main disadvantage of the lower precooler support, using the established maintenance ground rule of man access not being mandatory, is that the mechanical holddown must be done remotely. A holddown locator pinion is shown conceptually in Fig. 9-2, but the mechanism penetrating the bottom head will be complex when engineered. The objective of this brief study was to explore the bottom support concept, and, while the cavity height savings is significant, it is felt that more detailed design effort is needed to resolve the remote clampdown issue before this approach can be considered viable.

9.6. HEAT EXCHANGER INTEGRATION IN PCRV

The preceding sections have pointed out the influences that PCRV considerations have had on the design approaches adopted for the recuperator and the precooler. How the integration of the heat exchangers within the PCRV arrangement is accomplished depends heavily on the resulting interaction with the other components and gas flow paths within the system. In pursuing the basic design goal of simplicity, the integrated heat exchanger concepts developed thus far have taken advantage of utilizing the pressure containment role of the PCRV to eliminate the need for shells and to minimize the number of mechanical connections to the PCRV, thus simplifying heat exchanger installation and removal. In the recuperator, the functions of top support and high-pressure/low-pressure flow circuit segregation have been combined in the torispherical tubesheet to simplify the upper structure. These approaches, which are illustrated schematically in Fig. 9-23, have been continued in the investigations reported herein.

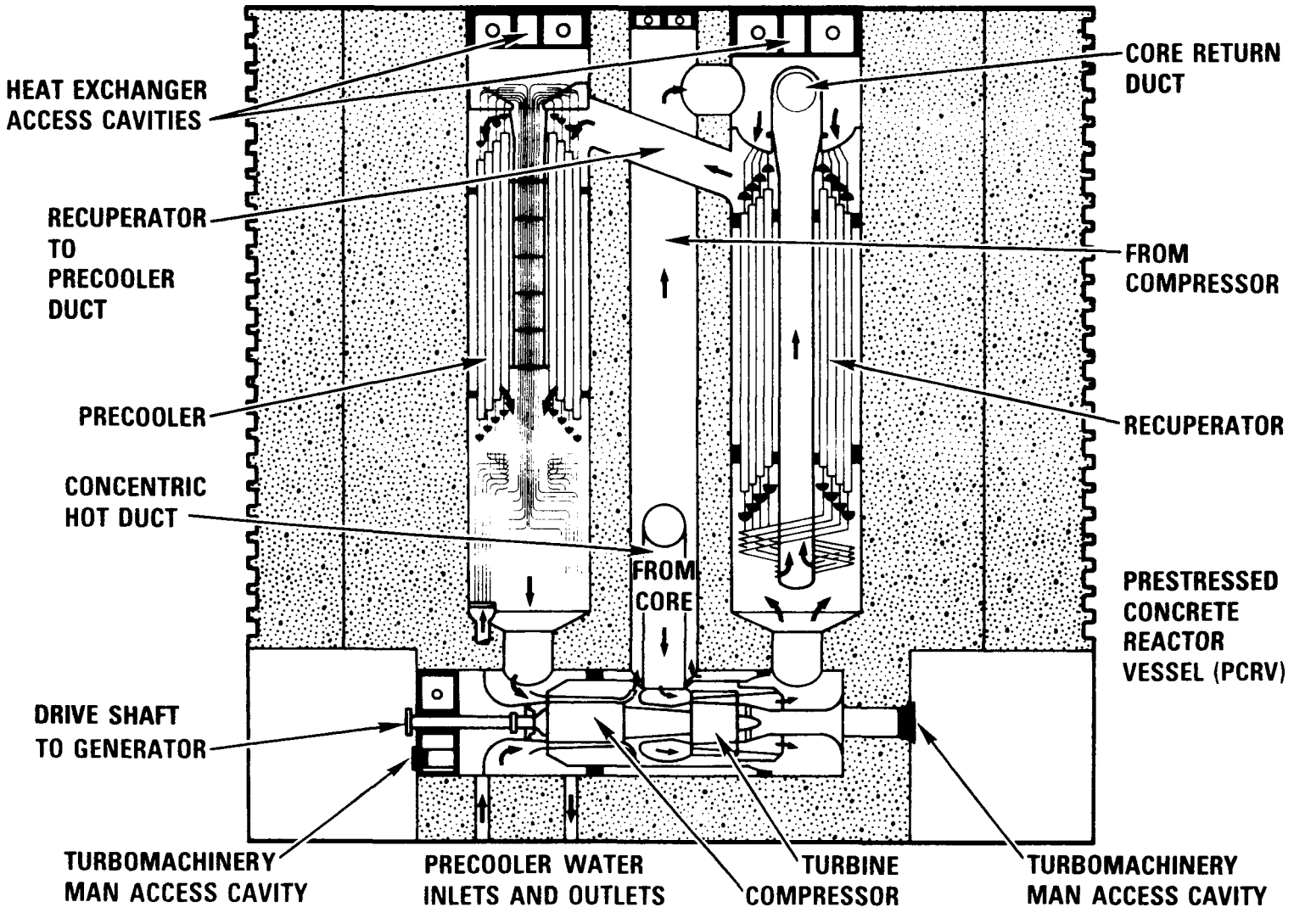

Fig. 9-23. Developed section through GT-HTGR vessel showing primary system helium flow path

Recent plant configuration studies have identified significant reductions in PCRV size and cost associated with reorienting the horizontal turbomachinery to a tangential, rather than radial, position, thus eliminating the size limitation on the PCRV previously imposed by the length of the gas turbine unit. The impact of this change on the integration of the heat exchangers in the four-loop, 4000-MW(t) and three-loop, 3000-MW(t) options for a 850°C ROT, 4000-MW(t), dry-cooled plant is discussed below.

9.6.1. Four-Loop Arrangement (Square PCRV)

Details of the four-loop plant configuration are shown in Fig. 9-24 which shows the four turbomachines arranged in a square pattern. With this configuration, it was possible to place the recuperator and the precooler directly above the turbine discharge and compressor inlet ends of the turbomachine, respectively. This considerably simplifies the interconnecting ducting between the turbomachine and the heat exchangers over that previously required for the radial PCRV arrangement, in which the vertical recuperator and precooler installations straddled the turbomachine cavity near its center. With the heat exchangers positioned directly above, instead of astride, the turbomachinery cavity, the depth of the heat exchanger cavities in the square PCRV design is just below the amount at which it governs the PCRV height, thus helping to produce a very efficient PCRV design.

In this four-loop design, considerations for the minimum ligament thickness in the area below the heat exchanger cavities made it necessary to move the turbine discharge and compressor inlet duct openings until they were no longer concentric with respect to their heat exchanger cavities. Whether or not additional measures will be necessary to prevent flow maldistribution in this arrangement remains to be analyzed.

The integrations of the recuperator and the precooler are quite similar, with the additional precooler requirements for section isolation capability, drainability, module plugging, and headering handled by the same methods developed for previous designs.

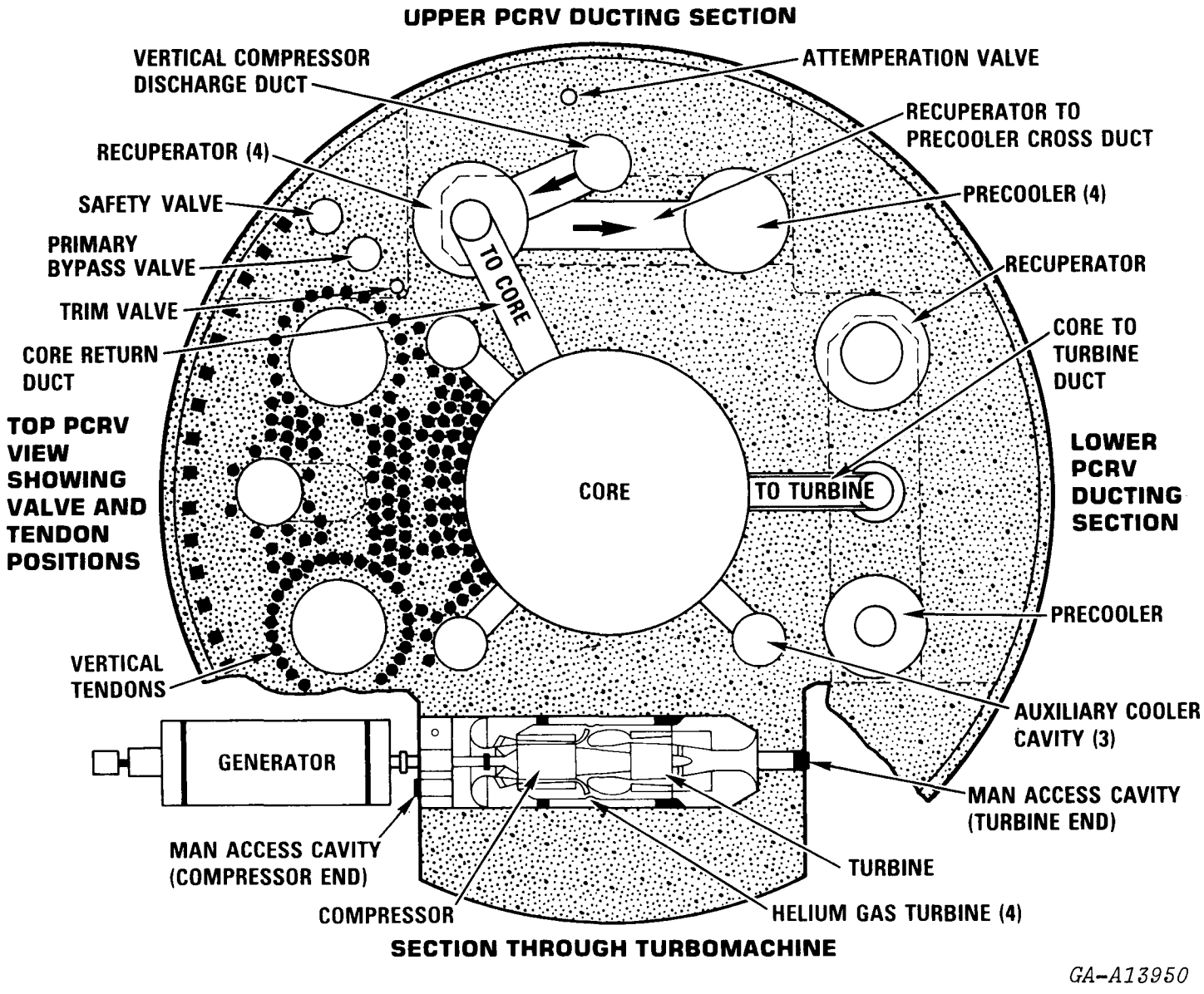

Fig. 9-24. Plan view of square PCRV arrangement for four-loop GT-HTGR plant

9.6.2. Three-Loop Arrangement (Delta PCRV)

Details of the three-loop plant configuration are shown in Fig. 9-25, which shows the three turbomachines arranged in a triangular, or delta, pattern. The advantages and general integration features of this design variant are the same as those discussed above for the square PCRV configuration, except that the extra ligament space afforded by the delta turbomachine arrangement permits the bottom duct penetrations into the heat exchanger cavities to be located centrally.

9.7. INTEGRATED HEAT EXCHANGER DESIGN CONCEPTS

As mentioned in the previous heat exchanger design study for the integrated plant, there is a strong interaction between the major components and the heat exchangers cannot be treated as isolated components. The combined effects of size constraint (integration in the PCRV side-wall cavities), in-service inspection, in-situ repair, and maintenance and fabrication considerations have a significant effect on the choice of surface geometry, flow configuration, and mechanical design.

The goal of the current heat exchanger design task was to select a configuration that had a minimum impact on the size of the PCRV. A module subheadering approach, in which the tube plate itself lies within the projected module flow field permitted better utilization of heat exchanger frontal area. With the contiguous hexagonal module array, the overall heat exchanger diameter was significantly reduced without incurring performance loss. From the heat exchanger standpoint, the proposed hexagonal module geometry has additional advantages (intermodule mixing, elimination of interstitial seals, and increased assembly rigidity) other than the main incentive for selection of this approach, namely, size and weight reduction and projected cost savings. The ramifications of the improved packing efficiency geometry go beyond mere heat exchanger diameter reduction, because this permits a reduction in the diameters of both the PCRV and the containment building, with attendant cost savings.

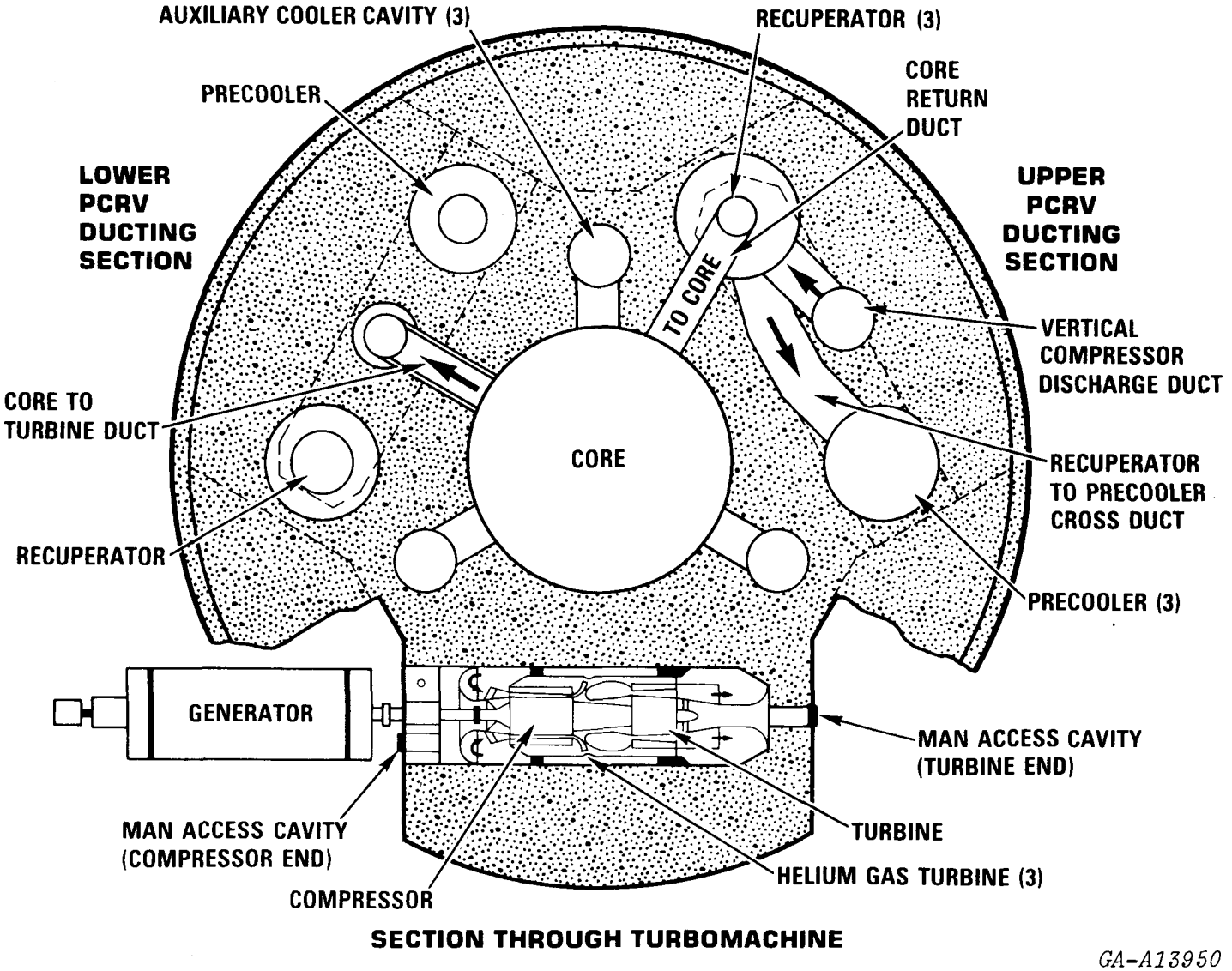

Fig. 9-25. Plan view of delta PCRV arrangement for three-loop GT-HTGR plant

The selected heat exchanger concept is applicable to the recuperator and the precooler for the various plant configurations currently being studied (i.e., dry-cooled and binary-cycle plants). During this phase of the program, the 950°C ROT case was selected for heat exchanger optimization because it represented the most severe conditions from the thermal and structural standpoints. The 850°C ROT cases, while embodying the same design approach, do not represent optimized heat exchanger design solutions but rather were prepared in support of primary system layout studies for the delta (three-loop) and square (four-loop) plant variants.

10. PROGRAM PLANNING (Task 189a, No. SU044)

Activities in the Program Planning task have been primarily directed toward development of more detailed planning for the program definition (preliminary design) phase and updating the existing GT-HTGR preliminary development program plan (Ref. 10-1). Additional effort was required to provide program approach input for the optional gas-cooled reactor (GCR) development strategies evaluated by ERDA GCR task force participants.

A preliminary work breakdown structure (WBS) has been developed to include all elements of a demonstration plant program. The format and the numbering system have been established to make it practical to utilize established computer methods for tracking progress and expenditures when program activities warrant this level of detail. The WBS hierarchy is as follows:

1. Task categories (100s level)

2. Tasks (10s level, representing systems, major structures, and activities

3. Subtasks (third digit), representing components and subsystems

4. Work packages, breaking down subtasks by activities

5. Assignments, within work packages

Major WBS headings and a typical task breakdown are illustrated in Fig. 10-1.

The preliminary program definition phase plan is nearing completion. The plan utilizes the preliminary WBS categories and task breakdown format. Individual tasks have been cost-estimated and time-phased in accordance with a reference 2-yr schedule. The plan is being documented according to the following outline:

A. Overview

1. GT-HTGR program summary
2. Program schedule, Phases I through V

B. Program definition phase plan

1. Objectives and basis
2. Work breakdown structure
3. Task descriptions
4. Schedule
5. Cost estimate - expenditure rate

It is anticipated that substantial cooperation and work-sharing with the German/Swiss Hochtemperaturreaktor mit Heliumturbine (HHT) project will occur during the program definition phase. However, because of current programmatic uncertainties and the early status of related agreements, current plans do not show work-sharing but are task-oriented to facilitate future division of work by task where appropriate. Liaison and activities associated with the adaptation of designs and systems analyses performed primarily by one side of the cooperation are not included in the preliminary plan. These efforts will necessarily have to be further defined when final cooperative plans are developed.

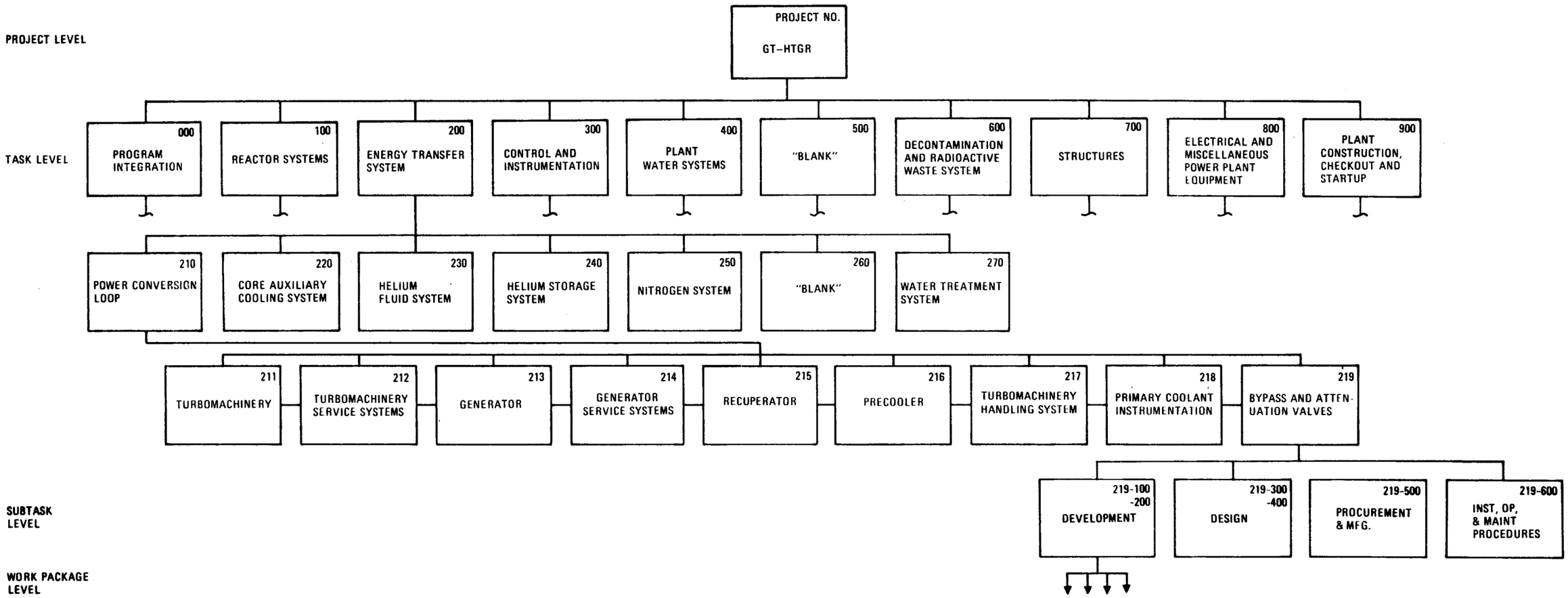

GA-A13950

Fig. 10-1. Work breakdown structure

REFERENCES

10-1. "Nuclear Gas Turbine Power Plant Preliminary Development Plan," Gulf Energy & Environmental Systems Report GA-A12709, August 1973.

11. SAFETY STUDIES (Task 189a, No. SU030)

11.1. INTRODUCTION

A preliminary Accident Initiation and Progression Analysis (AIPA) study was completed identifying the significant risk sequences for the GT-HTGR (see Section 11.2). Safety-related design criteria were developed for various subsystems. A summary of some of the major studies and resulting criteria is presented in Section 11.3. The mechanisms for fission product deposition and mass transfer in the turbine have been analyzed to establish an improved basis for activity of this component (see Section 11.4). The potential safety effects of the introduction of the binary-cycle (ammonia) plant have been assessed (see Section 22.5). The study indicates that the licensing questions appear to be resolvable. A seismic analysis of the PCRV has been performed and is briefly summarized in Section 11.6.

11.2. SIGNIFICANT RISK SEQUENCES

An AIPA study of the GT-HTGR was performed to determine the significant risk sequences. The details of the completed preliminary study are reported in Appendix B.

The AIPA study was largely based on the major SC-HTGR study completed early this year (Ref. 11-1). The GT-HTGR AIPA shows that the GT-HTGR risk envelope lies within that of the SC-HTGR. Thus, the following conclusion from Vol. I of Ref. 11-1 for the SC-HTGR applies equally well to the GT-HTGR:

> "It is concluded that, over a meaningful range of frequencies (say, once per year to once in ten million years), no accident sequence considered in this study would cause death by latent cancer. Events

that were even less frequent (less than once in a billion years) might be predicted to cause one or two latent cancer deaths during a period of approximately 25 years following the occurrence of such an event. This result would be overwhelmed by the normal occurrence of cancer-induced deaths which, during that same 25-year period, would typically be about 5700 in a population of comparable size."

The GT-HTGR risk during a loss of offsite power event is shown to be orders of magnitude below the relatively higher risk SC-HTGR event. The GT-HTGR does not have steam-related components; therefore, the relatively higher-risk SC-HTGR steam leak events are not within the spectrum of GT-HTGR events. The GT-HTGR adds one relatively higher-risk event to the SC-HTGR spectrum. Events related to the generator shaft that penetrates both the PCRV and the reactor containment building (RCB) are shown to be in the relatively higher risk category.

11.3. SAFETY-RELATED DESIGN CRITERIA

11.3.1. CACS Requirements

The CACS is designed to provide adequate core cooling following a reactor trip and shutdown of the PCLs either with the primary coolant system pressurized or following a Design Basis Depressurization Accident (DBDA). The system is composed of three independent auxiliary cooling loops, each designed with the capacity to remove 50% of the core decay heat. Each loop is composed of a core auxiliary heat exchanger, an auxiliary loop shutoff valve, and an electrical motor-driven auxiliary circulator. Hot and cold ducts carry the coolant from the bottom plenum and return it to the top plenum.

The core cooling requirements for the CACS are set to satisfy the intent of General Design Criteria 34 and 35 of 10CFR50, Appendix A.

11.3.1.1. CACS Performance Requirements. The estimated limiting thermal conditions for the GT-HTGR are listed in Table 11-1. Where similarities exist with the steam plant (such as the fuel and lower plenum thermal barriers), the safety limits are obtained directly from Ref. 11-2. For new components, the limits have been evaluated from consideration of the proposed materials. The safety limits are defined as the temperature at which damage may be incurred to the extent that it would interfere with effective core cooling. From Table 11-1 it can be seen that the high-temperature materials of the core itself are not limiting; rather, temperature limits occur in portions of the primary coolant boundary. Specifically, the upper plenum thermal barrier cover plates become limiting during pressurized loss of main loop cooling where natural circulation in the core cavity heats the upper plenum during the period between loss of main loop cooling and initiation of the CACS. Since the natural circulation driving forces are dependent density differences, the time to reach this limit will be a function of primary coolant pressure, which is dependent on helium inventory and volume. For the current design, somewhat more than 5 min was required to reach the upper plenum cover plate temperature limit. The lower plenum thermal barrier cover plates and auxiliary circulators approach their limits during depressurized transients.

11.3.1.2. Core Bypass Condition. The core bypass flow is important since it reduces the core cooling capacity of the CACS. The steam plant design includes main loop helium shutoff valves to minimize this bypass flow. Initial estimates of the flow in a shutdown PCL indicated that similar main loop valves are not necessary for the GT-HTGR. Three bypass conditions were recognized in the current study. The nominal case has the main loops shut down with the control valves closed. The dominant flow resistance in this case consists of the recuperator and the compressor. The second case recognizes the possibility that a main loop bypass valve may be in the open position. Here, the compressor and the recuperator may be partially bypassed, resulting in a larger bypass flow. The third case assumes that one turbomachine experienced a severe accident resulting in a loss of its flow

TABLE 11-1
SUMMARY OF TEMPERATURE LIMITS

Component	Safety Limit	Comment
Fuel particles	1649°C (3000°F)	Failure of fuel particle coatings
Graphite block	2371°C (4300°F)	Fuel-graphite loss of integrity
Control rod	2538°C (4600°F)	Possible boron migration [control rod cans melt 1316°C (2400°F) not considered a safety limit]
Core flow control orifice	1316°C (2400°F)	Allowable for 1 hr
Thermal barrier cover plate		
1. Upper plenum and cross ducts	649°C (1200°F)	Allowable for 1 hr
2. Lower plenum and cross ducts	1093°C (2000°F)	Allowable for 1 hr
Ambient gas temperature of auxiliary circulator		To be determined
Ambient gas temperature of upper plenum penetrations		To be determined
Gas inlet temperature to auxiliary exchanger	1038°C (1900°F)	Allowable for 4 hr
	1093°C (2000°F)	Allowable for 1 hr
Turbine inlet gas temperature[(a)]		To be determined
Recuperator temperature[(a)]		To be determined

[(a)] Not critical for CACS operation

resistance and larger bypass flow. Consequently, the only flow resistance in the faulted loop was assumed to be the high-pressure side of the recuperator.

Table 11-2 shows the calculated bypass fractions for the conditions studied. The nominal condition shows an 18% to 20% bypass. The other two cases show similar bypass fractions. Calculations indicate if the control valves are open in all three PCLs, more than 30% of the flow could bypass the core by way of the main loops. This situation appears to be unacceptable for depressurized accidents. Therefore, the load control and safety valve design criteria have been generated requiring provision for ensuring that these valves will be closed when the pressure difference across the valve is less than a preset minimum. The minimum pressure difference at which the valves can be open is significantly greater than the total pressure drop with CACS operation and is approximately equal to the total system absolute pressure under depressurized conditions (where the bypass is important).

TABLE 11-2
CORE BYPASS CONDITIONS

Condition	Bypass Flow, %	
	Pressurized	Depressurized
Nominal [a]	18 to 20	18 to 20
Valve open [b]	∿25	∿25
Void turbomachine [c]	∿25	∿25

[a] Three power conversion loops shut down with control valves closed

[b] A control valve from core inlet to turbine discharge open in one PCL

[c] Turbomachine void in one loop; remaining loops have control valves closed

11.3.1.3. Auxiliary Circulator Options. The results of analysis of various circulator options and bypass conditions are summzrized in Table 11-3. The primary concern for pressurized cases is the temperature developed in the top plenum during the period when forced circulation is absent; for this issue, the size of the CACS system is unimportant provided that all other cooling requirements are met. For Case 1, the reference 3000-MW CACS will be acceptable; consequently, other larger-capacity loops are also acceptable. Because of the large rotating inertia of the turbomachines, the GT-HTGR will have a minimum of about 80 sec before the machines can coast down. This minimizes the period for natural circulation in the GT-HTGR.

For the depressurized condition, several auxiliary circulator cases were run with various bypass conditions. For Case 3, the reference 3000-MW CACS system may not be acceptable. In addition, the results from Cases 2 and 3 show that the nominal bypass cases with two CACS loops are more severe than utilizing three CACS loops and allowing larger bypass flows, assuming that either a bypass valve opened or turbomachinery failed. Case 4 was run with three CACS loops of the reference 2000-MW circulator size and nominal bypass. From the results shown, it is expected that two loops of this size may not be acceptable, since only two-thirds of the flow is available. Case 5 shows that the Fulton Plant [0.67 MW (900 BHP) vs "standard" 0.45 MW (600 BHP)] circulators, in combination with the reference 3000-MW heat exchangers, are satisfactory for the worst case. It therefore appears appropriate that this size of circulator be used for the GT-HTGR.

11.3.1.4. Ambient Backpressure Studies. The studies described in Section 11.3.1.3 utilized some credit for an elevated containment equilibrium pressure following helium blowdown into the leak-tight containment. Recent licensing discussion for the steam plant required an analysis of the CACS performance assuming no credit for any containment backpressure. Also, recent discussions have indicated cost advantages of the low-pressure confinement building, which relieves directly to the atmosphere. These events have dictated reevaluation of the GT-HTGR CACS cooling capacity at atmospheric pressure. The recommended CACS system from Section 11.3.1.3 was used for the evaluation.

TABLE 11-3
CACS STUDY SUMMARY
(5-min delay before CACS put into operation)

Conditions	Peak Core Outlet Temp, °C (°F)	Max Core Average Outlet Temp, °C (°F)	Max Duct to CAHE, °C (°F)	Peak Fuel Temp, °C (°F)	Comment
1. Pressurized, two CACS loop (reference 3000 MW), nominal bypass	1031 (1888)	916 (1680)	787 (1448)	1097 (2006)	638°C (1180°F) max top plenum thermal barrier cover plate temperature
2. Depressurized, three CACS loops (reference 3000 MW), voided loop bypass	1117 (2043)	970 (1778)	699 (1290)	1186 (2167)	Appears to be acceptable
3. Depressurized, two CACS loops (reference 3000 MW), nominal bypass	>1316 (>2400)	>1090 (>1994)	>1459 (>1675)	>1443 (>2630)	Unacceptable (run stopped at 3 hr with temperature still rising)
4. Depressurized, three CACS loops (reference 2000 MW), nominal bypass	1114 (2038)	968 (1775)	836 (1536)	1183 (2162)	Two CACS loops with nomin nominal bypass may not be acceptable
5. Depressurized, two CACS loops (Fulton Plant size), nominal bypass	1107 (2025)	964 (1768)	841 (1546)	1174 (2145)	Acceptable

Three cases were evaluated in this study. For all three cases, the pressure was set at 101.3 KPa (14.7 psi). Cases 1 and 2 utilized two CACS loops with nominal bypass in the main loops; Case 3 was for three CACS loops and one damaged turbomachine. For Case 1, the gas (air) in the containment and in the PCRV (He) was considered to be mixed; then the pressure was relieved (though no credit was taken for backpressure during the mixing). For Cases 2 and 3, the initial containment gas was assumed to be pure air. The helium leaving the PCRV during the blowdown was assumed, in some manner, to leave the containment. For Case 2, the helium content drops continually over the period of concern, whereas Case 1 would eventually show an equilibrium gas composition of approximately 55% helium.

It was anticipated that the heavier gas circulating in the PCRV for Cases 2 and 3 would reduce the heat removal capacity of the CACS, since the heat capacity per unit mass is reduced. While this occurred in the overall core, the hot channel performance was reversed because of the increased mass flow of Case 2. Table 11-4 shows the heat removal from the total core and from hot region 11 as a function of time. The total heat removal rate is less for Case 2; however, the hot region heat removal rate was increased in Case 2 as compared with that of Case 1.

This phenomenon results in a reduction in peak fuel temperatures as well as a reduction in the maximum core outlet temperature. Case 2 shows a reduction in peak fuel temperatures from 1493°C (2720°F) to 1443°F (2630°F). Similarly, the hot streak temperature was reduced from 1377°C (2510°F) to 1332°F (2430°F). Case 3, which utilized three CACS loops and the larger bypass associated with a failed turbomachine, showed the lowest temperatures 1322°C (2412°F) peak fuel and 1232°C (2250°F) hot streak.

The coolant flow rates supplied by the CACS circulators vary for the three cases analyzed. For Case 1, the analysis showed that the circulator quickly became speed-limited, limiting the flow since the machine was not working at full power. For Case 2, the heavier gas resulted in a larger torque requirement and, hence, greater mass flow, even though the circulator was operating at somewhat lower speed. It should be noted that, even

TABLE 11-4
HEAT REMOVAL RATES

Hr	Case 1		Case 2	
	Total Core, W (Btu/hr)	Hot Region 11, W (Btu/hr)	Total Core, W (Btu/hr)	Hot Region 11, W (Btu/hr)
0.5	0.416 (1.42) x 10^8	0.647 (2.21) x 10^6	0.425 (1.45) x 10^8	0.741 (2.53) x 10^6
1.0	0.448 (1.53)	0.700 (2.39)	0.442 (1.51)	0.785 (2.68)
1.5	0.477 (1.63)	0.750 (2.56)	0.454 (1.55)	0.835 (2.85)
2.0	0.501 (1.71)	0.770 (2.63)	0.460 (1.57)	0.867 (1.96)
2.5	0.513 (1.75)	0.838 (2.86)	0.463 (1.58)	0.890 (3.04)
3.0	0.524 (1.79)	0.902 (3.08)	0.457 (1.56)	0.899 (3.07)
3.5	0.527 (1.80)	0.934 (3.19)	0.451 (1.54)	0.902 (3.08)
4.0	0.524 (1.79)	0.964 (3.29)	0.439 (1.50)	0.887 (3.03)
4.5	0.518 (1.77)	1.002 (3.42)	0.428 (1.46)	0.867 (2.96)

though the mass flow is greater in Case 2, the heat capacity is reduced, resulting in a reduction in the total heat removal rate.

The limiting component in the depressurized transients is generally the cross duct from the core to the core auxiliary heat exchanger. Using the methods described in Ref. 11-2, the maximum cover plate temperatures at the cross duct location were evaluated. Figure 11-1 shows the maximum thermal barrier cover plate temperature as a function of pressure. For all of the cases evaluated to date, the peak temperature remains below the maximum allowable temperature of 1093°C (2000°F). As shown in Fig. 11-1, it may be possible to continue to cool the core until a containment pressure of ∿69 KPa (∿10 psia) is reached.

11.3.2. Generator Housing/Mounting

Safety-related design criteria have been identified as a result of analyses of the potential hazard presented by a hydrogen explosion in a generator cell. The following design criteria are necessary to ensure that a hydrogen explosion in a generator cell can be sustained.

11.3.2.1. PCRV Shaft Penetration Plug.

1. This plug must be designed to allow for at least 2.54 mm (0.1 in.) of float so as to relieve sustained radial loads on the bearing.

2. The bearing itself must be capable of withstanding a radial load of 11,793 kg (26,000 lb) with the shaft at design speed.

11.3.2.2. Space Underneath Generator. Provisions must be made to ensure that the volume underneath the generator (between generator supports) is no greater than 61 m^3 (200 ft^3).

11.3.2.3. Generator Cell Head. The maximum effects of a hydrogen explosion can be sustained by a cell head with a hemispherical shape. For a shape other than hemispherical, some permanent plastic deformation does occur. Design features will be established such that catastrophic failure that could cause damage to either the PCRV or the primary system shaft seal will not occur.

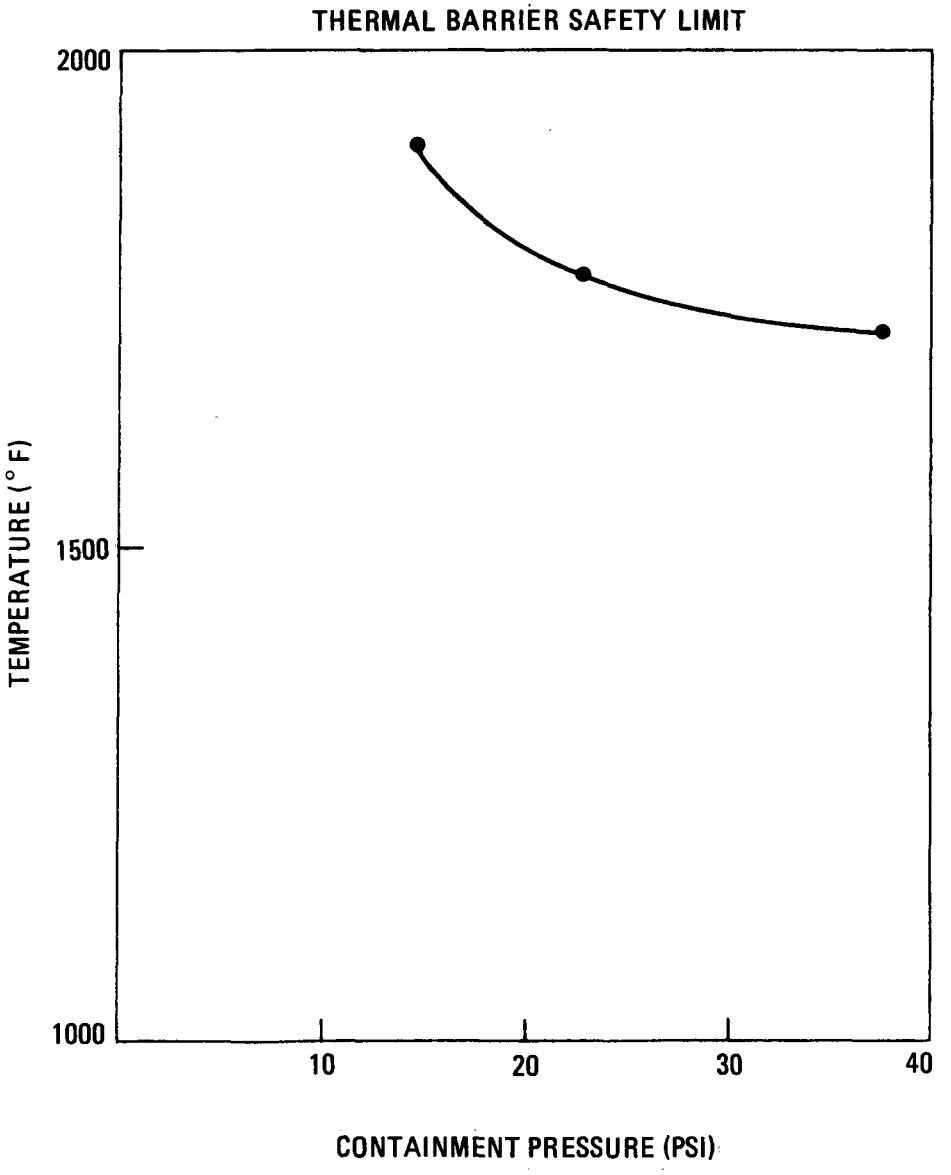

GA-A13950

Fig. 11-1. Maximum thermal barrier temperature vs containment pressure for two CACS loops with nominal bypass

11.3.3. Cooling Water System (CWS) Requirements

This section describes the results of an analysis to determine the CWS response to a precooler offset shear accident and the resulting safety-related design criteria generated. In particilar, it is concerned with identifying (1) the time required to detect that an accident has occurred and (2) the water ingress into the primary coolant. The conclusion of the study is that water ingress can be effectively eliminated by the specified choice of design parameters.

11.3.3.1. Water Ingress Requirements. The major facets of precooler failures along with the consequence of each incident have been identified and reported in previous progress reports. Water inleakage resulting from any single failure must be minimized to prevent core damage. A design value of less than 104 kg (230 lb) maximum has been chosen (GT-HTGR PSID) based on analyses demonstrating that at least this amount is acceptable. Therefore, for a precooler and CWS design to be acceptable from a safety standpoint, it must be possible to demonstrate that the worst credible accident will result in a water ingress below this level. It appears that the worst credible accident would result from an offset shear of one of the module supply lines.

In order to evaluate the transient resulting from such an analysis, it is not sufficient to consider only the precooler itself. Rather, the dynamic responses of the entire CWS must be evaluated. The reason for this will be evident from the discussion in the next section.

11.3.3.2. Systems Model. A schematic diagram of the CWS is given in Fig. 11-2. A qualitative description of the transient resulting from an offset shear is as follows: Helium will almost immediately (>>0.1 sec) purge the water in the faulted supply line then pressurizing the inlet header. The momentum of the inlet supply water will continue the flow for 0.2 to 0.6 sec, depending on water pressure. When the flow stops, helium will begin purging the 47 unfaulted modules; reverse flow in the supply line is

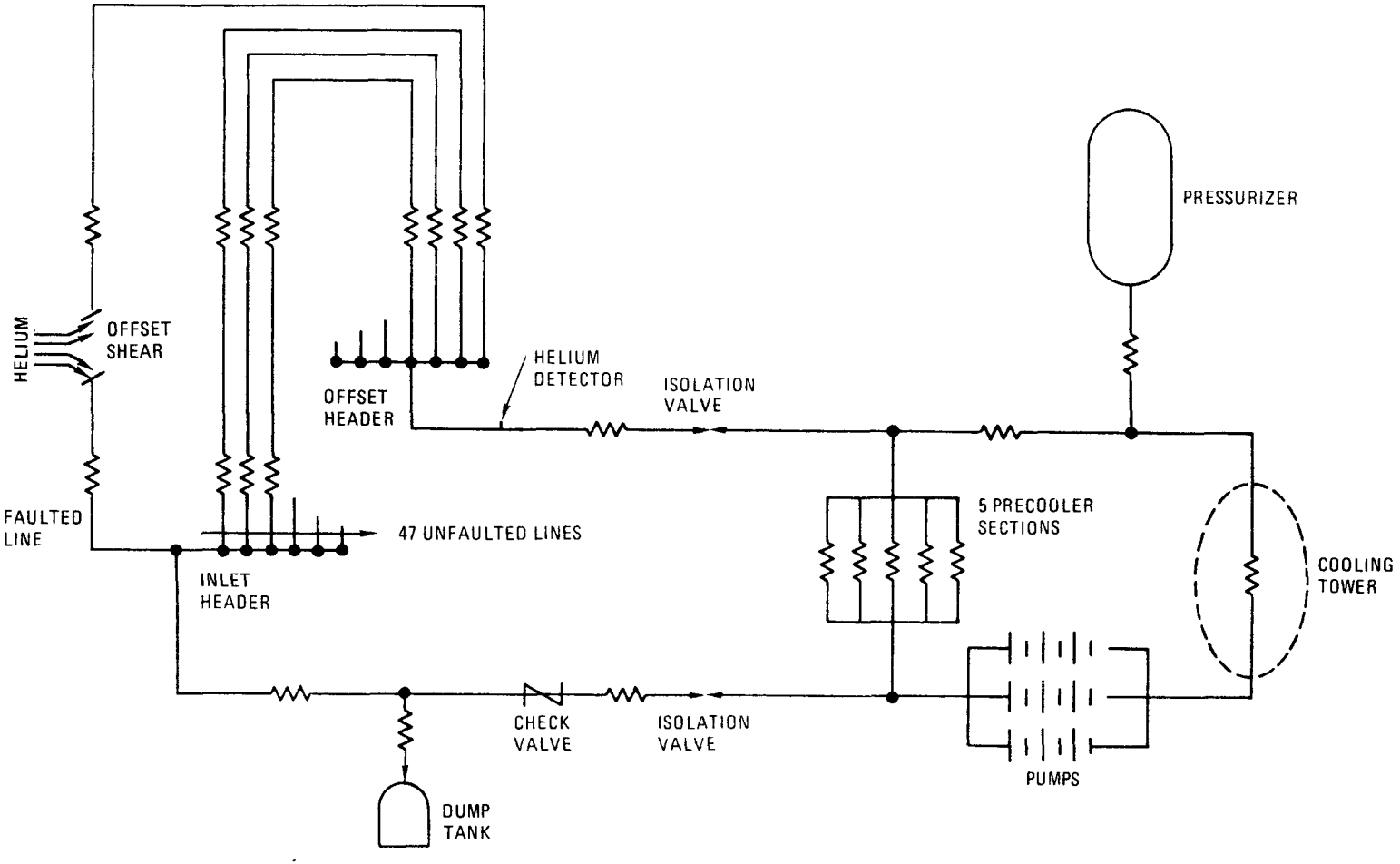

Fig. 11-2. Schematic of cooling water system (CWS)

prevented by a check valve. Helium will completely purge the faulted line reaching the outlet header where radiation detectors will signal that a failure has occurred. At this time, isolation of the faulted section can begin, and the dump tank valves can be opened. Determining the time required for this event was the first task of the study.

Closing the isolation valves on the faulted precooler section supply and return lines ∿356 mm (∿14 in.) will take 1 to 2 sec. During this time period, the pressurizer will continue to be charged, thus raising the pump outlet pressure. If the outlet pressure exceeds the helium pressure before the isolation valves are closed, water will be discharged into the primary coolant. Thus, the second task of the study was to determine the minimum pressurizer volume required to prevent this water ingress.

A computer code was developed that could simulate the dynamic response of the CWS to such an accident. To do this, it was necessary for the code to account for the following phenomena: friction as well as acceleration losses in the lines; line purging by the helium that continually changes the line resistance; system pressurization by the purged water being forced into the pressurizer; and variation in pump operating point due to changing flows and resistances.

11.3.3.3. Safety-Related Design Criteria. From the analysis, utilizing the requirements and model described, the following set of design requirements was developed:

1. Activity monitors

   Number: One set of three per precooler section

   Setpoint: 5 mR/hr (presently assumed to be equal to steam cycle reheater value)

2. Flow monitors

   Number: Two per precooler section (OPS)

   Response: 1 ∿ 5 sec

   Setpoint: ∿ $\sqrt{30\%}$ of flow

3. Isolation valves

Number: Two inlet + two outlet valves per section (24 total)
Closure time: <2 sec
Leakage rate: TBD
Pressure differential: ∿6.2 MPa (∿900 psi)
Safety class: 2

4. Check valves

Number: One inlet valve per section (12 total)
Pressure differential: ∿6.2 MPa (∿900 psi)
Safety class: 2

5. There must be a dump line connecting each precooler inlet line with the dump tank. Within each line, there must be a parallel leg with two isolation valves (safety class 2) in each leg. One of the valves in each leg must remain open to allow for in-service operational checks. Opening time must be less than 2 sec. Provision must be made to allow for dumping each precooler section from the outlet. This may be either an automatic or a manual system. One solution would be to connect inlet and outlet supply lines with a check valve. A lock-out system must be provided to ensure that only one precooler section may be dumped.

6. Dump tank

Volume: 1.5 times precooler water volume (one section)
Safety class: 3

7. CWS pressurizer

Free volume: 4.5 times precooler water volume (one section)

11.4. MASS TRANSFER IN THE TURBOMACHINE

11.4.1. Introduction

The prediction of the fission product plateout concentration on the turbomachine in the GT-HTGR is important in terms of accessibility, maintenance, and handling requirements including the turbomachine shipping cask design basis. The fission product distribution around the reactor circuit is needed to determine the potential liftoff fractions occurring during accidents. The gas turbine is the first major component that the gas "sees" after leaving the reactor core; as a consequence, the gaseous concentrations are greatest in this portion of the loop, which results in a large driving force for mass transfer.

Previous calculations performed at General Atomic (Ref. 11-3) for the GT-HTGR utilized an estimated mass transfer coefficient of 0.34 m/sec (1.11 ft/sec) for transfer to the turbine blades. In addition, a few calculations were performed varying the mass transfer coefficient in order to determine the sensitivity to changing mass transfer coefficient. These results indicated that additional study of the mass transfer process should be performed.

The mass transfer rate in the turbomachine is complicated by the complex flow distributions through the machine. One method for evaluating the mass transfer is to utilize the large amount of theoretical and experimental work accumulated on heat transfer under conditions applicable to turbomachine blades. Turbine blades are basically air foils having a convex (suction) surface and a concave (pressure) surface. The detailed aerodynamic evaluation of the blading designs utilizes boundary layer theory to analyze the velocity distributions along the blade surfaces (Ref. 11-4). These boundary layer calculations are required to demonstrate that the required velocity deflections can be obtained. Specifically, these calculations indicate whether a boundary layer separation could occur, the extent of the laminar sublayer, the location of the transition region, and the extent of the turbulent sublayer. The location of the transition region is important

since differing rates of heat transfer and, hence, mass transfer occur in the laminar and turbulent sublayer.

Brown and Martin (Ref. 11-5) have reviewed the methods for predicting heat transfer to gas turbine rotor blades. Specifically, they have reviewed the applicability of methods and data from isothermal, incompressible flow along flat plates to high-temperature flow along curved surfaces or rotating blades where pressure distributions and centrifugal effects can give rise to secondary flows. Their conclusions are that the flat plate data are useful in providing insight into the phenomenon, although further investigation is needed for predicting the onset of turbulence, particularly in favorable pressure gradients. Finally, in the actual engine operation where secondary flows do occur, these effects tend to increase the local heat transfer over flat plate or cascade measurements.

11.4.2. Mass Transfer Calculations

The mass transfer of circulating fission products to the turbomachine blades is considered to be a diffusion phenomenon. Using the PAD (Ref. 11-6) type of calculational procedure, the diffusion rate to the blade surface is expressed in the form of a mass transfer coefficient where the driving force is a concentration difference.

The general method of modeling the gas turbine in the PAD code (Ref. 11-3) would be to model each blade row or stage as a PAD node and to utilize an overall mass transfer coefficient (blade or stage average). Methods for predicting the overall mass transfer rate are discussed below.

11.4.3. Estimate of the Overall Mass Transfer Coefficient

The first method for estimating the overall mass transfer coefficient was to utilize the analogy between heat transfer and mass transfer. References 11-7 and 11-8 indicated that the satisfactory results for the

prediction of heat transfer coefficients were available in Reynolds number and Prandlt number form:

$$\frac{hc}{k} = a\, N_{RE}^{\alpha}\, N_{Pr}^{\beta}$$

where h = heat transfer coefficient

k = thermal conductivity

c = blade chord length

a, α, β = numerical coefficients

N_{Re} = Reynolds number

N_{Pr} = Prantl number

The Colburn analogy between heat transfer and mass transfer allows one to estimate the mass transfer coefficient (K) by substituting $\frac{Kc}{D}$ for $\frac{hc}{k}$ and replacing the Prandlt numbers by the Schmidt numbers (N_{Sc}):

$$\frac{Kc}{D} = a\, N_{Re}^{\alpha}\, N_{Sc}^{\beta}$$

where D = molecular diffusivity

11.4.4. Local Mass Transfer Coefficient

The mass transfer at the turbomachine blade has been evaluated as a function of location along the blade surface. The method used is an extension of Squires' calculations for local heat transfer in turbine blades (Ref. 11-9). This method is presented in Schlicting and is used by Parker and Lee (Ref. 11-10). For these calculations, the velocity profiles were obtained from turbomachine manufacturers, and the graphical calculations described by Parker and Lee and Wilson and Pope (Ref. 11-11) were performed numerically.

11.4.5. Laminar Boundary Layer

The mass transfer coefficient in the laminar portions of the boundary layer is calculated as follows:

$$\frac{sh}{\sqrt{Re_x}} = \frac{0.572}{\frac{\delta c}{c}\sqrt{Re_x}}$$

where sh = Sherwood number = $\frac{KC^o}{D}$

δc = concentration boundary layer thickness

C^o = concentration at boundary layer

Re_x = local Reynolds number based on cord length and discharge velocity

c = blade cord length

A value of $\frac{\delta c}{c}\sqrt{Re_x}$ was obtained using the methods presented in Ref. 11-10.

This allows direct calculation of the mass transfer coefficient.

11.4.6. Turbulent Boundary Layer

For the turbulent boundary layer, the local mass transfer rate was calculated using the equations developed by Lin et al. (Ref. 11-12):

$$K = \frac{FU}{2\Phi_D}$$

where U is the local velocity outside the boundary layer, F is the skin friction coefficient, and

$$\Phi_D = 1 + \left\{ \sqrt{\frac{F}{2}} \frac{14.5}{3} (N_{Sc})^{2/3} f(N_{Sc}) + \frac{1 + 5.64\ N_{Sc}}{6.64\ (1 + 0.41\ N_{sc})} - 4.77 \right\}$$

where $$f(N_{Sc}) = 0.5 \ln \left\{ \frac{\left[1 + \frac{5}{14.5} (N_{Sc})^{1/3}\right]^2}{1 - \frac{5}{14.5} (N_{Sc})^{1/3} + \left(\frac{5}{14.5}\right)^2 (N_{Sc})^{2/3}} \right\} + \frac{\pi\sqrt{3}}{6}$$

$$+ \sqrt{3} \tan^{-1}\left[\frac{\frac{10}{14.5} N_{Sc}^{1/3} - 1}{\sqrt{3}}\right]$$

These calculations were performed for the second stage of the turbine. Figure 11-3 shows the local mass transfer coefficient for both the pressure and suction surfaces. The overall mass transfer coefficient for the stage is 0.52 m/sec (1.70 ft/sec). For the eight turbine stage, similar calculations were performed. Figure 11-4 shows the local mass transfer rate along the blade surfaces. The overall mass transfer coefficient for this stage is 0.40 m/sec (1.30 ft/sec).

These calculations indicate that the mass transfer rate decreases through the turbine. This occurs because of the reduction in gas velocity which occurs in the turbine. Table 11-5 shows the values of mass transfer coefficient which have been evaluated to date.

TABLE 11-5
MASS TRANSFER COEFFICIENTS

Calculation	K, m/sec (ft/sec)
Initial estimate (Ref. 11-3)	0.34 (1.11)
Ellerbrock (Ref. 11-13)	0.15 (0.050)
Squires method (this study)	
Second stage	0.52 (1.70)
Eighth stage	0.40 (1.30)

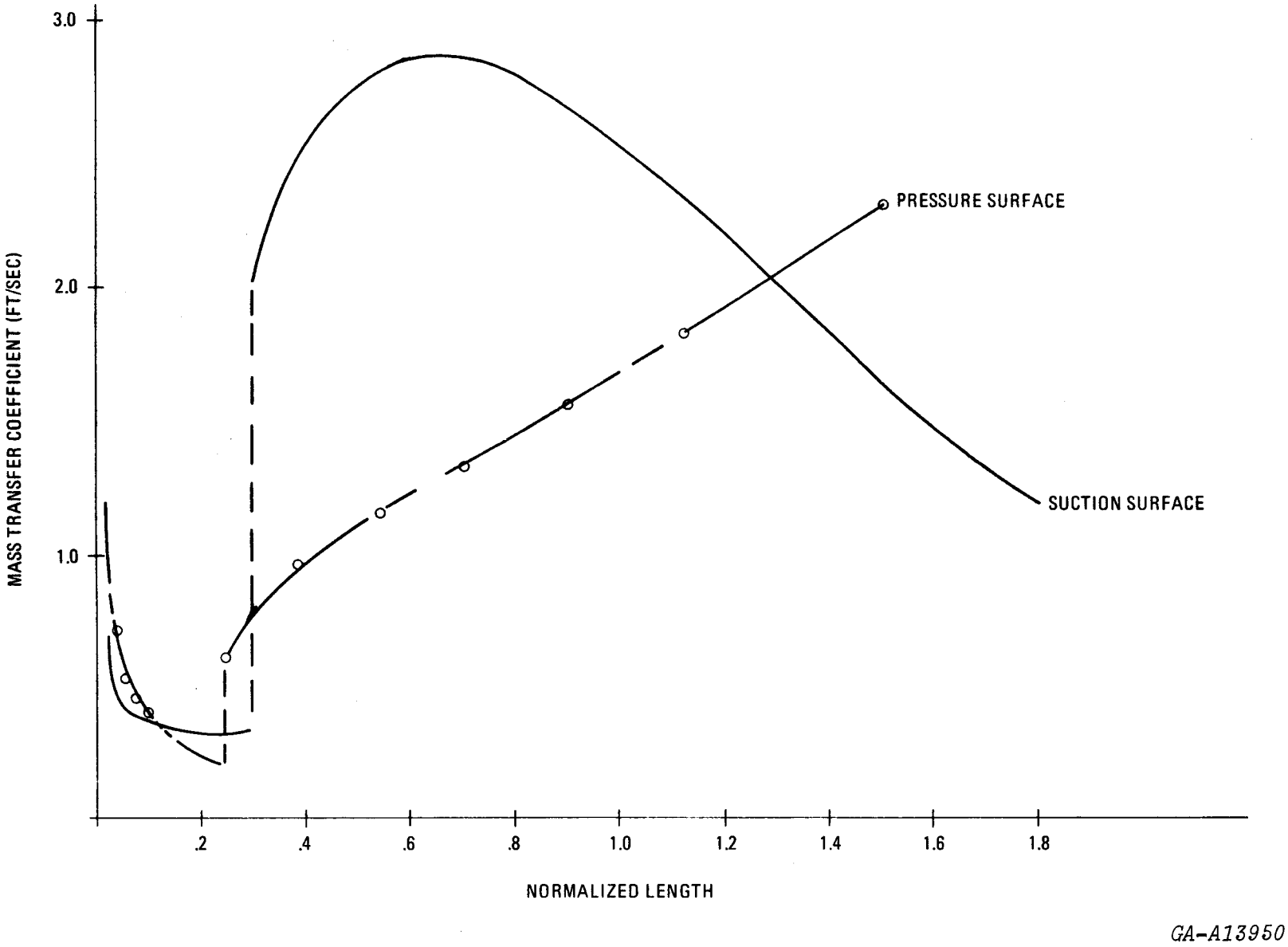

Fig. 11-3. Mass transfer coefficient for second stage

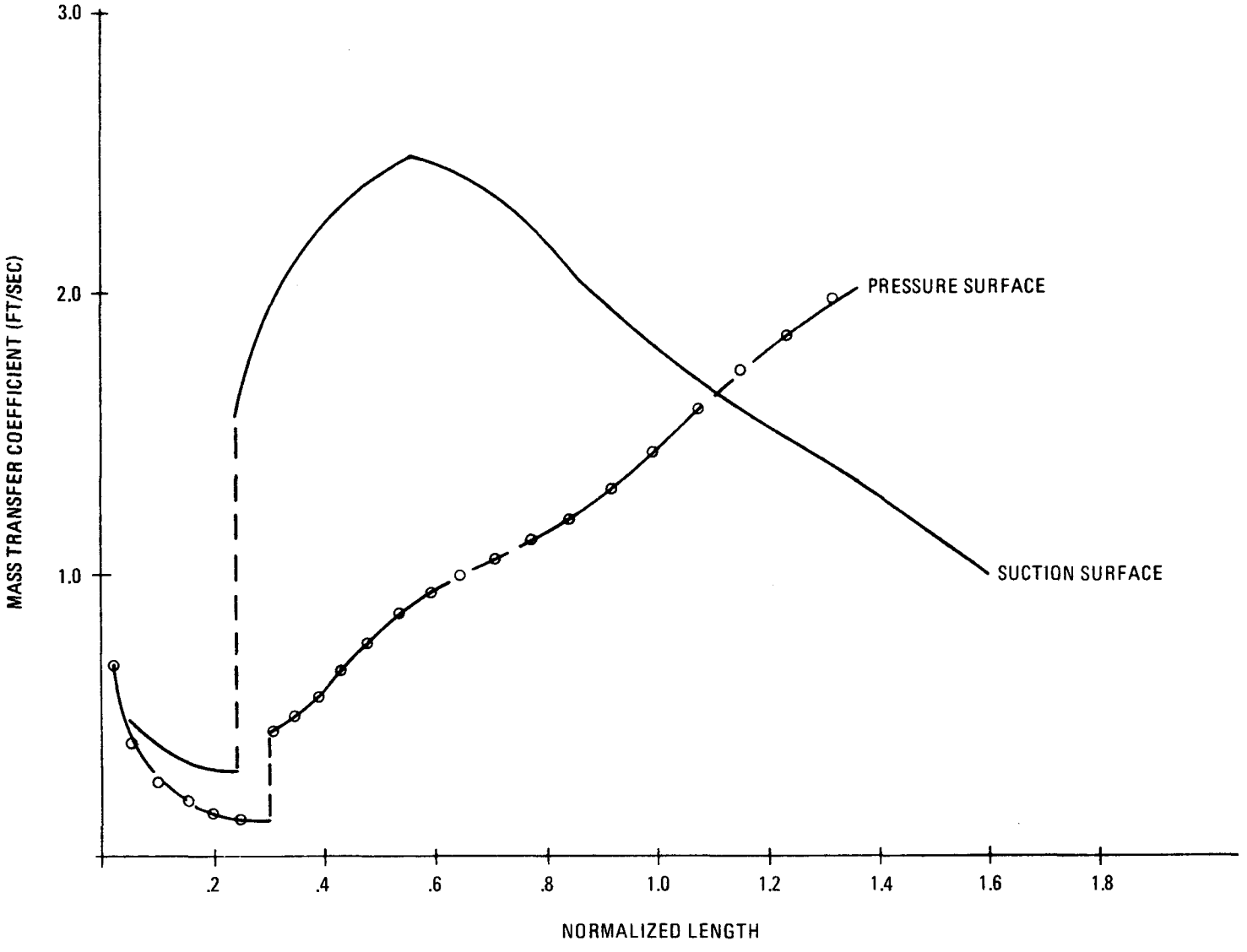

Fig. 11-4. Mass transfer coefficient for eighth stage

11.5. BINARY-CYCLE PLANT SAFETY

The use of ammonia as a binary-cycle fluid in the GT-HTGR presents new safety issues which complicate the design of a binary-cycle power plant. Any fluid, except the chemically inert noble gases such as helium, are in some respect incompatible with the HTGR core. As a consequence, the issue resolves into a consideration of the degree of incompatibility. In this respect, water is an acceptable working fluid provided that leakage to the primary coolant is controlled and detection methods are employed, etc. The chemical reactions subsequent to a steam leak have been subject to a substantial amount of experimental investigation. On the basis of this data, the plant has been designed such that steam leaks are negligible problems in terms of public safety and relatively minor in terms of plant damage. It is expected that proper engineering would lead to an equivalent situation for an ammonia system.

A binary-cycle plant which utilizes common components with a dry-cooled plant or can be easily converted from a dry-cooled plant to a binary-cycle plant has been promoted as an attractive concept. However, careful study shows that the binary-cycle plant will impose some additional design changes beyond the precooler design. First, the PCRV design pressure would need to be increased to the extent that the ammonia leakage increases the system pressure. Secondly, the presence of large amounts of ammonia on the plant site could necessitate redesign of the control room ventilation system in compliance with Regulatory Guide 1.78. Finally, the consequences of ammonia leakage present unique problems in terms of the refrigeration phenomena which can be expected.

11.5.1. Ammonia Leaks inside PCRV

The potential chemical reactions occurring subsequent to an ammonia leak inside the PCRV are (1) the thermal decomposition of ammonia, (2) the

ammonia-graphite reaction to form hydrogen cyanide, and (3) the decomposition of HCN to form nitrogen, hydrogen, and carbon:

$$2\ NH_3 \overset{\rightarrow}{\leftarrow} N_2 + 3H_2 \qquad (11\text{-}1)$$

$$NH_3 + C \overset{\rightarrow}{\leftarrow} HCN + H_2 \qquad (11\text{-}2)$$

$$2HCN \rightarrow 2C + H_2 + N_2 \qquad (11\text{-}3)$$

At normal core temperatures, the equilibrium favors the thermal decomposition of ammonia to nitrogen and hydrogen. However, some kinetic data (Ref. 11-14) indicate that this reaction may be relatively slow. In the limit, this reaction could be ignored in order to estimate the quantity of graphite consumed. (Equation 11-2 shows that 5.5 kg (12 lb) of graphite reacts with each 7.7 kg (17 lb) of ammonia.) Equations 11-2 and 11-3 may be combined to show the overall reaction of interest:

$$3NH_3 + C \overset{\rightarrow}{\leftarrow} HCN + N_2 + 4H_2 \qquad (11\text{-}4)$$

The equilibrium constant for this reaction at 816°C (1500°F) is about 10^6. For ammonia leaks of 454 kg (1000 lb) and 2270 kg (5000 lb), the equilibrium impurity composition would be as shown in Table 11-6.

TABLE 11-6
EQUILIBRIUM IMPURITY COMPOSITION

	454-kb (1000-lb) NH_3 Leakage		2270-kg (5000-lb) NH_3 Leakage	
	P, kPa	P, mole	P, kPa	P, mole
HCN	11.0	∿20	54.0	∿100
N_2	11.0	∿20	54.0	∿100
H_2	44.0	∿80	216.0	∿380
NH_3	0.2	0.3	1.0	∿2

The amount of graphite reacted is negligible compared with the amount of graphite in the core, even for a 2270 kg (5000 lb) ammonia leak.

The pressure response for the GT-HTGR would be approximately 15 MPa/kg (1 psi/100 lb) NH_3 introduced into the primary coolant, assuming that Eq. 11-4 describes the reactions. The overpressure protection system trip would occur at 0.71 MPa (1030 psi) if 1360 kg (3000 lb) of ammonia were to leak into the reactor. Assuming that the reference 64-mm (2.5-in.)-diameter precooler subheader pipes remain, leakage rates of thousands of kg/sec are possible for the classical offset shear pipe break. Assuming a detection time of 20 sec., large amounts of NH_3 could enter the primary system during the detection time. It would be difficult to avoid leakage during the isolation and dump period considering steam generator experience and the inventory in the ammonia heater. These results indicate that (1) PCRV design pressure may have to be raised, (2) orificing should be added to the precooler to limit leakage, or (3) smaller lead tubes may be needed.

Some increase in the PCRV design pressure will be needed for the binary-cycle plant. The incremental pressure increase is dependent on the allowable ammonia leakage. As stated above, the approximate relation is 15 MPa/kg (1 psi/100 lb) NH_3. This increment is applied to the design pressures of the low-pressure cavities (precooler and recuperator). For example, a 1360 kg (3000 lb) ammonia leak would necessitate a 20 kPa (30 psi) increment on the PCRV design pressure, and a 2300 kg (5000 lb) leak would require an additional 35 kPa (50 psi).

In order to reduce the extent of potential ammonia leakage, either precooler header orificing or a redesign which incorporates many more smaller-diameter lead tubes is needed. The orificing would require an additional 0.689 MPa (100 psi) loss on the ammonia inlet and outlet subheaders. This would be accomplished by 19-mm (0.75-in.) orifices on the inlet lines and 38-mm (1.5-in.) orifices on the outlet lines. Preliminary cycle calculations show that the overall plant efficiency is not very sensitive to an ammonia pressure loss increase of the above magnitude. Therefore,

orificing appears to be an acceptable method for limiting potential ammonia leakage.

The high-pressure ammonia inside the PCRV would require additional review of the pressure relief system, since a positive means of overpressurization is clearly available. A return to the external pressure relief system may be required. However, a positive external relief system presents additional problems. Failure of the ammonia detection system would lead to opening of the pressure relief valve and expulsion of combustible gas, as is postulated in the steam plant. The steam-graphite reaction rate is slow enough that only small amounts of flammable gas (H_2, CO) are released to the containment (Ref. 11-15) and a flammable mixture cannot be obtained. The equivalent accident for an ammonia leak is a more difficult problem. If the NH_3 decomposition reaction is slow, only ammonia and helium will be released should the detection system fail. Conversely, if the decomposition is fast, hydrogen could be released which could be a severe problem because of the wide flammability limits of hydrogen and the potential for hydrogen explosions. In this respect, ammonia is a more severe problem than water since it contains 58% more hydrogen per pound.

Figure 11-5 shows a hydrogen/air/helium plot which is useful for showing the process under consideration. (An equivalent hydrogen/ammonia curve is not available.) The relief valve effluent would be shown as a point on the base of the triangle. By connecting this point with the apex of the triangle (pure air), the mixing path is mapped. If the path crosses the flammability curve, combustion is possible. From this type of construction, one observes that approximately an 8% hydrogen-92% helium mixture would not be combustible; higher H_2 concentrations could burn.

Hydrogen mole fractions in the PCRV as a function of ammonia leakage quantities for the ammonia decomposition reaction are shown in Fig. 11-6. For complete reaction, 8% hydrogen concentrations can be avoided if ammonia leakage is limited to less than 5500 kg (12,000 lb), assuming complete mixing in the primary coolant system. It should be possible to limit ammonia leakage such that hydrogen combustion would not be a problem.

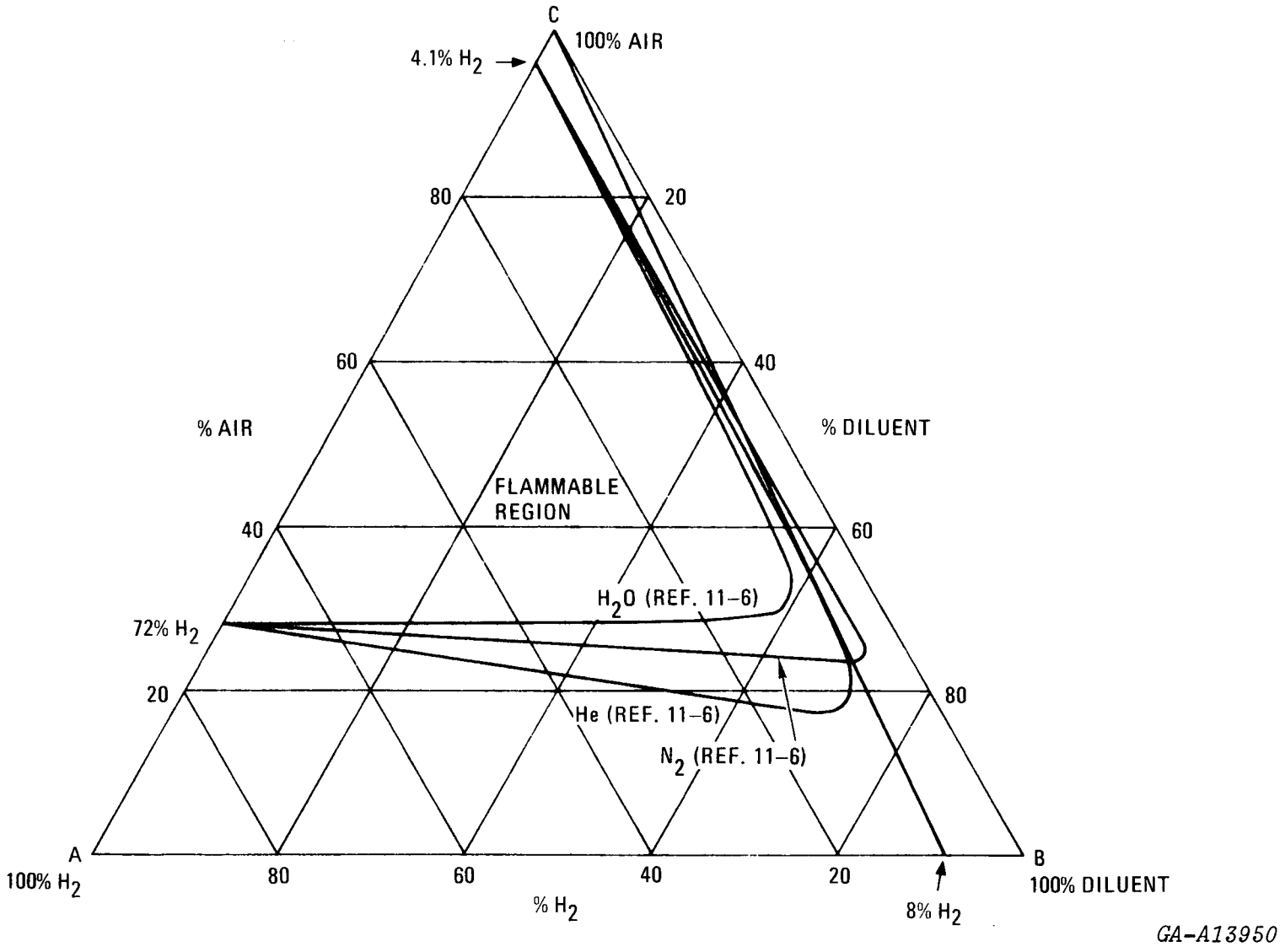

Fig. 11-5. Flammable limits of hydrogen in air diluted with N_2, He, and H_2O for upward flame propagation at ambient pressure and temperature

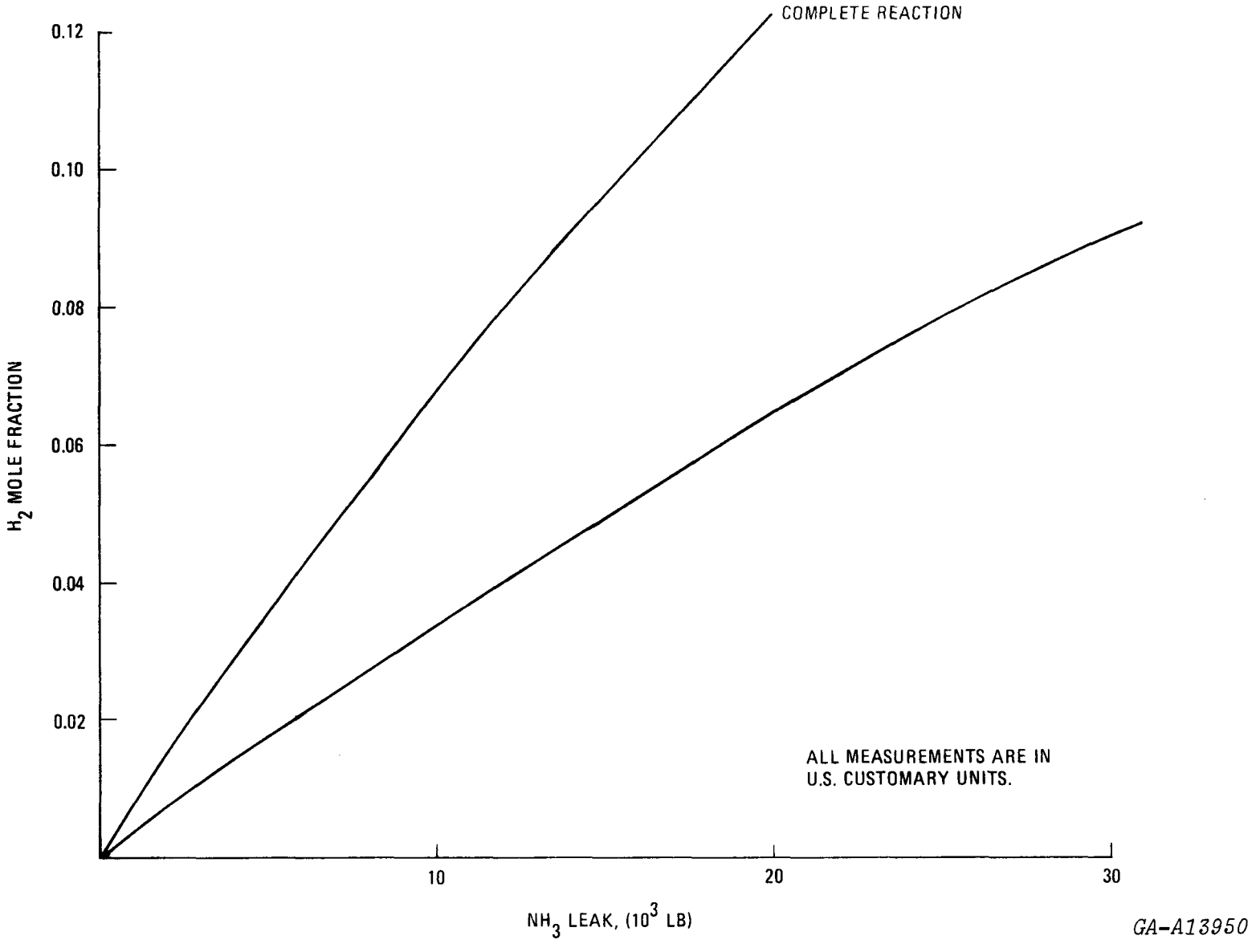

Fig. 11-6. PCRV gas composition as a function of NH_3 leakage

In order to quantify these issues further, additional information is needed on (1) chemical reaction rate data and (2) flammability limits for ammonia, hydrogen, helium, and air mixtures.

11.5.2. Ammonia Leaks Into Containment

The supercritical ammonia cycle utilizing ammonia pressure in excess of 1.4 MPa (2000 psi) presents a unique problem of ammonia depressurization in the event of a pipe rupture in the ammonia system. Any of the high-pressure pipes from the ammonia feed pump to the turbine are potential hazards. If the ammonia system is suddenly depressurized, the liquid portions of the ammonia system will vaporize and drop in temperature dramatically. For the ammonia feed lines, there is a potential for the heat of vaporization to be supplied from sensible heat of the steel piping; calculations show that significant cooling can be expected down to the saturation temperature at 0.1 MPa P (1 atm), which is about -36°C (-33°F). Such calculations indicate that difficult problems could exist in isolating ammonia feed lines in the event of a loss of pressure incident. These problems arise because of potential thermal contraction and resultant stresses in ammonia feed pipes and valves. Failure to isolate could result in unacceptable amounts of ammonia entering the containment. However, experience with commercial refrigeration units indicates that successful isolation was provided in cases where similar events occurred.

In order to evaluate the transient containment response, the CONTEMPT code (Ref. 11-16) was modified to model ammonia leaks. A design basis leakage of 4500 kg (10,000 lb) was assumed. For a precooler inlet line failure, the ammonia would flash immediately, cooling the containment air to approximately -36°C (-33°F). This cooling effect reduces the containment pressure to 8.4 KPa (12.2 psia). The containment atmosphere gradually warms up after the accident because of heat transfer from the structural members. After about 5 min, the containment temperature is about 4.4°C (40°F). The containment structures do not themselves experience such a cooling trend except for potential localized components such as ammonia

pipes and other components close to the spill. The CONTEMPT code cannot currently model such localized phenomena. For a precooler outlet linebreak, analysis which conservatively assumed constant enthalpy for the inleaking ammonia showed that the peak containment pressure would be below 240 kPa (35 psia) and that the peak temperature would be less than 177°C (350°F). These peak conditions are much less severe than those experienced during a design basis depressurization accident and are therefore well within acceptable limits.

A cooling effect can be expected in the precooler if the ammonia system is suddenly depressurized. However, the large mass of the precooler compared with that of the feed line [(11.4 kg (25 lb) metal/lb NH_3 vs 1.8 kg (4 lb) metal/lb NH_3] results in a less serious temperature drop.

11.5.3. Ammonia Combustion

During an ammonia pipe failure, the ammonia/air flammability limits have been reported to be 16% to 25% ammonia (Ref. 11-17). The heat of combustion is about 19 MJ/kg (8000 Btu/lb). The combustion products are water and nitrogen. Ammonia is normally considered difficult to burn; part of this experience is probably due to the narrow flammability limits. However, the heat of combustion is high enough to cause a potential containment overpressure transient if sufficient ammonia were burned in the containment. Approximately 2300 kg (5000 lb) of NH_3 would be limiting if burned quickly.

Approximately 9000 kg (20,000 lb) of NH_3 would be needed to reach an equilibrium at the lower flammability limit with the containment air. Furthermore, the containment contains enough oxygen to burn about 14,000 kg (30,000 lb) of ammonia. However, for any ammonia leak in the containment, the flammability limit is crossed as the ammonia mixes with the air. Figure 11-7 shows this process. The straight line connecting the ammonia corner with the air point is shown to pass through the flammability region, which is estimated from the four known flammability points.

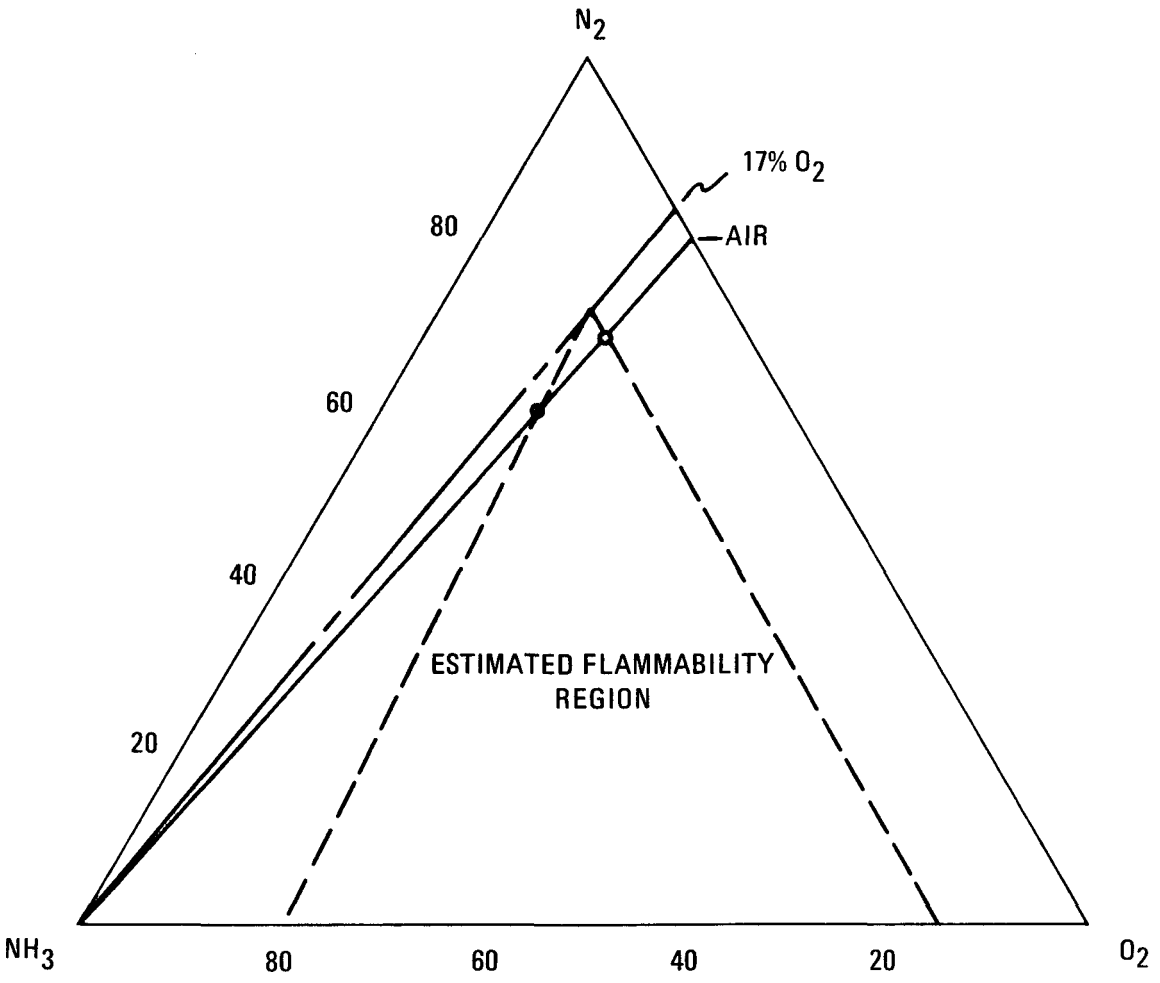

GA-A13950

Fig. 11-7. Ammonia-air flammability diagram

A second interesting phenomenon is shown in Fig. 11-7. Consider an NH_3-oxygen mixture located on the bottom of the triangle. Any composition between 15% and 80% NH_3 is flammable. As N_2 (a diluent) is added, the flammability limits become pinched until the limits have been reduced to 15% and 26% NH_3 for air mixtures. One can estimate the flammability region above the air-NH_3 line and estimate the N_2-O_2 composition which would not support ammonia combustion. From the data available, N_2-O_2 mixtures which contain an oxygen content of less than 16% to 17% should not support ammonia combustion. Since there is enough oxygen in this mixture to support life, it should be possible to add sufficient nitrogen to the containment to eliminate the ammonia combustion problem without going to a fully inert atmosphere.

11.6. RCB/PCRV SEISMIC ANALYSIS

11.6.1. Analysis Approach

The RCB/PCRV model, which was prepared for the preliminary seismic analysis, was described in Section 2.4 of the last semiannual progress report (Ref. 11-18). For the safety study, several seismic analyses were performed using the SAP IV program (Ref. 11-19). This program is a multipurpose program which is capable of performing static as well as dynamic analysis. Per Ref. 11-20, ground excitation in three orthogonal directions, namely, two horizontal and one vertical, were applied simultaneously to simulate the effects created by a random seismic event. The response spectra curves generated in Ref. 11-21 were applied in the RCB/PCRV response spectra analysis. On the other hand, artificial time histories of 15-sec duration whose response spectra envelop the NRC design response spectra curves (Ref. 11-21) were applied in the time history analysis. To assess the effects of the various soil conditions on the RCB/PCRV seismic response, the five different soil conditions shown in Table 11-17 were investigated. These soil conditions are expected to encompass all possible reactor site conditions within the United Stages.

TABLE 11-7
SOIL CONDITION DATA

Soil Condition	Soil Modulus (G), MPa (psi)	Poisson's Ratio
Competent rock	6.89×10^4 (10×10^6)	0.3
Extra firm	2.41×10^3 (3.5×10^5)	0.35
Firm	6.20×10^2 (9×10^4)	0.35
Soft	1.72×10^2 (2.5×10^4)	0.4
Very soft	2.48×10^1 (3.6×10^3)	0.4

11.6.2. Seismic Results

11.6.2.1. Frequency. For each soil condition, appropriate spring constants were calculated for the spring between the ground anchor points and the nodal point, as shown in Fig. 2-2 of Ref. 11-18. The frequency analysis results indicate that the mode shapes of the RCB/PCRV were essentially uncoupled but did not lie along the two horizontal global axes. Thus, a minor adjustment in the sectional properties was made to permit their alignment with the global axis.

Thirty-five modal frequencies and mode shapes were calculated for each soil condition. In order to demonstrate the effects of the soil conditions on the RCB/PCRV frequencies, the first 10 frequencies and mode shape characteristics are tabulated in Table 11-8. As expected, the fundamental frequency was found to decrease with a decrease in the soil stiffness.

11.6.2.2. Response Spectrum Analysis Results. The response spectrum analyses were carried out to calculate the most representative maximum values of response, i.e., deflections, stresses, etc., of the RCB/PCRV during the seismic excitation. Analyses were performed for the five different soil conditions. For each soil condition, the ground excitations in the three

TABLE 11-8
PCRV-REACTOR CONTAINMENT BUILDING
DAMPED[a] MODAL FREQUENCIES FOR VARIOUS SOIL CONDITIONS

Mode[b] No.	Frequencies (Hz)				
	Rock	Extra Firm Soil	Firm Soil	Soft Soil	Very Soft Soil
1	3.74[c]	3.07[c]	1.95[i]	1.16[i]	0.45[i]
2	3.81[c]	3.10[c]	1.95[i]	1.16[i]	0.45[i]
3	6.75[d]	5.12[e]	3.53[j]	2.04[j]	0.78[j]
4	6.89[d]	5.21[e]	4.30	2.81[k]	1.10[k]
5	7.33[e]	6.72[f]	4.36	2.97[i]	1.20[i]
6	7.36[e]	6.77[h]	4.84[k]	2.98[i]	1.20[i]
7	7.51	7.27	6.59[d]	5.32	5.04
8	10.79[f]	7.27	6.65[d]	5.41	5.14
9	11.34[g]	10.04[i]	7.30[e]	7.28[e]	7.28[e]
10	11.34[g]	10.17[i]	7.30[e]	7.28[e]	7.28[e]

[a] Critical damping of 2% and 10% was assumed for concrete and soil, respectively.

[b] Only the first ten modes are tabulated.

[c] Containment lateral modes

[d] PCRV lateral modes

[e] Fuel handling machine modes

[f] Containment vertical modes

[g] Generator lateral modes

[h] Containment torsional modes

[i] PCRV-containment lateral modes

[j] PCRV-containment vertical modes

[k] PCRV-containment torsional modes

Cartesian coordinate directions (see Fig. 2-2 of Ref. 11-18) were simultaneously applied. For each direction, modal responses, i.e., stresses, deflections, etc., at the various RCB/PCRV locations were calculated.

The response spectrum approach results in the loss of the time phase between the modal responses. Therefore, the NRC has published methods (Ref. 11-20) of calculating the representative maximum value of a particular response during the seismic excitation. On the basis of these guidelines, the maximum expected responses of a given element can be obtained from the corresponding maximum values of the responses of individual modes by taking the square root of the sum of the squares (SRSS) of the maximum values of each mode of the structure. This rule generally leads to acceptable results provided that individual modes are well-separated. In cases where individual modes are not well-separated, either the SRSS rule must be modified or the time history approach can be used to analyze the structure. After obtaining the representative maximum response in each direction, the SRSS method is again applied to take into account simultaneous three-dimensional seismic excitation.

Seismic loads at the RCB/PCRV interface were also obtained from the response spectrum analyses for the OBE and SSE events. From these results, the maximum interface loads, which do not necessarily occur simultaneously, were determined considering the entire range of soil condition. The results are presented in Table 11-9.

11.6.2.3. Time History Analysis Results. Time history analyses were performed to generate the in-structural response spectra at the various RCB/PCRV locations. The same five soil conditions were considered for these analyses. Artificial 15-sec time histories were used as input for the RCB/PCRV time history analysis. Ground excitations in three coordinate directions (see Fig. 2-2 of Ref. 11-18) were simultaneously applied to

TABLE 11-9
SEISMIC RESPONSE AT THE INTERFACE BETWEEN THE
PCRV SUPPORT AND THE FOUNDATION SYSTEM

Type of Loading	Response Intensities (SRSS Sum) at Interface	
	OBE (1.0 g)	SSE (1.0 g)
Axial force[(a)], MN (lb) (in vertical direction)	2.40×10^3 (5.4×10^8)	2.36×10^3 (5.3×10^8)
Shear force, MN (lb) (in two-orthogonal horizontal directions)	2.80×10^3 (6.3×10^8)	2.14×10^3 (4.8×10^8)
Flexure moment, MN-m (lb-in.) (in two-orthogonal horizontal directions)	7.68×10^4 (6.8×10^{11})	5.88×10^4 (5.2×10^{11})
Torsional moment[(b)], MN-m (lb-in.)	5.53×10^3 (4.9×10^{10})	4.18×10^3 (3.7×10^{10})

[(a)]These forces do not include the dead load of the PCRV and the PCRV support.

[(b)]Torsional moment is the maximum value either obtained from a dynamic analysis or computed by offsetting the design shear force from the center of rigidity by 5% of the diameter of the PCRV.

generate the structural response time history at the various RCB/PCRV support locations. The data were subsequently used to determine in-structural response spectra for the following locations:

1. Turbomachinery support
2. Reactor core support
3. Heat exchanger support
4. PCRV top head (fuel handling machine support)
5. RCB supports (top of base mat)

Since the dynamic behavior of the RCB/PCRV was found to be dominated by the motions of the symmetric RCB and PCRV (i.e., dynamic effect, if any, due to the asymmetric components was negligible), the response is obtained in only one horizontal direction, and the response in the other horizontal direction was assumed to be the same. Response spectra were generated for each soil condition and for an OBE event and an SSE event. Excitations were applied in one horizontal direction and the vertical direction. The five in-structure design response spectra for a given direction and earthquake event represent the envelope of spectra for each soil condition where the peaks have been widened by ±15% to account for uncertainties. The design response spectra are determined for 1%, 2%, and 5% damping. Typical horizontal and vertical response spectra curves (for an SSE event) for the turbomachinery support location are shown in Figs. 11-8 and 11-9.

11.6.2.4. Turbomachinery-Generator Displacements. During the response spectrum analyses, displacement components at the various RCB/PCRV locations were calculated. The relative displacements between the turbomachinery (TM) and the generator are of particular significance, since they impose substantial loads on the turbomachinery plug. The displacement results for the five selected soil conditions indicate that the absolute, as well as the relative, displacement between the TM and the generator increases with a decrease in the soil stiffness. It is observed that the relative displacement in the vertical direction between the TM and the generator is created partially by the RCB/PCRV rocking motions. When the TM and the generator rotate about the Z axis (see Fig. 2.2 of Ref. 11-18) by the same angle,

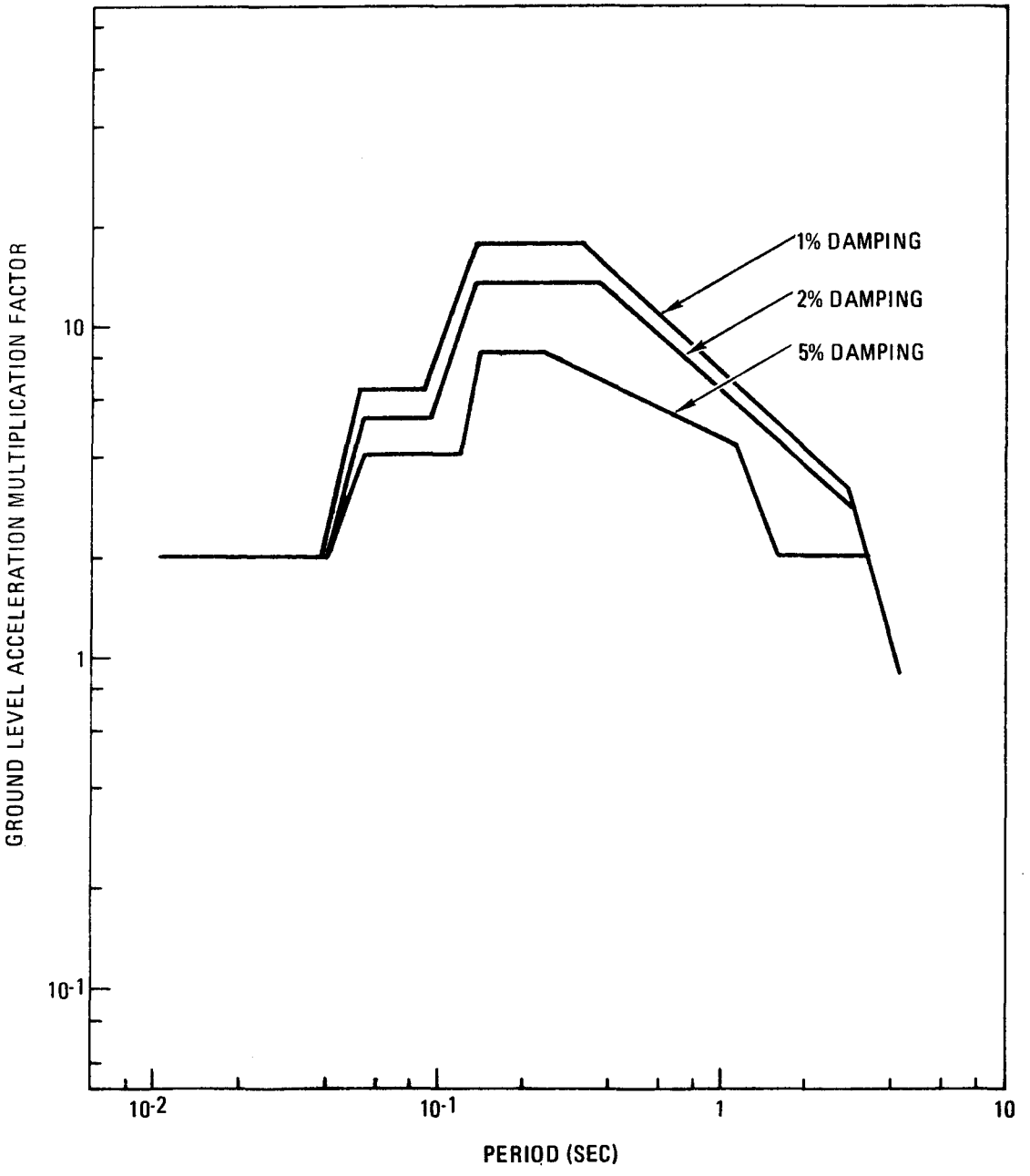

GA-A13950

Fig. 11-8. Horizontal response spectra for 1.0-g SSE for turbomachinery support location

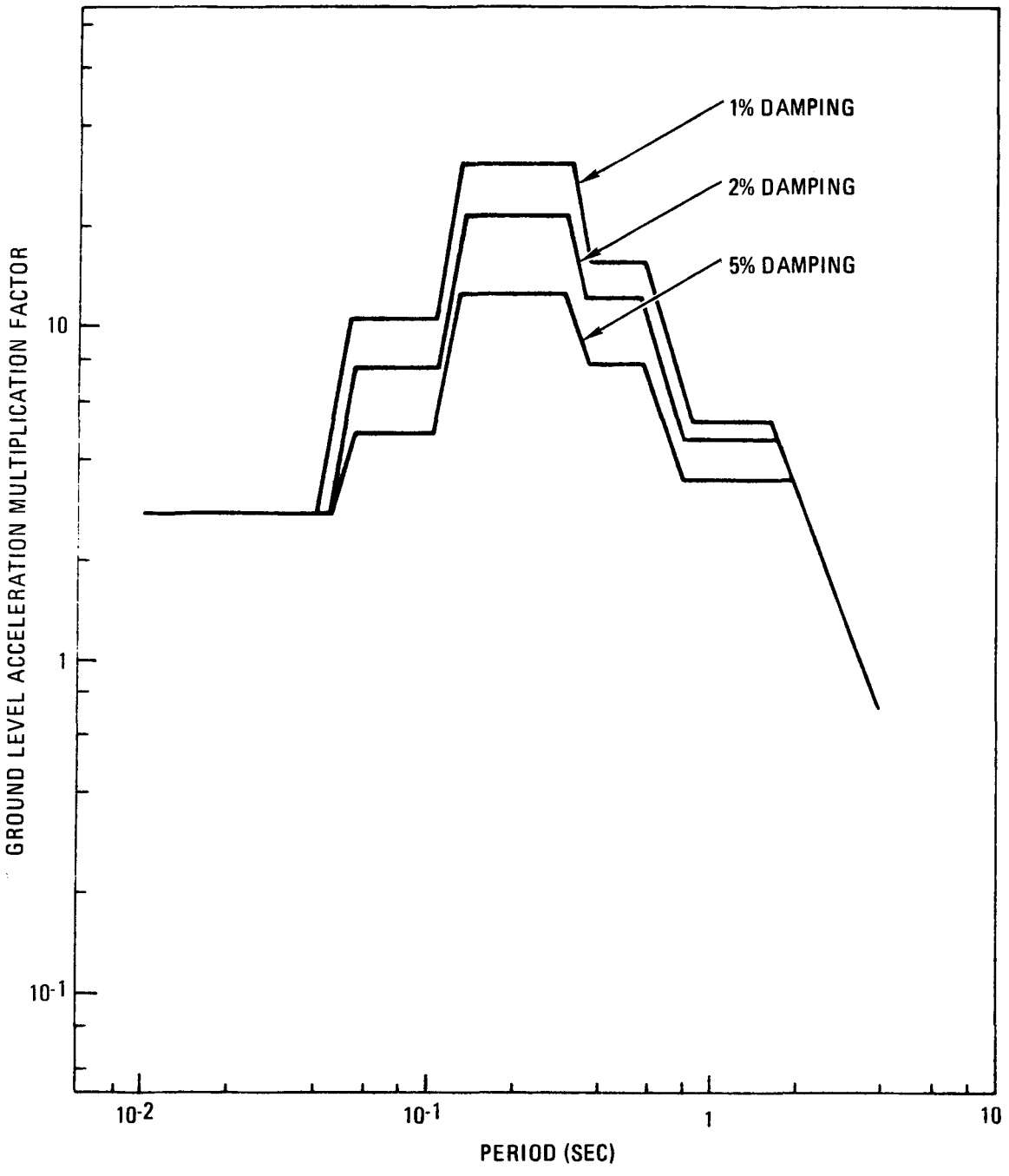

GA-A13950

Fig. 11-9. Vertical response spectra for 1.0-g SSE for turbomachinery support location

the loadings on the TM plug and the TM shaft are expected to be negligible, even though the vertical displacements between these components are different. In order to take into account rocking motions, vertical displacements of the TM and the generator are adjusted as follows:

$$\left[U_y\right]^{TM}_{Adjust} = \left[\left\{\left[U_y\right]^{TM}\right\}^2 - \left\{\left[\theta_z\right]^{*}_{PCRV\ @\ node\ 6} \times 13.72\ m\ (540\ in.)\right\}^2\right]^{1/2}$$

$$\left[U_y\right]^{Gen}_{Adjust} = \left[\left\{\left[U_y\right]^{Gen}\right\}^2 - \left\{\left[\theta_z\right]^{*}_{PCRV\ @\ node\ 6} \times 24.38\ m\ (960\ in.)\right\}^2\right]^{1/2} \qquad (11\text{-}5)$$

The adjusted vertical displacements for the SSE event are shown in Table 11-10. These calculations were performed for the SSE event based on a maximum horizontal ground acceleration of 1 g applied simultaneously in the two orthogonal horizontal directions and the vertical direction. If, for this preliminary analysis, we conservatively assumed that the GT-HTGR plant site is located in the high seismic zone, the maximum expected ground accelerations will be approximately 0.5 g. Thus, the expected relative displacement between the TM and the generator for the postulated SSE event based on the maximum ground acceleration of 0.5 g will be as follows:

$$\delta_{Vertical} = 0.5 \times \Delta U]_y$$

$$= 0.5 \times 8.38 \approx 4.2\ mm\ (0.5 \times 0.33 \approx 0.165\ in.)$$

*It is assumed that the TM shaft rocking motion is the same as the SRSS rocking motion (θ_z) of node 6 of the PCRV (see Fig. 2-2 of Ref. 11-18).

TABLE 11-10
TURBOMACHINERY-GENERATOR VERTICAL DISPLACEMENT DURING 1.0-g SSE

Soil Condition	Rocking Motion About Z Axis (see Fig. 4-8), Rad	Turbomachinery Displacements, mm (in.)		Generator Displacements, mm (in.)		$\Delta U\rfloor_y$ =
		$U_y\rfloor^{TM}_{Actual}$	$U_y\rfloor^{TM}_{Adjust}$	$U_y\rfloor^{Gen}_{Actual}$	$U_y\rfloor^{Gen}_{Adjust}$	$\text{abs}\left\{U_y\rfloor^{TM}_{Adjust} - U_y\rfloor^{Gen}_{Adjust}\right\}$
Rock	2.3×10^{-4}	3.05 (0.12)	0.76 (0.03)	1.02 (0.04)	5.59 (0.22)	4.83 (0.19)
Extra firm	6.6×10^{-4}	13.46 (0.53)	9.91 (0.39)	16.0 (0.63)	1.78 (0.07)	8.13 (0.32)
Firm	2.07×10^{-3}	50.8 (2.00)	42.16 (1.66)	63.5 (2.50)	38.61 (1.52)	3.56 (0.14)
Soft	4.16×10^{-3}	99.57 (3.92)	81.53 (3.21)	129.54 (5.10)	80.52 (3.17)	1.02 (0.04)
Very soft	1.38×10^{-2}	320.04 (12.6)	258.06 (10.16)	429.26 (16.90)	266.45 (10.49)	8.38 (0.33)

$$\delta^{*}_{\text{Horizontal}} = 0.5 \times \max \left[U_x \right]^{TM} - U_x \left]^{Gen} \right]$$

$$= 0.5 \times 3.56 \ (0.14)$$

$$= 1.78 \text{ mm } (0.07 \text{ in.}) \qquad (11\text{-}6)$$

The TM shaft and the TM plug will be designed to permit the relative vertical and lateral displacements determined by Eq. 11-6.

*Effect on the horizontal mismatch, if any, due to the RCB/PCRV torsional mode is assumed to be negligible.

REFERENCES

11-1. "HTGR Accident Initiation and Progression Analysis Status Report," General Atomic Report GA-A13617, January 1976, Volume I.

11-2. "An Analysis of HTGR Core Cooling Capability," Gulf Energy & Environmental Systems Report Gulf-GA-A12504, May 1973.

11-3. Chmielewski, R. D., and C. G. Hoot, "Fission Product Plateout Calculations for a Gas Turbine HTGR," General Atomic Report GA-A13213, November 1974.

11-4. Schlichting, H., Boundary Layer Theory, McGraw-Hill, New York, 1960.

11-5. Brown, A., and B. W. Martin, "A Review of the Bases of Predicting Heat Transfer to Gas Turbine Rotor Blades," ASME Paper 74-GT-27, 1974.

11-6. Vanslager, F. E., and L. D. Mears, "PAD, a Computer Code for Calculating the Plateout Activity Distribution in a Reactor Circuit," Gulf Energy & Environmental Systems Report GA-10460, January 1971.

11-7. Jakob, M. (ed.), Heat Transfer, Wiley, New York, 1975, Section VII.

11-8. Horlock, J. H., Axial Flow Turbines, Butterworth, London, 1966, pp. 223-228.

11-9. Squires, H. B., "Heat Transfer Calculations for Aerofoils," British ARC Report R&M 1986, 1942.

11-10. Parker, G. I., and P. Lee, "Studies of the Decomposition of Sub-micron Particles on Turbine Blades," Proc. Inst. Mech. Eng. 186, 519 (1972).

11-11. Wilson, D. G., and J. A. Pope, "Convective Heat Transfer to Gas Turbine Blade Surfaces," Proc. Inst. Mech. Eng. 168, 861 (1954).

11-12. Lin, C. S., R. W. Moulton, and G. L. Putman, "Mass Transfer between Solid Walls and Fluid Streams," Ind. Eng. Chem. 45 636 (1953).

11-13. Ellerbrock, H. H., in Heat Transfer, Volume II, M. Jakob (ed.), Wiley, New York, 1957, pp. 381-412.

11-14. Logan, S. R., et al., "The Catalytic Decomposition of Ammonia on Evaporated Iron Films," Trans. Faraday Soc., 922 (1957)

11-15. "General Atomic Standard Safety Analysis Report," USNRC Docket 50-535, 1974, Chapter 15.

11-16. Macnab, D. I., "The CONTEMPT Computer Program," General Atomic Report GA-A12692, February 1974.

11-17. Coward, H. F., and G. N. Jones, "Limits of Flammability of Gases and Vapors," U. S. Bureau of Mines Bulletin 503, 1952.

11-18. "Gas Turbine HTGR Program, Semiannual Progress Report for the Period July 1, 1975 through December 31, 1975," General Atomic Report GA-A13740, January 1976.

11-19. Bathe, K., et al., "Sap IV, a Structural Analysis Program for Static and Dynamic Response of Linear Systems," University of California, Berkeley Report EERC 73-11, June 1973.

11-20. "Combination of Modes and Spatial Components in Seismic Analysis," USAEC Regulatory Guide 1.92, December 1974.

11-21. "Design Response Spectra for Seismic Design of Nuclear Plants," USAEC Regulatory Guide 1.60 (Rev. 1), December 1973.

APPENDIX A

PCRV DESIGN APPROACH STUDIES

A.1. GENERAL

A study of PCRV configurations for two-, three-, and four-loop configurations of an advanced 4000-MW(t) GT-HTGR has been performed which included reactor outlet temperatures of 850°C (1562°F) and 950°C (1742°F). The turbomachine arrangements investigated were (1) radial arrangement and (2) nonradial arrangement. The radial arrangement is the arrangement of the reference design; in the nonradial arrangement, the turbomachine cavities form a horizontal delta in the three-loop configuration and a square in the four-loop configuration. For the two-loop configuration a delta arrangement and a parallel arrangement of the turbomachine cavities were studied.

The PCRV and cavity dimensions of all configurations studied are given in Table A-1. The table also indicates whether the PCRV diameter is determined by stress conditions (stress-limited) or by the arrangement of the cavities within the PCRV (geometry-limited).

A.2. BASIC DESIGN DATA

For the design of the PCRVs, it was assumed that the internal pressure relief system (Ref. A-1) as developed for the GT reference design will also be applied for the advanced GT-HTGR configurations. This resulted in the following maximum pressure for the core cavity:

$$MCP_C = 6.915 \text{ MPa (1003 psig)}$$

The maximum heat exchanger cavity pressure for the two-loop configuration was

$$MCP_{HX} = 5.447 \text{ MPa (790 psig)}$$

TABLE A-1
PCRV AND CAVITY DIMENSIONS

		Two Loops		Three Loops				Four Loops			
		Turbomachine Arrangement									
		Delta	Parallel	Radial		Delta		Radial		Square	
		Configuration									
		850/2-1	850/2-2	850/3-1	950/3-1	850/3-2	950/3-2	850/4-1	950/4-1	850/4-1	950/4-2
Reactor outlet temperature	°C	850	850	850	950	850	950	850	950	850	950
	°F	1562	1562	1562	1742	1562	1742	1562	1742	1562	1742
PCRV o.d.	m	39.32	38.77	40.54	40.54	40.54	39.41	39.93	39.93	39.93	39.93
	ft	129	127.2	133	133	133	129.3	131	131	131	131
PCRV height	m	34.75	34.75	34.14	34.14	31.49	31.49	34.14	34.14	31.49	31.49
	ft	114	114	112	112	103.3	103.3	112	112	103.3	103.3
Recuperator cavity diam	m	6.86	5.03	5.64	5.49	5.64	5.49	5.18	4.88	5.18	4.88
	ft	22.5	16.5	18.5	18	18.5	18	17	16	17	16
Recuperator cavity length	m	23.77	23.77	23.77	23.77	20.42	20.42	23.77	23.77	20.42	20.42
	ft	78	78	78	78	67	67	78	78	67	67
Precooler cavity diam	m	7.62	5.33	5.94	5.49	5.94	5.49	5.18	4.88	5.18	4.68
	ft	25	17.5	19.5	18	19.5	18	17	16	17	16
Precooler cavity length	m	23.77	23.77	23.77	23.77	20.42	20.42	23.77	23.77	20.42	20.42
	ft	78	78	78	78	67	67	78	78	67	67
Compressor discharge duct diam	m	2.97	2.97	2.97	2.97	2.97	2.97	2.59	2.59	2.59	2.59
	ft	9.75	9.75	9.75	9.75	9.75	9.75	8.5	8.5	8.5	8.5
Turbomachine cavity diam	m	4.57	4.57	4.11	4.11	4.11	4.11	4.11	4.11	4.11	4.11
	ft	15	15	13.5	13.5	13.5	13.5	13.5	13.5	13.5	13.5
Turbomachine cavity length	m	15.85	15.85	14.02	14.02	15.85	15.85	13.26	13.26	13.26	13.26
	ft	52	52	46	46	52	52	43.5	43.5	43.5	43.5
PCRV diam limited by		Stress	Geometry	Stress	Geometry	Stress	Stress	Geometry	Geometry	Geometry	Geometry

For the three- and four-loop configurations, an ammonia bottoming cycle was applied which required a slightly higher heat exchanger cavity pressure. This was determined to be

$$MCP_{HX} = 5.654 \text{ MPa (820 psig)}$$

The heat exchanger cavity dimensions are given in Table A-1, and the dimensions of the turbomachine cavities are given in Fig. A-1. The cavity lengths given in Fig. A-1 represent the minimum lengths required for the turbomachine including the minimum required space for compressor inlet and turbine outlet plenums.

Other design data are as follows:

Core cavity diameter	$D_c = 13.56$ m (44.5 ft)
Core cavity height	$H_c = 14.43$ m (47 ft 4 in.)
Heat exchanger cavity diameter	D_{HX} = See Table A-1
Precast panel thickness	$t = 0.61$ m (2 ft)
Safety factor	$F = 1.1$
Allowable compressive stress in concrete	$f = 15.685$ MPa (2275 psi)
Creep relaxation factor	$\eta = 0.8$

A.3. PCRV DIMENSIONS

A.3.1. PCRV Diameter

The PCRV diameter is determined by the cavity pressures and diameters according to the following equation:

$$D = \frac{(MCP_c D_c + 2MCP_{HX} D_{HX\ max}) F}{f\eta} + D_c + 2D_{HX\ max} + 2t \quad \text{(A-1)}$$

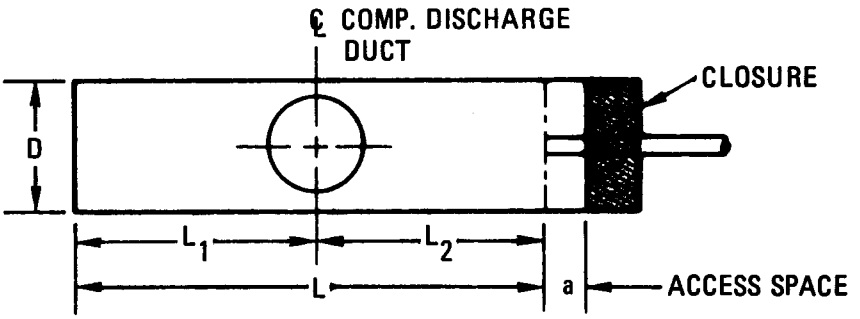

	D	L	L_1	L_2	a
2–LOOP	4 572	15 849	8 229	7 620	914
	(15.0)	(52.0)	(27.0)	(25.0)	(3.0)
3–LOOP	4 114	14 020	7 162	6 858	914
	(13.5)	(46.0)	(23.5)	(22.5)	(3.0)
4–LOOP	4 114	13 258	6 858	6 400	914
	(13.5)	(43.5)	(22.5)	(21.0)	(3.0)

NOTE: ALL DIMENSIONS IN MILLIMETERS (FT)

GA-A13950

Fig. A-1. Basic turbomachine cavity dimensions

where $D_{HX\ max}$ is the diameter of the largest-side cavity and t is the thickness of the precast wire wrapping panels.

The diameters of all configurations were first determined with Eq. A-1 and then checked by layout. As indicated in Table A-1, the PCRV diameter is determined either by stress conditions (determined by Eq. A-1) or by geometric conditions (determined by layout).

A.3.2. PCRV Height

A.3.2.1. Top and Bottom Head. The minimum PCRV height is determined by the sum of the core cavity height plus the top and bottom head thickness.

The top head thickness was determined with the following equation:

$$H_t = \frac{\overline{MCP}_c\ D_c}{4s} \qquad \text{(A-2)}$$

where s = allowable shear stress
$= 5\sqrt{f_{cua}}$

and f_{cua} = max concrete compressive stress
= 6500 psi = 44.82 MPa

With the values given in Section A.2, the top head thickness will be

$$H_t = \frac{(1003)\ (44.5)}{(4)\ (400)}$$

$$= 27.9 \text{ ft} = 8.53 \text{ m } (\sim 28 \text{ ft})$$

This would also be the bottom head thickness for the two-loop, the three-loop delta, and the four-loop square arrangements.

For the radial arrangement of the turbomachines, the bottom head thickness is dependent on the required ligaments between the core cavity and the

bottom surface of the PCRV. For this study the dimensions shown in Fig. A-2 were used, where the 6.248 m (20.5 ft) distance from the bottom of the core cavity to the centerline of the turbomachine cavity is the same as that used on the reference design. The dimension of 4.876 m (16 ft) from the turbomachine cavity to the bottom surface of the PCRV is shorter than that used for the reference design. It was selected because the PCRV is directly supported on the containment slab, which is considered integral with the PCRV (see Section A.6).

A.3.2.2. PCRV Overall Height. With the dimensions of top and bottom heads and the core cavity height, the minimum PCRV height will be

$$H_{min} = (47.3) + (2)\ (28)$$
$$= 103.3 \text{ ft} = 31.486 \text{ m}$$

For the configurations with a radial turbomachine arrangement, the PCRV height will be

$$H = 47.3 + 28 + 36.5$$
$$= 111.8 \text{ ft} = 34.077 \text{ m}$$

A height of 34.137 m (112 ft) was used.

A.3.3. Recuperator Length Limitation

The recuperator length which can be accommodated within a PCRV with minimum height is dependent on the slant angle of the core inlet duct and the required thickness of the top head. The slant angle of the duct, in turn, is dependent on (1) the requirement that the thermal barrier of the duct can be removed through the top of the heat exchanger cavity and (2) the stress conditions in the slanted duct area. A study of a duct arrangement with a slant angle of 45 deg was made (Ref. A-2) and showed that this arrangement is feasible and that only local high-tensile stresses occur which can be controlled by proper arrangement of steel reinforcements in these areas. The structural effect of changing this angle to a steeper

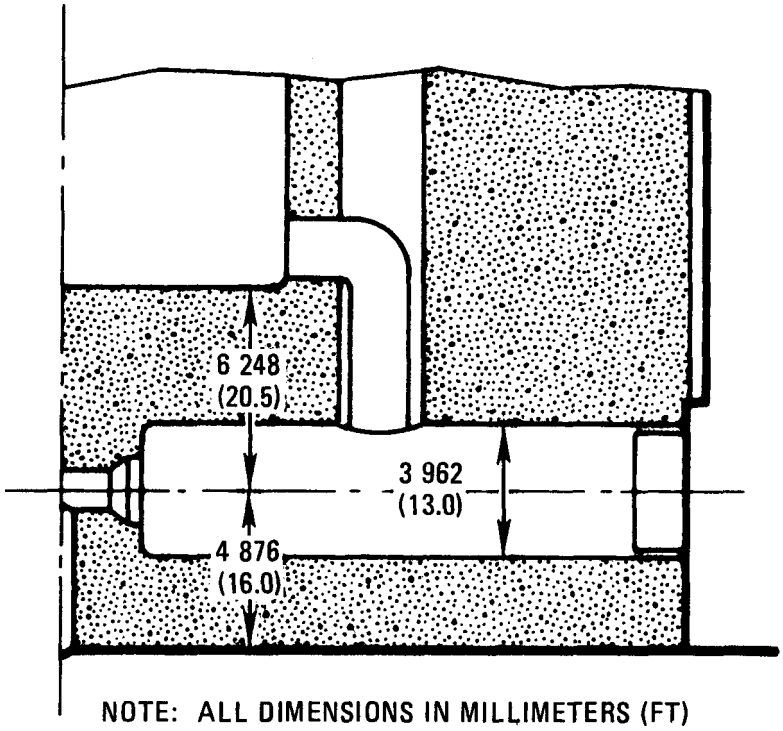

GA-A13950

Fig. A-2. Bottom head dimensions for radial turbomachine

angle than 45 deg on the top head design is not known and so was not considered. Therefore, for all designs a slant angle of the core inlet duct of 45 deg was used in spite of the resulting unused space below the heat exchanger closure (see Fig. A-3).

Because of these restrictions of the core inlet duct, the length of the recuperator is limited if it has to fit into a PCRV with minimum height, as applies to the delta and square configurations. For the configuration with radial turbine arrangement, the length of the recuperator can be extended approximately 3.05 to 3.35 m (10 to 11 ft) by eliminating a portion of the straight section of the turbine exhaust duct.

A.4. TWO-LOOP CONFIGURATIONS

A.4.1. General

Two configurations with reactor outlet temperature of 850°C were investigated: (1) with two heat exchangers (one recuperator and one precooler) per loop (Configuration 850/2-1); (2) with two pairs of recuperators and precoolers (Configuration 850/2-2). Configuration 850/2-1 has a delta arrangement of the turbomachine units and features an asymmetric PCRV design. Configuration 850/2-2 has the turbomachine units arranged in parallel and has the core cavity in the center of the PCRV.

Configuration 850/2-1 was not pursued further because the size of the heat exchangers would be too large and heavy for handling and shipping.

For Configuration 850/2-2, a preliminary layout was made in order to study the feasibility of the ducting system. This study showed that the ducting system is geometrically feasible within the PCRV.

The corresponding configurations with a reactor outlet temperature of 950°C were not investigated, but because of the slightly smaller heat exchanger cavity diameters the PCRV diameters would also be slightly smaller.

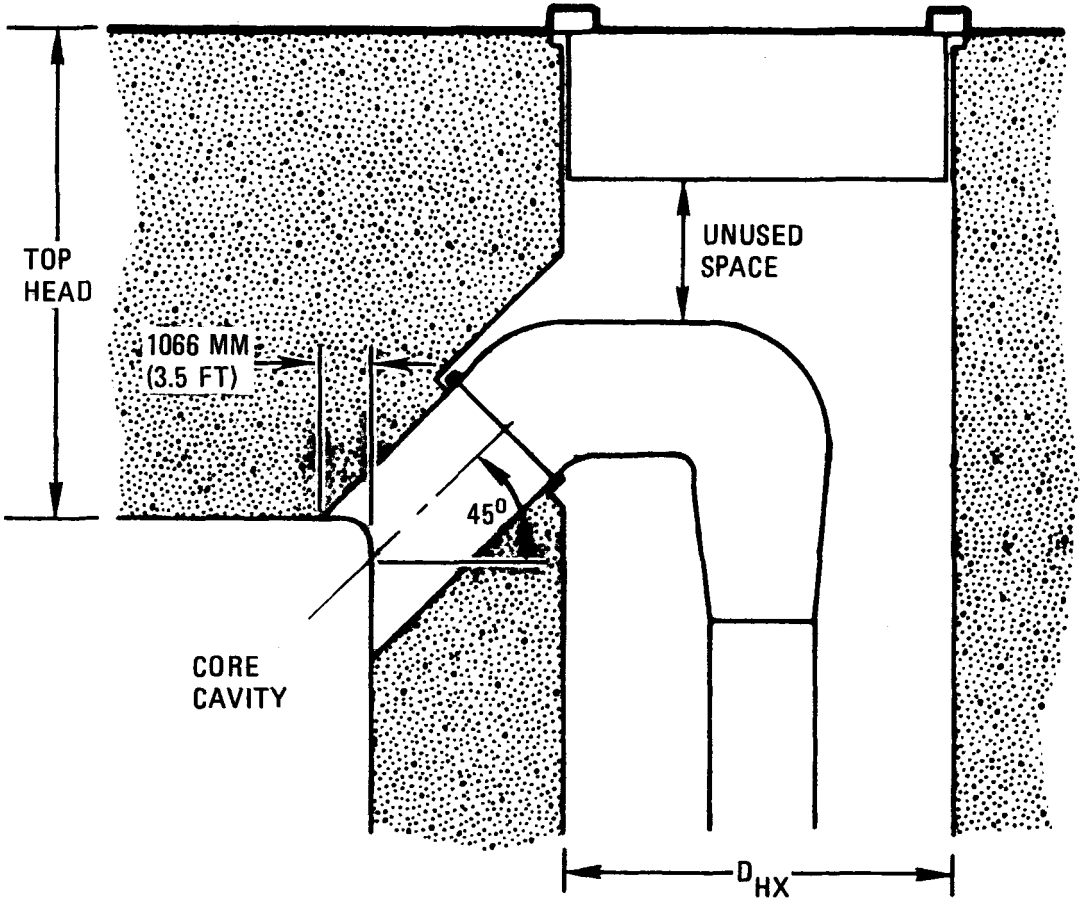

Fig. A-3. Slanted core inlet duct

A.4.2. PCRV Diameter

A.4.2.1. Configuration 850/2-1. Using Eq. A-1 and the design data from Section A.2, the diameter for a symmetrical PCRV design would be

$$D = \frac{[(1003)\ (44.5) + (2)\ (790)\ (25)]\ 1.1}{(2275)\ (0.8)} + 44.5 + (2)\ (25) + 2t$$

$$= 145.3 \text{ ft} + 4 \text{ ft}$$

$$= 44.287 \text{ m} + 1.219 \text{ m}$$

For the asymmetric design (see Fig. A-4), the radii R_1 and R_2 were determined by using the following modified equation of Eq. A-1:

$$R = \frac{(MCP_c\ D_{c/2} + MCP_{HX}\ D_{HX})F}{f\eta} + D_{c/2} + D_{HX}$$

Using this equation for R_1 and R_2, the radii would be:

$$R_1 = \frac{(1003)\ (22.25)\ (1.1)}{(2275)\ (0.8)} + 22.25$$

$$= 35.7 \text{ ft}$$

$$= 10.881 \text{ m}$$

$$R_2 = \frac{[(1003)\ (22.25) + (790)\ (25)]\ 1.1}{(2275)\ (0.8)} + 22.25 + 25$$

$$= 70.4 \text{ ft}$$

$$= 21.458 \text{ m}$$

These two radii were used for the layout of the PCRV shown in Fig. A-4 with a diameter of 39.319 m (129 ft) and a saving of approximately 6.1 m (20 ft) of PCRV diameter compared with the symmetrical design.

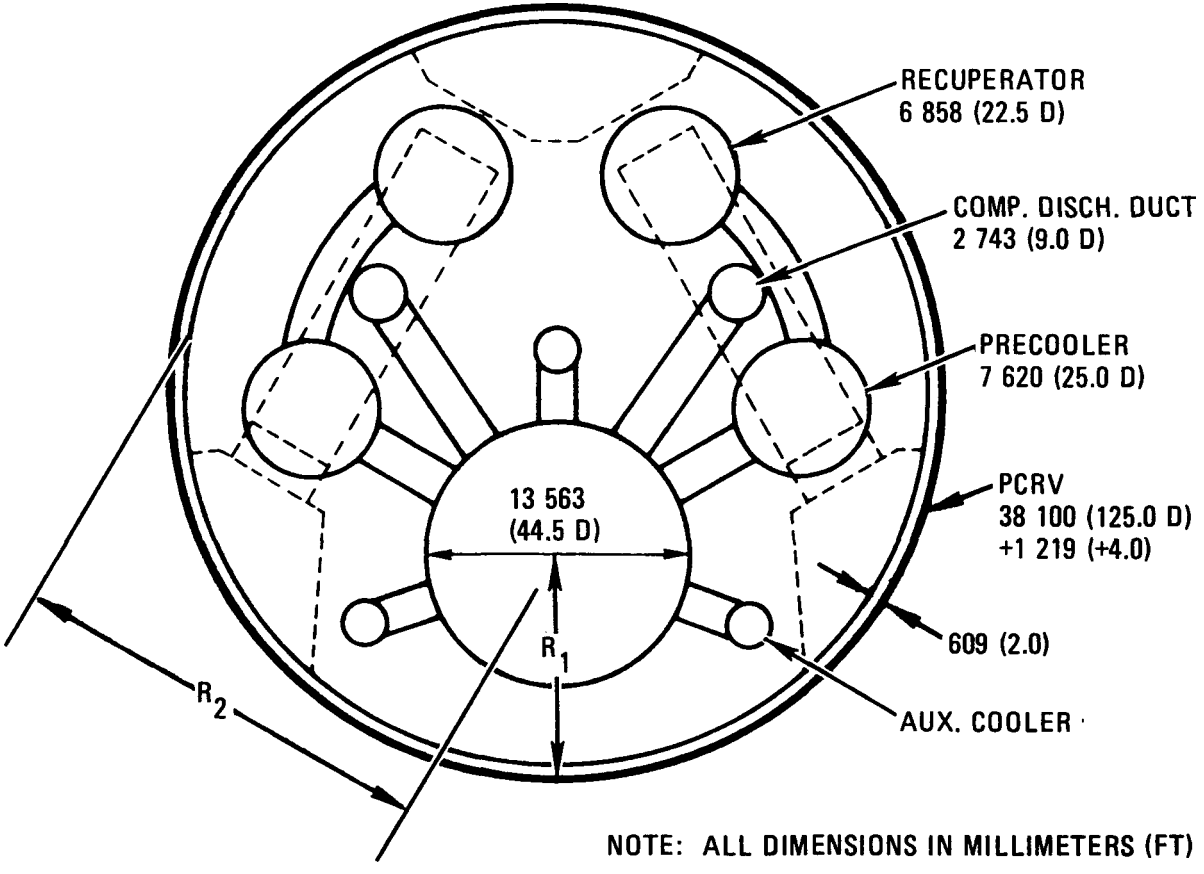

Fig. A-4. Configuration 850/2-1, two-loop, 4000-MW(t), delta

A.4.2.2. Configuration 850/2-2 (see Fig. A-5). The PCRV diameter for this configuration will be

$$D = \frac{[(1003)\ (44.5) + (2)\ (790)\ (17.5)]\ 1.1}{(2275)\ (0.8)} + 44.5 + (2)\ (17.5) + (2)\ (2)$$

$$= 123.2 \text{ ft} + 4 \text{ ft}$$

$$= 37.541 \text{ m} + 1.219 \text{ m}$$

A.4.3. Description of Configuration 850/2-2

The layout is shown in Fig. A-6. The dimensions used for the turbomachine unit are shown in Fig. A-1.

The basic components consist of two turbomachine units and four each recuperators and precoolers arranged in pairs.

The ducting arrangement appears to fit into the general PCRV layout. Twin ducts from the bottom of the core to the turbine were used. One duct goes directly into the turbine from the top, and the second goes into the outer side of the turbine (90 deg apart). An effort to arrange these ducts so that they entered on opposite sides of the turbine would require a much larger PCRV, and therefore the arrangement shown (of 90 deg apart) was considered to be a satisfactory compromise. Access for thermal barrier removal is also provided.

Twin exit ducts from the turbine are located on each side of the turbomachine cavity at the turbine exit plenum. These ducts are relatively short and feed the pair of recuperators for shell-side flow.

The flow exiting from the pair of recuperators (flow outside the tubes) is joined in a common single large duct directed to the pair of precoolers. Although the duct is rather large, it should be observed that its shadow in the plan view is within the profile of the turbomachine cavity. Therefore, the duct does not restrict the application of the vertical tendons.

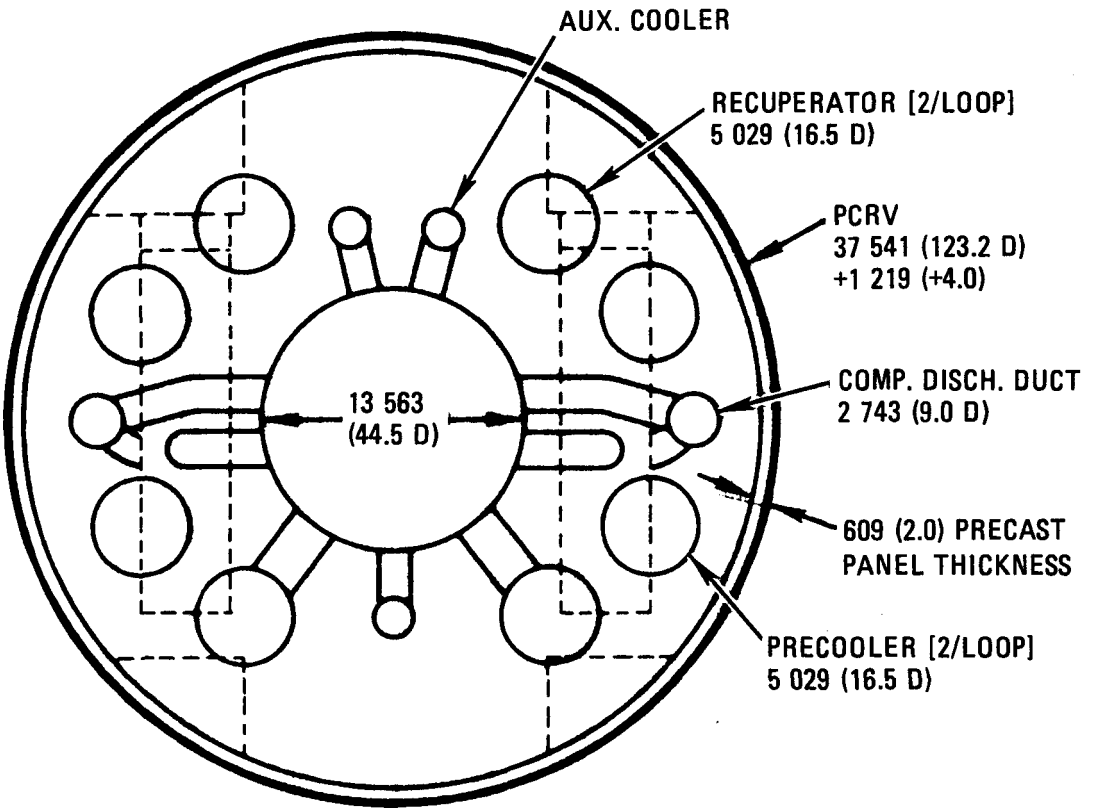

Fig. A-5. Configuration 850/2-2, two-loop, 4000-MW(t), parallel

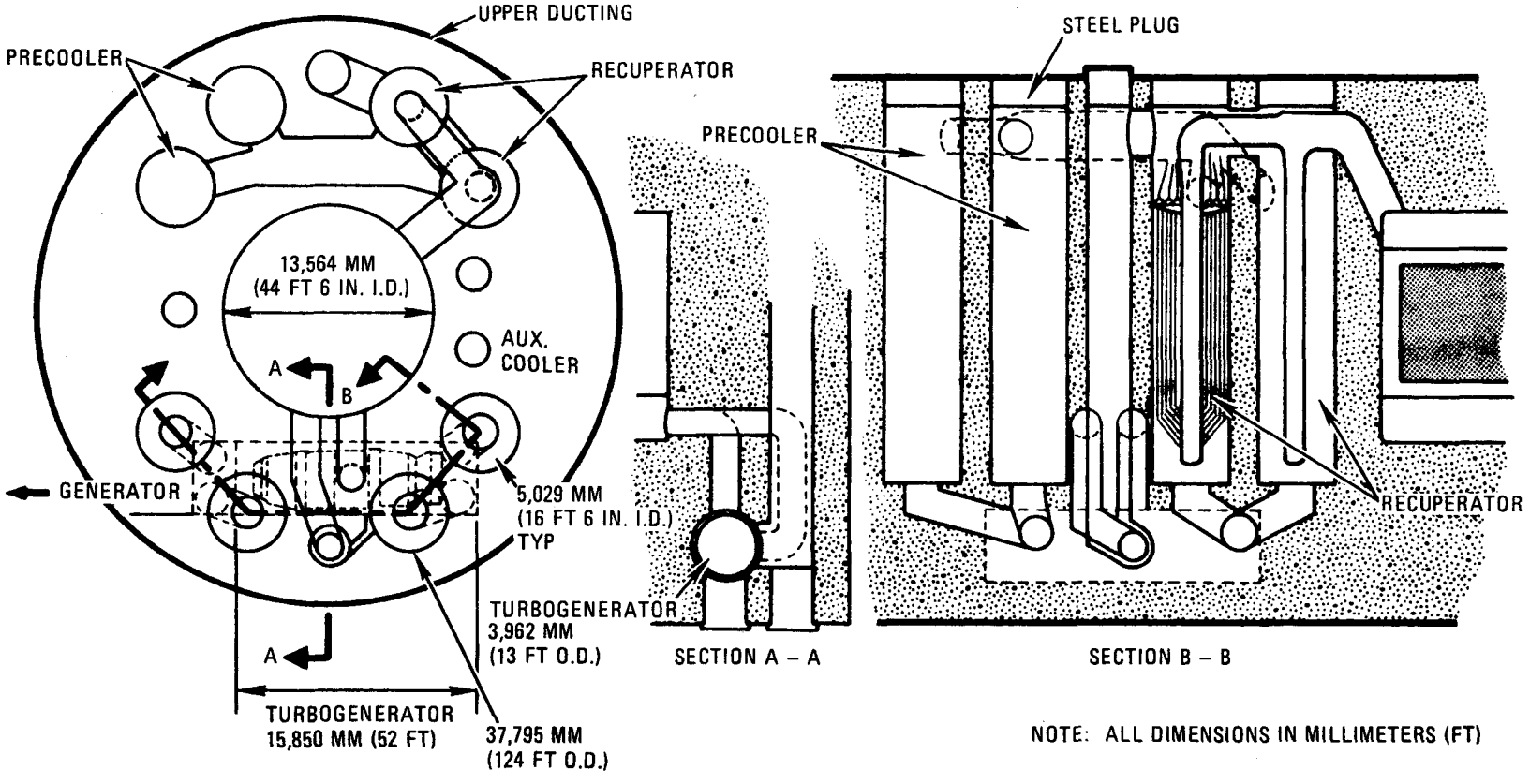

Fig. A-6. Configuration 850/2-2, preliminary layout

The branching of the ducting from the heat exchanger is rather unsymmetrical and will require some flow analysis and balancing.

The ducting exit between the precooler to the compressor inlet plenum is very similar to the turbine exit ducting.

The compressor exit ducting is concentric with one of the turbine inlet ducts, thereby assisting the concrete cooling in that area. One compressor outlet duct located above the outer turbine inlet duct directs the flow upward to the pair of recuperators (for tube-side helium flow). The flow is ducted directly to adjacent recuperators. The duct for the more distant of the pair of recuperators obtains its flow from the adjacent recuperators' plenum.

The return flow from inside the recuperator tubes is conducted upward through center ducts in the recuperators. The flow thus exiting from the inside of the recuperator tubes is joined into a single duct which returns the helium to the core.

A.5. THREE- AND FOUR-LOOP CONFIGURATIONS

A.5.1. General

The overall evaluation of the different three- and four-loop configurations resulted in the following:

1. PCRV size. As can be observed from Table A-1, the smallest PCRV can be achieved with a three-loop design with a reactor outlet temperature of 950°C which has a delta turbomachine arrangement and the following dimensions:

   Overall diameter: D = 39.411 m (129.3 ft)
   Overall height: H = 31.496 m (103.3 ft)

2. PCRV Diameter. The diameter of the PCRV is determined by stress conditions for the following three-loop configurations: 850/3-1, 850/3-2, and 950/3-2. For all other configurations, the diameters are determined by geometric conditions (see Table A-1) and are therefore not the most economical designs.

3. PCRV height. For the three-loop delta and four-loop square designs, the PCRV height is the minimum height. This height is determined by the required top and bottom head thickness plus the core cavity height and is 31.496 m (103.3 ft) (see Section A.3.2). The height for the configurations with the radial turbomachine arrangement is 34.137 m (112 ft), which is greater than the minimum height because of the required ligaments between turbomachine cavity, core cavity, and bottom head.

A.5.2. Discussion of Configurations

A.5.2.1. Three-Loop Configurations. The layouts of these configurations are shown in Figs. A-7 and A-8.

Configuration 850/3-1 has a radial arrangement of the turbomachine units and an outside PCRV diameter of 40.538 m (133 ft). The diameter is determined by Eq. A-1 and by stress conditions.

The PCRV height is determined by the core cavity height plus the thickness of the top and bottom heads as explained in Section A.3.2. The overall height of the PCRV is 34.137 m (112 ft).

The PCRV diameter of Configuration 950/3-1 is determined only by the geometry of the turbomachine. The heat exchanger cavity size is smaller than that of Configuration 850/3-1 and would allow a smaller PCRV diameter to meet stress criteria, but the turbomachine dimensions require a diameter of 40.538 m (133 ft).

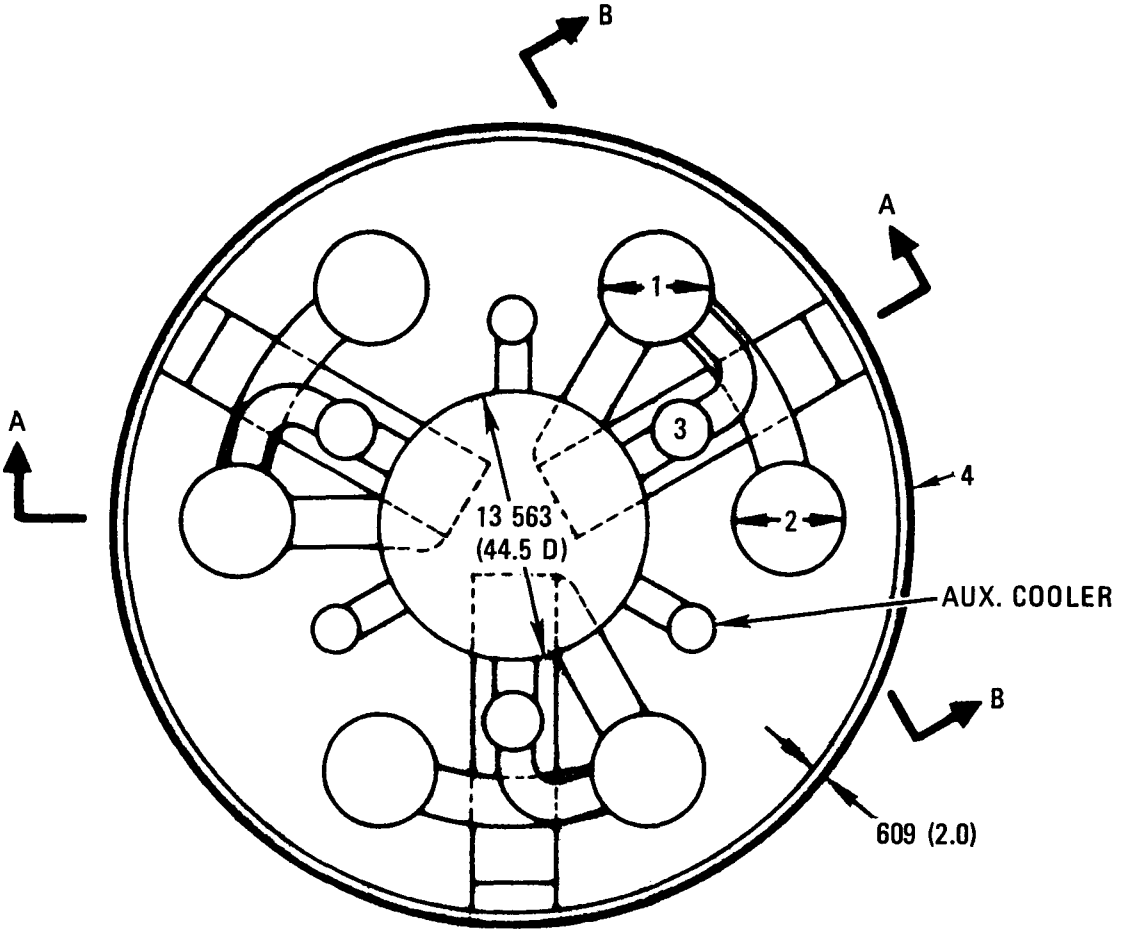

		850/3–1		950/3–1	
1	RECUPERATOR	5 638	(18.5) D	5 486	(18.0) D
2	PRECOOLER	5 943	(19.5) D	5 486	(18.0) D
3	COMP. DISCH. DUCT	2 946	(9.75) D	2 946	(9.75) D
4	PCRV	39 319	(129.0) D	39 319	(129.0) D
		+1 219	(+4.0)	+1 219	(+4.0)

NOTE: ALL DIMENSIONS IN MILLIMETERS (FT)

GA-A13950

Fig. A-7. Configuration 850-950/3-1, three-loop, 4000-MW(t), radial (sheet 1 of 2)

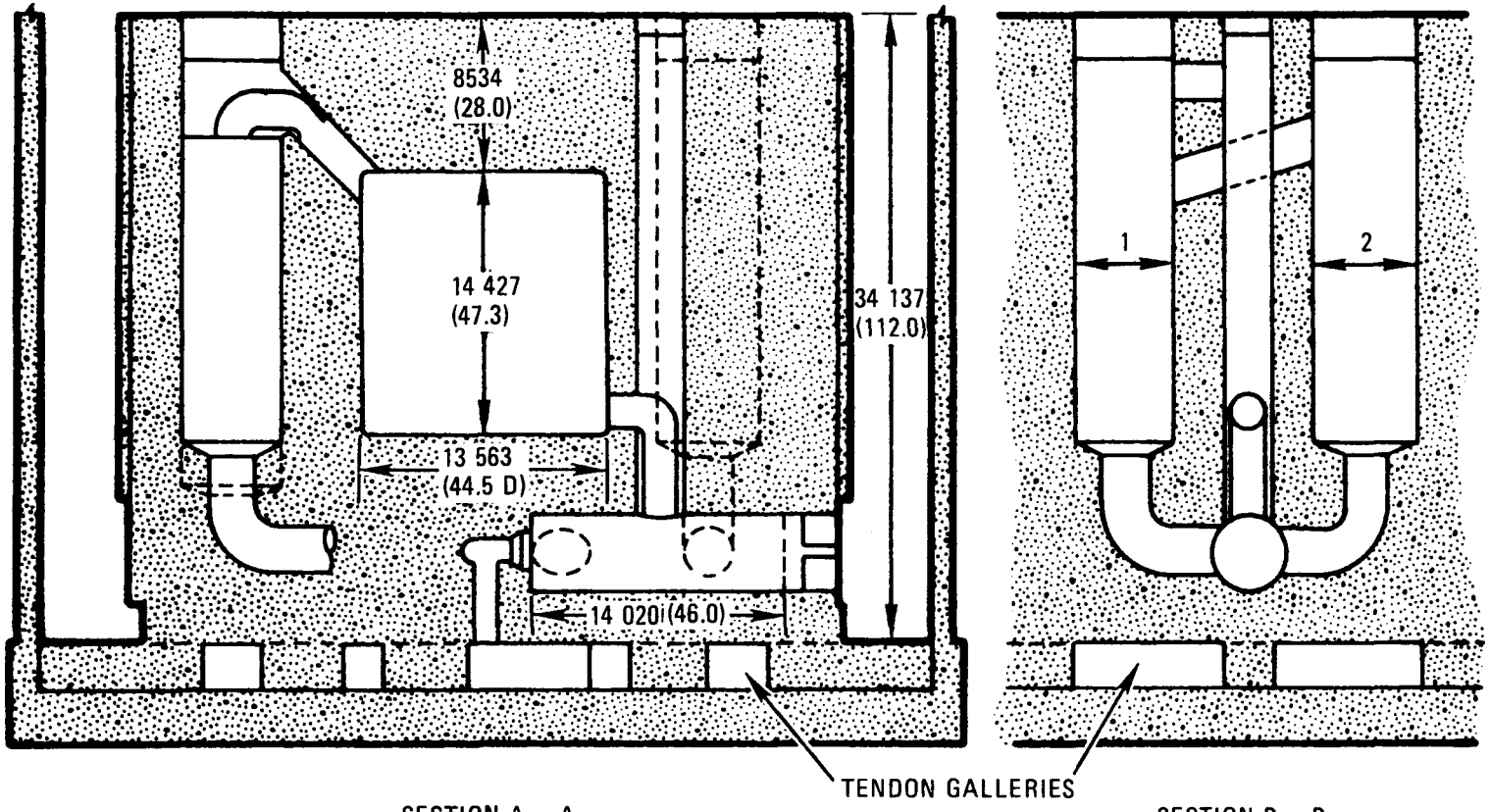

		850/3–1		950/3–1	
1	RECUPERATOR	5 638	(18.5) D	5 486	(18.0) D
2	PRECOOLER	5 943	(19.5) D	5 486	(18.0) D

NOTE: ALL DIMENSIONS IN MILLIMETERS (FT)

GA-A13950

Fig. A-7. Configuration 850-950/3-1, three-loop 4000-MW(t), radial (sheet 2 of 2)

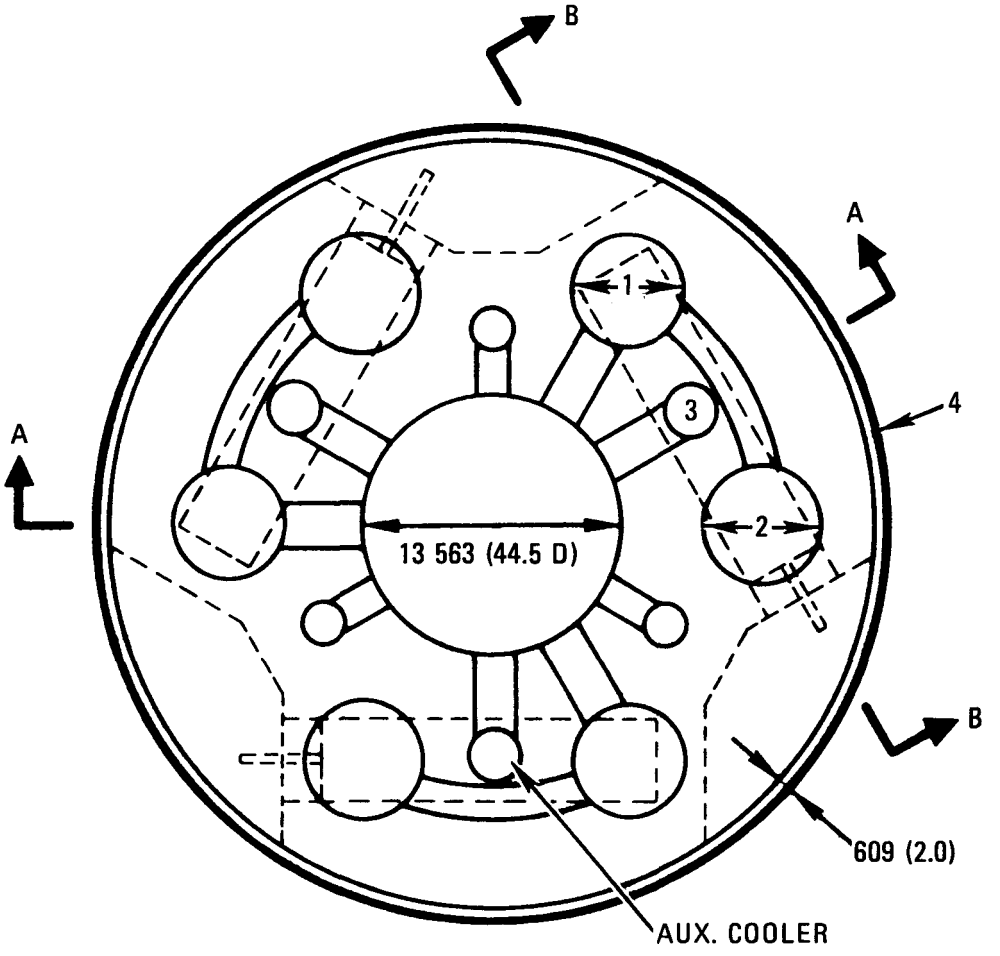

		850/3–2	950/3–2
1	RECUPERATOR	5638 (18.5) D	5486 (18.0) D
2	PRECOOLER	5943 (19.5) D	5486 (18.0) D
3	COMP. DISCH. DUCT	2946 (9.75) D	2946 (9.75) D
4	PCRV	39319 (129.0) D +1219 (+4.0)	38201 (125.3) D +1219 (+4.0)

GA-A13950

Fig. A-8. Configuration 850-950/3-2, three-loop, 4000-MW(t), delta (sheet 1 of 2)

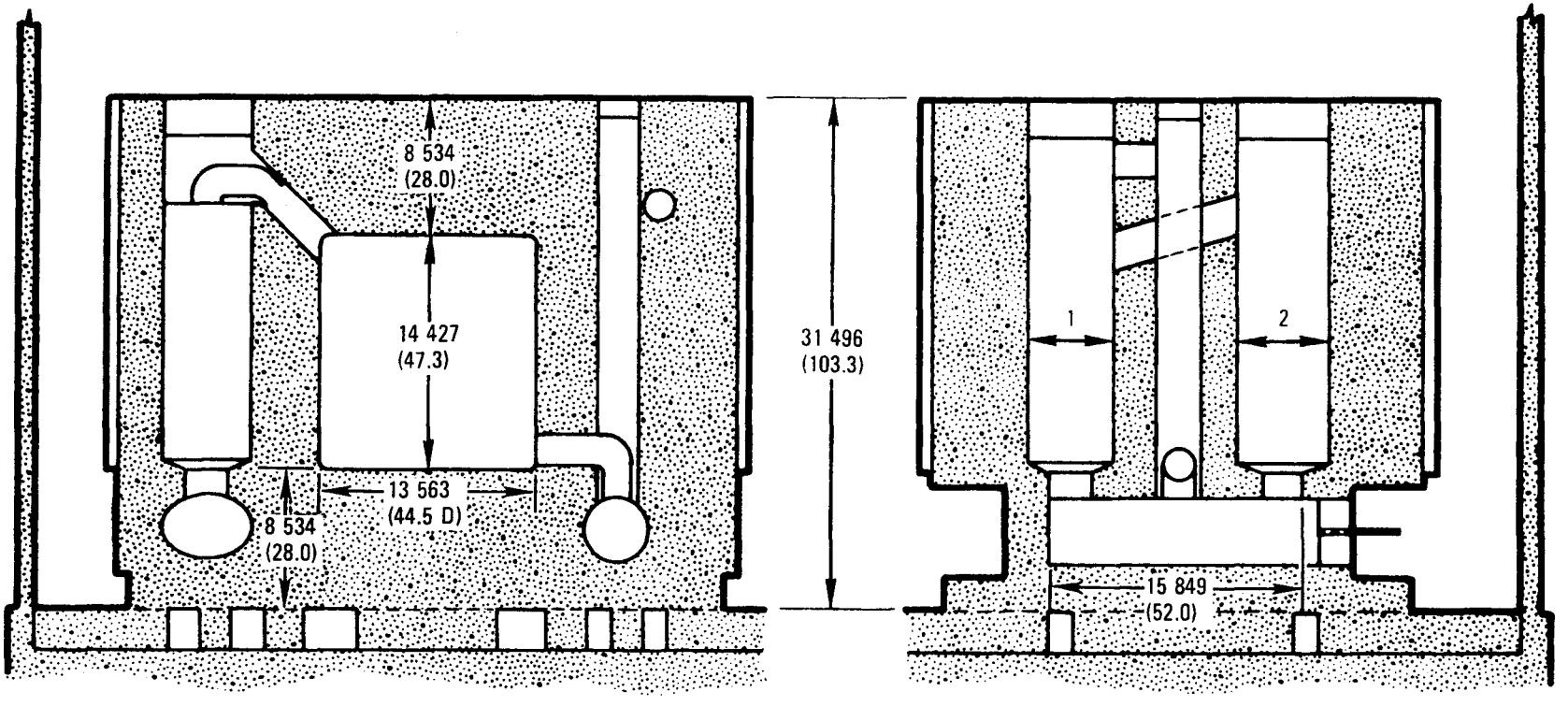

		850/3 2		950/3-2	
1	RECUPERATOR	(18.5) D	(18.0) D	5 486	(18.0 D)
2	PRECOOLER	(19.5) D	(18.0) D	5 486	(18.0 D)

NOTE: ALL DIMENSIONS IN MILLIMETERS (FT)

GA-A13950

Fig. A-8. Configuration 850-950/3-2, three-loop, 4000-MW(t), delta (sheet 2 of 2)

Because the PCRVs are designed to the turbomachine cavity dimensions, any axial growth of the turbomachine will therefore affect the PCRV diameter.

Configurations 850/3-2 and 950/3-2 have a triangular (delta) arrangement of the turbomachine units. The PCRV diameters for these configurations are determined by stress conditions in the ligaments only and were determined to be 40.538 m (133 ft) for Configuration 850/3-2 and 39.420 m (129.3 ft) for Configuration 950/3-2.

The PCRV height for both configurations is 31.496 m (103.3 ft), which is the minimum PCRV height.

Because of the arrangement of the heat exchangers directly above the turbomachine cavities, a reduction in the number of vertical tendons of approximately 5% is achieved. There will also be a primary coolant pressure drop reduction due to shorter ducts and elimination of two 90-deg bends in the ducting system.

The triangular arrangement of the turbomachine cavities allows a considerably growth of the turbomachine units without affecting the PCRV diameter. This is apparent in Fig. A-8, sheet 2 of 2, where the turbomachine cavity length has been made 15.849 m (52 ft) in order to provide more efficient compressor inlet and turbine outlet plenum chambers. This cavity length is available for a turbomachine growth.

A.5.2.2. Four-Loop Configurations. The layouts of these configurations are shown in Figs. A-9 and A-10.

Configurations 850/4-1 and 950/4-1 have a radial arrangement of the turbomachine cavities and outside diameter of 39.928 m (131 ft). The PCRV diameter is determined by the geometry of the turbomachine arrangement with respect to the location of the compressor discharge duct and the dimensions of the turbomachine cavities according to Fig. A-1.

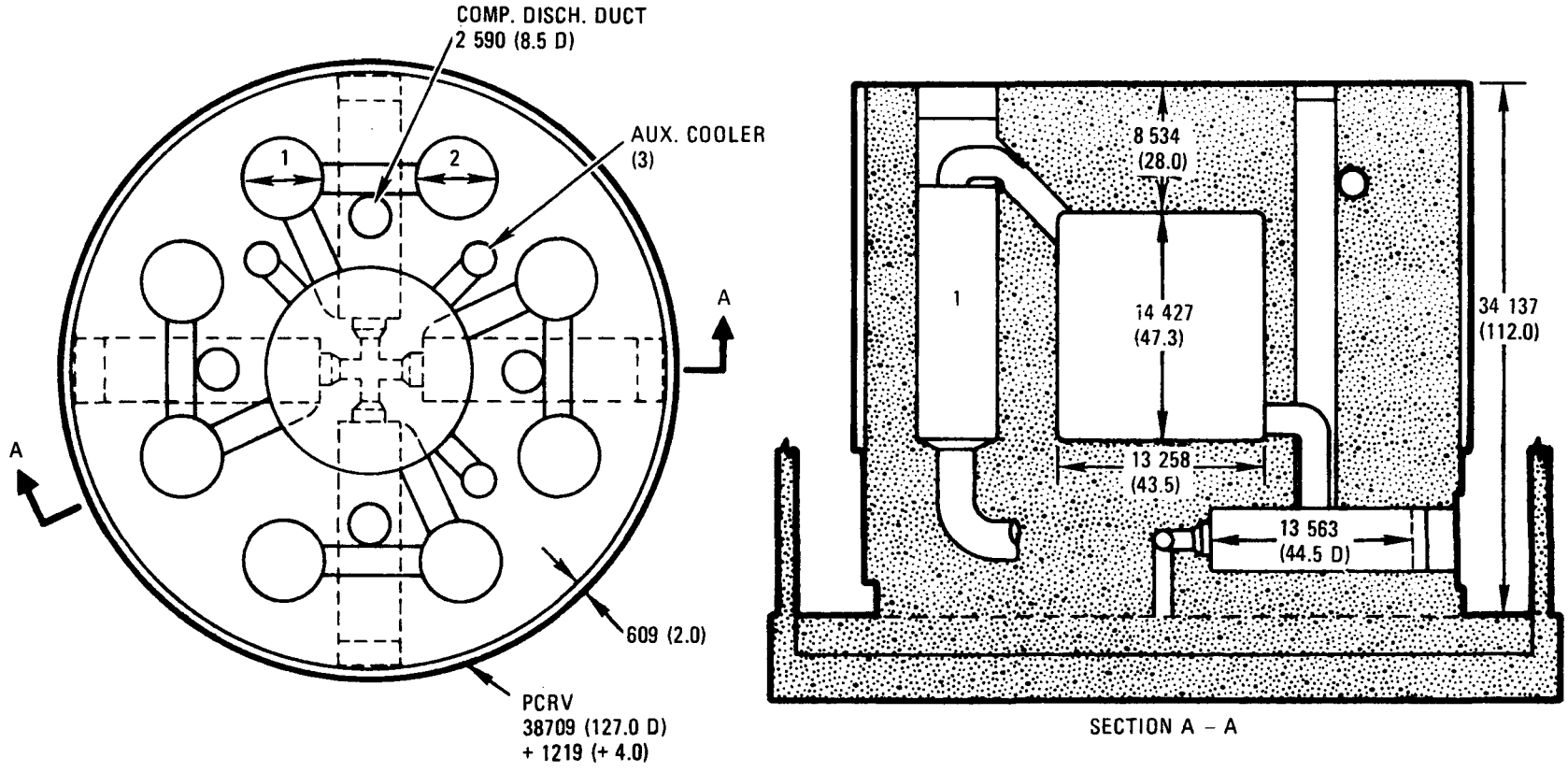

		850/4–1		950/4–1	
1	RECUPERATOR	5181	(17.0) D	4876	(16.0) D
2	PRECOOLER	5181	(17.0) D	4876	(16.0) D

NOTE: ALL DIMENSIONS IN MILLIMETERS (FT)

Fig. A-9. Configuration 850-950/4-1, four-loop, 4000-MW(t), radial

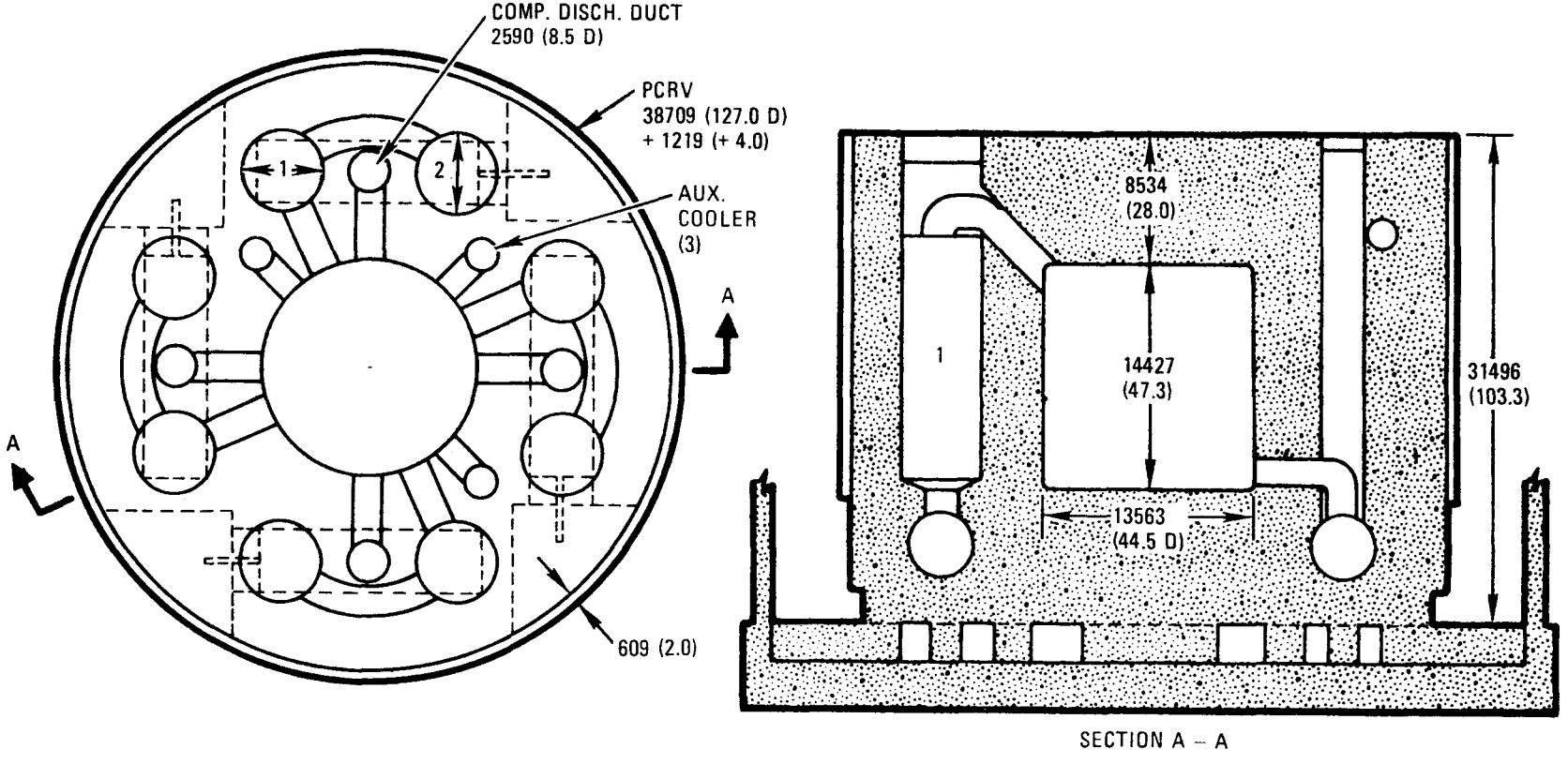

		850/4–2		950/4–2	
1	RECUPERATOR	5181	(17.0)	4876	(16.0)
2	PRECOOLER	5181	(17.0)	4876	(16.0)

NOTE: ALL DIMENSIONS IN MILLIMETERS (FT)

...-A13950

Fig. A-10. Configuration 850-950/4-2, four-loop, 4000-MW(t), square

The PCRV height of 34.137 m (112 ft) is the same as for the three-loop counterpart.

This configuration is also designed to the turbomachine cavity dimensions, and any axial growth of the turbomachine units will affect the PCRV diameter.

Configurations 850/4-2 and 950/4-2 have a square arrangement of the turbomachine cavities. The PCRV diameter for both configurations is determined by the geometric conditions of the turbomachine cavities in that square. The length of the turbomachine cavities and the space required for the horizontal prestressing tendons around the turbomachine cavity plugs were the determining geometric factors for the PCRV diameter of 39.928 m (131 ft). Because of these limiting conditions, there is no axial growth capability for the turbomachines without affecting the PCRV diameter.

The PCRV height is also the minimum height of 31.496 m (103.3 ft).

A.5.2.3. Technical Uncertainties. The technical uncertainty of the PCRV designs arises from the structural discontinuity of the bottom part for the delta design of the three-loop configuration and the square design of the four-loop configuration in the area where the turbomachine cavities are located.

A three-dimensional structural analysis of this section using the MARC code (Ref. A-3) with a simplified grid structure has been made. The preliminary evaluation of the results of this analysis is that the design is feasible and that no unusually high local stresses are apparent.

For the remaining part of the PCRV, all foreseen design or development problems are the same as those occurring with the reference design.

For the four-loop square configuration, the same uncertainty of the bottom part of the PCRV exists.

Because of the added cavities of the fourth loop and in spite of the fact that the heat exchanger cavities are smaller, the PCRV diameter is no longer determined by the stress conditions but rather by the geometry of the layout of the turbomachine cavities including their horizontal prestressing system. Future larger-scale investigation of this area may result in a slight increase of the PCRV diameter of the square configuration.

A.5.2.4. Growth Potential. The growth of the turbomachine length can be accommodated without a change in PCRV diameter only by the three-loop delta configuration. For all other configurations, an increase in PCRV diameter will result if the turbomachine length is increased.

A.6. PCRV FOUNDATION

The containment building designs with the PCRV placed directly on the slab of the containment building required a study of the arrangement of the vertical tendon heads on the bottom surface of the PCRV.

So long as unbonded tendons with their capability for replacement are required, access to both upper and lower tendon heads has to be provided. In this study, access has been provided as shown in Figs. A-11 and A-12 for the three-loop radial and delta designs, respectively, and in Fig. A-13 for the four-loop square arrangement.

The major problem with a design where the PCRV is placed directly on the slab of the containment is the arrangement of the containment liner. The objective of the liner is to provide a leak-tight boundary for the reactor to the outside atmosphere, and penetrations should be kept to a minimum. Therefore, the PCRV tendons should not penetrate the liner. The design described avoids this by placing the containment liner underneath the tendon galleries. Burying the liner under a thick layer of concrete is a disadvantage, however, for liner welds in the area directly beneath the PCRV require special leak check provisions in any case. In the annulus between the PCRV and the containment wall, the liner can be elevated to a

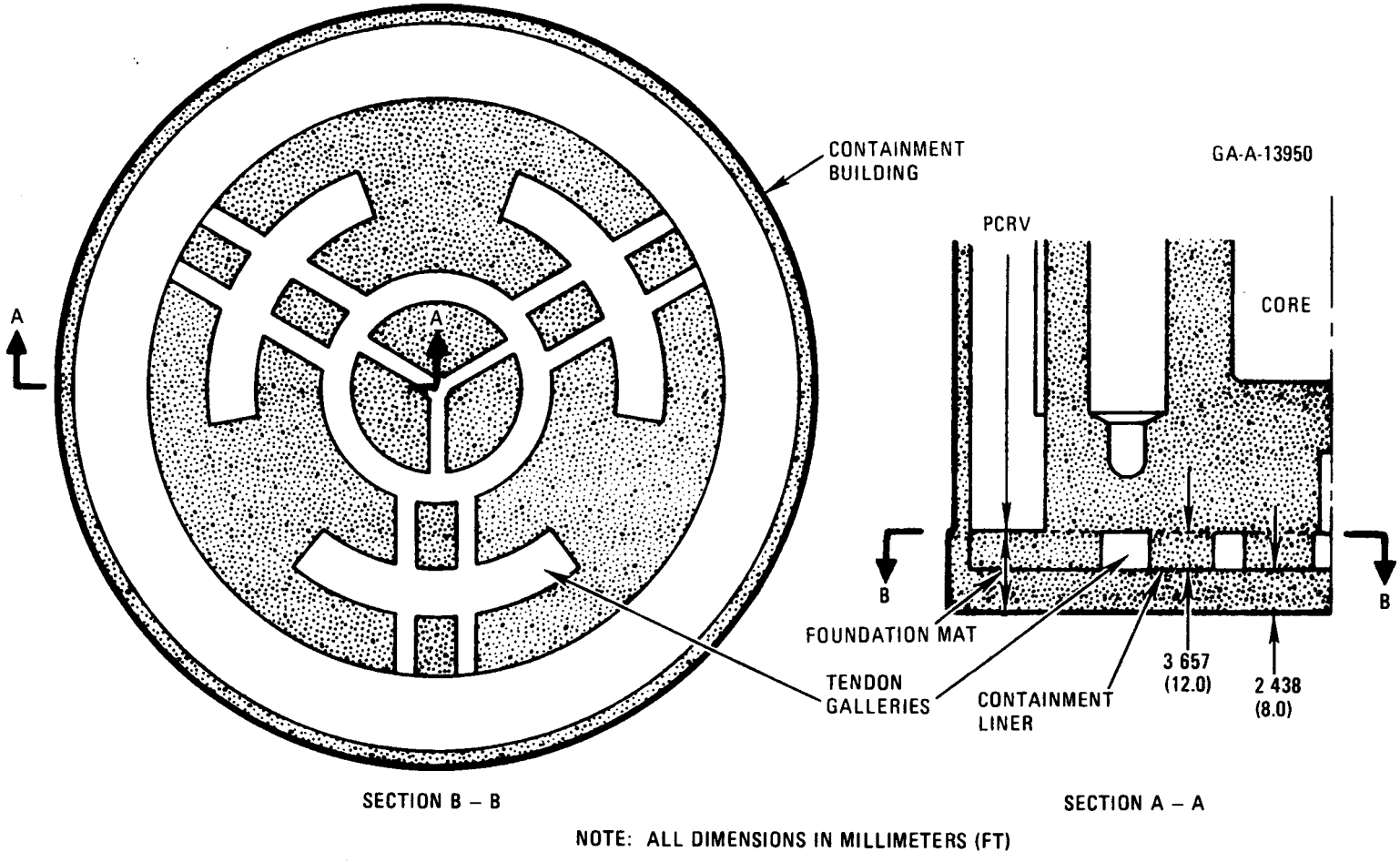

Fig. A-11. Foundation, three-loop, radial

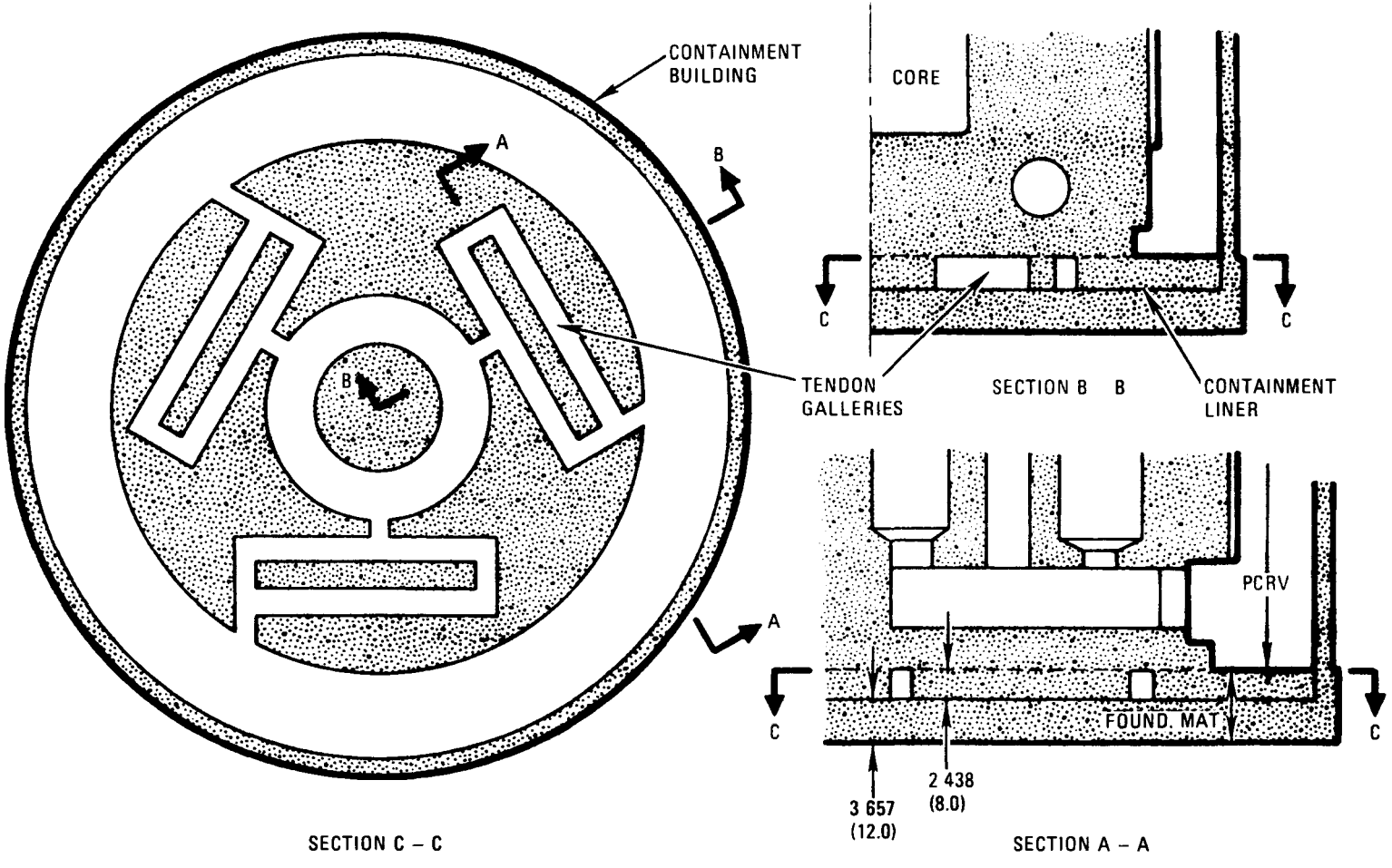

NOTE: ALL DIMENSIONS IN MILLIMETERS (FT)

GA-A13950

Fig. A-12. Foundation, three-loop, delta

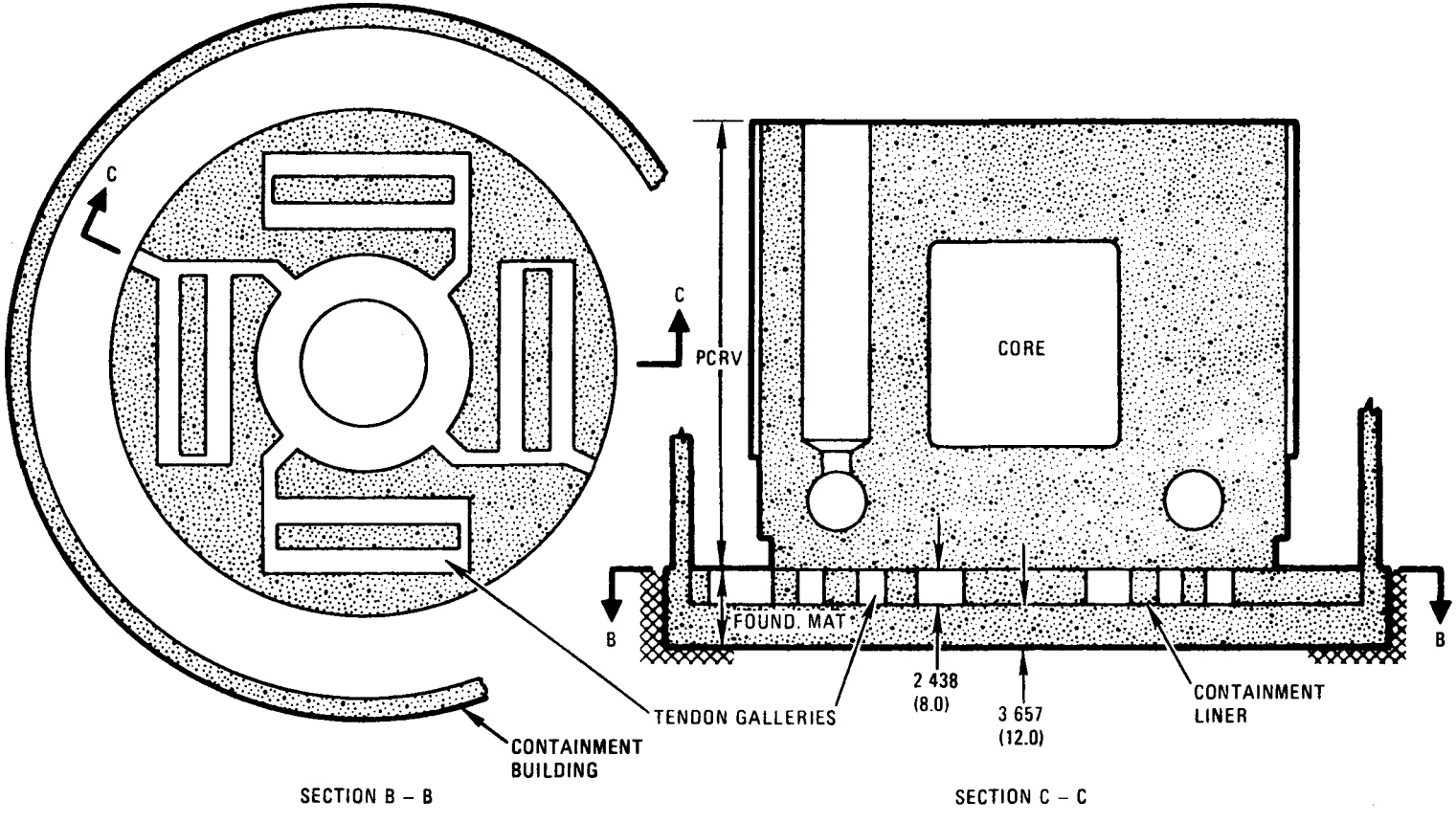

Fig. A-13. Foundation, four-loop, square

level 0.4572 m (1.5 ft) beneath the containment floor. All areas directly below the tendor galleries are readily available for leak testing.

The integrity of the foundation mat will be obtained by cadwelding the vertical reinforcing bars of the top and bottom layers of the mat to the liner. This will provide the required structural connection between the PCRV and the containment mat to resist the seismic overturning moment during an earthquake.

The tendon galleries should be minimized by leading tendons into common galleries.

REFERENCES

A-1. "Gas Turbine HTGR Program, Semiannual Progress Report for the Period July 1, 1975 through December 31, 1975," General Atomic Report GA-A13740, January 1976, Section 5.

A-2. "Gas Turbine HTGR Program, Quarterly Progress Report for the Period October 1, 1974 through December 31, 1974, "General Atomic Report GA-A13301, January 1975, Section 5.

A-3. "MARC-CDC Nonlinear Finite Element Analysis Program," Marc Analysis Corporation, Providence, Rhode Island.

APPENDIX B
SIGNIFICANT RISK SEQUENCES

The following Accident Initiation and Progression Analysis (AIPA) was developed specifically for the GT-HTGR. Every event discussed in the GCR AIPA (Ref. B-1) and the HTGR AIPA Status Report (Ref. B-2) is related to a comparable GT-HTGR event. The following events that are specific to the GT-HTGR are also discussed:

1. Loss of electric load (LOL)
2. Precooler failures
3. Turbomachine failures
4. Shaft seal failures
5. Generator failures
6. Cooling water system (CWS) pipe rupture

B.1. REPORT CONTENT

1. Table of events analyzed
2. Comments and/or development of each event
3. Summary risk plot for the GT-HTGR

B.2. REPORT METHODOLOGY

The methodology is described in Ref. B-2. Wherever possible, event and/or branch probabilities are taken from Ref. B-2. Thus, repair time and maintenance effects are implicitly included in the analysis. The philosophy of reliance on Ref. B-2 and on the advice of the engineers who authored the report was felt to increase the accuracy of the study over a direct analysis of the individual events for the GT-HTGR, particularly considering the preliminary design status of the plant.

B.3. CONSEQUENCE EVALUATION

All of the consequences were approximated by conservative comparison with Ref. B-2 events. GT-HTGR whole-body doses are estimated at 1.5 times the dose of Ref. B-2 and the bone dose at three times that of Ref. B-2 for a comparable event. These factors are well within the consequence uncertainty and have therefore been ignored.

B.4. EVENTS CHOSEN FOR ANALYSIS

The events listed in Table B-1 were not specifically developed in this study. The Table B-1 events are generic to the HTGR concept and are not expected to vary significantly between SC-HTGR and the GT-HTGR.

The events listed in Table B-2 are discussed in the following text. The selection of events for analysis followed the procedures detailed in Ref. B-2. A general discussion of the event selection process for the GT-HTGR is presented in Ref. B-3. Because the GT-HTGR is often compared with the SC-HTGR, the following discussion addresses all of the events covered in Ref. B-2.

B.5. GT-HTGR AIPA EVENT DISCUSSION

B.5.1. Helium Instrumentation Line Break

See Vol. III of Ref. B-2.

B.5.2. PCRV Purge Header Break

See Vol. III of Ref. B-2.

B.5.3. Rapid PCRV Depressurization

With one exception, Event 3 is substantially similar to the event in Vol. III of Ref. B-2. The GT-HTGR has an additional initiating event of a shaft seal failure. This additional event is analyzed as Event 20.

B.5.4. Slow PCRV Depressurization

See Event 3 comments.

B.5.5. Drop of Spent Fuel Shipping Container

See Vol. III of Ref. B-2.

TABLE B-1
EVENTS NOT DEVELOPED IN THIS STUDY

Section in This Report	Event	Section in Vol. III of Ref. B-2
B.5.1	Helium instrumentation line break	4.1
B.5.2	PCRV purge header break	4.2
B.5.5	Drop of spent fuel shipping container	4.5
B.5.6	Gas waste tank rupture	4.6
B.5.10	Drop of neutron source	4.10
B.5.12	Liquid waste tank rupture	4.12
B.5.13	Drop of solid waste container	4.13
B.5.14	Drop of irradiated hardware container	4.14
B.5.15	Drop of recycle fuel container	4.15
B.5.17	PCRV structural failure	4.17

TABLE B-2
EVENTS ANALYZED FOR THE GT-HTGR

Section in This Report	Event	Section in Vol. III of Ref. B-2
B.5.3	Rapid PCRV depressurization	4.3
B.5.4	Slow PCRV depressurization	4.4
B.5.7	Loss of offsite power (LOSP)	4.7
B.5.8	Moisture inleakage into primary coolant	4.8
B.5.9	Reheater tube leak	4.9
B.5.11	Main steam pipe rupture outside containment	4.11
B.5.16	Shafe shutdown earthquake (SSE)	4.16
B.5.18	Loss of electric load (LOL)	
B.5.19	PCRV pressure relief	
B.5.20	Shaft seal failures	
B.5.21	Precooler failures	
B.5.22	Turbomachine failures	
B.5.23	Generator failures	
B.5.24	CWS pipe rupture	

B.5.6. Gas Waste Tank Rupture

See Vol. III of Ref. B-2.

B.5.7. Loss of Offsite Power (LOSP)

This event differs considerably from that of the SC-HTGR. The GT-HTGR advantages are the lower probability of losing main loop cooling and the zero consequence during LOSP so long as either the CACS or the main loops can operate. The event logic tree for LOSP is shown in Fig. B-1. The non-zero consequence in the SC-HTGR following loss of load is discussed in Event 18. The large consequence following failure to isolate the containment is based on the SC-HTGR with external pressure relief.

B.5.8. Moisture Inleakage into Primary Coolant

The GT-HTGR does not have a source of high-pressure moisture with a potential for entry into the PCRV. The GT-HTGR event most similar to this is event 21.

B.5.9. Reheater Tube Leak

The GT-HTGR does not have a reheater. The GT-HTGR event most similar to this is Event 21.

B.5.10. Drop of Neutron Source

See Vol. III of Ref. B-2.

B.5.11. Main Steam Pipe Rupture Outside Containment

The GT-HTGR does not produce steam. The GT-HTGR event most similar to this is Event 24.

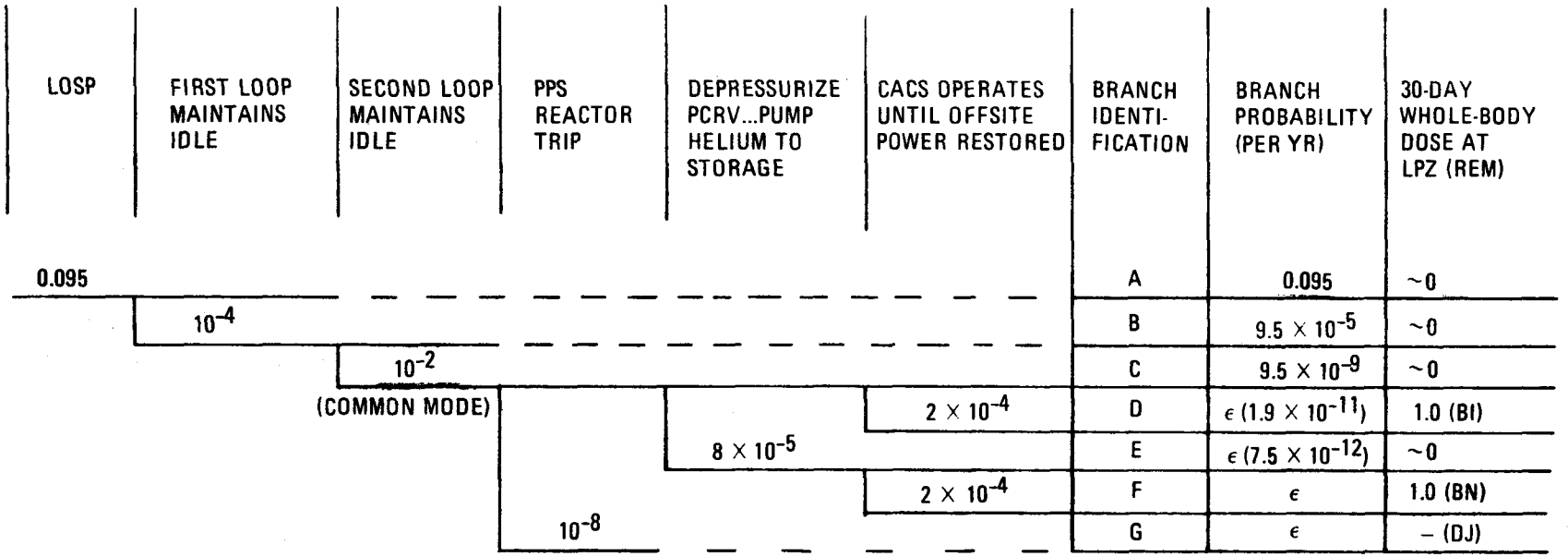

NOTES:

1. BRANCH PROBABILITIES FROM REFS. B–2 AND B–4.
2. CONSEQUENCES ARE ESTIMATED FROM THE PARENTHESIZED BRANCH OF THE EVENT IN VOL. III OF REF. B–2.
3. CONTAINMENT BUILDING IS ALWAYS ISOLATED.
4. LPZ = LOW POPULATION ZONE.

GA-A13950

Fig. B-1. Event logic tree for loss of offsite power (LOSP)

B.5.12. Liquid Waste Tank Rupture

See Vol. III of Ref. B-2.

B.5.13. Drop of Solid Waste Container

See Vol. III of Ref. B-2.

B.5.14. Drop of Irradiated Hardware Container

See Vol. III of Ref. B-2.

B.5.15. Drop of Recycle Fuel Container

See Vol. III of Ref. B-2.

B.5.16. Safe Shutdown Earthquake (SSE)

The assessment of SSE risk is not tractable at this stage of GT-HTGR preliminary design. The continuing enhancement of the GT-HTGR data base will enable a later SSE risk analysis. The qualitative opinion that the GT-HTGR SSE risk will not differ significantly from that of the SC-HTGR relies on the following factors:

1. The GT-HTGR and SC-HTGR core, CACS, and containment building are nearly identical.

2. The turbomachine and generator loads during an SSE are significantly smaller than the normal turbomachine stress during startup and shutdown (cf. critical speeds); therefore, the shaft seals are assured to be intact.

3. Both the precooler and the recuperator are designed such that their spectrum of credible failures does not include events with radiological consequences (see Vol. III of Ref. B-2 for the SC-HTGR event).

B.5.17. PCRV Structural Failure

See Vol. III of Ref. B-2.

B.5.18. Loss of Electric Load (LOL)

The radiological consequence of LOL differs considerably from that of the SC-HTGR. For several engineering reasons, the standard method for reduction of steam turbine drive is to vent the high-pressure steam to the atmosphere. Since the steam is lightly tritiated, the SC-HTGR LOL has a finite risk. The GT-HTGR reduces turbine drive following LOL by collapsing (within the PCRV) the turbine pressure ratio using the bypass valve system (BVS). Therefore, the GT-HTGR LOL is without radiological risk.

B.5.19. PCRV Pressure Relief

The SC-HTGR relieves PCRV overpressure, using pressure relief valves, to the reactor containment building (RCB). The SC-HTGR needs external pressure relief because of the 5.5 MPa (2250 psia) steam, which could overpressurize the PCRV. The GT-HTGR does not have a source of high-pressure fluid capable of overpressurzing the PCRV. (The precooler water pressure is always below the adjacent helium pressure.) No identified source for overpressure of the PCRV exists; however, the ASME Boiler and Pressure Vessel Code requires a pressure relief system. A proposal was presented to the ASME Code Committee for internal pressure relief. The proposal was accepted by the ASME Code Committee, and the code is to be amended. Therefore, there is no radiological risk to PCRV pressure relief.

B.5.20. Shaft Seal Failures

Unlike the SC-HTGR, the GT-HTGR has a generator shaft that penetrates both the containment building and the PCRV. The generator shaft will be constrained such that the conceivable shaft ejection event will require prior PCRV structural failure. Thus, the event will be incredible, as demonstrated in Vol. III of Ref. B-2.

The primary coolant boundary (PCB) in the PCRV generator shaft penetration is formed by the solid generator shaft, surrounded by various floating seals that are attached to the shaft and the PCRV. The seal failure risk was estimated in Ref. B-5 and is listed in Table B-3. The event logic tree is presented in Fig. B-2.

B.5.21. Precooler Failures

The GT-HTGR precooler leak has less radiological consequence than the similar SC-HTGR reheater leaks or steam generator leaks. The primary difference is the closed-loop cooling water system (CWS) (e.g., the secondary coolant) for the dry-cooled GT-HTGR. The only paths for radiation to the public are "shine" from the CWS lines and water release through relief valves should the CWS be overpressurized. The consequence was conservatively estimated from Vol. III of Ref. B-2. The event logic tree is presented in Fig. B-3.

B.5.22. Turbomachine Failures

Turbomachine failures are of three types: (1) bearing failure, (2) blade failure, and (3) disk failure.

Bearing failure is a progressive event that is independent of shaft seal lubricant failure. Thus, the PCB remains intact, and there is no radiological consequence.

The turbomachine is encased in a burst shield designed to contain disk fragments generated at up to 20% overspeed. The burst shield will contain all radial ejection of failed blades. Failed blades will be ejected according to the existing local pressure gradient. Both the shaft seals and the adjacent thermal barrier have passive protection that is proof against these low-energy missiles. Thus, this event is without radiological consequence.

TABLE B-3
PROBABILITY AND CONSEQUENCE OF EVENTS
ASSOCIATED WITH SHAFT SEAL FAILURE

Event Description	Initial Primary Coolant Leakage Flow	Probability of Occurrence (per plant yr)	Consequence: 30-Day Whole-Body Dose at LPZ (rem)
A. Slow PCRV depressurization	Approximately 2 lb/sec	5×10^{-5}	8×10^{-4}
B. Rapid PCRV depressurization	Approximately 88 lb/sec	4×10^{-9} low est. 1×10^{-5} high est.	8×10^{-4}
C. Rapid PCRV depressurization with loss of containment integrity	Approximately 88 lb/sec	$\varepsilon(6 \times 10^{-13})$ low est. $\varepsilon(6 \times 10^{-9})$ high est.	8×10^{-2}

NOTES:

Event A: A slow PCRV depressurization resulting from the loss of the sealing oil required for the functioning of the dynamic shaft seals, combined with a failure to subsequently secure static sealing.

Event B: A rapid PCRV depressurization resulting from mechanical damage to both the dynamic and the static seals caused by gross imbalance of the rotating parts of the turbine.

Event C: A rapid PCRV depressurization as in Event B, combined with the loss of containment integrity.

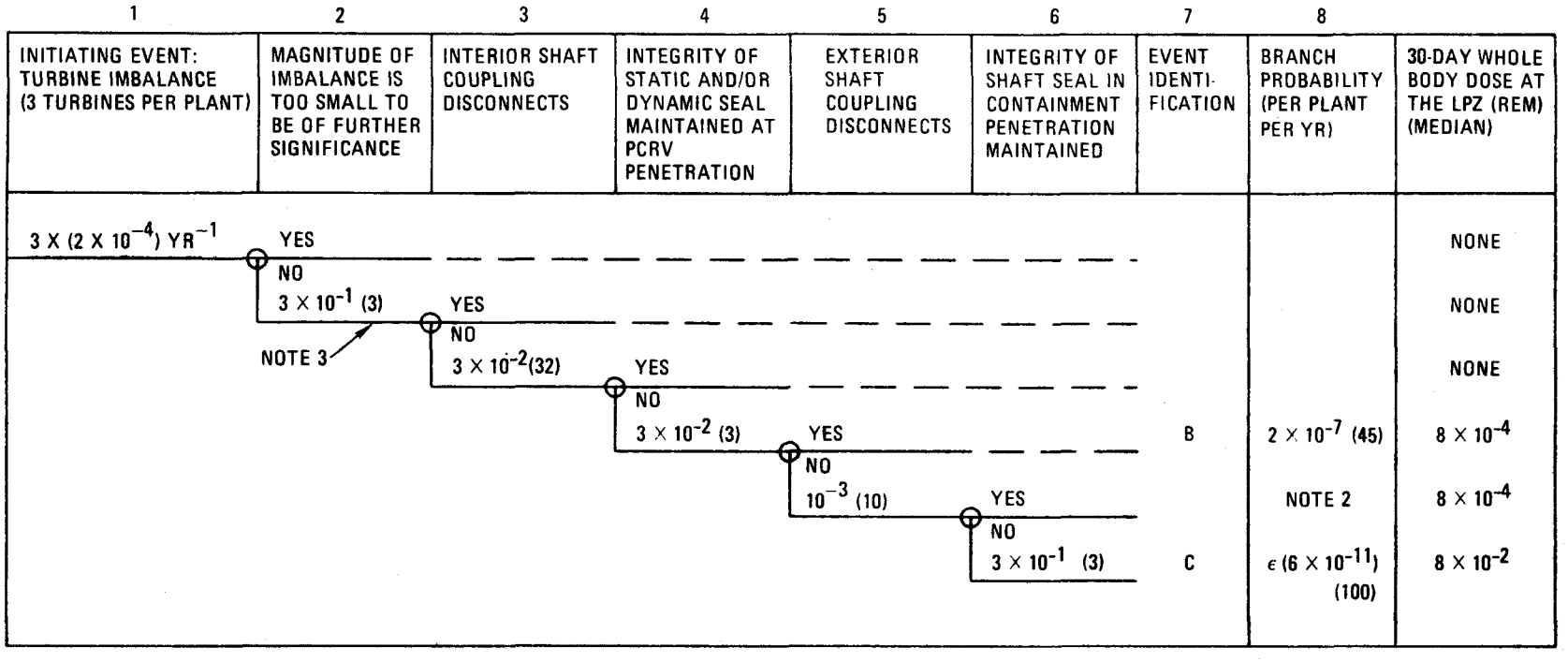

NOTES:

1. ϵ DENOTES AN EXTREMELY SMALL PROBABILITY.
2. BRANCH RESULTS IN AN INSIGNIFICANT INCREASE IN PROBABILITY OF BRANCH B.
3. VALUES IN PARENTHESES ARE MULTIPLICATIVE ERROR RANGE ESTIMATES.

GA-A13950

Fig. B-2. Event logic tree for shaft seal failure

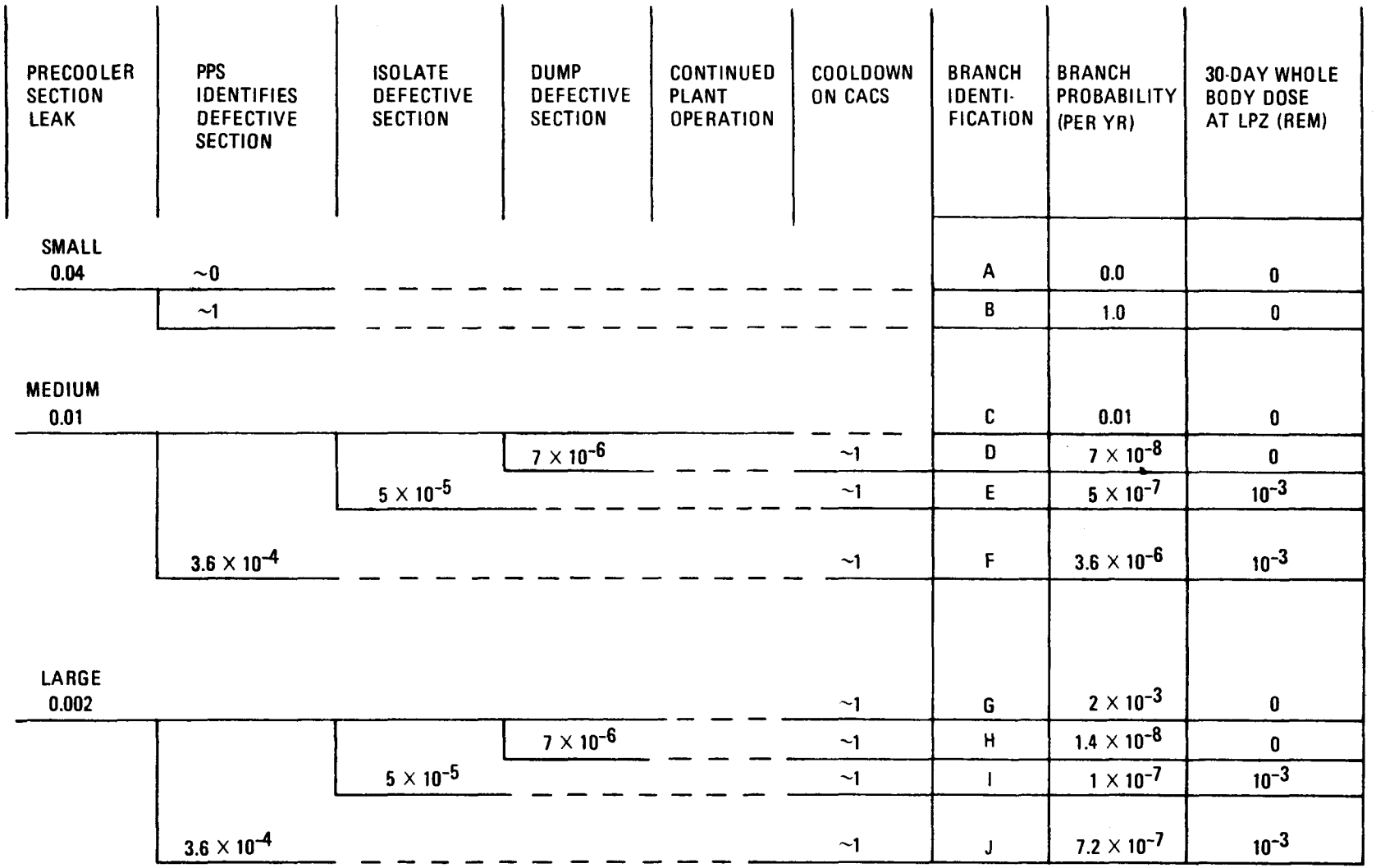

GA-A13950

Fig. B-3. Event logic tree for precooler leak (sheet 1 of 2)

NOTES:

1. A SMALL LEAK IS DEFINED TO BE UNDETECTABLE BY THE PLANT PROTECTION SYSTEM (PPS) MONITORS. THE OPERATOR HAS AN UNLIMITED TIME TO DISCOVER THE LEAK BECAUSE IT IS AN OUTWARD LEAK FROM THE PRIMARY COOLANT INTO THE CLOSED SECONDARY COOLANT SYSTEM. THE FOLLOWING CHECKS WOULD DISCOVER THE LEAK IN PROGRESS:

   a. HIGH CWS PRESSURE

   b. HIGH CWS PRESSURIZER LEVEL

   c. HIGH READINGS DURING THE FREQUENT ADMINISTRATIVE CHECKS OF CWS ACTIVITY LEVEL

   d. HIGH ACTIVITY IN THE CWS PURIFICATION SYSTEM WASTE

   e. DECREASING PRIMARY COOLANT PRESSURE

2. THE MEDIUM AND LARGE LEAKS DIFFER ONLY IN THE LIFTING OF THE CWS RELIEF VALVES AT THE PRESSURIZER. ISOLATION FOR THE MEDIUM LEAK WILL BE COMPLETED PRIOR TO LIFTING THE CWS RELIEF VALVE.

3. THE EVENT LOGIC TREE FOR THE PRECOOLER LEAK WAS SYNTHESIZED FROM THE REHEATER LEAK AND THE STEAM GENERATOR LEAK OF VOLS. III AND IV OF REF. B-2.

4. BRANCHES WHEREIN THE CWS RELIEF VALVES REMAIN CLOSED WILL RESULT IN ZERO CONSEQUENCE.

5. DEPENDING ON CWS CONSTRUCTION DETAILS NOT YET DEFINED, IT IS POSSIBLE THAT THE PRIMARY COOLANT COULD SIMPLY FORM A VOID SPACE IN THE CWS BY PUSHING CWS WATER THROUGH THE CWS RELIEF VALVE. A CONSEQUENCE COMPARABLE TO THE SC-HTGR LOSS OF LOAD EVENT (2×10^{-5} REM) WOULD RESULT.

6. ESCAPING PRIMARY COOLANT WILL PROBABLY BUBBLE THROUGH THE CWS WATER BEFORE BEING RELIEVED. LARGE FRACTIONS OF THE FISSION PRODUCTS AND NOBLE GASES CAN BE EXPECTED TO BE ABSORBED BY THE WATER.

7. THE CONSEQUENCE USED FOR BRANCHES WHEREIN THE CWS RELIEF VALVES OPEN HAVE BEEN PESSIMISTICALLY ESTIMATED AS EQUAL TO THE CONSEQUENCE FOR THE WORST BRANCH OF THE REHEATER LEAK FROM REF. B-2.

GA-A13950

Fig. B-3. Event logic tree for precooler leak (sheet 2 of 2)

The most serious turbomachine failure is a disk failure. Disk failure below 20% overspeed will be contained by the turbomachine burst shield. The turbomachine is prevented from exceeding 20% overspeed by the safety BVS. Failure of this system, as noted in the event logic tree presented in Fig. B-4, will result in turbomachine failure when the disk ultimate tensile strength is exceeded (at less than 50% overspeed). The worst case failure of a maximum penetration disk fragment that failed at 50% overspeed would penetrate the burst shield and at most 610 mm (2 ft) of the PCRV. This is less than the minimum ligament distance to penetrate to the PCRV outer surface. Thus, the primary coolant can reach the containment through only three mechanisms: (1) leaching through the concrete, (2) severing a concrete or liner cooling pipe, or (3) severing a vertical or horizontal prestressing tendon. The first two leaks are less serious than the slow PCRV depressurization for several reasons, particularly the improbability of an operator ignoring the event. The third leak may resolve itself into a leak of the first type if the adjacent tendons are grouted. A probabilistic model of the mechanism by which a disk failure could cause a tendon failure would include a distribution in disk fragment sizes, energies, orientation for burst shield penetration, direction in relation to tendon locations, and resiliency of the tendon during impact. Since the branches leading to the tendon failure must each have a subunity probability, a detailed study of this event would result in a lower event consequence. Figure B-4 assigns a probability of unity to the worst branches of the disk failure in order to develop a 522 cm^2 (100 $in.^2$) tendon tube leak path.

B.5.23. Generator Failures

Failure of the generator cannot have a radiological consequence unless it causes the failure of the containment building or the containment building shaft seal and a further failure in the PCB. Design provisions will ensure that this sequential failure is incredible. Data will be developed to probabilistically estimate the explosion hazard of the hydrogen-cooled generator, which is protected by the hydrogen combustion suppression system, and to assess the conceivable cause of common mode failures.

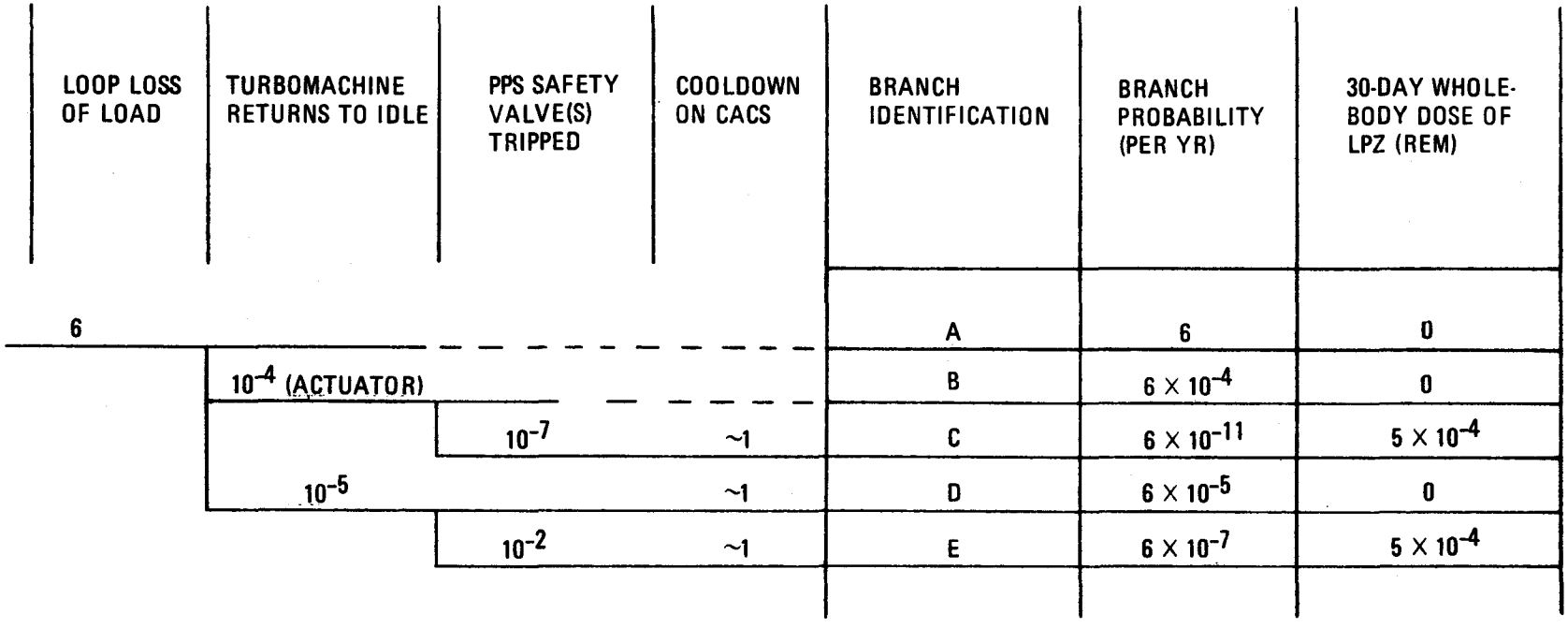

NOTES:

1. BRANCH E IS COMMON MODE FAILURE OF THE PRIMARY BYPASS VALVE AND SAFETY VALVE.
2. CONSEQUENCES C AND E ARE FROM THE RAPID DEPRESSURIZATION EVENT OF VOL. III OF REF. B–2. CACS FAILURE HAS $Q_d = 10^{-4}$ BUT CONSEQUENCE IS ONLY 10^0; THUS THE RISK IS UNCHANGED.
3. COOLDOWN ON CACS IS A SIMPLIFIED COMPOUND STATEMENT. TURBOMACHINE OVERSPEED IN ONE LOOP IS NOT EXPECTED TO AFFECT THE OTHER LOOPS. THEREFORE THE INITIAL CORE COOLING SHOULD USE THE MAIN LOOPS. THUS THE NOTE (2) ABOVE IS PESSIMISTIC IN THAT ONLY A SINGLE CACS UNIT WITH REDUCED POWER WOULD BE REQUIRED.

GA-A13950

Fig. B-4. Event logic tree for turbomachine failure

B.5.24. CWS Pipe Rupture Outside Containment

The present reference plant has a single CWS for the entire plant. A single failure in portions of the system will cause the lightly tritiated water to drain out of the CWS within seconds. Under these conditions, the only way to cool the reactor is with the CACS. During this event, offsite power is available. Figure B-5 presents the event logic tree for this event.

B.6. RESULTS

A summary risk plot for the GT-HTGR is presented in Fig. B-6, sheet 1. Figure B-6 is an overlay of Fig. B-6, sheet 1 onto the SC-HTGR summary risk plot. Figure B-6, sheet 3, briefly describes each plotted point.

B.7. RECOMMENDATIONS

Whereas the evaluated GT-HTGR risk envelope is below the SC-HTGR risk envelope and the SC-HTGR risk envelope is orders of magnitude lower than the light water reactor risk envelope, no specific recommendations to lower the risk envelope were developed. Later evaluation of the generator failure and SSE events is not expected to alter the risk envelope.

Several events should be reevaluated to reduce plant unavailability:

1. The precooler failure initiating event probability was estimated from the reheater analysis in Vol. IV of Ref. B-2. Milder precooler temperature and pressure conditions suggest the potential for lower initiating event probabilities in the GT-HTGR.

2. The CWS pipe rupture event probability was estimated from the main steam pipe rupture analysis of Vol. III of Ref. B-2. Milder CWS temperature and pressure conditions suggest the potential fow lower initiating event probabilities in the GT-HTGR.

3. Further development of the shaft seal system has the potential for reduced initiating event probabilities.

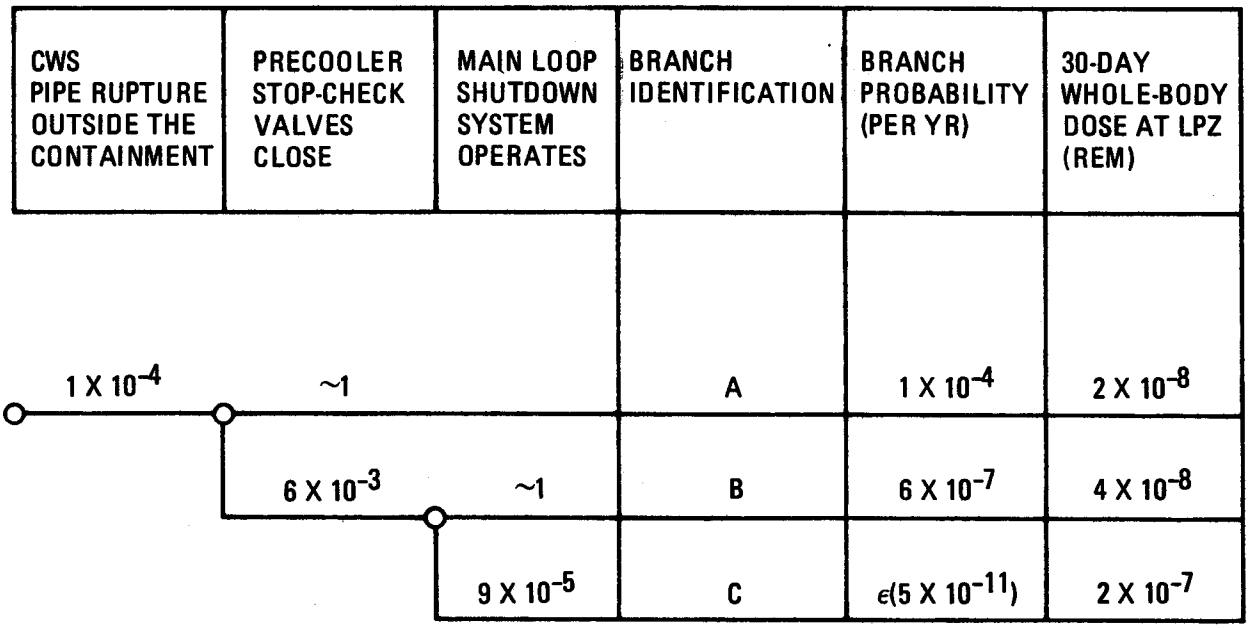

NOTE:

THIS FIGURE IS IDENTICAL TO FIG. 4–2 IN VOL. III OF REF. B–2, FOR A MAIN STEAM PIPE RUPTURE. THE EVENTS ARE TOO SIMILAR TO EXPECT ANY SIGNIFICANT DIFFERENCE BETWEEN THE SC–HTGR AND THE GT–HTGR.

GA-A13950

Fig. B-5. Event logic tree for CWS pipe rupture outside containment

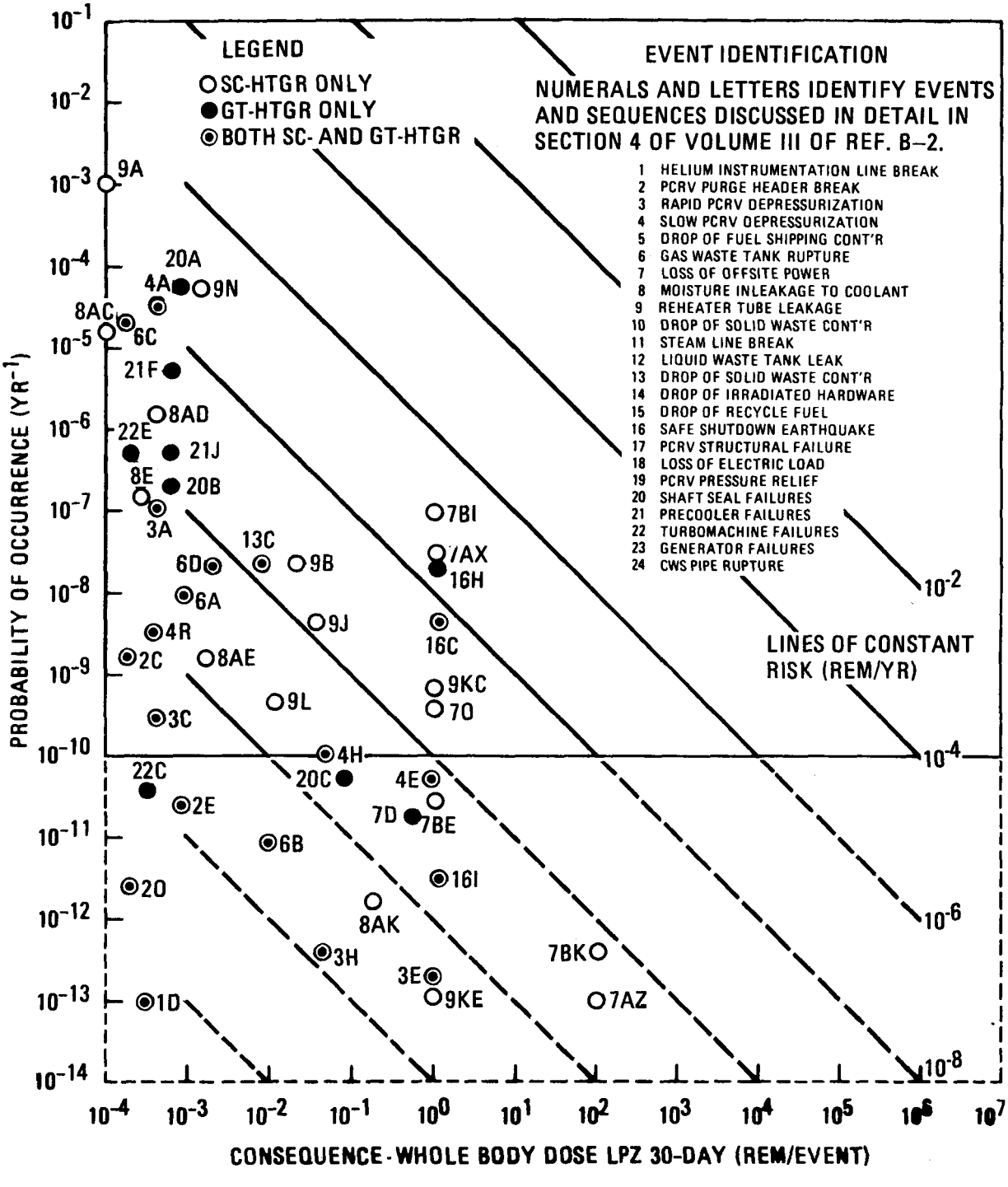

GA-A13950

Fig. B-6. Risk summary (sheet 1 of 3)

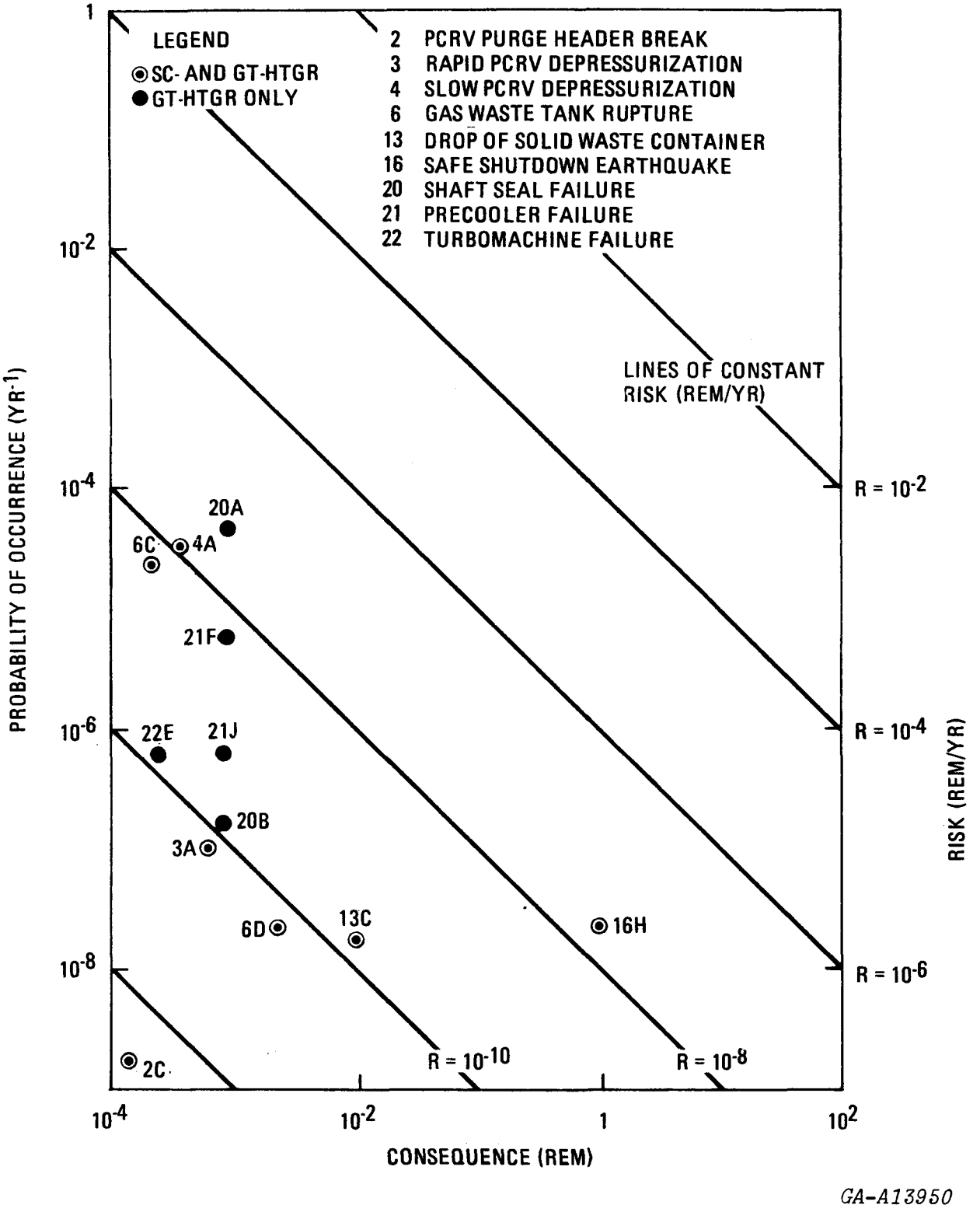

Fig. B-6. Risk summary (sheet 2 of 3)

POINT	DESCRIPTION
7D	LOSS OF OFFSITE POWER. FAILURE TO MAINTAIN IDLE.
20A	SHAFT SEAL FAILURE. SLOW DEPRESSURIZATION.
20B	SHAFT SEAL FAILURE. RAPID DEPRESSURIZATION.
20C	SHAFT SEAL FAILURE. RAPID DEPRESSURIZATION WITH LOSS OF CONTAINMENT INTEGRITY.
21F	PRECOOLER FAILURE. MEDIUM LEAK. FAILURE OF PPS TO IDENTIFY LEAK.
21J	(21F) FOR LARGE LEAK.
22C	TURBOMACHINE FAILURE. COMMON MODE SAFETY BYPASS VALVE SYSTEM FAILURE PRECEDED BY THE NONCOMMON MODE CONTROL ACTUATOR FAILURE.
22E	TURBOMACHINE FAILURE. COMMON MODE SAFETY BYPASS VALVE SYSTEM FAILURE CAUSING CONTROL ACTUATOR FAILURE.

GA-A13950

Fig. B-6. Risk summary (sheet 3 of 3)

REFERENCES

B-1. "GCR Accident Initiation and Progression Analysis," General Atomic Report GA-A13094, August 1974.

B-2. "HTGR Accident Initiation and Progression Analysis Status Report," General Atomic Report GA-A13617, November and December 1975, Volumes III and IV.

B-3. "Gas Turbine HTGR Program, Semiannual Progress Report for the Period July 1, 1975 through December 31, 1975," General Atomic Report GA-A13740, January 1976, Section 2.2.

B-4. "Reactor Safety Study," draft, USAEC Report WASH-1400, August 1974.

B-5. Scaletta, F. P., and J. H. Vrouwes, "Direct Cycle HTGR, a Preliminary Assessment of PCRV Depressurization Caused by Failure of the Turbine Output Shaft Penetration Seal," unpublished data, December 1975.